



**4th International Conference on
High-Performance Marine Vehicles**

HIPER'04

Rome, 27-29 September 2004

**4th International Conference on
High-Performance Marine Vehicles**

HIPER'04

Rome, 27-29 September 2004

Volker Bertram (Ed.)



Sponsored and co-organised by INSEAN



Edited by Volker Bertram
Published by INSEAN
ISBN 88-7617-001-4

Index

Volker Bertram, Ould El Moctar, Bruno Junalik, Stefan Nusser <i>Fire and Ventilation Simulations for Ship Compartments</i>	5
Volker Bertram, Ehsan Mesbahi <i>Estimating Resistance and Power of Fast Monohulls Employing Artificial Neural Nets</i>	18
Volker Bertram, Mohammad S. Seif <i>New Developments for Fast and Unconventional Marine Vehicles</i>	28
Yasushi Yoshida <i>Careful Selection of a Planing Boat's Hull Form Parameters</i>	44
Prasanta K Sahoo, Nicholas A Browne, Marcos Salas <i>Experimental and CFD Study of Wave Resistance of High-Speed Round Bilge Catamaran Hull Forms</i>	55
Ermina Begovic, Guido Boccadamo <i>Added Mass and Damping Coefficient Prediction – Results of Different Methods</i>	68
Adrian Constantinescu, Alain Nême, Volker Bertram <i>Hydro-Elastic Simulation of Simple 2-D Geometries in Water Entry</i>	83
Matthias Klemt, Gerhard Jensen, Olaf Lindenau <i>CFD Simulation and Virtual Reality Visualization for a Fast Monohull in Waves</i>	95
Hirotsugu Tanaka, Yasushi Yoshida <i>An Optimum Design of Monohull High-Speed Craft in Still Water</i>	103
Stefano Brizzolara, Dario Bruzzone <i>Automatic Optimisation of a New Fast Catamaran with Bulbous Bow</i>	116
Thomas Richir, Catalin Toderan, Jeom Kee Paik, Philippe Rigo <i>Effect of welding on ultimate compressive strength of aluminium stiffened panels</i>	129
Massimo Figari, Michele Viviani <i>Conceptual design of a Fuel Cell Electric Generator for a Ro/Ro Passenger Ferry Vessel</i>	140
Olaf Lindenau <i>Advances in Simulation of Ditching of Airplanes</i>	152
Giles Thomas, Michael Davis, Damien Holloway, Tim Roberts <i>An Investigation into the Whipping of Large High-Speed Catamarans</i>	162
Deniz Saydan, Grant E. Hearn <i>Damage Stability as a Safety Criterion for Optimisation Tools</i>	177
Maciej Pawlowski, Dracos Vassalos, Daria Cabaj, Cantekin Tuzcu, Dimitris Konovessis <i>Floodable Length Curves based on Probability of Survival</i>	192
Hajime Kihara <i>Numerical Models of Water Impact</i>	200

Marcello Barone, Carlo Bertorello, Mario Stella <i>Multi-Attribute Decision Techniques in Ship Design</i>	215
Marcos Salas, Richard Luco, Prasanta K. Sahoo, Nicholas Browne, M. López <i>Experimental and CFD Resistance Calculation of a Small Fast Catamaran</i>	229
Koos Frouws, Fons Huijs <i>The Applicability of Advanced Ship Types in the Dutch SAR Operations</i>	235
Ulf S. Tudem, Hans Liljenberg <i>Design Development and Model Testing of New Patented Air Supported Vessel (ASV) Designs - Leading to the Construction of a 24 m ASV Full-Scale Demonstrator</i>	249
Gregory Grigoropoulos, Dimitris Chalkias, Christos Tikkos <i>Multi-Objective Hull Form Optimization of High-Speed Vessels</i>	264
Michael S. Bruno, Brian J. Fullerton, Raju Datla, Peter A. Rogowski <i>Field and Laboratory Investigation of High-Speed Ferry Wake Impacts in New York Harbor</i>	277
Sayyad-Hamid Sadathosseini, Mohammad S. Seif <i>A Boundary Element Method for the Wave Making Resistance of a Displacement Catamaran</i>	287
Karsten Fach <i>Corrosion and Damages on High Speed Craft</i>	295
Dario Boote, Tommaso Colaianni, Enrico Pino <i>Seakeeping Analysis of a Trimaran Fast Ferry</i>	304
Karsten Fach <i>Classification Aspects of HSC Multihulls</i>	317
Claudio Lugni, Andrea Colagrossi, Guiseppina Colicchio, Odd Faltinsen <i>Numerical and Experimental Investigation on Semi-Displacement Mono- and Multi-Hulls</i>	323

Field and Laboratory Investigation of High-Speed Ferry Wake Impacts in New York Harbor

Michael S. Bruno, Brian J. Fullerton, Raju Datla, Peter A. Rogowski

Center for Maritime Systems, Davidson Lab., Stevens Inst. of Technology, Hoboken, N.J. 07030
mbruno@stevens.edu

1. Introduction

The last 10 years have witnessed a tremendous growth in passenger ferry service in the New York metropolitan region, a growth that is mirrored in many other areas of the world as more and more urban shorelines experience revitalization – some would say a transformation. This revitalization has in a very real sense been brought about by success in restoring our urban waterways. Estuaries like the Hudson-Raritan Estuary are once again vital and vibrant habitat, and offer recreational and commercial opportunities to thousands of residents and visitors. Urban waterways also serve as hosts to the US Marine Transportation System (MTS), a system that is responsible not only for passenger ferry transportation, but also for more than 95% of U.S. international trade. The Port of New York and New Jersey, among the largest in the nation, is a critical component of the national and global MTS.



Fig.1: Ferry route map for NY Waterways

The mixed use of the urban estuary – including marine transportation, commercial and recreational fishing, and pleasure boating, among others - creates complex user needs and, unfortunately, conflicts. The recent rapid growth in high-speed ferry service in the Hudson River (see Fig.1 for a route map of the primary ferry service) has created the potential for one such conflict – the need to provide reliable waterborne passenger transportation while at the same time ensuring that wave-sensitive shoreline facilities and activities are not adversely impacted. Of particular concern are:

- Impact to vessels in exposed and partially-protected dock areas and marinas
- Damage to bulkheads and other shoreline structures
- Erosion of natural shorelines and wetlands
- Impacts to sea grass and shellfish beds
- Safety of passing vessels, particularly small craft

In response to this issue, the State of New Jersey requested that Stevens Institute of Technology conduct a comprehensive study of the New York Harbor wake problem with a view toward developing recommendations to enable efficient passenger ferry service while also minimizing any identified adverse impacts associated with ferry wakes. The Stevens study is now complete and has been approved by the Harbor Operations Committee of New York – New Jersey Harbor. We here summarize our findings and recommendations, and also provide the preliminary findings from more recent field measurements in the Harbor.

2. Study description and results

The study of ferry-generated wakes in New York Harbor involves the consideration of various factors: complicated bathymetry, ambient wave field, various types of vessels, their speed, acceleration and course changes. With this in mind, it was decided to study the problem by a combination of qualitative and quantitative field measurements, and laboratory measurements of wake wash from small-scale models.

The study contained several elements, including:

- field observations of wave characteristics in the Hudson River over a multi-week period;
- visual observations of ferry wake generation, ferry routing, docking and departing procedures, etc.;
- scale model studies of ferry wake generation using the Stevens high-speed towing tank and scale models representing a variety of ferry hull forms, including monohulls and catamarans, operating over a wide range of speeds;
- meetings with the full range of stakeholders, including ferry captains, marina owners and operators, commercial vessel captains, the New York Harbor Operations Committee, and Federal, State and local government officials.

2.1. Field Observations, July, 2002

A field study was undertaken in July, 2002. High-resolution pressure gauges were deployed for slightly over eight days beginning the afternoon of July 10th. Two gauges were situated so as to obtain time series pressure records that would provide a description of the wave heights and wave periods found in the Harbor. The Harbor bathymetry is characterized by a deep (~20 m) channel flanked in most areas by a narrow, flat, and shallow (~3 m) shelf. One gauge was placed at a depth of 11 m in the channel, approximately 100 m seaward of the pier head line. The second gauge was placed at a depth of 4 m, inshore of the pier head line. The two gauges were located near the NY Waterways Lincoln Harbor ferry terminal (see Fig.1) and as such near an active fast ferry route.

The 8-day surface elevation time series for the offshore gauge is given in Fig.2. The time series indicates a strong diurnal pattern of relatively calm overnight periods followed by very energetic periods. The highest waves in the day occur during two peak periods. The first peak period of each day begins as a gradual increase starting at approximately 0530 EDT and peaking at approximately 0915 EDT,

which corresponds to the morning rush hour. Wave heights then gradually diminish, but only to levels well above the typical overnight values, until approximately 1245 EDT when they again begin to increase as the evening rush hour is approached. After the second and typically highest peak of the day at approximately 1745 EDT, the wave heights gradually diminish until they reach the typical overnight values some time shortly after 2330 EDT. Overnight maximum wave heights range from 4 inches to 6 inches (10 to 15 cm). The morning peak heights are typically between 12 inches and 16 inches (30 to 40 cm). Similar behavior was observed by the inshore gauge, although the inshore gauge typically recorded wave heights between 5% and 10% higher than the offshore gauge, likely because of the effect of shoaling and/or wave reflections from the shoreline.

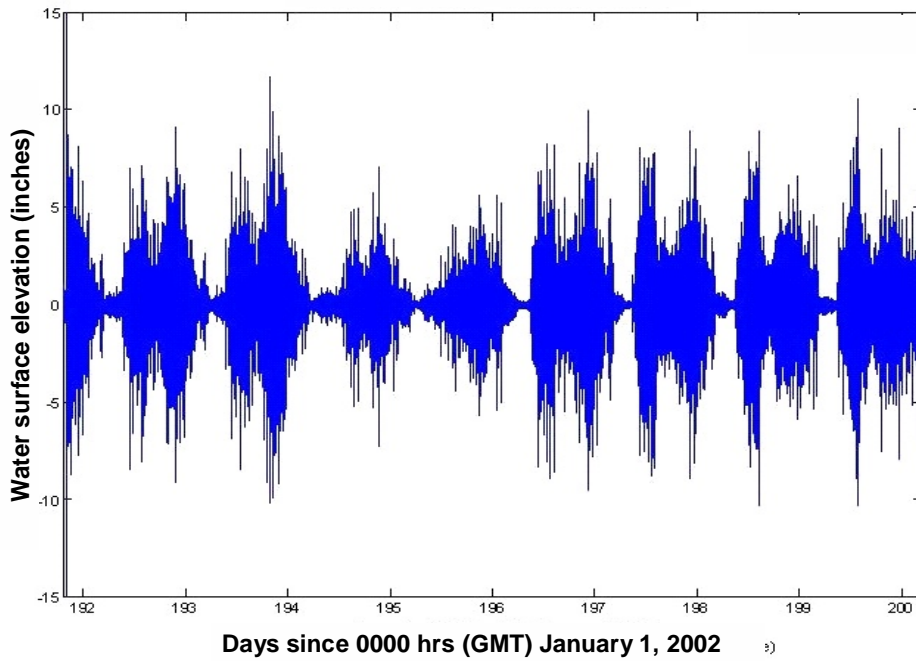


Fig.2: Time history of water surface elevation for 8-day period

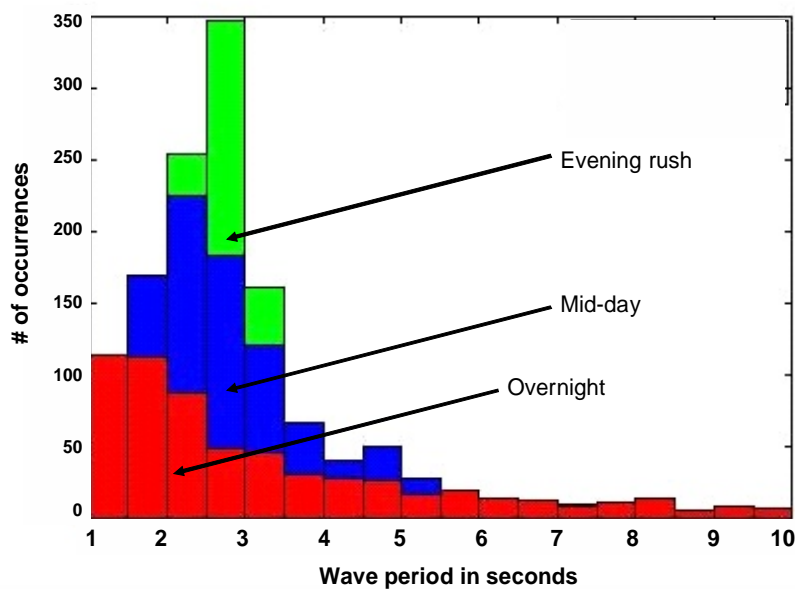


Fig.3: Histogram of wave period

Until this point in the report, discussion of the observed waves has been limited to describing wave height. However, wave period is a critical measure not only of the energy contained in the wake field, but also of the potential influence of the wakes on vessels and shoreline infrastructure. In addition, the performance of partial wave barriers, such as floating breakwaters, is strongly affected by wave period. Observed wave periods ranged from 1 to 10 seconds. Histograms of wave period for different time periods are presented in Fig.3. The peak of the histogram falls in the 1 to 2 second range during a typical overnight hour. During the typical midday hour, the peak moves to the 1.5 to 3.0 second range and the number of occurrences in the 3 to 5 second range increases by nearly 50%. During a typical hour in the evening rush, the peak period again moves up, now to the 2.5 to 3.0 second range. During the evening rush, the number of occurrences of periods greater than 3.0 seconds is very similar to that which was observed during the midday, which is significantly greater than is observed in the calm overnight hours.

2.2. Field Observations, July, 2004

A follow-up field study was conducted in July, 2004 in order to obtain a higher-resolution dataset regarding wake characteristics, and the relationship between time of ferry vessel passage and associated wave characteristics. In order to accomplish this task, an ultrasonic acoustic water level gauge operating at a frequency of 10 Hz was used to measure wave activity in New York Harbor. The gauge was located at the western Hudson River Shoreline just south of the Hoboken North ferry terminal, Fig.1. Wave data was logged on July 20th starting at 5:20 am before any boat activity in the harbor. Times of ferry vessel passage were noted, and measurements were taken throughout the day until 7 pm.

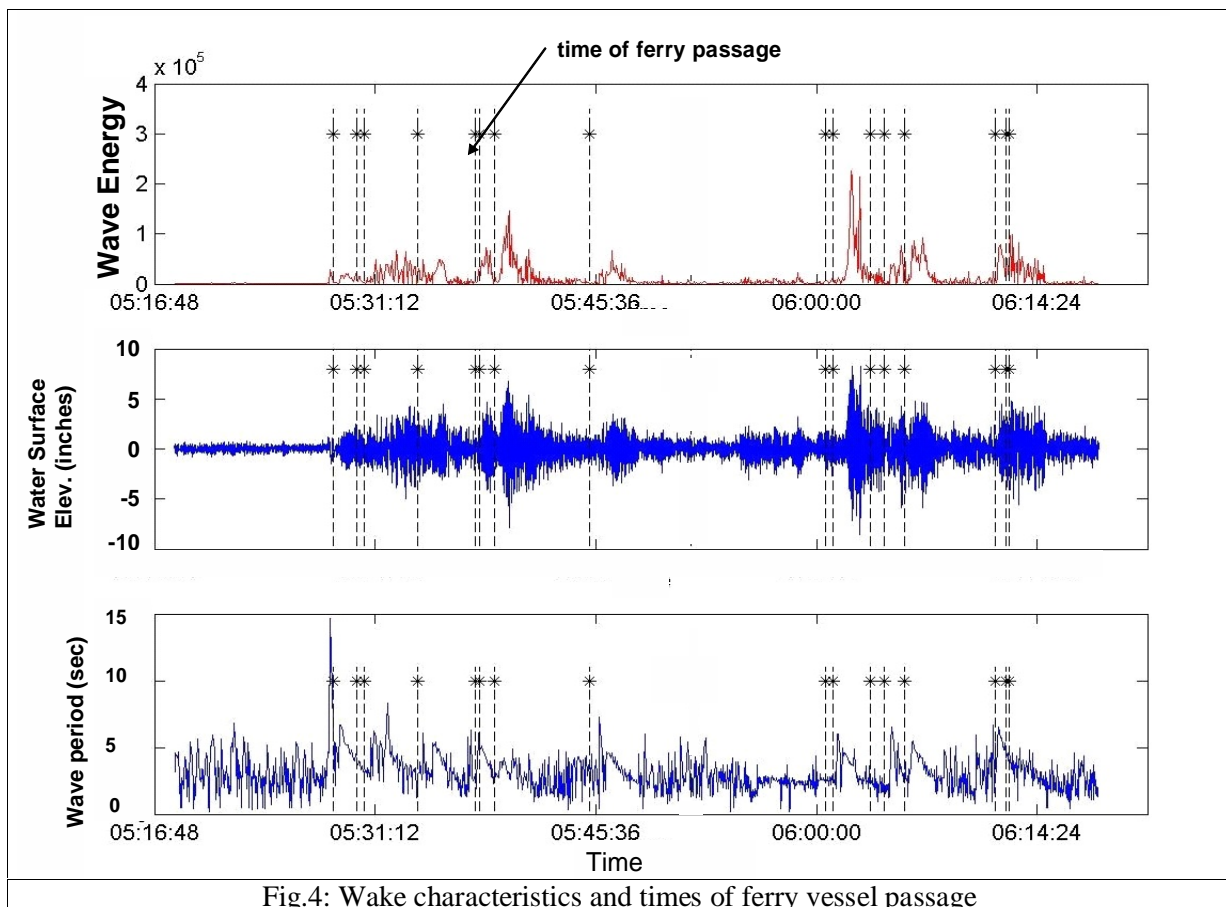


Fig.4: Wake characteristics and times of ferry vessel passage

Fig.4 illustrates the wave energy, water surface elevation (with tide removed) and wave period for the first hour of measurements, at the start of the morning rush hour. Clearly, the times of vessel passage are associated with sudden increases in the measured wave energy, with maximum wave energy levels experienced during time periods when several vessels passed in close proximity to one another. This

finding is likely at least in part attributable to the wave summation associated with reflections from the shoreline. The figure does not indicate the type and speed of the ferry in each instance, although these records do exist. A computer modeling effort is underway to examine the wake generation characteristics of each vessel type under the observed speed and water depth conditions. This analysis will help explain the variability in wave height and period observed here.

2.3. Laboratory studies

Tests were conducted in the Davidson Laboratory High-Speed Towing Tank, which is 313 ft (95.5 m) long, 12 ft (3.7 m) wide and 6 ft (1.8 m) deep, and has a top speed of 100 ft/s (30.5 m/s). Four different vessels, whose characteristics are given in Table I, were tested to study their wake characteristics in addition to the standard resistance and seakeeping performance characteristics.

Table I: Model characteristics

Hull	Catamaran	Monohull	Catamaran	Catamaran
Length	71.2 ft (21.7 m)	65 ft (19.8 m)	105 ft (32 m)	90 ft (27.4 m)
Beam	27.5 ft (8.4 m)	14 ft (4.3 m)	28.4 ft (8.7 m)	34 ft (10.4 m)
Draft	3.4 ft (1 m)	3 ft (0.9 m)	3.45 ft (1.1 m)	5 ft (1.5 m)
Model scale	1/12	1/12	1/20	1/16

The first model, that of the 71 ft Catamaran, was tested in October 2000 but NY Waterway decided not to consider it for their fleet. The 65 ft Monohull, “The Sea Otter”, was tested in April 2001 and NY Waterway currently operates 3 of these vessels. The 105 ft catamaran design was tested in July 2001 and NY Waterway is in the process of commissioning a few of these vessels. Finally, the 90 ft Catamaran that was tested in September 2002 will be part of the future NY Waterway fleet.

Each model was free to trim and heave, but fixed in yaw, roll, surge and sway. The vertical motion of the tow-point was measured using a motion transducer attached to the free-to-heave apparatus. Trim of the model keel relative to the horizon was measured using an inclinometer mounted on the connecting platform. Resistance was measured using a drag balance located directly above the pivot box. Two accelerometers were mounted near the bow and CG to record vertical acceleration in wave tests. Wake height measurements were made in calm water tests using two resistance-type wave probes at fixed locations in the tank. The two probes were located in that section of the tank where the model runs at constant speed and at transverse distances of 3 ft and 5 ft (model scale) from the ship centerline. The time history of the wake was recorded as the model passed by. A video camera was located on the carriage and video recordings were made of each run. Still photographs using a camera mounted on the carriage were also taken for most of the runs. Data were acquired at 250 Hz in a 100 ft “data trap”.

The full-scale wake heights measured from each of the model test are presented in Tables II to V. Some of the typical trends that can be observed are: the wake heights increase with the displacement, the newer designs tend to have lesser wake heights, the wake heights are higher at the transition (hump condition) speeds and decrease at higher speeds, wake heights depend on the location of the center of gravity and the running trim. To emphasize the wake height variation with speed, the data from the 71 ft Monohull “Sea Otter” is presented in Fig.5.

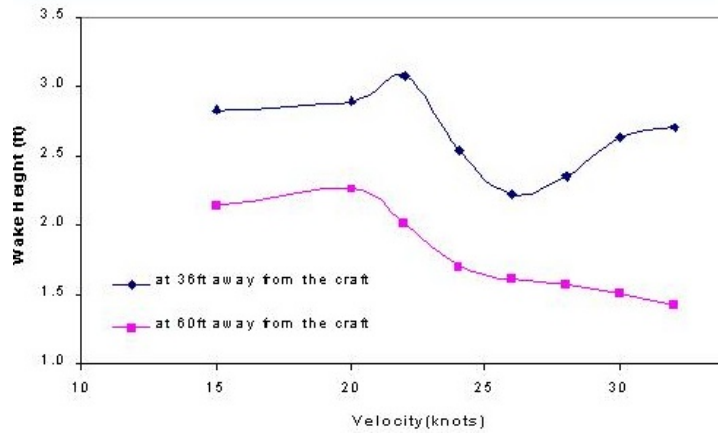


Fig.5: Wake characteristics for the 71 ft. monohull ferry: wake height vs. speed

Table II: Wave heights for 71 ft catamaran (different displacements and LCGs)

Run #	Speed (knots)	Wake Heights (ft)		Run #	Speed (knots)	Wake Heights (ft)	
		Measured at 36 ft	Measured at 60 ft			Measured at 36 ft	Measured at 60 ft
55 LT - 3 ft				65 LT - 3 ft			
27	15	2.9	2.9	64	15	2.8	2.6
28	20	3	2.8	66	20	3.6	3.2
29	22	2.8	2.8	67	22	2.8	2.8
30	24	2.2	2	68	24	2.6	2.6
31	26	2.2	1.8	69	26	2.2	2.2
55 LT - 5 ft				65 LT - 5 ft			
33	20	3.2	2.8	71	15	2.8	2.8
34	22	2.8	2.4	72	20	3.6	3.2
35	24	2.4	2.2	73	22	3	2.8
36	26	2	1.8	74	24	2.6	2.6
37	28	1.8	1.7	75	26	2.2	2.2
38	30	1.6	1.5				
60 LT - 3 ft				65 LT - 7 ft			
41	15	2.5	2.4	77	20	2.7	2.7
42	20	3	3	78	22	3.4	2.9
43	22	3.2	3	79	24	2.8	2.6
44	24	2.8	2.7	80	26	2.5	2.5
45	26	1.9	1.9				
46	28	1.8	1.7	55 LT - 3 ft			
47	30	1.4	1.3	82	20	3	2.8
60 LT - 5 ft				83	22	2.8	2.5
49	15	2.5	2.5	84	24	2.4	2.1
50	20	2.9	2.9	85	26	2	1.9
51	22	3.2	2.8				
52	24	2.8	2.8	50 LT - 5 ft			
53	26	2.4	2.3	88	15	3.2	2.9
54	28	2	2	89	20	2.8	2.6
55	30	1.8	1.7	90	22	2.5	2.3
60 LT - 7 ft				91	24	2	1.7
59	20	2.7	2.7	92	26	1.9	1.6
60	22	3.2	2.8	93	28	1.5	1.3
61	24	2.8	2.6	94	30	1.4	1.2
62	26	2.4	2.2				

Table III: Wave heights for 65 ft monohull (different displacements and LCGs)

Run # No.	Velocity (kn)	Wake Height(ft)		Run # No.	Velocity (kn)	Wake Height(ft)	
		at 36ft	at 60ft			at 36 ft	at 60 ft
73,990lb. - 39.8 ft				62,500 lb. - 39.8 ft			
4	15	2.8	2.1	49	20	2.5	2.0
5	20	2.9	2.3	50	22	2.4	1.6
6	22	3.1	2.0	52	24	2.2	1.3
7	24	2.5	1.7	53	26	2.2	1.2
8	26	2.2	1.6	54	30	2.3	1.2
9	28	2.4	1.6	55	32	2.2	1.1
10	30	2.6	1.5	<u>40.8 ft</u>			
11	32	2.7	1.4	63	30	2.4	1.2
<u>repeat check</u>				Tests using 2.75" interrupters at 62,500 lb.			
13	24	2.7	1.6	<u>1/16" projection - 39.8 ft LCG</u>			
Tests with LCG variation at 73,990 lb.				57	15	1.9	0.8
<u>37.8 ft</u>				59	26	1.7	1.3
15	26	2.4	1.6	<u>1/16" projection - 40.8 ft LCG</u>			
<u>38.8 ft</u>				61	26	1.9	1.3
17	26	2.3	1.6	62	30	1.9	1.1
<u>41.8 ft</u>				<u>1/32" projection - 40.8 ft LCG</u>			
21	26	2.7	1.8	67	30	1.8	0.9
<u>40.8 ft</u>				Tests using interrupters at 73,990 lb.			
19	26	2.7	1.6	<u>2.75" long - 1/32" projection - 39.8 ft LCG</u>			
23	28	2.7	1.5	70	26	1.2	1.8
24	30	2.7	1.5	<u>1.4" long - 1/32" projection - 39.8 ft LCG</u>			
25	32	2.7	1.5	72	26	2.3	1.6
49,640 lb. - 39.9 ft				73	30	2.3	1.4
27	10	0.7	0.2	<u>1.4" long - 1/32" projection - 40.8 ft LCG</u>			
28	15	1.5	0.7	75	30	2.3	1.3
29	20	2.0	1.6	76	26	2.5	1.6
30	22	1.9	1.3	Tests using Trim Wedges at 73,990 lb. And 39.8 ft			
31	24	1.7	1.1	<u>3.5"X1" - 5 deg. Wedges</u>			
32	26	1.5	1.2	79	26	2.0	1.5
33	28	1.8	1.0	<u>3.5"X1" - 3 deg. Wedges</u>			
34	30	1.8	1.0	82	30	2.4	1.4
35	32	1.8	0.8				
<u>repeat check</u>							
36	24	1.8	1.2				
49,640 lb. - 40.9 ft							
40	26	1.8	1.0				
41	28	2.0	1.0				
42	30	1.9	0.9				
43	32	1.8	0.9				
44	40	1.6	0.7				
45	42	1.5	0.8				

3. Results and discussion

The wake heights and periods found in the field measurements agree qualitatively with what was observed during the physical model tests. For this reason, it would be expected that modification of operational parameters such as speed and trim to be more in line with the optimum values predicted by the physical model tests would lessen wakes created by a particular vessel. For vessels currently operating in their most inefficient regimes, the potential reduction in wake energy can be substantial.

Table IV: Wave heights for 105 ft catamaran (different displacements and LCGs)

Run # No.	Vs (kn)	Wake Heights (ft)		Run # No.	Vs (kn)	Wake Height (ft)	
		at 60ft	at 100 ft			at 60ft	at 100 ft
195,610 lb - 59.5 ft				195,610 lb - 59.5 ft			
9	10	0.6	0.5	49	20	4.0	3.2
10	15	1.5	0.9	50	24	2.5	2.0
11	20	2.2	1.0	51	27	2.2	1.9
12	22	2.6	1.5	52	30	1.9	1.6
13	24	2.6	2.5	55	34	1.6	1.1
15	26	2.5	1.9	150,850 lb. - 61.25 ft			
14	28	2.2	1.8	57	19	3.1	1.3
16	30	1.8	1.6	58	20	2.3	1.7
195,610 lb - 62.5 ft				59	24	2.0	1.5
19	20	2.9	2.2	60	28	1.7	1.4
21	24	2.7	2.4	61	30	1.5	1.2
22	26	2.4	2.1	62	32	1.4	1.1
23	28	2.0	1.8	64	36	1.2	0.9
24	30	2.0	1.5	66	40	1.1	0.8
25	32	2.0	1.4	150,850 lb. - 63.25 ft			
26	34	1.8	1.4	68	20	2.2	1.7
27	36	1.6	1.1	69	24	2.1	1.5
28	38	1.7	1.1	70	24	2.1	1.5
29	40	1.6	1.0	71	28	1.8	1.3
30	41	1.6	1.0	72	30	1.6	1.2
* Chines Widened near the Bow				73	32	1.5	1.1
195,610 lb - 62.5 ft				75	41	1.3	0.8
32	20	1.6	1.2	225,000 lb. - 62.5 ft			
33	24	2.5	1.9	77	20	2.3	1.1
34	28	1.9	1.8	78	24	2.9	2.2
35	30	1.8	1.6	79	28	1.7	2.0
37	32	1.7	1.4	80	30	2.4	1.7
38	34	1.7	1.2	81	32	1.9	1.4
195,610 lb - 59.5 ft				82	34	1.8	1.4
40	20	2.2	2.1	225,000 lb. - 64 ft			
41	24	2.6	1.9	84	24	2.9	2.2
44	26	2.0	1.8	85	28	2.3	2.1
45	30	1.9	1.6	86	32	2.0	1.4
46	32	1.8	1.3				

The largest amount of wake energy created per unit time occurs during the transition from displacement to planing mode. This was observed in the physical model tests and suggested in the qualitative field study. In many cases (especially the newer hulls), higher speeds result in lower wave energy. Again, with the guidance provided by physical model tests of hulls, these optimum speeds must be known and adhered to by vessel operators whenever possible to minimize wake. As little time as possible should be spent in the transition zone. Again, for vessels that are currently being operated for long periods of time at the very high end of displacement (very low end of planing) substantial decreases in wake energy will be possible by this optimization.

Table V: Different loads and trims

Run #	Vel (fps)	Wake Height (ft) (at 80 ft)	Run #	Vel (fps)	Wake Height (ft) (at 80 ft)
100 LT - Level Trim			110 LT - Level Trim		
1	0.00	0.0	19	0.00	0.0
2	4.02	--	20	8.37	3.2
3	6.23	2.8	21	10.52	--
4	8.37	3.1	22	11.38	--
5	10.52	--	23	12.69	1.1
6	11.36	2.1	24	13.54	1.2
7	12.68	1.3	25	14.82	1.2
8	13.51	1.2	26	15.69	1.2
9	14.82	1.1	27	16.99	0.9
10	15.67	1.1	90 LT - Level Trim		
11	17.00	0.9	28	0.00	0.0
12	12.67	1.2	29	8.38	2.9
100 LT - 2 deg Trim			30	10.54	2.5
14	0.00	0.0	31	11.39	--
15	8.37	3.5	32	12.70	1.2
16	10.52	--	37	13.55	1.2
17	12.67	1.1	34	14.86	1.2
18	14.84	0.8	35	15.71	1.1
			36	17.01	0.9

The qualitative field study also strongly suggested that sharp turns in the transition phase could result in the focusing of wave energy, especially to the inside of turns. The qualitative evidence is strong enough on its own in this specific area to warrant the minimization of any sharp turns during the transition phase if any wake-sensitive areas are located on the inside of the turn.

Wave shoaling is taking place during at least some stages of the tide in the shallowest areas of the shorelines, some of which contain marinas. Deepening (dredging) these specific areas has the potential to reduce wave heights by 30% in some of the shallowest regions. Deepening by itself will not completely mitigate any wake problem in this harbor, but should be considered part of the total approach.

In places where reflective shorelines (vertical or near vertical walls) border water deeper than 2 feet MLLW, most of the incoming wave energy is simply reflected back into the Harbor. Efforts should be taken wherever possible to limit reflective shorelines. Again, simply replacing reflective shorelines with dissipative shorelines will not completely mitigate the wake problem, but will prevent exacerbating the situation and is an important part of any total approach.

Our study indicated that ferry wakes are responsible for a good portion of the wave energy in the ferry operating region, with maximum contribution during the weekday rush hours. Our analysis indicates that the wakes produced by high-speed ferry vessels differ in many important respects from wakes produced by more slowly moving vessels. The most damaging wakes, in terms of height, occur at low speeds, particularly during the transition from low-speed displacement mode to planing mode, and during certain turning maneuvers. The length of the ferry wakes is in general significantly longer than the length of wakes associated with even larger, slow-moving (displacement-mode) vessels operating in the Harbor. It is this large wavelength that allows wake energy to pass through the various wave protection devices in use at marinas along the Hudson River shoreline, including floating barriers and partial-depth wave screens.

Wake characteristics vary not only as a function of the vessel's speed, trim, and direction of travel, but also as a function of hull characteristics. Hull designs that more easily achieve high-speed planing are far more energy efficient and generate far lower wake energy than less efficient hull designs. Clearly, hull designs that minimize wake production are desirable from both an adverse impacts standpoint and an operational standpoint.

These findings have led to the following recommendations:

- 1) **Ferry Operators**
 - Assign the most efficient hulls to the most wake-sensitive areas.
 - Determine the most efficient operating range (speed and trim) for each vessel class and operate each vessel within this range as much as is practicable, with as little time as possible spent in the transition phase between the displacement and planing modes.
 - Ferry routing should be carefully evaluated, and modified to ensure minimal time spent in the transition phase while adjacent to or pointing toward wake-sensitive shoreline areas, and to avoid turning with a wake-sensitive area inside the turn. In general, a ferry should proceed from the dock to the center of the navigation channel at a speed well below transition (that is, well within displacement mode), then make its turn to proceed in an along-channel direction, rapidly accelerate to high-speed planing mode until adjacent to the next stop, decelerate to a speed well within displacement mode, then turn toward the dock.
 - We recommend against blanket speed restrictions, as such restrictions will very likely have the unintended effect of increasing the height of wakes produced by ferry vessels that are designed for efficient operation at high speeds.
- 2) **Marina Operators**
 - Should be permitted to construct wave protection systems that can protect the dock areas from waves exceeding 20 inches in height and 4.25 seconds in period. An example of such a system is a full-depth timber wave screen.
 - Avoid reflective side banks to the degree possible.
 - Optimize entrance channel design to avoid direct exposure to wakes produced by passing vessels.
- 3) **Regulatory Authorities**
 - Examine permitting requirements that prohibit the installation of effective wave protection systems along marina and other wake-sensitive shoreline areas.
- 4) **General Public**
 - As the revitalization of waterways and shorelines continues, and as more people take to the water in vessels of all sizes and types, there will be an increasing need to educate the boating public about the rules of the road when operating a vessel in a commercial harbor. The production and widespread dissemination of Harbor maps that clearly delineate active navigation channels, loading and unloading areas, and ferry routes, would be an important first step in this regard, as would public outreach activities that would include the participation of commercial vessel operators in the Harbor.

Estimating Resistance and Power of Fast Monohulls Employing Artificial Neural Nets

Volker Bertram, ENSIETA, 2 rue François Verny, F-29806 Brest Cd 9, bertravo@ensieta.fr
Ehsan Mesbahi, University of Newcastle, Armstrong Bldg, UK Newcastle NE1 7RU,
ehsan.mesbahi@newcastle.ac.uk

Abstract

Simple design formulae for resistance and power prediction for fast semi-displacement monohulls are derived using Artificial Neural Nets. These formulae can be programmed easily in spreadsheets or optimization routines. The formulae were derived from curves based on database evaluation of the Hamburg Ship Model Basin.

1. Fast monohulls

Fast monohulls are very different in hull shape from conventional low-speed hulls, Fig.1. We focus here on the most common representatives of fast ships: displacement, semi-displacement and planing monohulls, Fig.1. We focus here on fast monohulls. See *Fritsch and Bertram (2002)* for conventional monohulls and catamarans, *Azcueta and Bertram (2002)* for unconventional high-performance marine vehicles.

Typical examples of fast displacement ships are corvettes, frigates, working boats and similar ships. These are characterized by straight V-shaped sections in the forebody, slender waterlines, round bilge with decreasing radius going to the transom stern and centerline skeg. They are frequently fitted with an integrated trim wedge. The LCB positions usually lie between 2% and 3% aft of $L_{pp}/2$ for larger ships. Displacement ships operate up to $F_n=0.4\dots0.6$, i.e. they approach only the begin of the planing condition. Advantages of this hull form are good seakeeping behavior, good course-keeping ability, and – if the vessel operates above the resistance hump – relatively low dynamic trim at top speed. The steep run of the power curve at higher speeds caused by the fact that little hydrodynamic lift is produced, is a main disadvantage and determines the operational limits of this type.

Semi-displacement ships integrate the attributes of displacement and planing hulls. Semi-displacement ships achieve higher speeds than displacement ships due to increased dynamical lift and corresponding reduction in resistance. The most common examples of this type are patrol boats, special navy craft, pleasure yachts, pilot boats, etc. Vessels can reach the planing condition with speeds of up to $F_n\approx 1$. The course-changing and course-keeping behavior is similar to that of pure displacement ships. The seakeeping is in general good. At high speeds, roll-induced transverse instability can arise under certain circumstances.

Real planing hull designs should normally be used for high-speed vessels only. The stations have straight sections and knuckle lines (with a bilge knuckle running from the stem over the entire length to the transom), relatively large deadrise angles in the forebody decreasing further aft to about $L/2$ and continuing at nearly constant angles of not less than 10° to the transom. Early planing hull designs with warped deadrise are not very common today. The forward part of the longitudinal knuckle is designed to work as a spray rail. Trim wedges with adjustable tabs are often installed to control the dynamic trim. These become less effective for $F_n>1$ as there is generally a reduction in dynamic trim in that speed range. Typical examples are fast patrol boats, racing yachts, S&R boats, fast small passenger ferries, and similar vessels. For lower speeds, the resistance of this hull form is slightly higher than that of a semi-displacement vessel with the same length and displacement. The typical advantages of this hull form develop at speeds $F_n>1$. The seakeeping qualities of these vessels are not as good as for displacement and semi-displacement hulls. This disadvantage can be partially compensated by selecting relatively high L/B ($L/B\approx 7\dots 8$) and deadrise angles $\tau>10^\circ$ in the aft part. The high-speed stability problem of semi-displacement hulls may also occur with planing hulls.

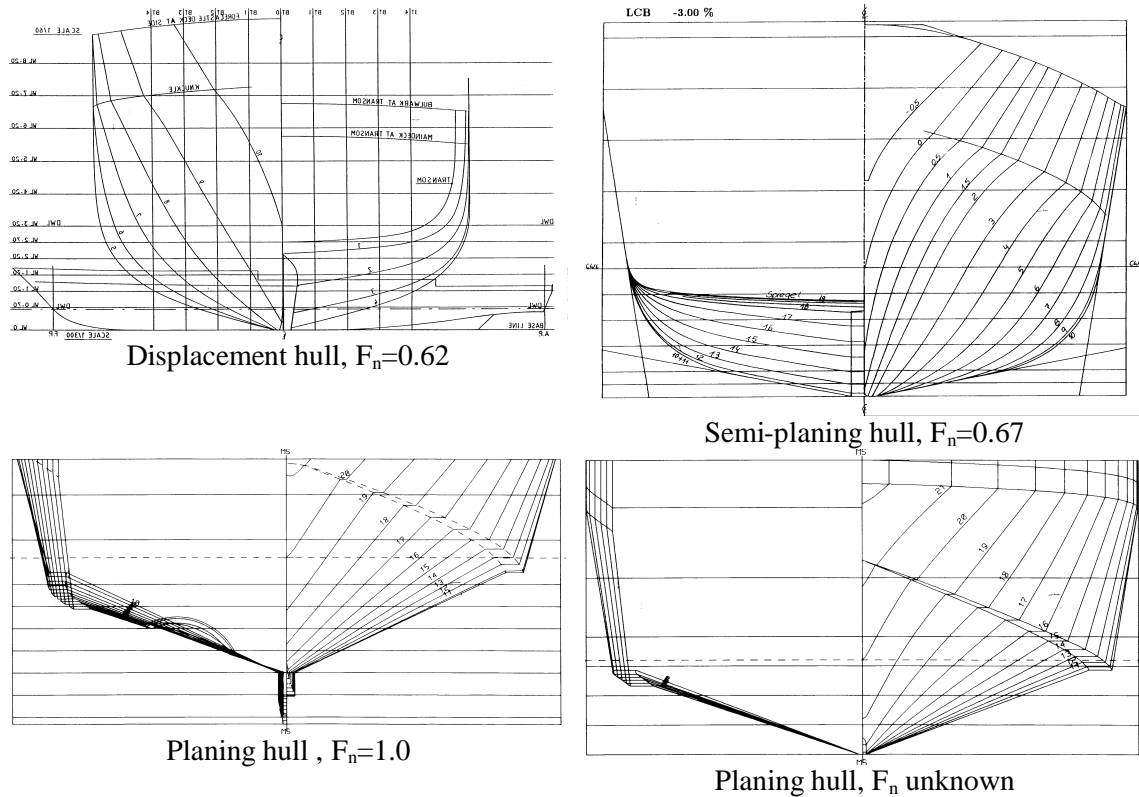


Fig.1: Body plans of typical representatives of fast monohulls, *Fritsch and Bertram (2002)*

2. Artificial Neural Nets for functional approximation

Conventional regression has been extensively used in naval architecture in system identification to provide required factors and coefficients. Based on databases of existing designs, coefficients are then interpolated or even extrapolated to calculate coefficients for a new application. This procedure requires the engineer to specify not only which input parameters mainly influence one or more output parameters, but also to specify the type of functional relation between input and output parameters. Most often in the past, simple linear relations have been chosen. Designers plotted data and by visual inspection sometimes chose also simple polynomial relations. This approach is cumbersome and unsuitable for many nonlinear relations. Shortcomings are especially apparent for multi-dimensional input/output data sets. Here we apply a more versatile and user-friendly approach to system identification: Artificial Neural Networks (ANNs) may be used to find functional relationship for certain ship data, *Mesbahi (2003)*. ANNs are increasingly used in naval architecture and marine engineering for system identification. *Hess and Faller (2000)* give an overview of ANN application in naval architecture, *Bertram and Mesbahi (2000)*, *Mesbahi and Bertram (2000)* further applications to ship design.

ANNs have the capability of storing data during a learning process and then reproducing these data during a recall process. ANNs can generally represent the mapping of multi-dimensional input/output data sets as:

$$f: \mathbf{X} \rightarrow \mathbf{Y} \quad (1)$$

f is a non-linear function, $\mathbf{X}=(x_1, x_2, \dots, x_n)$ is real input vector, $\mathbf{Y}=(y_1, y_2, \dots, y_m)$ is real output vector, Fig.1. ANNs are best used for interpolation, but in some cases have also been demonstrated to yield valid extrapolations.

An ANN structure consists of several layers. Each layer consists of several nodes. In the example shown in Fig.2 we have input layer, output layer, and one hidden layer. The values of the previous

layer are weighted, reach a node, summed up and are transformed by a function F , before passed on to the next layer. Typically, this function is a sigmoid function of the form:

$$\text{sig}(x) = 1/(1+e^{-x}) \quad (2)$$

In this study, we have used fully-connected feed-forward ANNs with one hidden layer. Hidden layer and output layer use sigmoidal activation functions. The hidden layer may have different number of processing elements (neurons), which depend on the number of patterns and complexity of the relationship to be approximated. The standard choice is one hidden layer. Conventional back-propagation is used for network training. Momentum terms are added to the learning algorithm to achieve a higher convergence rate, *Rumelhart and McClelland (1986)*.

x_i and y_i are input and output data respectively, which are normalised between 0 and 1:

$$\text{Normalised value} = (\text{Real value} - \text{Min. Value}) / (\text{Max. value} - \text{Min. value})$$

Therefore, as far as ANN training is concerned, the units of the input and output data sets are irrelevant; they are only used when the output data is to be de-normalised to its real value.

The following equation shows the mathematical relationship between x and y the single-input/single-output (SISO) ANN used here:

$$y = c_0 + c_1 \cdot \text{sig}[b_0 + b_1 \cdot \text{sig}(a_{10} + a_{11} \cdot x_1 + a_{12} \cdot x_2 + \dots) + b_2 \cdot \text{sig}(a_{20} + a_{21} \cdot x_1 + a_{22} \cdot x_2 + \dots) + \dots] \quad (3)$$

After sufficient training, adjusted values for the coefficients a , b , and c are derived and the non-linear relationship is determined.

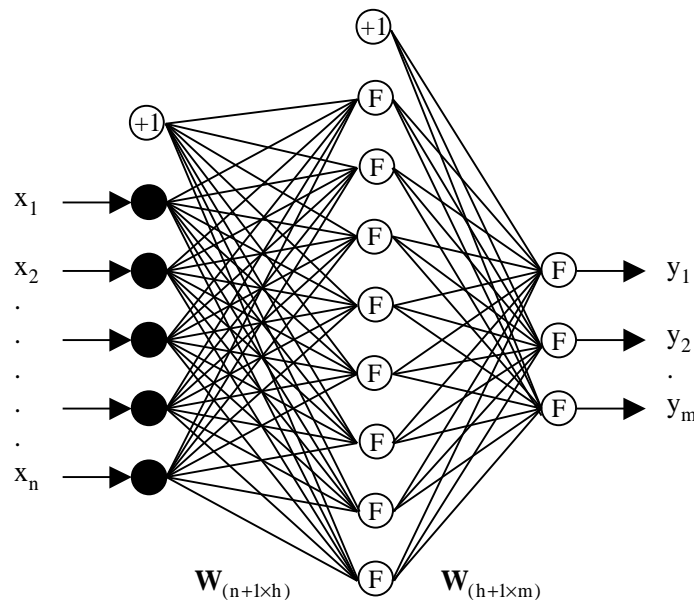


Fig.2: General structure of an Artificial Neural Network

3. Resistance and power prediction formulae

After the general hull type has been selected, the main dimensions of the hull are settled and the hull form can be worked out based on the designer's experience, data for comparable ships or systematical series of hull forms. A speed/power prediction is needed early in the design to select the engine. This prediction is usually based on a resistance computation and an estimation of overall efficiency. Closely connected with the propulsion plant are details of the appendages such as shafts, brackets, propellers, stabilizer fins and steering system. Based on a general arrangement plan, more detailed computations of LCG and LCB as well as stability are carried out. Static trim can significantly influence power consumption.

The resistance of high-speed vessels is primarily a function of the vessel's displacement, wetted length and surface, speed and additionally breadth for planing hulls. Therefore significant parameters are the slenderness $L/\nabla^{1/3}$ and the specific resistance R_T/∇ . The total resistance R_T is decomposed as usual with notation following ITTC unless otherwise specified, *Bertram (2000)*:

$$R_T = R_F + R_R \quad (4)$$

$$R_F = C_F \cdot \rho / 2 \cdot V^2 \cdot S \quad (5)$$

$$R_R = R_W + R_{APP} + R_{AA} + R_{PARAS} \quad (6)$$

ρ denotes the water density, V the ship speed, S the wetted surface (at rest except for planing hulls as described in more detail below), C_F follows ITTC'57 with Reynolds number is based on L_{wl} . The appendage resistance R_{APP} , the air and wind resistance R_{AA} , and the parasitic resistance R_{PARAS} (resistance of hull openings such as underwater exhaust gas exits, scoops, zinc anodes, etc.) can be estimated globally with 3-5% R_F for a projected vessel, but the determination of R_W (which includes wave, wave-making, spray and viscous pressure (or separation) resistance) is more difficult.

Considering the propulsive efficiencies yields the necessary engine power P_B from effective power $P_E = R_T \cdot V$:

$$P_B = P_E / (\eta_D \cdot \eta_M) \quad (7)$$

$\eta_M = 95\%$ is the mechanical efficiency of gear box and shaft bearings. The propulsive efficiency is $\eta_D = \eta_H \cdot \eta_R \cdot \eta_0$. Since $\eta_H \approx 1$ and $\eta_R \approx 1$ for these hull forms, the main influence is the propeller efficiency η_0 . Modern propeller designs and water jet propulsion systems can reach values of more than 70% under good operational conditions.

3.1. Power prediction for planing hulls

Fritsch and Bertram (2002) give already a simple procedure easy to program and suitable to estimate the power of planing hulls. The brake horsepower P_B [kW] required by a ship of displacement Δ [kg] at maximum speed V_K [kn] is then:

$$P_B = 0.7354 \cdot (\Delta \cdot V_K / 765.2 + B^2 \cdot V_K^3 / 1051.1) \quad (8)$$

Here B is the mean of the maximum beam at chines and the chine beam at the transom. If B is not known at an early design stage, we estimate:

$$B = 0.215 \cdot \Delta^{0.275} \quad (9)$$

The accuracy of this formula has been confirmed by many high-speed vessels tested at the Hamburg Ship Model Basin HSVA. One of the advantages of this equation is obviously the simple application when compared with other methods based on systematical series. The formula is given here only for completeness, although no neural net evaluation was involved.

3.2. Power prediction for semi-displacement hulls

The procedure for estimating resistance and power is very similar as for planing hulls. At HSVA, statistical data has been compiled for the prediction of the bare hull effective power P_E . These statistics are based on a slenderness coefficient $C_V = \nabla / L^3$. The resistance coefficient C_{TV} is defined by:

$$R_T = C_{TV} \cdot \rho / 2 \cdot V^2 \cdot \nabla^{2/3} \quad (10)$$

C_{TV} is a function of the Froude number, given in *Fritsch and Bertram (2002)* as diagrams. The corresponding formulae derived by ANN evaluation are:

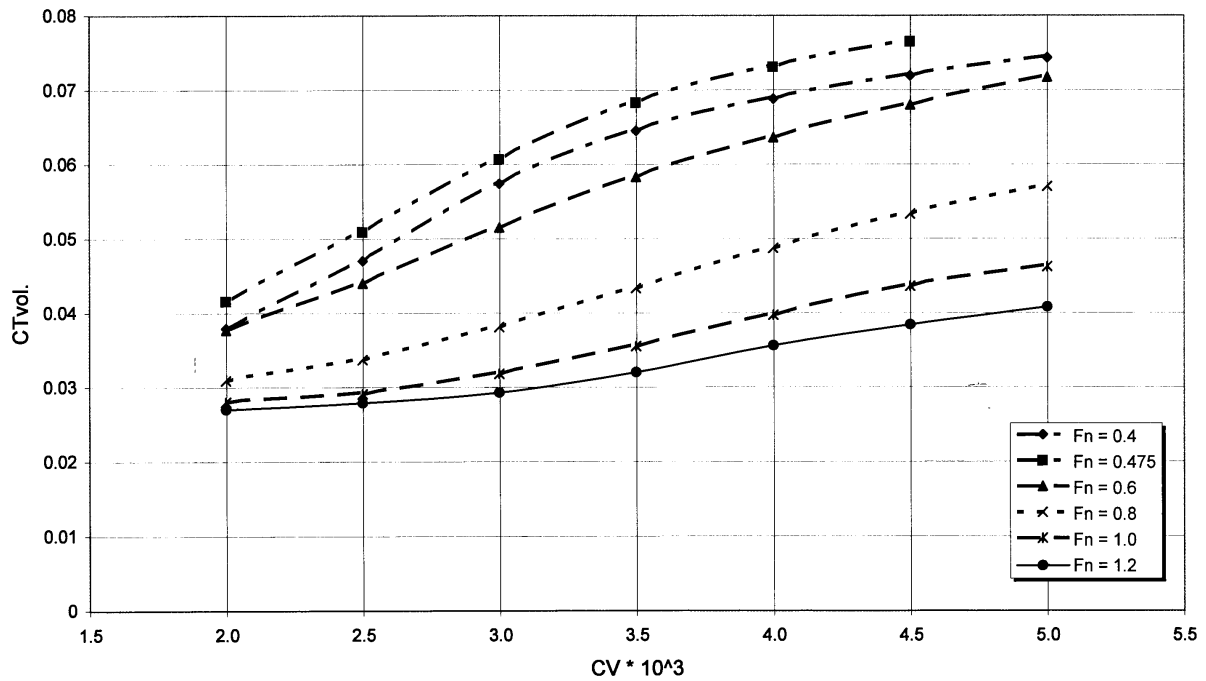


Fig.3: Bare hull resistance for high-speed vessel, *Fritsch and Bertram (2002)*
Curves labeled $F_n=0.4$ and $F_n=0.475$ are to be interchanged

For $0.002 < C_V < 0.005$, $0.4 < F_n < 1.2$, Fig.3:

$$C_{TV} = c_0 + c_1 \cdot \text{sig} [b_0 + b_1 \cdot \text{sig}(a_{10} + a_{11} \cdot x_1 + a_{12} \cdot x_2) + b_2 \cdot \text{sig}(a_{20} + a_{21} \cdot x_1 + a_{22} \cdot x_2) + b_3 \cdot \text{sig}(a_{30} + a_{31} \cdot x_1 + a_{32} \cdot x_2) + b_4 \cdot \text{sig}(a_{40} + a_{41} \cdot x_1 + a_{42} \cdot x_2) + b_5 \cdot \text{sig}(a_{50} + a_{51} \cdot x_1 + a_{52} \cdot x_2)] \quad (11)$$

$x_1 = 1.125 \cdot F_n - 0.4$	$x_2 = 300 \cdot C_V - 0.549$	
$a_{10} = -0.3260$	$a_{11} = 0.1852$	$a_{12} = 0.1022$
$a_{20} = 3.9759$	$a_{21} = -7.5136$	$a_{22} = -1.6368$
$a_{30} = 1.3266$	$a_{31} = 1.6764$	$a_{32} = -4.9726$
$a_{40} = 3.1882$	$a_{41} = 4.1851$	$a_{42} = -5.2130$
$a_{50} = 1.4979$	$a_{51} = -0.8394$	$a_{52} = -6.2047$
$b_0 = 0.9473$	$b_1 = 0.1904$	$b_2 = 2.4479$
$b_3 = -1.5372$	$b_4 = -1.7522$	$b_5 = -1.8346$
$c_0 = 0.024806$	$c_1 = 0.05389$	

For $0.0025 < C_V < 0.007$, $0.2 < F_n < 0.45$, Fig.4:

$$C_{TV} = c_0 + c_1 \cdot \text{sig} [b_0 + b_1 \cdot \text{sig}(a_{10} + a_{11} \cdot x_1 + a_{12} \cdot x_2) + b_2 \cdot \text{sig}(a_{20} + a_{21} \cdot x_1 + a_{22} \cdot x_2) + b_3 \cdot \text{sig}(a_{30} + a_{31} \cdot x_1 + a_{32} \cdot x_2) + b_4 \cdot \text{sig}(a_{40} + a_{41} \cdot x_1 + a_{42} \cdot x_2)] \quad (12)$$

$x_1 = 3 \cdot F_n - 0.55$	$x_2 = 199.3 \cdot C_V - 0.44642$	
$a_{10} = 3.20130$	$a_{11} = -6.76554$	$a_{12} = 2.88373$
$a_{20} = 8.00008$	$a_{21} = -4.98452$	$a_{22} = -5.99841$
$a_{30} = 1.43160$	$a_{31} = 3.79446$	$a_{32} = -3.92012$
$a_{40} = -1.55789$	$a_{41} = 0.34187$	$a_{42} = 5.01403$
$b_0 = 0.03358$	$b_1 = -2.38217$	$b_2 = -2.95919$
$b_3 = 2.42695$	$b_4 = 2.41849$	
$c_0 = 0.019134$	$c_1 = 0.05333$	

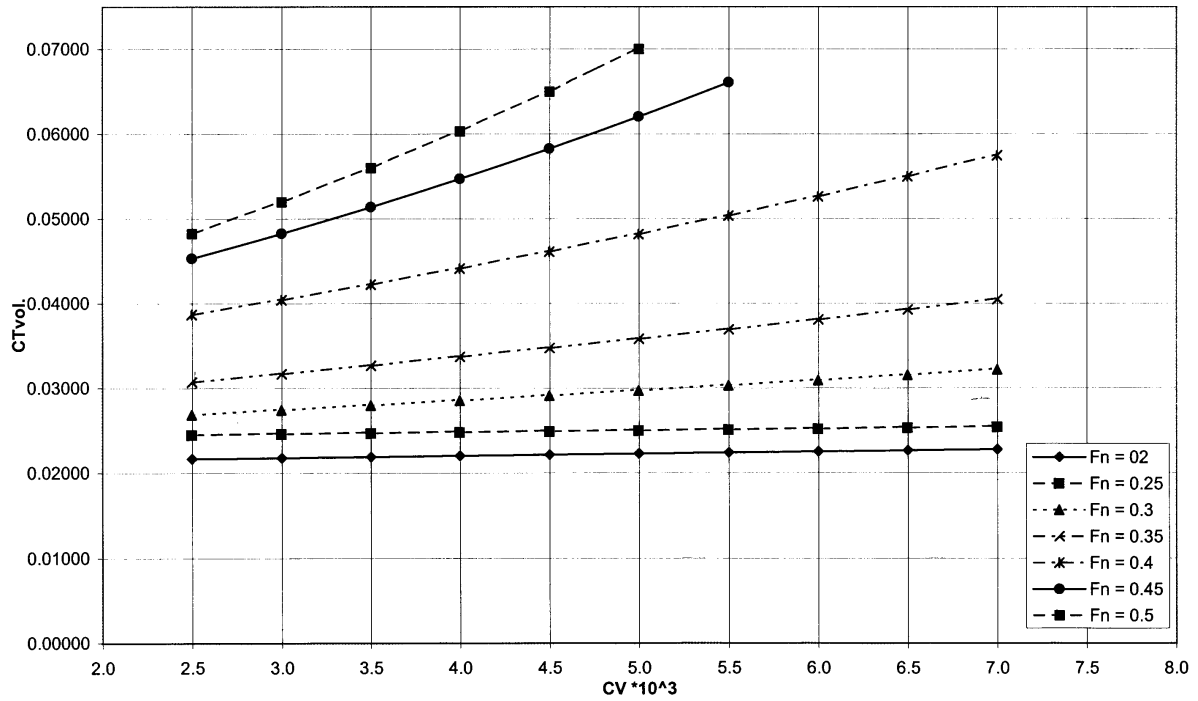


Fig.4: Bare hull resistance for high-speed vessel, *Fritsch and Bertram (2002)*

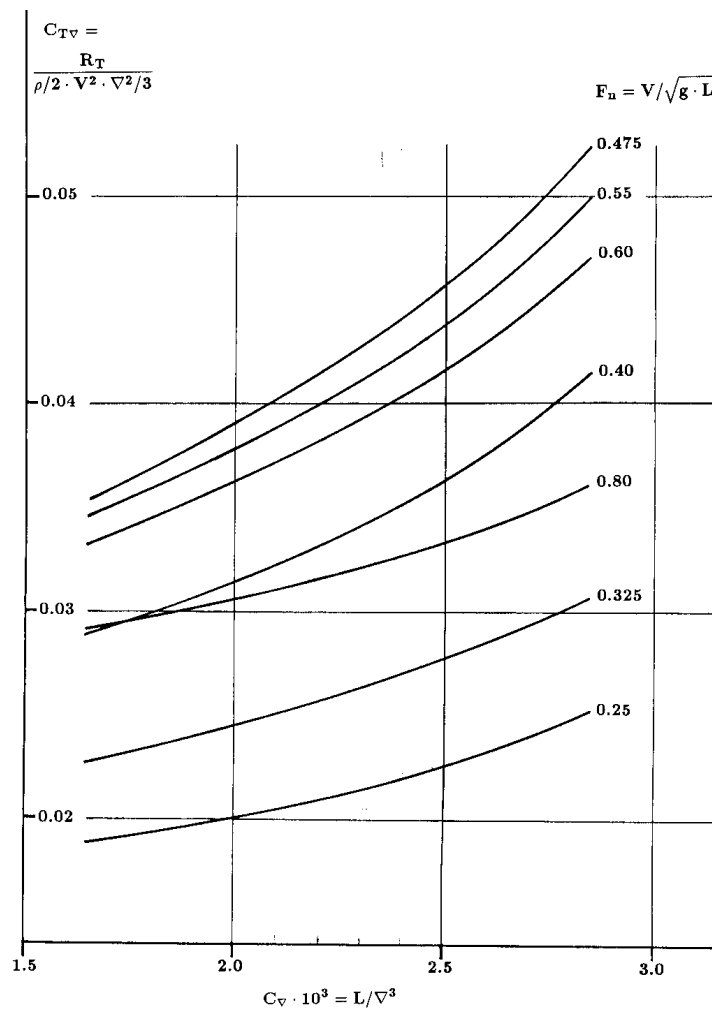


Fig.5: Bare hull resistance for frigates and corvettes, *Fritsch and Bertram (2002)*

For frigates and corvettes, for $0.0016 < C_V < 0.0029$, $0.25 < F_n < 0.8$, Fig.5:

$$C_{TV} = c_0 + c_1 \cdot \text{sig} [b_0 + b_1 \cdot \text{sig}(a_{10} + a_{11} \cdot x_1 + a_{12} \cdot x_2) + b_2 \cdot \text{sig}(a_{20} + a_{21} \cdot x_1 + a_{22} \cdot x_2) + b_3 \cdot \text{sig}(a_{30} + a_{31} \cdot x_1 + a_{32} \cdot x_2)] \quad (13)$$

$$\begin{aligned} x_1 &= 1.6364 \cdot F_n - 0.3591 & x_2 &= 751.6 \cdot C_V - 1.1849 \\ a_{10} &= -1.5048 & a_{11} &= -5.0786 & a_{12} &= 4.7309 \\ a_{20} &= 2.9204 & a_{21} &= -5.7543 & a_{22} &= 0.9466 \\ a_{30} &= 2.1448 & a_{31} &= -4.52883 & a_{32} &= 2.0804 \\ b_0 &= -0.6757 & b_1 &= 2.2364 & b_2 &= -4.8354 & b_3 &= 2.1233 \\ c_0 &= 0.01788 & c_1 &= 0.036444 \end{aligned}$$

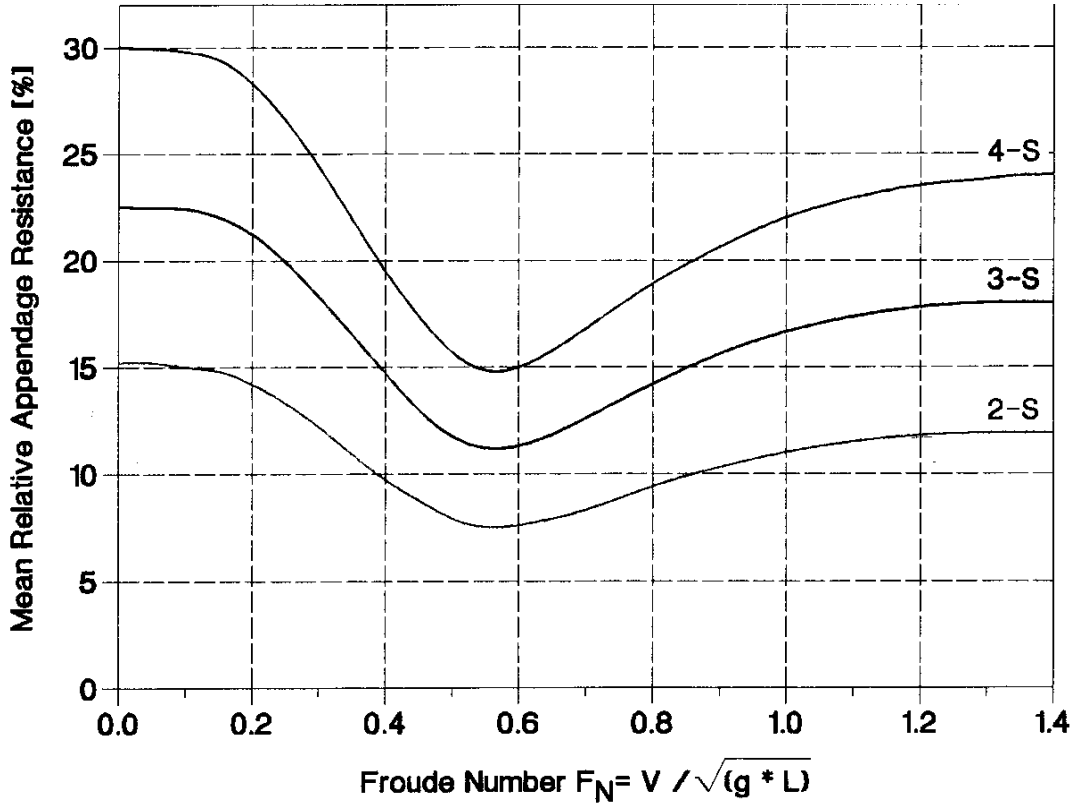


Fig.6: Mean relative appendage resistance R_{APP}/R_T for 4-screw, 3-screw and 2-screw vessels, *Fritsch and Bertram (2002)*

Since the value found for the effective power is valid for the bare hull only, allowances for R_{APP} and R_{AA} must be added. R_{APP} can be estimated from statistical data, Fig.6, *Fritsch and Bertram (2002)*. Again we applied artificial neural nets to convert diagrams into equivalent formulae. The mean relative appendage resistance R_{APP}/R_T is then:

$$2 \text{ propellers : } R_{APP}/R_T [\%] = c_0 + c_1 \cdot \text{sig} [b_0 + b_1 \cdot \text{sig}(a_{10} + a_{11} \cdot x_1) + b_2 \cdot \text{sig}(a_{20} + a_{21} \cdot x_1)] \quad (14)$$

$$\begin{aligned} x_1 &= 0.6544 \cdot F_n + 0.0338 \\ a_{10} &= -7.346 & a_{11} &= 14.118 \\ a_{20} &= -3.545 & a_{21} &= 13.394 \\ b_0 &= 2.996 & b_1 &= 4.070 & b_2 &= -6.837 \\ c_0 &= 7.023 & c_1 &= 8.718 \end{aligned}$$

$$3 \text{ propellers : } R_{APP}/R_T [\%] = c_0 + c_1 \cdot \text{sig} [b_0 + b_1 \cdot \text{sig}(a_{10} + a_{11} \cdot x_1) + b_2 \cdot \text{sig}(a_{20} + a_{21} \cdot x_1)] \quad (15)$$

$$\begin{aligned} x_1 &= 0.6453 \cdot F_n + 0.0477 \\ a_{10} &= -4.232 & a_{11} &= 15.07 \end{aligned}$$

$$\begin{array}{lll}
a_{20}= -7.375 & a_{21}= 14.00 & \\
b_0= 2.737 & b_1= -6.481 & b_2= 4.046 \\
c_0= 10.72 & c_1= 12.55 &
\end{array}$$

$$4 \text{ propellers : } R_{APP}/R_T [\%] = c_0 + c_1 \cdot \text{sig} [b_0 + b_1 \cdot \text{sig}(a_{10} + a_{11} \cdot x_1) + b_2 \cdot \text{sig}(a_{20} + a_{21} \cdot x_1)] \quad (16)$$

$$\begin{array}{lll}
x_1 = 0.686F_n - 0.008 & & \\
a_{10}= 3.797 & a_{11}= -16.43 & \\
a_{20}= 5.965 & a_{21}= -11.99 & \\
b_0= 0.3438 & b_1= 6.215 & b_2= -3.746 \\
c_0= 14.23 & c_1= 16.42 &
\end{array}$$

R_{AA} can be calculated following *Schneekluth and Bertram (1998)*.

3.3. Trim for fast ships

The resistance of a fast ship is fundamentally linked with the dynamic trim. *Fritsch and Bertram (2002)* give diagrams for optimum trim angle θ for fast vessels. Incorporating their recommendation to use 30% smaller values than given in the diagrams, we obtain the following formulae for recommended trim angle (bow up) at zero speed:

Displacement and semi-displacement hulls:

$$\theta = 0.7 \cdot \{c_0 + c_1 \cdot \text{sig} [b_0 + b_1 \cdot \text{sig}(a_{10} + a_{11} \cdot x_1 + a_{12} \cdot x_2) + b_2 \cdot \text{sig}(a_{20} + a_{21} \cdot x_1 + a_{22} \cdot x_2) + b_3 \cdot \text{sig}(a_{30} + a_{31} \cdot x_1 + a_{32} \cdot x_2) + b_4 \cdot \text{sig}(a_{40} + a_{41} \cdot x_1 + a_{42} \cdot x_2)]\} \quad (17)$$

$$\begin{array}{lll}
x_1 = 0.9 \cdot (\nabla^{2/3} / B \cdot T) - 1.975 & x_2 = 0.71 \cdot F_n - 0.0795 & \\
a_{10}= -3.75198 & a_{11}= -1.69432 & a_{12}= 9.49288 \\
a_{20}= -2.49216 & a_{21}= 3.86243 & a_{22}= -1.65272 \\
a_{30}= 3.87188 & a_{31}= 0.61239 & a_{32}= -17.00609 \\
a_{40}= -2.68088 & a_{41}= -3.55418 & a_{42}= 3.42624 \\
b_0= 1.63558 & b_1= -2.18713 & b_2= 2.15603 \\
b_3= -4.84437 & b_4= -1.51677 & \\
c_0= -0.17276 & c_1= 2.364 &
\end{array}$$

B is the width, T the draft, ∇ the volumetric displacement.

Planing hulls

$$\theta = 0.7 \cdot \{c_0 + c_1 \cdot \text{sig} [b_0 + b_1 \cdot \text{sig}(a_{10} + a_{11} \cdot x_1 + a_{12} \cdot x_2) + b_2 \cdot \text{sig}(a_{20} + a_{21} \cdot x_1 + a_{22} \cdot x_2)]\} \quad (18)$$

$$\begin{array}{lll}
x_1 = 0.6 \cdot (\nabla^{2/3} / B \cdot T) - 0.85 & x_2 = 0.6624 \cdot F_n - 0.01936 & \\
a_{10}= -2.66906 & a_{11}= 0.12856 & a_{12}= 8.06127 \\
a_{20}= 6.30112 & a_{21}= -3.37513 & a_{22}= -3.66594 \\
b_0= -0.83869 & b_1= 4.16294 & b_2= -2.71566 \\
c_0= -0.39046 & c_1= 6.535 &
\end{array}$$

4. Validation against external test data

We compare the resistance prediction of our ANN formulae with experimental data supplied in personal communication by Prof. Prasanta Sahoo of Australian Maritime College (AMC) and the commercial program Navcad (using the prediction for planing hulls). We compare resistance values, assuming in all cases a density $\rho = 1000 \text{ kg/m}^3$.

The first test case is 'model 5' of the AMC series with the following particulars: displacement $\nabla = 25.34 \cdot 10^{-3} \text{ m}^3$, $L = 1.6 \text{ m}$, $B = 0.4 \text{ m}$, $T = 0.1 \text{ m}$, $C_B = 0.395$, $C_V = \nabla / L^3 = 6.186 \cdot 10^{-3}$. These parameters lie in the middle of the parameter variations investigated by the AMC series. We considered this model therefore as 'typical'. The measured resistance lies for all investigated Froude numbers above the

ANN (Eq.(11)) and Navcad predictions, Fig.7. The ANN formula gives very similar estimates as Navcad.

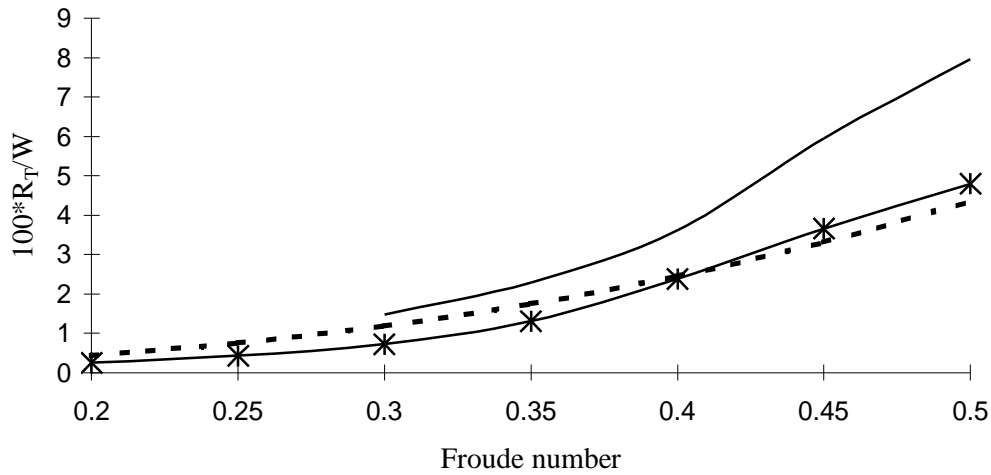


Fig.7: Resistance for 'AMC model 10' : -*- ANN ; — Exp. ; - - - Navcad

The second test case is the 'model 10' of the AMC test series with the following particulars : displacement $\nabla=8.003 \cdot 10^{-3} \text{ m}^3$, $L=1.6 \text{ m}$, $B=0.2 \text{ m}$, $T=0.05 \text{ m}$, $C_B=0.5$, $C_V=\nabla/L^3=1.953 \cdot 10^{-3}$. This model is thus very slender with an unusually small wave resistance. The ANN prediction following Eq.(11) extrapolates slightly beyond the interval of applicability. The predicted resistance lies consistently (typically 30%) below the measured value. Navcad has similar errors for small to medium Froude numbers and then over-predicts the resistance. While the ANN prediction has at least a similar characteristics, both Navcad and ANN show that statistical predictions perform poorly for extreme test cases. While this is generally known and unavoidable, it is good to recall and demonstrate this fact on occasion.

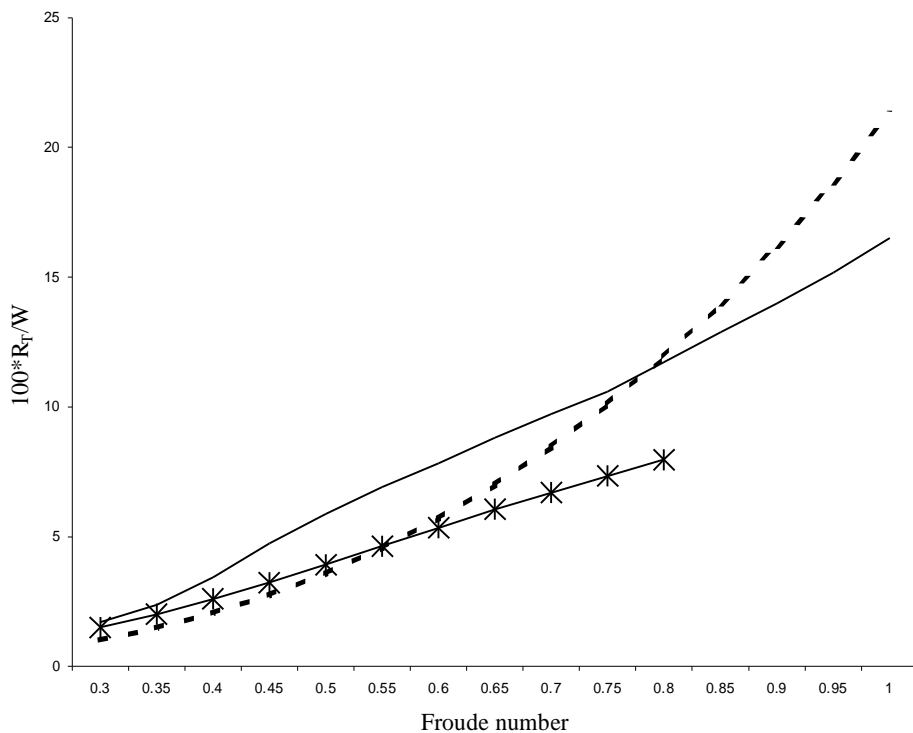


Fig.8: Resistance for 'AMC model 10' : -*- ANN ; — Exp. ; - - - Navcad

5. Conclusions

Once a suitable data base is compiled and the significant parameters are determined, the evaluation with Artificial Neural Nets proved to be straight-forward. The resulting formulae are easy to program, either in higher programming languages like Fortran or in spreadsheets like Excel.

The formulae – as the underlying diagrams – are simple approximation through scattered original data. They give rough estimates and reflect to some extent the influence of main parameters. The simplicity comes at the expense of accuracy, i.e. these formulae cannot substitute accurate first-principle approaches (computational fluid dynamics) or professional model tests. However, the validation studies served to ensure that the given formulae reflect the original diagrams in good accuracy and should prove to be valuable in early design studies, particularly if budget restriction prohibit more expensive approaches.

References

- AZCUETA, R.; BERTRAM, V. (2002), *High-performance marine vehicles as naval platforms – An overview*, 3rd Int. Conf. High-Performance Marine Vehicles (HIPER), Bergen, pp.22-33
- BERTRAM, V. (2000), *Practical ship hydrodynamics*, Butterworth+Heinemann, Oxford
- BERTRAM, V.; MESBAHI, E. (2000), *Adaptive Neural Network Applications in Ship Design*, Jahrbuch der Schiffbautechnischen Gesellschaft, Springer
- FRITSCH, M.; BERTRAM, V. (2002), *Power prediction and hull improvement for conventional fast vessels*, 3rd Int. Conf. High-Performance Marine Vehicles (HIPER), Bergen, pp.167-177
- MESBAHI, E. (2003), *Artificial neural networks – Fundamentals*, 39th WEGEMT School OPTIMISTIC – Optimization in Marine Design, Mensch&Buch Verlag, pp.191-216
- MESBAHI, E.; BERTRAM, V. (2000), *Empirical design formulae using artificial neural networks*, 1st Int. Conf. Computer und IT Applic. Mar. Industries, COMPIT, Potsdam, pp.292-301
- SCHNEEKLUTH, H.; BERTRAM, V. (1998), *Ship design for efficiency and economy*, Butterworth+Heinemann, Oxford
- HESS, D.; FALLER, W. (2000), *Simulation of ship maneuvers using recursive neural networks*, 23rd Symp. Naval Hydrodyn., Val de Reuil
- RUMELHART, D.E.; McCLELLAND, J.L., (1986), *Parallel distributed processing: Explorations in the microstructure of cognition*, I&II, MIT Press, Cambridge MA.

New Developments for Fast and Unconventional Marine Vehicles

Volker Bertram, ENSIETA, Brest/France, volker.bertram@ensieta.fr

Mohammad S. Seif, Sharif University of Technology, Teheran/Iran, seif@sharif.edu

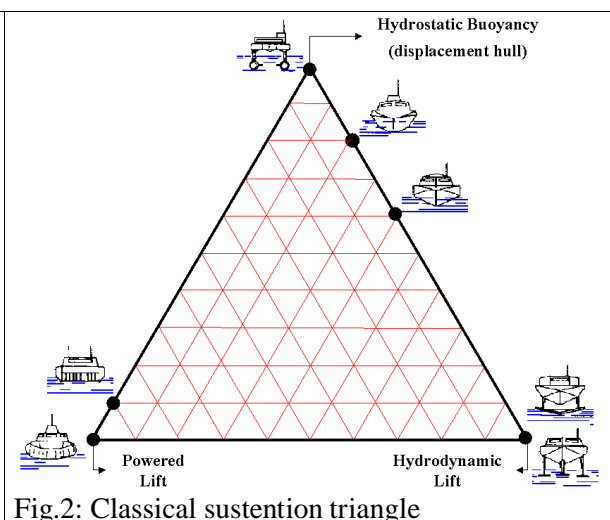
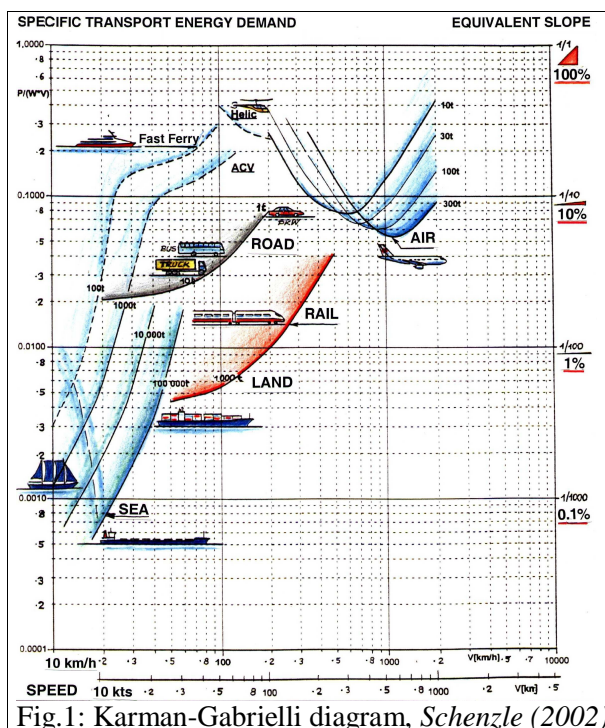
Abstract

This paper reviews different methods used for increasing the speed of marine vehicles in recent years. For this purpose, different components of resistance and methods of resistance reduction are investigated. Moreover, methods of weight saving and improvement of propulsion system efficiency are also discussed.

1. Introduction

The past two decades have witnessed a multitude of developments for fast and unconventional marine vehicles for various applications, notably navy applications, fast ferries and racing boats/fast yachts. These vehicles are frequently referred to as high-performance marine vehicles (HPMV) or high-speed craft (HSC). The term HPMV is more popular with navies, while HSC is adopted by various rules of IMO (International Maritime Organisation) and classification societies. This review of assorted HPMV draws on previous publications. Papanikolaou (2001) focuses in his HPMV review rather on the commercial market, ANEP (1996), Azcueta and Bertram (2002), on HPMV as naval platforms. The technological feedback from the racing scene into military and commercial fast vessels often is considerable, e.g. Acampora (1995). Advantages and disadvantages of the different advanced and hybrid vehicles can generally be looked at with regard to their characteristics:

1. Design: platform stability, general arrangement (deck area and volume space), maximum draft.
2. Hydrodynamic: range of operating speed, propulsion configuration, speed loss in waves, seakeeping, maneuverability, weight and trim sensitivity.
3. Structural: global strength, local strength, dynamic loads (slamming), use of advanced materials, complex structures.
4. Others: acquisition and operating costs, state of development of the technology, survivability (detectability or stealth characteristics and vulnerability for naval vessels).



Conventional displacement ships operate at relatively low speeds and feature high transport efficiency (= mass * distance/installed power). Fig.1 shows the Karman-Gabrielli diagram, *Gabrielli and Karman (1950)*, in the updated form of *Schenzle (2002)*. Conventional ships are one order of magnitude more efficient than land transport and two orders of magnitude than air transport. However, as speed increases, ships become less and less efficient and land transport (by trains) is the most efficient alternative, until at really high speeds airplanes become more economical. Very fast ships have similar transport energy demands as airplanes, albeit at much lower speed. Continuous research aims at improving the performance of fast ships and shift extend thus the region where ships have competitive advantages over land transport. This is also driven by a political desire to shift transport from road (expensive infrastructure) to sea (cheap infrastructure).

2. Classification

The classification of advanced vehicles and their hybrid derivations usually follows the classical sustentation triangle, *Jewell (1973,1976)*. The corners of this triangle represent the vessels supported by hydrostatic buoyancy, hydrodynamic lift and powered lift. The edges and the inside of the triangle represent the hybrids, Fig.2.

Hybrid vehicles combine more than one source of sustentation or lift simultaneously and may combine the advantages of the different types of advanced craft from which they derive. To address all the various hybrids – of which more than 100 different concepts exist – would go far beyond the scope of this paper. Therefore we will focus only on the most promising types, which are in different stages of development: preliminary concept, prototypes and demonstrators or in operation.

3. Displacement multihulls

In the hydrostatic buoyancy corner we find displacement monohulls and multihulls. Increasing the speed of a conventional displacement ship is only possible to a certain extent. At Froude numbers approximately $F_n > 0.4$, wave resistance increases disproportionately with ship speed for most ship hull forms. One approach for fast ships, particularly those requiring or benefiting from considerable deck area, are multihulls allowing very thin waterline entrance angles while ensuring sufficient stability. The most popular multihulls are catamarans, *Jansson and Lamb (1992)*. Conventional displacement catamarans operate at $F_n > 0.4$. They are well proven in commercial applications, usually as fast ferries. Wave piercers are a popular catamaran design. Examples for navy applications are the ‘Jervis Bay’ (500 fully equipped troops, 40+ knots, 1000 nm) chartered by the Royal Australian Navy, Fig.3, *Moss (2001)*, and the ‘Joint Venture’ HSV-X1 chartered by the US army. The main advantage of catamarans compared to monohulls are: larger deck area, higher speeds at same cost, reduced roll motions, higher initial stability, better maneuverability and better survivability. The main disadvantages are greater heave and pitch motions and structural problems in the transversal box connection.

SWATH (Small Waterplane Area Twin Hull) ships are semi-submerged catamarans, Fig.4, *Gore (1985)*, *Lang and Slogett (1985)*, *Papanikolaou (1996)*, www.swath.com. SWATH advantages are seakeeping superior to similar-sized conventional and unconventional craft and a large deck area for helicopter operation. Disadvantages are its higher resistance and installed power requirements due to greater wetted surface, its sensitivity to displacement changes and to trim, large draft, increased acquisition and operating costs compared to monohulls. Early SWATH prototypes have been built as technology demonstrators for the US navy (T-AGOS) and the Japanese navy. One of the Japanese SWATH built by Mitsui is the surveillance vessel ‘Hibiki’ for the Japanese defense forces, *Hynds (2001)*. A noteworthy recent delivery is the SWATH for the German navy built by TNSW in 2003, *Bormann (2003)*, Fig.5. Abeking+Rasmussen has built various SWATH ships for pilot transfer, Fig.6, and has also proposed naval SWATHs based on that experience, *Spethmann (2000,2001)*. One of the envisioned applications is in cooperation with the Lürssen shipyard for the mine hunting improvement programme MJ2000 of the German navy, where a SWATH parent vessel acts as a control ship for at least two surface drones, *N.N. (2002a)*.

The 'Sea Shadow', Fig.7, www.fas.org, a stealth technology demonstrator of the US Navy, is also based on SWATH technology. Most SWATH ships were designed for speeds lower than 25 knots. Almaz Shipbuilding Company in Russia has built a 32 m vessel in 1998 with a service speed of 28 knots. Other research in Russia has led to the development of a semi-planing SWATH concept designed for higher speeds with patrol craft applications, *Dubrovskiy (2000)*. A variant of a SWATH is the HSS (High Speed SWATH), which combines a SWATH bow section with a planing catamaran astern section, combining the good seakeeping of a SWATH and the high performance of a catamaran, Fig.8. Fig.9 shows the HSS 40+ knot car/passenger ferry built for STENA Lines. The US Navy 'X-Craft', Fig.10, is designed to become the Navy's largest and fastest aluminum catamaran with speeds exceeding 50 knots. The X-craft has moderate SWATH geometry and will also test polymer drag reduction technology (Prof. R. Latorre (UNO) in personal communication).

The High Aspect Ratio Twin Hull (HARTH) is a catamaran with very slender and high struts, Fig.11, *N.N. (2002c)*, foxxaero.homestead.com/indrad_018.html. Such a design would feature very good seakeeping. So far has remained only in the 'artist vision' stage with little information available. One may have severe doubts concerning passenger handling, both in regular service and emergency evacuation, and structural integrity/cost for such a design. Weinblume, *Söding (1997)*, Fig.12, are catamarans with staggered hulls excellent wave resistance at moderate speeds, acceptable seakeeping, and low wash. However, disadvantages in deck arrangement and structural problems have prevented so far any demonstrator to be built.

Displacement trimarans are a recent development. Their overall advantages compared to monohulls are claimed to be, *Smith and Jones (2001)*: lower resistance at high speed, better damage stability, good seakeeping, efficient layout of payload, good survivability, reduced operating costs. The 21 m trimaran yacht 'Ilan Voyager', Fig.13, built in 1988 proved the trimaran speed, economy and range capability by making a record-breaking un-refueled voyage around Britain in 72 hours. The success of this prototype has led to the design and construction of a 35m yacht 'Cable & Wireless Adventurer' which successfully completed a circumnavigation of the world in a record time of less than 75 days. The futuristic design study super-slender monohulls of Kvaerner Shipbuilding of Finland is also a slender monohulls with outriggers, thus a trimaran, Fig.14. The designers feel the craft will be capable of speeds of 40-60 knots. Fig.15 shows the trimaran demonstrator research vessel 'Triton', www.naval-technology.com/projects/trimaran/, www.trimaran.dera.gov.uk. The US Littoral Combat Ship (LCS) program aims to develop a new, high-speed (40-50 knots) combatant for coastal operations. Up to 60 ships are planned and the Navy hopes to begin construction in 2006. One of the three design studies kept for further investigation, is a trimaran, Fig.16, *N.N.(2003)*, www.globalsecurity.org/military/systems/ship/lcs-refs.htm, <http://peoships.crane.mil/lcs/>. Contrary to wide-spread belief, the trimaran side hulls should not be designed as thin as possible. The side hulls create wave systems that shall interfere with the wave system of the center hull to provide maximum mutual cancellation to achieve the desired resistance reduction at design speed. For this, the wave systems of the side hulls must have a similar magnitude as the wave system of the center hull.

The SLICE of Lockheed Martin, Figs.17 and 18, *Schmidt (2001)*, features four semi-displacement hulls with surface-piercing struts making it actually a 'quadramaran'. The staggered hull arrangement causes at certain speeds favorable interaction between upstream/downstream hulls, reducing the resistance compared to standard SWATH designs. www.aerohydro.com/products/marine/navatek.htm. Another US four-hull ship is the 20-m, 14 t aluminum prototype Q18 of Quadrimaran, which achieved top speeds of 63 knots planing in headwinds. www.quadrimaran.com

The 'ultimate' in multihulls so far are pentamarans, i.e. ships with five surface piercing hulls. As for the trimaran and the SLICE, the design feature fortunate wave interaction at design speed and sufficient stability despite slender hulls with low wave and spray formation. For military applications the protection of the center hull by the outriggers is also used as an argument. IZAR shipyards pursue actively the realization of a demonstrator pentamaran, teaming up with Nigel Gee Assoc., Fig.19, *Moret and Gee (2001)*. BMT has presented a frigate design study based on a pentamaran hull, Fig.20.



Fig.3: INCAT 045, HMS 'Jervis Bay'
 → Fig.4: SWATH principle

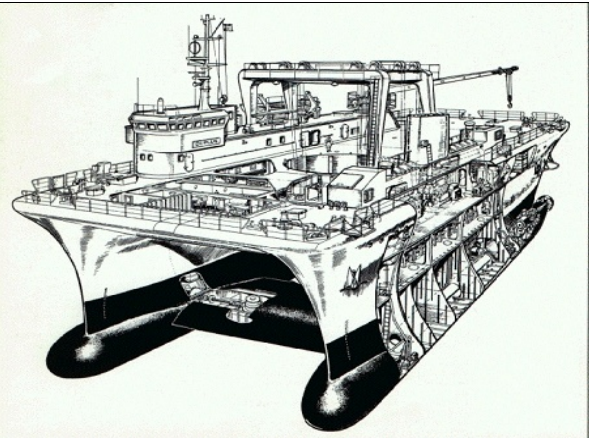


Fig.5: Germany navy SWATH 'Planet'



Fig.6: SWATH by Abeking+Rasmussen for pilots



Fig.7: Stealth SWATH 'Sea Shadow' of US Navy

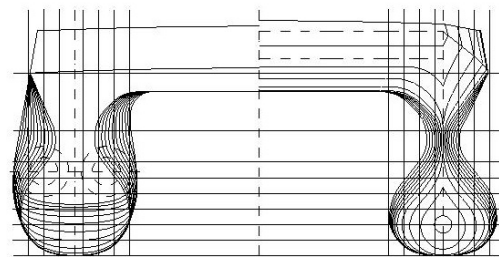


Fig.8: HSS designed by MTG



Fig.9: GTS Stena Explorer (HSS)



Fig.10: X-craft of US Navy



Fig.11: HARTH 360 passenger ferry

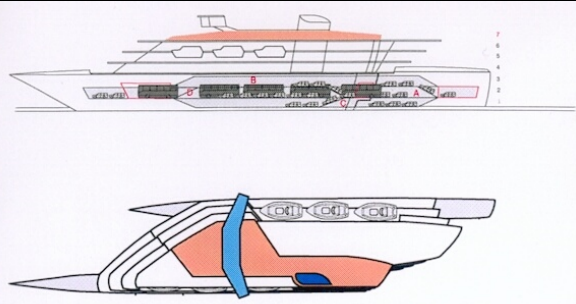


Fig.12: Weinblum design



Fig.13: Record-breaking trimaran 'Ilan Voyager'



Fig.14: Super-slender ferry (Kvaerner-Masa)



Fig.15: UK Navy Trimaran demonstrator 'Triton'



Fig.16: General Dynamics design study for US Navy littoral combat ship as trimaran

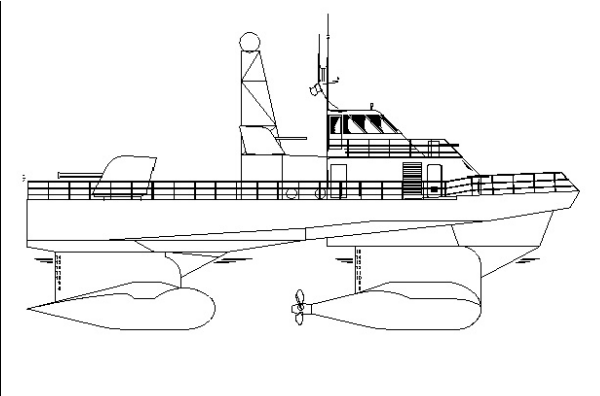


Fig.17: SLICE by Lockheed Martin



Fig.18: SLICE in building dock



Fig.19: Pentamaran design of Nigel Gee Assoc.

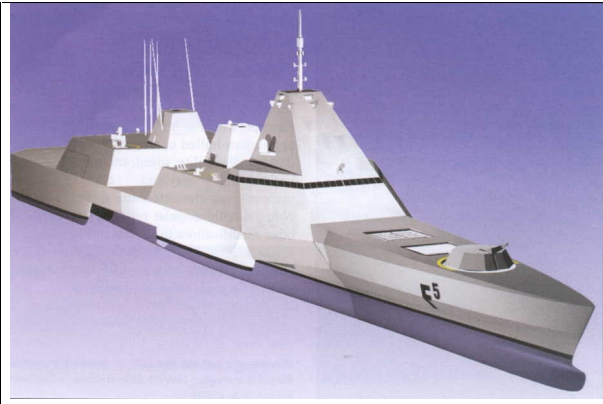


Fig.20: Pentamaran design of BMT



Fig.21: UK Stealth frigate study 'Sea Wraith'

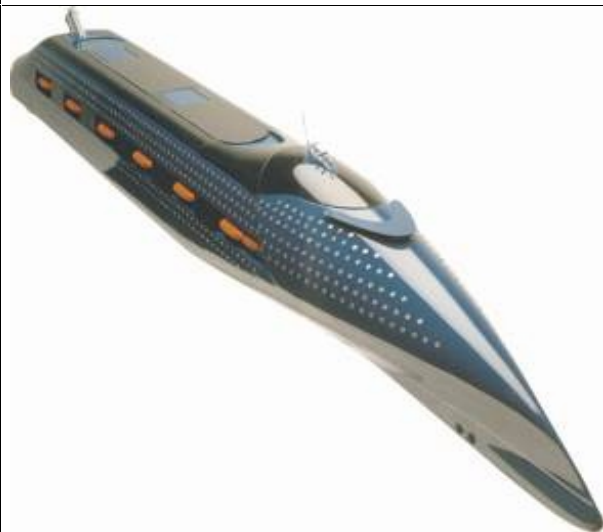


Fig.22: Euroexpress of Kvaerner



Fig.23: VSV Paragon Mann



Fig.24: Rolls-Royce FNSLV

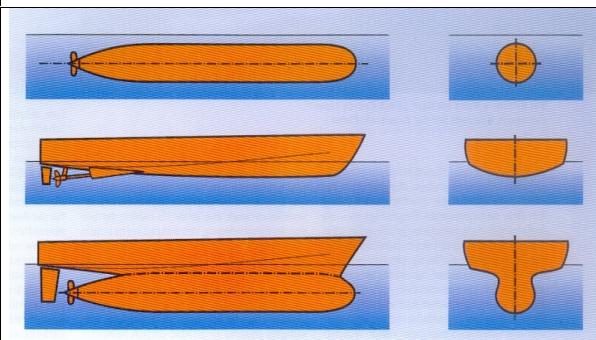


Fig.25: Fast Monohull of Blohm & Voss



Fig.26: Typical planing hull



Fig.27: Typical surface-piercing hydrofoil



Fig.28: Jetfoil – fully submerged hydrofoils

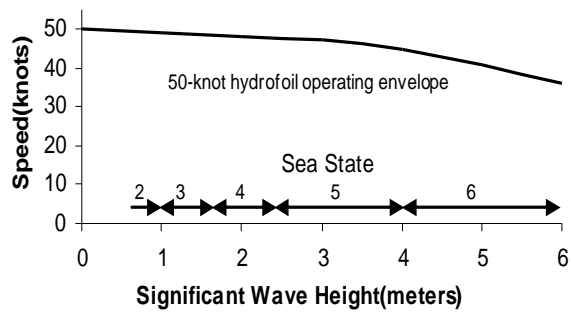


Fig.29: Effect of sea state on hydrofoil speed
www.foils.org/basfigs.htm

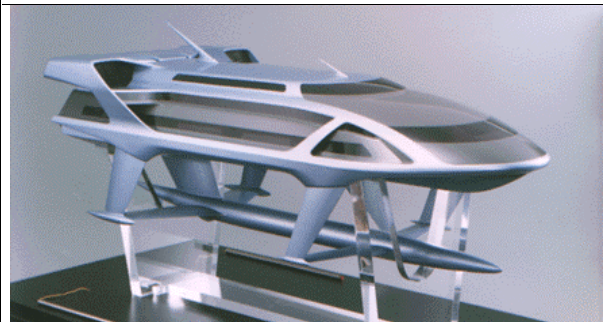


Fig.30: HYSWAS design TSL-F (Japan)



Fig.31: 'Quest' HYSWAS



Fig.32: US HYSWAS patrol boat study



Fig.33: German HYSWAS design study



Fig.34: Midfoil demonstrator (Navatek)

4. Monohulls

The wave-piercing principle can also be applied to displacement monohulls like the British project for a stealth frigate 'Sea Wraith', Fig.21, the US navy project DD21 'Zumwalt' class destroyer, or the German MTG project of a 7000 t frigate. Kvaerner Masayards and Guy Design Group in Finland teamed up to develop the 'Euroexpress' design, a futuristic wave-piercing fast car ferry design, Fig.22, http://foxxaero.homestead.com/indrad_038.html. In 1990, the designer Adrian Thompson began developing the concept of VSV (Very Slender Vessels), Fig.23, www.vsvboats.com. A number of these wave-piercing designs have been built since then. The craft has a long slender hull shape with two large chines to generate lift and dynamic stability. Limited interior space means the craft is most suited to military roles where speed and stealth are required. The designers feel the craft will be capable of speeds in the 40-60 knot range with a length to beam ratio of about 9:1.

Rolls-Royce launched in 2003 designs for a 40-knot, 2500t-payload fast naval logistics ship, Fig.24. The Fast Navy Sea-Lift Vessel is equipped with Rolls-Royce waterjets. Its high-tensile structure has aluminum accommodation and bridge decks. FNSLV technical details are: Lpp=177m, B=24m, T=4.15m; 4000 tons tdw; 1800m lane meters. The Fast Monohull by Blohm+Voss, *Langenberg (1995)*, is a displacement hull with the hull volume as deep submerged as possible, Fig.25. The ship type has been proposed for naval applications, but so far only two fast cruise vessels of this type have been built, *Engelskirchen and Marzi (2001)*.

Planing craft, Fig.26, *Savitsky (1985)*, are usually cheaper than other high-speed craft of similar speed, having relatively simple structure and equipment. In consequence, very many planing craft are used worldwide for passenger transportation, military purposes, racing, pleasure, etc. In planing condition, when almost 80% of the weight of the boat is supported by hydrodynamic lift, these craft can go very fast, but need to overcome a resistance hump to get into planing. Planing craft have typically payload problems as heavy boats are need excessive power to get into planing. They also have infamously bad seakeeping performance with considerable speed loss in high sea states. More than any other ship type, they benefit from early design trade-offs between calm-water performance and seakeeping, as optimum calm-water planing geometries have worst seakeeping characteristics. Modern simulation techniques can now aid the design for high-performance planing craft, *Bertram et al. (2003)*.

5. Pure and hybrid hydrofoils

Hydrofoils, *Johnston (1985)*, *Meyer and Wilkins (1992)*, *Meyer and Wilkins (1992)*, www.foils.org, similar to airplanes, use wing surfaces to generate lift. They have surface-piercing (SPH), Fig.27, or fully submerged foils (FSH), Fig.28. Since water density is much greater than that of the air, the area of hydrofoil surface can be very small compared to airplane wings. Overall advantages of these craft compared to other types of fast vessels of the same size are the higher cruising speed and the higher level of comfort up to wave heights preventing foil-born mode. Fig.29 shows the effect of sea state on hydrofoil speed for a submerged-foil hydrofoil ship in actual sea conditions. There is only a modest reduction in speed as wave heights increase. Principal disadvantages of hydrofoil craft are cost, limited payload capability, and large draft. Different types of hydrofoils were developed in Western Europe, USA and Japan; but about 80% of all hydrofoils have been built in the Soviet Union, both for military and fast ferry applications. While hydrofoils were largely abandoned by NATO navies in the 1980's, Russia continued operation, e.g. with the Russian fast attack patrol hydrofoil of Mukha class.

Several hybrid designs combine buoyancy and hydrodynamic lift, *Meyer (1991)*. The HYSWAS (hybrid small waterplane area single hull) is a monohull hybrid hydrofoil with a deeply submerged torpedo-like buoyancy body and hydrofoils giving 30%-70% of the required lift force, Figs.30-33, *Meyer (1992)*, *Bertram (1994)*. HYSWAS have been projected up to frigate size, but so far only the TSL-F (Techno-Superliner) demonstrator, www.khi.co.jp/products/ship/index.html, Fig.30, and the US Navy 'Quest', Fig.31, *Meyer et al. (1995)*, have been built. HYSWAS feature higher payload and larger range than pure hydrofoils at the price of a slightly reduced speed.

Pacific Marine patented in 1998 a design combining elements of a SLICE design and a hydrofoil with

smaller forward and large aft foil. In 1998, a 65-foot 52-ton technology demonstrator MIDFOIL was launched. An improved design refitted with a new lifting body was re-launched in 2000. In the modified configuration, Fig.34, the original foil was replaced with a composite three-dimensional lifting body, the angled control fins were replaced with a centerline “T” foil, and an improved ride control system was installed. MIDFOIL has demonstrated outstanding ride quality at all speeds and headings during trials in Hawaiian waters. www.navships.com/midfoil.html

Hydrofoil-assisted catamarans have been more widely accepted. A typical representative is the South African HYSUCAT, *Migeotte and Hoppe (1999)*, *Hoppe (2001)*, Fig.35, www.hydrospeed.co.za, www.unistel.com/technologies/hysucatl/. The HYSUCAT (hydrofoil supported catamaran) is a catamaran hull fitted typically with a tandem hydrofoil system. The dynamic lift reduces the wetted area of the catamaran, resulting in up to 45% resistance reduction. Several types have been built as patrol boats reaching speeds up to 50 knots. The design features good seakeeping and relatively low resistance, but the foil design is sensitive and requires tailoring towards specific design conditions.

6. Pure and hybrid air cushion vehicles

An Air Cushion Vehicle (ACV), *Lavis (1985,1992)*, is supported totally by its air cushion, with an air curtain (high pressure jet) or a flexible skirt system around its periphery to seal the cushion air. ACVs can operate at very high speeds, have low vulnerability to underwater explosions, small draft and underwater signatures, and are amphibious. However, they are affected by wind, sensitive to trim changes and have high acquisition and maintenance costs due to the seals and lift fan system and specific electronic equipment for ride-control device. Fig.36 shows the Russian landing craft (LCAC) of Pomornik class (Zubr class), currently the world’s largest ACV with 150 t payload and a maximum operating speed of 63 knots. The Greek Navy operates 4 of such boats as well. Fig.37 shows the Russian landing craft (LCAC) of Aist class (Dzheyran class). Its operating speed is 70 knots. Fig.38 shows the USN LCAC I, *Bobeck (1992)*. Beyond its basic mission of transporting personnel and equipment from ship to shore, LCAC I has become a multi-mission craft. LCAC I is an effective mine-hunter-sweeper or a troop carrier. The Finnish navy has started a ‘squadron 2000’ of future fast combat vehicles with the ACV ‘Tuuli’, Fig.39, *N.N. (2002b)*. The 50-knot ACVs are designed for year-round operation allowing also moving over ice.

Air cushion catamarans, *Butler (1985)*, *Lavis and Spaulding (1991)*, are commonly known as SES (surface effect ships), although there is no surface effect involved. SES are able to operate at high speeds ($V > 40$ knots, $F_n > 1.0$), have reduced underwater signature levels and improved shock resistance to underwater explosions, good platform stability, shallow draft, and large deck area. Disadvantages are speed loss in head seas, the loss of amphibious capability compared to the ACV, and relatively high production and maintenance costs. Examples of this type of craft are: The French AGNES-200, in 1992 the largest SES in the world with 250 t displacement, the German MEKAT class ‘Corsair’ Blohm+Voss, Fig.40, *N.N. (1989)*, *Bohlayer (1999)*, the Norwegian Oksøy class mine-hunter, and the Norwegian Skjold class fast patrol boat, *Kilhus (2001)*, Fig.41, and the Russian missile corvette ‘Bora’ (SES with hydrofoils, 53 knots), Fig.42, and the Swedish stealth SES ‘Smyge’, Fig.43, www.canit.se/~griffon/diverse/miltech/stealthships.html. Raytheon resorted also to SES technology in its design study for the US ‘Littoral Combat Ship’, Fig.44.

Air-cavity ships (ACS) have been investigated for some time in the Soviet Union, Fig.45, and more recently also in Western Europe, www.dkgroup.dk/design.html. The basic idea is to use of bottom ventilation to reduce friction resistance. Air is supplied under the specially profiled bottom, Fig.46, so that a steady air layer is formed separating a considerable part of the bottom from direct contact with water. Around the cavity are rigid bottom sections which are in stationary contact with water, however the layer is much thinner and smaller than for an SES. The side hulls are planing. The ACS uses 1.5-2.5% of the engine power for the air cavity compared to typical 20-30% for an SES. Air escapes constantly at the back end of the cavity, thus requiring a constant new supply of air and the concept is only attractive at higher speeds, *Matveev (2003)*, www.hydrofoils.org.



Fig.35: HYSUCAT (South Africa)



Fig.36: Russian landing craft Pomornik class



Fig.37: Russian landing craft Aist class



Fig.38: USN LCAC I, www.tmls.textron.com



Fig.39: Finnish ACV 'Tuuli'



Fig.40: German 'Corsair', www.blohmvooss.com



Fig.41: Norwegian Skjold class SES



Fig.42: Russian missile corvette 'Bora'



Fig.43: Swedish SES 'Smyge'



Fig.44: SES project of Raytheon for US LCS ship



Fig.45: Sokzhoy, 55 knot Air Cavity Ship

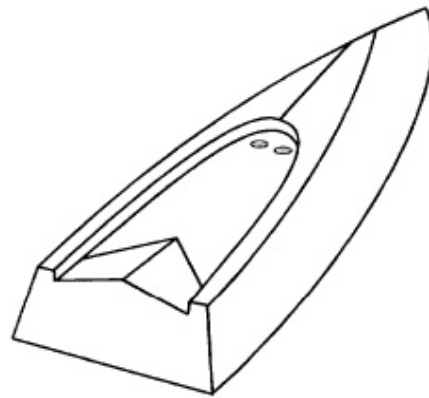


Fig.46: Bottom geometry of Air Cavity Ship



Fig.47: 'SeaCoaster' bottom view

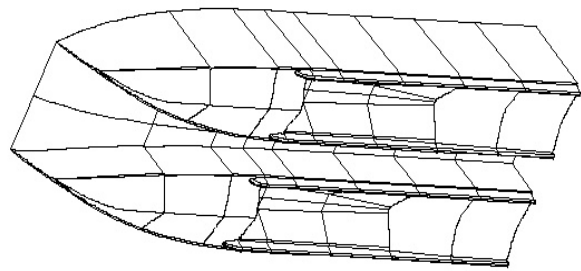


Fig.48: Micro-bubble drag reduction catamaran



Fig.49: 'Caspian Sea Monster' built 1966

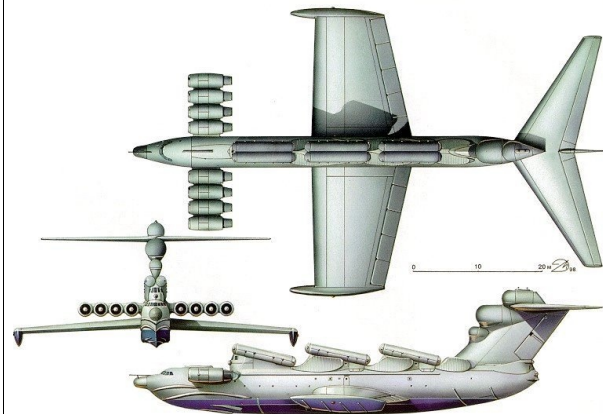


Fig.50: Russian missile launcher 'Lun' WIG

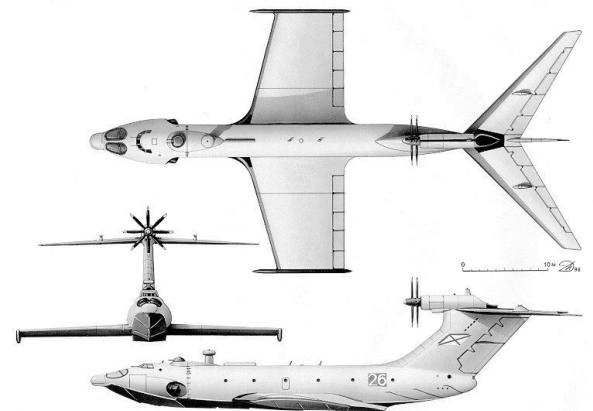


Fig.51: WIG 'Orlyonoks' (built in 1973); plan (left) and unloading an armored carrier (right)



> Avec la fin de la guerre froide et la chute vertigineuse des moyens financiers soviétiques, les projets militaires furent mis de côté et leurs enseignements exploités à des fins civiles, comme le montre cette chronologie de la flotte russe d'avions à effet de sol...

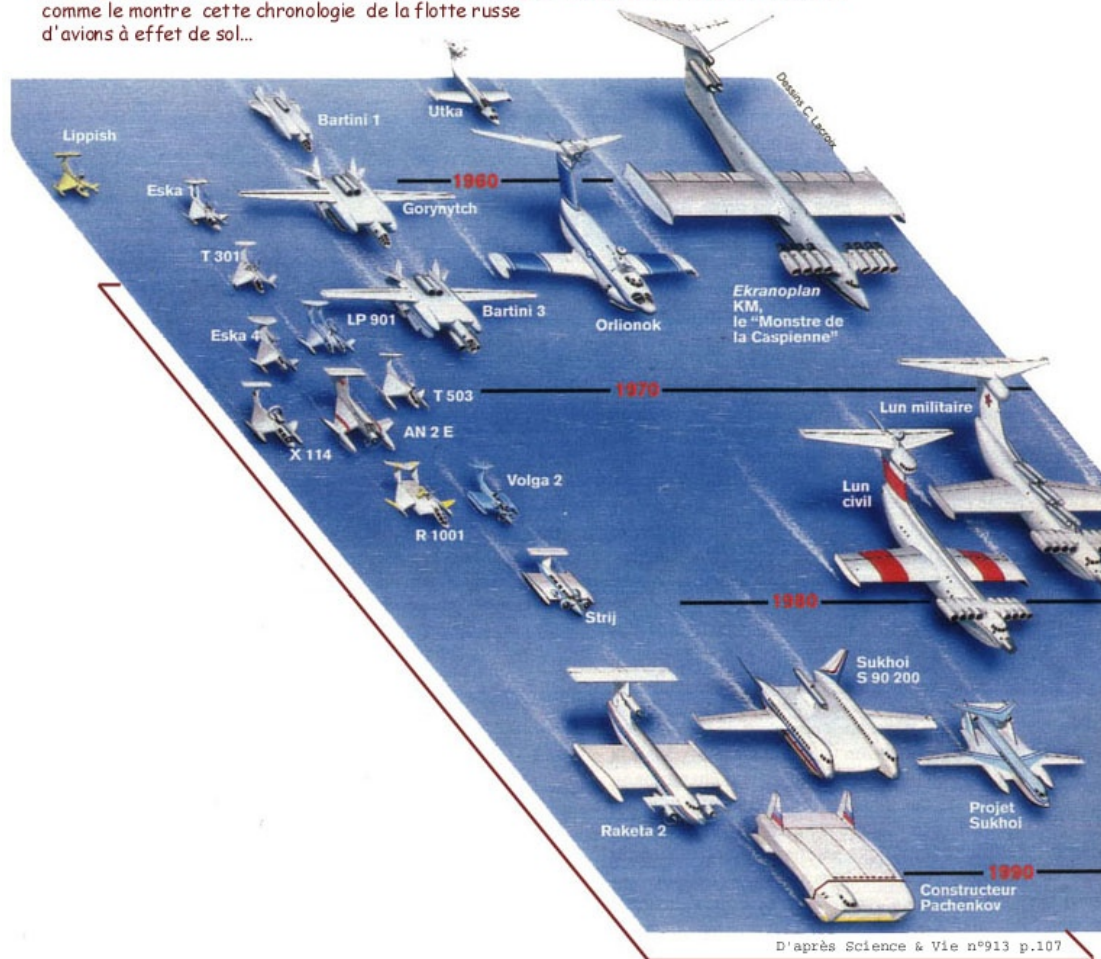


Fig.52: Overview of WIG developments, jpcolliat.free.fr/ekra/ekraA.html



Fig.53: WIG ferry Flightship



Fig.54: Atlantis I – WIG project



Fig.55: Stolcraft



Fig.56: Tunnel boat

Fig.47 shows an image of the 'SeaCoaster'. Recesses are built into the underside of each catamaran side hull. When pressurized air is supplied to the recesses, the pressurized air cushions support about 80% of total displacement. This results in a decrease in draft and a substantial reduction in wetted area resistance and impact. Total power requirements including fans for the air-cushions is only 60% of a conventional catamaran, *N.N. (2002c)*. The SeaCoaster is used since 1999 as a fast ferry on Lake Erie. A related idea to reduce frictional drag is using micro-bubbles. In the USA, a catamaran has been fitted with a micro-bubble drag reduction (MBDR) system, Fig.48. This vessel uses two micro-bubble injections from the vertical hull sides. After initial model tests, full-scale trials with a 16.6 m catamaran were completed in July 2001. Full-scale trials recorded a 2.5-3% speed increase at 40-45 kn, *Latorre et al. (2002,2003)*. Japanese researchers have also worked extensively on micro-bubble drag reduction, www.nmri.go.jp/spd/drag/drag2e.htm

7. Pure and hybrid aerodynamic lift vehicles

The wing-in-ground (WIG) or ekranoplan is essentially an aircraft flying close to the water surface exploiting the 'ground effect' which improves the drag/lift ratio of a foil, *Butler (1985)*, *Hooker and Terry (1992)*, jpcolliat.free.fr/ekra/ekraA.html, www.se-technology.com, operating at speeds of 100 to 500 km/h. WIGs could be an efficient replacement of conventional transport systems (ships, aircraft) on existing routes and also where there is no infrastructure such as airports. Due to the ground effect, WIGs are much more fuel efficient than airplanes. A main problem with WIG technology is the power requirement for take-off, which is several times larger than that required for cruising and determines thus the installed power. There are also safety concerns for craft operating in densely populated areas at such speed and low altitude. Some WIGs like the Soviet 'Caspian Sea Monster' (550t, 500 km/h), Fig.49, and the 'Lun' (400t, 450 km/h), Fig.50, are larger than a Boeing 747! Fig.51 shows the 110 t Soviet 'Orlyonoks', a troop and assault vehicle transport operating at 400 km/h (payload of 15 t). There is limited WIG experience outside Russia, Fig.52. The German military developments of WIGs were stopped some years ago. However, under the sponsorship of the German Ministry of R&D a program was started in the commercial field for the development of a 80 passenger WIG ferry, *Hynds (2000)*, based on the Hoverwing family, Fig.53, *Fischer and Matjasic (1998,1999)*. Such a WIG classified by Germanischer Lloyd operates now as fast ferry in Australia. The US Atlantis 1 project contemplates a WIG design for fast troop transport, Fig.54, i.e. with 5000 t total weight (incl. 1500t payload) a much bigger WIG than ever built, *Losi (1995)*.

The Stolkraft hull form, Fig.55, has been exhaustively model tested at the US Naval Surface Warfare Center (NSWC) and at MARIN in the Netherlands. The hull form combined planing, aerodynamic lift and displacement buoyancy. At high speeds the vessel will plane with minimal wake and with 80% of its weight supported by the dynamic forces. www.artanderson.com/stolkraft/hulldesign.html, www.intbrokers.com.au/stolkraft/stolkraft.html. The Tunnel boat combines similarly aerodynamic lift with a planing hull, Fig.56. The planing component contributes to a stable and controlled 'flight'. The tunnel roof and the upper deck surface form an aerofoil, giving the major part of the lift. www.funrcboats.com/, <http://boatdesign.net/articles/tunnel-hull-design/>

5. Summary

The development of high-performance marine craft is far from being finished. New concepts evolve, particularly attractive for navy and fast ferry applications.

Acknowledgement

We thank our assistants. Pauline Prönnicke performed valuable Internet research for references and pictures.

References

- ACAMPORA, B. (1995), *SM Racer: Design and operation of one of the world's fastest monohulls*, Marine Technology 32/3, pp.197-208
- ANEP (1996), *The application of costing and operational effectiveness methods for the selection of hull types*, ANEP 52, NATO
- AZCUETA, R.; BERTRAM, V. (2002), *High-performance marine vehicles as naval platforms*, HIPER'02, Bergen, pp.22-33
- BERTRAM, V. (1994), *Tragflügelgestützte Hybridschiffe*, Jahrbuch Schiffbautechnische Gesellschaft, pp.355-362
- BERTRAM, V.; MARZI, J.; SCHMIDT, J. (1995), *Hybrid hydrofoil monohulls*, FAST'95, Travemünde
- BOBECK, D.F. (1992), *LCAC: A system evolution*, High-Performance Marine Vehicles Conf., Arlington, ACV113-122
- BOHLAYER, W. (1999), *High speed craft for governmental maritime services*, 1st High-Performance Marine Vehicles Conf., Zevenwacht, pp.20-27
- BORMANN, D.U. (2003), *Class 751 research and test vessel*, Naval Forces 5, pp.52-55
- BUTLER, E.A. (1985), *The surface effect ship*, Naval Engineers Journal, pp.200-258
- DUBROVSKIY, V. (2000), *SWATH seakeeping allows growth in speed*, Speed at Sea, Feb., pp.27-28
- ENGELSKIRCHEN, J.; MARZI, J. (2001), *Development of a fast displacement hull form for a RoPax day ferry*, 2nd High-Performance Marine Vehicles Conf., Hamburg, pp.139-148
- FISCHER, H.; MATJASTIC, K. (1998), *Die Nutzung des Bodeneffektes zur Verbesserung der Wirtschaftlichkeit beim Transport über Wasser*, Schiff&Hafen 6, pp.61-65
- FISCHER, H.; MATJASTIC, K. (1999), *The hoverwing technology - Bridge between WIG and ACV*, 1st High-Performance Marine Vehicles Conf., Zevenwacht, pp.72-78
- GABRIELLI, G.; von KARMAN, T. (1950), *What price speed?*, Mech. Eng. 72, pp.775-781
- GORE, J.L. (1985), *SWATH ships*, Naval Engineers Journal 97/2, pp.83-112
- HOKER, S.F.; TERRY, M.R. (1992), *Hydroaviation*, High-Performance Marine Vehicles Conf., Arlington, WS1-8
- HOPPE, K.G.W. (2001), *Recent applications of hydrofoil supported catamarans*, Fast Ferry International, September, pp.30-36
- HYNDS, P. (2000), *Commercial interest revived in WIG technology*, Speed at Sea, Feb., pp.45-48
- HYNDS, P. (2001), *SWATH designs continue to make steady headway*, Speed at Sea, Aug., pp.28-29
- JANSSON, B.O.; LAMB, G.R. (1992), *Buoyantly supported multihull vessels*, High-Performance Marine Vehicles Conf., Arlington, MH1-17
- JEWELL, D.A. (1973), *Hybrid fluid-borne vehicles*, The Senior Engineer 23/9, pp.7-11
- JEWELL, D.A. (1976), *Possible naval vehicles*, Naval Research Reviews, ONR, October
- JOHNSTON, R.J. (1985), *Hydrofoils*, Naval Engineers Journal 97/2, pp.142-199
- KILHUS, G. (2001), *Operational experience with the Skjöld-class SES-FPD's*, Jahrbuch Schiffbautechnische Gesellschaft, Springer
- LANG, T.G.; SLOGETT, J.E. (1985), *SWATH developments and performance comparisons with other craft*, Int. Conf. SWATH Ships and Advanced Multi-Hulled Vessels, RINA, pp.7-23
- LANGENBERG, H. (1995), *Fast displacement ships - An economical option for high speed*

transport, FAST'95, Travemünde, pp.283-294

LATORRE, R.; MILLER, A.; PHILIPS, R. (2002), *Micro-bubble resistance reduction for high speed craft*, SNAME Trans 110, pp.259-277

LATORRE R., MILLER A., PHILIPS R. (2003a) *Micro-bubble resistance reduction on a model SES catamaran*, Ocean Engineering 30/17, pp.2297-2309

LATORRE R., MILLER A., PHILIPS R. (2003b) *Drag reduction on a high speed trimaran*, 7th FAST Vol. I, Ischia, pp.87-92

LAVIS, D.R. (1985), *Air cushion craft*, Naval Engineers Journal 97/2, pp.259-316

LAVIS, D.R. (1992), *Hovercraft development*, High-Performance Marine Vehicles Conf., Arlington, ACV1-38

LAVIS, D.R.; SPAULDING, K.B. (1991), *Surface effect ship (SES) developments worldwide*, Naval Engineers Journal, September, pp.39-83

LOSI, P.C. (1995), *The wingship potential for strategic lift*, Industrial College of the Armed Forces, Washington, www.ndu.edu/library/ic6/95-S12.pdf

MATVEEV, K.I. (2003), *Air cavity ships are ready for a wider market*, Speed at Sea 9(1), pp.13-16, <http://docs.hydrofoils.org/acs.pdf>

MEYER, J.R. (1991), *Hybrid hydrofoil technology - An overview*, FAST'91, Trondheim, pp.623-640

MEYER, J.R. (1992), *Hybrid hydrofoil technology applications*, High-Performance Marine Vehicles Conf., Arlington, HF25-36

MEYER, J.R.; DeVENY, J.A.; JORDAN, P.D. (1995), *HYSWAS concept demonstrator*, Int. Hydrofoil Society 25th Anniversary Conf., Arlington, pp.203-213

MEYER, J.R.; WILKINS, J.R. (1992), *Hydrofoil development and applications*, High-Performance Marine Vehicles Conf., Arlington, HF1-24

MIGEOTTE, G.; HOPPE, K.G.W. (1999), *Developments in hydrofoil assistance for semi-displacement catamarans*, FAST'99, Seattle, pp.631-642

MORET, J.A.; GEE, N. (2001), *The pentamaran fast ferry – The ultimate step forward in passenger and cargo transportation at high speed*, www.wemt.nl/papers.htm

MOSS, S. (2001), *A wave-piercing catamaran as fast troop transport vessel*, Jahrbuch Schiffbautechnische Gesellschaft, Springer

N.N. (1989), *Lufkissen-Katamaran SES "Corsair", ein neuartiges Hochgeschwindigkeitsfahrzeug*, Hansa 126/11,12, pp.800-801

N.N. (2002a), *FLW, Specialist of naval craft*, Hansa 139/9, pp.178-183

N.N. (2002b), *Finnish hovercraft Tuuli*, Hansa 139/7, pp.53

N.N. (2002c), *Survey of alternative waterborne technologies*, Appendix C in The Survey of Transit Technologies, rttg.org/pdf/alt-tech/Appendix_C.pdf

N.N. (2003), *Three industry teams selected for LCS preliminary design*, Warship Technology, October, pp.12-13

PAPANIKOLAOU, A. (1996), *Developments and potential in open sea SWATH concepts*, WEGEMT workshop Conceptual Designs of Fast Sea Transportation, Glasgow

PAPANIKOLAOU, A. (2001), *Review of advanced marine vehicles concepts*, Norwegian Maritime Technology Forum

RITTER, O.K.; TEMPLEMAN, M.T. (1998), *High Speed Sealift Technology Vol.1*, Report CDNSWC-TSSD-98-009, www.ccdott.org/hss_volume2/01_hss_workshop_tech.pdf

- SAVITSKY, D. (1985), *Planing craft*, Naval Engineers Journal 97/2, pp.113-141
- SCHENZLE, P. (2002), *Wind propulsion for coastal and ocean transport*, 1st World Wind Energy Conf., Berlin
- SCHMIDT, T.W. (2001), *Technology for the 21st century: SLICE - A revolutionary new ship*, Jahrbuch Schiffbautechnische Gesellschaft, Springer
- SMITH, R.P.; JONES, J.B. (2001), *Design, construction and trials of the trident trimaran test craft*, Jahrbuch Schiffbautechnische Gesellschaft, Springer
- SÖDING, H. (1997), *Drastic resistance reduction in catamarans by staggered hulls*, FAST'97, Sydney, pp.225-230
- SPETHMANN, K. (2000), *Nach Ablieferung des Stationsschiffes "Elbe" ist das neue Lotsenversetzsystem komplett*, Schiff&Hafen 10, pp.121-130
- SPETHMANN, K. (2001), *A realised SWATH-application as an example for naval purposes*, Jahrbuch Schiffbau-Technische Gesellschaft, Springer

Careful Selection of a Planing Boat's Hull Form Parameters

Yasushi Yoshida, Technical University of Varna¹/Japan, yyoshida@fg8.so-net.ne.jp

Abstract

A planing boat's resistance has been estimated by non-dimensional values made of length, half width and chine height at midship, and initial trim angle. The parameters have been selected by applying principal component analysis to the data of a series of towing tank tests by using thirteen kinds of 2.5m length models up to 3.5 in Froude number based on displacement volume. The estimation has been checked against the PT boat's propulsive coefficient, thrust and scale effect, showing reasonable values. The parameters are compared with those three other ships (planing boat, fishing boat, merchant ship).

Nomenclature

C_f	frictional resistance coefficient
C_i	set of coefficients
C_t	model's total resistance coefficient (total resistance divided by $(\frac{1}{2}) \rho V^2 (\sqrt[3]{\nabla})^2$)
d_i	set of coefficients
EHP	effective horsepower
F	Froude number based on displacement volume: $F=V/\sqrt{g \cdot \sqrt[3]{\nabla}}$
$F(\mathbf{X})$	Prediction such as resistance, EHP, etc.
f_i	set of coefficients
R_S	total resistance at speed V_S
S	wetted surface area
T	thrust
V	velocity
\mathbf{X}	set of hull form parameters X_1, X_2, X_3 , etc.
Z_i	set of principal components $Z_1 > Z_2 > Z_3 > Z_4$ (eigenvalue's order)
ΔD	non-dimensional draft change at transom (draft change divided by $\sqrt[3]{\nabla}$), positive for draft decrease
$\Delta \theta$	trim angle change; positive for bow up
∇	displacement volume
ρ	density

(Yoshida's planing boat hull form)

b_1	half width at Ord.10 (stern)
b_2	half width at Ord.5 (midship)
b_3	half width at Ord.2
H_3	keel height at Ord.2
H_4	keel height at Ord.0 (bow)
h_1	chine height at Ord.10
h_2	chine height at Ord.5 (midship)
h_3	chine height at Ord. 2
L	length from Ord.0 through 10
ℓ	transom's overhang
θ	initial trim angle
χ_i	set of non-dimensional hull form parameters

1 Formerly Wessex Institute of Technology, UK
Warship Research Division of First Research Center in Japan Defense Agency's Technical Research and Development Institute, Japan

(Keuning's et al. planing boat hull form)

$A_p/\sqrt[3]{\nabla}$	planing area
L	planing length
LCG	ratio of distance from stern through center of gravity to planing length
L/Bpx	ratio of planing length to width

(Tsuchiya's fishing boat hull form)

B/T	ratio of maximum width under water to draft at midship
C_M	coefficient of cross section at midship
L	total length
LCB	distance between midship and center of gravity
t/L	tangent of trim angle
α_{BS}	angle of buttock line's slope
$0.5\alpha_e$	bow's incident angle into water plane
$0.5\alpha_r$	stern's angle at water plane
ξ_i	set of non-dimensional hull form parameters

(Tagano's merchant ship hull form)

B	width at midship
d	draft
C_m	coefficient of cross section at midship
L	total length
LBd/∇	reciprocal of block coefficient

1. Introduction

Although planing boat hulls are traditional, there are few reasonable design bases. Engineers typically have to design boats by the method of trial and error through their experience and sense. At higher speeds, planing boats change their floating position, complicating the prediction of their resistance performance. Dynamic lift together with arranging trim tabs at the transom (which may be considered as increasing the boat's overall length) should be taken into consideration together with resistance. These phenomena complicate analyses and the design process to the point where some naval architects have stopped relying on theoretical-based work to results for design work.

Experimental analyses require (1) tanks in which large models can be towed with high speed and (2) a long time against damping of wave after a towing test. Few such towing tanks produce the experimental data. Recent advances in advanced numerical approaches have not really changed the situation and the demand for simple, practical design tools remains.

Nagai and Yoshida (1993) presented coefficients of quadratic equations to estimate a set of C_t , $\Delta \theta$ and ΔD (called "resistance performance") of a planing boat model. The equations were based on data of a series of the towing tank tests using thirteen kinds of 2.5m length models in Japan Defense Agency's Towing Tank (Meguro Towing Tank, Tokyo), *Nagai and Yoshida (1993)*, *Degtyarev et al. (1998)*, *Yoshida (1999)*. Each model's displacement and center of gravity was changed by six ways, which makes 78 data. The equations covered Froude numbers up to 3.5 in intervals of 0.5. The resistance performance of the PT boat, *Raymond and Blackmann (1975-1976)*, was estimated by the equations up to Froude number 3.0 (top speed). The estimation was checked against the PT boat's trial test data. The propulsive coefficient is about 50%, which is a reasonable value. Trim angles were under-estimated for all Froude numbers. Further checks against the equation and careful selection of hull form parameters will be clarified. For the first time the prediction of resistance performance against scale effect 1:14 will be shown with the check of the full-scale's thrust.

2. Principal Component Analysis

2.1 Principal component axes

Fig.1 shows the model's principal dimensions. Initially eleven non-dimensional hull form parameters were selected, Fig.2, which enable us to draw a minimum lines plan.

The correlation matrix is made from the total hull form data (11×78), which shows all correlation coefficients of each pair of hull form parameters. Principal component analysis to the matrix give us principal component axes Z_i , $i=1, 2, 3$, and 4. Z_1 is the predominant axis, Z_2 next to Z_1 , Z_3 next to Z_2 etc. in eigenvalue or data distribution direction. Z_4 's eigenvalue is greater than 1. The axes are perpendicular to each other. Each Z_i can be expressed by a linear equation of the eleven hull form parameters in Fig.2. Each hull form parameter's coefficient is called as a factor load, which means the correlation coefficient between the hull form parameter and the axis Z_i . The coefficient is also the element of Z_i 's eigenvector. Taking scores by these axes, we can see the distribution of all data like an ellipse on the rectangular coordinates of Z_1 , Z_2 and Z_3 . Large coefficients in absolute value on each axis are selected in Fig.2 to look at the axis' characteristics, which enable us to make the standard of discussing hull form parameters. More than 0.60 in absolute value is selected in Fig.2.

2.2 The axes' characteristics

2.2 (a) Z_1

Judging from the four major factor loads on Z_1 in Fig.2, we regard Z_1 as "the axis of chine height and width" or "the axis of cross section". We call Z_1 "axis of cross section" from now on.

2.2 (b) Z_2

Judging from the three major factor loads on Z_2 in Fig.2, we regard Z_2 as "the axis of length and transom" or "the axis of planing area". Considering that the theme is a planing boat, we call Z_2 "axis of planing area" from now on. Similarly Z_3 and Z_4 are as follows:

2.2 (c) Z_3

Z_3 "the axis of width".

2.4 (d) Z_4

Z_4 "the axis of initial trim angle".

According to these axes, each hull form's parameters were arranged to predict total resistance, EHP and wave resistance etc., Fig.3.

3. Yoshida's hull form parameters

3.1 Boat's total resistance

A planing boat's total resistance R_s at speed V_s is expressed as:

$$R_s = [C_t - \{ C_{fm} S_m / (\sqrt[3]{\nabla m})^2 \}]^{(1/2)} \rho_s (\sqrt[3]{\nabla s})^2 V_s^2 + C_{fs}^{(1/2)} \rho_s S_s V_s^2 \quad (1)$$

"m" of each suffix is taken for a model, "s" for a boat. The equation is derived from the same residual resistance coefficient at a Froude number between model and boat. C_t is obtained by the Eqs. (2) to (4) in the next section, which were derived by principal component analysis.

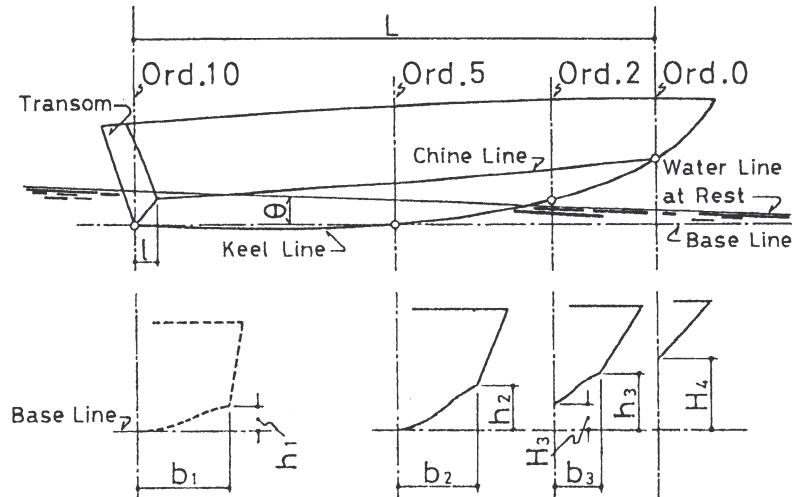


Fig.1: Principal dimensions, which enable us to draw a minimum lines plan

	Z_1	Z_2	Z_3	Z_4
$h_1/\nabla^{1/3} (= \chi_2)$				
$h_2/\nabla^{1/3} (= \chi_3)$	0.87			
$h_3/\nabla^{1/3} (= \chi_4)$	0.93			
$H_3/\nabla^{1/3} (= \chi_5)$				
$H_4/\nabla^{1/3} (= \chi_6)$	0.96			
$L/\nabla^{1/3} (= \chi_7)$		-0.61		
$b_2/\nabla^{1/3} (= \chi_8)$	0.63		-0.65	
$b_3/\nabla^{1/3} (= \chi_9)$			-0.78	
$\ell/\nabla^{1/3} (= \chi_{10})$		0.89		
$\theta (= \chi_{11})$				-0.65
$b_1/\nabla^{1/3} (= \chi_{12})$		0.80		

Fig.2: Hull form parameters' major factor loads at each axis

	Yoshida's Planing Boat	Keuning's et al. Planing Boat	Tsuchiya's Fishing Boat	Tagano's Merchant Ship
F(X)	Total Resistance & Floating Position		EHP	Wave Resistance
Z ₁	b ₂ / $\sqrt[3]{\nabla}$ (χ_8) h ₂ / $\sqrt[3]{\nabla}$ (χ_3) H ₄ / $\sqrt[3]{\nabla}$ (χ_6) h ₃ / $\sqrt[3]{\nabla}$ (χ_4)		B/T (ξ_2) C _M (ξ_3) 0.5 α_e (ξ_6)	B/d C _m LBd/ ∇
Z ₂	L/ $\sqrt[3]{\nabla}$ (χ_7) b ₁ / $\sqrt[3]{\nabla}$ (χ_{12}) ℓ / $\sqrt[3]{\nabla}$ (χ_{10})	L/B _{px} A _p / $\sqrt[3]{\nabla}$	L/ $\sqrt[3]{\nabla}$ (ξ_1) 0.5 α_r (ξ_7) α_{BS} (ξ_8)	LBd/ ∇
Z ₃	b ₂ / $\sqrt[3]{\nabla}$ (χ_8) b ₃ / $\sqrt[3]{\nabla}$ (χ_9)		B/T (ξ_2)	B/L B/d LBd/ ∇
Z ₄	θ (χ_{11})	LCG	LCB t/L (ξ_5) (ξ_9)	
F	0.5 – 3.5	0.75 – 3.0	0.45 – 0.80	0.3 – 0.65
Terms	5, 7, 44	13	72	Selected-point Numbers
Power	1, 2	3	4	7 (Coefficients 4 + Curve 3)

Points that are used to form prismatic curve

Fig.3: Hull form parameters, term numbers and max. power in equation, applicable speed range

3.2 Model's resistance performance

A set of C_t , $\Delta \theta$ and ΔD is called "resistance performance". C_t is a model's total resistance coefficient predicted by the empirical equation made of four non-dimensional hull form parameters as Eq.(2). The parameters are length, half width and chine height at midship, and initial trim angle, which have major factor loads on the axes in Fig.2. Major factor load means more than 0.60 in correlation coefficient's absolute value.

$$C_t = d_0 + d_1 h_2 / \sqrt[3]{\nabla} + d_2 L / \sqrt[3]{\nabla} + d_3 b_2 / \sqrt[3]{\nabla} + d_4 \theta \quad (2)$$

Also $\Delta \theta$ and ΔD , which are necessary to determine the floating position of a model, are expressed by this kind of linear equation.

Adding two squared hull form parameters, namely length and initial trim angle, to Eq.(2), yields the quadratic equation, *Nagai and Yoshida (1993)*:

$$C_t = f_0 + f_1 h_2 / \sqrt[3]{\nabla} + f_2 L / \sqrt[3]{\nabla} + f_3 b_2 / \sqrt[3]{\nabla} + f_4 \theta + f_5 (L / \sqrt[3]{\nabla})^2 + f_6 \theta^2 \quad (3)$$

If we want to use eleven hull form parameters to predict resistance performance, two kinds of equations are considered. The first one is the linear equation made of eleven hull form parameters in Fig.2. The second one is the linear equations made of principal components as in Eq.(4).

$$C_t = C_0 + C_1 Z_1 + C_2 Z_2 + C_3 Z_3 + C_4 Z_4 \quad (4)$$

The four principal components have no relation to each other. Then Eq.(4) has the highest accuracy among these kinds of equations. As each principal component term has eleven terms, the total number of terms is 44. These eleven hull form parameters are used to obtain a set of optimum hull form parameters and draw the plan, *Degtyarev et al. (1998)*, *Yoshida (1999)*.

In initial design, Eqs.(2) and (3) are used because they contain the major hull form parameters and are concise. Both equations have reasonable accuracy. As an example, the PT boat's total resistance is predicted in Fig.4. The PT boat has 35m in overall length, 9m in width, 133 tons in displacement and three propellers, *Raymond and Blackmann (1975-1976)*. The total resistance values by the Eqs.(1), (2) and (3) have been checked against the total thrust values from the trial test data, *Yoshida (2002a)*, showing that the estimate is reasonable. Trim angle changes by Eqs. (2) and (3) under-estimated the PT boat's trial test data, Fig.5. It is due to scale effects, *Yoshida (2002b)*. *Sottorf (1938)* showed the scale effect of rectangular plate models under several scale ratios, Fig.6. Then the limitation of Yoshida's equations may be about 25m in overall length.

4. Discussion

4.1 Cross section

The planing boat's cross section is a main factor for its contribution to the total resistance. The main part of the cross section at midship seems to be shaped by the isosceles triangle having the deadrise angles' both alternate angles on the width $2b_2$'s ends in Fig.1. Chine height h_2 and half width b_2 at midship determine the deadrise angle. The cross section was not selected directly as a parameter for two reasons: From low speed to high speed the correlation coefficients at midship between total resistance coefficient and the cross section, between total resistance coefficient and the chine height and between total resistance coefficient and the width had similar tendency in the whole speed range, Table I. The cross section, the chine height and the width have highly correlated to each other, which explains the similar tendency. If we use a pair of the terms having high correlation coefficient each other in these kinds of equations, the sign of the terms will be irregular.

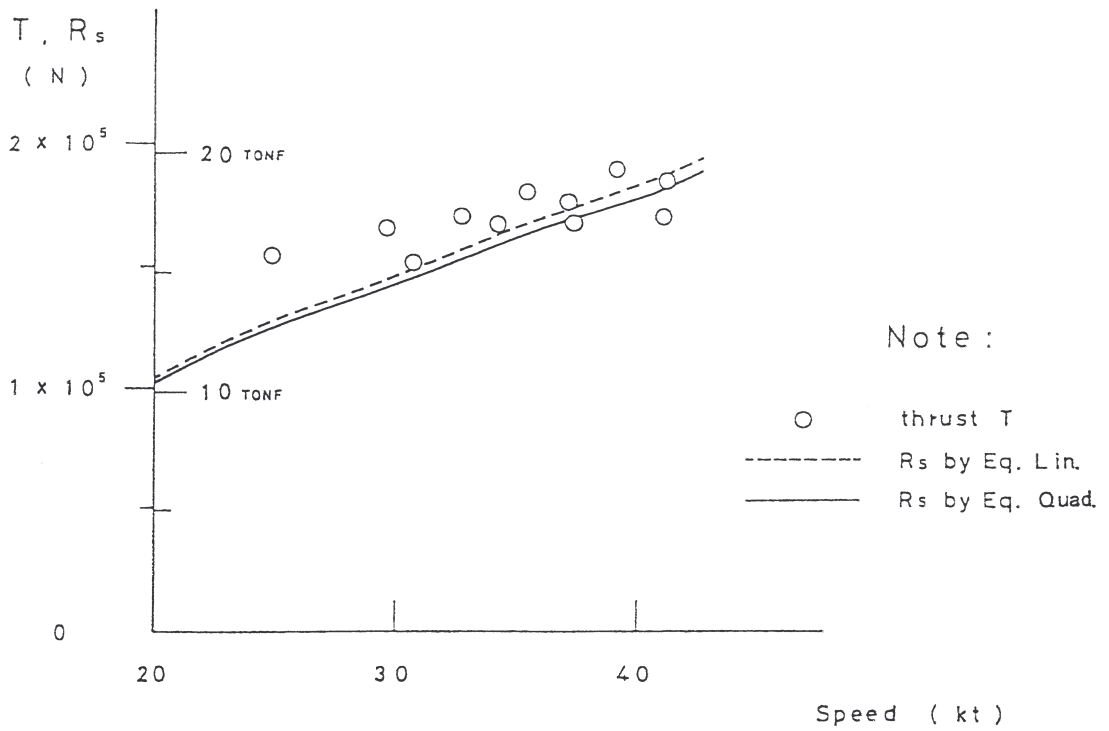


Fig.4: Thrust balances with resistance at top speed; additional thrust is confirmed up to top speed

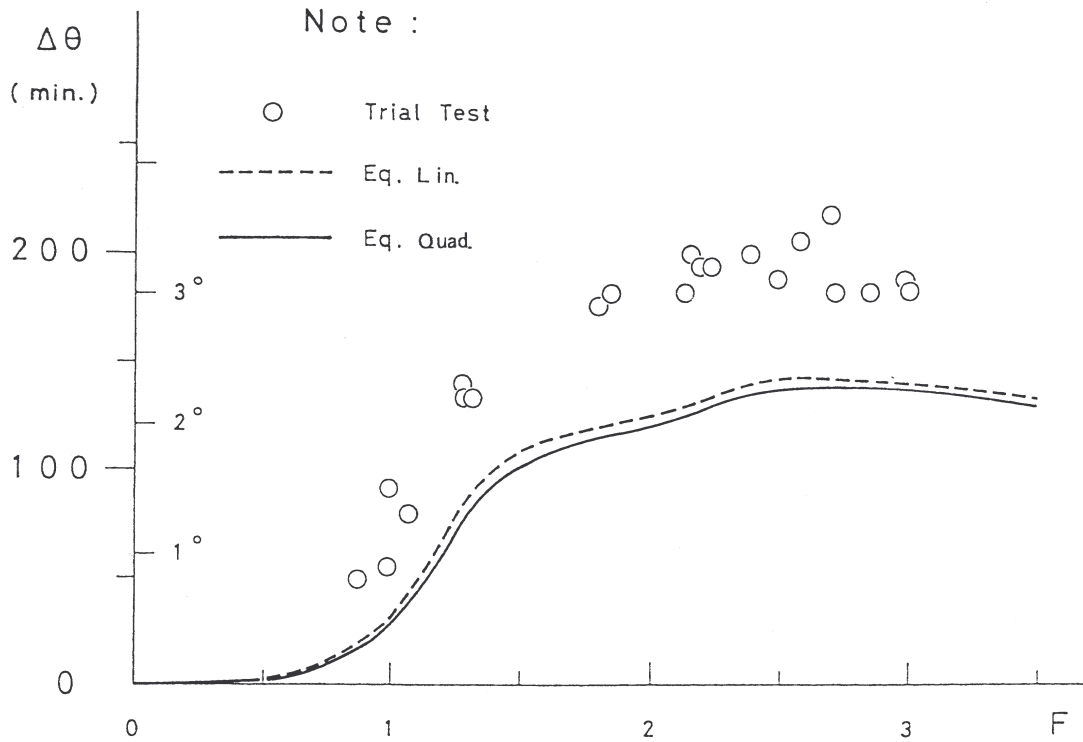


Fig.5: Trim angle change is under-estimated for all Froude numbers

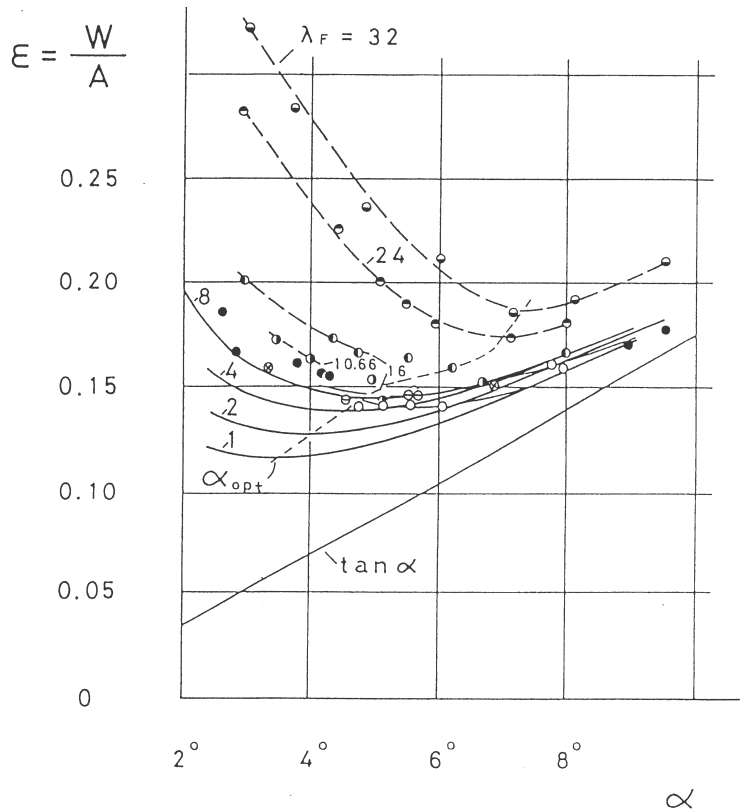


Fig.6: Scale effect λ begins about 1:10 in scale ratio, *Sottorf (1938)*

Each term's sign of the Eq.(2) is almost correct because the terms are independent from each other. For example, increasing length decreases total resistance, thus length's sign must be minus. All signs have been checked in such a way. As the second reason, designers face the problem how to decide chine height and deadrise angle for given cross section. Then including chine height and deadrise angle in the equation is desirable.

Keeping width constant, a hull form with higher chine height (sharp pointed bottom) gets less total resistance for low speeds and more total resistance for high speeds, Table I.

Table I: Correlation coefficients between total resistance coefficient and cross section, etc. at midship

F	0.5	1.0	1.5	2.0	2.5	3.0	3.5
Cross Section	-0.68	-0.35	-0.44	-0.19	0.88	0.66	0.00
Chine Height	-0.73	-0.35	-0.43	-0.28	0.30	0.57	0.00
Width	-0.32	-0.19	-0.29	-0.00	0.42	0.52	0.00

The centreline contour, Fig.1, (chine line H_4 - h_3 - h_2 or bow shape) affects the flow or total resistance.

$b_2/\sqrt[3]{\nabla}$, $h_2/\sqrt[3]{\nabla}$, $H_4/\sqrt[3]{\nabla}$ and $h_3/\sqrt[3]{\nabla}$ are included in Z_1 .

Tsuchiya (1972) selected B/T and C_M as cross section factor and $0.5\alpha_e$ against flow to predict EHP of a fishing boat. *Tagano (1973)* selected B/d and C_m as cross section factor to predict wave resistance of a merchant ship.

4.2 Planing area

Lengths L and ℓ , Fig.1, affect the wetted length of the plan area and thus the total resistance. The area at water plane level is mainly determined by the isosceles triangle having perpendicular L to the middle of the width $2b_1$ at transom. The apex corresponds to the incident angle against flow.

$L/\sqrt[3]{\nabla}$, $b_1/\sqrt[3]{\nabla}$ and $\ell/\sqrt[3]{\nabla}$ are included in Z_2 .

Keuning et al. (1993) selected L/B_{px} and $Ap/\sqrt[3]{\nabla}$ to predict resistance performance of a planing boat.

Although the fishing boat does not get into planing, *Tsuchiya (1972)* selected $L/\sqrt[3]{\nabla}$, $0.5\alpha_r$ and α_{BS} by evaluating the area at water plane level to predict EHP of a fishing boat.

4.3 Width

The width at Ord.2 and 5 in Fig.1 are important factors for the hull form. The author selected $b_2/\sqrt[3]{\nabla}$ and $b_3/\sqrt[3]{\nabla}$ in Z_3 . *Tsuchiya* selected B/T to predict EHP of a fishing boat. *Tagano* selected B/L and B/d to predict wave resistance of a merchant ship.

4.4 Initial trim angle

The location of center of gravity is connected with the initial trim angle. The author selected θ in Z_4 . Setting center of gravity toward the transom is desirable to get fine planing. Porpoising will occur for center of gravity near the bow. *Keuning et al.* selected LCG to predict resistance performance of a planing boat. *Tsuchiya* selected LCB and t/L to predict EHP of a fishing boat.

4.5 Block coefficient

Tagano selected LBd/∇ to predict wave resistance of a merchant ship. LBd/∇ is connected with previous sections 4.1 through 4.3.

5. Keuning's et al. hull form parameter

Keuning et al. (1993) have selected hull form parameters from the consideration of the model tests by *Clement and Blount (1963)*. L/B_{px} , $Ap/\sqrt[3]{\nabla}$ and LCG were selected. $Ap/\sqrt[3]{\nabla}$ on water plane will make an approximate isosceles triangle having the perpendicular L/B_{px} to transom, which we may call planing area. The isosceles triangle on water plane together with the location of the center of gravity is the essence of discussion on planing phenomenon. But there are two problems in the view of designers:

- (1) How to determine the principal dimension of the planing area and
- (2) How the change of deadrise angle should be dealt with.

6. Equations

6.1 Yoshida's equation

Eq.(2) has five terms, Eq.(3) seven, Eq.(4) 44. In addition to three kinds of equations, the author has a linear equation composed of eleven hull form parameters expressed by χ_i , $i=2,3,\dots,12$. (See Fig.2). The highest power is 2. Yoshida's equations should be used to predict a planing boat's resistance and floating position up to Froude number 3.5. The equations are obtained at intervals of

0.5 in Froude number. The wetted surface area at a floating position enables us to calculate the frictional resistance. Excepting the clean condition on transom, the author regards the wetted surface area as the area the under water plane. The maximum wave resistance occurs at about 1.0 in Froude number. For Froude numbers slightly above 1.0, the transom stern clears. Semi-planing starts at Froude numbers around 2.0, planing around Froude number 2.5.

6.2 Keuning's et al. equation

The equation has 13 terms. The highest power is 3. The equation should be used to predict a planing boat's total resistance and floating position up to Froude number 3.0.

6.3 Tsuchiya's equation

The equation has 72 terms. The hull form parameters ξ_i , $i=1,2,\dots,9$ are used. The highest power is 4. His equation should be used to predict a fishing boat's EHP up to Froude number 0.8. The author converted length based Froude number into displacement volume based Froude number, referring to *Komatsu and Yamaguchi (1989)*. A fishing boat has complex hull form and is used in lower speed range.

6.4 Tagano's equation

The number of terms is equal to the plotted point numbers to form the prismatic curve. The highest power is 7. Power 4 is used for coefficients and power 3 for curve. His equation should be used to predict a merchant ship's wave resistance up to Froude number 0.65. The Froude number was converted as for Tsuchiya's equation, *Komatsu and Yamaguchi (1989)*. A merchant ship's main part has nearly similar cross section and the ship is used in lower speed range.

7. Conclusions

(1) After extensive model tests and the full-scale tests, practical equations together with important hull forms to predict resistance performance have been obtained. These were confirmed by thrust checks for full-scale experiments.

(2) This paper shows the scale effect. Sottorf's (1938) data using the rectangular plates in Hamburg Ship Model Basin showed that the effective scale ratio is up to 1:10. The present work shows that the case of 1:14 scale is still effective for the prediction except for the trim angle change.

References

NAGAI, T.; YOSHIDA, Y. (1993), *Estimation of Resistance, Trim and Draft of Planing Craft*, Ship Technology Research, Vol.40/3, pp.133-137

DEGTYAREV, A.B.; KROLENKO, S.I.; YOSHIDA, Y. (1998), *A Mathematics for Design and Development of Optimum Hull Form Applying to Obtain a Planing Boat's Hull Form Parameter Set with the Minimum*, Proc. ISC'98 KSRI, (eds.) Spiro, V. E. & Polonsky, B. P., St Petersburg, Section A, Vol.1, pp.207-214

YOSHIDA, Y. (1999), *Optimum Design of a Planing Boat's Hull Form*, Marine Technology 3, (eds.) Graczyk, T., Jastrzëbski, T. & Brebbia, C. A., WIT Press, Southampton, Boston, pp.3-13

RAYMOND, V.; BLACKMANN, B. (eds.) (1975-1976), *Jane's Fighting Ships*, London, p.213

YOSHIDA, Y. (2002a), *Apply Tanaka's Nomogram to the PT Thrust Estimation*, Int. Conf. High Speed Craft Technology and Operation of RINA, London, pp.125-131

- YOSHIDA, Y. (2002b), *A Scale Effect Check about Resistance Estimation of Planing Boats*, 3rd Int. Conf. High-Performance Marine Vehicles (HIPER'02), Bergen, pp.448-456
- SOTTORF, W. (1938), Versuch mit Gleitflächen, 4.Teil. Analyse, Werft, Reeder, Hafen, 19 Jahrgang, Heft 6, pp.66-67
- TSUCHIYA, H. (1972), *Statistical Analysis to Fishing Boat Hull Forms' Effective Horsepower*, J. Soc. Naval Arch. Japan, Vol.132, pp.63-80
- TAGANO, H. (1973), *The Statistical Method of Estimating Hull Forms' Wave Making Resistance*, J. Kansai Soc. Naval Arch. Japan, Vol.147, pp.43-52
- KEUNING, J. A.; GERRITSMA, J.; VAN TERWISGA, P. F. (1993), *Resistance Tests of a Series Planing Hull Forms with 30° Deadrise Angle, and a Calculation Model based on This and Similar Systematic Series*, Int. Shipbuild. Progr. Vol.40, No.424, pp.333-385
- CLEMENT, E.P.; BLOUNT, D.L. (1963), *Resistance Tests of a Systematic Series of Planing Hull Forms*, Trans. SNAME, Vol.71
- KOMATSU, M.; YAMAGUCHI, M.(1989), *The Propulsive Performance of High Speed Crafts*, Symp. High-speed Crafts and the Performance, Soc. Naval Arch. Japan, pp.75-118

Experimental and CFD Study of Wave Resistance of High-Speed Round Bilge Catamaran Hull Forms

Prasanta K Sahoo, Australian Maritime College, Launceston/Australia, P.Sahoo@mte.amc.edu.au
Nicholas A Browne, Australian Maritime College, Launceston/Australia,
Marcos Salas, University Austral of Chile, Valdivia/Chile, msalas@uach.cl

Abstract

Although catamaran configuration has been around for a longtime, it is only in the recent past that such hull forms have seen unprecedented growth in the high-speed ferry industry. One of the design challenges faced by naval architects is accurate prediction of the hydrodynamic characteristics of such vessels primarily in the areas of resistance, propulsion and seakeeping. Even though considerable amount of research has been carried out in this area, there remains a degree of uncertainty in the prediction of calm water resistance of catamaran hull forms. This research attempts to examine the calm water wave resistance characteristics of a series of round bilge transom stern, semi-displacement slender catamaran hull forms based on computational fluid dynamics (CFD) modeling.

While maintaining the same center of buoyancy and displacement, the influence of hull shape has been examined, specifically the effects of demi-hull spacing in the speed range corresponding to Froude numbers of 0.2 to 1.0. The results of CFD analysis have been compared with experimental towing tank results of NPL series, which closely resemble the systematic series developed here. The results obtained show considerable promise and development of an industry standard regression equation based on the data obtained from CFD analysis, model experiments and full-scale ship trials, can be seen as achievable.

1. Introduction

This paper attempts to investigate the calm water resistance for a systematic series of round bilge catamarans hull forms. The systematic series tested consists of high-speed semi-displacement hull forms. This analysis was undertaken using the computational fluid dynamics (CFD) package SHIPFLOW. SHIPFLOW is a useful alternative to model testing as the requirement to produce several different models can be very expensive. The capabilities of SHIPFLOW enable the user to obtain all of the information that model testing can produce, and therefore SHIPFLOW is commonly referred to as a numerical towing tank. The numerical results obtained were then used to carry out a regression analysis enabling a generalized equation to be produced to predict the wave resistance coefficient. The research primarily concentrated on the following:

- a) To examine the variation in C_w for a slender catamaran hull form, due to changes in the vessels slenderness ratio, while maintaining the same displacement and centre of buoyancy over the range indicated in Table 1.
- b) To examine the variation in C_w for a more general range of catamaran hull forms over a range of Froude numbers.

Table 1: Demi-hull Geometric Parameters

Geometric Parameters	$L/\nabla^{1/3}$	LCB/LCF	s/L	C_B
Range of Application	8 to 11	1.03 to 1.12	0.20 to 0.40	0.40 to 0.50

2. Literature Survey

An exhaustive literature survey had been carried out earlier Schwetz and Sahoo (2002) where various papers have been quoted regarding the resistance prediction of catamarans. Essentially the present paper was an attempt to evaluate results based purely on round bilge catamaran hull forms so as to remove some of the earlier inconsistencies faced in the paper of Schwetz and Sahoo (2002). The paper by Insel and Molland (1992) summarizes a calm water resistance investigation into high-speed semi-displacement catamarans, with symmetrical hull forms based on experimental work carried out at the University of Southampton.

Two interference effects contributing to the total resistance effect were established, being viscous interference, caused by asymmetric flow around the demihulls, which affects the boundary layer formation and wave interference, due to the interaction of the wave systems produced by each demihull. Particulars of models tested by Insel and Molland (1992) are presented in Table 2. The particulars of the models used in their investigation are presented in Table 3.

Table 2: Catamaran geometric parameters [Insel and Molland (1992)]

Geometric Parameters	$L/\nabla^{1/3}$	L/B	B/T	C_B
Range of Application	6 to 9	6 to 12	1 to 3	0.33 to 0.45

Table 3: Model Particulars [Insel and Molland (1992)]

Models	$L/\nabla^{1/3}$	L/B	B/T	C_B	LCB/L from transom
C2	7.1	10	1.6	0.44	50%
C3	6.3	7	2	0.397	43.6%
C4	7.4	9	2	0.397	43.6%
C5	8.5	11	2	0.397	43.6%

Models C3, C4 and C5 were of round bilge hull form derived from the NPL series and model C2 was of the parabolic Wigley hull form. All models were tested over a range of Froude numbers of 0.1 to 1.0 in the demi-hull configuration and catamaran configuration with separation ratios, S/L, of 0.2, 0.3, 0.4 and 0.5. Calm water resistance, running trim, sinkage and wave pattern analysis experiments were carried out.

The authors proposed that the total resistance of a catamaran should be expressed by equation (1):

$$C_{TCAT} = (1 + \phi k) \sigma C_F + \tau C_w \quad (1)$$

The authors state that for practical purposes, σ and ϕ can be combined into a viscous resistance interference factor β , where $(1 + \phi k) \sigma = (1 + \beta k)$ whence:

$$C_{TCAT} = (1 + \beta k) C_F + \tau C_w \quad (2)$$

It may be noted that for demi-hull in isolation, $\beta = 1$ and $\tau = 1$, and for a catamaran, τ can be calculated from equation (3).

$$\tau = \frac{C_{W\,CAT}}{C_{W\,DEMI}} = \frac{[C_T - (1 + \beta k) C_F]_{CAT}}{[C_T - (1 + k) C_F]_{DEMI}} \quad (3)$$

The authors conclude that the form factor, for practical purposes, is independent of speed and should thus be kept constant over the speed range. This was a good practical solution to a complex engineering problem at that point in time. However this view is in sharp contradiction following research conducted by Armstrong (2000). The derived form factors for the mono-hull configuration are shown in Table 4.

Table 4: Derived form factors [Insel and Molland (1992)]

	C2	C3	C4	C5
(1+k)	1.10	1.45	1.30	1.17

The paper by Molland et al (1994), is an extension of the work conducted by Insel and Molland (1992). Additional models are tested with the particulars listed in Tables 6 and 7. The research and results are also detailed in the University of Southampton Ship Science Report 71, (1994).

Armstrong's thesis entitled "*A Thesis on the Viscous Resistance and Form Factor of High-speed Catamaran Ferry Hull Forms*", [Armstrong (2000)], examines the current methods for predicting the resistance of recently designed high-speed catamarans. Current literature suggests large form factors are needed for correlation between model scale and full scale, which Armstrong claims, contradicts the expectation that long slender hull forms would have low values. Form factors as per Molland et al (1994) are shown in Table 5.

Table 5: Model Form Factors [Molland et al (1994)]

Model	Monohull (1+k)	s/L=0.2		s/L=0.3		s/L=0.4		s/L=0.5	
		1+βk	β	1+βk	β	1+βk	β	1+βk	β
3b	1.45	1.60	1.33	1.65	1.44	1.55	1.22	1.60	1.33
4a	1.30	1.43	1.43	1.43	1.43	1.46	1.53	1.44	1.47
4b	1.30	1.47	1.57	1.43	1.43	1.45	1.50	1.45	1.50
4c	1.30	1.41	1.37	1.39	1.30	1.48	1.60	1.44	1.47
5a	1.28	1.44	1.57	1.43	1.54	1.44	1.57	1.47	1.68
5b	1.26	1.41	1.58	1.45	1.73	1.40	1.54	1.38	1.46
5c	1.26	1.41	1.58	1.43	1.65	1.42	1.62	1.44	1.69
6a	1.22	1.48	2.18	1.44	2.00	1.46	2.09	1.48	2.18
6b	1.22	1.42	1.91	1.40	1.82	1.47	2.14	1.44	2.00
6c	1.23	1.40	1.74	1.40	1.74	1.45	1.96	1.44	1.91

3. Research Program

The present research program was devised to:

- Examine variations in C_w using CFD, while modifying basic hull parameters, including the displacement and LCB.
- Compare C_w results of CFD with results from towing tank tests and develop regression model.
- Perform a comparative analysis of regression model against experimental results.

4. Systematic Series Development

The systematic series that was used for this analysis is based on typical hull forms used by the high-speed ferry industry in Australia. A parametric transformation procedure was used to produce the desired demi-hull series. Table 6 illustrates the geometrical parameters of the demi-hull series developed. For each model, hydrostatic information was extracted as presented in Table 7, containing parameters relevant to the regression analysis. It may be noted that LCB and LCF locations are with respect to the transom. The systematic series of demi-hulls thus produced was confined to:

$$0.2 \leq \frac{s}{L} \leq 0.4$$

while the speed range was constrained to $0.2 \leq Fn \leq 1.0$

Froude number of less than 1 is based on the restrictions imposed by SHIPFLOW. The lower limit of separation ratio was decided on as 0.2, and this was due to the fact that most demihull separations are within this region. At the upper limit, any greater separation would result in little deviation of the results. The body plans of models developed during this research study are illustrated in Figures 1 to 7 as shown below.

Table 6: Geometrical Parameters of Systematic Series of Catamarans

Model	L/B	B/T	C_B	$L/\nabla^{1/3}$
1	15.00	1.50	0.40	9.45
2	15.00	1.50	0.45	9.08
3	15.00	2.50	0.50	10.40
4	15.00	2.50	0.40	11.20
5	12.50	1.50	0.45	8.04
6	12.50	2.50	0.45	9.54
7	10.00	2.50	0.45	8.22

Table 7: Hydrostatics of Systematic Series

Model	Length (m)	Beam (m)	Draught (m)	Δ (tonnes)	i_E (deg)	β (deg)	WSA (m^2)	LCB (m)	LCF (m)
1	50.00	3.33	2.22	151.93	5.43	42.99	246.10	22.30	20.70
2	50.00	3.33	2.22	170.91	7.18	44.32	256.20	22.27	21.54
3	50.00	3.33	1.33	113.90	7.03	24.94	195.89	22.34	21.41
4	50.00	3.33	1.33	91.08	4.00	23.32	181.97	22.29	19.99
5	50.00	4.00	2.67	246.10	8.60	44.11	307.57	22.27	21.54
6	50.00	4.00	1.60	147.69	8.60	30.37	231.71	22.27	21.54
7	50.00	5.00	2.00	230.77	10.71	30.37	289.80	22.27	21.54

5. Theory of SHIPFLOW

In order to utilize the software correctly, it is necessary to understand the background theory, which is relevant to this analysis. SHIPFLOW (2003) uses panel methods to calculate the co-efficient of wave resistance, and therefore it is necessary to define the grid of panels that will be used for the analysis. The module XMesh is used to define the groups/surfaces that are to be considered. The three groups are body, free, and transom. The body group represents the hull surface. To define the grid of panels representing the body, the number of stations to be used along the length of the hull and the number of points across each station must be specified. A stretch function has been used, which produces smaller panels of $0.01L_{PP}$ at the bow to help define the significant changes in geometry that exist. As SHIPFLOW moves further aft the panels become increasingly larger until at the stern they are $0.02L_{PP}$ where little change in sectional area exists.

The free group represents the free surface. The free surface can be considered as the water surrounding the body group, which is used to model the waves created. Therefore it is necessary to create a free surface that extends forward of the bow, well aft of the model (approximately two wave lengths), and a considerable distance abeam of the vessel. After the limits of the free surface have been introduced, it is necessary to once again define the number of stations along the length of the free surface and the number of points across each station to create the grid.

The transom group represents a part of the free surface which extends directly aft of the transom.

This group is therefore quite long and only as wide as the vessel. As in the previous section, it is necessary to define the number of stations and points required to produce a grid. For consistency, the number of stations aft of the body must be the same for the free surface as it is for the transom group so that the panels are aligned.

The module XPAN is the solver that iteratively converges on the value of co-efficient of wave resistance. It is therefore necessary to input the maximum number of iterations that are to be used. In addition to this, the type of solver that will be used must be specified. The non-linear solver will generally produce a more accurate result than the linear solver, however it is more unstable particularly at high speeds and the solution may not converge. If reference is not made to the type of solver then the linear solver is used as the default. The other important feature of XPAN is whether the model is enabled to freely sink and trim. It is important to note that SHIPFLOW undergoes its analysis by non-dimensionalising the vessel down to a model of unity. Therefore all of the co-ordinates are non-dimensionalised by the length between perpendiculars L_{pp} . As mentioned XMesh module enables the user of SHIPFLOW to construct a grid of panels to illustrate the scenario to be tested. Due to the flexibility of SHIPFLOW to be applied to many different applications, it can produce varying results, which will not match model testing, or full-scale data. The program will produce an accurate result of co-efficient of wave resistance based on the grid supplied, however if the grid is not well set-up the result does not have much validity.

One of the major limitations of SHIPFLOW is its inability to model spray and wave-breaking phenomena at high speeds with a Froude number of 1.0 considered as the upper limit. Therefore the investigation has been restricted to this speed. When considering the validity of results there are two key aspects, the precision and the accuracy. If SHIPFLOW is used correctly very precise results may be obtained however these results cannot be considered as accurate until they have been scaled according to some model testing or full-scale data. Therefore, when constructing the grid in SHIPFLOW the aim is to achieve precise results, which can then be altered for accuracy.

At low Froude numbers the transom wave has a small wavelength and a large wave height. Conversely, at high Froude numbers the transom wave has a large wavelength with small wave amplitude. Therefore if a constant grid is applied to all of the models at the full range of speeds the degree of precision varies. Therefore caution must be taken when comparing results at different speeds. To overcome this problem, the grid must be systematically altered as the speed is increased to take into account the larger wavelength. This was achieved by increasing the free and transom surfaces further aft until two wavelengths are included as a guideline. On the other hand, at lower speeds it is not necessary to extend the free and transom surfaces further aft of the body group, but it will be necessary to include smaller panels in the grid to account for the significant changes in wave height.

If the grid is not altered it can be expected that as the Froude number is increased the results can be considered as becoming increasingly precise. However, as previously mentioned when the speed is increased SHIPFLOW becomes increasingly unstable in its ability to model spray and wave breaking phenomena. Therefore, using this software is a balance of stability and precision and to produce valid results an extensive amount of time is required to analyse the different scenarios. The change in grid density was applied to this analysis to account for changes in Froude numbers.

6. Regression Analysis

The type of regression analysis that was performed is called a Forward Stepwise Regression. For this analysis, the wave-resistance co-efficient is the dependent variable. A forward stepwise regression uses one independent variable, and gradually increases the number of variables used in each iteration. The number of iterations is usually the same as the number of cases that are presented for analysis. If an introduced variable is insignificant to the regression analysis it will be discarded.

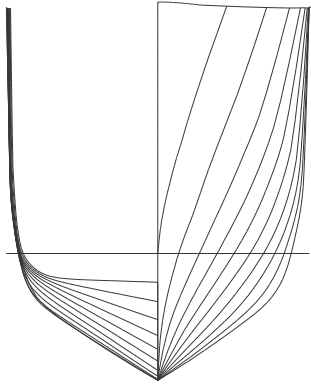


Fig.1: Body Plan of Model 1

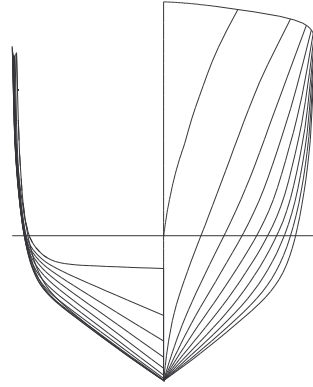


Fig.2: Body Plan of Model 2

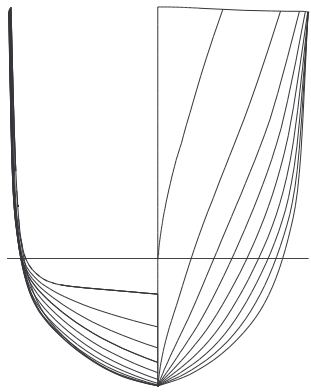


Fig.3: Body Plan of Model 3

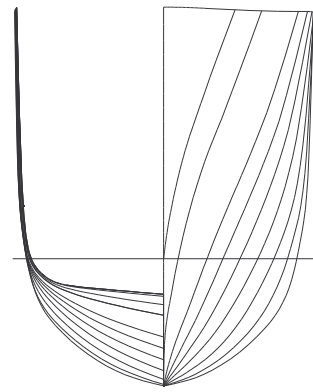


Fig.4: Body Plan of Model 4

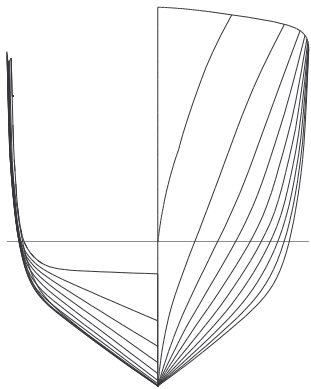


Fig.5: Body Plan of Model 5

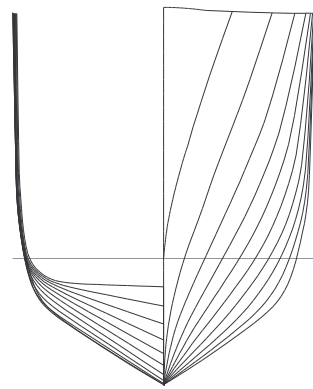


Fig.6: Body Plan of Model 6

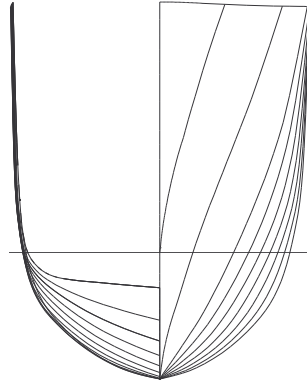


Fig.7: Body Plan of Model 7

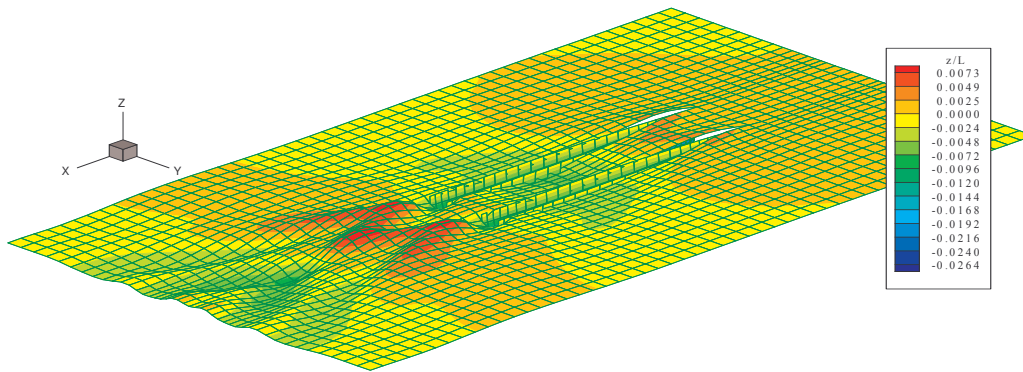


Fig.8: Model 3 in SHIPFLOW at Fn 0.4, s/L 0.2

The regression analysis was undertaken by separating the data into two sections, the demi-hull and the various catamaran configurations. This data was further broken down into individual Froude numbers tested, and then the analysis was carried out. The reason for testing Froude numbers independently is due to the inability to gain accurate regression co-efficients for varying speeds. The co-efficient of wave resistance can be considered to be a function of several geometrical parameters. As suggested by Schwetz and Sahoo (2002) C_w would be a function of several parameters as shown in equation 4:

$$C_w = f(L, B, T, C_B, C_P, C_M, \nabla, LCB, LCF, i_E, Fn, s, hullform) \quad (4)$$

From the list of parameters above, not all of these must be included in the generalized regression equation. Terms such as LCB and LCF have been used by Schwetz and Sahoo (2002) as means of representing the ‘semi-swathness’ of a hull form and therefore are not required. So the generalized equations for a demi-hull and catamaran are given by equations 5 and 6.

$$C_{Wdemi} = e^{C_1} \left(\frac{L}{B}\right)^{C_2} (C_B)^{C_3} \left(\frac{L}{\nabla^{1/3}}\right)^{C_4} (i_E)^{C_5} (\beta)^{C_6} \quad (5)$$

$$C_{Wcat} = e^{C_1} \left(\frac{L}{B}\right)^{C_2} \left(\frac{B}{T}\right)^{C_3} (C_B)^{C_4} \left(\frac{L}{\nabla^{1/3}}\right)^{C_5} (i_E)^{C_6} (\beta)^{C_7} \left(\frac{s}{L}\right)^{C_8} \quad (6)$$

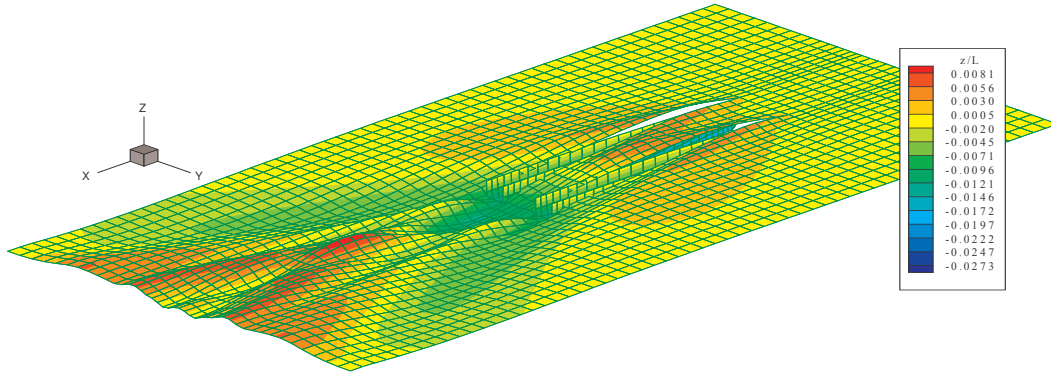


Fig.9: Model 3 in SHIPFLOW at Fn 0.7, s/L 0.2

Equation 6 above was applied to the catamaran regression analyses; however for a demi-hull the (s/L) term becomes insignificant. In addition to this, due to the number of variables compared with the number of cases for a demi-hull analysis, the (B/T) term was not included in the regression (due to the fact that there would be seven models seven independent variables and therefore can not be solved).

Table 8: Regression Coefficients and R² for demi-hull Configuration

Fn	C₁	C₂	C₃	C₄	C₅	C₆	R²
0.2	3.001	-0.159	0.515	-3.666	-0.194	0.000	0.967
0.3	1.221	0.000	0.815	-3.445	0.218	0.000	0.985
0.4	3.180	-0.702	0.377	-3.114	-0.390	0.000	1.000
0.5	2.519	0.396	-0.775	-4.175	0.000	-0.410	0.999
0.6	2.031	-0.239	0.000	-3.402	-0.138	-0.091	0.999
0.7	1.130	-0.220	0.000	-3.221	-0.043	-0.081	0.999
0.8	0.600	-0.272	0.000	-3.079	0.000	-0.063	0.999
0.9	-0.216	0.000	-0.228	-3.158	0.173	-0.178	0.999
1.0	-1.086	0.000	-0.396	-2.965	0.300	-0.203	0.998

In Table 8 the coefficients for the regression analysis have been shown for demi-hull configuration. Also included is the R² value, which represents the accuracy of the results with 0 providing no correlation and 1 providing complete correlation with the data. As seen above the regression analyses performed are quite good, with the exception being at Fn 0.20. The slightly lower correlation of results is due to the peak is observed on the C_w curve, which varies significantly between different models making it harder to model.

Also included is the R² value, which represents the accuracy of the results with 0 providing no correlation and 1 providing complete correlation with the data. As can be seen in figures 10 to 12, the regression analyses performance is quite good for speeds above Fn = 0.5. The slightly lower

correlation of results in the lower speed region is due to the peak observed on the C_w curve, which varies significantly between different models making it harder to model.

There is generally a very good correlation between results obtained from SHIPFLOW and regression analysis, and therefore the regression analysis can be considered a very good representation of the SHIPFLOW data. The only question to ponder is whether the results obtained from SHIPFLOW are reasonable. Table 9 illustrates the regression coefficients for catamaran configuration.

Table 9: Regression Coefficients and R^2 for Catamaran Configuration

Fn	C₁	C₂	C₃	C₄	C₅	C₆	C₇	C₈	R²
0.2	2.571	0.436	0.000	0.000	-4.124	-0.039	-0.199	0.037	0.995
0.3	0.585	0.000	0.000	0.945	-3.282	0.246	0.087	-0.089	0.989
0.4	3.324	0.000	-0.471	-0.963	-3.523	0.000	-0.688	-0.035	0.984
0.5	2.439	0.379	0.000	-0.600	-4.262	0.000	-0.337	-0.368	0.999
0.6	1.809	-0.110	0.000	0.000	-3.625	-0.061	-0.095	-0.314	0.997
0.7	1.055	0.000	0.082	-0.025	-3.617	0.000	-0.064	-0.181	0.997
0.8	0.603	0.222	0.266	0.000	-3.869	0.000	0.000	-0.069	0.998
0.9	-0.466	0.049	0.162	0.000	-3.322	0.128	0.000	-0.006	0.999
1.0	-1.221	0.000	0.117	0.000	-3.046	0.264	0.000	0.075	0.995

7. Results

Only three vessels from the series tested by Molland et al (1994) coincided with the series produced for this analysis. It is observed that above a Froude number of 0.5 the correlation of results is extremely good. The NPL series tested by Molland et al (1994) is based on a mono-hull series that has been put into a catamaran configuration. The other problem with using this work is the insufficient information available in their paper on the hydrostatics of each model. The value especially for dead-rise amidships and half angle of entrance have been kept constant at 7° and 30° respectively for NPL models and regression analysis for comparison purposes, and therefore a closer correlation would hopefully exist when the input is more accurate.

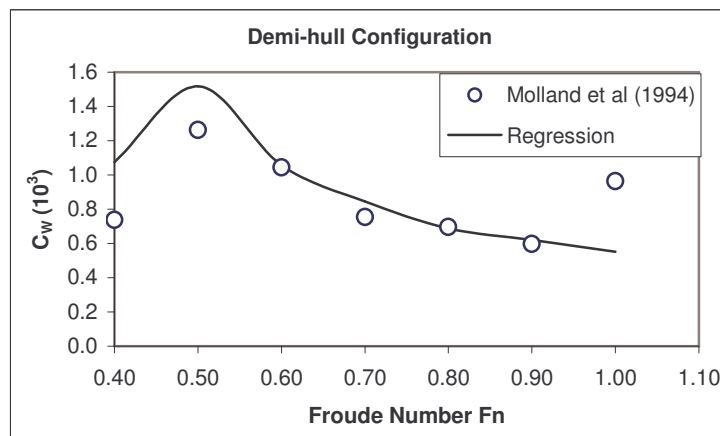


Fig.10: Validation of Regression Analysis against Molland et al (1994) Model 6a, demi-hull Configuration.

It is interesting to note the variables that have been included in the different equations for each Froude Number for a catamaran and demi-hull. The main variable that becomes apparent as having the most influence on resistance is the wet volume slenderness ratio ($L/\nabla^{1/3}$). Half angle of entrance, dead-rise, and separation ratio are also significant throughout the speed range. The breadth to draft ratio becomes significant only at the higher speeds.

It is interesting to note the variables that have been included in the different equations for each Froude Number for a catamaran and demi-hull. The main variable that becomes apparent as having the most influence on resistance is the slenderness ratio ($L/\nabla^{1/3}$).

The form factor due to viscous resistance interference factor is another aspect of catamaran resistance that could be further analysed. The work by Armstrong (2000) is limited to the applicable range of low Froude numbers that can be used. Therefore if a similar analysis was undertaken with carefully monitored SHIPFLOW and model testing results, an equation for form factor of catamarans could be produced. This seems to be the least researched aspect of determining catamaran resistance.

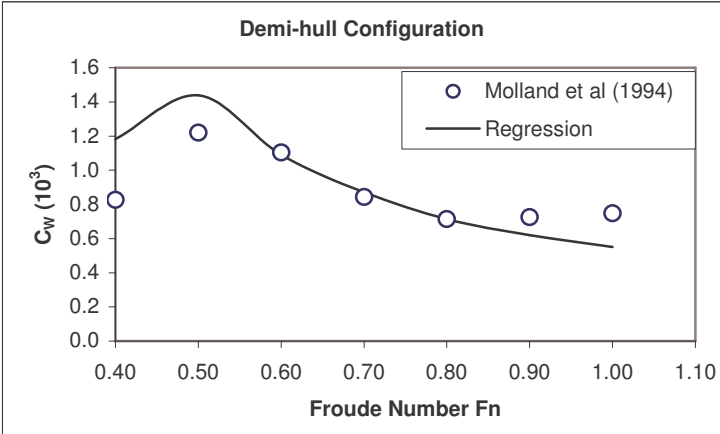


Fig.11: Validation of Regression Analysis against Molland et al (1994) Model 6b, demi-hull Configuration

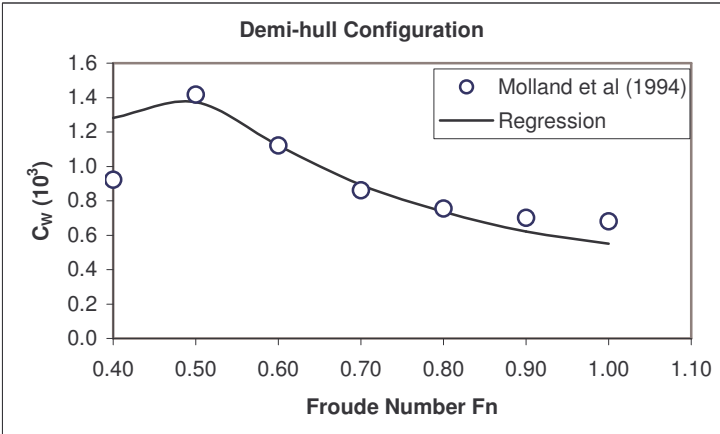


Fig.12: Validation of Regression Analysis against Molland et al (1994) Model 6c, demi-hull Configuration

Figures 10 to 12 illustrate the close correlation between the monohull NPL (Models 6a, 6b and 6c) series against regression analysis in demi-hull configuration. Figures 13 to 15 represent similar correlation analysis in catamaran configuration. As these are catamaran hull forms suitable for high-speed range the results have been presented for Fn values of 0.4 to 1.0. It is apparent from the above figures that the regression analysis developed from CFD analysis is robust enough to predict the wave resistance coefficient in both demi-hull and catamaran configurations.

8. Final Remarks

The variation of grid density must be very precise in order to obtain accurate results over the whole speed range. Therefore time must be spent before analysis to set-up a grid for each Froude number so that the results are consistently precise. In order to perform suitable

analysis on round bilge catamaran hull forms the constraints as shown in Table 10 should be strictly adhered to.

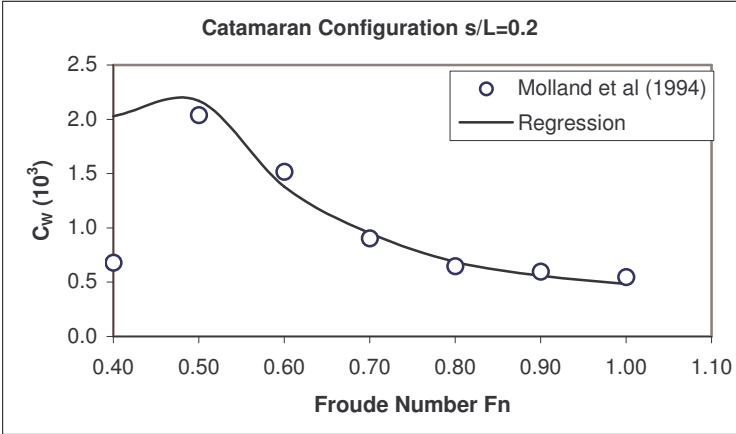


Fig.13: Validation of Regression Analysis against Molland et al (1994) Model 6a, Catamaran Configuration

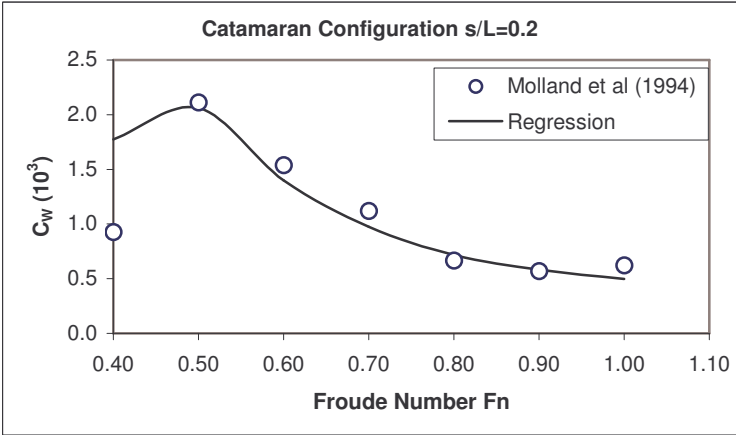


Fig.14: Validation of Regression Analysis against Molland et al (1994) Model 6b, Catamaran Configuration

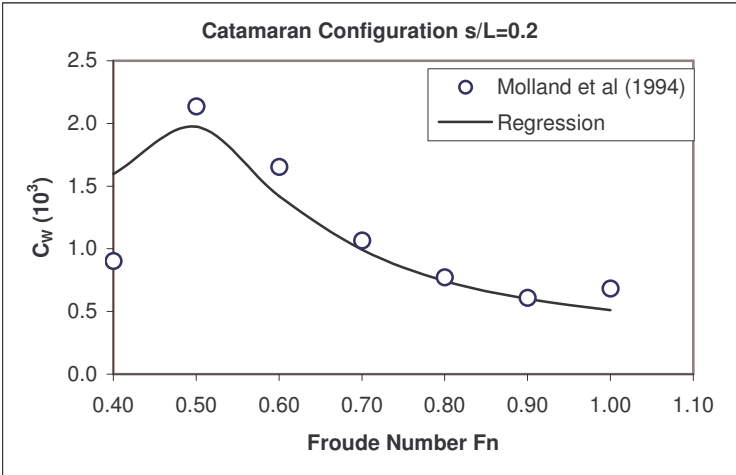


Fig.15: Validation of Regression Analysis against Molland et al (1994) Model 6c, Catamaran Configuration

In order to calculate the total resistance, if actual data is unavailable, the following empirical formulae may be used:

Wetted Surface Area: $S = 1.7LT + \frac{\nabla}{T} m^2$ as per Mumford.

$$S = \frac{\nabla}{B} \left[\frac{1.7}{C_B - 0.2(C_B - 0.65)} + \frac{B}{T} \right] m^2$$

Form factor as per Armstrong (2000) is given by $(1+k)_{ship} = 1.72 - f \left(\frac{L}{\nabla^{1/3}} \right)^g \left(\frac{B}{T} \right)^{-0.1}$

where $f = -2.25Fn^2 + 4.47Fn - 1.61$ and $g = 0.76 - 1.09f$

The wave resistance interference factor can be determined from the expression given by:

$\tau = \frac{C_{WCAT}}{C_{WDEMI}}$ valid for $0.4 < Fn < 1.0$ and the viscous resistance interference factor, β , can be obtained from the experimental data of Molland et al (1994).

Table 10: Range of Parameter Constraints

Parameter	Range
L/B	10 to 15
B/T	1.5 to 2.5
C_B	0.4 to 0.5
$L/\nabla^{1/3}$ (slenderness ratio)	8 to 12
s/L (separation ratio)	0.2 to 0.4
i_E (half angle of entrance)	4 to 11 degrees
β (average deadrise angle)	23 to 45 degrees
Fn	0.4 to 1.0
LCB as % of L aft of mid-ship	5 to 6

9. Conclusions and Discussion

In view of the analysis and validation process undertaken in this research work the following conclusions can be drawn:

- A systematic series of round bilge catamaran hull forms have been designed and wave resistance coefficients for demi-hull as well as catamaran hull form configurations have been determined using CFD (SHIPFLOW) for a range of Froude numbers.
- A regression analysis has been performed based on CFD results and has been compared with experimental results of NPL series hull forms as conducted by Molland et al (1994).
- It appears that the regression equation is robust enough as it compares favorably, specially at $0.5 < Fn < 1.0$, with experimental results for the three NPL models whose geometrical parameters closely match the constraints of the regression analysis.

It is imperative to note that a limited number of models have been created in this instance, which implies that the range could be further enlarged and more rigorous validation is required against experimental results.

10. Nomenclature

B	Demihull beam at the waterline (m)	C_T	Total resistance coefficient
C_B	Block coefficient	C_W	Wave resistance coefficient
C_F	ITTC (1957) ship model correlation line: $C_F = 0.075(\log R_n - 2)^{-2}$	C_{WCAT}	Wave resistance coefficient for a catamaran
C_R	Residuary resistance coefficient	C_{WDEMI}	Wave resistance coefficient for a demihull in isolation.

F_n	Froude number based upon waterline length.	S	Wetted surface area (m^2)
i_E	Half waterline entry angle	T	Draught (m)
L	Waterline length (m)	$(I+k)$	Form factor
P_E	Effective Power (kW)	$(I+\beta k)$	Form factor including the viscous. interference resistance factor β .
R	Vessel Resistance (N)	V	Velocity (m/s)
R_n	Reynolds number	β	Viscous interference resistance factor
s	Catamaran demihull spacing (m)		
ρ	Fluid density (kg/m^3)		
τ	Wave resistance interference factor		
ν	Kinematic viscosity of fluid (m^2/s)		
∇	Volumetric Displacement (m^3)		
Δ	Displacement (tonne)		

11. Abbreviations

CFD	Computational Fluid Dynamics
LCB	Longitudinal centre of buoyancy, reference from the transom
LCF	Longitudinal centre of floatation, reference from the transom
DWL	Design waterline
ITTC	International Towing Tank Conference
WSA	Wetted Surface Area

12. Acknowledgement

The authors would like to express their sincere gratitude to The Australian Maritime College, Australia and The University of Austral, Chile for their support, encouragement and financial help rendered throughout the course of this research work.

References

- ARMSTRONG, N.A (2000), *On the Viscous Resistance and Form Factor of High-Speed Catamaran-Ferry Hull Forms*, Ph.D Thesis, The University of New South Wales, Sydney, Australia.
- INSEL, M.; MOLLAND, A.F. (1992), *An Investigation into Resistance Components of High-Speed Displacement Catamarans*, Trans. of Royal Institute of Naval Architects, Vol.134, pp 1-20
- MOLLAND, A.F.; WELLICOME, J.F.; COUSER, P.R. (1994), *Resistance Experiments on a Systematic Series of High Speed Displacement Catamaran Forms: Variation of Length-Displacement Ratio and Breadth-Draft Ratio*, Ship Science Report No.71, University of Southampton, UK.
- SCHWETZ, A.; SAHOO, P.K. (2002), Wave Resistance of Semi-Displacement High Speed Catamarans Through CFD and Regression Analysis, *3rd Int. Conf. High Performance Marine Vehicles (HIPER'02)*, Bergen, Norway, pp 355-368.
- SHIPFLOW User's Manual, Flowtech International, Edition 1, December 2003.

Added Mass and Damping Coefficient Prediction – Results of Different Methods

Ermina Begovic, University of Naples Federico II, Naples/Italy, begovic@unina.it
Guido Boccadamo, University of Naples Federico II, Naples/Italy, boccadam@unina.it

Abstract

The evaluation of ship motions and loads obtained through seakeeping calculations is continuing to be one of the most important research subject. Numerical procedures used for this purpose are generally validated by ship motions experiment; evaluation of motion equation coefficients is carried out experimentally by forced motions and measurement of exciting forces on restrained model in regular seaway. Even if the motion prediction by some numerical method is satisfactory, the predicted values of particular coefficients from the motion equation (added mass and damping coefficients) and of exciting forces are not always satisfactory. This can affect heavily loads assessment that is fundamental for structure scantlings. In particular, for the widely studied Wigley based hulls, big discrepancies between numerical and experimental values have been noted. In this work the review of experimental results for added mass and damping coefficients for heave and pitch available in literature is given. For two Wigley models and for a high-speed model, heave and pitch added mass and damping coefficients are calculated by 2.5D high-speed theory with and without cross-flow corrections. Results are compared with numerical results of similar works where different 3D time domain calculation methods were used. Significant differences in some coefficients are found, calling for further investigation on the matter.

1. Introduction

The importance of ship motions and global wave loads assessment is highlighted by the considerable number of ship disasters or damages to their structures and cargo in extreme weather conditions. At the same time ship behaviour in the most frequent sea states is important for commercial effectiveness and passenger comfort. Inaccuracy of determining ship responses arises from the very complex hydrodynamic problems of describing the flow around the ship moving in waves. Mathematical models, which would include the major part of the physical properties of ship behaviour in waves, are almost impossible to solve in reasonable time. Therefore, significant simplifications have been used in the development of *state-of-the art* methods to make them practically useful.

Presently, different hydrodynamic models (linear or non-linear, in frequency or in time domain) are used and efforts are concentrated to estimate more accurately ship motions and pressure distributions. For the engineering purposes, the essential features of the ship responses to waves can be described by linear theories and reliable theories were developed in past years. At the 14th International Ship and Offshore Structures Congress, *ISSC 2000* it was pointed out that the two-dimensional strip theories are still considered as the most practical design tool to assess the vessels seakeeping characteristics. Even if it can be true for determining ship motion for low and moderate speed in head sea, 2D strip theories are not adequate either for pressure distribution assessment or motion responses at high forward speed. At present, 3-D theories are gaining importance, although the state of the art indicates that significant work is still required to develop practically reliable 3-D computational methods.

Even if the motion prediction by some numerical method is satisfactory, the predicted values of particular coefficients from the motion equation (added mass and damping coefficients) and of exciting forces are not always satisfactory. This can affect heavily loads assessment that is fundamental for structure scantlings. The problem is that developed numerical procedures are generally validated by ship motions experiment; evaluation of motion equation coefficients is carried out experimentally by forced motions and measurement of exciting forces on restrained model in regular seaway. The traditional seakeeping practice: comparison of the predicted ship motions and global hydrodynamic force with the measured not demonstrate the advantage of the advanced

numerical methods nor show the deficiency of them. It is because the ship motion and the global hydrodynamic force are the result of many factors integrated and do not provide high grade information on hydrodynamic model involved in.

Here, added mass and damping coefficients by different numerical methods are determined. Obtained numerical results are compared with the experimental ones and the differences are analysed.

2. Theory Overview

We consider the ship as a rigid body travelling at the constant forward speed U . Furthermore, we assume that the rigid body will oscillate harmonically in time with six degrees of freedom with the complex amplitudes: η_j ($j=1, 2, \dots, 6$), where $j=1, 2, \dots, 6$ refer to surge, sway, heave, roll, pitch and yaw respectively, as shown in the *Fig.1*.

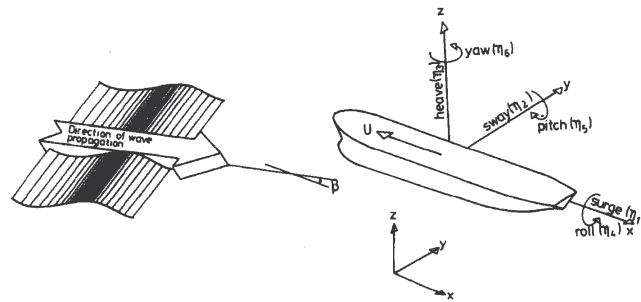


Fig.1: Motions, VERES User's Manual

The problem of flow determination caused by the ship presence and her advancing velocity means, mathematically, to find velocity and pressure. The first step in solving a boundary value problem is the set up of differential equations to describe the fluid flow. The level of complexity of these equations depends on the mathematical formulation of fluid properties and flow field. In the physically exact formulation mathematical model becomes very difficult to solve, so it is necessary to introduce a certain number of simplifications. The most common assumptions are:

- homogenous fluid
- incompressible fluid ($\nabla \cdot \mathbf{V} = 0$)
- non viscous fluid
- irrotational fluid motion ($\omega = \nabla \times \mathbf{V} = 0$ everywhere in the fluid)
- negligible surface tension

In order to solve the problem, significant simplification can be done using the linearization. The linearization means that all the quadratic terms appearing in the boundary conditions are assumed to be sufficiently small to be negligible. In developing the linearized boundary-value problem, the invoked mathematical model losses contact with the reality to a great extent, but it gains the capacity to construct the new solutions. In the linearized problems every linear operator could be considered as the linear combination of linear terms and gives us the possibility to consider hydrodynamic problem of body moving in the regular waves as two separate sub-problems (steady and non-steady problem). It also means that the small amplitude incident waves will produce small amplitude ship motions. As the consequence of the superposition the responses of a ship to an irregular wave spectrum can be considered as the sum of the responses to regular waves of all frequencies present in the spectrum, *St. Denis and Pierson (1953)*.

Through the linearization process it is possible to consider separately external unsteady forces associated with the diffraction and the radiation problems. The diffraction problem deals with the forces produced by the waves on the body fixed at its mean advancing position.

The radiation problem considers the forces induced by the harmonic oscillations of the rigid body described through added mass A_{jk} and damping B_{jk} coefficients concept. The true meaning of added mass concept is apparent increasing in inertia of the body which moves in fluid and spends some kinetic energy to accelerate surrounding fluid so it should be understood in terms of hydrodynamic pressure induced force. The damping coefficient B_{jk} represents a measure of energy dissipation through the radiated waves. The coefficients A_{jk} and B_{jk} are functions of body form, mode of motion, frequency of oscillation and forward speed. There are 36 added mass coefficients and 36 damping coefficients.

In the diffraction problem, the body is restrained for any oscillatory motion and is subjected to incident waves of known length, amplitude and heading. The resultant force experienced by the body from incident waves is known as hydrodynamic exciting force and it is directly proportional to the wave amplitude. It is also function of the wave frequency, of the heading, of the forward speed and of the body geometry. Hydrodynamic exciting force is composed of Froude-Krylov force and diffraction forces and moments.

The hydrostatic restoring force is defined as the fluid force to restore the body to its static equilibrium when the body is displaced freely from the rest position. This force is obtained by integrating the hydrostatic pressure due to the variation in displacement express through C_{jk} - hydrostatic restoring coefficient. It is a function of the body geometry only and in the linear theory it is independent from the motion η_k . The indices j and k indicate the mode of the restoring force and the mode of motion respectively.

2.1. Ship Motions

When the hydrodynamic forces are determined, the procedure is straightforward to set up the equations for rigid body motions equating the exciting forces with the inertial forces associated with the accelerations of rigid body. We have:

$$\sum_{k=1}^6 [(M_{jk} + A_{jk}) \cdot \ddot{\eta}_k + B_{jk} \cdot \dot{\eta}_k + C_{jk} \cdot \eta_k] = F_j e^{i\omega_e t}, j=1,2,\dots,6$$

where

M_{jk} - generalised mass matrix for the body

A_{jk} - added mass coefficients matrix

B_{jk} - damping coefficients matrix

C_{jk} - hydrostatic restoring coefficients matrix

F_j - complex amplitudes of the exciting forces and moments - given by $F_j e^{i\omega_e t}$

ω_e - encounter frequency

$\eta_k, \dot{\eta}_k, \ddot{\eta}_k$ - displacement, velocity and acceleration terms

The indexes j and k indicate the direction of the fluid force and the mode of motion respectively.

3. Experimental Results

To get better insight into the “accuracy of added mass and damping coefficient prediction” of different numerical methods from the literature the experimental results of forced motions are collected. From the rare experimental data for added mass and damping coefficients presented until now, only two works with all necessary data were identified and used as references in this work.

The first work is by *Journee (1992)* who performed vertical motions and forced motions tests (determination of added mass and damping coefficients) at three velocities corresponding to $F_N=0.2, 0.3$ and 0.4 of four models based on Wigley hull forms. Tests were performed at University of Delft. From these four models in this work only two very slender models with $L/B=10$ are considered. The

second work by *Keuning (1990)* deals with well known high speed Model 5 by *Blok and Beukelman (1984)*. The experiments of forced motions at $F_n=0.57$ and 1.14 are performed for segmented and for unsegmented 2m length model at University of Delft. Blok and Beukelman performed at MARIN seakeeping tank the vertical motion tests of 5m length model at the same F_n . The main dimensions are summarized in the Table I, while the body plans are shown in the Figs.2 to 4.

Table I: Models Main Dimensions

	WIGLEY I	WIGLEY III	MODEL 5
L_{WL} (m)	3.0000	3.0000	2.0000
B (m)	0.3000	0.3000	0.2500
T (m)	0.1875	0.1875	0.0624
C_B	0.5606	0.4622	0.396
C_M	0.9090	0.6667	0.633
F_N	0.20; 0.30; 0.40	0.20; 0.30; 0.40	0.57; 1.14
R_{55} (m)	0.25 L_{WL}	0.25 L_{WL}	0.25 L_{WL}
X_{CG} (m)	0.0000	0.0000	0.1022
Z_{CG} (m)	0.1700	0.1700	0.1690*
$\xi_{a-Heave \& Pitch}$ (m)	0.018	0.019	0.01 L_{WL}
$\xi_{a-ForcedHeave}$ (m)	0.050	0.050	0.01; 0.02
$\xi_{a-ForcedPitch}$ ($^{\circ}$)	3	3	
λ_{SHIP}	15.0	15.0	22.085
$L_{WL-ship}$ (m)	45.000	45.000	44.170

*This value was used originally in experiments performed by Blok and Beukelman determined as 60% of depth of 5m length model. In Keuning's work the CG value is not specified. In this work the original value by Blok and Beukelman was scaled to the ship values

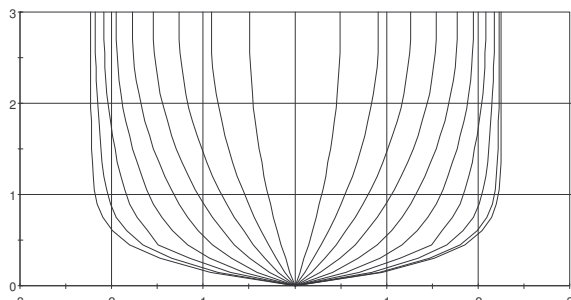


Fig.2: Body Plan of Model Wigley I

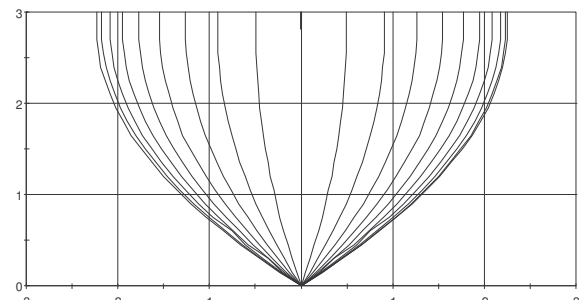


Fig.3: Body Plan of Model Wigley III

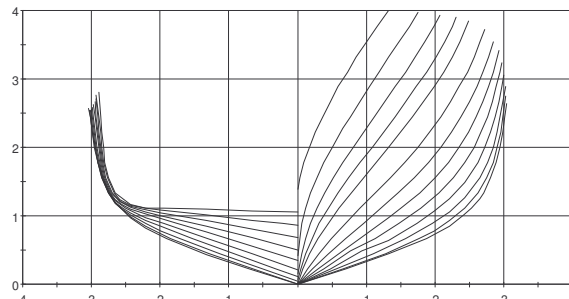


Fig.4: Body Plan of Blok and Beukelman Model 5

4. Comparison of Numerical and Theoretical Results for Added Mass and Damping Coefficients Prediction

For the described Wigley models the vertical motions were calculated using the strip theory by *Salvesen et al. (1970)* while for the Model 5, the calculations were performed using the 2.5 D high-speed theory by *Faltinsen and Zhao (1990)*, both implemented in program VERES. For all three models the calculations with the numerical code TRIM developed by authors and described in *Begovic et al. (2002)* using the cross-flow correction were performed with the cross flow coefficient values equal to: $\alpha=0.035$ and $C_D=0.25$.

As the interest of this paper was focused on the added mass and damping coefficients prediction, the comparison of experimental results and results obtained by described programs were performed. The numerical results from literature for the same models were collected and are compared too. The numerical results presented by *Journee (1992)* are obtained by two different 3D methods: WAMIT, *Newman (1988)* and DELFRAC, *Pinkster (1992)*. *Kara and Vassalos (2003)* presented the results for Wigley I at $F_n=0.4$ obtained by 3D time domain program with satisfied exact body boundary condition. *Yasukawa (2003)* presented results for modified Wigley hull (Wigley III) at $F_n=0.3$ obtained by 3D time domain panel method including nonlinearity of hull and free surface boundary condition.

In all diagrams heave results are in non-dimensional form η_3/A , while pitch results for both Wigley models are originally presented not as: $\frac{\eta_5 \cdot \lambda}{2 \cdot \pi \cdot A} = \frac{\eta_5}{kA}$ but as $\frac{\eta_5 \cdot L}{2 \cdot \pi \cdot A}$ and here mark η_5 has the same meaning.

Added mass and damping coefficient are presented always in non-dimensional form as:

$$A_{33}'' = \frac{A_{33}}{\rho \nabla}; B_{33}'' = \frac{B_{33}}{\rho \nabla \cdot \sqrt{\frac{g}{L}}}; A_{55}'' = \frac{A_{55}}{\rho \nabla \cdot L^2}; B_{55}'' = \frac{B_{55}}{\rho \nabla \cdot L^2 \cdot \sqrt{\frac{g}{L}}}$$

while the abscissa is non-dimensional frequency of oscillation calculated as:

$$\omega_E'' = \frac{\omega_E}{\sqrt{\frac{g}{L}}}$$

where L was the ship dimension as reported in Table I.

4.1. Model Wigley I

For both Wigley models very satisfactory results for heave motion were obtained showing that at low speed the strip theory is still giving sufficiently accurate results and there is no necessity for cross-flow correction. Pitch results are not that good and in some way it was not expected because is simple mathematical form, symmetrical with respect to longitudinal and transversal plane and even more the F_n is equal to 0.2 or max 0.4. Therefore, the same calculations were performed by program SHIPMO using the strip theory by *Gerritsma and Beukelman (1967)*. The legend used in diagrams is: VERES, SHIPMO, CF, EXP referring to the results obtained by strip theory implemented in VERES, strip theory implemented in SHIPMO, results from TRIM using the cross-flow coefficients $\alpha=0.035$ and $C_D=0.25$ and experimental data respectively. As regard vertical motions no significant difference is found between trend of SHIPMO and VERES results.

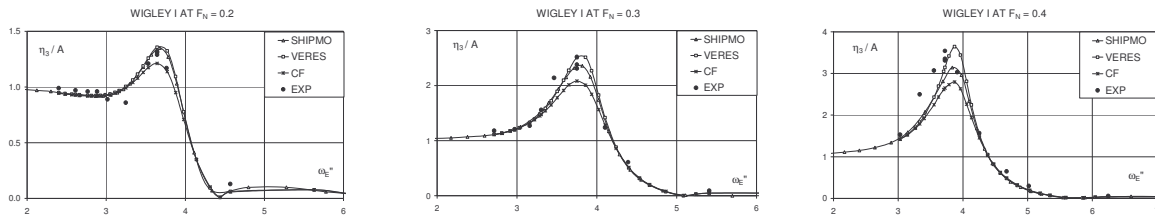


Fig.5: Heave results for Model Wigley I

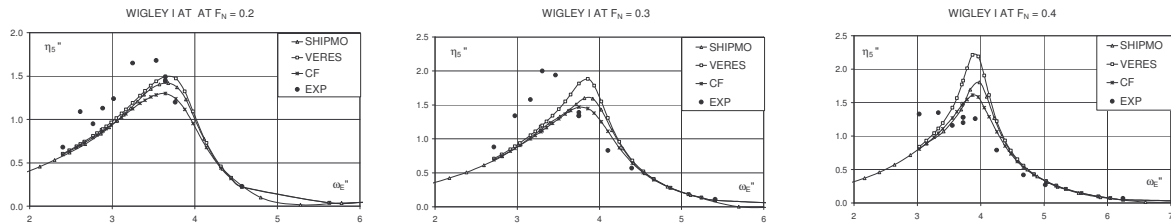


Fig.6: Pitch results for Model Wigley I

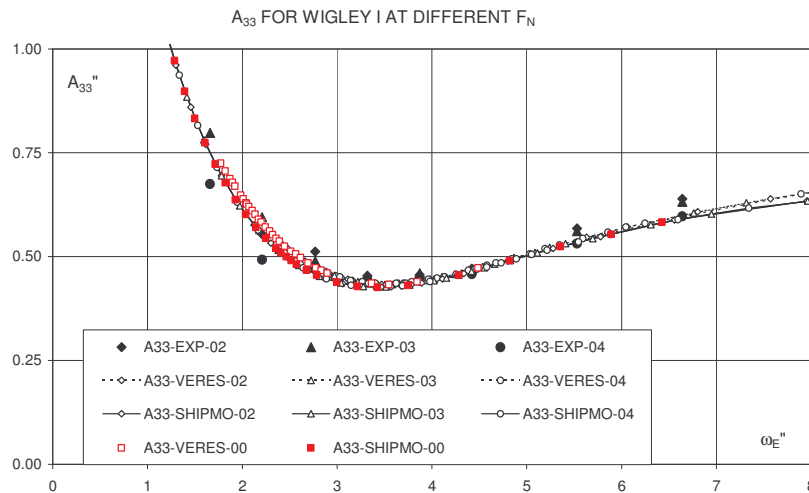


Fig.7: A₃₃ for Model Wigley I

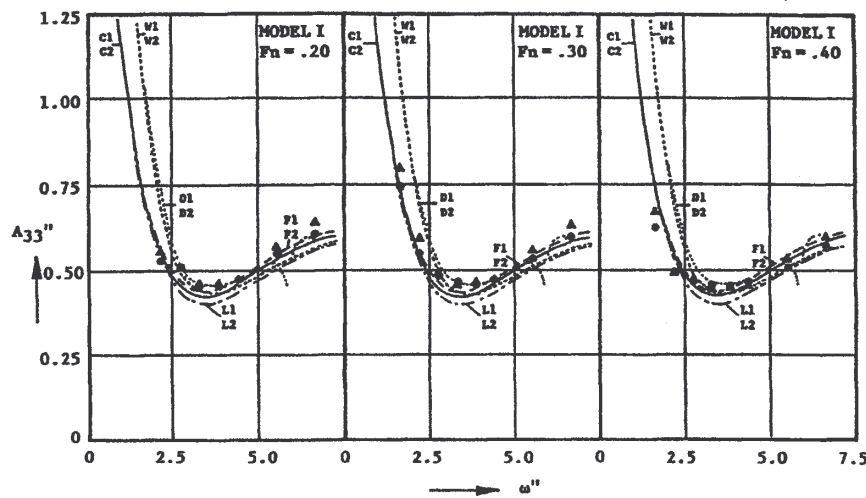


Fig 7-1: A₃₃ for Model Wigley I from *Journee (1992)*

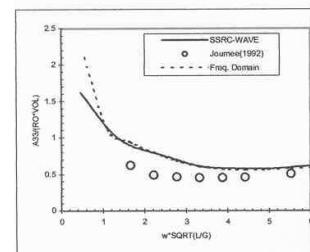


Fig 7-2: A₃₃ for Model Wigley I at $F_N=0.4$ from *Kara and Vassalos (2003)*

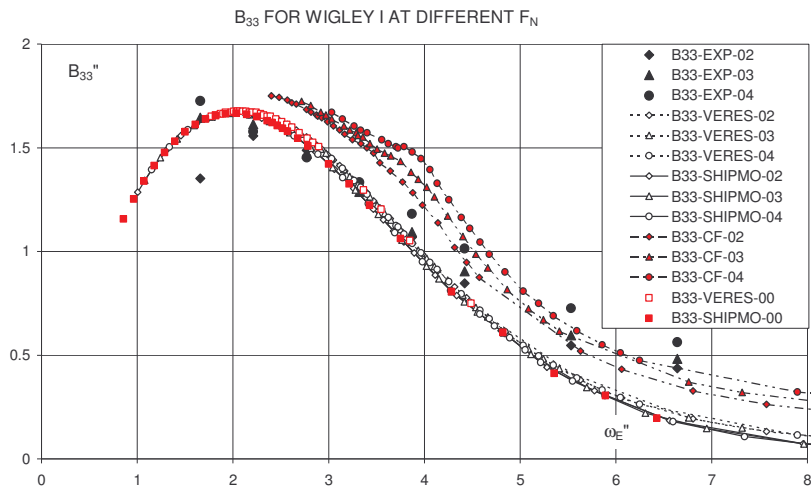


Fig.8: B_{33} for Model Wigley I

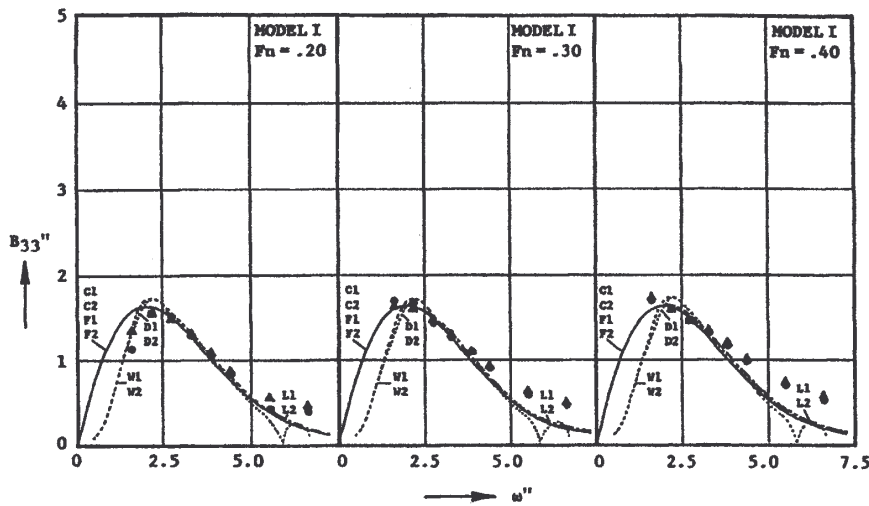


Fig.8-1: B_{33} for Model Wigley I from *Journee (1992)*

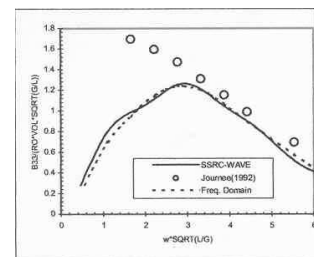


Fig.8-2: B_{33} for Model Wigley I at $F_N=0.4$ from *Kara and Vassalos (2003)*

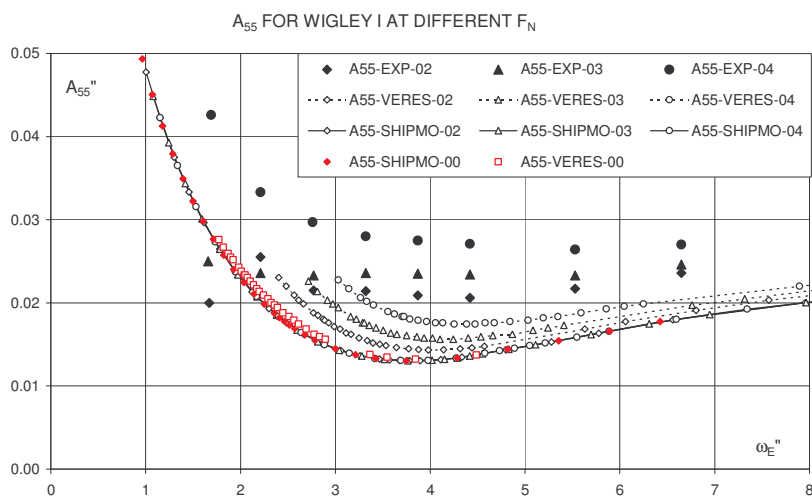


Fig 9: A_{55} for Model Wigley I

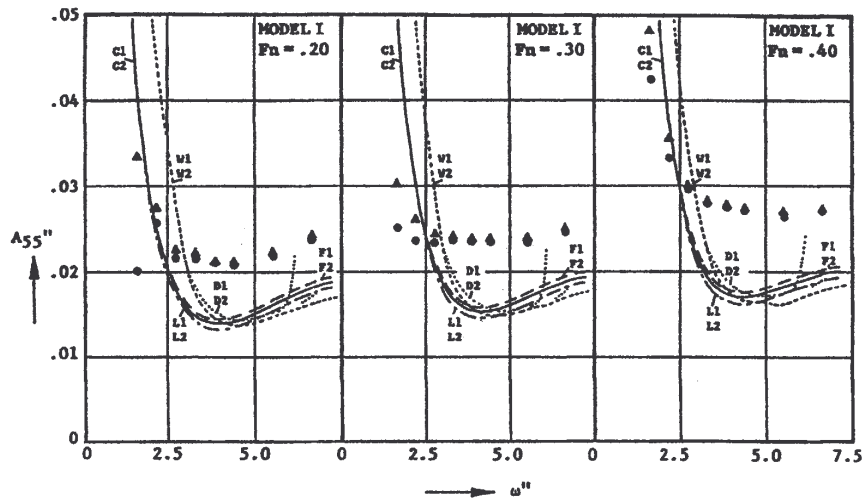


Fig.9-1: A_{55} for Model Wigley I from *Journee (1992)*

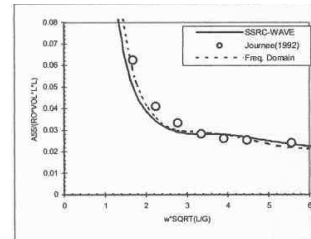


Fig.9-2: A_{55} for Model Wigley I at $F_N=0.4$ from *Kara and Vassalos (2003)*

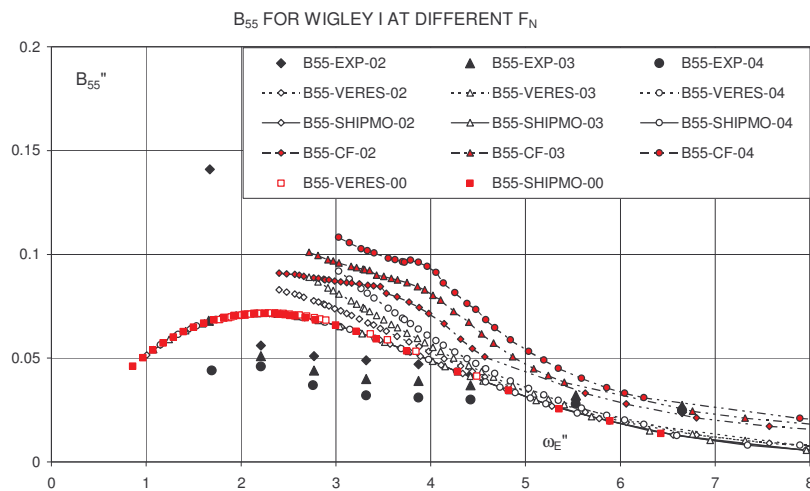


Fig.10: B_{55} for Model Wigley I

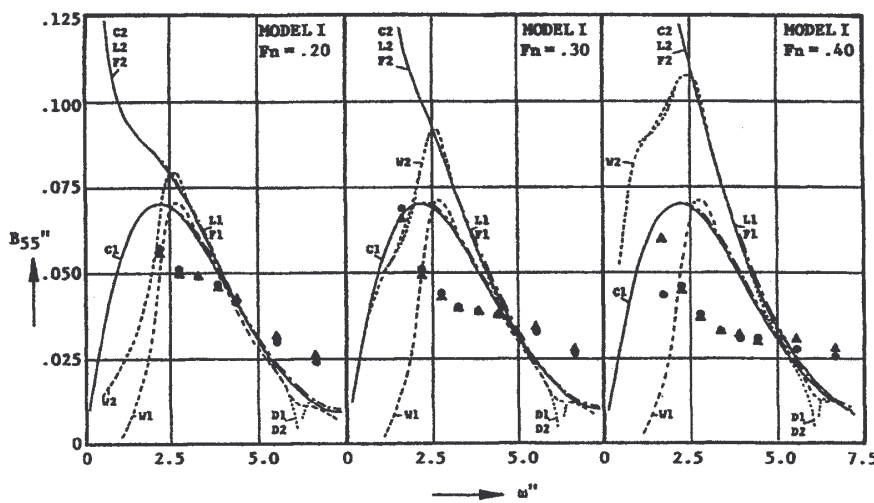


Fig.10-1: B_{55} for Model Wigley I from *Journee (1992)*

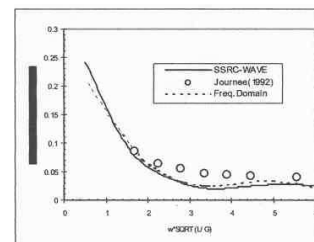


Fig.10-2: B_{55} for Model Wigley I at $F_N=0.4$ from *Kara and Vassalos (2003)*

For the Model Wigley I, the results obtained for A_{33} by both 2D strip theory fit very well the experimental results at all F_N . The SHIPMO strip theory do not have the terms with advancing velocity so for all speeds, coefficient values are equal a priori. The Salvesen et al. strip theory has this term but as the considered hull form is symmetrical as regard transversal plane, these members are cancelled and again for all three considered speeds the coefficient value is constant. It can be noted that these simple theories are better than Journee and Kara-Vassalos predictions. Among 3D theories, WAMIT reported by Journee seems slightly better than others.

As regard B_{33} again 2D theories give better fitting of experimental data than 3D. In particular the cross flow correction seems very beneficial in high frequency range. It can be noted quite different trend among 3D methods. While frequency domain methods by Journee give very fair prediction in low frequency range and in high frequency the experimental results are underestimated, the time domain results has completely opposite trend in low frequency and almost perfectly fit experimental results in high frequency.

Pitch-pitch added mass coefficient A_{55} is rather poor predicted by all frequency domain methods and it seems again that 2D are little bit better than 3D theories. Again, the results from SHIPMO strip theory are constant for all speeds because of missing advancing velocity term. Results presented by Kara and Vassalos perfectly fit experimental data. The same comments are valid for B_{55} , where surprisingly can be noted that among frequency domain methods, the most simple one (SHIPMO) seems the best one. Also should be noted that cross flow correction is giving no benefit.

4.2. Model Wigley III

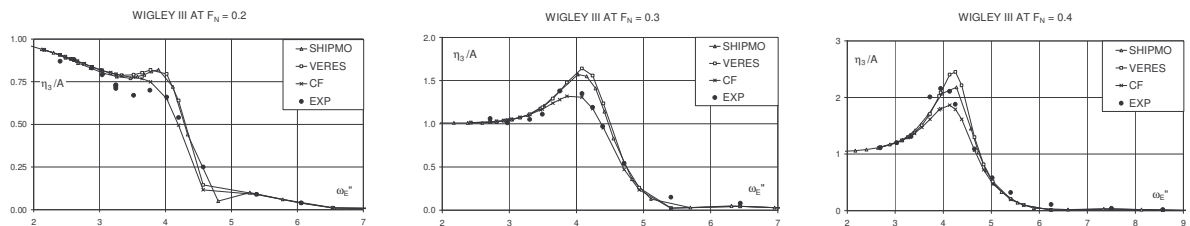


Fig.11: Heave results for Wigley III

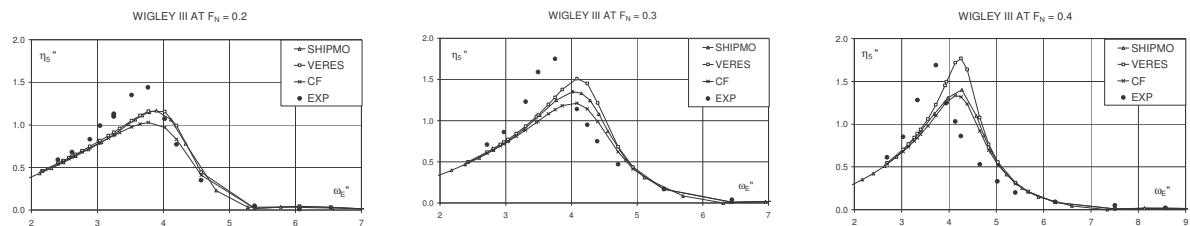


Fig.12: Pitch results for Wigley III

Analysing the results for added mass and damping coefficients for model Wigley III obtained by different theories it can be noted that only Yasukawa results (white circles at Figs. 13-2, 14-2, 15-2 and 16-2) perfectly fit all the experimental results. As regard considered frequency domain methods, no significant preferences among them could be identified, generally heave-heave coefficients are better predicted than pitch-pitch. 3D theories are slightly better for heave-heave coefficients but are also significantly worse in pitch-pitch coefficients prediction. Cross flow correction for B_{33} gives perfect fitting and some improvement in very high frequency range for B_{55} .

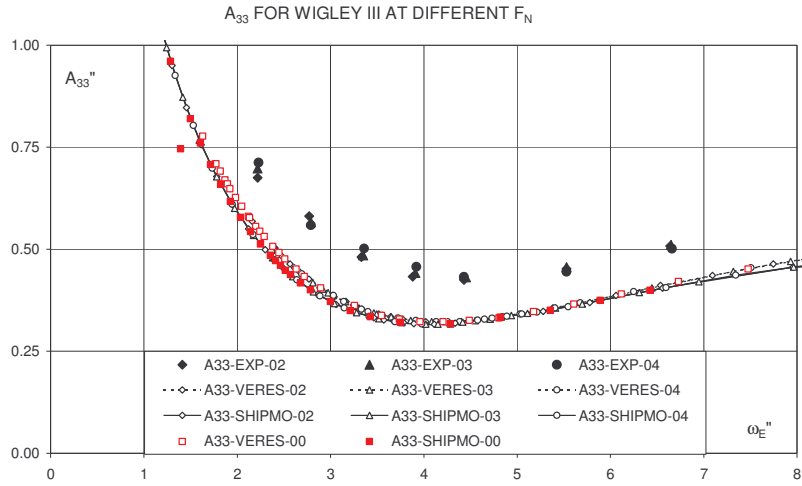


Fig. 13: A_{33} for Model Wigley III

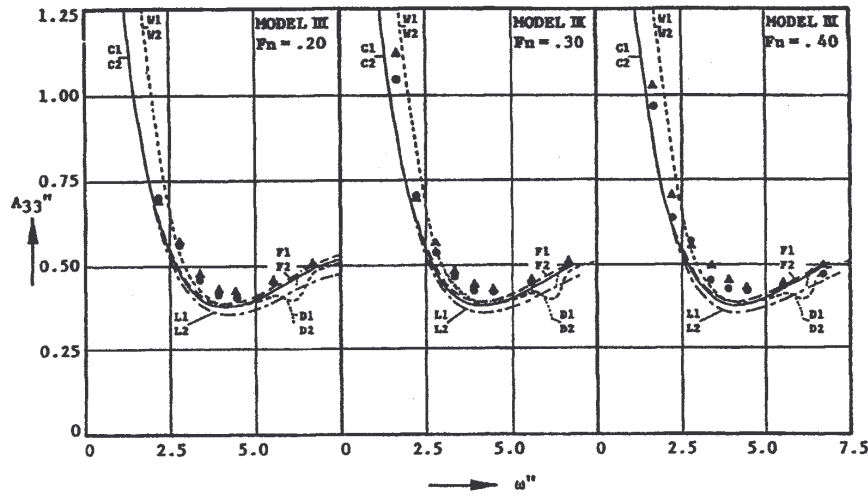


Fig.13-2: A_{33} for Model Wigley III at $F_N=0.3$ from Yasukawa (2003)

Fig.13-1: A_{33} for Model Wigley III from Journee (1992)

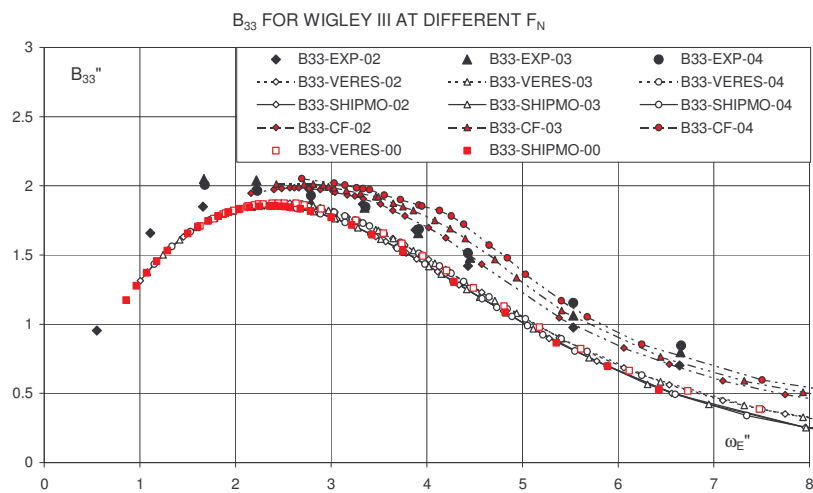


Fig.14: B_{33} for Model Wigley III

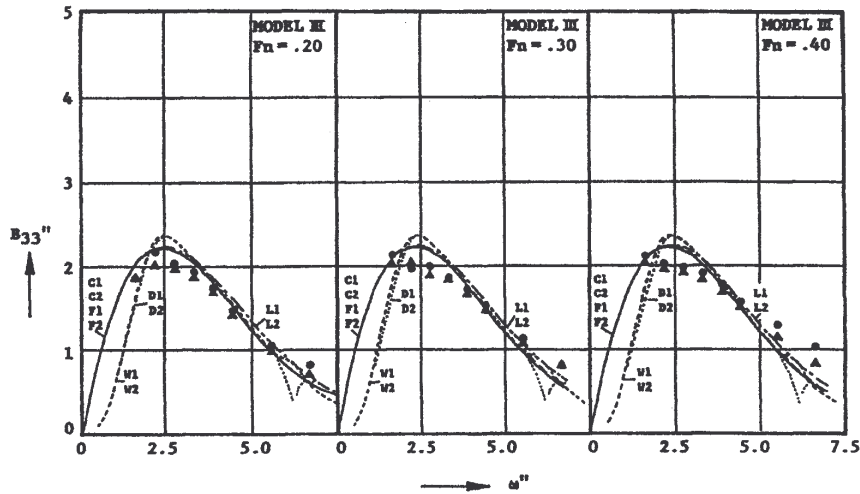


Fig.14-1: B_{33} for Model Wigley III from *Journee (1992)*

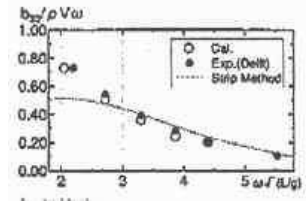


Fig.14-2: B_{33} for Model Wigley III at $F_N=0.3$ from *Yasukawa (2003)*

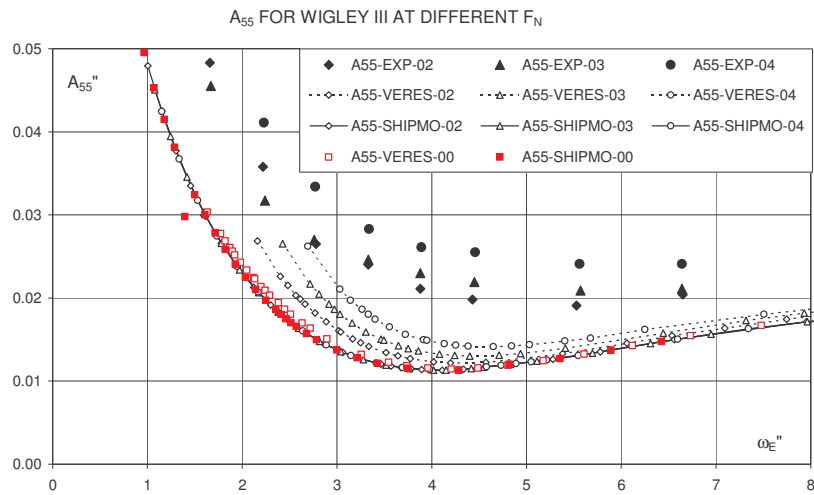


Fig.15: A_{55} for Model Wigley III

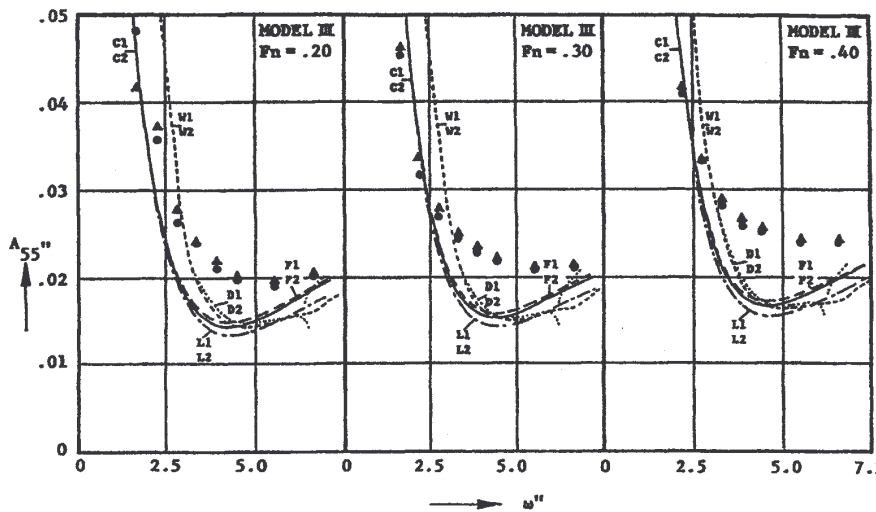


Fig.15-1: A_{55} for Model Wigley III from *Journee (1992)*

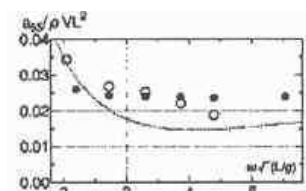


Fig.15-2: A_{55} for Model Wigley III at $F_N=0.3$ from *Yasukawa (2003)*

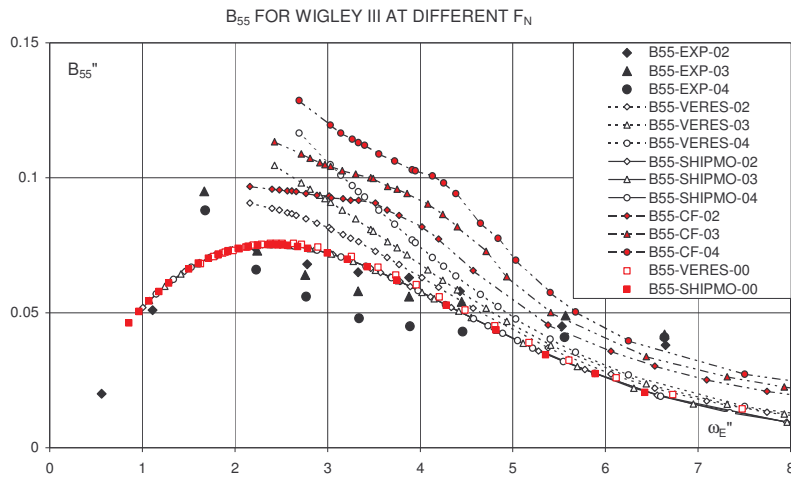


Fig.16: B_{55} for Model Wigley III

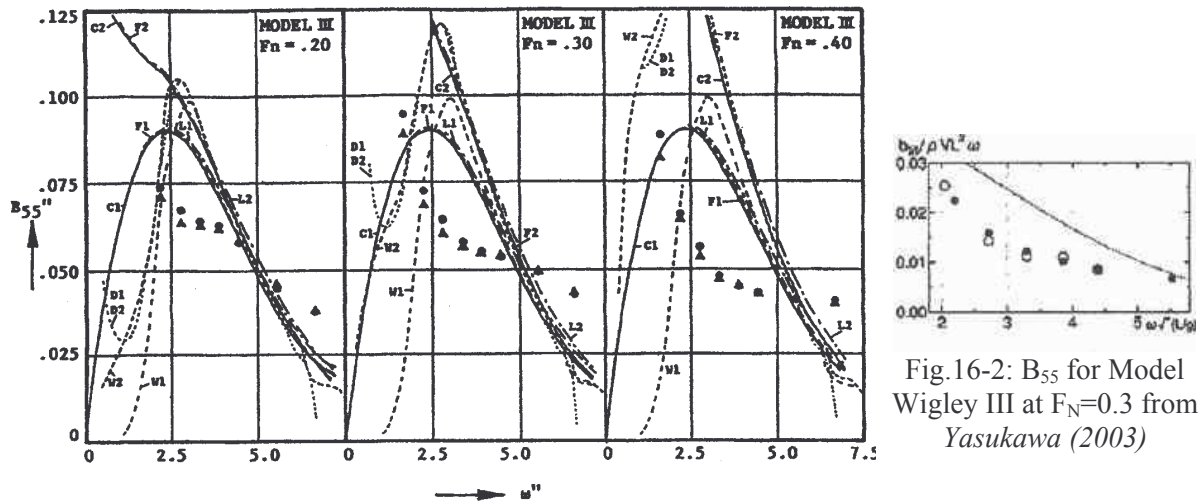


Fig.16-1: B_{55} for Model Wigley III from *Journee (1992)*

Fig.16-2: B_{55} for Model Wigley III at $F_N=0.3$ from *Yasukawa (2003)*

4.3. Blok and Beukelman MODEL 5

For Model 5 the vertical motion and added mass and damping coefficient prediction is done by 2.5 D high speed theory by *Faltinsen and Zhao (1991)* with and without cross-flow correction. In this case, the vertical motions results obtained using the cross flow correction are giving much better fitting of experimental data as can be seen from Figs. 17-20. Originally only heave-heave added mass and damping coefficients are given and only for segmented model (7 segments) at 8 frequencies. *Faltinsen and Zhao (1991, 1993)* used these results as the test case for 2.5 D high speed theory accuracy and presented results for every segment at 3 frequencies. In this work the experimental results for segmented model are integrated and are presented as function of frequencies (same as *Journee's* data).

It can be seen that at $F_N = 0.57$ for whole model both coefficients: A_{33} and B_{33} are predicted quite good. At $F_N=1.14$, except for high frequencies, there is a big difference between numerical results for A_{33} from the experimental. Numerical prediction of damping coefficient B_{33} at $F_N=1.14$ has completely different trend from the experimental results. The cross flow correction is not beneficial when the results are overestimated because it increases even more the gap between the results.

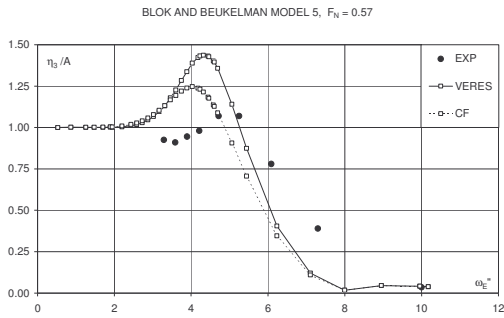


Fig.17: Heave results for Model 5 at $F_N=0.57$

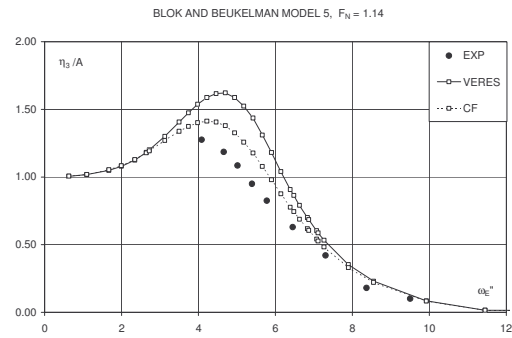


Fig.18: Heave results for Model 5 at $F_N=1.14$

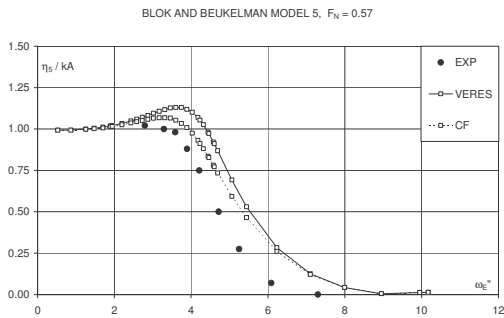


Fig.17-1: Pitch results for Model 5 at $F_N=0.57$

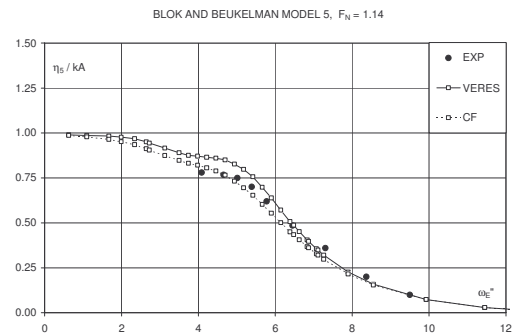


Fig.18-1: Pitch results for Model 5 at $F_N=1.14$

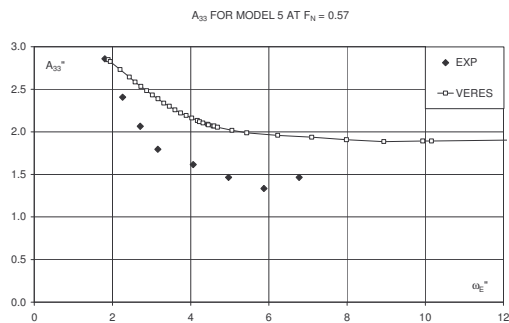


Fig.19: A_{33} for Model 5 at $F_N = 0.57$

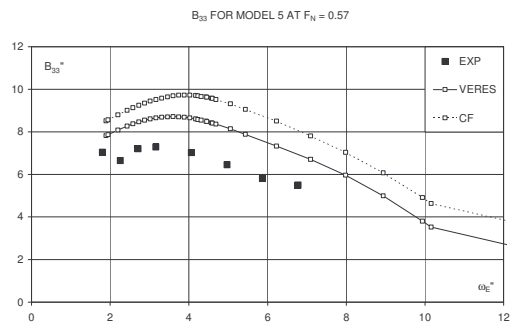


Fig.20: B_{33} for Model 5 at $F_N = 0.57$

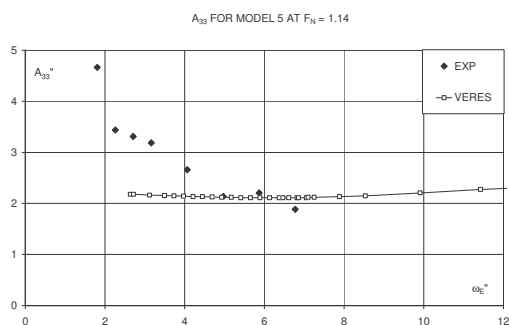


Fig.21: A_{33} for Model 5 at $F_N = 1.14$

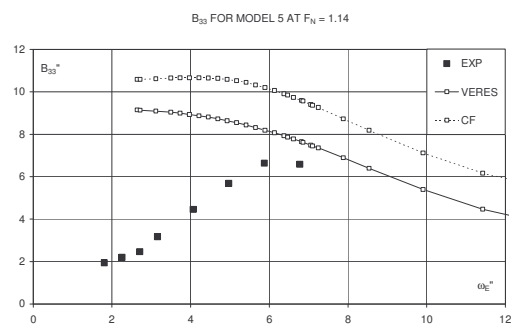


Fig.22: B_{33} for Model 5 at $F_N = 1.14$

5. Conclusions

Collection of experimental data from forced motions experiments and restrained model experiment are very useful tools to validate hydrodynamic theories but the available results are scarce. Analysing the results for added mass and damping coefficients obtained by different theories it can be noted that 2-D theories show not expected poor results in cases in which due to hull form and low speed they should be suitable.

3-D theories show the better coefficient prediction but not in all cases, only Yasukawa results perfectly fit the experimental results for all coefficients. The improvements of his method are nonlinear boundary conditions on hull surface and on free surface in 3-D time domain code. Results presented using 3-D time domain code with non-linear hull boundary condition by Kara and Vassalos improve significantly pitch - pitch coefficients while heave-heave coefficients do not present some benefit comparing them with Journee numerical data or by simple strip theories. Cross-flow correction is beneficial in B_{33} prediction for both Wigley models while in B_{55} offers some improvement only in high frequency range. 2.5 D high speed theory is giving fair results for considered coefficients at $F_N=0.57$ but at very high speed $F_N=1.14$ the predicted results for whole model are quite poor. On the other hand, in *Faltinsen and Zhao (1991)* the results of this method was presented for segmented model with trim at 3 frequencies: the results show partly satisfactory agreement with experimental ones, but using a non linear version of 2.5 D theory.

From the designer point of view, motion and wave loads prediction (rather than coefficient prediction) is of interest, so future work should be in direction of forces evaluation instead of coefficients only.

Acknowledgements

The work was financed by University of Naples "Federico II", research funds 2002 and 2003.

References

BEGOVIC, E., (2002), *Cross-flow effects in the vertical motions prediction of fast slender ships*", Ph.D. Thesis, University of Naples Federico II ", Naples, Italy

BEGOVIC, E; BOCCADAMO, G.; ZOTTI, I.(2002), *On The Effect Of Viscous Forces On The Motions Of High Speed Hulls*, 3rd Int. Conf HIPER'02, Bergen, Norway, pp.47-59

BLOK, J.J.; BEUKELMAN, W. (1984), *The High-Speed Displacement Ship Systematic Series Hull Forms - Seakeeping Characteristics*, Trans. SNAME, Vol. 99, pp.125-150

FALTINSEN, O. (1993), *On Seakeeping of Conventional and High Speed Vessels*, J.Ship Research, Vol 37, No.2, pp.87-101

FALTINSEN, O.; ZHAO, R. (1991), *Numerical predictions of ship motions at high forward speed*, Phil. Trans. R. Soc. London, No. 334, pp.241-252

GERRITSMA, J.; BEUKELMAN, W. (1967), *Analysis of the Modified Strip Theory for the Calculation of Ship Motions and Wave Bending Moments*, Int. Shipb. Progr., Vol. 14, pp.319-337

JOURNEE, J.M.J. (1992), *Experiments and Calculations on 4 Wigley Hull Forms in Head Waves*, Report 0909, Delft University of Technology

JOURNEE, J.M.J. (2001), *Discrepancies in Hydrodynamic Coefficients of Wigley Hull Forms*, MARIND 2001, Varna, Bulgaria

KARA, F.; VASSALOS, D. (2003), *Time-Domain Prediction of Steady and Unsteady Motion of High Speed Crafts*, 7th Int. Conf. FAST 03, Ischia, Italy, pp.27-36

KEUNING, J.A. (1990), *Distribution of Added Mass and Damping Along the Length of a Ship Model Moving at High Forward Speed*, Int. Shipbuilding Progress, Vol. 37, pp.123-150

SALVESEN, N.; TUCK, E.O.; FALTINSEN, O. (1970), *Ship Motions and Sea Loads*, Trans. of SNAME, Vol. 78, pp.250-287

THWAITES B. (1960), *Incompressible Aerodynamics*, Oxford University Press, UK

YASUKAWA H. (2003), *Application of a 3-D Time-Domain Panel Method to Ship Seakeeping Problems*, 24th Symp. Naval Hydrodynamics

MARINTEK - Sintef Group: *VERES Version 3.18 - User's Manual*, January 1999

MARIN Wageningen - *SHIPMO - User's Manual*, Release 3.11, July 1992

Hydro-Elastic Simulation of Simple 2-D Geometries in Water Entry

Adrian Constantinescu, Alain Nême, Volker Bertram
ENSIETA, Brest/France, volker.bertram@ensieta.fr

Abstract

This paper describes a pre-study of fluid–structure interaction during the impact of a ship on the water surface. The paper compares two different approaches for numerical simulation of the impact of simple rigid and deformable shells on water with experiments.

1. Introduction

Slamming is particularly important for fast ships:

- Slamming loads are often the largest loads and determine structural dimensions, particularly sensitive for light-weight, fast ships.
- Even if each impact load is small, frequent impact loads accelerate fatigue failures of hulls.
- Fast ships usually transport passengers and slamming loads affect passenger comfort.

A fully satisfactory theoretical treatment of slamming has been prevented so far by the complexity of the problem:

- Slamming is a strongly non-linear phenomenon which is very sensitive to relative motion and contact angle between body and free surface.
- Predictions in natural seaways are inherently stochastic; slamming is a random process in reality.
- Since the duration of wave impact loads is very short, hydro-elastic effects are large.
- Air trapping may lead to compressible, partially supersonic flows where the flow in the water interacts with the flow in the air.
- Most theories and numerical applications are for two-dimensional rigid bodies (infinite cylinders or bodies of rotational symmetry), but slamming in reality is a strongly three-dimensional phenomenon.

Bertram (2000) gives an overview of the most important analytical approaches to slamming, pointing out that in the end only computational fluid dynamics (CFD) methods are expected to bring considerable progress, while classical theories work well in two-dimensional flow for certain geometries.

We focus here on the aspect of hydro-elasticity, limiting the study to simple geometries and 2-d flows, as a first step to develop more sophisticated 3-d numerical methods.

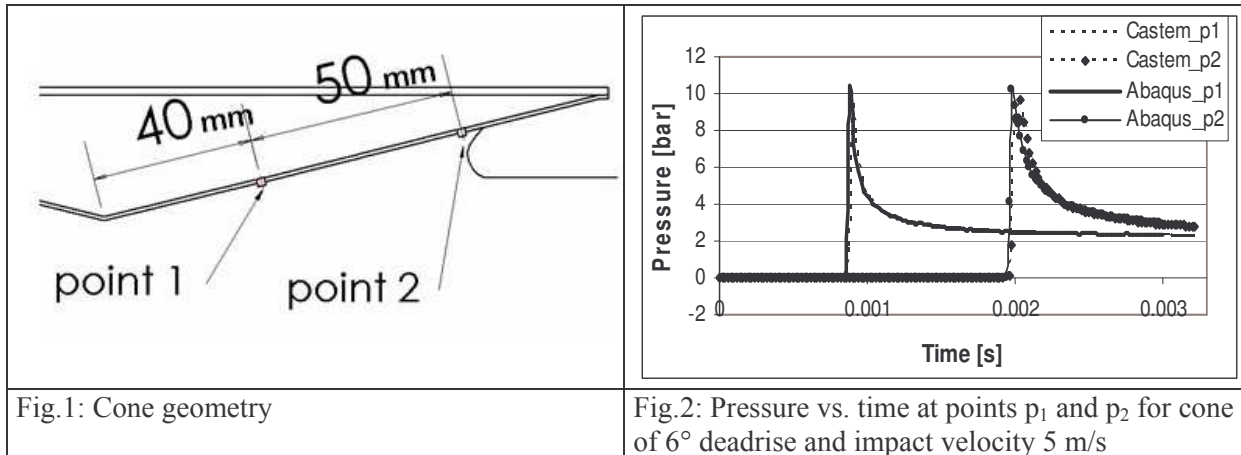
2. Numerical approach

Donguy et al (2001) developed a numerical approach to simulate 3-d slamming problems, combining the assumption of small displacement for the fluid and the solid with an asymptotic formulation for accurate pressure evaluation on the wetted surface of the body. For solving the fluid problem, they used a fluid–heat analogy under the hypothesis of incompressibility and irrotational initial velocity field for the fluid, considering the velocity potential or the displacement potential as temperature. The finite element code CASTEM was employed for solving fluid (heat) and solid evolutions. The fluid–structure interaction generates a coupling matrix which has been implemented in CASTEM.

We have globally followed the same approach using the commercial finite element code ABAQUS associated with PYTHON and FORTRAN languages instead of CASTEM. Thus, some procedures have been modified and several numerical aspects improved. We considered only wedges and cones as geometries. Three deadrise angles β (6° , 10° , and 14° between the body and the calm water surface),

three initial impact velocities (2.5, 5, and 8 m/s) and three thickness values of the outer body shell (0.5, 1, and 1.5 mm) were considered.

An additional mass of 30 kg was attached in a ring around the deformable steel shells. The typical dimensions of the structure are the same as those used by *Donguy et al. (2001)* in the experiments. The pressure was measured at two points (p_1 and p_2), Fig.1.



For the rigid cases, the velocity was assumed constant. Our simulation of the maximum pressure values agrees very well with those determined with CASTEM, Fig.2. We also obtain the same wet-surface propagation velocity, as well as the resulting vertical force on the solid. The study of impact with deformable structures is more complicated. A finite element method (FEM) must be employed to find the shell evolution in parallel with the fluid calculation. To couple these two simulations, we project the pressure obtained at the nodes of the fluid mesh onto the Gauss points of the solid surface and the nodal displacements or nodal velocities of the structure onto the Gauss points of the water surface.

3. Mathematical Formulation

We consider the problem of impact of a 3-d body on a water surface, Fig.3. The fluid problem is formulated within potential flow theory for an ideal fluid (incompressible, inviscid, irrotational). The velocity vector anywhere in the fluid domain follows from $\mathbf{v} = \text{grad}\Phi$. $\Phi(x,y,z,t)$ is the velocity potential. We assume small disturbances both for the solid and the fluid.

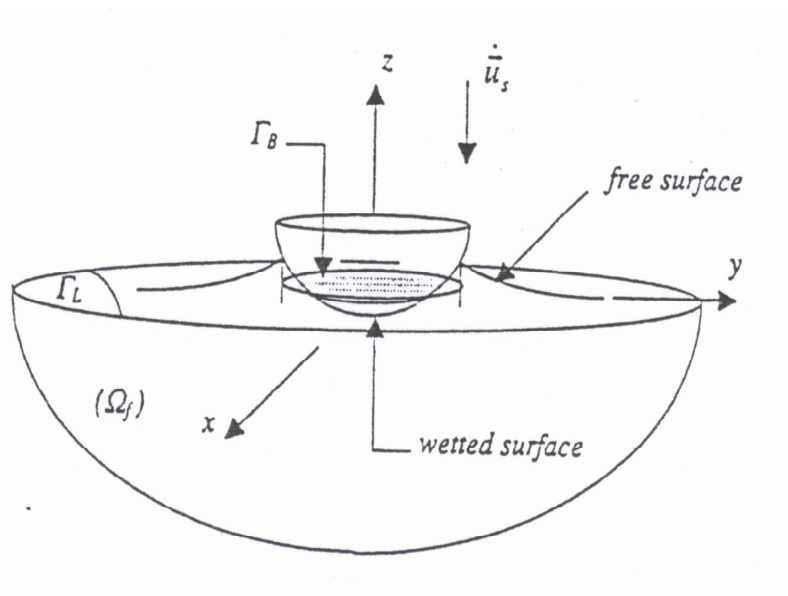


Fig.3 : Geometric definitions

Then, the velocity potential must satisfy the following conditions:

$$\Delta\Phi = 0 \quad \text{in } \Omega_f \quad (1)$$

$$\text{grad}\Phi \cdot \mathbf{n} = \dot{\mathbf{u}}_s \cdot \mathbf{n} = \frac{\partial \mathbf{u}_s}{\partial t} \cdot \mathbf{n} \quad \text{on the wet surface} \quad (2)$$

$$\Phi=0 \quad \text{on the free surface} \quad (3)$$

$\mathbf{u}_s(x,y,t)$ the displacement of the structure. Eq.(2) represents no-penetration condition for the body surface.

Eq.(3) expresses the condition of zero relative pressure on the free surface. Everywhere at the free surface and at all times, we have atmospheric pressure. The linearized Bernoulli equation gives then at the free surface: $\partial\Phi/\partial t - gz=0$. Neglecting gravity (wave making) for high impact speeds, we then obtain: $\partial\Phi/\partial t=0$, which after integration becomes $\Phi=\text{const}$. As only derivatives of the potential are of interest here, we can set the constant arbitrarily to zero.

The fluid is initially at rest:

$$\Phi(x_0, y_0, z_0, 0) = 0 \quad (4)$$

The flow is not disturbed far from the body:

$$|\text{grad}\Phi| \rightarrow 0 \quad \text{for } (x_0^2 + y_0^2 + z_0^2)^{1/2} \rightarrow \infty \quad (5)$$

Once the potential is determined, the fluid pressure is calculated by the (linearized) Bernoulli equation:

$$p = -\rho_0 \frac{\partial\Phi}{\partial t} \quad (6)$$

The conditions on the initial water surface ($z_0 = 0$) are:

$$\frac{\partial\Phi}{\partial z_0} = \dot{u}_{sz} = \frac{\partial u_{sz}}{\partial t} \quad \text{on } \Gamma_B \quad (7)$$

$$\Phi = 0 \quad \text{on } \Gamma_L \quad (8)$$

$$\frac{\partial\Phi}{\partial z_0} = \frac{\partial h}{\partial t} \quad \text{on } \Gamma_L \quad (9)$$

$$\text{where } h = \int_0^t \frac{\partial\Phi}{\partial z_0} \Big|_{(x,y,0,\tau)} d\tau \quad (10)$$

Γ_B is vertical projection of the body wetted surface on $z_0 = 0$ and Γ_L the liquid surface, i.e. the free water surface.

An analogy to fluid-thermodynamics can be employed to solve our fluid dynamics problem with the commercial finite element code ABAQUS/Standard and its module of thermal resolution. The heat transfer model is given by the following equations:

$$\Delta T = 0 \quad \text{in } \Omega_f \quad (11)$$

$$\lambda \frac{\partial T}{\partial z_0} = -q \cdot z \quad \text{on } \Gamma_B \quad (12)$$

$$T = 0 \quad \text{on } \Gamma_L \quad (13)$$

$$\frac{\partial h}{\partial t} = \frac{\partial T}{\partial z_0} \quad \text{on } \Gamma_L \quad (14)$$

$$\text{where } h = \int_0^t \frac{\partial T}{\partial z_0} \Big|_{(x,y,0,\tau)} d\tau \quad (15)$$

An equivalent system to Eq.(1) and Eqs.(7)-(10) is obtained if the temperature T is expressed in [m²/s], the thermal conductivity set to $\lambda=1$, and q expressed in [m/s] in the thermal module of ABAQUS/Standard.

In addition, it is necessary to know the extent of the wet surface d . Physically, the position of this surface is given by imposing the condition of conservation of the volume of the fluid. In an equivalent way, this condition results in finding the intersection between the rise in the free face and the position of the solid body. The rise in the free surface is expressed as the integral in time of the normal derivative of the velocity potential in Eq.(10). More simply, we can solve the problem of the displacement potential $\Psi = \Psi(x_0, y_0, z_0, t)$ such that:

$$\Psi = \int_0^t \Phi(x_0, y_0, z_0, \tau) d\tau \quad (16)$$

and $h = \Psi(x_0, y_0, 0, t)$. Thus the potential Ψ must satisfy:

$$\Delta \Psi = 0 \quad (17)$$

$$\frac{\partial \Psi}{\partial z_0} = u_{sz} \quad \text{on the wet surface} \quad (18)$$

$$\Psi = 0 \quad \text{on the free surface} \quad (19)$$

Again, we utilize the fluid-heat analogy to calculate the equivalent system formed by Eqs.(17)-(19), the temperature T will be expressed in [m²], thermal conductivity $\lambda=1$, and q in [m] in the thermal module of ABAQUS/Standard.

4. Rigid Structures

We limit ourselves to two simple shapes, namely wedges and cones. Employing rotational symmetry, cones can be treated as two-dimensional bodies. The deadrise angle β of either form is defined between the body and the free surface at rest.

The two fundamental assumptions in this case are: the entry speed of the solid into the fluid is constant; the numerical time increment Δt is constant at $2 \cdot 10^{-5}$ s. The method of resolution does not require a finite element calculation, as we know exactly the position of the body surface at each time. To determine the pressure exerted by the fluid on the structure, a time increment $\delta t_i = i \Delta t / 60 = t_i / 60$ was used. The fluid time step δt_i thus exceeds the structure motion time step Δt after 60 time increments, i.e. after $12 \cdot 10^{-4}$ s for $\Delta t = 2 \cdot 10^{-5}$ s. The small time steps at the initial water entry are necessary to capture the high gradient of the potential and the corresponding pressure peak. The increasingly large time steps make the algorithm efficient and stable.

The time increment for the fluid problem was optimized. A small mesh size M_s around the contact surface border is required to take into account the high potential gradient in this zone. According to the estimated wet surface velocity $\dot{d} = \frac{4}{\pi} \frac{V}{\tan(\beta)}$ for cones and $\dot{d} = \frac{\pi}{2} \frac{V}{\tan(\beta)}$ for wedges, where V is

the impact velocity, δt must be greater than M_s/\dot{d} to compute accurately the contact surface dimension. On the other hand, δt must be small enough to well determine the pressure field, Eq (20).

The calculation of the final numerical pressure in several stages, *Donguy (2002)*, is associated with an asymptotic development at the wetted surface boundary. This method is classically used to model the problem of the hydrodynamic impact, e.g. *Wagner (1932)*. The asymptotic study led to the determination of two zones (near-field and far-field) in which two asymptotic developments are obtained then connected. Within first order, the composite solution for the pressure includes a far-field solution (fulfilling conditions far from the body-surface intersection, but being singular at the intersection) and a near-field solution (valid in the vicinity of the intersection, describing the formation of a jet). The far-field pressure is approximated by central differencing of the Bernoulli equation (20). For the correct evaluation of the resulting total effort, it is necessary to consider also the near-field pressure, Eq.(21). For 2-d flows and very small deadrise angle ($\beta < 1^\circ$), combining near-field and far-field solutions allows to obtain an analytical so-called ‘composite’ solution which is continuous in the whole domain, Eq.(22). However, in reality air-trapping occurs for such small deadrise angles, making classical potential flow approaches questionable, *Bertram (2000)*. Since we utilized numerical resolution and finite distances from the exact wetted surface boundary, an approximate model is necessary to connect analytical far-field and near-field pressure solutions, Eq.(23). The operating range of this connection is limited to the distance r in front of the end of wet surface.

$$p_{edfc} = -\rho_f \frac{\Phi^{t_j} - \Phi^{t_j - \delta t_j}}{\delta t_j} \quad (20)$$

$$p_i(x_0, t) = \rho_f \frac{\dot{d}^2}{2} \left[1 - \left(\frac{1-u}{1+u} \right)^2 \right], \quad u \in [0, 1]$$

$$x_0 - d(t) = \frac{\delta \delta(t)}{\pi} \left(-2 \ln u - \frac{4}{u} - \frac{1}{u^2} + 5 \right) \text{ for } x_0 < d(t) \quad (21)$$

$$x_0 - d(t) = \frac{\delta \delta(t)}{\pi} \left(-2 \ln u - 4u - u^2 + 5 \right) \text{ for } x_0 > d(t)$$

$$\delta \delta(t) = \frac{\pi V^2 d(t)}{8 \dot{d}^2(t)}$$

$$(p_i)_e(x_0, t) = \rho_f \frac{V d \dot{d}}{\sqrt{2d(d-x_0)}} \quad (22)$$

$$(p_i)_e^{num}(x_0, t) = (p_i)_e(x_0, t) \text{ for } x_0 < d - r(t)$$

$$(p_i)_e^{num}(x_0, t) = \frac{(p_i)_e(x_0, t) - p_{edfc}}{r(t)} (d - x_0) + p_{edfc} \text{ for } x_0 > d - r(t) \quad (23)$$

In these expressions, ρ_f stands for the fluid density, taken as 1000 kg/m^3 for fresh water. The final pressure is given by the composite numerical corrected pressure:

$$p_{num} = p_{edfc} + p_i - (p_i)_e^{num} \quad (24)$$

From these previous set of equations we can prove that the maximal pressure equals to :

$$\rho_f \frac{d^2}{2} \quad (25)$$

Fig.4 shows the first grid of the fluid domain used in our calculations. The zone with a fine grid corresponds to the intersection between the fluid surface and the body surface.

As in the drop tests of *Donguy (2002)*, we calculated with CASTEM and ABAQUS the time histories of the pressure at the two points p_1 and p_2 , at a distance of 40 mm and 90 mm, respectively, of the top of the body, Fig.2. The results obtained with ABAQUS and CASTEM were very similar. For rigid cones, the results were also satisfactory. Table I compiles the maximum values of the pressures for various configurations. The maximum values calculated with ABAQUS are very close to those given with CASTEM. Both differ from experimental values, because the sensors average the pressure over the sensor area. Averaging our numerical results over the sensor area gives then also much better agreement with experiments.

Table I: Pressures [bar] on rigid cone for deadrise angle 10°

Speed	2.5 m/s		5 m/s	
	p_1	p_2	p_1	p_2
ABAQUS	1.67	1.68	6.7	6.7
CASTEM	1.6	1.6	5.4	6.6
Experiment	1.0	1.4	4.1	5.6
ABAQUS averaged	1.12	1.6	4.5	5.6

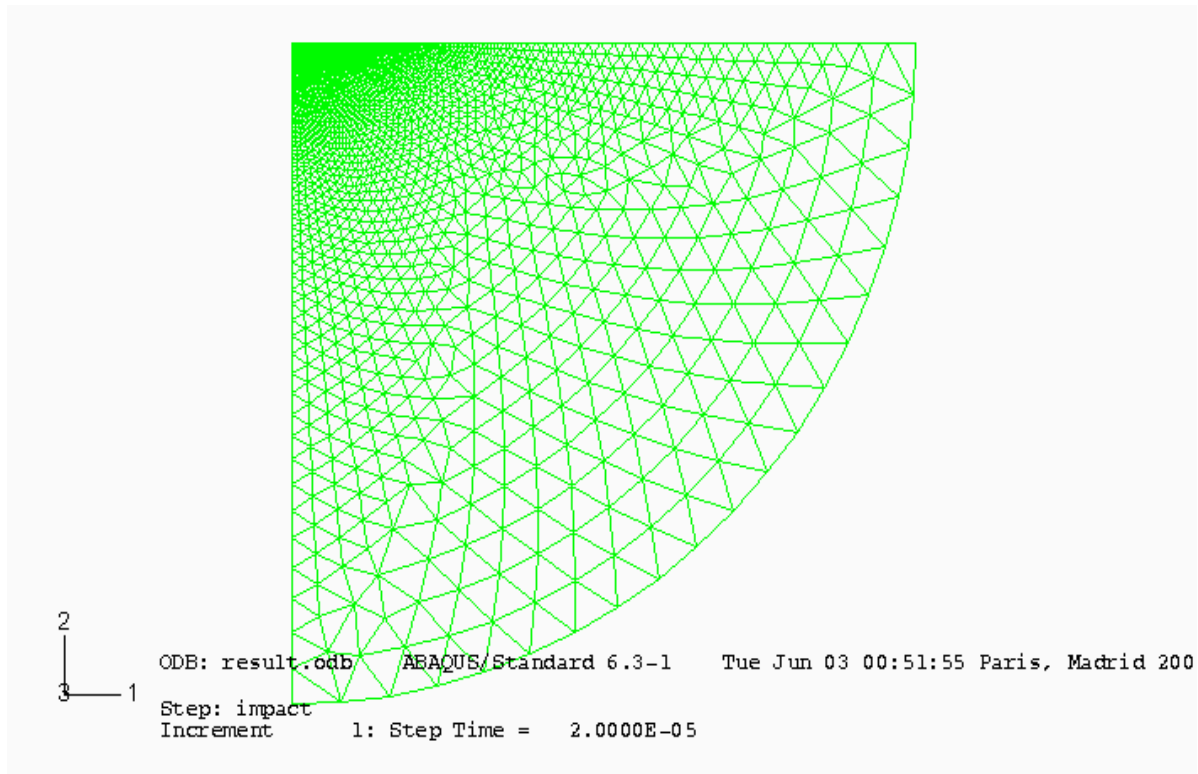


Fig.4 : Fluid mesh

The time history of the force as function of deadrise angle is very close to that obtained with CASTEM, as well as with the analytical non-linear solution determined by *Zhao and Faltinsen (1992)*. The peak pressure obtained by Zhao and Faltinsen corresponds to the analytical expression derived by combining Eq.(24) with the expressions for the wet surface velocity for cones and wedges given above:

$$\frac{\rho_f}{2} \left[\frac{4}{\pi \tan(\beta)} V \right]^2 \text{ for cones} \quad (26)$$

$$\frac{\rho_f}{2} \left[\frac{\pi}{2 \tan(\beta)} V \right]^2 \text{ for wedges} \quad (27)$$

We optimized the fluid mesh reducing the number of elements successively while checking that the results still agreed with Eqs.(26) and (27), respectively. Without apparent loss of accuracy in results, we thus reduced the mesh size from initially 30000 linear triangular elements to 2000, Fig.5. The drastic reduction in elements resulted in a much smaller, but still considerable reduction in CPU time by a factor 2. The reason is that the pressure interpolation between fluid and structure nodes depends on the number of elements on the body contour, not on the elements on the free surface. Also, the number of necessary iterations to determine the wetted surface increases as the mesh becomes coarser.

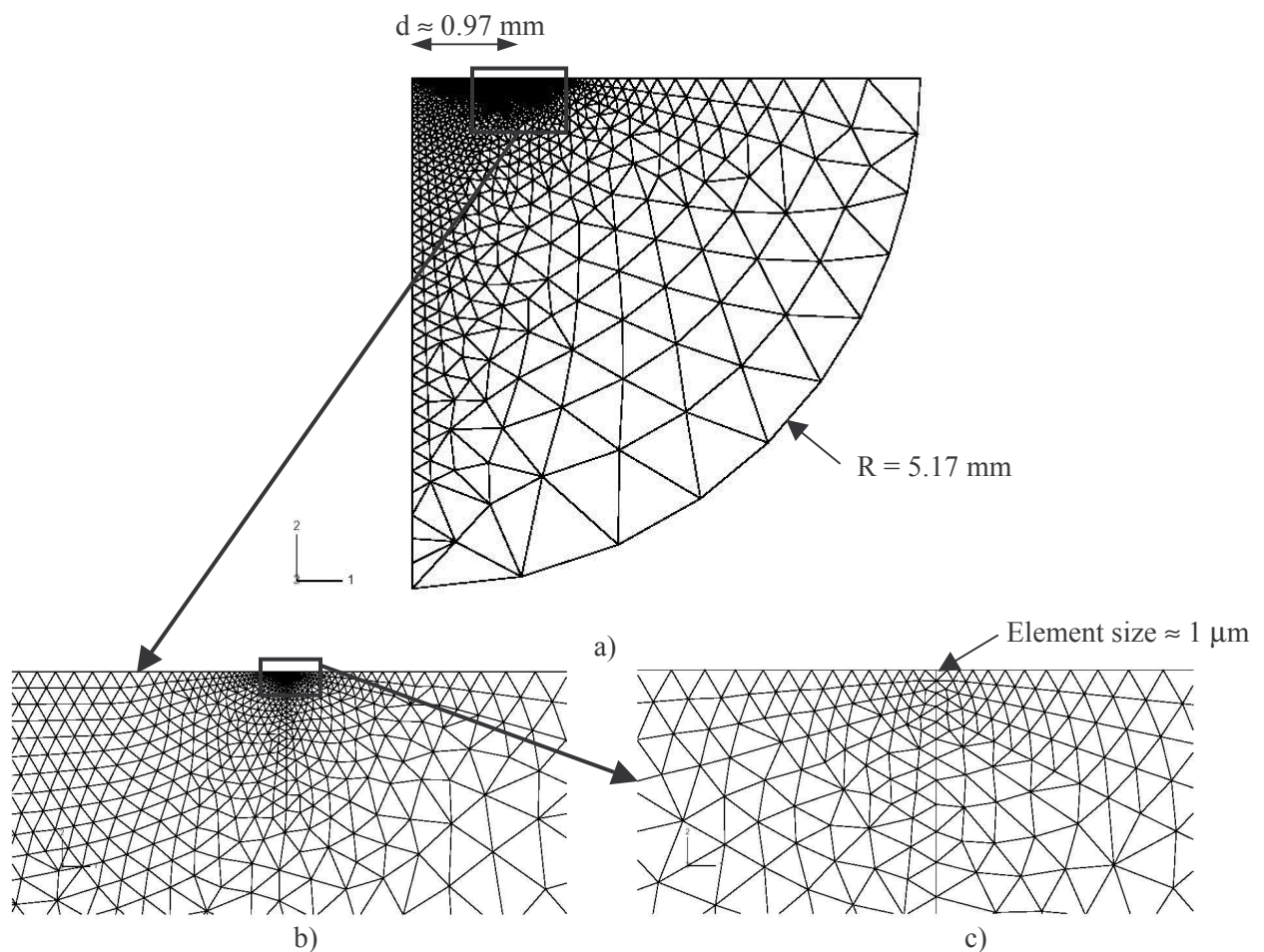


Fig.5: Fluid mesh at the first increment (20µs), for a 6° cone impacting the water surface at 4 m/s
a) complete mesh, b) zoom on 'a', c) zoom on 'b'

We can also check after post-processing if the Neumann condition (no penetration) are correctly prescribed along the contact line between solid and fluid, Fig.6.

5. Deformable Structures

The impact study of deformable structures is more complicated as it requires simultaneous computations of fluid and structure. The flow computations remain very similar to the rigid body case, but the

structure calculation and its coupling to the fluid calculation differ considerably between our approach using ABAQUS and *Donguy's (2002)* approach using CASTEM. Donguy used a strong fluid-structure coupling iterative process – only one iteration – during the time step Δt . Instead, we employ the *RESTART function of ABAQUS. This command allows to stop and restart a simulation without losing the history of the positions, velocities and accelerations at nodes. During the resulting pauses, we carry out a fluid calculation. Thus an explicit integration, denoted here ‘ping-pong scheme’, is achieved in our case.

Fluid pressures and position of the body are expressed by values at the nodes. Because the fluid grid does not coincide with structure grid, we use a cubic spline to interpolate pressures from the fluid grid to the structure grid (Gauss points) and displacements and velocities from the structure grids to the fluid grid.

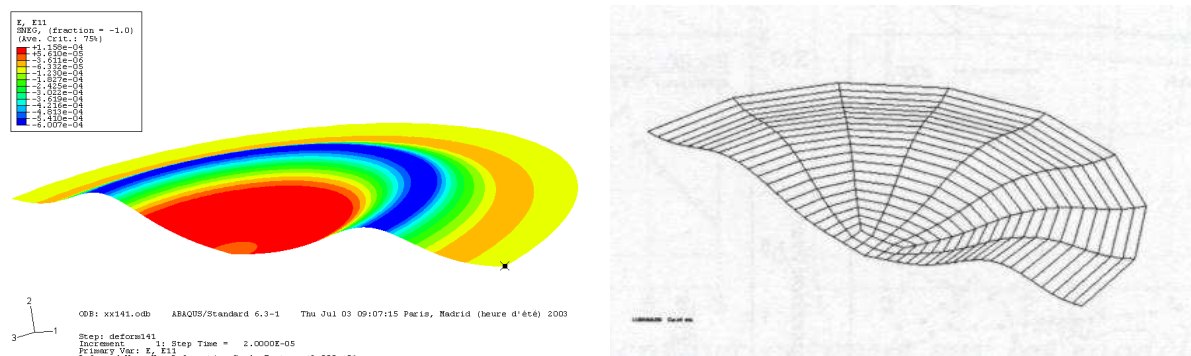


Fig.6: Scaled deformation of a cone: ABAQUS (left) and CASTEM (right)

Wedges are modeled as a 3d shell of small length – one element in the y-direction – with a longitudinal symmetry on the two sides of this shell band. All elements used are linear: triangle DC2D3 (2D fluid), triangle DCAX3 (axisymmetric fluid), 4-node shell element S4 (wedge) and axisymmetric shell element SAX1 (cone). The mesh size of the solid structures is around 10 μm .

Compared to the rigid case, in the deformable case we record important differences for the wedge between the two approaches, ABAQUS and CASTEM. For instance, the pressure p_1 obtained with CASTEM is 2.7 bars and 11.5 bars with ABAQUS for velocity 5 m/s, shell thickness 1mm and deadrise angle 6° . For cones, the results between the two approaches agree qualitatively well, Fig.6. A quantitative comparison is impossible because not all details were documented in *Donguy (2002)*.

The calculated average pressure gives values close to the experiment. The maximum values of the pressures decrease less over time (compared to values obtained with the wedge) due to the relatively larger rigidity of cones.

We tried to improve our explicit fluid-structure interaction scheme. We went further than Donguy's model by computing a totally implicit fluid-structure interaction. The main idea is to calculate alternatively up to the complete plunging of the structure into water both the time history of displacement and velocity of the structure nodes, and the fluid pressure time history along the contact surface for prescribed deformation. This iterative process starts with the flow computation, considering a rigid body motion for the solid.

The obtained fluid pressure time history along the contact surface is transferred to the transient dynamic finite element analysis of the structure. The post-processing of this finite element analysis allows to determine the time history of displacement and velocity of the structure nodes which it is transferred to the fluid finite element analysis, and so on. This iterative scheme, denoted here ‘process scheme’, is carried on until convergence.

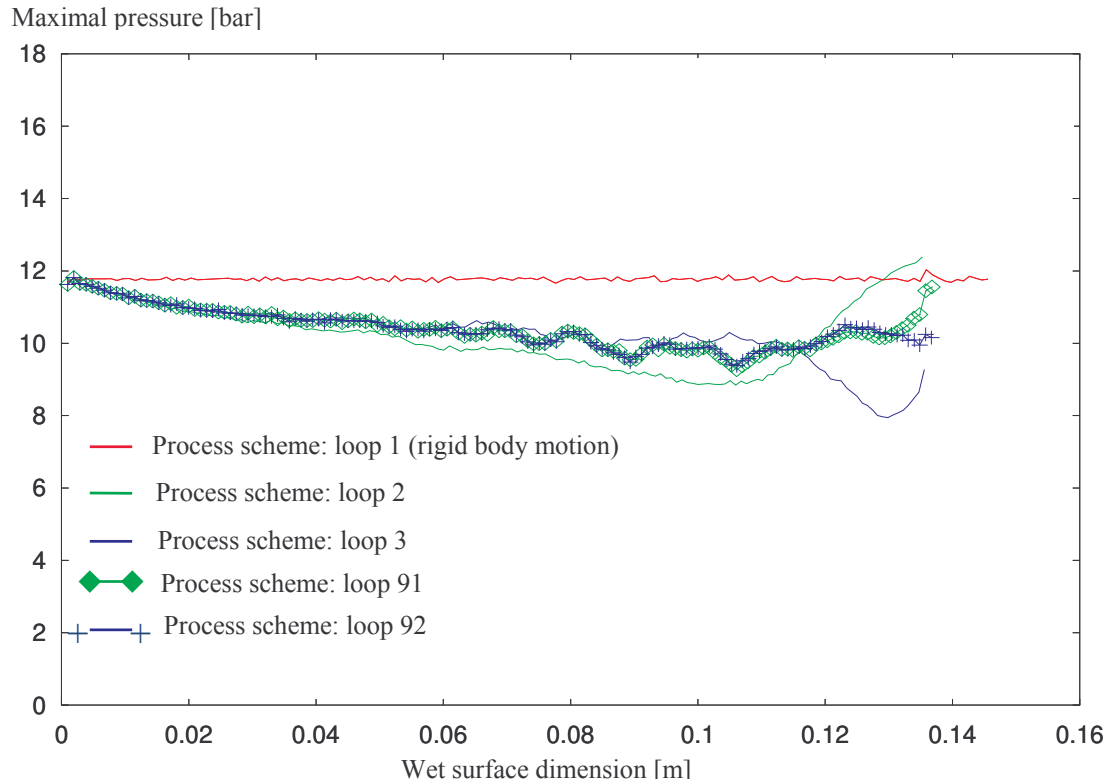


Fig.7: Maximal pressure distribution after different loops of the process scheme

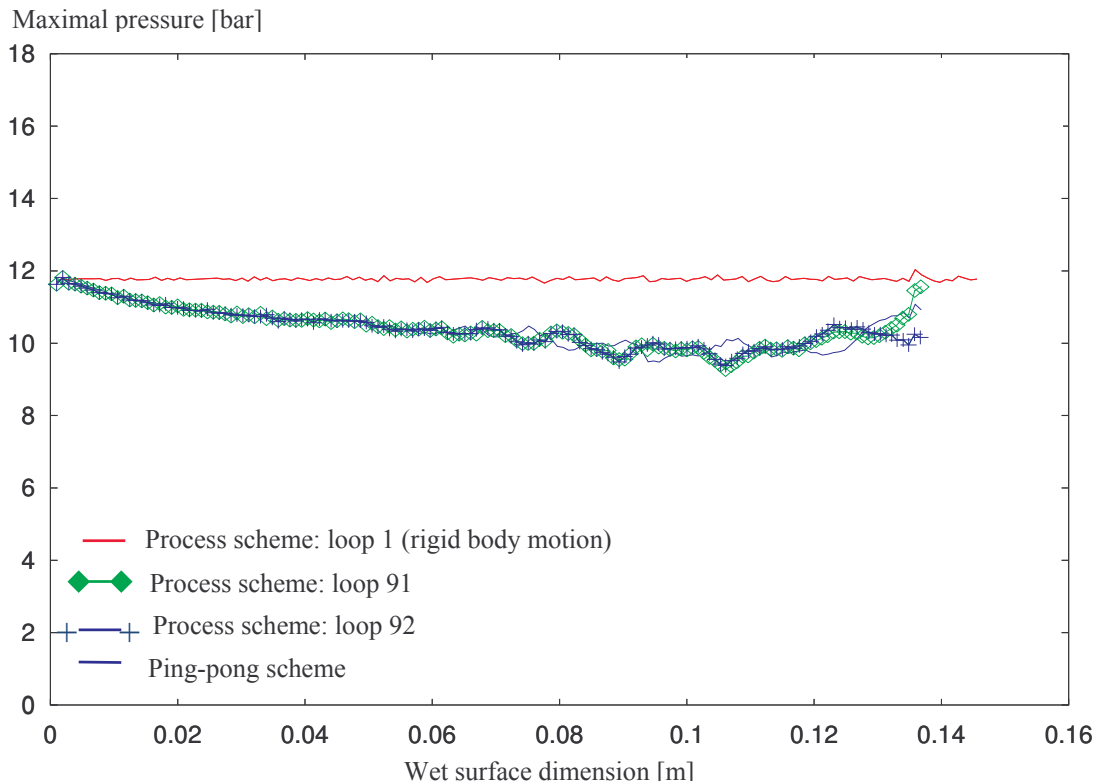


Fig.8: Maximal pressure distribution; process scheme and ping-pong scheme

We conducted the simulation of a 6° cone impacting the water surface at 4 m/s. The structure was 1.5 mm thick. The cone meridian was 16 cm long. We made the assumption of elastic behavior for the material (steel) with a Young modulus 210 GPa, a Poisson ratio 0.3, and a density 7800 kg/m^3 . The Fig.7 represents the peak pressure distribution along the solid structure after the first return loop, the second, the third, the 91st and the 92nd of the implicit iterative process. More loops are necessary to

obtain the convergence over 0.12 m of wet surface. Fig.8 compares our explicit ‘ping-pong’ and implicit ‘process’ fluid-structure interaction schemes. The explicit ‘ping-pong’ scheme and the final iterations of the implicit scheme yield similar results. The apparent wiggles may be due to numerical instabilities, but also due to beginning vibrations of the body. This question is subject to current discussion and further research.

6. First studies for an improved hydrodynamic model

For most practical impact problems, the body shape is complex and the effect of gravity is considerable. In such cases, analytical solutions are very difficult or even impossible. This leaves CFD as a tool. Various researchers have approached slamming problems, usually employing surface-capturing methods, e.g. Volume-of-Fluid or level-set techniques. (See *Bertram (2000)* for a discussion these various CFD techniques). Although viscosity plays a less important role for slamming than for many other problems in ship hydrodynamics, usually RANSE (Reynolds-averaged Navier-Stokes equations) solvers were employed, e.g. *Muzaferija and Peric (1998)*, *Muzaferija et al. (1998)*, Fig.9, *Sames et al. (1998)*, Fig.10, and most noteworthy for planing hulls *Caponnetto (2002)*.

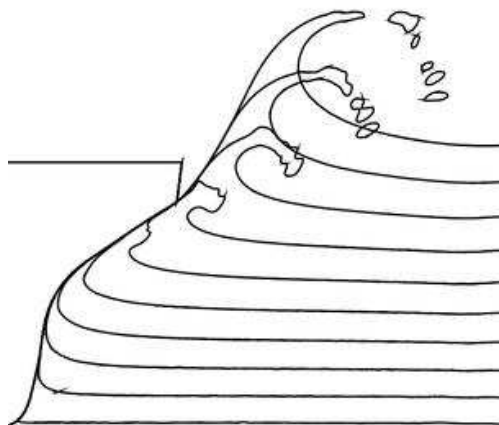


Fig.9: 2-d Slamming simulation using CFD, *Muzaferija et al. (1998)*

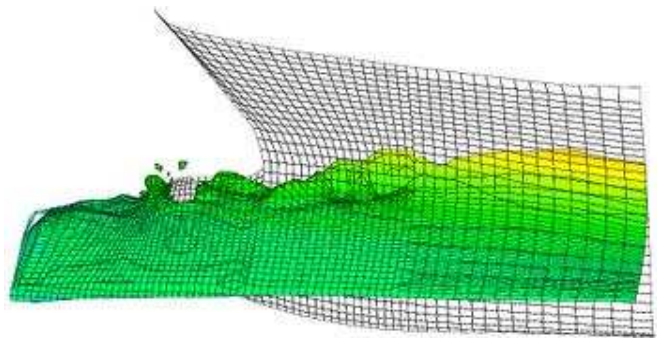


Fig.10: 3-d slamming simulation using CFD, *Sames et al. (1998)*

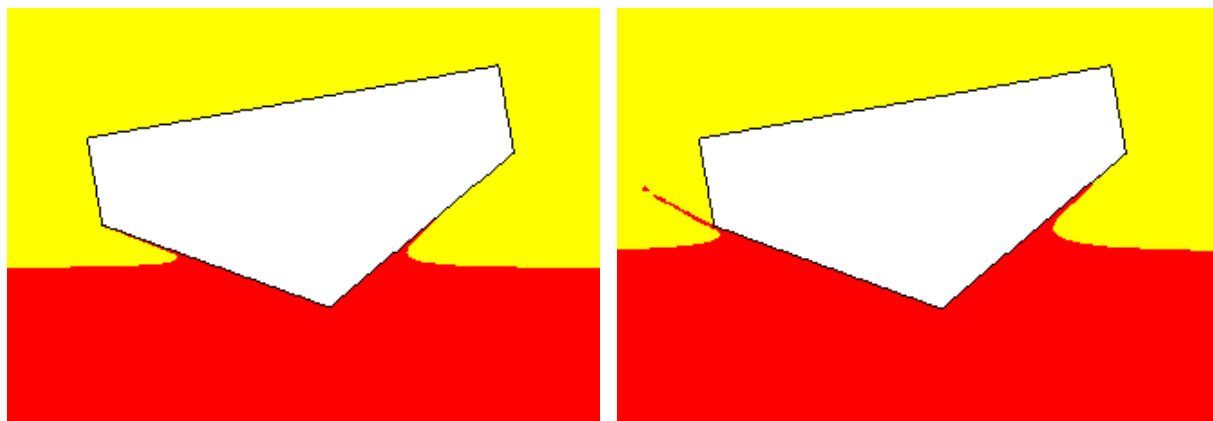


Fig.12: Water surface deformation for wedge with deadrise angle $\beta=30^\circ$ computed with Fluent

Our hydrodynamic model is so far insufficient for practical work, as it is fundamentally limited to 2-d and even there to a narrow bandwidth of deadrise angles. While the approach was justified by advancing more rapidly on the fluid-structure interaction aspect and testing the ABAQUS software, we will eventually use CFD methods to model the fluid aspects. In cooperation with the Sharif

University/Tehran, we reproduced the complex free-surface deformation with detaching jet and droplets for the water entry of a wedge with deadrise angle 30° , both for the symmetric case and the case of the wedge tilted by 10° , Fig.11, *Seif et al. (2004)*. In this case, we employed the commercial RANSE solver Fluent in version 6.0.

7. Conclusion

For the rigid-body water entry, the hybrid fluid-structure approaches based on CASTEM and ABAQUS give practically identical results for the propagation velocities of the wetted surface and differences in pressure of approximately 5%. Numerical values for maximum pressures are higher than measured due to the averaging effect of finite sensor areas. Analytical results obtained by *Zhao and Faltinsen (1992)* for the evolution of force as function of time, deadrise angle, and entry speed were well reproduced by our approach.

For the deformable body case, differences between ABAQUS and CASTEM are larger, undoubtedly related to the differences in modeling. In general, the time steps for the deformations are similar between the two codes. Note that partially plastic deformation was observed for the cone and the wedge with 6° deadrise in experiments.

There is general consensus for the need of proper validation for numerical slamming simulations. A shock machine allowing controlled water entry velocity and hydro-elastic detailed pressure measurements will help to validate CFD simulations, finding suitable grid and other input parameters for quasi-3d cases like cones.

Once these parameters are established and sufficient computing power available, CFD methods will allow to predict rather detailed pressures on complex ship structures needed both for ultimate strength design (single impact leading to plastic deformation) and fatigue strength design (high-frequency load of moderate amplitude leading to material failure due to microscopic structure failure).

At ENSIETA, such machines are at present installed and expected to be operational next year. The resultant validation data should aid further progress in numerical methods as well.

Acknowledgements

We are grateful for discussions and encouragement from Bernard Peseux (ECN, Nantes) and Yann Doutréleau (ENSIETA, Brest), Mohammad Seif (Sharif Univ., Tehran) for supplying initial grids for the CFD computations, and François Grosjean (ENSIETA, Brest) for his help on Fluent.

References

- BERTRAM, V. (2000), *Practical ship hydrodynamics*, Butterworth+Heinemann, Oxford
- CAPONNETTO, M. (2002), *Sea keeping simulation of fast hard chine vessels using RANSE*, NuTTS'02, Pornichet
- DONGUY, B.; PESEUX, B.; FONTAINE, F. (2001), *Numerical and experimental investigation of a rigid cone striking the free surface of an incompressible fluid*, ASME, PVP Conf., Atlanta
- DONGUY, B. (2002), *Study of the fluid interaction structure at the time of the hydrodynamic impact*, Doctoral Thesis, Ecole Centrale de Nantes
- MUZAFERIJA, S.; PERIC, M. (1998), *Computation of free-surface flows using interface tracking and interface-capturing methods*, Nonlinear Water Wave Interaction, Comp. Mech. Publ.
- MUZAFERIJA, S.; PERIC, M.; SAMES, P.; SCHELLIN, T. (1998), *A two-fluid Navier-Stokes solver to simulate water entry*, 22nd Symp. Naval Hydrodyn., Washington
- SAMES, P.; SCHELLIN, T.; MUZAFERIJA, S.; PERIC, M. (1998), *Application of two-fluid finite volume method to ship slamming*, OMAE'98, Lisbon
- SEIF, M.S.; MOUSAVIRAAD, S.M.; SADDATHOSSEINI, S.H.; BERTRAM, V. (2004), *Numerical modeling of 2-d water impact in one degree of freedom*, Sintesis Tecnologica (submitted)
- ZHAO, R.; FALTINSEN, O. (1992), *Slamming loads on high-speed vessels*, 19th Symp. Naval Hydrodyn., Seoul

CFD Simulation and Virtual Reality Visualization for a Fast Monohull in Waves

Matthias Klemt, Plaza Compositor Miguel Asíns Arbó 16, 46013 Valencia, Spain, klemt@freenet.de
Gerhard Jensen, Technical University of Hamburg-Harburg, Germany, g.jensen@tu-harburg.de
Olaf Lindenau, Technical University of Hamburg-Harburg, Germany, lindenau@tu-harburg.de

Abstract

Within the Navier-Stokes-Equation-Solver "Comet", based on finite volume method, via the user-coding interface routines are programmed to predict forces and moments on floating bodies and to calculate the body motions according to these. An overlapping grids method has been developed and employed to avoid the difficult grid-management caused by the change of the body location. The post-processing of the simulation has been done by transforming the results into a 3D-model using the "Virtual Reality Modelling Language". Interactive choice of the data to be displayed and interactive navigation in space and time offers the viewer the ability to analyse the results in more detail. As applications in this paper a RoRo ship in extreme waves and the wind induced motion of a sailing yacht are presented.

1. Introduction

Ship motions and associated loads on a ship hull are usually predicted with methods based on potential flow assumptions. Large errors can be introduced by these assumptions for some practically important cases like ship motions in large amplitude waves, ship responses under a wave impact (slamming), or ship capsizing etc. The need for a numerical tool that can predict the motions and loads in large waves, taking into account viscous effects, turbulence, flow separation and wave-breaking phenomena is obvious.

The objective of this research is to develop and validate a computational technique for the coupled analysis of viscous flow and flow-induced body-movements in large waves. For this purpose, some cases are selected to be investigated using this method and compared with experimental results.

2. Numerical Method

The program "Comet", version 2.000, has been used, which employs a finite volume method to predict forces acting on a body and free surface deformations by solving the Navier-Stokes equations, *ICCM (2001)*. The two-fluid system is modelled by a two-phase formulation of the governing equations. No explicit free surface is defined during the computations. The location of the free surface between air and water is obtained by solving an additional transport equation for the volume fraction of one of the fluids (interface capturing). To obtain a sharp interface, the high resolution interface capturing (HRIC) scheme has been used, *Muzaferija et al. (1999)*. Overturning (breaking) waves as well as buoyancy effects of the trapped air is considered automatically by the model. The flow is assumed to be laminar and incompressible.

The Navier-Stokes-Equations and the body dynamic equations are to be solved in a coupled manner. Applying the finite volume method on block structured grids, the viscous flow around a floating-body is predicted. The floating body dynamic has been implemented into the program via the user-coding interface. The body motions are calculated according to the forces and moments obtained by integrating pressure and shear stress over the body surface. The velocity of the floating body is corrected by a Crank-Nicholson-Method after every iteration (fully implicit), taking advantage of the iterative nature of the fluid-flow solver. An Approximation for the hydrodynamic masses is used to make the coupled procedure robust. Nonlinear effects like impact loads, *Sames et al. (2001)*, ship responses in large waves and viscous effects are considered.

An approach with overlapping grids has been developed and employed to avoid the difficult grid-management caused by changing of the body position. There is a space-fixed grid with a hole close to the body and a body-fixed grid. Fig.1 shows the principle of this approach.

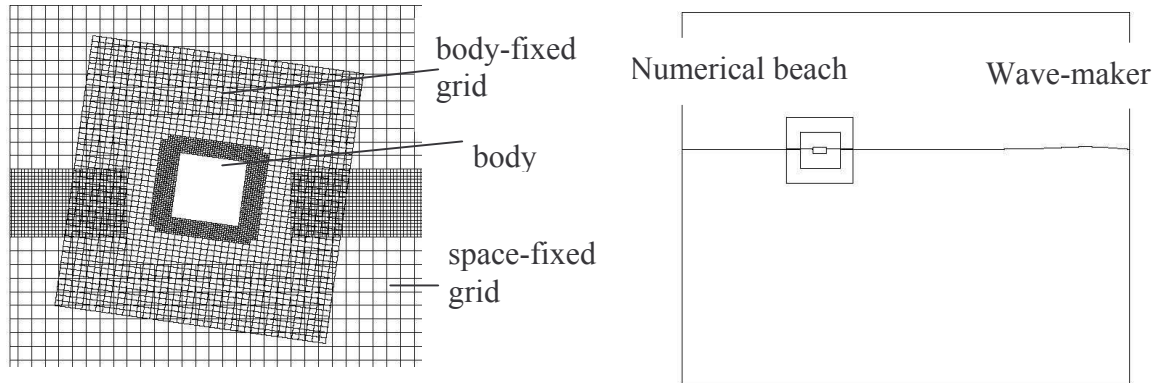


Fig.1: 2-d body with overlapping grids

Fig.2: Numerical tank for body motion

The flow solution has to be interpolated on the boundaries of every grid from each other to force a unique solution on both grids in the overlapping area. Finally a correction of the convective velocities makes sure that the mass conservation law will be satisfied. This correction is getting smaller with a greater number of iterations.

There are two ways to calculate the flow in the case of body-movement. First by changing the coordinates of the body-fixed grid in every iteration (moving grid) and after that solving the Navier-Stokes-Equations in the space-fixed coordinate system. The disadvantage of this method is, that the geometry in the program is only written in single precision, while all variables are in double precision. In case of small time steps this could lead to problems.

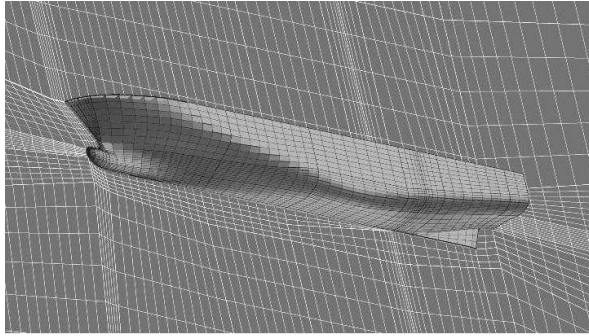
The other way, which is employed here, is to keep the coordinates of the body-fixed grid fixed and the Navier-Stokes-Equations will be solved in the body-fixed coordinate system. Considering grid-accelerations and velocities is necessary in this case. This could be done in double precision. Another advantage is the reduced requirement of memory because there is no need for saving the updated vertex nodes of the grid during the calculation.

The numerical tank into which the floating bodies are placed consists of a fluid domain with two phases (water and air) bounded by a layer of air on top, a bottom surface in water and four vertical boundaries. Regular waves are generated by giving inlet velocity and water height based on potential theory (Airy, Stokes I-IV) at the inlet boundary, *Clauss et al. (1998)*. At the other side of the tank a numerical beach is defined to avoid reflection of the waves.

3. Applications

3.1 Motions of a fast conventional passenger ferry in waves

A fast conventional RoRo passenger ferry was selected as reference ship for the study. The ship was designed by IZAR for the European research project *DEXTREMEL (1997)*. Model tests were carried out at a scale of 1/40 in a sea keeping basin by MARIN. Fig.2 shows the discretisation of the ship and its main particulars are listed there.



	Symbol	Value	Unit
Length between perpendiculars	Lpp	173.00	m
Beam	B	26.00	m
Draft	T	6.50	m
Displacement	Δ	16800	t
Service Speed	Vs	28	kts

Fig.2: Discretisation and main particulars of RoRo passenger ferry

The computation was done for a ship speed of 26 knots (93 % of service speed) in head waves. Only half of the ship at model scale has been discretized and pitch and heave were the degrees of freedom. At the beginning of the calculation the whole computation domain was initialized with undisturbed waves and the ship was at rest. Fig.3 shows the calculated heave and pitch motion in waves with $\omega=0.6$, $H=7.3$ m and a plot of the situation at $t=32.1$ s is presented in Fig.4.

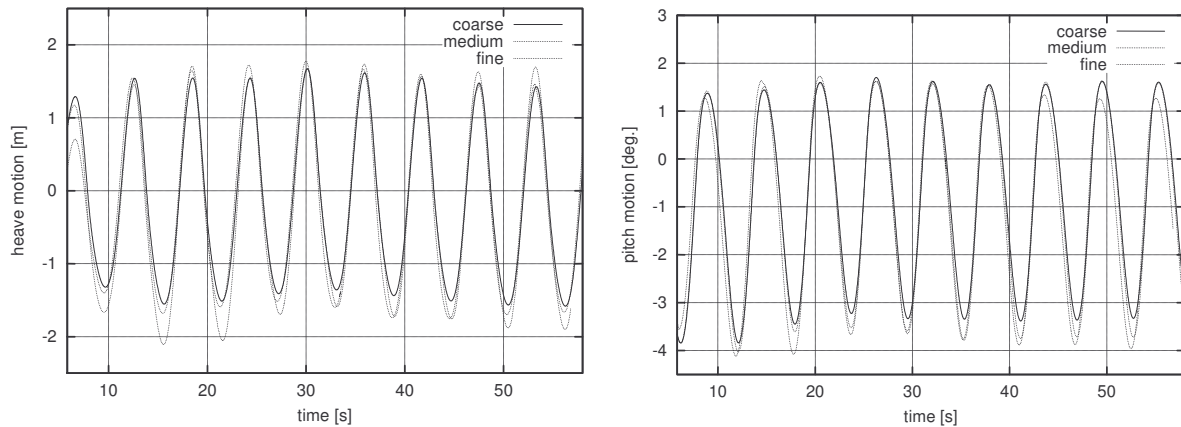


Fig.3: Calculated heave and pitch motions of RoRo passenger ferry

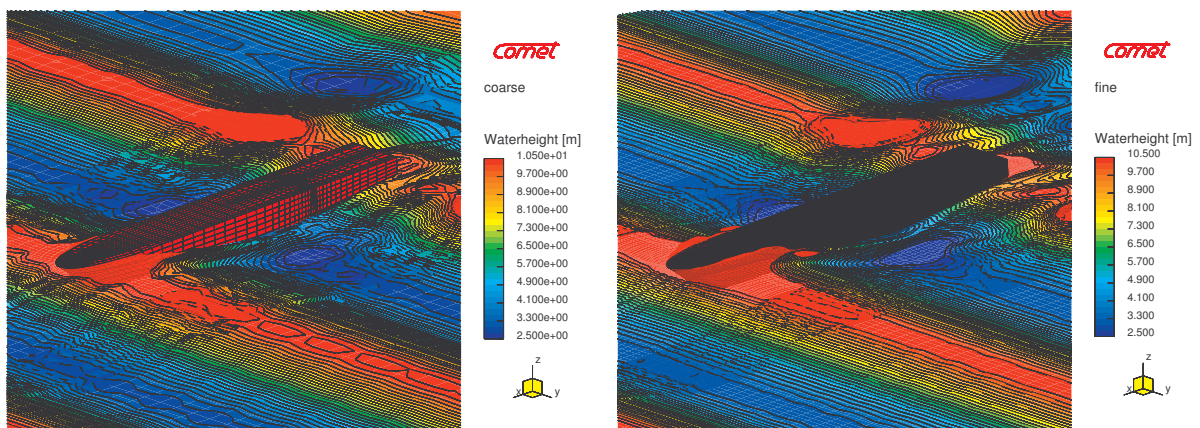


Fig.4: RoRo passenger ferry in head waves, $\omega=0.6$, $H=7.3$ m at $t=32.1$ s; coarse grid (left) fine grid (right)

Noted is that the amount of the negative pitch angle is much higher than the positive one caused by bow flare effects and impact loads. The corresponding force and moments acting on the hull are shown in Fig.5.

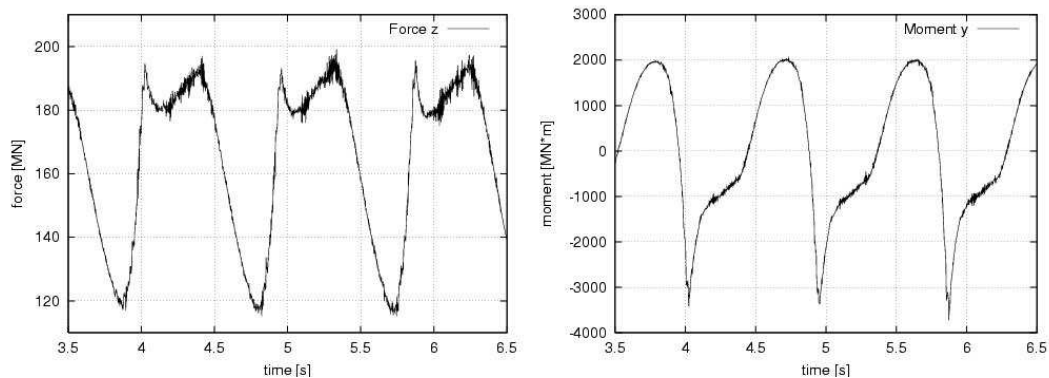


Fig.5: Calculated heave force and pitch moment of RoRo passenger ferry

The time traces of the forces have a nonlinear appearance due to the impact loads during the water entry. Fig.6 presents the comparison of calculated and measured response amplitude operators (RAO) of heave and pitch motion.

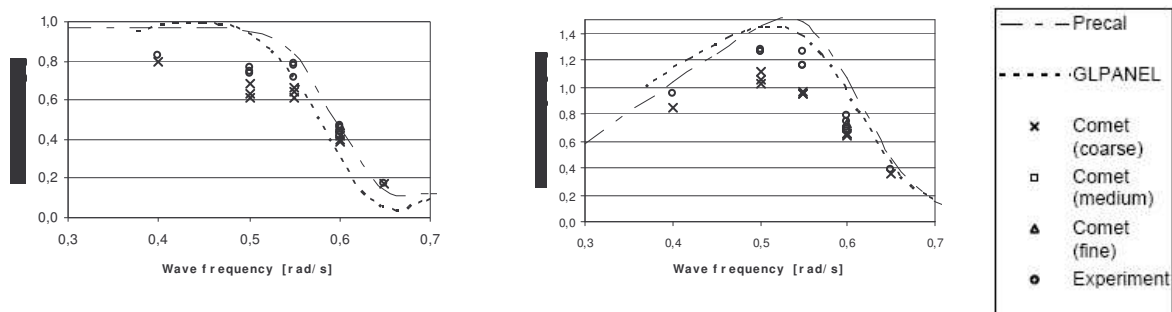


Fig.6: Comparison of RAOs of heave and pitch motion of RoRo passenger ferry

The heave and pitch response are a bit under predicted by the computational method compared to the experiments and methods based on potential theory. This effect might be caused by numerical damping due to the generally coarse discretisation of the ship, as grid refinement produces higher amplitudes of motion.

3.2 Wind induced motion of sailing yacht

Usually CFD analysis of the sails and the hull of a sailing yacht are each done with separate methods and independently. Here a modern sailing yacht designed for racing is chosen to prove the capability of the numerical method to calculate the flow both in water and air simultaneously in an accurate way. The “propulsion” of the sailing yacht is induced only by the air flow around the sails. The objective is finding the state of equilibrium with air and water flow with respect to all degrees of freedom.

The simulation is carried out without using the overlapping-grid technique. Fig.7 presents the surface grid for the hull with about 5200 elements and the sails with about 2300 elements within a grid for the fluid domain of 700 000 cells. The main parameters of the sailing yacht are presented in the table of Fig.7.

The sails are treated as rigid and there was no detailed information for the sail geometry available.

To steer a ship within manoeuvring simulations using Navier-Stokes-Equation solvers the rudder is usually placed within a cylindrical block. This block then is rotated according to the rudder angle. At the interfaces of this block with the surrounding grid often numerical problems appear, especially when the rudder is only partly submerged. To avoid these problems here a routine I used to move the vertices of the grid using spring analogies according to the rudder angle. Rudder angles of up to 10 degrees to both sides are possible without too large deformations of the cells around the rudder.

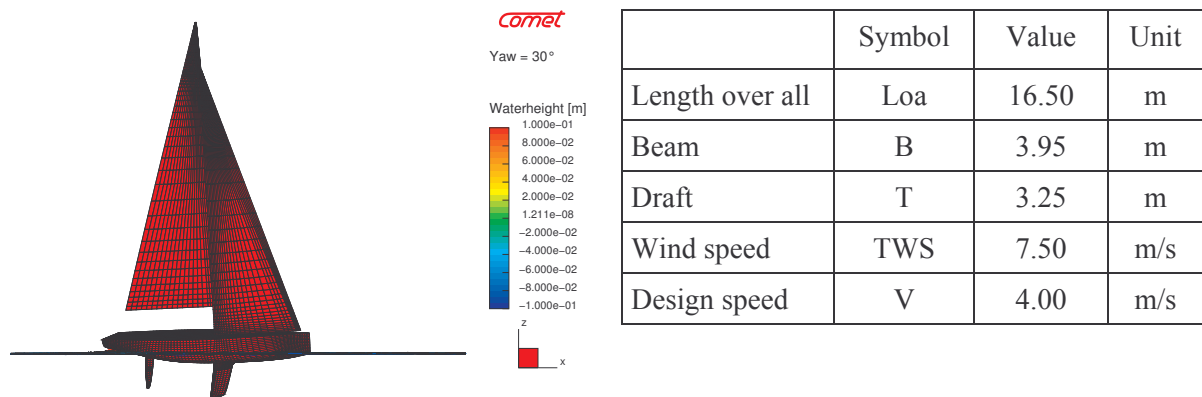


Fig. 7 Surface discretisation and main parameters of sailing yacht

During first calculations it became obvious that the yacht could not sail with the chosen initial geometry of foresail and main sail. The pressure distribution at a plane 12m above the water level shows for the initial geometry, that only the foresail produced lift forces in the right direction, Fig.8 left. As the opening between foresail and main was too small in practice the main would have avoid this condition by evading to the windward side or the main would be hauled in. With the rigid sails the flow separated from the main and the main did not contribute to the propulsion of the yacht, but only slowed it down. By modifying the grid in such a way, that the main was hauled in 9° a desirable configuration could be found, Fig.8 right.

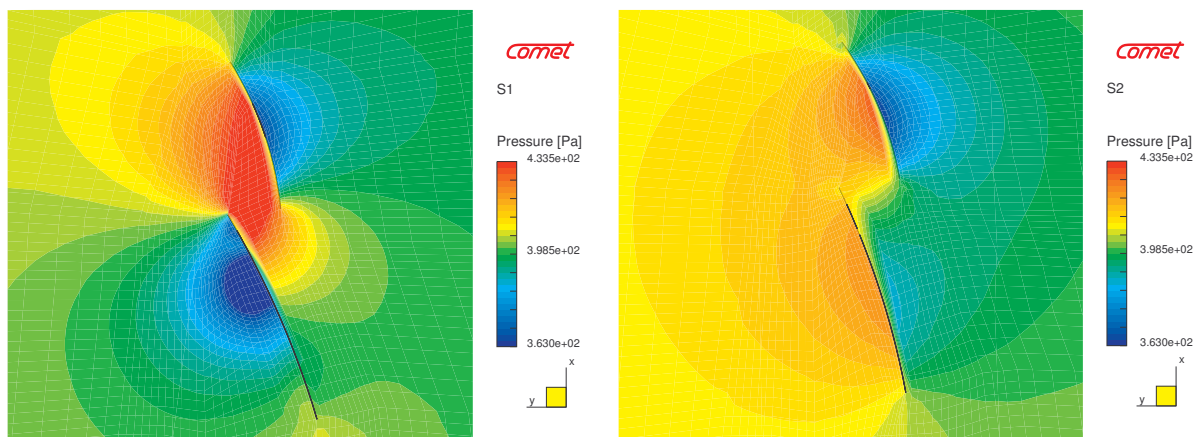


Fig.8: Pressure distribution in plane 12 m above water level; initial sail geometry (left) and improved sail geometry (right)

A series of calculations with fixed yaw angle revealed, that with this sail configuration the sailing yacht still was not capable of sailing as close to the wind as designed for. For larger angles of apparent wind, the results for the forward speed were close to the designed values.

As a last step all 6 degrees of freedom of the sailing yacht were let free. The navigation of the yacht was carried out by programming an autopilot with a given yaw angle as target. The autopilot gives information on the required rudder angle and the grid is changed to that. Although the controller was

not optimal adapted to the problem of steering a sailing yacht, the sailing yacht was kept on track for quite a while. Some more results are presented in the next section.

4. VRML for CFD Post-processing

During a CFD-simulation of the kind presented here a huge amount of data is generated. Saving the data of every control volume at every time step to hard disk is neither feasible nor will the disk space be enough. Thus the usual way of post processing is to do part of the post processing already during every time step of the simulation, e.g. save the pressure at certain locations to a file, calculate and save forces and moments acting on the body as well as the motion of the body. With a specified frequency restart-files containing the data of all flow properties for every control volume are saved, which are used to make some pictures of some quantities of the flow field (e.g. pressure distribution, free-surface elevation). Out of a series of such pictures often movies are generated. Once the restart-file is deleted no other pictures or quantities may be visualized. An external viewer usually has no access to the data of the restart-file and so can not do his own post-processing by visualizing the quantities he wants and view them from his own chosen view point. The objective is to improve the post-processing procedure, to extract more of the most important information from the restart-file and to provide them in a form the user may easily navigate in these data in space and time. As proposed by other authors (see *Lindenau et al. (2003)* for some references in naval architecture and some basics) the “Virtual Reality Modeling Language” (VRML), <http://www.web3d.org/x3d/vrml/>, solves this purpose. As interpreter we use the “Cosmos player”, which is a share-ware plug-in for standard internet browsers. The VRML-model comprises the geometry of the ship, some flow quantities to be visualized and a control panel.

The VRML player provides the necessary means to navigate in space: zoom in/out, rotate, pan and for easy navigation it is possible to view the model from predefined view points. The navigation in time is realized by programming in javascript some buttons similar to an audio player: start, halt and stop the process in time and step forward and backward in time. With the help of several other buttons on the control panel the quantities of the flow field which are to be displayed are chosen. This control panel is more or less independent of the VRML-model and can be reused (also by others) for further applications.

The surface of the ship is discretised finer for the CFD simulation than needed for the visualization of the geometry in a VRML model. First the geometry exported from the CFD code and saved as VRML model in the format of polygons (`IndexedFaceSet`). As the performance of the VRML-model is based on the polygon count of the model a routine by *Lindenau et al. (2003)* is used to enhance the performance of the VRML-model. This routine checks in a first step the distortion of a quadrilateral and if it is greater than a specified limit than it is split into two triangles. The next step checks whether the normal vectors of adjoining polygons are within a specified limit and than joins them to one larger polygon. This reduces the number of polygons necessary to display the geometry. In a similar way the edges of the polygon are checked and superfluous points are deleted. Within the routine also the order of points describing each polygon is arranged in such an order, that all normal vectors point out of the geometry. This further increases the performance of the VRML-model as the inside of the geometry is now not rendered by the VRML player. Another performance increase is gained by providing only the data for one symmetry half of the geometry and the flow data and mirroring them to the other side within the VRML-model. The motion of the ship is introduced into the VRML-model by moving the coordinate system in which the ship is given. For this the VRML player is given a discrete time series of the motion and the VRML player performs a linear interpolation in-between giving a for visualization purposes sufficient fluent motion.

The data of the flow field are import in the IBM data explorer, where the data of the body-fixed grid and the space-fixed grid are joined together. The free surface near the ship is also built of polygons allowing large deformations of the surface such as breaking waves and air entrapment. The region far away from the ship is displayed as `ElevationGrid` which gives the heights of a surface relative to reference plane with a regular grid for the heights. This reduces the amount of data necessary for

displaying the free-surface and thus increases the performance of the VRML-model. The user has the chance of coloring the waves according to height and to make the free-surface transparent in steps allowing a view on other flow properties. For every display time step a new wave geometry is loaded into the VRML-model.

As boundary values the time dependent pressure distribution or shear forces on the hull can be switched on and off by the user. This makes it possible to study the pressure distribution together with the motion of the ship and the wave elevation. These distributions are realized within the VRML-model by assigning pre-calculated colors to the points of the geometry. The VRML player then makes the interpolation between the colors of the points resulting in a smooth color distribution. A color map gives the relation between color and flow quantity.

Although 3-dimensional navigation is easy in a VRML model the viewer soon gets confused if too many data of the flow field are presented within the space. It is only is only feasible to present some selected data, e.g. in form of trajectories or vectors visualizing the velocity of the fluid. Fig.9 shows screen shots of the VRML models for the RoRo ship, Fig.10 for the sailing yacht.

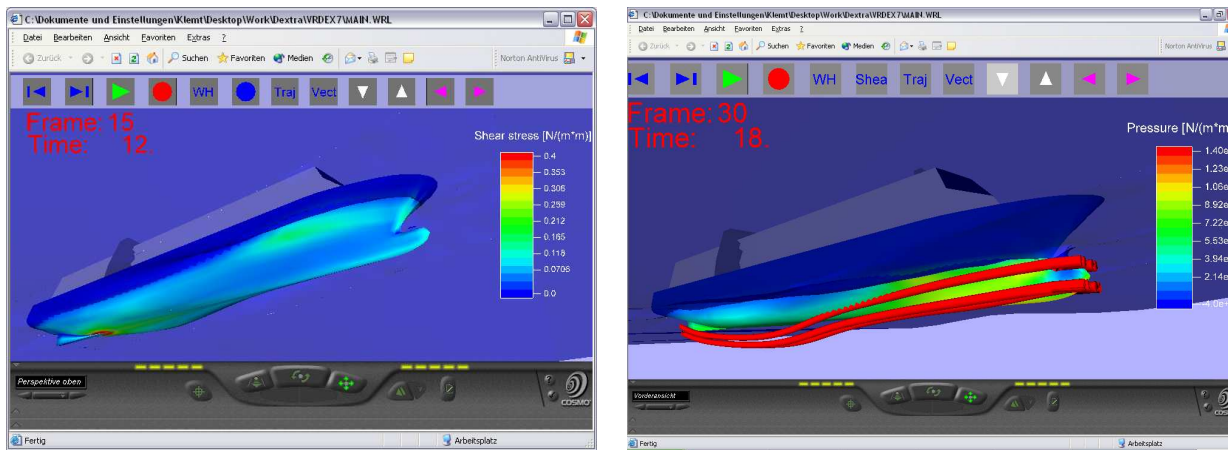


Fig.9: VRML model for RoRo ship: shear stress on hull (left), pressure distribution together with trajectories and free surface at hull

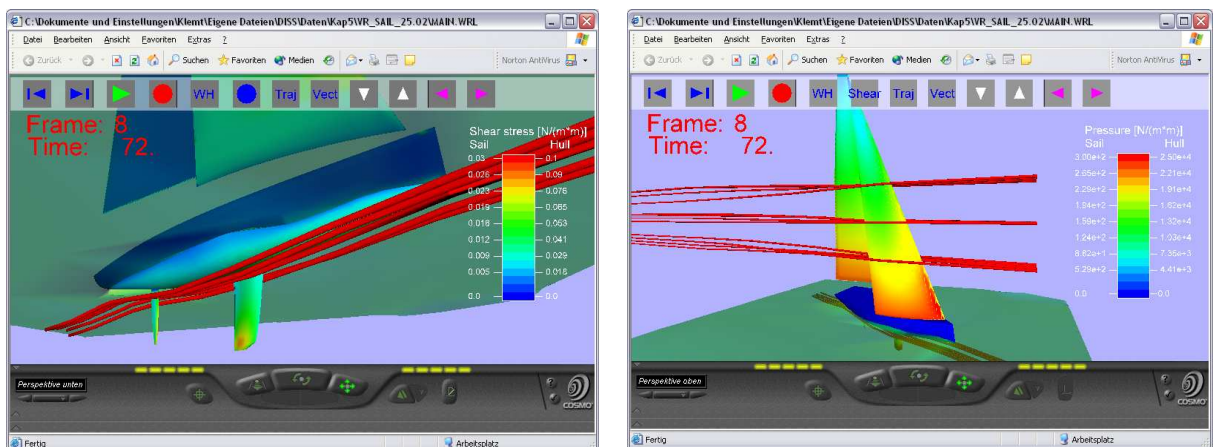


Fig.10: VRML model of sailing yacht: shear forces on hull, water elevation on lee side and trajectories in water (left), pressure distribution on sails and trajectories in air (right)

5. Conclusion

It has been shown that the present method using overlapping grid technique can be used for the calculation of wave loads and associated motions of a ship advancing in waves. Even the calculation of wave loads and the resultant motions of a ship in large waves can be carried out without any major difficulty, as shown for the application to a RoRo ship. The comparison of experimental results and computational method shows a good agreement in case of motions.

The application of the method to the wind induced motion of a sailing yacht shows the capability of the method to deal with two fluids with the necessary accuracy.

In addition, a VRML-based method for post-processing has been shown. The 3D-model of the computation results allow the viewer to get a better impression of the details of the flow around the ship.

References

CLAUSS, G.; LEHMANN, E.; ÖSTERGAARD, C. (1998), *Meerestechnische Konstruktionen*, Springer-Verlag Berlin Heidelberg New York

ICCM (2001), *Comet user manual*, ICCM (Institute of Computational Continuum Mechanics GmbH), Hamburg

DEXTREMEL (1997), *Design for structural safety under extreme loads*, BriteEuRam project, contract BPPR-CT97-0513, <http://research.germanlloyd.org/Projects/DEXTREMEL/index.html>

MUZAFERIJA, S.; PERIC, M. (1999), *Computation of free-surface using interface-tracking and interface-capturing methods*, Chap.2, O. Mahrenholtz and M. Markiewicz, eds., *Nonlinear Water Wave Interaction*, WIT Press, Southampton, pp. 59-100

SAMES, P.C.; KLEMT, M.; SCHELLIN T.E. (2001), *Prediction of wetdeck slamming loads for a catamaran*, HIPER 2001, Hamburg

LINDENAU, O.; BERTRAM, V. (2003), *The making of a VRML model for an SES with streamlines and pressure distribution*, COMPIT'03, Hamburg, pp.5-14, http://www.tu-harburg.de/fds/Arbeitsschwerpunkte/VRML_HTML/vrml_main.htm

An Optimum Design of Monohull High-speed Craft in Still Water

Hirotsugu Tanaka, Tanaka Propeller & Boat Research/Japan

Yasushi Yoshida, Technical University of Varna/Japan, yyoshida@fg8.so-net.ne.jp

Abstract

An optimum design parameter set has been obtained on the basis of the data of a series of towing tank tests by using thirteen models of 2.5m length up to 3.5 in Froude number based on displacement volume. The objective function is defined as the total resistance at Froude number 3.5, in which deadrise angle, warp, length, initial trim angle, width of planing area at midship and ratio of planing area's width at transom to the width at midship are taken as design parameters. As the constraints the following items are considered: (1) empirical equation's tolerance range (2) control of maximum trim angle change (3) total resistance hump in lower speed range and (4) deadrise angle. It is confirmed that the obtained hull has the minimum total resistance and controls of restrictive conditions are fine.

1. Optimisation problem

Optimum designs must always satisfy suitable constraints. Typical constraints for planing hulls are acceleration at bow, heeling angle in turn, and maximum trim angle change. Optimisation can be applied if objective function and constraints can be properly mathematically formulated.

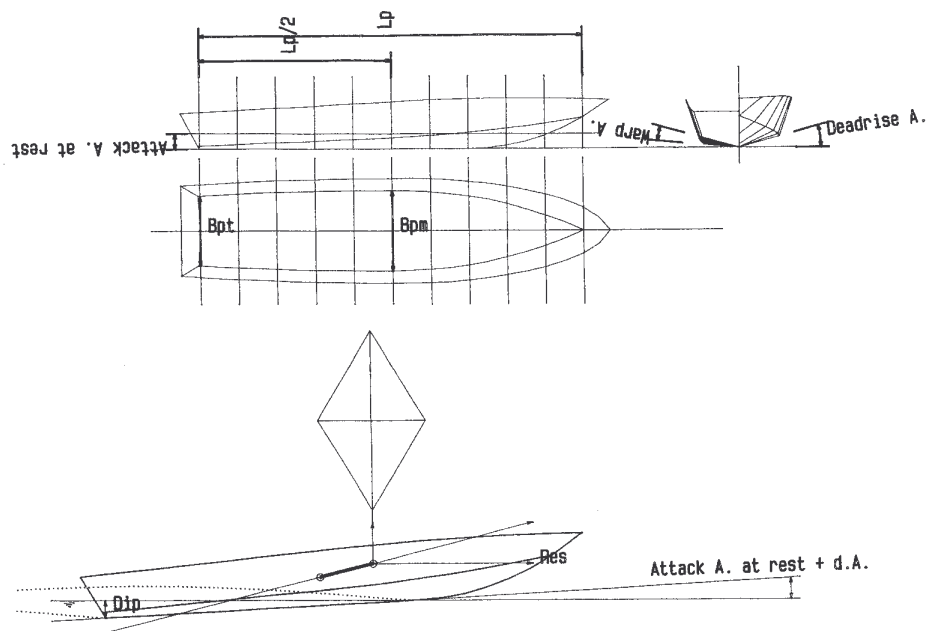


Fig.1: Towing tank test of 2.5m-length model in the First Research Center

Six design parameters $X(i)$, $i=1,2, \dots, 6$ are taken for the analysis:

$X(1)$ for deadrise angle (deg.)

$X(2)$ for warp angle (deg.)

$X(3)$ for planing area's total length L_p (m) from the displacement volume 0.060m^3

$X(4)$ for attack angle against base line or initial trim angle (deg.)

$X(5)$ for planing area's width at midship B_{pm} (m) from the displacement volume 0.060m^3

$X(6)$ for ratio of planing area's width at transom to the width at midship B_{pt}/B_{pm} , Fig.1

2. Experiments and empirical equations for objective function and constraints

A series of towing tank tests was done without appendages. The model's connective pin, installed at the bottom of dynamometer, lied on the shaft line, Fig.1. Then the model was towed toward the propeller shaft line. The dynamometer moves up and down according to change of the floating positions. Total resistance Res, trim angle change d.A. and dip at transom Dip were measured. The 78 design parameter sets in Table I yielded the measured values in Table II up to 3.5 in Froude number Fn (based on displacement volume ∇) at intervals of 0.5, in which the calculations based on displacement mass $\Delta = 60\text{kg}$ or cube root of displacement volume $\nabla^{1/3} = 0.060^{1/3}\text{ m}$ were done by the method described in Nagai *et al.* (1976) and Tanaka(1987).

All regression equations for Res, d.A. and Dip were fitted for quadratic Eqs.(1) to (3) by the least squares method to the data of Tables I and II.

$$\begin{aligned} \text{Res}(\mathbf{X}) = & S(1)*X(1)*X(1)+S(2)*X(1)+S(3)*X(2)*X(2)+S(4)*X(2)+S(5)*X(3)*X(3) \\ & +S(6)*X(3)+S(7)*X(4)*X(4)+S(8)*X(4)+S(9)*X(5)*X(5)+S(10)*X(5) \\ & +S(11)*X(6)*X(6)+S(12)*X(6)+S(13) \end{aligned} \quad (1)$$

$$\text{d.A.}(\mathbf{X}) = S(1)*X(1)*X(1)+S(2)*X(1)+S(3)*X(2)\dots\dots\dots+S(12)*X(6)+S(13) \quad (2)$$

$$\text{Dip}(\mathbf{X}) = S(1)*X(1)*X(1)+S(2)*X(1)+S(3)*X(2)\dots\dots\dots+S(12)*X(6)+S(13) \quad (3)$$

Table III gives the coefficients S(i). The relative errors in predicting the original measured data were e.g. for Res up to Froude number 3.5 are 9.9%, 3.5%, 2.3%, 1.9%, 2.2%, 3.1% and 3.2%. This is reasonable.

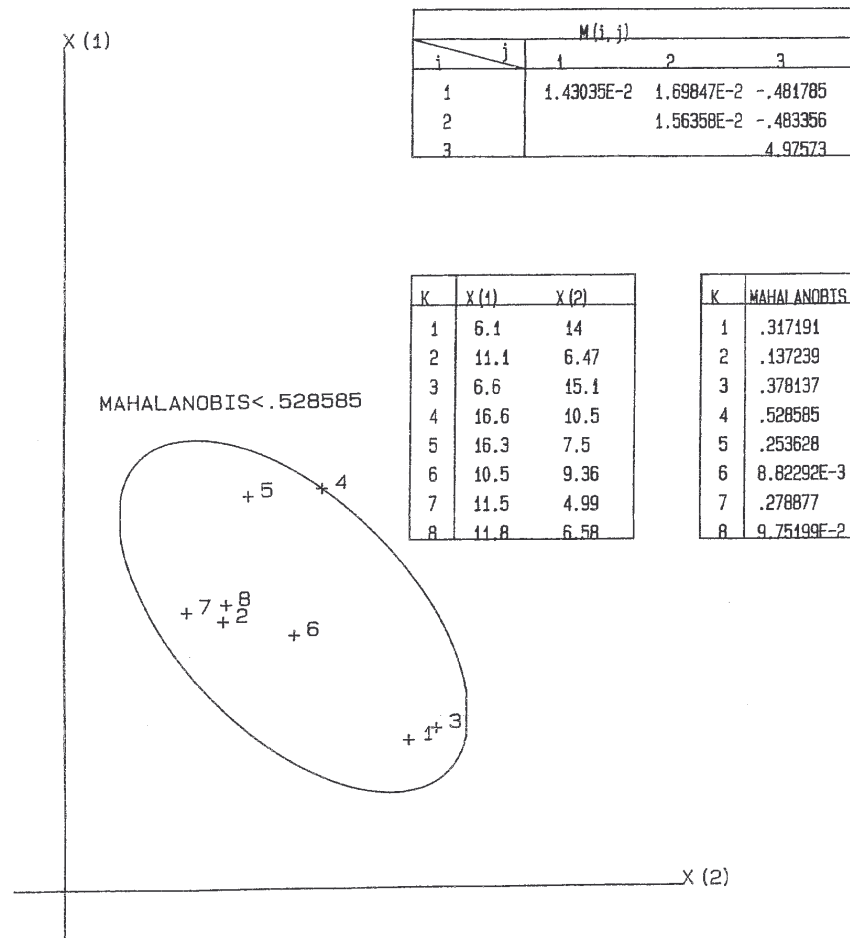


Fig.2: Mahalanobis's distance in case of two dimension coordinates and its kernel matrix M(i, j)

Table I: 78 design parameter sets experimented

K	X (1) D.A. (deg)	X (2) W.A. (deg)	X (3) Lp (m)	X (4) A.A. at rest (deg)	X (5) Bpm (m)	X (6) Bpt/Bpm
1	16.1193	14.0575	2.66692	-.932	.586136	.9
2	16.1193	14.0575	2.51058	-.932	.551775	.9
3	16.1193	14.0575	2.38545	.107	.524275	.9
4	16.1193	14.0575	2.38545	-.412	.524275	.9
5	16.1193	14.0575	2.38545	-.932	.524275	.9
6	16.1193	14.0575	2.28049	-.932	.501207	.9
7	21.1066	6.47872	2.12375	0	.575541	.999
8	21.1066	6.47872	2.21946	0	.601479	.999
-	-	-	-	-	-	-
-	-	-	-	-	-	-
-	-	-	-	-	-	-
-	-	-	-	-	-	-
75	19.1368	3.16565	2.61433	1.15	.623944	.764
76	19.1368	3.16565	2.53471	0	.604943	.764
77	19.1368	3.16565	2.70847	0	.646413	.764
78	19.1368	3.16565	2.61736	0	.624668	.764

Table II: Measured values of total resistance, trim angle change and draft at transom

		Res (kg)						
K \ Fn	0	.5	1	1.5	2	2.5	3	3.5
1	0	.863	2.784	5.526	6.96	8.639	9.599	11.04
2	0	.9	2.838	5.778	7.14	8.4	9.24	10.26
3	0	.966	3.6	7.62	8.58	9	9	9.3
4	0	.93	3.198	6.72	7.859	8.82	9.18	9.72
5	0	.924	3.126	6.36	7.56	8.639	9.42	10.019
6	0	.87	3.174	6.42	7.5	8.639	9.12	9.42
7	0	.606	3.756	6.779	8.16	9.059	9.66	11.28
8	0	.606	3.654	6.42	7.92	9.12	9.9	11.4
-	-	-	-	-	-	-	-	-
-	-	-	-	-	-	-	-	-
-	-	-	-	-	-	-	-	-
-	-	-	-	-	-	-	-	-
75	0	.624	3.342	6.42	7.859	9.42	10.68	12.66
76	0	.565	2.904	5.946	7.74	9.3	11.04	12.84
77	0	.552	2.85	5.61	7.68	9.9	12.179	14.519
78	0	.493	2.574	5.292	6.779	8.34	9.78	11.34

		d.A. (deg)						
K \ Fn	0	.5	1	1.5	2	2.5	3	3.5
1	0	0	.367	2.182	2.222	2.822	2.512	2.512
2	0	0	.62	2.652	2.722	2.842	3.031	3.031
3	0	0	.983	3.603	4.053	4.243	3.972	3.972
4	0	0	.867	3.152	3.372	3.892	3.462	3.462
5	0	0	.682	2.652	3.112	3.642	2.502	2.502
6	0	0	.908	3.372	3.352	3.952	4.032	4.032
7	0	.038	.836	2.92	3.14	3.65	3.45	3.45
8	0	0	.771	2.62	2.64	3	3.08	3.08
-	-	-	-	-	-	-	-	-
-	-	-	-	-	-	-	-	-
-	-	-	-	-	-	-	-	-
-	-	-	-	-	-	-	-	-
75	0	.07	.659	2.21	2.48	2.71	2.46	2.13
76	0	.02	.476	2.11	2.32	2.71	2.75	2.75
77	0	.041	.394	1.68	1.86	2.05	2.26	2.34
78	0	.02	.394	1.84	2.05	2.36	2.44	2.49

		Dip (cm)						
K \ Fn	0	.5	1	1.5	2	2.5	3	3.5
1	6.668	6.768	9.649	11.152	9.86	8.662	7.665	6.668
2	7.205	7.392	9.176	12.27	10.855	9.551	8.332	7.205
3	9.35	9.529	11.403	14.163	12.724	10.509	9.35	8.727
4	8.524	8.702	10.93	13.337	11.898	10.218	8.702	7.722
5	7.683	7.861	9.646	12.142	11.246	9.913	8.665	7.772
6	8.147	8.318	10.696	13.425	11.711	9.938	9.254	8.914
7	11.09	11.26	13.045	15.316	14.137	13.467	12.111	11.09
8	10.786	10.963	12.829	14.841	13.628	12.916	11.852	10.786
-	-	-	-	-	-	-	-	-
-	-	-	-	-	-	-	-	-
-	-	-	-	-	-	-	-	-
-	-	-	-	-	-	-	-	-
75	11.8	12.094	13.178	15.828	14.732	13.571	11.8	10.718
76	9.988	10.179	11.8	14.471	13.593	12.946	11.992	10.751
77	9.611	9.915	11.039	13.587	12.772	12.155	11.446	11.039
78	9.8	9.997	11.277	14.214	13.331	12.448	11.375	10.981

Table III: Coefficients of regression equations

		S(i)												
Fn \ i		1	2	3	4	5	6	7	8	9	10	11	12	13
Wres (kg)	0	0	0	0	0	0	0	0	0	0	0	0	0	0
	.5	3.3335E-3	-1.82059	-2.57392E-3	4.36617E-2	3.23942E-2	-2.204773	-1.00437E-2	7.37353E-2	1.53448	-2.40124	-6.77927	1.62649	3.04926
	1	-5.21646E-3	.227339	3.63762E-3	-3.12353E-2	.607244	-4.46636	5.94782E-2	.407102	11.9458	-13.8895	4.50197	-7.30821	14.3527
	1.5	4.00471E-3	-2.17247	-1.67337E-3	4.21222E-2	1.69618	-11.0983	.103736	.560137	1.19511	-1.75308	-6.84364	11.2085	21.7132
	2	-5.63769E-4	-1.48334E-2	3.19571E-3	-6.46372E-2	1.98206	-11.5479	.162779	.307374	10.1385	-10.9257	1.19526	-1.35013	27.7963
	2.5	-9.99806E-4	4.15218E-2	1.15238E-2	-2.63005	2.23724	-11.6848	.241927	-4.57739E-2	26.937	-29.7164	10.6057	-16.0921	38.2201
3	9.06993E-3	-2.96115	2.23067E-2	-5.05867	3.63503	-17.0184	.357905	-3.11642	30.145	-30.0195	19.6465	-31.6922	53.6817	
3.5	1.13941E-2	-2.60692	3.64349E-2	-7.95043	5.40334	-25.3822	.407391	-3.36388	8.77042	1.52086	36.3964	-61.6881	66.1057	
W.A. (deg)	0	0	0	0	0	0	0	0	0	0	0	0	0	0
	.5	4.301E-4	-5.23773E-3	1.21593E-3	-8.26649E-3	9.35309E-2	.374128	-7.15656E-3	4.51888E-2	-1.98011	3.19494	-1.57426	2.62469	-2.67709
	1	-6.72311E-5	2.68434E-2	.001871	1.13391E-2	.258085	-2.12088	2.36055E-3	.26346	2.07971	-1.98704	-4.31987	6.96876	1.31189
	1.5	2.38563E-3	-1.24188	-3.71114E-3	.105107	1.58246	-10.4128	8.66879E-2	.410054	7.42109	-10.1059	-16.1505	27.4193	11.2048
	2	7.44241E-3	-3.63971	-6.55819E-3	.137634	1.41948	-9.44345	3.38637E-2	.358781	-3.18688	2.10747	-17.9016	29.8043	8.51373
	2.5	5.06885E-3	-3.12351	-1.17197E-2	.218772	1.37841	-9.47814	5.09211E-2	.316064	-4.80228	3.3085	-21.0879	35.6248	6.081
3	-2.07989E-3	7.89016E-5	-1.04046E-2	.170823	9.05249E-3	-1.94069	6.82695E-2	9.00608E-2	2.47012	-6.24628	-18.4035	32.342	-3.39425	
3.5	2.76878E-3	-2.28111	-1.20628E-2	.153494	.202638	-2.19313	9.76369E-2	-8.06631E-2	8.70572	-15.1365	-13.3733	25.3627	4.07582	
W.DP (cm)	0	-1.99332E-3	.332779	3.67572E-3	-3.100727	.82813	-7.16829	-1.18654E-2	1.72095	11.2462	-14.1281	-5.44584	7.71105	19.2155
	.5	-2.43188E-4	.320212	8.31116E-3	-152453	.751751	-7.33175	-3.95215	1.74567	20.0662	-23.5399	-8.52049	12.3691	20.7107
	1	1.23304E-2	-2.237819	8.75908E-3	-120905	1.45083	-12.2573	-1.5908	1.83461	-5.22327	10.429	-23.832	38.2148	14.1119
	1.5	9.63647E-3	-2.12666	-1.71584E-3	-2.21699E-2	-3.82286	-4.03177	.111945	1.73285	4.7575	-4.94621	-31.6884	51.8108	7.57282
	2	7.23462E-3	-1.61709	-1.04749E-2	7.59136E-2	.926344	-8.16909	5.84701E-3	1.47897	-13.9347	13.7489	-31.0509	51.4681	3.84176
	2.5	1.21188E-3	.097627	-1.13539E-2	6.35282E-2	.382484	-4.81411	.113998	1.23311	-23.5762	26.7969	-21.3514	36.8462	-3.78979
3	-3.87963E-3	.291157	-9.48566E-3	-4.90599E-2	-1.16693	4.62121	5.97206E-2	.584066	4.69125	-10.0056	-10.8117	21.191	-2.42162	
3.5	6.45525E-3	-1.47376	-9.65226E-3	-1.24177	-1.54469E-2	-2.9015	8.04455E-2	.287057	17.6846	-27.7099	-6.13676	4.63822	19.4222	

We propose a tolerance ellipse for the equations, where many design parameters investigated exist. The parameters X(1) to X(6) should be used within experiment data range. 78 sets of X(1) to X(6) form an ellipse on the six dimension coordinates. Several ellipse surfaces as the limitation will be considered. A probability-distance from the data' center to the surface is called "Mahalanobis's distance", Nagai *et al.* (1977). Taking an example for X(1) and X(2) against eight data, Fig.2 shows a tolerance ellipse. The point No.4 or data at k=4 lies on the curve of the maximum Mahalanobis's distance as 0.528585. The applicable range is limited within the ellipse's curve. Then the tolerance ellipse Eq. is selected as Eq.(4). X(3) equals to 1.

$$1.43035E-2 * X(1) * X(1) + 1.69847E-2 * X(1) * X(2) - 0.481785 * X(1) * X(3) + 1.56358E-2 * X(2) * X(2) - 0.483356 * X(2) * X(3) + 4.97573 * X(3) * X(3) = 0.528585 \quad (4)$$

These coefficients in the kernel matrix M(i, j) are also shown in Fig.3.

Table IV: Mahalanobis's distance about 78 test data and its kernel matrix M(i, j)

		M(i, j)						
i \ j	1	2	3	4	5	6	7	
1	2.68802E-3	3.11566E-3	-2.13124E-2	1.38147E-2	7.51054E-2	-8.34419E-2	-4.82364E-2	
2		.002411	-1.69681E-2	1.73471E-2	.121473	-5.46444E-2	-7.62673E-2	
3			.47285	-4.30583E-2	-1.06696	.954077	-2.02453	
4				.068244	.347466	-.214528	-.248619	
5					8.25428	2.59808	-11.8505	
6						3.10701	-7.20796	
7							9.96265	

K	MAHALANOBIS										
1	7.93524E-2	14	8.86679E-2	27	9.15098E-2	40	5.07231E-2	53	2.78006E-2	66	.135627
2	6.83784E-2	15	6.65274E-2	28	8.68654E-2	41	1.94969E-2	54	5.27267E-2	67	.099081
3	.131905	16	8.93545E-2	29	.063139	42	6.14748E-2	55	7.28655E-2	68	.089983
4	8.85763E-2	17	9.93977E-2	30	.091464	43	2.07891E-2	56	6.38762E-2	69	.138894
5	8.20341E-2	18	.150347	31	2.38609E-2	44	6.63652E-2	57	5.84536E-2	70	8.66489E-2
6	.108871	19	7.86314E-2	32	1.13277E-2	45	.112323	58	.114082	71	.100604
7	9.93309E-2	20	7.32412E-2	33	2.58512E-2	46	6.51093E-2	59	7.71532E-2	72	.122076
8	9.30452E-2	21	9.73358E-2	34	4.19378E-2	47	.064105	60	.131123	73	5.81856E-2
9	.146659	22	9.40561E-2	35	2.00834E-2	48	9.81951E-2	61	4.66967E-2	74	7.07874E-2
10	8.42438E-2	23	.087698	36	6.79579E-2	49	6.50635E-2	62	4.39405E-2	75	.144978
11	.104767	24	.13873	37	3.18766E-2	50	3.73869E-2	63	6.72188E-2	76	5.26276E-2
12	.150294	25	8.69026E-2	38	1.54533E-2	51	6.32915E-2	64	6.52456E-2	77	4.08678E-2
13	9.88998E-2	26	6.68182E-2	39	2.45571E-2	52	5.59616E-2	65	6.63004E-2	78	4.18501E-2

By similar way, the applicable range of the Eqs.(1) to (3) for the design parameters X(1) to X(6) in Table I was obtained as the coefficients or kernel matrix M(i, j) in Table IV, by which each Mahalanobis's distance about 78 test data can be calculated as Table IV.

```

----- Question [A] -----
----- minimize -----
*Res (Fn=3.5)
----- subject to -----
MAHALANOBIS<.1503
M1=1, M2=0, M3=0
----- ans. by new method -----
Deadrise A. (deg) = 15.4852
Warp A. (deg) = 10.3716
Lp (m) = 2.35038
Attack A. at rest (deg) = .12718
Bpm (m) = .49264
Bpt/Bpm = .86599
----- check -----
*Res (Fn=3.5) (kg) =7.99085
-----
MSHALANOBIS = .150299 (<.1503)
-
-
-
-
-

```

Fn	0	.5	1	1.5	2	2.5	3	3.5
*Res (kg) [A]	0	1.005	3.324	6.924	7.759	8.276	8.287	7.99
*d.A (deg) [A]	0	-.048	.825	3.318	3.726	4.347	3.99	4.048
*Dip (cm) [A]	9.54	9.66	11.6	14.57	13.67	11.37	10.57	9.82

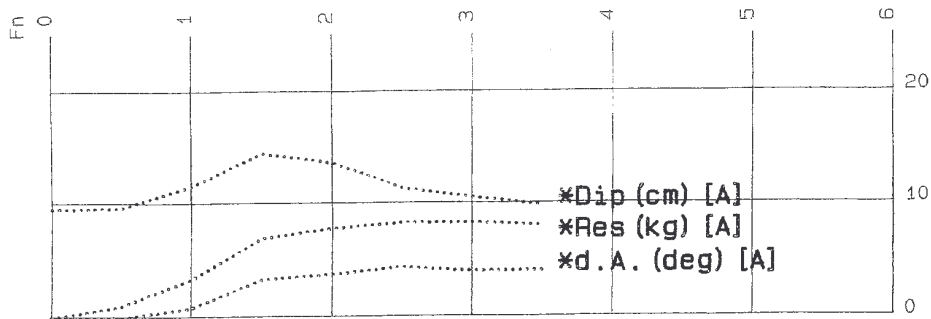


Fig.3: Optimum hull, satisfying inside of Equations' tolerance ellipse

We developed three computer programs for optimum designs, Appendix 1 to 3. Program 1 covers regression equations by quadratic form against experimental data. Program 2 should be used to limit the applicable range of the equations by the Program 1. The range can be defined within a tolerance ellipse of Mahalanobis's distance. Mahalanobis's distance is probability-distance from the distribution center of data to a data. Without the ellipse, any optimum problems will fail to obtain the optimum value. The reason is that every equation requires tolerance range. Alternatively many kinds of areas on two dimension coordinates against multi-variable analysis may be considered, which requires many equations to form even an area.

Program 3 works for an optimum problem, having four characteristics:

- (1) approachable without higher knowledge about mathematics
- (2) quick convergence
- (3) robustness against hard convergence problems such as Rosen-Suzuki problem
- (4) usable against both maximum and minimum problems

```

----- Question [B] -----
---- minimize ----
*Res (Fn=3.5)
---- subject to ----
MAHALANOBIS<.1503; *Res (Fn=1.5) <6kg; Deadrise A.>20deg; *d.A. (Fn=3.5) =3.3deg
M1=2, M2=1, M3=1
---- ans. by new method ----
Deadrise A. (deg) = 20.0001
Warp A. (deg) = 10.7993
Lp (m) = 2.52318
Attack A. at rest (deg) = -.087743
Bpm (m) = .475938
Bpt/Bpm = .849962
----- check -----
*Res (Fn=3.5) (kg) =8.713198
-----
MSHALANOBIS=.143371 (<.1503)
*Res (Fn=1.5) (kg) =5.996208 (<6)
Deadrize A. (deg) =20.000072 (>20)
*d.A. (Fn=3.5) (deg) =3.300126 (=3.3)
-
-

```

Fn	0	.5	1	1.5	2	2.5	3	3.5
*Res (kg) [B]	0	.697	3.22	5.996	7.216	8.245	8.554	8.713
*d.A (deg) [B]	0	-.048	.758	2.649	2.792	3.222	3.341	3.3
*Dip (cm) [B]	9.89	10.17	11.19	13.77	13.15	11.44	10.89	10.05

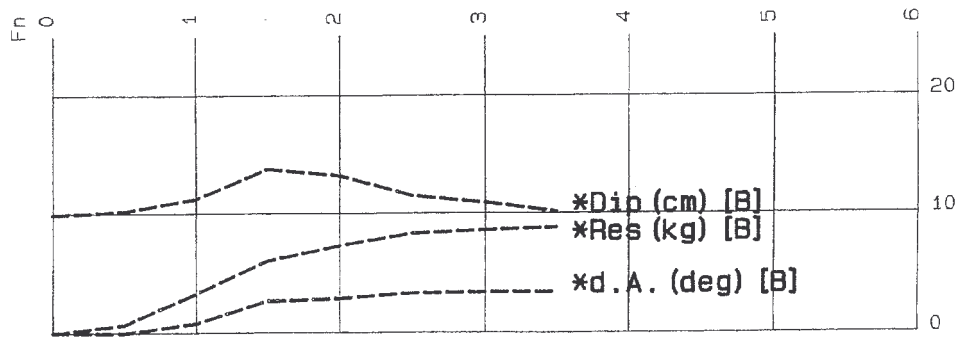


Fig.4: Optimum hull controlled against resistance hump in lower speed range, maximum trim angle change and deadrise angle, satisfying inside of Equations' tolerance ellipse

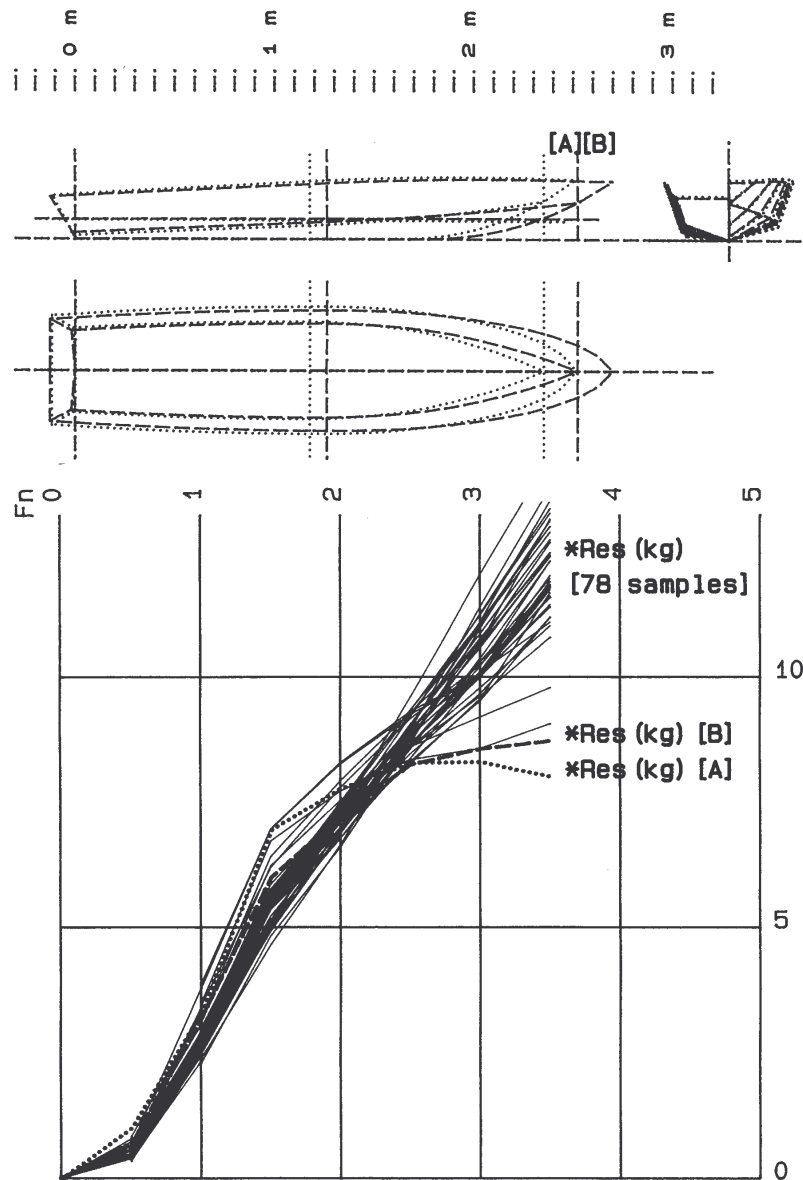


Fig.5 : Comparing optimum hulls in case of question A and B with test models against total resistance

3. Optimum design of hull forms

In order to obtain a hull with minimum total resistance at the top speed, the objective function is set for the predicted resistance Res at $Fn=3.5$. The tolerance ellipse of the objective function is needed as constraint. Other constraints are added to this condition successively.

3.1 Constraint “inside tolerance ellipse”

Similarly, the applicable range of the Eqs.(1) to (3) for the design parameters $X(1)$ to $X(6)$ in Table I was obtained as the coefficients or kernel matrix $M(i, j)$ in Table IV, by which each Mahalanobis’s distance about 78 test data can be calculated as Table IV. Under the Mahalanobis’s distance less than 0.1503, the hull form with the minimum total resistance was searched as question [A] in Fig.3. The minimum total resistance was obtained as 7.990085kg for the design parameters $X(1)$ to $X(6)$:

X(1) = 15.4852 deg., deadrise angle
X(2) = 10.3716 deg., warp angle
X(3) = 2.35038m, Lp
X(4) = 0.12718 deg., attack angle at rest
X(5) = 0.49264m, Bpm
X(6) = 0.86599, Bpt/Bpm

Checking against the Mahalanobis's distance of question [A], the distance was well controlled until the result. Up to Froude number 3.5 the predictions of total resistance Res, trim angle change d.A and dip at transom Dip were obtained as the curves in Fig. 3.

3.2 Lowering maximum wave resistance and maximum trim angle change

In the previous section total resistance at Froude number 1.5, where the maximum wave resistance or hump of total resistance will occur, equals to 6.924 kg, trim angle change at Fn=3.5 4.048 and deadrise angle 15.4852 deg.

Total resistance at Froude number 1.5 is controlled as less 6 kg level, trim angle at Fn=3.5 3.3 deg. level and deadrise angle greater 20 deg. level. Pilot and crew want lowering the trim angle change for sight, steering and safe working. If we add these three constraints, the question [B] is formed. Fig.4 shows the result of solving question [B] for hull and total resistance etc.

4. Discussion

The reformation of hull form was done as Fig.5, satisfying the constraints against both cases [A] and [B] as two kinds of dotted lines etc. in Fig.3 and 4. The predictions of total resistance at Froude number 3.5 of the cases show lower values than that of 78 test models as the lines. The hulls are also shown by the dotted lines in Fig.5.

A sharp pointed bottom and long hull will be favourable against decreasing total resistance in lower speed range. In general, lowering resistance in low speed range makes higher resistance in high-speed range. Against this tendency the optimum technique in design works will work well. As another problem, even regressions with small error may not realize boats' floating positions.

In conclusion, an optimum design parameter set was obtained under the restrictive conditions (1) empirical equations' tolerance ellipse limit (2) control of maximum trim angle change (3) control of total resistance hump in lower speed range and (4) deadrise angle. We compared prediction of total resistance, trim angle change and draft at transom up to Froude number 3.5 for the obtained model with all test models' one. Then hull reformation was confirmed.

References

NAGAI, T.; TANAKA, H.; YOSHIDA, Y. (1976), *On the planing hull form with minimum resistance in still water*, J. West Japan Soc. Naval Arch. Japan, Vol.52, pp.33-43

TANAKA, H. (1987), *An design example of a planing boat's propeller and hull*, J. Boating World, publisher Boating World, Dec., p.55

Appendix 1: Program 1 to regression Eq.

Program 1 is used for the fitting Eqs. (1) to (3) by the least squares method. The step numbers No.115 to 161 is the items for the fitting. The design parameter sets in Table I is written at No.9010 to 9780, and, for example, Res at Froude number 3.5 in Table II at No.10010 to 10730. The regression coefficients S(i) are out putted at No.5001, after running the program for the form "S(1)*F1(X)+S(2)*F2(X)+.....+S(M9)*FM9(X)". M9 means the number of terms, S(i) coefficient of ith term and Fi(X) function of X for ith term. For example, A3(1,k)=X(k,1)*X(k,1) at No.120 is set for X(1)*X(1) at the first term of Eq.(1) and so on.

```

25 DIM X(150,30),A3(30,150),S(30),P3(150),
   F(150),I(150),J(150),D(30),T(30,30)
50 READ N9,N2
60 FOR K=1 TO N2
61 FOR I=1 TO N9
70 READ X(K,I)
80 NEXT I
81 NEXT K
115 FOR K=1 TO N2
120 A3(1,K)=X(K,1)*X(K,1)
121 A3(2,K)=X(K,1)
122 A3(3,K)=X(K,2)*X(K,2)
123 A3(4,K)=X(K,2)
124 A3(5,K)=X(K,3)*X(K,3)
125 A3(6,K)=X(K,3)
126 A3(7,K)=X(K,4)*X(K,4)
127 A3(8,K)=X(K,4)
128 A3(9,K)=X(K,5)*X(K,5)
129 A3(10,K)=X(K,5)
130 A3(11,K)=X(K,6)*X(K,6)
131 A3(12,K)=X(K,6)
132 A3(13,K)=1
160 NEXT K
161 M9=13:GOSUB 170
166 END
170 FOR K=1 TO N2
174 READ P(K)
175 NEXT K
176 GOSUB 420:RETURN
420 FOR I=1 TO M9
430 FOR J=1 TO M9
440 T(I,J)=0
450 FOR L=1 TO N2
460 T(I,J)=T(I,J)+A3(J,L)*A3(I,L)
470 NEXT L
480 NEXT J
490 NEXT I
500 FOR I=1 TO M9
510 T(I,M9+1)=0
520 FOR L=1 TO N2
530 T(I,M9+1)=T(I,M9+1)+P(L)*A3(I,L)
540 NEXT L
550 NEXT I
560 E=1E-11:GOSUB 870:RETURN
870 M=M9+1:D=1
890 FOR K=1 TO M9
900 K1=K-1:P=0
920 FOR I=1 TO M9
930 FOR J=1 TO M9
940 IF K=1 THEN 1010
950 FOR I2=1 TO K1
960 FOR J2=1 TO K1
970 IF I=I(I2) THEN 1050
980 IF J=J(J2) THEN 1050
990 NEXT J2
1000 NEXT I2
1010 IF ABS(T(I,J))<=ABS(P) THEN 1050
1020 P=T(I,J):I(K)=I:J(K)=J
1050 NEXT J
1060 NEXT I
1070 IF ABS(P)>E THEN 1100
1080 D=0:RETURN
1100 I3=I(K):J3=J(K):D=D*P
1130 FOR J=1 TO M
1140 T(I3,J)=T(I3,J)/P
1150 NEXT J
1160 T(I3,J3)=1/P
1170 FOR I=1 TO M9
1180 T= T(I,J3)
1190 IF I=I3 THEN 1240
1200 T(I,J3)=- (T/P)
1210 FOR J=1 TO M
1220 IF J<>J3 THEN T(I,J)=T(I,J)-T*T(I3,J)
1230 NEXT J
1240 NEXT I
1250 NEXT K
1260 FOR I=1 TO M9
1270 I4=I(I):J4=J(I):D(I4)=J4:S(J4)=T(I4,M)
1310 NEXT I
1650 GOSUB 5000:RETURN
5000 FOR I=1 TO M9
5001 PRINT "I,S(I)";I,S(I)
5010 RETURN
9000 DATA 6,78
9010 DATA 16.1193,14.0575,2.66692,-.932,.586136,.9
9020 DATA 16.1193,14.0575,2.51058,-.932,.551775,.9
9030 DATA 16.1193,14.0575,2.38545,.107,5.24275,.9
9040 DATA 16.1193,14.0575,2.38545,-.412,.524275,.9
9050 DATA 16.1193,14.0575,2.38545,-.932,.524275,.9
9060 DATA 16.1193,14.0575,2.28049,-.932,.501207,.9
9070 DATA 21.1066,6.47872,2.12375,0,.575541,.999
9080 DATA 21.1066,6.47872,2.21946,0,.601479,.999
9750 DATA 19.1368,3.16565,2.61433,1.15,.623944,.764
9760 DATA 19.1368,3.16565,2.53471,0,.604943,.764
9770 DATA 19.1368,3.16565,2.70847,0,.646413,.764
9780 DATA 19.1368,3.16565,2.61736,0,.624668,.764
10010 DATA 11.04,10.26,9.3,9.72,10.02,9.42
10070 DATA 11.28,11.4,10.98,12.06,11.94,13.14
10730 DATA 14.34,13.08,12.66,12.82,14.52,11.34

```

Appendix 2: Program 2 to applicable range of regression Eq.

Program 2 is used for applicable range of Eqs.(1) to (3) that is limited by a tolerance ellipse. The coefficients of kernel matrix of the ellipse $M(i, j)$ and Mahalanobis's distance of data number k are outputted at No.6003 and 6012, after inputting a set of the number of dimensions and data points at No.20000 and all design parameter sets like Table I at No.20010.

```

20 DIM X(100,20),X1(20),A1(20,20), 3100 NEXT I
   MAHALANOBIS(100),M(20,20),N2(20) 3101 NEXT K
60 READ N9,N2 3102 RETURN
61 FOR K=1 TO N2 3160 E=1E-10
70 FOR I=1 TO N9 3170 FOR N1=1 TO N
80 READ X(K,I) 3180 N2(N1)=N1
90 NEXT I 3190 NEXT N1
95 X(K,N9+1)=1 3200 FOR N1=1 TO N
100 NEXT K 3210 P=0
107 GOSUB 2000:GOSUB 6000 3220 FOR I=N1 TO N
165 END 3230 IF P>=ABS(A1(I,1)) THEN 3260
2000 FOR J=1 TO N9 3240 P=ABS(A1(I,1)):I1=I
2880 X1(J)=0 3260 NEXT I
2890 FOR I=1 TO N2 3270 IF P>E THEN 3290
2900 X1(J)=X1(J)+X(I,J) 3280 I2=1:END
2910 NEXT I 3290 N3=N2(I1):N2(I1)=N2(N1):N2(N1)=N3
2920 X1(J)=X1(J)/N2 3320 FOR J=1 TO N
2930 NEXT J 3330 W=A1(I1,J):A1(I1,J)=A1(N1,J):
2970 FOR I=1 TO N9 A1(N1,J)=W
2980 FOR J=1 TO N9 3360 NEXT J
2990 A1(I,J)=0 3370 W=A1(N1,1)
3000 FOR K=1 TO N2 3380 FOR J=2 TO N
3010 A1(I,J)=A1(I,J)+(X(K,I) 3390 A1(N1,J-1)=A1(N1,J)/W
   -X1(I))*X(K,J)-X1(J)) 3400 NEXT J
3020 NEXT K 3410 A1(N1,N)=1/W
3030 NEXT J 3420 FOR I=1 TO N
3040 NEXT I 3430 IF I=N1 THEN 3490
3050 N=N9:GOSUB 3160 3440 W=A1(I,1)
3060 FOR I=1 TO N9 3450 FOR J=2 TO N
3061 M(I,I)=A1(I,I) 3460 A1(I,J-1)=A1(I,J)-W*A1(N1,J-1)
3062 NEXT I 3470 NEXT J
3063 FOR I=1 TO N9-1 3480 A1(I,N)=-W*A1(N1,N)
3064 FOR J=I+1 TO N9 3490 NEXT I
3065 M(I,J)=A1(I,J)*2 3500 NEXT N1
3066 NEXT J 3510 FOR N1=1 TO N
3067 NEXT I 3520 FOR J=N1 TO N
3070 FOR I=1 TO N9 3530 IF N2(J)=N1 THEN 3550
3071 M(I,N9+1)=0 3540 NEXT J
3072 FOR J=1 TO N9 3550 N2(J)=N2(N1)
3073 M(I,N9+1)=M(I,N9+1) 3560 FOR I=1 TO N
   -2*X1(J)*A1(I,J) 3570 W=A1(I,J):A1(I,J)=A1(I,N1):A1(I,N1)=W
3074 NEXT J 3600 NEXT I
3076 NEXT I 3610 NEXT N1
3080 M(N9+1,N9+1)=0 3630 RETURN
3081 FOR I=1 TO N9 6000 FOR I=1 TO N9+1
3082 FOR J=1 TO N9 6002 FOR J=I TO N9+1
3083 M(N9+1,N9+1)=M(N9+1,N9+1) 6003 PRINT "I,J,M(I,J)";I,J,M(I,J)
   +X1(I)*X1(J)*A1(I,J) 6004 NEXT J
3084 NEXT J 6005 NEXT I
3085 NEXT I 6010 FOR K=1 TO N2
3091 FOR K=1 TO N2 6012 PRINT "K,MAHALANOBIS";K,MAHALANOBIS(K)
3092 MAHALANOBIS(K)=0 6013 NEXT K
3096 FOR I=1 TO N9+1 6020 RETURN
3097 FOR J=I TO N9+1 20000 DATA 2,8
3098 MAHALANOBIS(K)=MAHALANOBIS(K) 20010 DATA 6.1,14,11.1,6.47,6.6,15.1,16.6,
   +M(I,J)*X(K,I)*X(K,J) 10.5,16.3,7.5,10.5,9.36,11.5,
3099 NEXT J 4.99,11.8,6.58

```

Appendix 3: Program 3 to optimum design

Program 3 is used to obtain an optimum design parameter set such as $X(i)$, $i=1,2,\dots,6$ having the minimum total resistance. The calculation results are outputted at No.6000 to 6180, after inputting at 10000 to 10500 as follows: (1) a negative value having small one in absolute value such as -0.01 and -0.001 at No.10012 (2) the number of dimensions at No.10014 (3) initial values at No.10017 (4) objective function at No.10050 (5) number of restrictive conditions etc.; M1 for the number of "<" conditions, M2 for ">" ones and M3 for "=" ones, which are arranged by the order of M1, M2 and M3 to input the conditions by the order at 10060 and (6) the arranged restrictive conditions in the order at No.10100 to 10500.

```

30 DEFDBL A,B,C,D,E,X,Y
35 DIM C(10),A(10),X(10),X1(10)
36 DIM XO(10),YO(10),Y(10)
50 READ E8,KO,DO,CO,N:C8=E8:A8=E8:X8=E8
70 FOR I=1 TO N
80 READ X(I)
90 NEXT I
100 X(N+1)=1:READ M1,M2,M3:K=0
505 IF K=KO THEN END
506 K=K+1
510 FOR I=1 TO N
515 YO(I)=FIX(X(I)*E8)/E8
520 NEXT I
525 GOSUB 8850
530 FOR I=1 TO N
535 Y(I)=FIX(X(I)*E8)/E8
540 NEXT I
545 FOR I=1 TO N
550 IF YO(I)=Y(I) THEN 555 ELSE 505
555 NEXT I
560 CO=CO/10:IF CO=0 THEN 565 ELSE 505
565 END
1000 GOSUB 1140
1040 FOR I=1 TO N
1050 X1(I)=X(I)
1060 NEXT I
1070 FOR I=1 TO N
1080 X1(I)=X1(I)+C(I)*CO
1090 NEXT I
1100 FOR I=1 TO N
1110 X(I)=X1(I)
1120 NEXT I
1130 RETURN
1140 FOR I=1 TO N
1150 XO(I)=X(I)
1160 NEXT I
1170 GOSUB 10050:CD=C
1180 FOR I=1 TO N
1190 X(I)=X(I)+DO
1200 GOSUB 10050
1201 C(I)=(C-CD)/DO:X(I)=XO(I)
1210 NEXT I
1220 RETURN
2000 GOSUB 9000
2040 GOSUB 2090:A=A0:A0=(A-B)/A1
2050 FOR I=1 TO N
2060 X(I)=X(I)-A0*A(I)
2070 NEXT I
2080 RETURN
2090 GOSUB 2150:A1=0
2110 FOR I=1 TO N
2120 A1=A1+A(I)^2
2130 NEXT I
2140 RETURN
2150 FOR I=1 TO N
2160 XO(I)=X(I)
2170 NEXT I
2180 GOSUB 9000:A0=A
2200 FOR I=1 TO N
2210 X(I)=X(I)+DO:GOSUB 9000:A(I)=(A-A0)/DO
2220 X(I)=XO(I)
2240 NEXT I
2250 RETURN
6000 PRINT "*****"
6105 PRINT "CO=";CO;"K=";K
6110 FOR I=1 TO N
6120 PRINT"X(";I;")=";FIX(X(I)*X8)/X8
6130 NEXT I
6140 GOSUB 10050
6145 PRINT"****":PRINT "C=";FIX(C*C8)/C8:PRINT "****"
6150 IF M1=0 THEN 6155
6151 FOR M=1 TO M1
6152 GOSUB 9000
6153 PRINT "A";M;"=";FIX(A*A8)/A8;"( < ";B;")"
6154 NEXT M
6155 IF M2=0 THEN 6160
6156 FOR M=M1+1 TO M1+M2
6157 GOSUB 9000
6158 PRINT "A";M;"=";FIX(A*A8)/A8;"( > ";B;")"
6159 NEXT M
6160 IF M3=0 THEN 6180
6161 FOR M=M1+M2+1 TO M1+M2+M3
6162 GOSUB 9000
6163 PRINT "A";M;"=";FIX(A*A8)/A8;"( = ";B;")"
6164 NEXT M
6180 RETURN
8850 GOSUB 1000
8852 IF M1=0 THEN 8858
8853 FOR M=1 TO M1
8854 GOSUB 9000
8855 IF A<B THEN 8857
8856 GOSUB 2000
8857 NEXT M
8858 IF M2=0 THEN 8864
8859 FOR M=M1+1 TO M1+M2
8860 GOSUB 9000
8861 IF A>B THEN 8863
8862 GOSUB 2000
8863 NEXT M
8864 IF M3=0 THEN 8868
8865 FOR M=M1+M2+1 TO M1+M2+M3
8866 GOSUB 2000
8867 NEXT M
8868 GOSUB 6000:RETURN
8869 RETURN
9000 ON M GOSUB 10100,10200,10300,10400,10500
9010 RETURN
10000 *****E8,KO,DO*****
10004 DATA 100000000,100000,.0000001
10010 *****CO*****
10012 DATA -.01
10013 *****N*****
10014 DATA 4
10015 *****X(I);I=1 to N*****
10017 DATA 0,0,0,0
10020 *****object*****
10050 C=-5*(X(1)+X(2))-7*(3*X(3)-X(4))+X(1)^2+X(2)^2+2*X(3)^2+X(4)^2
10060 *****M1:(<),M2:(>),M3:(=)*****
10061 DATA 3,0,0
10090 *****subject to*****
10100 A=X(1)^2+X(2)^2+X(3)^2+X(4)^2+X(1)-X(2)+X(3)-X(4):B=8:RETURN
10200 A=X(1)^2+2*X(2)^2+X(3)^2+2*X(4)^2-X(1)-X(4):B=10:RETURN
10300 A=2*X(1)^2+X(2)^2+X(3)^2+2*X(1)-X(2)-X(4):B=5:RETURN
10400 RETURN
10500 RETURN

```

Automatic Optimisation of a New Fast Catamaran with Bulbous Bow

Stefano Brizzolara, Dario Bruzzone

Università di Genova - DINAV, Italy,
brizzolara@dinav.unige.it, bruzzone@dinav.unige.it

Abstract

The paper presents a theoretical investigation into the wave resistance characteristics of a new typology of fast catamarans with an internal underwater body between the two demihulls, which can grant a considerable reduction in total resistance. The effect of the underwater body is investigated in a systematic way by the application of an automatic parametric optimisation method on the longitudinal and vertical position of the body. The wave pattern and wave making resistance of each investigated solution is evaluated by means of a free surface potential flow panel method. The inviscid resistance reductions predicted by the numerical method show comparable trends with experimental results. The optimum “catamaran with bulb” configuration, at different design speeds, is found by the automatic optimisation method, based on a differential evolution algorithm, which drives the entire numerical procedure (i.e. variation of free parameters, the panel mesh discretisation, the prediction of wave resistance) varying in each iteration the free parameters in an “intelligent way”. The analysis of the results is made at two different levels: a preliminary comprehensive investigation of the wave patterns generated by each “BulbCat” hull component and their quantitative interference effects; and the discussion of the optimised configurations for different speeds through the correlation between the parameters considered in the optimisation problem and the analysis of the objective function variation over the free variable design space. Interesting conclusions are drawn about the effectiveness of the underwater bulb, of the optimisation method, and practical guidelines are given for the application of a “BulbCat” typology in the design of new fast catamarans.

1. Introduction

A cooperative research project, funded by the Italian Ministry of Research and held by the three Italian Universities of Naval Architecture: Genova, Napoli and Trieste, is dedicated to the study of modern and efficient multi-hull vessels for fast sea transportation of passengers and cars, among which trimaran, pentamarans and unconventional catamarans are taken under consideration.

This study here presented is part of the activity of this research project and deals with a novel typology of catamaran first presented by Zotti (2003). In fact, through a systematic series of towing tank tests, he proved that some typologies of fast catamaran hulls can improve their residual resistance by the use of an underwater body of revolution placed at the bow, as an isolated submerged bulb between the two demihulls. The effect of the underwater body is not only beneficial around a single design speed, but also over an appreciable speed range. This new catamaran hull typology is briefly referred to as “BulbCat” in the rest of the paper. An example of this kind of new composite multihull is described in more detail in the next section.

The intention of this study is to further analyse the hydrodynamic behaviour and the interference effects of the underwater body on the whole ship wave-making resistance and to complement the inevitably limited experimental investigation with a higher number of configurations, especially for what regards the influence of the longitudinal and vertical position of the submerged internal body. Other motivations of the present study are aimed to the enhancement of the experience in the application of parametric optimisation algorithms to the design of fast ship hulls with improved powering characteristics, that brought already interesting results in another study (Brizzolara, 2004), and to extend the application of the free surface potential flow methods on a new multi-hull typology trying to verify the accuracy and the stability of the results.

2. The “BulbCat” concept

Following Zotti (2003), the catamaran base hull form to which the underwater body of revolution is applied, has been taken from a currently existing fast catamaran passenger ferry operating on short routes between the Italian coast and the closer islands (range less than 50 miles).

Table I gives the main characteristics of the hull of this ship. Fig.1 shows transverse sections of the body plan. The demihulls are hard chine deep-V hulls. It is interesting to analyse the resistance of the vessel in the whole high speed regime, corresponding to $Fn_L=0.45-0.9$.

Table 1: Main characteristics of the base catamaran hull (full scale values):

Length at waterline	$L_{WL} = L = 35.87$ m	O.A. beam-length ratio	$L/B_{WL} = 3.16$ m
Demihull breadth ratio	$L/B_{WL} = 12.6$	Demihull draught ratio	$B_{WL}/T_{des} = 1.80$
Demihull relative length	$L/\nabla^{1/3} = 8.84$	Total displacement	$\Delta = 137$ t
Wetted Surface ratio	$S/\nabla^{2/3} = 10.4$	Demihull Separation	$S/L = 0.225$

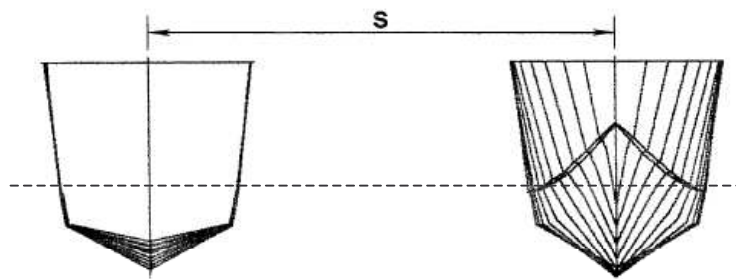


Fig. 1: Body plan of the base catamaran hull used in the study

In his work, Zotti added three different bodies of revolution taken from Series 58 of DTMB (Gertler, 1950), having three different length diameter ratios, $L_b/D_b=5.0, 6.0, 7.0$, and same longitudinal prismatic coefficient $C_p=0.65$, and built them in order to keep the same length, varying the diameter. Moreover, he kept the same longitudinal position of the bulb, which features its leading edge placed at the fore perpendicular of the catamaran, during all the experimental tests. However, from the experimental results, appreciable differences are not noted between these three bodies as far as the residuary resistance is concerned. Some changes of the residuary resistance, on the contrary, has been noted either with a variation of the length or a variation of the draft of the bulb.

So in our this study we assumed and kept the dimension and shape of the underwater body as the one nominated BC1 in the cited work ($L_b/D_b=5, L_{WL}/L_b=5, C_p=0.65$), and took as free parameters the longitudinal (Δx) and vertical shifts (Δz) of the position of the submerged body, with respect to the reference one used by Zotti (L.E. of bulb on the FP of the catamaran, axis at half draft of the vessel).

The reference configuration of the “BulbCat” is illustrated by the 3D views of Fig.2, which also gives an appreciable idea of the relative dimension of the bulb compared with that of the hull.

To compare the hydrodynamic characteristics of the original catamaran with the modified “BulbCat” version, Zotti kept the same draft and static attitude of the original catamaran hull. By this assumption (static draft fixed), it is possible to better isolate the effects caused by the addition of the internal bulb from the hydrodynamic point of view, since the catamaran submerged hull form remains unvaried. Anyhow the additional submerged appendage, causes noticeable geometry variation to the BulbCat: it increases the displacement by about 5.7%, increases the wetted surface of about 9.5% and shifts forward the longitudinal position of the centre of buoyancy of about $2.7\%L_{WL}$ when the leading edge of the bulb is at the fore perpendicular of the catamaran ($\Delta x/L=0$, reference condition).

These variations must be taken into account especially when the comparison is made with respect to the resistance coefficients referenced to the wetted surface or to the displacement.

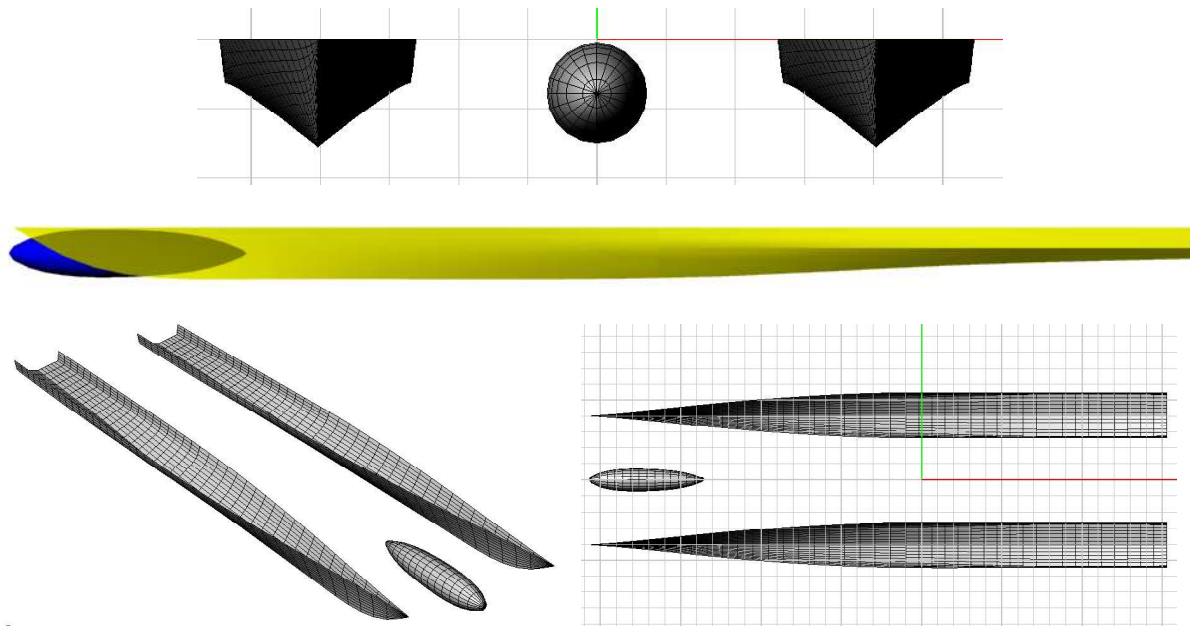


Fig.2: 3D views of the reference geometry configuration of the “BulbCat” hull form (L.E. of the internal bulb on FP and at T/2), with details of the panel mesh used for the wave resistance calculations.

3. The CFD method

The solution of the free surface potential flow around the multi-hull is obtained by a linear Rankine sources panel method, developed at the University of Genova, initially for conventional ships (Bruzzone, 1994), and continuously extended and validated especially for the case of fast multihull ships (Brizzolara et al., 1998; Brizzolara & Bruzzone, 2000; Bruzzone et al., 2000) also for far field wash problems in case of limited bottom depths (Brizzolara & Bruzzone, 2003).

Assuming inviscid and irrotational flow, the problem of the steady fluid motion around a ship advancing at a constant speed can be described by a velocity potential from which the velocities and all the other relevant flow quantities can be derived. The Laplace equation, the body boundary condition of no flow penetration into the hull, the kinematic and dynamic boundary conditions on the free surface, combined with the radiation condition of no upstream waves, set up the boundary value problem in terms of the unknown velocity potential. The non linear free surface boundary condition may be linearised by expressing the total velocity potential as the sum of a reference potential and of a perturbation potential having a lower order of magnitude. The reference potential is assumed as that describing the deeply immersed double model flow: the so called double model potential. A Rankine source distribution is assumed on the hull and on the free surface so the integral boundary value problem is expressed in terms of the related unknown source density. The discretisation of the hull and of a part of the free surface surrounding the hull is realised by means of quadrilateral panels and leads to the numeric formulation of the boundary value problem. The method is of the indirect type in which the relevant terms of the boundary equations are expressed recurring to the influence coefficients for the velocities (i.e. the first order partial derivatives of the potential) that are obtained according the Hess and Smith procedure. The second order derivatives of the velocity potential are computed by a backward finite difference operator in the longitudinal direction and by an outward finite difference operator in the transverse direction. Collocating the boundary equations at the centre of each panel, a linear system of equations for the unknown source densities on each panel is obtained and solved after LU factorisation. Then, the wave resistance can be determined by integration of the pressure forces on the hull which are derived by the application of the Bernoulli equation. Computations can be performed either in a given fixed position, as in this study, or an iterative procedure converging to balanced forces and moments can be followed, to obtain sinkage, trim and

wave resistance in the free attitude. An alternative way of determining the wave resistance is possible exploiting the numerical wave pattern analysis.

4. The Optimisation Method based on a DE Algorithm

The CFD solver, concisely described in the previous section, is integrated into a more comprehensive optimisation code, being coupled with the parametric geometry generation module, the automatic panel mesh generation module and the post-processing module. All these codes, integrated in SCILAB[®], a public domain scientific computing environment (www.scilab.org), are driven by an optimisation algorithm, also written in Scilab.

The optimisation method used is a differential evolution method: a global convergence, stochastic, unconstrained, single-objective, minimisation method, more efficient than well known GA methods. The method was developed in a relative recent time by Price and Storn (1995, 1996) and demonstrated a very good efficiency.

The advantage of stochastic type methods is that they do not require the evaluation of the gradient of the minimizing (objective) function with respect to the free variables of the problem which would take a prohibitive time each convergence step if the objective function is evaluated, as in our case, by the CFD solver. This kind of optimisation algorithm was already used with success in the similar but more complex case of the optimisation of the total resistance of a SWATH ship by variation of the lower hull forms (Brizzolara, 2004).

To address the reader to the specialised references, the basic idea behind DE method is briefly introduced hereinafter. The objective function \mathfrak{S} to be minimised is a general function of the N independent (or free) variables of the problem. In our case of the minimisation of the hull calm water resistance, in the most general sense, we can define the objective function as a weighted sum over the index i (with weights p_i) of the resistance reduction ΔR_i evaluated at NV different speeds V_i :

$$\mathfrak{S}(\bar{\psi}) = \sum_{i=1}^{NV} p_i \cdot \Delta R_{\%}(V_i) \quad (1)$$

$$\Delta R_{\%}(V_i) = 10^2 \frac{R(V_i) - R_{Ref.Hull}(V_i)}{R_{Ref.Hull}(V_i)}, \quad \sum_{i=1}^{NV} p_i = 1, \quad \bar{\psi}_j = [\Delta x / L, \Delta z / T, S / L]_j$$

The free variable values are ordered in a vector $\bar{\psi}_j$ which is referenced as the j^{th} member of the population formed by all the ∞^N vectors that belong to the N free variable domain. Each member has a distinct characteristic identified by the value of the free variable vector components.

By hypothesis there is a special member of the population which is capable of realising the minimum of the objective function over the considered domain. The iterative process act on a series of 'generations' formed by NP population members. The generation individuals do not change during the minimisation process. The first generation has individuals uniformly (in probabilistic sense) distributed inside a certain guessed initial domain, or around a known approximate solution. Up to this point, like genetic algorithms. The new idea behind DE algorithm is in the scheme used to find the individuals which will belong to the next generation. The new tentative individual is characterised by a trial free variable vector $\bar{\psi}_{new}$, found by linear combination of one random individual $\bar{\psi}_1$ of the current generation with the difference $\bar{\psi}_2 - \bar{\psi}_3$ between two other random individuals (of the current generation) through a linear factor F :

$$\bar{\psi}_{new} = \bar{\psi}_1 + F \cdot (\bar{\psi}_2 - \bar{\psi}_3) \quad (2)$$

F is a constant that regulates the amplification of the differential variation.

If the new (individual) vector realises a lower objective function value with respect to the value obtained with a comparison vector, then the new trial vector replaces the vector with which it was compared. The comparison vector can, but not need to be, a member of the population.

Moreover, in order to increase the diversity of the individuals between successive generations, a certain random permutation or exchange of elements in the trial vector just formed as per (1) is performed. As in genetic algorithms, this technique is called direct (because it acts directly on the elements of the vector) cross-over. The parameter which control the number of substituted vectors elements during the cross-over function is the *cross-over factor* $CR \in [0;1]$.

Several variation of the algorithm exist, depending on the way of calculating the trial vector and of choosing the comparison vector, but basically in addition to the one seen in eq. (2), named DE1, there is another (named DE2) which generates the trial vector in the following way:

$$\bar{\psi}_{new} = \bar{\psi}_1 + \lambda \cdot (\bar{\psi}_{Best} - \bar{\psi}_1) + F \cdot (\bar{\psi}_2 - \bar{\psi}_3) \quad (3)$$

where the additional control variable λ regulates the greediness of the scheme to converge towards a local minimum by adding a vector deviation which depends also by the distance to the best member of the current generation $\bar{\psi}_{best}$. Other modifications may be introduced by changing the crossover function (exponential or binomial) and the base vector $\bar{\psi}_1$ that instead of being randomly selected may be fixed to the best vector of the current generation.

For the time being, no attempt of personalizing the algorithm has been done for this study, and the standard DE/rand/1/exp algorithm has been used with the following constant factors: $F=0.6$, $CR=0.8$, $NP=10 \cdot size(\bar{\psi})$. In the future, it will be interesting to verify the dependence of the convergence speed on the control parameters of the DE algorithm.

Our optimisation problem has a bounded domain. Since the DE method is naturally unbounded, the only way to include these boundary constraints is inside the objective function: an additional penalty function will be added to the value of \mathfrak{J} found from eq. (1), which returns an higher value if the trial vector is outside the domain of investigation. In general in our case:

Condition:	$\Delta x/L \notin [-0.4;0.4]$	$\Delta z/T \notin [-1.0;0.05]$
Penalty Value:	100	100

The domain limits, though, have been adapted for the different speeds to be relatively close around the possible minimum, to avoid a dispersion of time in the convergence.

Finally a simple check of numerically unstable results is used to avoid unrealistic results which very seldom the CFD code can generate: the cases for which a negative wave resistance is predicted are evaluated with a very high penalty value. Another more consistent check, perhaps using a criteria based on the analysis of the wave pattern formation, is necessary to avoid also few other unrealistic results, not so drastic in terms of global wave resistance, that at the moment must be excluded ‘a posteriori’ and do prevent the convergence of the optimisation algorithm.

5. Wave pattern characteristics of Bulbcat, Catamaran and single components

A series of computation have been preventively done for the isolated demihulls, for the catamaran, for the isolated underwater body of revolution (internal bulb) and for the complete BulbCat in the reference geometry configuration ($\Delta x/L=0$; $\Delta z/T=0$), covering the complete speed range $Fn=[0.45:0.90]$, of interest for possible full scale applications.

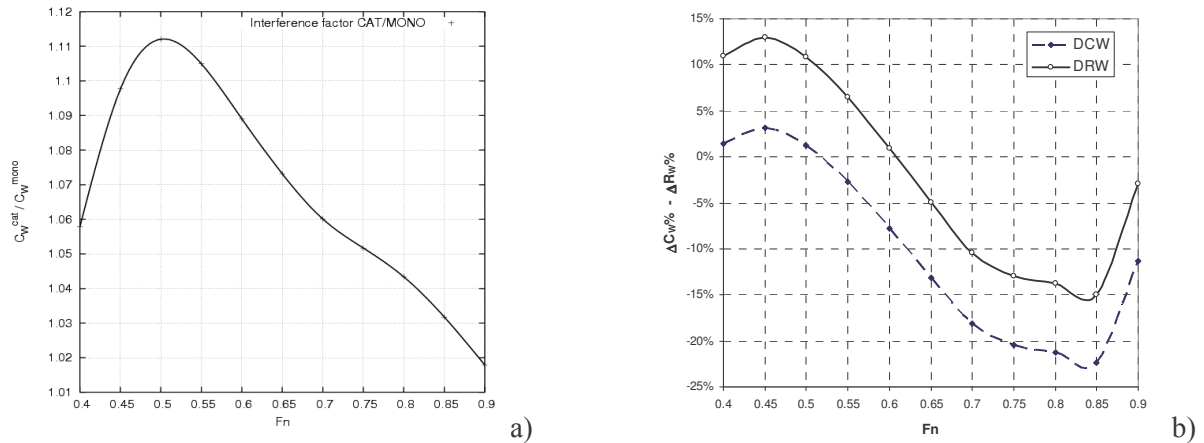


Fig.3: Interference factor for the catamaran (a) and relative difference in wave resistance (b) of the BulbCat in the reference geometry configuration ($\Delta x=0$, $\Delta z=0$) with respect to the catamaran.

The calculations were done with the hull fixed at the initial (static) attitude, congruently with the calculations done for the optimisation study. In fact, the CFD panel method, described in section 3, is capable of finding the dynamic trim and sinkage of the fast hull, as demonstrated already in many studies, e.g. Brizzolara & Bruzzone (2000), and in general for the accurate prediction of the wave resistance of fast ship the hull must be calculated at its dynamic attitude. To avoid prohibitive calculation times during the optimisation procedure, the attitude was then fixed, believing that main trends of the dependence of the wave resistance to the free geometric parameters can still be captured.

A first interesting indication of these preliminary calculations comes from Fig.3a. The wave resistance interference factor of the catamaran, defined as $I.F. = C_w^{CAT} / C_w^{MONO}$, is always greater than unity, that means an increase of wave resistance when the two hulls are coupled. This global result can be explained by the analysis of the observation of the first two graphs of Figs.4 and 5, which represent the wave pattern predicted for the demihull and catamaran at $F_n=0.55$ and $F_n=0.70$, respectively. An appreciable difference is not seen in the divergent waves aside the hull and the relative wave resistance increase may be due to the waves generated inside the two demihulls, starting with the first crest, caused by the focussing of the two first (bow) divergent waves of the two demihulls. This sharp peaked wave is shed also in the wake. From the third graph of Figs.4 and 5, it can be noted that the bulb at the same high speeds tends to form a peaked crest and trough close to its symmetry plane and one divergent wave system. The wave pattern generated by the BulbCat (last graphs of Figs.4 and 5), which combines the catamaran hull with the internal submerged body, is strongly changed respect to the that generated by the catamaran, by the presence of the internal body. In general, the first internal divergent bow wave of the demihulls is partially cancelled by the wave of the submerged body, which effectively changes the whole wave pattern inside the demihulls. Even the divergent wave trains outside the demihulls are beneficially influenced by the presence of the internal body. The global effect is captured in Fig.3b, which represents the difference in wave resistance or wave resistance coefficient between the BulbCat and the catamaran. The two curves are shifted by effect of the difference in wetted surface between the two ships (about 9.5% more for the BulbCat). In general at highest speed the effect of the submerged bulb, even though not placed in the optimum position, is still beneficial for the wave resistance.

When the bulb is in the optimum position all the described interference effects are positively enhanced, as shown in Figs.8 and 9, which present the comparison of the wave patterns of the optimum BulbCat and catamaran at $F_n=0.55$ and 0.70 respectively.

6. Optimisation of the BulbCat geometry at different speeds

The optimisation method briefly introduced in section 4 has been applied to the BulbCat configuration to find the optimum vertical and longitudinal position of the internal submerged body, at different

design speeds. The separation of the demihulls was not taken into account, so the free parameters vector has only two components $\vec{p} = [\Delta x/L, \Delta z/T]$. Total maximum number of generations was set to 20 for a maximum of $20 \times 20 = 400$ calculation cases (generated individuals). The optimisation procedure took some 40-48 hours to run on a Pentium 2.8 Ghz PC.

The history of the free parameters chosen by the optimisation algorithm and the correlation of the objective function with them is interesting to be analysed. Fig.6 represents, in this respect, the correlation between the longitudinal ($\Delta x/L$) and vertical position ($\Delta z/T$) of the internal body, relative to the reference position assumed by Zotti (2003) in his work (see Fig.2), with the wave resistance reduction with respect to that of the catamaran, at $F_n = 0.55$ and 0.70 respectively. It is clear that a strong correlation exists between the longitudinal position and the resistance, whereas the objective function seems to be independent from the other free variable (the depth). The dependence shows a minimum around $\Delta x/L = 0.22 \div 0.25$, slightly varying with the design speed. On the contrary, the dependence of the resistance on the submergence of the body is not so well individuated. These trends are confirmed by the contour plots of Figs.7 and 9 which represent the space dependence of the objective function from the two independent variables, at the two considered speeds respectively.

These plots show that the local minimum areas highlighted by a pale colour are almost narrow vertical bands parallel to Δz axis, since they are low sensitive to this parameter. In any case, an absolute minimum exists inside these areas and is highlighted with a bold cross in the figure.

Some of the lowest points of figure 6 (roughly those achieving less than 20% of reduction) have been implicitly excluded by the research of the minimum, since they correspond to unrealistic calculation cases, in which the numerical method used for the wave resistance prediction failed. As already discussed in section 4, at the moment this analysis is made 'a posteriori', is time consuming and still rely on an expert evaluation. A deterministic criterion is necessary and will be searched to make the optimisation procedure fully automatic and the convergence to the real minimum reliable and fast.

The best configurations found at the two considered speeds and their gains in wave resistance with respect to the catamaran are summarised in Table II. The resistance reductions are quite remarkable. The best theoretical position of the bulb is shifted rather forward and practically impossible for a realistic construction.

The hydrodynamic effect of the immersed body is evident from Figs.8 and 10 for the two considered speeds, respectively. It is clear that when the bulb is too advanced, i.e. $\Delta x/L > 0.3$, and the divergent wave system it creates is not captured anymore between the two demihulls, then the beneficial interference effects of the body are lost and in fact the wave resistance increases (dark areas in the graphs of Figs.7 and 9). In effect, by interpretation of Fig.6, the relative increase of wave resistance occurs rather steeply when the bulb is moved forward from the optimum position.

7. Conclusions and future prospects

The wave resistance characteristics and wave pattern formation of a fast catamaran hull with bulb have been investigated and discussed in the paper. In particular the effect of the internal submerged bulb is predicted to positively interfere with the first internal divergent bow wave of the demihulls, but it has effects also on the outside divergent wave trains.

An automatic optimisation method based on series of interfaced codes, featuring a linear panel method, an automatic mesh generator and a differential evolution optimisation algorithm has been described and applied with success to find the optimum vertical and longitudinal position of the internal submerged body of the BulbCat.

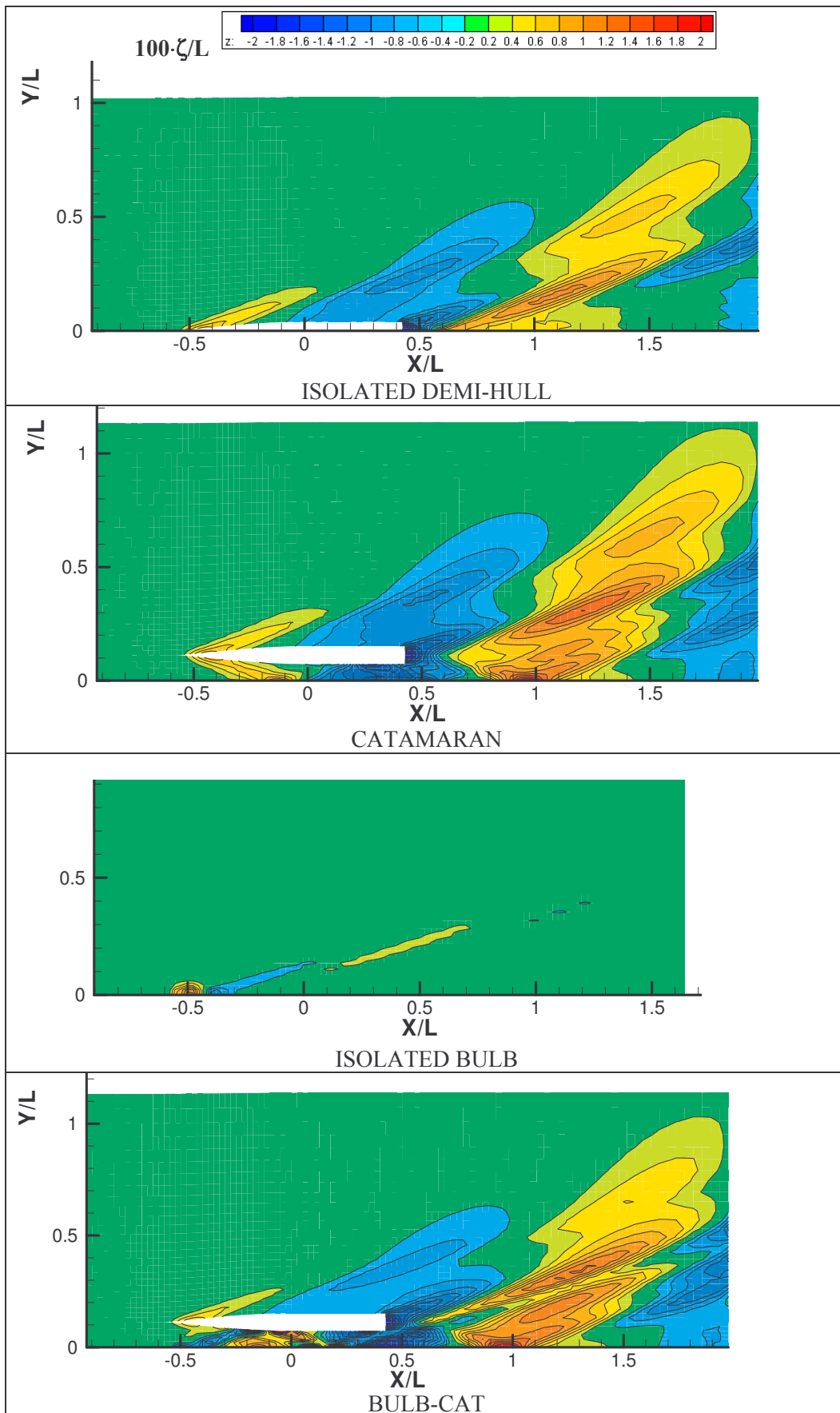


Fig.4: Wave contours (contour scale refers to $100 \cdot \zeta/L$) generated by BulbCat hull components and the whole BulbCat hull: $F_n=0.55$, $x_{LE}=0.0$, $z_{TE}=T/2$

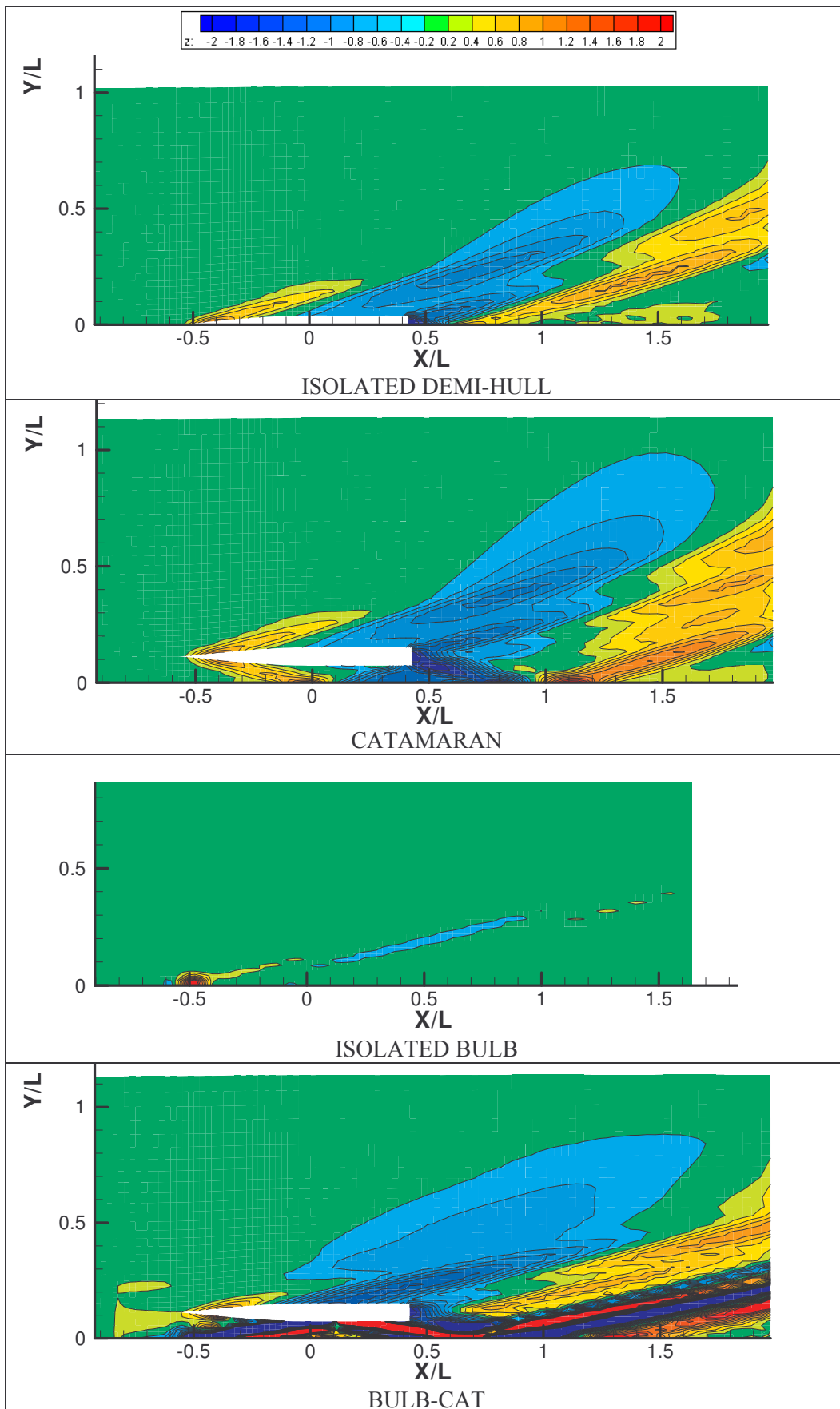


Fig.5: Wave contours (contour scale refers to $100 \cdot \zeta/L$) generated by BulbCat hull components and the whole BulbCat hull: $Fn=0.70$, $x_{LE}=0.0$, $z_{TE}=T/2$

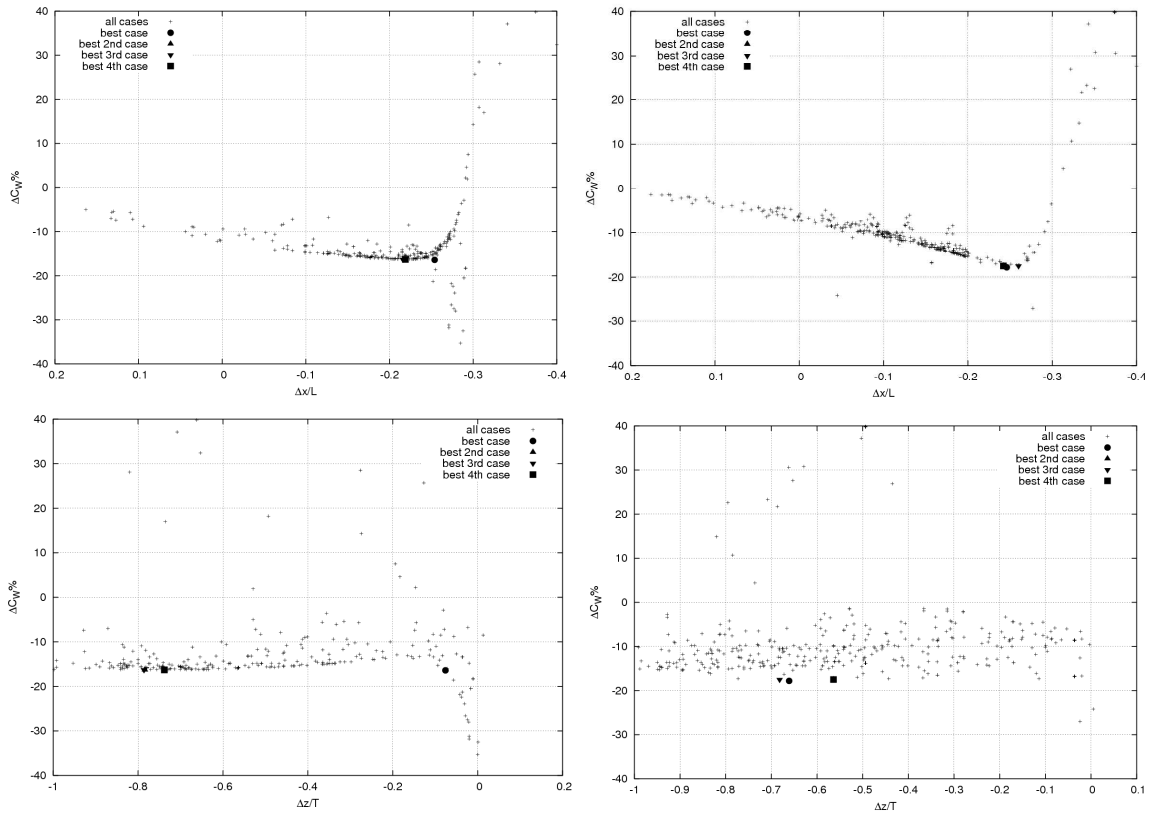


Fig.6: Correlation plot between the free variables (top: $\Delta x/L$, bottom: $\Delta z/T$) and the wave resistance gains respect to the reference catamaran, obtained during the optimisation calculations at two different speeds F_n : 0.55 (left), 0.70 (right).

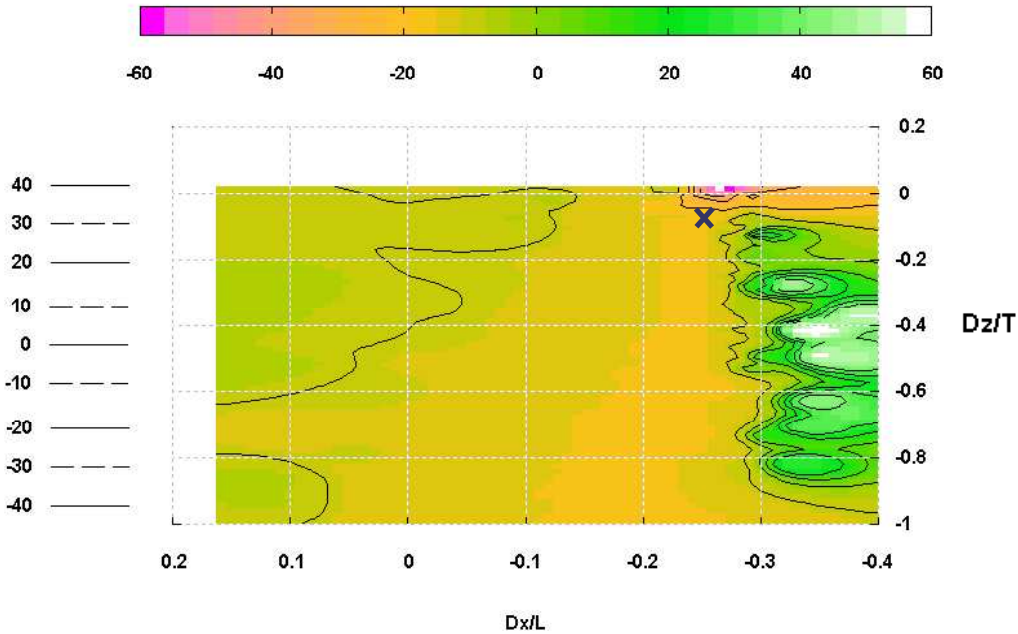


Fig.7: Contour plots of the objective function (C_w percent reduction with respect to that of the catamaran) over the optimisation design space: $F_n=0.55$. Bold cross indicates found optimum.

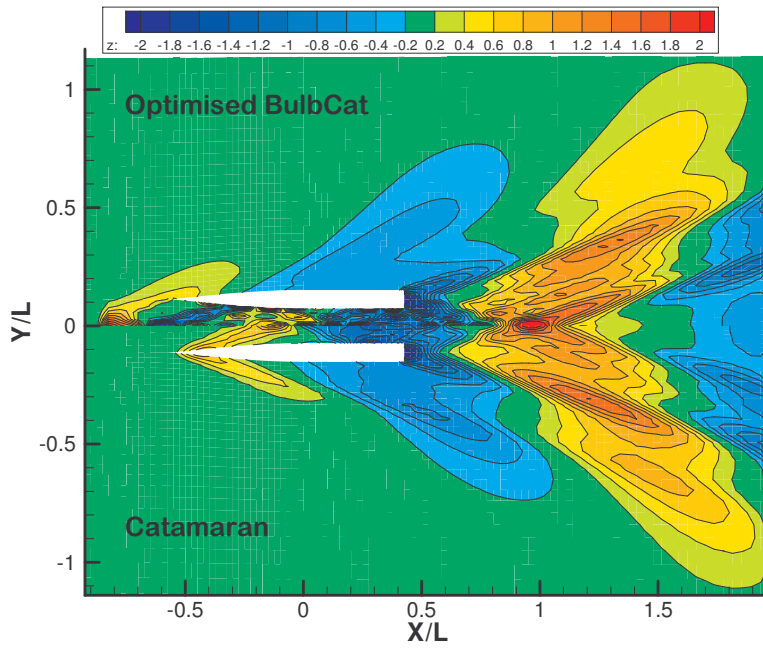


Fig.8: Near field free wave patterns generated by the catamaran and the optimised “BulbCat” at $Fn=0.55$. Contour level of the non-dimensional wave height $100 \cdot \zeta / L$

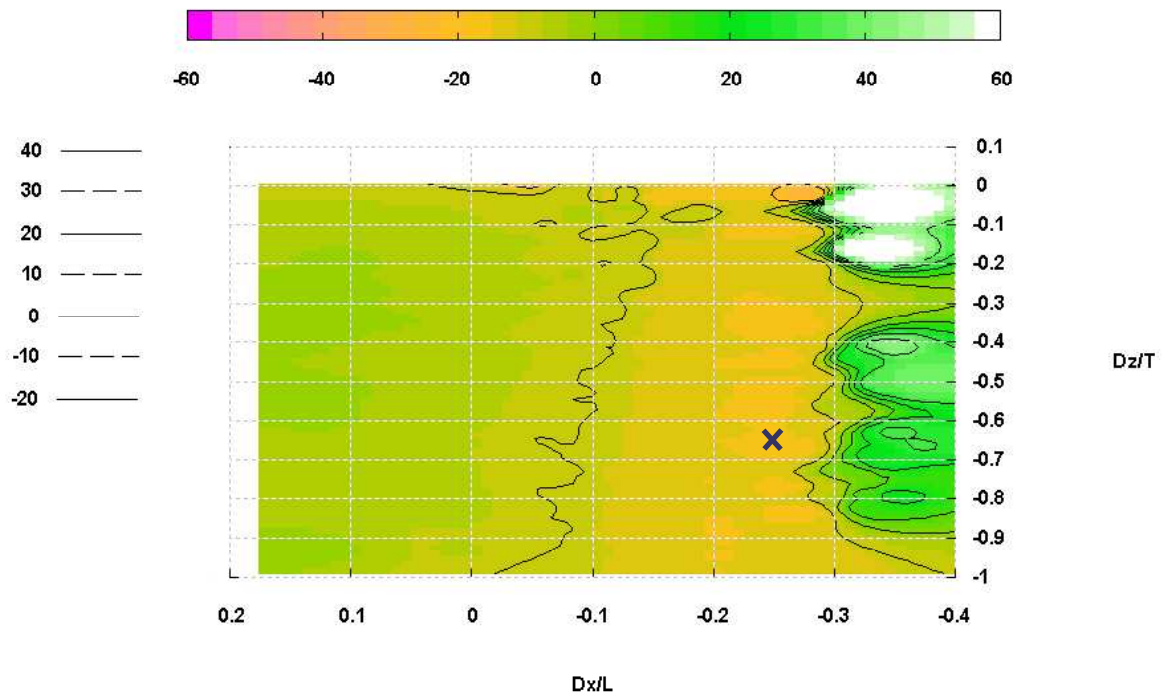


Fig.9: Contour plots of the objective function (C_w percent reduction with respect to that of the catamaran) over the optimisation design space: $Fn=0.70$. Bold cross indicates found optimum.

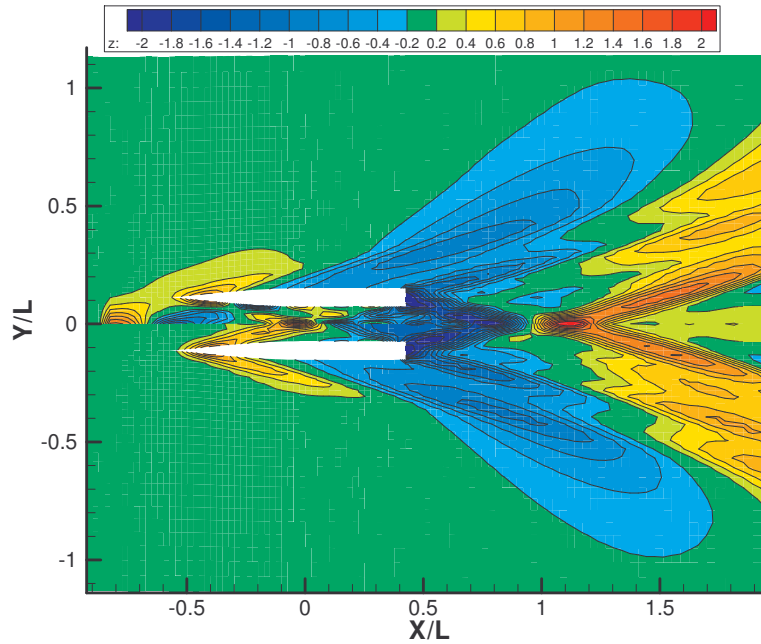


Fig.10: Comparison of the near field free wave patterns generated by the catamaran and the optimised “BulbCat” at $F_n=0.70$. Contour level of the non-dimensional wave height $100 \cdot \zeta/L$

The best position and relative resistance reduction with respect to the catamaran hull are summarised in Table II and are quite relevant. The optimum position of the body results too advanced for practical applications, but an shift aft the body of 10%, corresponds to wave resistance increase of the order of $2\% \div 5\%$, for $F_n=0.55$ and $F_n=0.70$ respectively. Furthermore the dependence of the wave resistance to the immersion of the bulb is not so pronounced, if inside the range assumed for numerical optimisation.

Table II: Optimum configuration found for the two considered speeds and relative gains in wave resistance with respect to the catamaran

F_n	$\Delta x/L$	$\Delta z/T$	C_{wcorr}	$\Delta C_w\%$	$\Delta R_w\%$
0.55	-0.254	-0.076	1.463200e-003	-16.4	-8.5
0.70	-0.246	-0.661	9.487000e-004	-17.8	-10.0

Next interesting research topics related to this study are:

- to devise a method that detects a numerical failure of the wave resistance numerical evaluation and include a penalty function into the objective function, to exclude these unrealistic solutions. Some preliminary idea are directed to some quantitative criteria based on the analysis of the energy spectrum of the generated free wave patterns;
- to apply and test the performance of other types of optimisation algorithms, including the deterministic types;
- to extend the optimisation also of the form and dimension of the internal submerged body;
- to include in the optimisation other design constraints relevant for specific design problems such as the fixed LCB position or constant displacement.

References

- BRIZZOLARA, S. (2004), *Parametric Optimization of SWAT-Hull Forms by a Viscous-Inviscid Free Surface Method Driven by a Differential Evolution Algorithm*, 25th Symp. Naval Hydrodynamics, St. John's, CANADA
- BRIZZOLARA, S.; BRUZZONE, D. (2000), *Numerical Wave Resistance and Dynamic Trim for High Speed Crafts*, NAV 2000 Int. Conference, Venice, Vol. I, pp. 4.2.1-4.2.13.
- BRIZZOLARA, S.; BRUZZONE, D. (2003), *Near and Distant Waves of Fast Ships in Limited and Unlimited Depths*, 7th Int. Conf. Fast Sea Transportation FAST 2003, Ischia, vol. III, pp. H1-H12
- BRIZZOLARA, S.; BRUZZONE, D.; CASSELLA, P.; SCAMARDELLA, I.; ZOTTI, I. (1998), *Wave Resistance and Wave Pattern for High Speed Crafts; Validation of Numerical Results by Model Tests*, 22nd Symp. Naval Hydrodynamics, Washington D.C., pp. 69-83.
- BRUZZONE, D. (1994), *Numerical Evaluation of the Steady Free Surface Waves*, CFD Workshop Tokyo, Ship Res. Inst. Tokyo, Vol. I, pp. 126-134.
- BRUZZONE, D.; CASSELLA, P.; ZOTTI, I. (2000), *Resistance Components on a Wigley Trimaran: Experimental and Numerical Investigation*, 4th Int. Conf. Hydrodyn., Yokohama, Vol. I, pp.115-120
- GERTLER, M. (1950), *Resistance Experiments on a Systematic Series of Streamlined Body of Revolution for Applications to the Design of High Speed Submarine*, DTMB report C-297, 1950.
- STORN, R.; PRICE, K. (1995), *Differential Evolution – A Simple and Efficient Adaptive Scheme for Global Optimization over Continuous Spaces*, TR-95-012, Int. Computer Science Institute, Berkeley, California.
- STORN, R. (1996), *On the usage of Differential Evolution Algorithms for Function Optimization*, NAFIPS, Berkeley, California, pp. 519-523.
- ZOTTI, I. (2003), *Hydrodynamic Improvement of Catamaran Hulls When Using Streamlined Bodies of Revolutions*, 7th Int. Conf. Fast Sea Transportation FAST 2003, Ischia

Effect of welding on ultimate compressive strength of aluminium stiffened panels

Thomas Richir, ANAST, Univ. of Liege, Liege, Belgium, thomas.richir@ulg.ac.be
Catalin Toderan, ANAST, Univ. of Liege, Liege, Belgium, catalin.toderan@ulg.ac.be
Jeom Kee Paik, NAOE, Pusan National University, Busan, Korea, jeompaik@pusan.ac.kr
Philippe Rigo, ANAST, Univ. of Liege, Liege, Belgium, FNRS, ph.rigo@ulg.ac.be

Abstract

Aluminium structures for marine applications have normally been built by welding. It is recognized that welding significantly affects the behaviour of aluminium alloys. In particular, heat-affected zone (HAZ) is softened by welding, and this reduces the ultimate strength of welded aluminium structures. It is of vital importance for structural designers to better understand how fabrication by welding affects the aluminium panel ultimate strength characteristics. This paper investigates the ultimate compressive strength characteristics of welded aluminium stiffened panels with varying welding related parameters such as weld type, width of HAZ (heat-affected zone) and reduction of yield stress due to HAZ softening. The non-linear finite element methods and the Paik empirical formulae are employed for the sensitivity analyses on the parameters.

1. Introduction

Both steel and aluminium structures for marine applications have usually been built by welding for the benefits in terms of fabrication efficiency and cost. However, welding can give rise to some problems during fabrication of aluminium structures in terms of softening in heat-affected zone (HAZ), among others, in contrast to low alloy steel structures. This may reduce the ultimate strength of welded aluminium structures.

It is commonly accepted that the collapse characteristics of welded aluminium structures are similar to those of welded steel structures until and after the ultimate strength is reached, regardless of the differences between them in terms of material properties. However, it is also recognized that the ultimate strength design formulae available for steel panels cannot be directly applied to aluminium panels even though the corresponding material properties are properly accounted for. One of the major reasons for this is due to the fact that the softening in HAZ significantly affects (reduces) the ultimate strength behaviour of welded aluminium structures, whereas it can normally be neglected in welded steel structures, Paik et al. (2004a).

A variety of parameters may affect the ultimate strength characteristics of welded aluminium structures as well as welded steel structures, and it is of vital importance for structural designers to better understand the sensitivity of the ultimate strength characteristics on such parameters. The aim of this paper is to provide one such contribution with the focus on the effect of welding on ultimate strength characteristics of welded aluminium panels, among other parameters. The parameters considered in the present paper are: weld type, HAZ width, and reduction of yield stress in the HAZ. The sensitivity on thickness of plating between stiffeners is also studied. With varying the parameters, a series of the ultimate strength calculations are undertaken. Non-linear finite element methods, Rigo et al. (2004), Simonsen (2003), and the empirical formulae of Paik et al. (2004a,b,c) are used for that purpose.

2. Methods of analysis

2.1 Non-linear finite element methods

Non-linear finite element solutions previously obtained by the ISSC Committee III.1 on Ultimate Strength, Simonsen et al. (2003), are adopted for the present sensitivity analyses. An elaborate

description of the ISSC FEA is given by Simonsen et al. (2003) and Rigo et al. (2003). The FEA solutions previously obtained by Rigo et al. (2004) are also used for the present sensitivity analysis on weld locations.

2.2 The Paik empirical formulae

A first-cut estimate of the panel ultimate strength is very important in terms of ultimate limit state (ULS) based reliability analyses. In this case, an empirical formulae is often useful. Paik et al. (2004a,b) derived the ULS formulae for both welded aluminum plating (between stiffeners) and welded aluminum stiffened panels, by regression analyses of FE computations obtained with varying related parameters. Details of the FEA to develop the empirical formulae are given by Paik et al. (2004a,b).

Three different levels of initial deflections were considered for the FE computations (see section 3.6), while welding residual stresses were not considered. Therefore, the three different types of ultimate strength formulae for the three different levels of initial deflections were derived. The following is the Paik empirical formulae for aluminium stiffened panels with the symbols defined in Fig.1, Paik et al. (2004b,c):

$$\sigma_{xu} = \frac{\sigma_{Y,seq}'}{\sqrt{C_1 + C_2(\lambda')^2 + C_3(\beta')^2 + C_4(\lambda'\beta')^2 + C_5(\lambda')^4}} \leq \frac{\sigma_{Y,seq}'}{(\lambda')^2} \quad (1)$$

σ_{xu} ultimate strength of the aluminium stiffened panel;
 $\sigma_{Y,seq}'$ equivalent yield stress of plate-stiffener combination as representative of a stiffened panel with considering HAZ effect,

$$= \frac{P_s}{bt + h_w t_w + b_f t_f},$$

$$P_s = (b - 2b_p') t \sigma_{Yp} + 2 b_p' t \sigma_{Yp}' + (h_w - b_s') t_w \sigma_{Ys} + b_s' t_w \sigma_{Ys}' + b_f t_f \sigma_{Ys} \quad (2)$$

b breadth of plating;
 b_f breadth of stiffener flange;
 b_p' HAZ breath at plate;
 b_s' HAZ breadth at stiffener;
 h_w height of stiffener web;
 t thickness of plating;
 t_f thickness of stiffener flange;
 t_w thickness of stiffener web;
 σ_{Yp} yield stress of plating at 0,2% offset;
 σ_{Yp}' yield stress of plating in HAZ;
 σ_{Ys} yield stress of stiffener at 0,2% offset;
 σ_{Ys}' yield stress of stiffener in HAZ;
 λ' column slenderness ratio with considering the HAZ effect;

$$= \frac{a}{\pi r} \sqrt{\frac{\sigma_{Y,seq}'}{E}} \quad (3)$$

a length of a stiffened panel between transverse frames
 E Young's modulus of elasticity
 r radius of gyration,

$$r = \sqrt{\frac{I}{bt + A_w + A_f}};$$

I moment of inertia,

$$I = \frac{bt^3}{12} + bt \left(z_0 - \frac{t}{2} \right)^2 + \frac{h_w^3 t_w}{12} + A_w \left(z_0 - t - \frac{h_w}{2} \right)^2 + \frac{b_f t_f^3}{12} + A_f \left(t + h_w + \frac{t_f}{2} - z_0 \right)^2$$

$$A_w = h_w t_w ;$$

$$A_f = b_f t_f ;$$

z_0 distance from the outer surface of the attached plate to the elastic horizontal neutral axis of the plate-stiffener combination;

$$z_0 = \frac{0.5bt^2 + A_w(t + 0.5h_w) + A_f(t + h_w + 0.5t_f)}{bt + A_w + A_f}$$

β' plate slenderness ratio with considering the HAZ effect;

$$= \frac{b}{t} \sqrt{\frac{\sigma_{Y,p}}{E}}$$
(4)

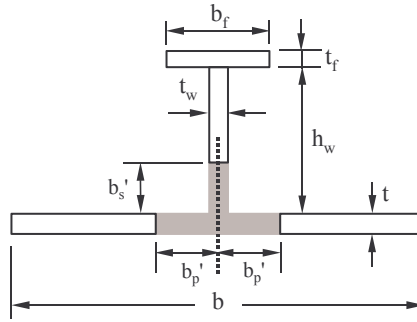


Fig.1: Cross section of the plate-stiffener combination with softening zones

In Eq.(1), the coefficients $C_1 - C_5$ are defined depending on the level of initial deflections of plating and stiffeners, as indicated in Table I, Paik et al. (2004b,c).

Table I: Coefficients depending on the levels of initial deflections of plating and stiffeners

Coefficient	Slight	Average	Severe
C_1	0.878	1.038	1.157
C_2	0.191	1.099	2.297
C_3	0.106	0.093	0.152
C_4	-0.017	-0.047	-0.138
C_5	1.30	1.648	3.684

3. Description of the standard panel considered

3.1 Geometry

For the present study, a reference panel is selected from welded aluminium stiffened panels used for collapse testing undertaken by Aalberg et al. (2001). The panel has angle type (or L-shaped) aluminum extrusions (6082 temper T6) of stiffeners, while the stiffeners are welded to plating. Fig.2 indicates the geometry of the reference panel.

3.2 Material properties

While the details of the material properties are described in the paper of Aalberg et al. (2001), the Young modulus is 70,475 MPa and the Poisson ratio is 0.3. The transverse frames have the same material properties to plating. Welding significantly influences the properties of aluminium alloys.

Due to welding, the yield stress in HAZ can be decreased. Depending on the weld type, the width of HAZ can increase. In this regard, the HAZ width and the reduction amount of yield stress in HAZ will be varied in the present sensitivity analyses.

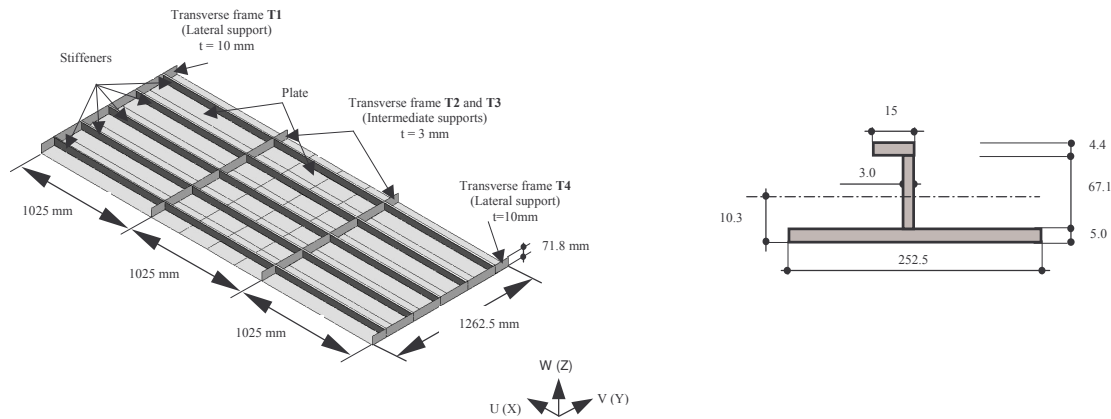


Fig.2: The reference aluminium stiffened panel

3.3 Loads

The panel is subjected to axial compressive loads in the longitudinal direction applying displacement control. Loading is applied at the initial neutral axis of cross section at both ends (no shift due to eccentric load, etc. is considered).

3.4 Extent of the analysis

In the ISSC FEA, the entire panel, i.e., with a three-bay was taken as the extent of the analysis. The Rigo FEA takes a two-bay model, i.e., 1/2+1+1/2 panels as shown in Fig.3. On the other hand, a plate-stiffener combination model, i.e., a single stiffener with associated plating between transverse frames was taken for the Paik et al. (2004a) FEA which produced the Paik empirical formulae.

3.5 Boundary conditions

In the ISSC FEA, all (four) edges of the panel are almost clamped, while both the Rigo FEA and the Paik FEA consider that the panel is simply supported.

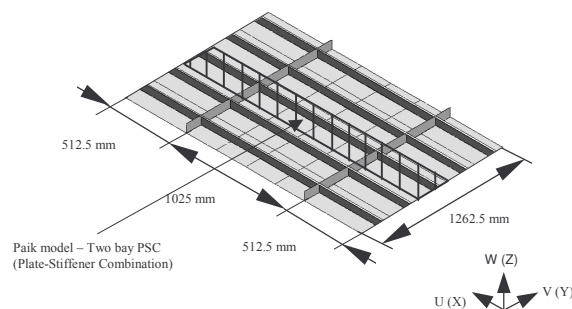


Fig.3: Extent of the analysis used for the Rigo FEA

3.6 Initial imperfections

In the ISSC FEA, a unique type of initial deflection is artificially generated as shown in Fig.4. A uniform lateral pressure loading is applied until the maximum deflection of plating between stiffeners is 2mm.

It is important to realize that the resulting initial deflection pattern generated by the ISSC FEA is quite different from the collapse mode of the continuous stiffened panel under predominantly axial compressive loads. That is, all sub-panels in this situation deflect in the same direction, although one sub-panel buckles up while the adjacent sub-panels deflect down as long as axial compressive loads are predominant. As a result, this unique pattern of initial deflection considered in the ISSC FEA can increase the panel ultimate strength to some extent.

Also, the ISSC FEA does not properly consider the initial deflection of stiffeners in the direction parallel or normal to stiffener web, the former being called column type initial deflection of stiffener and the latter being called sideways initial deflection of stiffeners.

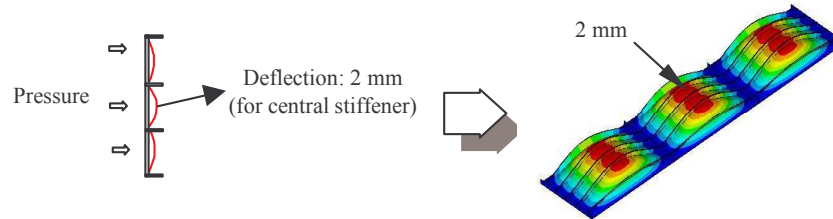


Fig. 4: Generation of initial deflection - Procedure to define the initial imperfections adopted for the ISSC FEA

The Rigo FEA considers two types of initial deflection pattern: One is the same to that of the ISSC FEA noted above, and the other is that the initial deflection pattern of plating between stiffeners is the same to the original buckling half wave.

While the Paik FEA assumes that plating between stiffeners has the same pattern to the original buckling half wave, it considers the three types of initial deflections, namely the initial deflection of plating between stiffeners, the column type initial deflection of stiffeners and the sideways initial deflection of stiffeners. Also, three different levels of initial deflections were considered in the Paik FEA, as follows

Slight level : $w_{opl} = 0.003b$, $w_{oc} = w_{os} = 0.001a$
Average level : $w_{opl} = 0.009b$, $w_{oc} = w_{os} = 0.0025a$
Severe level : $w_{opl} = 0.015b$, $w_{oc} = 0.005a$, $w_{os} = 0.008a$

where w_{opl} = maximum initial deflection of plating between stiffeners, w_{oc} = maximum column type initial deflection of stiffeners in the direction parallel to stiffener web, w_{os} = maximum sideways initial deflection of stiffeners in the direction normal to stiffener web, b = breadth of plating between stiffeners, and a = length of a stiffened panel between transverse frames.

Welding induced residual stresses are not considered for both the ISSC and Paik finite element analyses.

3.7 Modelling of HAZ

According to several standards, one shall consider the width of the reduced strength zone (noted η_1 and η_2 in the following) to extend 25 mm at each side of the weld (note that 20 mm is proposed in Eurocode 9, ENV (1998)). In the present study (Fig.6), this indicates that $2\eta_1 = 50$ mm in the plate and $\eta_2 = 25$ mm in the stiffener web (measured from the mid-plate and not from the plate surface). The extension (width) of the HAZ is mainly affected by the applied welding process and the welding parameters, as well as the material properties.

Therefore, the following weld zones are considered in the mesh modelling (Fig. 6):

- five longitudinal welds at the junction between the transverse plate and the five stiffeners,
- four longitudinal welds at the intersection between the five extruded elements,
- two transverse welds between plates.

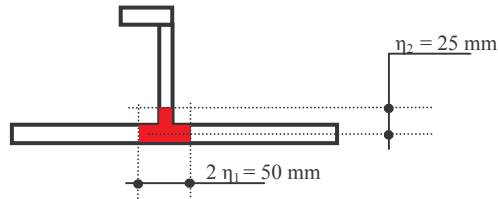


Fig. 5: Standard HAZ width ($2 \eta_1$ in plate = 50 mm, η_2 in stiffener web = 25 mm)

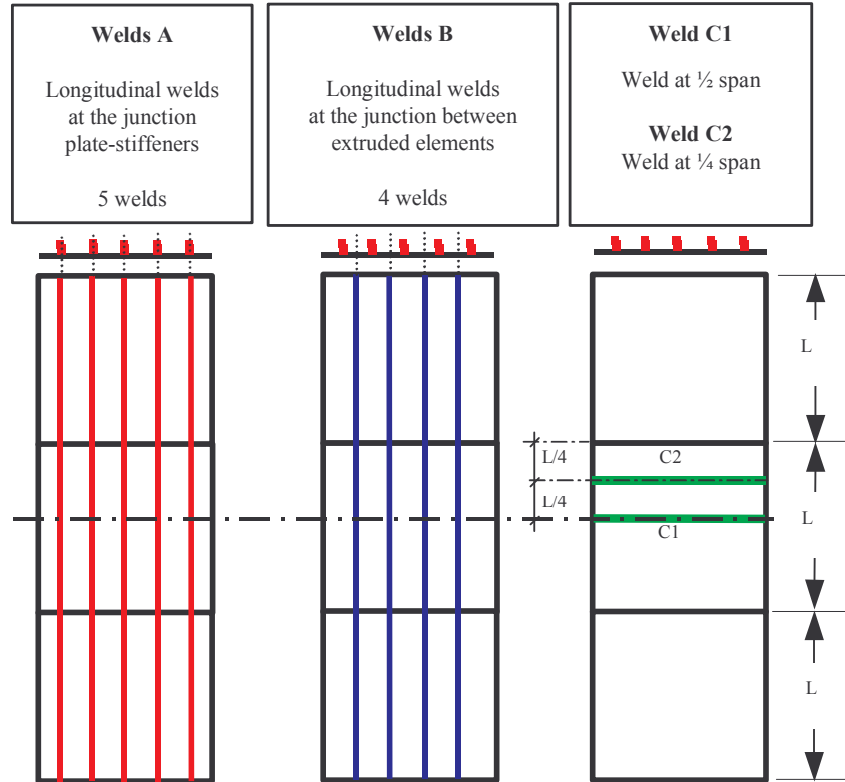


Fig. 6: Weld positions considered

It is assumed that welding does not affect material in HAZ of the transverse frames (i.e., T1,...,T4). Unless otherwise specified, the FEA is conducted with the HAZ width of 50 mm, i.e. $2 \eta_1 = 50$ mm (2×25 mm in the plate) and $\eta_2 = 25$ mm in the stiffener flange, with η_1 and η_2 defined in Fig. 5.

4. Sensitivity analysis

4.1 Weld locations

The ISSC FEA, Simonsen et al. (2003):

Table II: Effect of the weld locations investigated by the ISSC FEA

	Without HAZ (reference)	Welds A	Welds B	Welds B+C1	Welds A+C1	Welds A+C2	Welds B+C2
Ultimate strength (N/mm ²)	167.5	140.3	159.6	144.1	126.0	133.7	142.1
Difference to reference (%)	Ref.	-16.2	-4.7	-14.0	-24.8	-20.2	-15.2

Rigo et al. (2004) FEA:

Table III: Effect of the weld locations investigated by the Rigo FEA with the initial deflection pattern of the ISSC FEA

	Without HAZ (reference)	Welds A	Welds B	Welds B+C1	Welds A+C1	Welds A+C2
Ultimate strength (N/mm ²)	159.6	146.8	151.0	141.7	130.6	128.3
Difference to reference (%)	Ref.	-8.0	-5.4	-11.2	-18.2	-19.6

Table IV: Effect of the weld locations investigated by the Rigo FEA with the initial deflection pattern of the buckling half wave

	Without HAZ (reference)	Welds A	Welds B	Welds B+C1	Welds A+C1	Welds A+C2
Ultimate strength (N/mm ²)	141.2	127.9	139.6	139.8	128.4	128.5
Difference to reference (%)	Ref.	-9.4	-1.1	-1.0	-9.1	-8.9

Paik et al. (2004a,b,c) empirical formulae:

Table V: Effect of the weld locations investigated by the Paik empirical formulae for an average level of initial deflection

	Without HAZ (reference)	Welds A	Welds B
Ultimate strength (N/mm ²)	125.1	117.8	119.5
Difference to reference (%)	Ref.	-5.8	-4.5

It tends that the reduction of the ultimate strength due to weld type A is more serious than that due to weld type B. Compared to those by the ISSC FEA or the Rigo FEA, the reduction amount of the ultimate strength for welds B (extruded element) is similar to that for welds A (stiffeners welded on the plate) when the Paik empirical formulae are used. This may be due to the fact that in using the Paik empirical formulae, welds B are only taken into account through the P_s expression (Eq.(2)) which becomes:

$$P_s = (b-2b_p') t \sigma_{Yp} + 2 b_p' \sigma_{Yp}' + h_w t_w \sigma_{Ys} + b_f t_f \sigma_{Ys} \quad (5)$$

Transverse weld location seems insignificant but cannot be neglected as a difference is recorded between weld C1 and weld C2. Note that the Paik formulae does not consider the effect of welding along transverse frames as well since the plate-stiffener combination model is employed for the ULS calculation of a stiffened panel.

4.2. Effect of HAZ width (with Welds A – welded Stiffeners)

Four HAZ widths ($2 \eta_1$ in plate and η_2 in web) are considered (Fig. 5): $2 \eta_1 = 25, 50, 75, 100$ mm ($\eta_1 = \eta_2$). The yield stress in the HAZ is fixed at 115 MPa.

The ISSC FEA, Simonsen et al. (2003):

Table VI: Effect of the HAZ width investigated by the ISSC FEA

	Without HAZ (reference)	HAZ width			
		25 mm	50 mm	75 mm	100 mm
Ultimate strength (N/mm ²)	167.5	157.2	149.8	142.3	137.0
Difference to reference (%)	Ref.	-6.1	-10.6	-15.0	-18.2

Paik et al. (2004a,b,c) empirical formulae:

Table VII: Effect of the HAZ width investigated by the Paik empirical formulae

Initial deflection level		Without HAZ (reference)	HAZ width (mm)			
			25mm	50mm	75mm	100mm
Slight level	Ultimate strength (N/mm ²)	143.7	135.3	125.4	113.8	100.1
	Difference to reference	Ref.	-5.9	-12.7	-20.8	-30.4
Average level	Ultimate strength (N/mm ²)	125.1	117.6	108.9	98.9	87.1
	Difference to reference	Ref.	-6.0	-13.0	-21.0	-30.4
Severe level	Ultimate strength (N/mm ²)	95.3	90.3	84.5	77.7	69.6
	Difference to reference	Ref.	-5.2	-11.3	-18.5	-27.0

Fig.7 shows the effect of the HAZ width on the panel ultimate compressive strength when weld type A is applied. The panel ultimate compressive strength decreases significantly as the HAZ width increases. The reduction tendency of the ultimate strength with increase in the HAZ width is similar for both the ISSC FEA and the Paik empirical formulae regardless of the differences in terms of the panel edge conditions and the magnitude of initial deflections considered. The panel ultimate compressive strength is also affected significantly by the initial deflections.

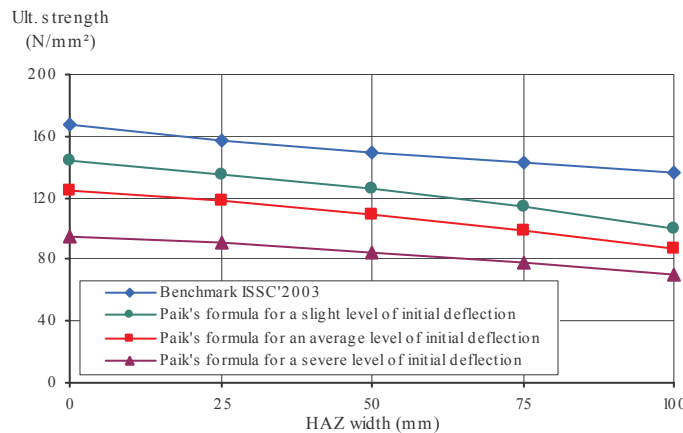


Fig.7: Sensitivity on HAZ width

4.3. Effect of yield stress reduction in the HAZ

The yield stress in the HAZ is varied when the HAZ width is fixed at $2\eta_1 = 50$ mm.

The ISSC FEA, Simonsen et al. (2003):

Table VIII: Effect of the yield stress reduction in the HAZ investigated by the ISSC FEA

	Without HAZ (reference)	Yield stress (N/mm ²)					
		$S_{v.ref}-10$	$S_{v.ref}$	$S_{v.ref}+10$	$S_{v.ref}+20$	$S_{v.ref}+40$	$S_{v.ref}+60$
Ultimate strength (N/mm ²)	167.5	148.4	150.3	152.4	154.4	160.0	167.7
Difference to reference (%)	Ref.	-1.3	0.0	1.4	2.7	6.4	11.6

Paik et al. (2004a,b,c) empirical formulae:

Table IX: Effect of the yield stress reduction in the HAZ investigated by the Paik empirical formulae

Initial deflection level		Without HAZ (reference)	Yield stress (N/mm ²)					
			S _{y, ref} - 10	S _{y, ref}	S _{y, ref} + 10	S _{y, ref} + 20	S _{y, ref} + 40	S _{y, ref} + 60
Slight level	Ultimate strength (N/mm ²)	143.7	134.6	135.3	135.9	136.5	137.7	138.9
	Difference to reference	Ref.	-7.2	-6.7	-6.2	-5.7	-4.8	-3.8
Average level	Ultimate strength (N/mm ²)	125.1	117.0	117.6	118.1	118.7	119.8	120.8
	Difference to reference	Ref.	-6.5	-6.0	-5.6	-5.2	-4.3	-3.4
Severe level	Ultimate strength (N/mm ²)	95.3	89.9	90.3	90.7	91.0	91.8	92.5
	Difference to reference	Ref.	-5.9	-5.5	-5.1	-4.7	-3.6	-3.1

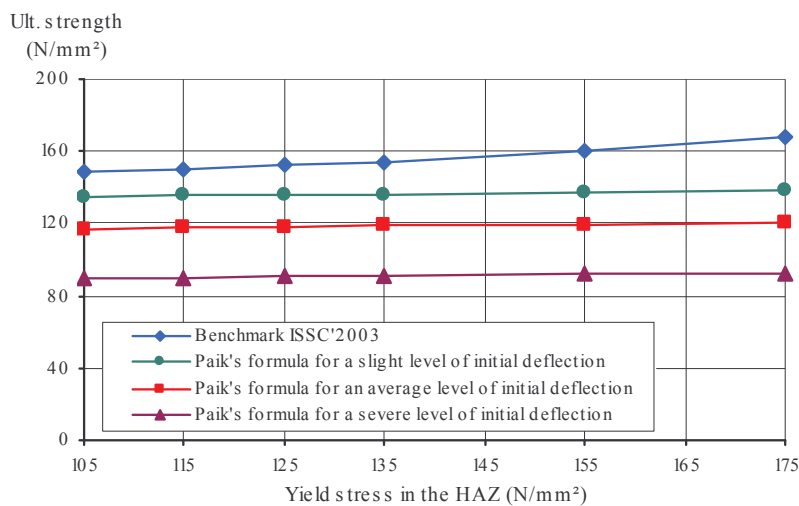


Fig.8: Sensitivity on yield stress of the HAZ

Fig.8 shows the effect of yield stress in HAZ on the panel ultimate compressive strength. The Paik empirical formulae indicates that the sensitivity of the panel ultimate strength on the yield stress in the HAZ is very small, while a reduction of 10% yield stress in the HAZ results in an ultimate strength reduction varying from 2% to 5% in the ISSC FEA. While further study is pending, this might be due to the fact that the tensile residual stresses exist in the HAZ after welding and this should usually not affect the ultimate strength of the panel as long as compressive loads are applied and the HAZ width is relatively small.

4.4. Effect of plate thickness

The thickness of the plate between stiffeners was increased to 7 mm, keeping the rest of the geometry of stiffeners unchanged. The material properties correspond to welds A, where the width of the HAZ is $2 \eta_1 = 50$ mm.

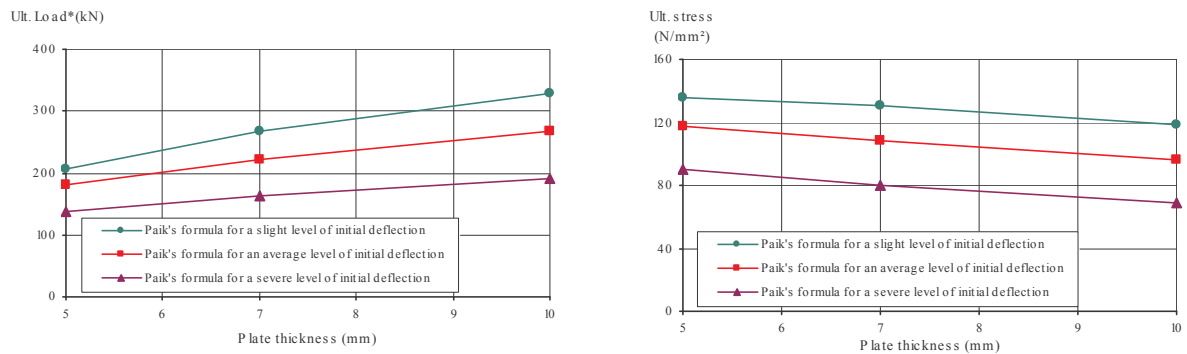
Paik et al. (2004a,b,c) empirical formulae:

Table X.a: Effect of plate thickness on the ultimate load investigated by the Paik empirical formulae

Initial deflection level		Plate thickness (mm)		
		5mm	7mm	10mm
Slight level	Ultimate load (kN)	206.9	266.8	329.9
	Difference to reference	Ref.	28.9	12.7
Average level	Ultimate load (kN)	179.9	221.1	267.8
	Difference to reference	Ref.	22.9	48.9
Severe level	Ultimate load (kN)	137.9	162.7	191.4
	Difference to reference	Ref.	18.0	38.8

Table X.b: Effect of plate thickness on the ultimate stress investigated by the Paik empirical formulae

Initial deflection level		Plate thickness (mm)		
		5mm	7mm	10mm
Slight level	Ultimate strength (N/mm ²)	135.3	131.1	118.1
	Difference to reference	Ref.	-3.1	-12.7
Average level	Ultimate strength (N/mm ²)	117.6	108.6	95.9
	Difference to reference	Ref.	-7.6	-18.4
Severe level	Ultimate strength (N/mm ²)	90.1	79.9	68.5
	Difference to reference	Ref.	-11.3	-24.0



*Ultimate load = resultant of the ultimate stress on the section of the plate-stiffener combination (Fig.2)

Fig 9: Sensitivity on plate thickness

Fig.9 shows the effect of plate thickness on the ultimate load and the ultimate stress of the panel, respectively. As would be expected, the ultimate load (force) increases with increase in the thickness of plating between stiffeners. However, the ultimate stress decreases as the thickness of plating increases while the dimensions of stiffeners are kept unchanged. This is due to the fact that for this specific case, the panel collapses by lateral-torsional buckling (or tripping) when the thickness of plating was increased to 7mm, while the standard panel reached the ultimate limit state by the so-called beam-column type collapse mode.

This is because stiffeners are likely to fail prior to plating as stiffeners are comparatively weak than plating with increased thickness, while the panel cross sectional area increases. It may be surmised from this study that a careful design of panel structures is required considering the potential collapse modes to occur as well as scantlings themselves.

5. Conclusions

In this paper, the effects of welding related parameters on the ultimate compressive strength of aluminium stiffened panels are investigated. The following conclusions can be drawn:

- (1) Welding related parameters studied in the present study are weld locations, HAZ width and yield stress reduction in HAZ. In addition, the effect of plate thickness on the panel ultimate strength is also studied.
- (2) It is concluded that fillet-welding at the junction between plating and stiffeners is more likely reducing the panel ultimate compressive strength than that by butt-welding of I-shaped extrusions. This is because the stiffener web as well as plate part is also softened in the former type of welding, while only plate part is softened in the latter.
- (3) As the width of HAZ increases keeping the yield stress in HAZ constant, the panel ultimate compressive strength decreases significantly.
- (4) As long as the HAZ width is relatively small and compressive loads are applied, the effect of yield stress reduction in the HAZ is small. This is because the tensile residual stresses existed in HAZ may offset the reduction of the ultimate strength of the panel in axial compression, while further study is pending when the HAZ width becomes larger.
- (5) When the dimensions of stiffeners are kept unchanged, the panel ultimate compressive strength (stress) can rather decrease with increase only in the thickness of plating between stiffeners. This is due to the fact that the collapse mode of the panel can become changed from the beam-column type collapse to lateral-torsional buckling of stiffeners as the stiffeners become weak compared to plating between stiffeners so that stiffeners likely fail prior to plating between stiffeners.

References

- Aalberg, A.; Langseth, M.; Larsen, P.K. (2001), *Stiffened aluminium panels subjected to axial compression*, Thin-Walled Structures, Vol.39, pp. 861–885.
- ENV (1998), European Committee for Standardization, *Eurocode 9: Design of Aluminium Structures-Part 1-1: General Rules and Rules for Buildings*, ENV 1999-1-1
- Paik, J.K.; Duran, A. (2004a), *Ultimate strength of aluminium plates and stiffened panels for marine applications*, Marine Technology, Vol.41, No.3, pp.108-121.
- Paik, J.K.; Hess, P.; Hughes, O.F. (2004b), *Ultimate strength failure of lightweight, multi-hull ships*, Progress Report to US Office of Naval Research, Washington, D.C.
- Paik, J.K.; Veen, S. van der; Duran, A.; Collette, M. (2004c), *Considering aluminium welded panel structures for aerospace, marine and land-based applications: a comparison of ultimate compressive strength design methods*, PRADS'2004, Luebeck.
- Rigo, P. et al. (2003), *Sensitivity analysis on ultimate strength of aluminium stiffened panels*, Marine Structures, Vol.16, pp 437-468
- Rigo, P. et al. (2004), *Ultimate strength of aluminium stiffened panels: Sensitivity analysis*, PRADS'2004, Luebeck.
- Simonsen, B.C. et al. (2003), *Benchmark, 15th Int. Ship and offshore Structures Congress (ISSC'2003)*, San Diego, Publ. Elsevier, pp. 304-313

Conceptual design of a Fuel Cell Electric Generator for a Ro/Ro Passenger Ferry Vessel

Massimo Figari, University of Genoa - Naval Architecture and Marine Engineering Department (DINAV), Genoa/Italy, figari@dinav.unige.it

Michele Viviani, Fincantieri, Naval Ship Business Unit, Genoa/Italy, michele.viviani@fincantieri.it

Abstract

The paper presents and compares different solution strategies for the installation of a fuel cell electric generator onboard a typical ro/ro-pax ferry. The work has been developed in the framework of the EU funded FCSHIP project. The main expected benefit of the presented solutions are reduction of environmental impacts of ships engaged in European trade (Short Sea Shipping) and reduction of environmental impacts of ships during stay in ports and harbours. The concept designs presented in this paper consider different fuel cells types (PEFC, MCFC, SOFC) and different fuels (marine diesel oil, hydrogen). Main advantages and main drawbacks of each solution are identified and discussed.

1. Introduction

The European Union strategy to reduce atmospheric emissions from shipping has presented a clear demand on reduction exhaust emissions from ships. A strategic document issued by the Commission addresses an urgent need of research and technology development on low-emission ships and bringing the technology to market in a foreseeable future.

Also the Italian Government pushes the modal shift from road to the sea in order to reduce traffic and pollution. Applying fuel cell (FC) technology to convert energy from hydrogen has been identified as one of the most promising element for future sustainable transportation. This has already been demonstrated by the automotive industry, while limited activity has taken place to demonstrate the feasibility of the FC technology in maritime sector. The major research effort for the application of FC onboard ships is developed in the USA, as deduced from literature. *Kumm (1990)* described a possible procedure for the selection of FC for ship applications; the procedure was used during the conceptual design of a FC propelled combatant ship for the US Navy. *Allen (1998)* provided an assessment of the progresses of some research studies of FC marine applications promoted by different US governmental Agencies; the paper also focus on the joint effort that the Agencies interested in the marine sector are doing to promote shipboard application of FC. *Karni (1999)* described the conceptual design of a FC propelled US Coast Guard vessel. *Bolind (2000)* published a SNAME research report focused on the potential of FC application on merchant ships. *Corbett (2000)* proposed an hydrogen fuelled ship with FC to reduce both air pollution and greenhouse gas emissions. *McMullen (2003)* presented a feasibility study for a FC propelled small passenger ferry in the San Francisco Bay.

Basurto (2002) presented a study for the propulsion of a luxury yacht with a combine FC-gas turbine cycle. The paper mainly covers the thermodynamic aspects of the plant and is not focused on the ship design aspects, such as the storage of the natural gas required to operate the proposed plant.

At European level the project "Fuel Cell technology for SHIPs" (FCSHIP) is the first major attempt of the European Commission to establish a roadmap for the marine industry to adopt this sustainable technology. The project had a two year duration and finished on June 2004. The project FCSHIP aimed to :

- enable EU fuel cell technology providers to be more competitive in the perspective future market for maritime applications;
- enable EU ship owners to utilise this new technology whose application to ship is expected to generate a lasting competitive advantage for ship owners and shipbuilders;
- to assist EU in meeting sustainable development, energy saving and air pollution reduction objectives.

In the framework of the FCSHIP project, one of the tasks was the feasibility study for the electric generation onboard ships by means of Fuel Cell systems. The main benefits were expected to be:

- the reduction of environmental impacts of ships engaged in European trade (Short Sea Shipping);
- the reduction of environmental impacts of ships during stay in ports and harbours.

In this paper a design procedure for the conceptual design of Fuel Cell Systems (FC) onboard ships is presented and the application to a car-passenger ferry is illustrated.

2. Marine Application of Fuel Cells

Fuel cells are electrochemical reactors which convert the chemical energy of the reactants directly into electricity, with high efficiency, due to the absence of any intermediate thermodynamic cycle (whose efficiency is limited by the Carnot efficiency). Furthermore, fuel cells offer significant improvements compared to traditional technologies also in terms of emissions, since (i) due to the operating temperature (always below 1000°C) no NO_x are produced; (ii) low CO emission; (iii) no formation of soot or powders, typical of combustion processes; (iv) no emissions of organic reactive compounds, typical of combustion processes; (v) CO₂ emissions lower than with traditional technologies, due to the higher efficiency.

From the technological point of view, fuel cells and batteries have similar components (anode, electrolyte, cathode). Nevertheless, the latter ones are closed systems, able to supply electricity until there are chemical reactant stored inside, while the previous ones are open systems, continuously supplied with chemical reactants and thus able to supply electricity under steady-state conditions.

Different types of fuel cells are currently been studied; they are usually classified according to the type of electrolyte employed:

1. proton exchange membrane fuel cell (PEFC, operating at 80°C),
2. alkaline fuel cell (AFC, operating at about 80°C),
3. phosphoric acid fuel cell (PAFC, operating at about 200°C),
4. molten carbonate fuel cell (MCFC, operating at about 650°C),
5. solid oxide fuel cell (SOFC, operating at about 1000°C).

Different types of fuel cells are addressed to different applications. In particular, high temperature fuel cells (MCFCs and SOFCs) offer higher efficiency and lower mechanical strength than the others, and thus they are considered to be suitable for small-medium size power plants.

FC systems with a high power (mainly stationary) are currently characterised in general by rather high volume and weight compared to conventional marine power systems. This will have a rather significant impact on ship design in the case of full electric ships powered by fuel cells.

Furthermore, hybrid systems coupling high temperature fuel cells to gas turbines are expected to reach efficiencies as high as 65% or even more. From the environmental point of view, the positive aspects described above for fuel cells are expected to hold also for hybrid systems, provided that the fuel treatment part of the plant is designed in a suitable way. The high interest that hybrid systems are receiving worldwide is demonstrated by the high number of research project currently in progress, and by the level of investments currently devoted to this subject from both companies and national energy agencies.

2.1 FC requirements

This paragraph addresses the main characteristics and requirements that a FC system has to have for the purpose of the conceptual design in FCSHIP project. Data in this section constitute the framework for the conceptual design. The FC has been considered subdivided into four main subsystems, as illustrated in Fig.1.

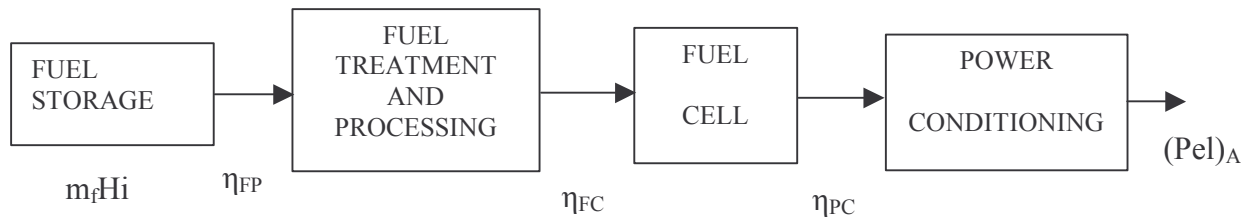


Fig.1: Fuel Cell (FC) subsystems

The overall system efficiency is: $\eta_{\text{sys}} = \eta_{\text{FP}}\eta_{\text{FC}}\eta_{\text{PC}}$

2.1.1 Fuel

Among the different possibilities of fuels presently available, three have been considered promising for this project:

- Marine Diesel Oil (MDO)
- Natural Gas (CH₄)
- Hydrogen (Compressed H₂ or Liquefied H₂)

MDO is a commonly used fuel in marine application. Presently it is mainly used for military vessels and for minor commercial vessels that have high speed diesel engines or gas turbines as prime movers. FC systems like MCFC have already been experienced with a diesel feed, through a reformer. The choice of this type of fuel is compatible with present FC experience and with actual state of the art of shipboard fuel systems. The main problem related to the application of MDO with FC systems is related to the sulphur content of the fuel itself, since it affects significantly the volume and weight of the whole fuel processing plant.

Hydrogen is the fuel that allows the better FC performances and highlights their potential benefits on the environment, but it has been never experienced for shipboard fuelling applications. The choice of this fuel represents a breakthrough for ship fuelling systems. It requires the development of new concepts for all the fuel chain (refuelling, storage, feed). It is a major challenge for the ship design. It has been decided to analyse hydrogen as fuel in connection with PEFC, with the aim of investigating the impact of the direct use of hydrogen (both liquefied and compressed) on the ship internal layout. Hydrogen storage and handling is a rather complex and unconventional task, especially if it has to respect the strict volume constraints inside a ship. In order to avoid too high specific volumes, hydrogen has to be stored in a liquefied form (at about 21K) or at high pressures (300÷700 bar). Both methodologies are related, contrarily to what occurs for conventional fuels, to significantly high energy requirements to fulfil the storage conditions. Moreover, it has to be underlined that these methodologies are, in many cases, just at the study or first demonstrator phase, and strong research efforts are being made in order to improve them in view of large scale applications in the automotive industry.

Natural Gas can be seen as a “compromise” choice, which allows to obtain higher benefits for the environment than MDO (because of its lower carbon content) and which contemporarily presents lower problems for what regards storage and handling with respect to pure hydrogen. Nevertheless, LNG storage and handling still represent a challenge, especially considering the particular kind of ship analysed. This particular problem has been covered in *Levander (2004)* (Annex 2).

2.1.2 Power

Power range is a main issue for shipboard application. Ship systems requires high power with high transient loads. On the base on the survey of present state of the art and on future foreseen, two power levels have been considered for FCSHIP conceptual design:

- a constant power generator of about 1000 kW
- the full electric power generation of about 2500-3000 kW

The first hypothesis refers to a FC system that is used for the 'base' generation, also in ports where the ship is close to urban areas. To supply the entire power demand of the ship there will be the necessity of diesel generators, which contemporarily allow to follow in a better way the typical transients in the electrical power requirements. In the second hypothesis the complete electric power demand is supplied by FC modules.

2.1.3 Weight and volume

Volume, weight and deck area are key aspects of any system for shipboard applications. The data used for the conceptual design comes from the gathering of multiple sources: a deep literature survey of previous, current and future projects, direct simulations and manufacturers data. Regarding MCFC and SOFC, there is a significant difference between data collected from FC manufacturers and data about current studies. One of the reasons for this gap is that data provided by FC manufacturers mainly refer to “stationary applications” (as most of the high power range FC currently developed), and therefore they are characterized by rather high volumes and weights (if compared to traditional Marine Diesel Generators). On the contrary, data from current studies are mainly related to transport applications, but they represent only future goals and not data about actual demonstrators or existing plants. We decided, therefore, to consider some different steps, starting from manufacturers data and considering also possible future developments, in order to give an impression of the possible impact on the ship of different FC solutions and to find which should be the research goals for FC manufacturers in the following years.

Table I: Fuel Cell Manufacturers data

	FC type	5 years	10 years	
Power	SOFC	50	250	[kW]
	MCFC	250-500	500	[kW]
Efficiency	SOFC	42	47	%
	MCFC	33-41	47-53	%
Specific Area	SOFC	0.15	0.03-0.06	[m ² /kW]
	MCFC	0.14	0.07	[m ² /kW]
Specific Volume	SOFC	375	45-112	[l/kW]
	MCFC	364	212	[l/kW]
Specific Weight	SOFC	100	32-48	[kg/kW]
	MCFC	144	85	[kg/kW]

Table II: Fuel Cell data from literature

	FC type	Near Term	Long Term	
Power	SOFC	250	50000	[kW]
	MCFC	3000	20000	[kW]
Efficiency	SOFC	55	75	%
	MCFC	40	70	%
Specific Area	SOFC			[m ² /kW]
	MCFC			[m ² /kW]
Specific Volume	SOFC	9.5	6.9	[l/kW]
	MCFC	56	48	[l/kW]
Specific Weight	SOFC	6.0	2.9	[kg/kW]
	MCFC	18.2	13.6	[kg/kW]

For what regards PEFC systems, on the contrary, current available systems have been developed for mobile applications, thus resulting in lower specific volumes and weights.

In order to complete the analysis also the impact of the use of alternative fuels on the ship's internal volumes was assessed. In the case of high temperature FC (MCFC and SOFC) using marine diesel oil

as fuel, the impact on the general arrangements of the ship is limited to the FC system itself (with connected auxiliaries). In fact the same tanks used for fuel oil can be adopted also for MDO, and the required volume is comparable, without any limitation in the ship operating profile and without limiting the ship range.

Table III: Target Fuel Cell characteristics (PEFC)

	5 years	
Fuel	Hydrogen (LH ₂ , CH ₂)	
Normal power	500	[kW]
System Efficiency	55	%
System sfoc	55	[g/kWh]
System volume	21	[l/kW]
System Weight	10.5	[kg/kW]
System Area	0.011	[m ² /kW]

On the contrary, in case different fuels are used (LNG or H₂), the impact on the ship's internal arrangements is not limited to the plants, but it is strongly influenced by the significant volumes needed for fuel storage. Furthermore natural gas and hydrogen cannot be stored in the ship structural tanks but it is necessary to use containment vessels.

This aspect, regarding hydrogen fuel, was assessed considering both LH₂ and CH₂ with two different storage pressures, 300 and 700 bar (while problems related to LNG are covered in *Levander (2004)* (Annex 2). In order to evaluate volumes and weights, the following values reported in Table IV: have been adopted (where the total weight and volume of the storage system per unit mass of fuel are specified); it has to be noted that, in the case of compressed hydrogen, the values of weights reported are referred to vessels built using composite materials.

Table IV: Weights and volumes of storage system per unit mass of fuel

Storage form	Specific volume [l/kg _{H2}]	Specific weight [kg/kg _{H2}]
LH ₂	30	11.2
CH ₂ (700 bar)	36	16.8
CH ₂ (300 bar)	62	13

2.1.4 FC System Rules Requirements

General rules requirements regarding the use of FC Systems on board ships have been developed by Germanischer Lloyd. The GL requirements address the following subjects:

1. Installation
2. Fuel Systems
3. Fuel Cell Stacks
4. Inverters following Fuel Cells
5. Ventilation Systems
6. Materials
7. Fire Extinguishing Systems
8. Explosion Protection
9. Control, Regulating, Monitoring and Alarm Devices
10. Protective Devices and Protective Systems
11. Trials of the System

Regarding the fuel tanks location, DNV and Norwegian Maritime Directorate rules for LNG storage have been considered pertinent to H₂ storage also and adopted as a guidance for the conceptual design. The different layouts proposed in this work take into account all the above mentioned rules

requirements, even if not all the pertinent requirements can be properly addressed at the early stage of the design.

2.2 Ship type for FC application

Among the different ship types and application analysed, the choice that offers the best opportunities with respect to:

- assure a significant reduction of pollutants emissions, mainly in highly populated areas;
 - assure the required ship volumes for the FC plant without a significant change of the ship layout;
 - assure a low impact on the overall ship cost, due to the high initial cost of this ship type
- seemed to be a ferry type ship. Two sizes of ferry were analysed: a medium-large size Ro/Ro-Pax vessel for short sea shipping and an harbour ferry.

This paper addresses the Ro/Ro-pax ferry design, while the harbour ferry design was performed by *Huismans (2004)* (Annex 4).

For this ship type, the application of Fuel Cells have to be limited to the electric power generation only, since the propulsive power requirement is too high compared to the power of current Fuel Cells applications. On the contrary, the 3 MW electrical power demand seems to be in a “feasible range” for FC; it allows to obtain significant environmental benefits, mainly for this kind of ship that has an operating profile characterized by frequent port stops with auxiliary power demand.

Other aspects in favour of a Ro/Ro-Pax are:

- assure a lower impact on the ship running costs with respect to other ship types, due to the lower incidence of the fuel costs (higher incidence of personnel costs);
- helping European shipping industry to maintain world-wide leadership in this market segment.

Table V lists the characteristics of a Ro/Ro-Pax vessel suitable for the conceptual design in FCSHIP project.

Table V: Main ship characteristics

		Machineries	
Length o.a.	138.8 m	Main Engines	4*8000kW, 750 RPM
Length p.p.	127.4 m	Aux. Diesel Engines	3*1000kW, 900 RPM
Breadth mld.	21.6 m	Emergency Diesel	1*400kW, 1800 RPM
Max. draught (SWL)	5.6 m	Propeller	2 CPP, 180 RPM
Displacement	9300 t	Service speed (85% MCR)	26.00 kn
Lane metres; cars	530m;365		
Passengers	1500		

The operational profile of the target ship was chosen with reference to short sea shipping routes. The reason of the choice is to maximise the benefits of exhaust emissions reduction. In fact, presently about 40% of the EU inter trade is operated by short sea shipping. The observed growth was about 27% over the past ten years. Two main typologies of short sea shipping routes were identified for the European waters, Table VI.

Table VI: Operational schedule

	long route: average 420 nm	short route: average 210 nm
voyage duration	16-20 hours	8-12 hours
stay at quay	8-4 hours	16-12 hours (or 4 hours if two voyages per day are scheduled)
winter:	1 voyage per day , 6 days every week	1 voyage per day , 6 days every week
summer	1 voyage per day , 7 days every week	2 voyages per day, 7 days every week

With a ship’s operating speed of about 26 kn, the most likely operating profile is associated to a short route with 2 voyages per day in peak traffic periods (typically summer period, e.g. from June to September), with speed reductions and 1 voyage per day during low traffic periods. The long route the voyage time is about 20 hours, with an approximate speed of 21 kn. In this case, the power installed into the concept design ship is under utilized (with a ship speed similar to the one we have in the short route in the low traffic period). In the following, typical time schedules for a long routes is reported; the propulsive power includes 15% sea margin; moreover, the power percentage is referred to the number of engines inside brackets (for example 84% with two engines for auxiliary power means $0.84 \cdot 2 \cdot 1080 \text{ kW}$).

Table VII: Operational profile - long route

Operation Mode	Location	Time from Start	Speed [knots]	% Propulsion power	% Aux. power
Manoeuvring	1	0:30	0-6	15 (2 engines)	87 (2 engines)
Cruise	-	20:00	21	85 (2 engines)	84 (2 engines)
Manoeuvring	2	0:30	0-6	15 (2 engines)	87 (2 engines)
At berth	2	3:00	0	0	73 (2 engines)
Manoeuvring	2	0:30	0-6	15 (2 engines)	87 (2 engines)
Cruise	-	20:00	21	85 (2 engines)	84 (2 engines)
Manoeuvring	1	0:30	0-6	15 (2 engines)	87 (2 engines)
At berth	1	3:00	0	0	73 (2 engines)
Total voyage	Round trip	48:00	-	-	-

3. Preliminary layout of the generator units in the engine room

We present some layout solutions, together with the present engine room layout for comparison. Fig.2 shows original engine room layout, with the 4 main propulsion engines driving two shaft lines and the 3x1000 kW Diesel Generators. The following FC electric generation configurations were considered:

- MCFC based on manufacturers data (1000 kW and full power) fuelled with diesel
- MCFC based on target data (full power) fuelled with diesel
- SOFC GT based on target data (full power) fuelled with diesel
- PEFC (1000 kW and full power) fuelled with hydrogen

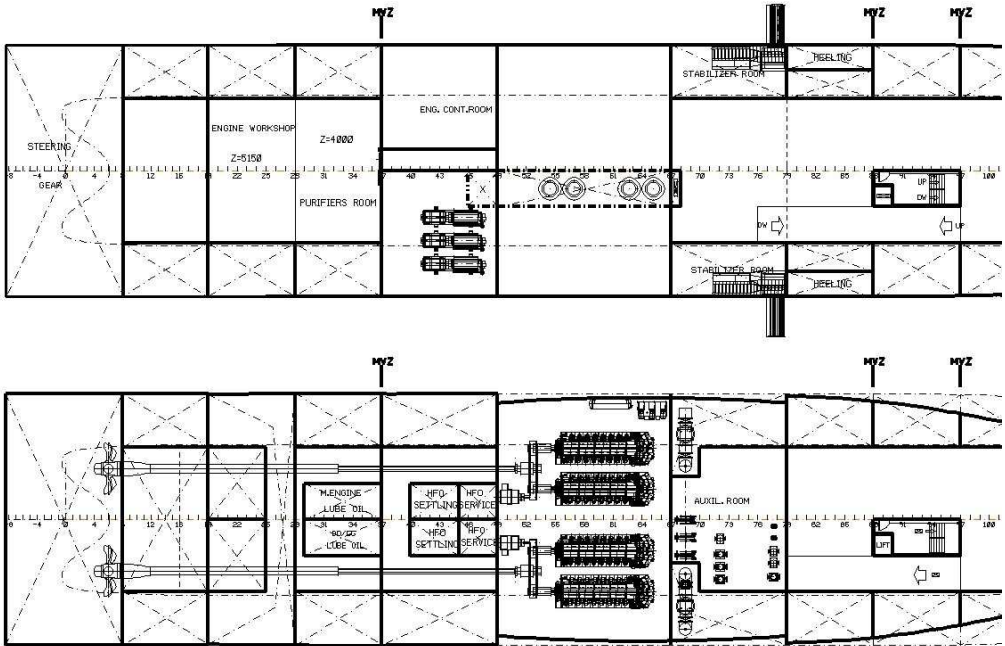


Fig.2: Original ship Engine Room layout

The use of diesel fuel (MDO) onboard does not require significant differences in the tanks arrangements and in the operational range with respect to a normal HFO fuelled ship; for this reason the sketches of the fuel tanks arrangements (fuel capacity plan) are not reported here.

A more detailed analysis was made in the case of hydrogen fuel, which is expected to have an higher impact on the ship. In particular, it was considered to reduce the number of voyages between refuelling in order to avoid a too strong impact of the hydrogen containment system volume on the ship internal layout and on the total cargo capacity. Moreover the short time scheduled into ports could represent an additional problem, limiting the maximum amount of fuel which can be loaded at every refuelling.

From the point of view of the range, the ship in her original configuration has the capability to sail about 5 voyages at 26 knots consecutively between refuelling (considering the long route of 420 nm), maintaining about 30% fuel stock (with a total range of about 3000 nm). For diesel fuel, the ship range is mainly limited by propulsive power requirements, being the electrical power requirements just a small percentage (about 6%) of the total. For the hydrogen fuelled ship, the range is limited by the electrical power requirements, due to the low specific volumes of the hydrogen storage.

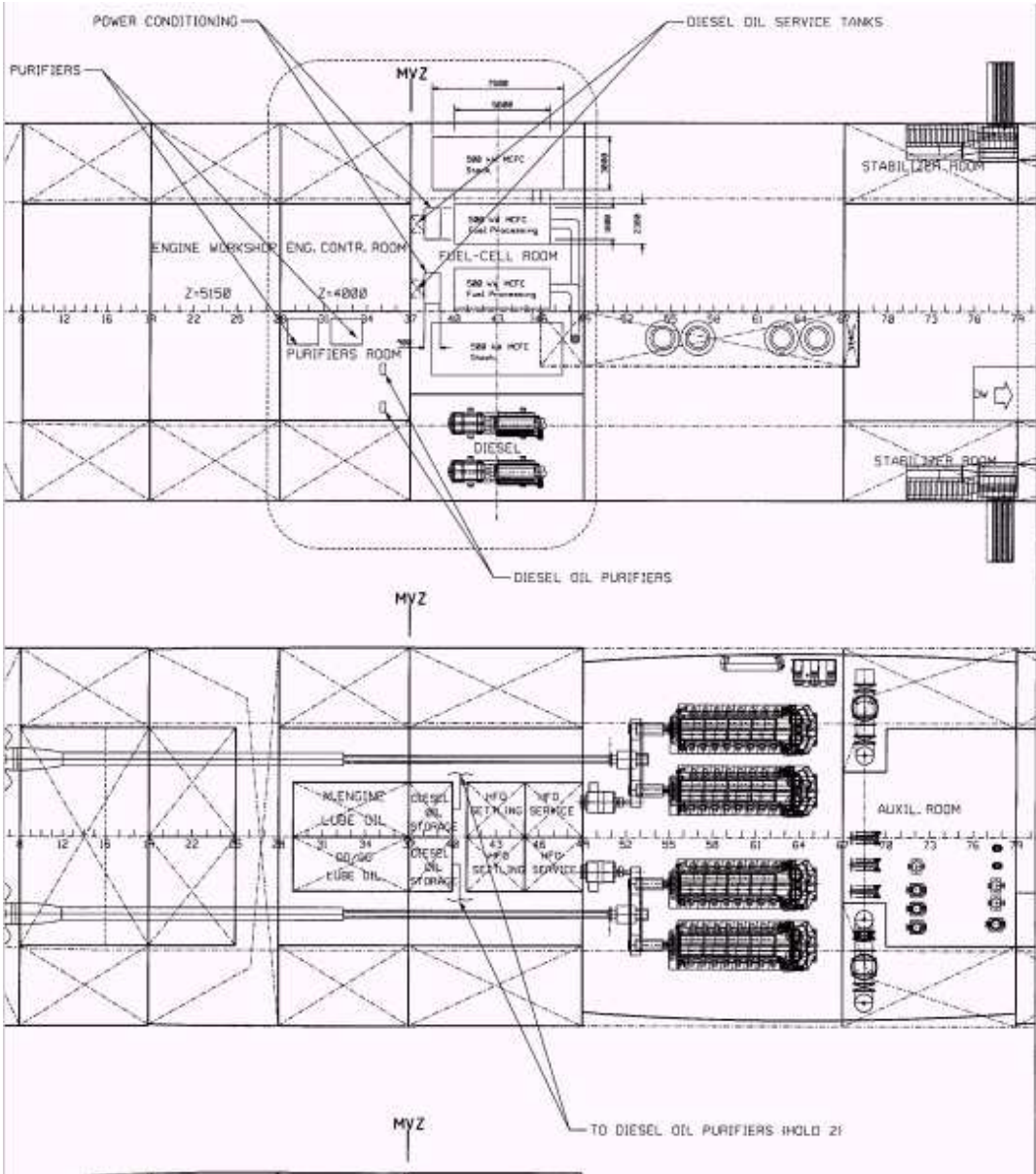


Fig.3: Engine room arrangement MCFC 1000 kW

3.1 1000 kW MCFC fuelled with Marine Diesel Oil

Figs.3-5 represent a possible solution where Generator System is composed by two Diesel Generators (2000 kW) and two MCFC Modules (500 kW each). All FC Modules have their own Diesel Oil Fuel Processing Module and Power Conditioning dedicated. MCFC characteristics are based on manufacturers data (10 years), Table I. The overall space required by the solution is greater than original configuration, Fig.3, with a higher volume requirement. However the required increase in space may be accomplished by a modest modification of the general arrangements of machinery spaces.

3.2 PEFC, hydrogen fuelled

The PEFC system presents significant differences from the other FC systems analysed previously. PEFC systems themselves, which already have a brand oriented to mobile applications, do not cause any problem in the ship arrangements. On the other hand, the main problems are expected to be: the high amount of required volume for the fuel storage, that can have a major impact on the ship layout, and the difficulties related to hydrogen storage and handling. In order to evaluate the volume needed for hydrogen storage, a preliminary calculation of the amount of H₂ consumption was performed. Two cases were considered: FC providing only 1000 kW or full electrical power; the ship range was halved to 3 days.

Table VIII: Hydrogen quantities needed for three days operation

Operational profile	Hydrogen needed [t] 1000 kW	Hydrogen needed [t] All electrical power
Long route	3.93	7.17
Short route (summer)	3.93	7.06
Short route (winter)	3.88	5.62

From the knowledge of hydrogen quantities needed to assure the operational range and from the values of the specific volumes of the storage system, an estimation of the dimensions of the storage systems has been performed and reported in the following.

Table IX: H₂ Storage, 1000 kW, 3 days operation

Storage form	Long route and short route summer		Short route winter	
	Storage volume [l]	Storage weight [kg]	Storage volume [l]	Storage weight [kg]
LH ₂	118000	44000	116000	43400
CH ₂ (700 bar)	141500	66000	140000	65000
CH ₂ (300 bar)	244000	51000	240500	50400

However, that the data reported in the present tables are subject to high uncertainties, due to the nature of data for hydrogen storage. Those data, in fact, are related to studies and future developments of advanced techniques with composite materials, for which in many cases no demonstrator exists. Moreover, all these studies, up to now, are related to very small tanks, and their direct application to the higher volumes required in this case is doubtful, with increased volumes which are likely to occur. Moreover, the LH₂ storage is related to a very high energy loss, with remarkable losses in the overall cycle. For compressed hydrogen, finally, lower but still significant energy losses could be expected. Furthermore some Classification Societies (e.g. DNV) would not allow gaseous storage below deck at pressures higher than 10 bar.

Figs.4 and 5 show the general arrangements of the solution with PEFC delivering 1000 kW electric power. Fig.4 shows the generators room layout, Fig.5 the fuel containment system layout. The 1000

kW PEFC solution can be easily accommodated in the ship, without any significant modification with respect to a conventional diesel generator layout. Instead the fuel containment requires an entire ship compartment with consequent reduction in cargo space.

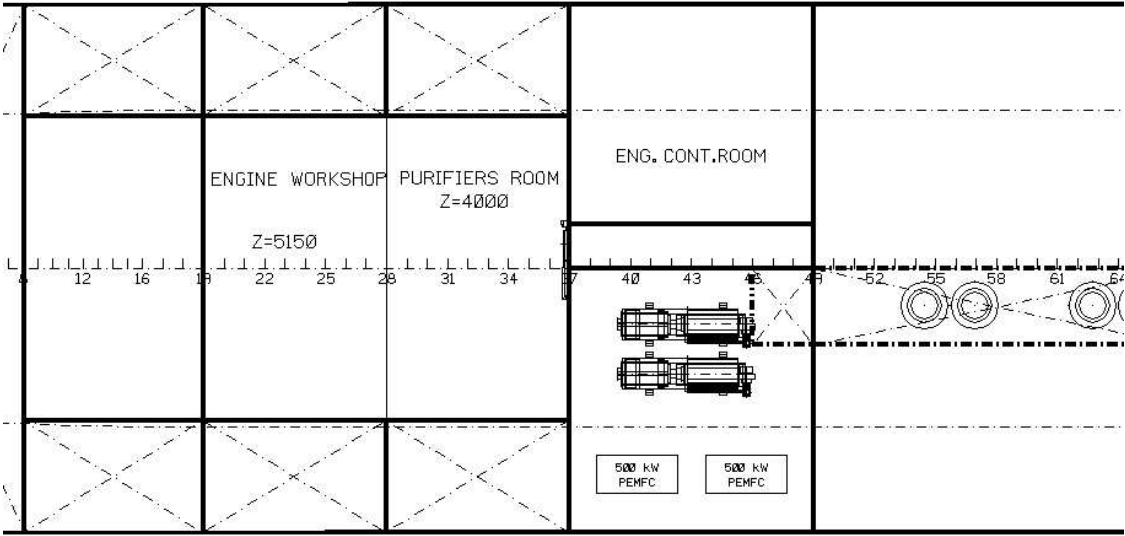


Fig.4: 1000 kW PEFC, generators room

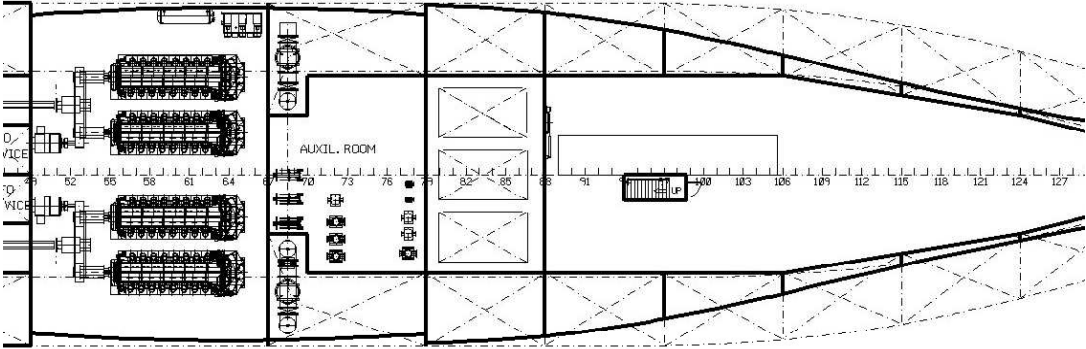


Fig.5: 1000 kW PEFC, storage arrangements, deck 1

3.3 Comparison of the analysed solutions

A comparison among all the analysed solutions has been performed in order to quantify and highlight possible benefits and drawbacks of each solution.

The following parameters have been considered for the comparison :

- cargo space (number of cars/length of cargo lanes in the lower hold)
- ship range
- electric generation system weight
- electric generation system efficiency

The considered parameters were selected due to their high importance for the design of the ship under consideration (Ro/Ro-Pax ferry). This choice does not exclude that other parameters may be of interest and further comparison may be assessed. The output of the comparison shows, for each parameter, the difference between the considered solution and the original ship. A positive value means that the value of the considered solution is higher than the correspondent value of the original ship. The results are reported in Table X:.

Table X: Results of analysed solutions

Solution	1 MCFC 1000 kW 10 years	2 MCFC 2500 kW 10 years	3 MCFC 2500 kW ?? years	4 MCFC 2800 kW ?? years	5 SOFC-GT 2500 kW/??	6 PEFC 1000 kW/5y.	7 PEFC 2500kW/5 y.
Cargo space	as ship 1 (365 cars)	- 40 m -10cars, -2.7%	as ship 1 (365 cars)	as ship 1 (365 cars)	+12 m (+3/4 cars +1%)	- 30 m (-8 cars, - 2.1%)	- 50 m (-14 cars, -3.8%)
Ship range	as ship 1 (3000 nm)	as case 1 (3000 nm)	as ship 1 (3000 nm)	as ship 1 (3000 nm)	as ship 1 (3000 nm)	1870 nm	1870 nm
El. Gen. Effic.	4 (+9%)	11(+28%)	31 (+79%)	31 (+79%)	31(+79%)	5 (+14%)	16 (+41%)
El. Gen. weight*	+58 t +89%	+134 t +206%	-33 t -50%	-29 t -44%	-38 t -58%	+55 t (+84%) (CH2 700) +33 t (+50%) (LH2)	+81 t (+124%) (CH2 700) +41 t (+63%) (LH2)

* The system weight considers both FC system weight and storage tanks weight

Cargo space has been evaluated on the base of preliminary general arrangements drawings. Regarding hydrogen storage, volumes correspond to LH₂ and CH₂ at 700 bar. Regarding solution 5, the increased cargo space is estimated basing on a possible new arrangement for the auxiliaries which could allow to save some space. All cargo space variations are very limited, this is a result of the ship choice, which was made in order to assure the required ship volumes for the FC plant without a significant change of the ship layout. However, for hydrogen fuel, in order to avoid too high cargo space reductions, ship range was reduced significantly.

The electric generation system efficiency was evaluated as a weighted average of the efficiencies of the electric generation gensets. Weight of electric generation systems was assessed on the base on the specific weight data reported in the previous tables. The weights are compared to a system with diesel Genset with a total power of 3x1080 kW, therefore some of the weight reduction are directly connected to the reduction in total power which was introduced in the FC systems. The percentage refers only to the variation of the electric generation system weight, it does not include any other machinery or ship weight. Since the electric generation system weight represent about 1 % of the ship weight, the influence on the ship displacement is limited in all cases to small percentages. Regarding hydrogen, that weights are significantly affected by a strong uncertainty.

4. Comments and Conclusions

The following final comments addresses only some preliminary ship design aspects (weight, space, global electric balance, buoyancy and stability, safety, Rule Requirements). Considerations concerning environmental aspect are not considered here, because matter of different tasks of the project.

All the proposed solutions offer an increase of electric generation efficiency. It represents a save in ship running costs (MDO fuel) and a reduction of mass flow emissions. The increased efficiency cannot practically influence the ship range (MDO fuel, hydrogen fuel lower the range), because the fuel consumption is greatly influenced by the propulsion.

Solution 1, that may represent the present 'entry level' of the FC technology onboard ships, seems to have no major impacts on general ship design. The ship maintains the original cargo capacity and range. The influence of the increased system weight on the ship displacement can be considered negligible at this stage.

Solution 2, the complete FC electric generation with the present state of the MCFC technology, presents some drawbacks. The cargo capacity is slightly reduced and the weight is increased in a significant way.

Solution 3 and 4, the complete FC electric generation with possible future MCFC technology, presents some improvements with respect to the traditional DG systems. The system weight is halved with some benefits on the whole ship.

Solution 5, the complete FC electric generation with the foreseen state of the SOFC technology, presents some significant improvements with respect to the traditional DG systems, with reduced volumes and slightly increased cargo capacity, with an efficiency increased by 80% and weight reduced more than 50%.

Solutions 6 and 7 consider the direct hydrogen storage and fuelling. They represent major challenges mainly due to the storage high volume requirements and safety problems. The main negative impacts are represented by the reduction of cargo capacity and the reduction of ship range, moreover a higher overall weight can be foreseen because of the high weight of the storage tanks.

The mid term targets of current RTD programs on FC systems for transportation have shown that it can be expected that the main gaps between current stationary and marine applications of fuel cells could be reduced by a significant reduction in volume and weight. Most recently, volume and weight of mobile high temperature fuel cell systems have reached 10 l/kW and 10 kg/kW, respectively (the target for aircraft applications is about 1 l/kW and 1 kg/kW). It is expected that with the state of the art technology system efficiency >65% is achievable for combined systems.

The improvement of efficiency, weight and cost reduction would be of great importance in reducing fuel cell operational costs and thus make FC systems more attractive to marine industry even if a wide range of open problems exists and further RTD efforts are required to 'load' a fuel cell onboard.

References

KUMM WILLIAM H. (1990), Marine and naval applications of Fuel Cells for propulsion: the process selection, *Journal of Power Sources*, 29 (1990), pp 169-179

ALLEN S.; ASHEY E.; GORE D.; WOERNER J.; CERVI M.. (1998), Marine Applications of Fuel Cells, *Naval Engineers Journal*, January 1998, pp 92-106

KARNI Z.; FONTNEAU P. (1999), Marine Molten Carbonate Fuel Cell demonstration module, US Coast Guard Research and Development Center, Report n. CG-D-12-99, May 1999

BOLIND A.M. (2000), An Evaluation of Fuel Cells for Commercial Ship Applications, SNAME Technical and Research Report n. 55, 2000

CORBETT J.J.; KEITH D.W.; FARRELL A. (2000), Towards true zero-emission vehicles in a single step: air pollution and greenhouse gas reduction through hydrogen fueled ships with carbon management, *IEEE Proceedings* 2000

MCMULLEN J.J. Associates Inc. (2003), Development of a Hybrid Fuel Cell Ferry, San Francisco Bay Area Water Transit Authority, August 2003

BASURTO M.T.; PILIDIS P.; HALES R. (2002), Molten Carbonate Fuel Cell Gas Turbine Combined Cycle for Marine Propulsion, ASME Turbo Expo 2002, Amsterdam

SKJOLSVIK K.O.; WURSIG, (2002) Results from screening process and summary of functional requirements, FCSHIP report

FIGARI M.; VIVIANI M.; LEVANDER O.; HUISMANS J.M.; FRACCHIA M., (2004), Description of conceptual ship design with fuel cell application, FCSHIP report DTR - 3.2 - FC - 02.2004

Advances in Simulation of Ditching of Airplanes

Olaf Lindenau, Hamburg Ship Model Basin (HSVA), lindenau@tu-harburg.de

Abstract

A simulation method to calculate the planned ditching of an aircraft is presented. The method is based on a modified Wagner method for the hydrodynamic force calculation with empirical corrections for ventilation and cavitation. Fuselage and wings of the aircraft are modelled as finite-element beams to account for the global elasticity of the aircraft. The time history of the aircraft motion and of the beams deformations are the main result. The core parts of the method are also applicable to planing and slamming of ships.

1 Introduction

In aviation planned ditching is a controlled emergency landing of an aircraft on water. Hence, during ditching the pilot keeps some control over the airplane and is able to perform a landing close to instructions given in the flight manual. Regulations require that the manufacturer of an aircraft has to prove the survivability of the ditching for the passengers and a safe post-ditching egress. The simulation of planned ditching can be subdivided into four major phases: approach, impact, landing and floatation, each of which gives its output as input to the next one. The approach phase gives the initial conditions for the impact scenario like pitch angle, aircraft speed and flap setting. The impact phase yields local deformations along the fuselage due to the hydrodynamic pressure. The landing phase covers the dynamic response due to the impact, as well as, possibly, the detachment of engines and flaps. Once the airplane comes to rest the floatation phase starts, which is governed by water ingress and ends with the sinking of the airplane.

The ditching simulation method presented here was first developed by Söding (1999) and is used for the impact and landing phases. The progressive flooding may be simulated with suitable extensions to a program for damage calculations of ships as presented by Shigunov et al. (2001). Söding (2002) used a simplified version of the ditching simulation program to calculate the motion of planing boats in waves.

2 Simulation method

The method is based on the following suppositions: the steering flaps are held in fixed position; the aircraft moves only in its vertical symmetry plane (3 degrees of freedom); there is no wind and the water surface is without waves.

The basic approach for the simulation is solving Newton's equation

$$\mathbf{M}\ddot{\delta} = \vec{f} \quad (1)$$

where \mathbf{M} is a mass matrix, $\ddot{\delta}$ a vector of accelerations and \vec{f} a vector of forces. For each time step of the simulation (1) is solved after forces and added (hydrodynamic) masses have been determined for one symmetry half of the aircraft. The accelerations are then integrated to obtain velocities and displacements.

The calculation of the hydrodynamic forces is based on an extension of v. Karman's (1929) and Wagner's (1932) "momentum method". Aerodynamic forces and the thrust of engines are also considered.

The flexible aircraft (AC) structure is modelled by two beam chains with a series of finite elements: one beam chain for the fuselage (FU) and one for the (right) wing (WR).

2.1 Coordinate systems and model of aircraft

The inertial frame of reference is the earth-fixed coordinate system (EF-CS) (ξ, η, ζ) with origin in the water surface in which the aircraft moves in 3 degrees of freedom: translation ξ and ζ and rotation ϑ . The body-fixed coordinate system (BF-CS) is (x, y, z) with the origin at the center of gravity of the aircraft G , the x -axis points towards the nose, the y -axis to starboard (right), and the z -axis downwards. y and η axes have the same direction; the other two axes differ by the pitch angle ϑ (positive: nose up). The finite elements have knots k at the ends. Each knot has a local coordinate system (x', y', z') with the same orientation as the body-fixed coordinate system (Fig. 1).

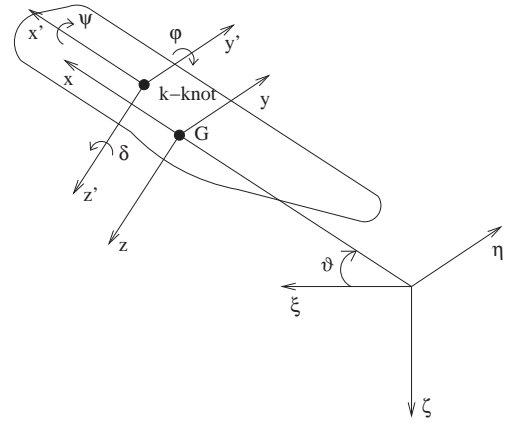


Figure 1: Main coordinate systems

The position of the aircraft as a function of time t is described by the coordinates of the center of gravity G : $\xi_G = \xi_G(t)$, $\zeta_G = \zeta_G(t)$, and by the pitch angle about the y -axis $\vartheta = \vartheta(t)$. The horizontal and vertical speed of the center of gravity are $\dot{\xi}_G = u$ and $\dot{\zeta}_G = w$. The angular velocity of the aircraft is $\dot{\vartheta}$. The corresponding accelerations are $\ddot{\xi}_G = \dot{u}$, $\ddot{\zeta}_G = \dot{w}$ and $\ddot{\vartheta}$.

For the force calculation the aircraft is composed of a number of components=“half-bodies” (two for the fuselage, wings and horizontal tails, several for the engines or flaps). The components are described by offsets arranged in a regular grid with spacing Δx and Δy .

Along the fuselage a number of knots nkn marking the ends of a number of finite elements $ne = nkn - 1$ are distributed. The knots of the finite elements have two degrees of freedom: displacement dz_k in z -direction and rotation $d\varphi_k$ about the y' -axis. $\vec{\delta}_{k0} = (z_{k0}, \varphi_{k0})^T$ is the undeformed position of the knot k of the FU.

Also along the wing a number of knots $nkwr$ marking the ends of a number of finite elements $ne = nkwr - 1$ are distributed. Here the knots have three degrees of freedom: displacement dz_{kWR} in z -direction, rotation $d\psi_{kWR}$ about the x' -axis and rotation $d\varphi_k$ about the y' -axis. $\vec{\delta}_{kWR0} = (z_{kWR0}, \psi_{kWR0}, \varphi_{kWR0})^T$ is the undeformed position of the knot k of the WR.

2.2 Equations of motion

The following equations of motion for the aircraft as beam model are derived by considering the aircraft as built up of numerous mass particles. These mass particles move in the non-inertial frame of reference of the aircraft (BF-CS), which itself moves in the inertial frame of reference (EF-CS) following the approach by Shigunov (2000). Integration over the mass particles belonging to one knot of the beam model give the equations of motion of the knot and the mass properties of the knot. Summation over all knots of the beam model yields the equations of motion of the aircraft in x, z, ϑ :

$$\ddot{\xi}_G m^{AC} \cos \vartheta - \ddot{\zeta}_G m^{AC} \sin \vartheta + \sum_{\text{f. e.}}^{\text{FU}} \ddot{\varphi}_k S'_{xy_k} + \sum_{\text{f. e.}}^{\text{WR}} \ddot{\varphi}_k S'_{xy_k} =$$

$$\begin{aligned}
&= F_x - 2\dot{\vartheta} \sum_{f. e.}^{FU} \dot{z}_k m_k + 2\dot{\vartheta} \sum_{f. e.}^{FU} \dot{\varphi}_k S'_{yz_k} + \sum_{f. e.}^{FU} \dot{\varphi}_k^2 S'_{yz_k} \\
&\quad - 2\dot{\vartheta} \sum_{f. e.}^{WR} \dot{z}_k m_k - 2\dot{\vartheta} \sum_{f. e.}^{WR} \dot{\psi}_k S'_{xz_k} + 2\dot{\vartheta} \sum_{f. e.}^{WR} \dot{\varphi}_k S'_{yz_k} - \sum_{f. e.}^{WR} \dot{\psi}_k \dot{\varphi}_k S'_{xz_k} + \sum_{f. e.}^{WR} \dot{\varphi}_k^2 S'_{yz_k} \quad (2)
\end{aligned}$$

$$\begin{aligned}
&\ddot{\xi}_G m^{AC} \sin \vartheta + \ddot{\zeta}_G m^{AC} \cos \vartheta + \sum_{f. e.}^{FU} \ddot{z}_k m_k - \sum_{f. e.}^{FU} \ddot{\varphi}_k S'_{yz_k} + \sum_{f. e.}^{WR} \ddot{z}_k m_k + \sum_{f. e.}^{WR} \ddot{\psi}_k S'_{xz_k} - \sum_{f. e.}^{WR} \ddot{\varphi}_k S'_{yz_k} = \\
&F_z + 2\dot{\vartheta} \sum_{f. e.}^{FU} \dot{\varphi}_k S'_{xy_k} + \sum_{f. e.}^{FU} \dot{\varphi}_k^2 S'_{xy_k} + 2\dot{\vartheta} \sum_{f. e.}^{WR} \dot{\varphi}_k S'_{xy_k} + \sum_{f. e.}^{WR} \dot{\psi}_k^2 S'_{xy_k} + \sum_{f. e.}^{WR} \dot{\varphi}_k^2 S'_{xy_k} \quad (3)
\end{aligned}$$

$$\begin{aligned}
&\ddot{\vartheta} J_y^{AC} - \sum_{f. e.}^{FU} \ddot{z}_k (x_k m_k + S'_{yz_k}) + \sum_{f. e.}^{FU} \ddot{\varphi}_k (x_k S'_{yz_k} + z_k S'_{xy_k} + J'_{y_k}) \\
&\quad - \sum_{f. e.}^{WR} \ddot{z}_k (x_k m_k + S'_{yz_k}) - \sum_{f. e.}^{WR} \ddot{\psi}_k (x_k S'_{xz_k} + R'_{xy_k}) + \sum_{f. e.}^{WR} \ddot{\varphi}_k (x_k S'_{yz_k} + z_k S'_{xy_k} + J'_{y_k}) = \\
&M_y - \sum_{f. e.}^{FU} \dot{\varphi}_k^2 (x_k S'_{xy_k} - z_k S'_{yz_k}) - 2\dot{\vartheta} \sum_{f. e.}^{FU} \dot{z}_k (z_k m_k + S'_{xy_k}) - 2\dot{\vartheta} \sum_{f. e.}^{FU} \dot{\varphi}_k (x_k S'_{xy_k} - z_k S'_{yz_k}) \\
&\quad - \sum_{f. e.}^{WR} \dot{\psi}_k^2 (x_k S'_{xy_k} + R'_{xz_k}) - \sum_{f. e.}^{WR} \dot{\varphi}_k^2 (x_k S'_{xy_k} - z_k S'_{yz_k}) - \sum_{f. e.}^{WR} \dot{\psi}_k \dot{\varphi}_k (z_k S'_{xz_k} + R'_{yz_k}) \\
&\quad - 2\dot{\vartheta} \sum_{f. e.}^{WR} \dot{z}_k (z_k m_k + S'_{xy_k}) - 2\dot{\vartheta} \sum_{f. e.}^{WR} \dot{\psi}_k (z_k S'_{xz_k} + R'_{yz_k}) - 2\dot{\vartheta} \sum_{f. e.}^{WR} \dot{\varphi}_k (x_k S'_{xy_k} - z_k S'_{yz_k}) \quad (4)
\end{aligned}$$

The equations of motion in z, φ for the knot k of the fuselage are:

$$\begin{aligned}
&\ddot{\xi}_G m_k \sin \vartheta + \ddot{\zeta}_G m_k \cos \vartheta - \ddot{\vartheta} (x_k m_k + S'_{yz_k}) + \ddot{z}_k m_k - \ddot{\varphi}_k S'_{yz_k} = \\
&F_{z_k} + \dot{\vartheta}^2 (z_k m_k + S'_{xy_k}) + 2\dot{\vartheta} \dot{\varphi}_k S'_{xy_k} + \dot{\varphi}_k^2 S'_{xy_k} \quad (5)
\end{aligned}$$

$$\begin{aligned}
&\ddot{\xi}_G (S'_{xy_k} \cos \vartheta - S'_{yz_k} \sin \vartheta) - \ddot{\zeta}_G (S'_{xy_k} \sin \vartheta + S'_{yz_k} \cos \vartheta) + \ddot{\vartheta} (J'_{y_k} + x_k S'_{yz_k} + z_k S'_{xy_k}) \\
&\quad - \ddot{z}_k S'_{yz_k} + \ddot{\varphi}_k J'_{y_k} = \\
&M'_{y_k} - 2\dot{\vartheta} \dot{z}_k S'_{xy_k} + \dot{\vartheta}^2 (x_k S'_{xy_k} - z_k S'_{yz_k}) \quad (6)
\end{aligned}$$

The equations of motion in z, ψ and φ for the knot k of the wing are:

$$\begin{aligned}
&\ddot{\xi}_G m_k \sin \vartheta + \ddot{\zeta}_G m_k \cos \vartheta - \ddot{\vartheta} (x_k m_k + S'_{yz_k}) + \ddot{z}_k m_k + \ddot{\psi}_k S'_{xz_k} - \ddot{\varphi}_k S'_{yz_k} = \\
&F_{z_k} + \dot{\vartheta}^2 (z_k m_k + S'_{xy_k}) + 2\dot{\vartheta} \dot{\varphi}_k S'_{xy_k} + \dot{\psi}_k^2 S'_{xy_k} + \dot{\varphi}_k^2 S'_{xy_k} \quad (7)
\end{aligned}$$

$$\begin{aligned}
&\ddot{\xi}_G S'_{xz_k} \sin \vartheta + \ddot{\zeta}_G S'_{xz_k} \cos \vartheta - \ddot{\vartheta} (x_k S'_{xz_k} + R'_{xy_k}) \\
&\quad + \ddot{z}_k S'_{xz_k} + \ddot{\psi}_k J'_{x_k} - \ddot{\varphi}_k R'_{xy_k} = \\
&M'_{x_k} + \dot{\varphi}_k^2 R'_{yz_k} + \dot{\psi}_k \dot{\varphi}_k R'_{xz_k} + 2\dot{\vartheta} \dot{\varphi}_k R'_{yz_k} + \dot{\vartheta}^2 (z_k S'_{xz_k} + R'_{yz_k}) \quad (8)
\end{aligned}$$

$$\begin{aligned}
& \ddot{\xi}(S'_{xy_k} \cos \vartheta - S'_{yz_k} \sin \vartheta) - \ddot{\zeta}(S'_{xy_k} \sin \vartheta + S'_{yz_k} \cos \vartheta) + \ddot{\vartheta}(J'_{y_k} + x_k S'_{yz_k} + z_k S'_{xy_k}) \\
& - \ddot{z}_k S'_{yz_k} - \ddot{\psi}_k R'_{xy_k} + \ddot{\varphi}_k J'_{y_k} = \\
& M'_{y_k} - \dot{\psi}_k^2 R'_{xz_k} - \dot{\psi}_k \dot{\varphi}_k R'_{yz_k} - 2\dot{\vartheta}(\dot{z}_k S'_{xy_k} + \dot{\psi}_k R'_{yz_k}) + \dot{\vartheta}^2(x_k S'_{xy_k} - z_k S'_{yz_k}) \quad (9)
\end{aligned}$$

The symbols in the above equations designate:

m^{AC}	mass of aircraft
J_y^{AC}	mass moment of inertia of aircraft about y -axis
F_x, F_z	external force on aircraft in x - and z -direction
M_y	external moment on aircraft about y -axis
m_k	mass of knot k
J'_{x_k}, J'_{y_k}	mass moments of inertia of knot k about x' - and y' -axis
$S'_{xy_k}, S'_{yz_k}, S'_{xz_k}$	mass moments referring to plane $x'y'$, $y'z'$ and $x'z'$ of knot k
$R'_{xy_k}, R'_{yz_k}, R'_{xz_k}$	mixed mass moments of inertia of knot k
F_{z_k}	external and elastomechanical force on knot k ; z component
M'_{x_k}, M'_{y_k}	external and elastomechanical moments about x' - and y' -axis on knot k
$\sum_{f. e.}, \sum_{WR}$	summation over knots of the fuselage and of the wing, respectively.

For the rigid aircraft these equations of motion reduce to the 3 ordinary equations of motion for a body moving with 3 degrees of freedom in an inertia frame of reference.

The above stated equations of motion are combined to the matrix equation system (1). The forces and displacements of the knots are given in the body-fixed coordinate system whereas the motion of the aircraft is calculated in the earth-fixed coordinate system. Hence, the vector of accelerations is:

$$\begin{aligned}
\vec{\delta} = & \left[\underbrace{\ddot{\xi}_G}_1, \underbrace{\ddot{\zeta}_G}_2, \underbrace{\ddot{\vartheta}}_3, \underbrace{\ddot{z}_1}_4, \underbrace{\ddot{\varphi}_1}_5, \dots, \underbrace{\ddot{z}_k}_{3+2k-1}, \underbrace{\ddot{\varphi}_k}_{3+2k}, \dots, \underbrace{\ddot{z}_{nkn}}_{3+2nkn-1}, \underbrace{\ddot{\varphi}_{nkn}}_{3+2nkn}, \right. \\
& \underbrace{\ddot{z}_1}_{3+2nkn+1}, \underbrace{\ddot{\psi}_1}_{3+2nkn+2}, \underbrace{\ddot{\varphi}_1}_{3+2nkn+3}, \dots, \underbrace{\ddot{z}_k}_{3+2nkn+3k-2}, \underbrace{\ddot{\psi}_k}_{3+2nkn+3k-1}, \underbrace{\ddot{\varphi}_k}_{3+2nkn+3k}, \dots, \\
& \left. \underbrace{\ddot{z}_{nknr}}_{3+2nkn+3nknr-2}, \underbrace{\ddot{\psi}_{nknr}}_{3+2nkn+3nknr-1}, \underbrace{\ddot{\varphi}_{nknr}}_{3+2nkn+3nknr} \right]^T \quad (10)
\end{aligned}$$

The factors appearing in (2) to (9) together with the accelerations contribute the elements of the mass matrix \mathbf{M} .

Apart from the first term of the right hand side of the equations (2) to (9) all other terms are put into a vector of mass inertia force \vec{f}_M . The total right hand sides may be expressed as:

$$\vec{f} = \vec{f}_G + \vec{f}_M - \vec{f}_E + \vec{f}_F - \vec{f}_D \quad (11)$$

Here \vec{f}_G is the vector of gravity forces and moments acting on the aircraft and on the knots of the beam model.

\vec{f}_E is the vector of explicit part of the elastic forces and moments acting on the knots of the beams (taking values of the displacement, the velocity and acceleration of the displacement of the knots from the previous time step). The implicit part of the elastic forces $\vec{\mathbf{K}}$ is added to the mass matrix (also see section 2.5):

$$\mathbf{K}\Delta\vec{\delta}^{jt+1} = \vec{f}_E + \tilde{\mathbf{K}}\ddot{\delta}^{jt+1} \quad (12)$$

The stiffness matrix \mathbf{K} is built up by taking the usual stiffness matrices for Timoshenko beams and by adding elements to account for torsion of the wing.

\vec{f}_F comprises for the aircraft itself the total forces and moments due to aerodynamics, thrust and hydrodynamics. The components of \vec{f}_F relating to a single knot cover the parts of these forces acting on the respective knot. \vec{f}_D (only relevant for the equations of motion of the knots) takes account of structural damping. The empirical formula used here contains the velocity of deformation, the stiffness coefficient of this degree of freedom, and a chosen factor.

2.3 Aerodynamic forces

For the aerodynamic forces acting on the wings and horizontal tails of the aircraft basically the simple approach by Söding (1999), presented by Shigunov et al. (2000), is used. It is assumed that, for the given initial conditions before water contact, the aircraft experiences no accelerations, i.e. that it is in equilibrium under the influence of weight, engine thrust and aerodynamic forces and moment. Thus the aerodynamic force and moment are known for $t = 0$. For later time it is assumed that the lift is proportional to the overall speed squared and that the lift of wings and horizontal tails change proportional the angle of attack. The induced drag is calculated from the lift. For elastic wings the aerodynamic pressure distribution over the wings has to be known. Instead of calculating a detailed pressure distribution, the initial lift force is assumed to be distributed elliptically in span-wise direction and parabolic over wing chord with maximum at the leading edge. The change of local angle of attack due to the motion of the aircraft and the displacement of the knots of the wing are considered.

2.4 Hydrodynamic forces

As presented by Söding (1999) the momentum equation introduced to the problem of hydrodynamic loads during contact of a body with a free surface by v. Karman (1929) and Wagner (1932) will be applied here:

$$f = -k \frac{d}{dt} \left(\rho_W \frac{\pi}{4} c^2 V \right) \quad (13)$$

f is the vertical dynamic force per length on one half of the symmetrical body, excluding hydrostatic buoyancy. The factor $\rho_W \pi / 4 \cdot c^2$ approximates the added mass per length. ρ_W is the water density, c the body halfbreadth at the water line. f and the immersion velocity V are positive in $+z$ -direction, i.e. downward. d/dt designates the time derivative and k a correction factor.

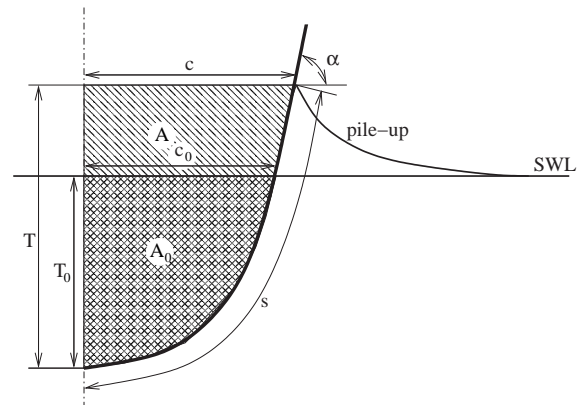


Figure 2: Most important force calculation parameters

As the forces on slender bodies with forward speed u shall be calculated the time derivative in

(13) is replaced by the substantial derivative:

$$\frac{D}{Dt} = \frac{\partial}{\partial t} - u \frac{\partial}{\partial x} \quad (14)$$

Thus (13) becomes:

$$f = -k\rho_W \frac{\pi}{4} \left(c^2 \frac{DV}{Dt} + V \frac{Dc^2}{Dt} \right) \quad (15)$$

The parameters c and A should not be taken at the undisturbed water level on submergence T_0 . According to Wagner (1932) and adapted by Söding (1999) to measurements for sections of various shapes, these parameters are dependent on the increased water surface level T . Söding gives an estimation for the pile-up $T - T_0$ of the water besides the body.

Söding applies corrections to (15) taking into account flow separation for upward motion of the body, hydrostatic forces, sections with knuckles and blunt bodies. Averaged pressure limits are introduced for stagnation pressure in stationary flow as well as for limits due to cavitation and ventilation.

More details on these corrections and evaluation of this approach can be found in Söding (1999), Shigunov (2000) and Shigunov et al. (2001).

According to the theory by Wagner (1932) used by Shigunov (2000), the pressure distribution along one section can be calculated as:

$$p(y^*) = k\rho_W \frac{DV}{Dt} \sqrt{c^2 - y^{*2}} + k\rho_W \text{Max}(V, 0) c \frac{Dc}{Dt} \frac{1}{\sqrt{c^2 - y^{*2}}} + \rho_W g \zeta_p \quad (16)$$

$y^* = y - y_0$ is the distance of a point on the section contour from the cut through the deepest points of the component and ζ_p is the submergence at that location. This approach already takes the modifications for upward motion of the body, for the hydrostatic pressure and a correction factor k into account. Further modifications account for emerging sections with knuckles as well as pressure limits due to ventilation and cavitation and to stagnation pressure for stationary flow.

2.5 Added mass and time integration

As the hydrodynamic forces on the right hand side of (1) also depend on the accelerations, this contribution is considered in form of an added mass matrix on the left hand side. Other than in the first versions of the ditching code using “test accelerations” to determine the elements of the added mass matrix presented by Shigunov et al. (2001), now the method proposed by Söding (2001) is implemented. This method updates the added mass matrix of the previous time step using the hydrodynamic forces of several preceding time steps and iteration steps within an implicate time integration method. This method reduces the computational effort for the calculations of the flexible aircraft considerably.

The following equation system is solved in each implicate step:

$$(\mathbf{M} + \mathbf{A}) \ddot{\delta} = \vec{f}, \quad (17)$$

giving the accelerations $\ddot{\delta}^{jt+1}$ at time step $it + 1$.

For the time integration the following implicate formulae are applied:

$$\ddot{\delta}^{jt+1} = \ddot{\delta}^{jt} + \left[(1 - \gamma) \ddot{\delta}^{jt} + \gamma \ddot{\delta}^{jt+1} \right] \Delta t \quad (18)$$

$$\vec{\delta}^{it+1} = \vec{\delta}^{it} + \left[(1 - \gamma) \dot{\vec{\delta}}^{jt} + \gamma \dot{\vec{\delta}}^{jt+1} \right] \Delta t + \left[(1 - \gamma) \ddot{\vec{\delta}}^{jt} + \gamma \ddot{\vec{\delta}}^{jt+1} \right] \frac{\Delta t^2}{2} \quad (19)$$

$\gamma = 1$ gives the implicate Euler method of first order, $\gamma = 1/2$ leads to the Crank-Nikolson scheme of second order, which is generally used, and $\gamma = 0$ gives the explicite Euler method of first order.

Inserting (18) into (19) yields:

$$\vec{\delta}^{it+1} = \vec{\delta}^{it} + \dot{\vec{\delta}}^{jt} \Delta t + \left(\gamma + \frac{1}{2} \right) \ddot{\vec{\delta}}^{jt} \Delta t^2 + \left(\gamma^2 + \frac{\gamma}{2} \right) \ddot{\vec{\delta}}^{jt+1} \Delta t^2 \quad (20)$$

(20) is used in (12) for splitting up the elastic forces into an implicate and an explicite part. The equation system for the motion of the aircraft and the knots of the beam model which is now solved can be written as:

$$(\mathbf{M} + \mathbf{A} + \tilde{\mathbf{K}}) \ddot{\vec{\delta}} = \vec{f} \quad (21)$$

2.6 Other features

The landing gears and niches for landing gear etc. are accounted for by their estimated drag force (force acting in negative x -direction). Their drag force are calculated with a user defined drag coefficient and an area of the parts given as input.

From reports of ditching incidents it is known that some parts of the aircraft, e.g. flaps and engines, are torn off during ditching. Thus for such body components a maximum force is given as input. If the actual force exceeds this maximum force, the component is excluded from the further simulation.

3 Results

Results are presented here for the VFW 614 designed and built by the Vereinigte Flugtechnische Werke, Germany. The VFW 614 is a short-range airplane for about 40 passengers. Unusual is the low-wing configuration with engines mounted on top of the wings. Some of the airplane main technical data are listed together with the initial conditions in Table 1. For the simulation the half-bodies fuselage, wing and horizontal tail are considered, and their underside is discretised, Fig 3.

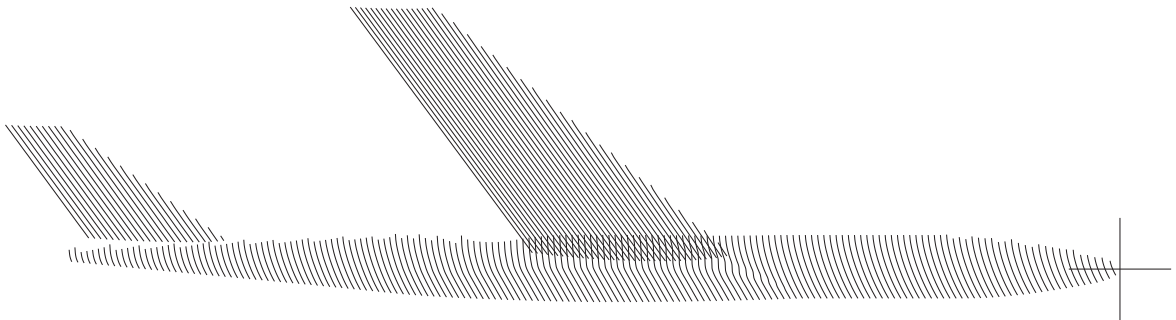


Figure 3: Discretisation of underside of a VFW 614; for wing and horizontal tail only every second section is plotted

Table 1: Main technical data of airplane and initial conditions for simulation

overall length	20.6m	initial pitch angle	10°
wing span	21.5m	initial horizontal velocity	50m/s
fuselage diameter	2.87m	initial vertical velocity	1m/s
mass	18.7t	density of water	1000kg/m^3
moment of inertia	255.5tm^2	density of air	1.28kg/m^3
thrust	0	kinematic viscosity of water	$1.4 \cdot 10^{-6}\text{m}^2/\text{s}$
		cavitation pressure	$p_{atm} - 100\text{kPa}$
		ventilation pressure	$p_{atm} - 0\text{kPa}$

For this aircraft ditching model tests with scale 1/8.5 were carried out and used by Bensch et al. (2001) and (2003) for validation of the method.

Here full scale simulations are made for the rigid aircraft as well as for the aircraft with the fuselage and/or the wing modelled as beams. Fig. 4 shows the time function of the height ζ_G of the center of gravity of the aircraft above the sealevel, the pitch angle ϑ , the horizontal velocity u , the vertical velocity w and the forces in z -direction on wing, fuselage and horizontal tail. The displacements of the knots near to the nose and the tail of the aircraft for the elastic fuselage are given in Fig. 5 and for the knot near to the tip of the wing in Fig. 6.

Only slight differences are visible between the rigid and the elastic fuselage, while the wing elasticity has moderate influence on forces and motions. During most time of the simulation the knots at the ends of the fuselage are displaced downwards. The knot at the tip of the wing is displaced upward at the beginning; this displacement is reduced later on.

4 Conclusion

A numerical method to simulate the planned ditching of aircrafts is presented. Especially the treatment of the elasticity of the aircraft structure by modelling the fuselage and the wings as beam models is described. Results for the motion and forces of the aircraft VFW 614 during ditching are presented together with some deformations.

Validation of the elastic simulations is still in progress, and the stability of the method has to be improved.

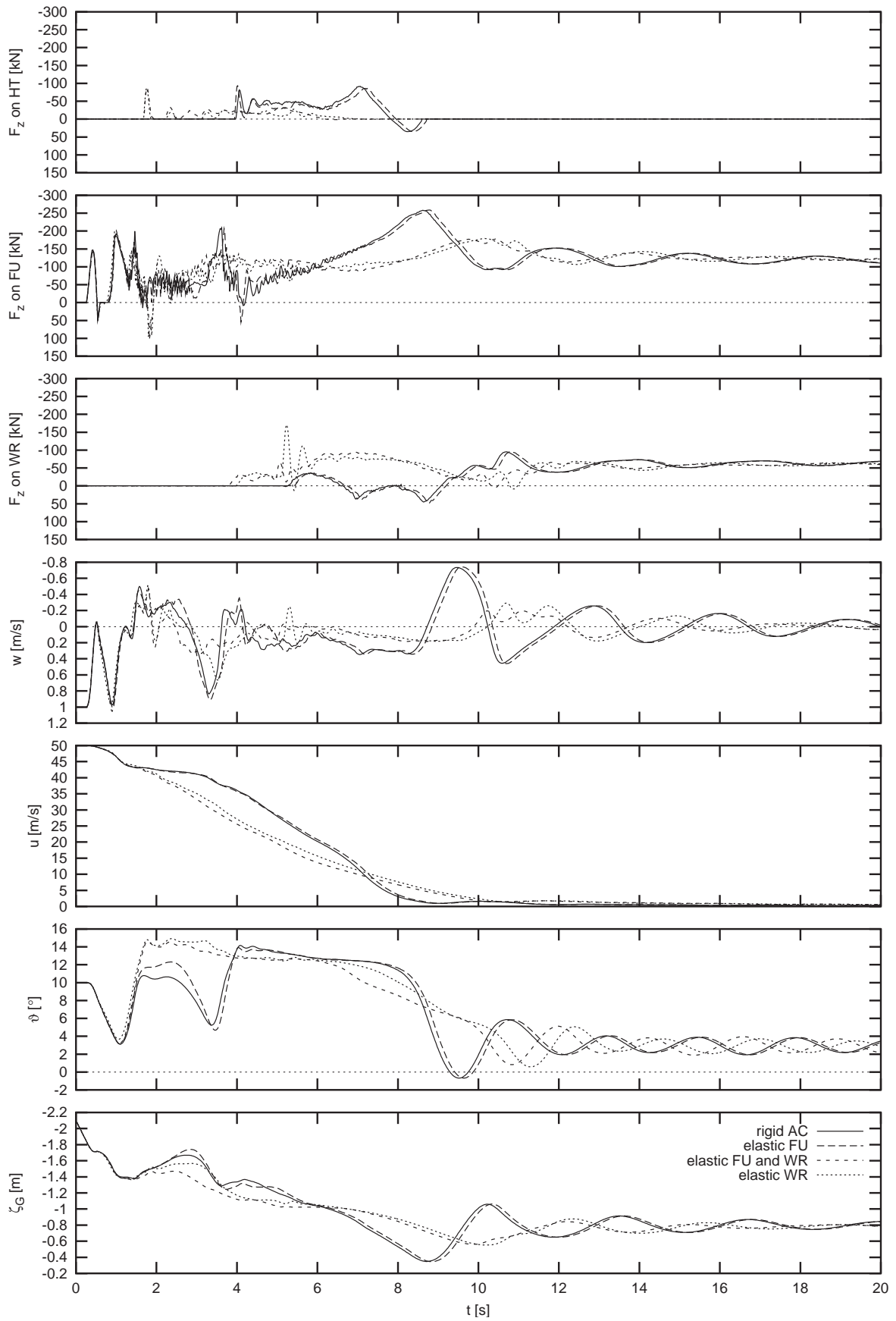


Figure 4: Results of ditching simulation of a VFW 614 for 4 cases: fuselage (FU) and wing (WR) both rigid, or both elastic, or one of them elastic

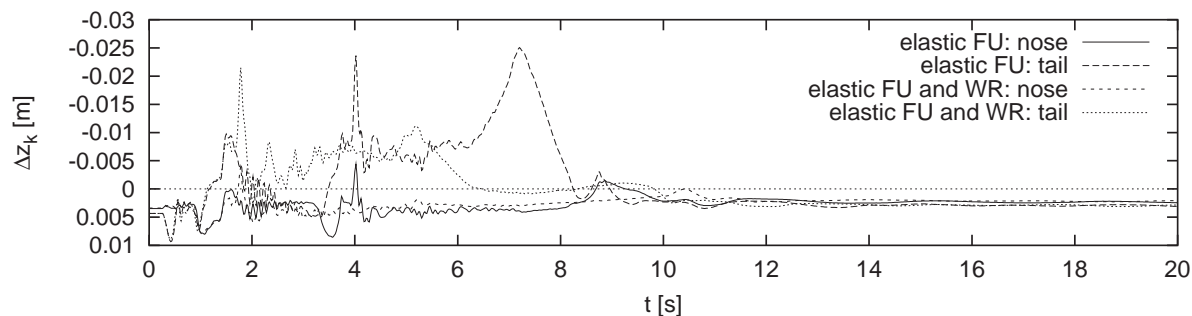


Figure 5: Displacement of knot near to the nose and near the tail of the aircraft over time for elastic fuselage and rigid wing (FU) and for elastic fuselage and elastic wing (FU WR)

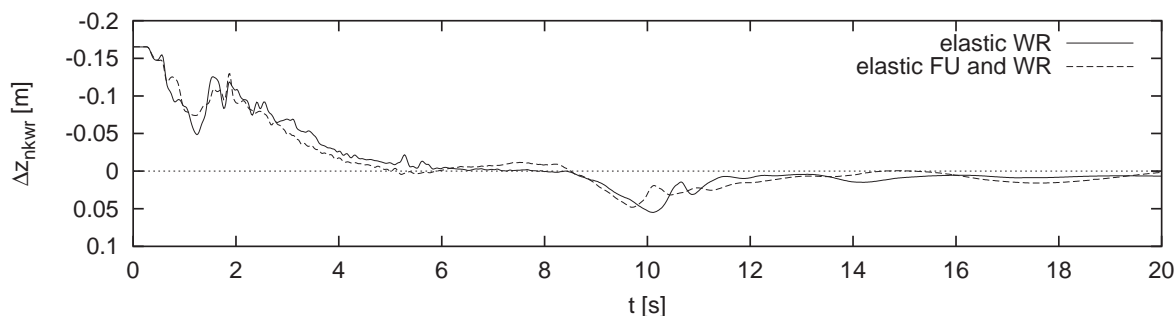


Figure 6: Displacement of knot near to the wing tip over time for rigid fuselage and elastic wing (WR) and for elastic fuselage and elastic wing (FU WR)

5 References

- BENSCH, L.; SHIGUNOV, V.; BEUCK, G.; SÖDING, H. (2001), *Planned Ditching Simulation of a Transport Airplane*, KRASH Users' Seminar, Phoenix/Arizona, pp. 1-11
- BENSCH, L.; SHIGUNOV, V.; SÖDING, H. (2003), *Computational method to simulate planned ditching of a transport airplane*, 2nd MIT Conference on Computational Fluid and Solid Mechanics, Boston, pp. 1251-1254
- V. KARMAN, T. (1929), *The impact on seaplane floats during landing*, NACA-TN 321, Washington, 8 p.
- SHIGUNOV, V. (2000), *Berechnung der Flugzeugbewegung beim Notwassern*, Report Nr. 608, Dept. of Fluid Dynamics and Ship Theory of the Technical University Hamburg-Harburg
- SHIGUNOV, V.; SÖDING, H.; ZHOU, Y. (2001), *Numerical Simulation of Emergency Landing of Aircraft on a Plane Water Surface*, HIPER'01, Hamburg, pp. 419-430
- SÖDING, H. (1999), *Berechnung der Flugzeugbewegung beim Notwassern*, Report Nr. 602, Dept. of Fluid Dynamics and Ship Theory of the Technical University Hamburg-Harburg
- SÖDING, H. (2001), *How to Integrate Free Motions of Solids in Fluids*, 4th Numerical Towing Tank Symposium, Hamburg, 4 p.
- SÖDING, H. (2002), *Planing boats in waves*, 5th Numerical Towing Tank Symposium, Pornichet/France, 4 p.
- WAGNER, H. (1932), *Über Stoß und Gleitvorgänge an der Oberfläche von Flüssigkeiten*, Zeitschrift für Angewandte Mathematik und Mechanik 12/4, Berlin, pp. 193-215

An Investigation into the Whipping of Large High-Speed Catamarans

Giles Thomas, Australian Maritime College, Tasmania, Australia, gthomas@amc.edu.au

Michael Davis, University of Tasmania, Tasmania, Australia, m.r.davis@utas.edu.au

Damien Holloway, University of Tasmania, Tasmania, Australia, damien.holloway@utas.edu.au

Tim Roberts, Revolution Design, Tasmania, Australia, troberts@revolutiondesign.com.au

Abstract

An investigation into the whipping behaviour of large high-speed aluminium catamarans, and its influence on fatigue life, is reported on. A combination of full-scale measurements of slam events and exciter tests were conducted on two large high-speed catamarans to investigate the modes, frequencies and damping of their whipping response. Modal analysis was also conducted utilising finite element analysis and including the fluid-structure interaction. Good correlation between the predicted and measured frequencies and mode shapes was found. The whipping behaviour was found to have a strong influence on the theoretical fatigue life of high-speed catamarans.

1. Introduction

In order to satisfy the high-speed sea transportation requirements of both commercial and military applications large, fast, lightweight vessels have been developed in the last 10 years. If optimisation of the structural design of such vessels is to take place, knowledge is required of the effect of sea loads on their structures (Morris 1991, Humphrey & Nybø 2002) with regard to both ultimate strength and fatigue life. Severe wet deck slam events, which occur when the vessel's motion causes an impact between the cross deck structure and the water surface, are of particular importance for high-speed catamarans. Whipping is the vibration of the hull girder induced by a slam event, and may be felt on board as a shudder after a slam impact. The corresponding vibratory stresses may be of equal order of magnitude to those induced by quasi-static wave bending moments, though they have a higher fundamental frequency.



Fig.1: Incat Hulls 042 and 050

The structural damage that may occur due to the whipping behaviour of large monohulls when operating in rough weather was first investigated in the 1970s (Ochi & Motter 1973, Kawakami et al. 1977). It has also been studied through full-scale measurements (Aertsen 1979, Clarke 1987) and towing tank tests (Fukasawa et al. 1981, McTaggart et al. 1997), with semi-empirical methods being developed for estimating the influence of whipping on bending moments and fatigue (Evans 1982, Clarke 1982). Friis-Hansen et al. (1995) developed a long-term probabilistic method to investigate the whipping of large fast monohulls, and whipping was found to have a significant effect on the predicted fatigue life of a small fast aluminium patrol boat (Kannari et al. 1998) by using the Rainflow method to determine equivalent stress variation. Although large high-speed vessels, due to the flexible nature of their hull girders, are especially susceptible to whipping vibrations following slam events, little work has been conducted on the whipping of large fast catamarans.

The natural modes of ships may be determined by finite element analysis (Louarn & Ternal 1999, Price & Temarel 1994). However there are few comparisons of the results, from using such techniques, with full-scale measurements available (Oei 1976). There is also a paucity of data available on the damping of hull girders when subjected to vibratory behaviour. Since the survey of available full-scale results by Betts et al. (1977) there has been little progress in increasing knowledge in this area.

This paper reports on a study into the whipping behaviour of large, high-speed catamarans. Extensive full-scale measurements of slam events were conducted on two large high-speed Incat catamarans (86m and 96m in length) during delivery voyages and regular service operations. These measurements were utilised to investigate the frequency and damping of the whipping behaviour of the vessels. Exciter tests were also conducted on the vessels, whilst stationary in calm water, in order to further examine the whipping modes, frequencies and damping. A theoretical investigation of the whipping behaviour of the vessels utilising finite element modal analysis including the fluid-structure interaction is also reported. The calculated whipping modes are then compared with those found through the full-scale measurements and exciter experiments, and the results discussed. Finally fatigue estimates are made of the effect of whipping on a large high-speed vessel's fatigue life.

2. Full-Scale Trials

To investigate the frequency and damping of the whipping behaviour extensive full-scale measurements of slam events were conducted, during delivery voyages and regular service operations, on two large high-speed Incat catamarans, Hulls 042 and 050.

2.1. Vessel Details

Incat Hulls 042 and 050 are large high-speed aluminium catamaran ferries, as pictured in Fig. 1. The principal parameters of the vessels are shown in Table I.

Table I: Principal parameters of Hulls 042 and 050

	Hull 042	Hull 050
Length overall	86.6m	96.0m
Length waterline	76.4m	86.0m
Beam overall	26.0m	26.0m
Draft	3.5m	3.7m
Hull beam	4.33m	4.5m
Deadweight	415 tonnes	800 tonnes
Speed, fully loaded condition	40 knots	40 knots

2.2. Measurements

A series of 16 strain gauges was fitted to each vessel at the locations shown in Figs. 2 and 3. An on board radar based wave meter, supplied by TSK, was fitted to the bow of each vessel to give readings of instantaneous absolute wave height. The motions of the vessels were also monitored using accelerometers and rate gyroscopes. Further details on the measurement systems may be found in Thomas et al. (2001, 2003).

Hull 042 was monitored during a delivery trip from Sydney, Australia to Portland, UK and during regular services across the English Channel. The monitoring of Hull 050 took place during regular services across Cook Strait between the North and South Islands of New Zealand.

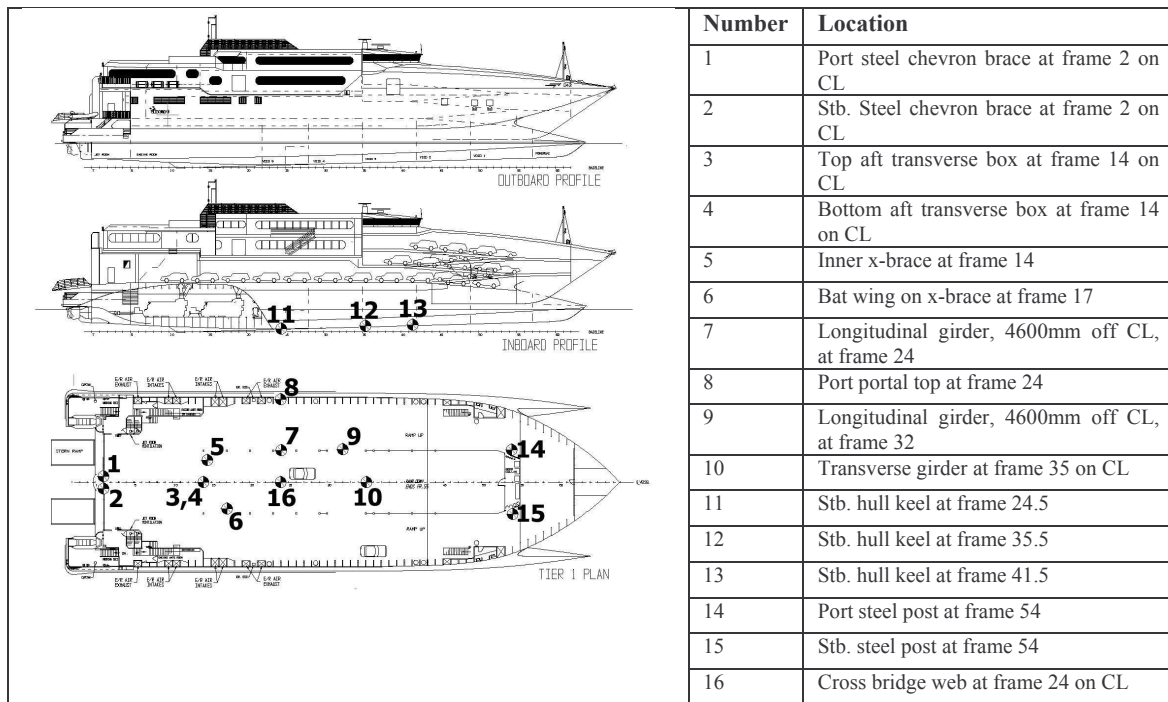


Fig. 2: Hull 042 strain gauge locations

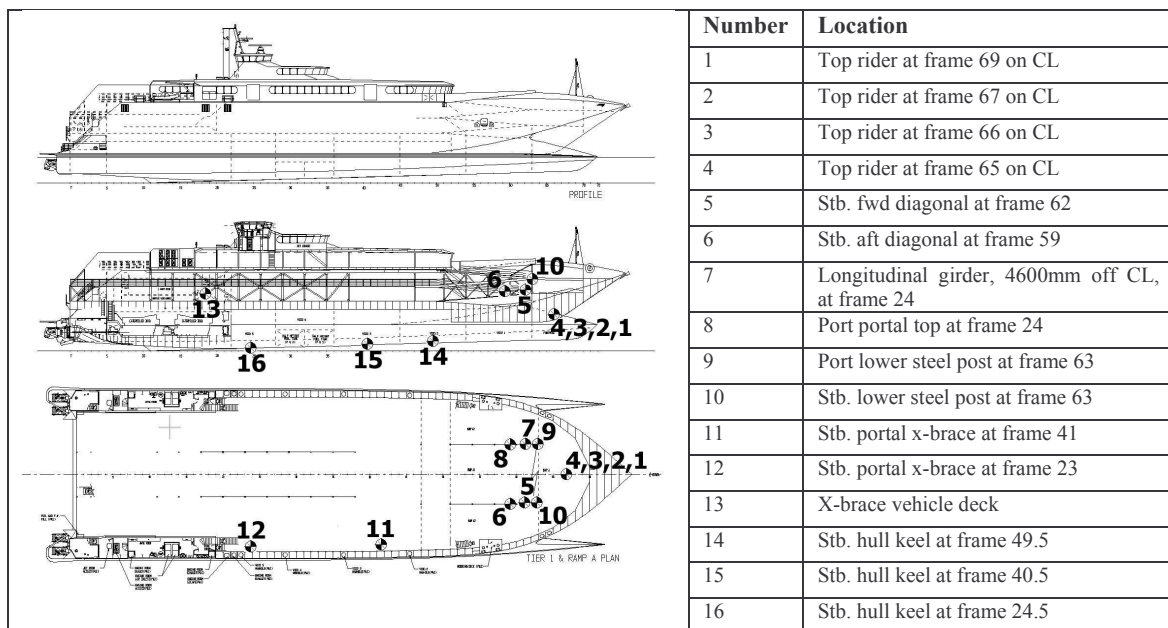


Fig. 3: Hull 050 strain gauge locations

2.3. Whipping Analysis

To investigate the structural whipping response, spectral analysis was conducted on the strain gauge data traces of slam events. The 20 Hz raw data was highpass filtered at 0.04 Hz to remove low frequency drift and windowed using a Hanning window to reduce spectral leakage. The power spectra for the strain gauge records for a 15 second window surrounding the slam event were then determined. These spectra were used to determine the whipping response frequencies of the vessel. The decay coefficient was estimated from the decaying oscillation by determining the ratio between

pairs of successive amplitudes. The decay coefficient is given in terms of successive stress peak values as defined in Fig. 4.

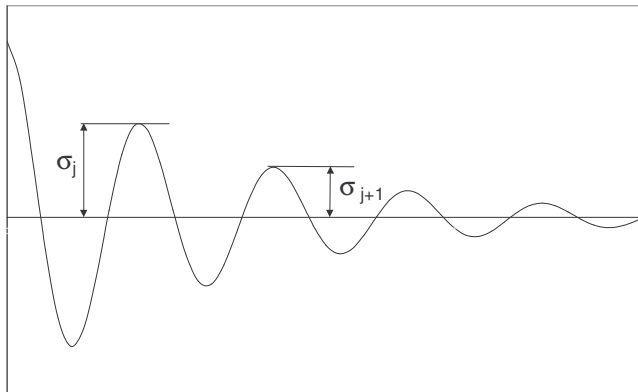


Fig. 4: Definition of decay coefficient

$$\eta = \frac{1}{\pi} \log_e \left(\frac{\sigma_j}{\sigma_{j+1}} \right)$$

Comprehensive analysis of other aspects of the slamming events including a definition of a slam event, frequency of slamming occurrence and magnitude of impulsive slam peak forces may also be found in Thomas et al. (2001, 2003).

2.4. Results

Fig. 5 shows examples of raw strain gauge data traces of a slam event measured on Hull 042. The traces clearly illustrate the initial dynamic impact loading due to the slam event (at time, $t = 168$ seconds) and the subsequent whipping of the structure, which decays away by approximately $t = 178$ seconds for the gauges on the steel chevron brace and the inner crossbrace, and by $t = 175$ for the two keel gauges.

The maximum slam stresses experienced by the top rider in the centre bow of Hull 050 were determined. Fig. 6 shows that the majority of slam events occurred with low stress levels: slam peak stress levels of greater than 50% of the yield stress (yield stress = 110 MPa) were achieved in less than 2% of slam events for this structural location.

For each vessel the principal frequencies of the whipping responses were averaged for individual strain gauges and are shown in Figs. 7 and 8. The range bars for each point indicate the range of the data prior to averaging. The results for four gauges were not included in Fig. 7 since they were located in close proximity to other gauges and exhibited identical frequencies.

For Hull 042, information was available on the vessel displacement during the delivery voyage and thus the whipping frequencies were found for two differing loading conditions. The results for Hull 042 clearly show two distinct frequencies for all of the gauges, except the steel chevron braces and the cross braces which only featured a single whipping frequency. The two frequencies are at approximately 1.5 Hz and 2.6 Hz. Four gauges exhibited the lower frequency of 1.5 Hz only. It is proposed that these gauges, due to their transverse orientation, were dominated by the lateral torsion mode (the mode which is equivalent to pitch connecting moment, PCM, for a catamaran) as opposed to the longitudinal mode and hence do not feature the 2.6 Hz frequency. The shift in frequencies for the two displacements is small, though it may be clearly seen. Henceforth the 1150 tonnes displacement will be known as trials condition 1 and the 970 tonnes displacement as trials condition 2. Two whipping response frequencies are also clearly visible in the Hull 050 results, except for the steel posts and cross braces. The frequencies are at approximately 1.3 Hz and 2.8 Hz.

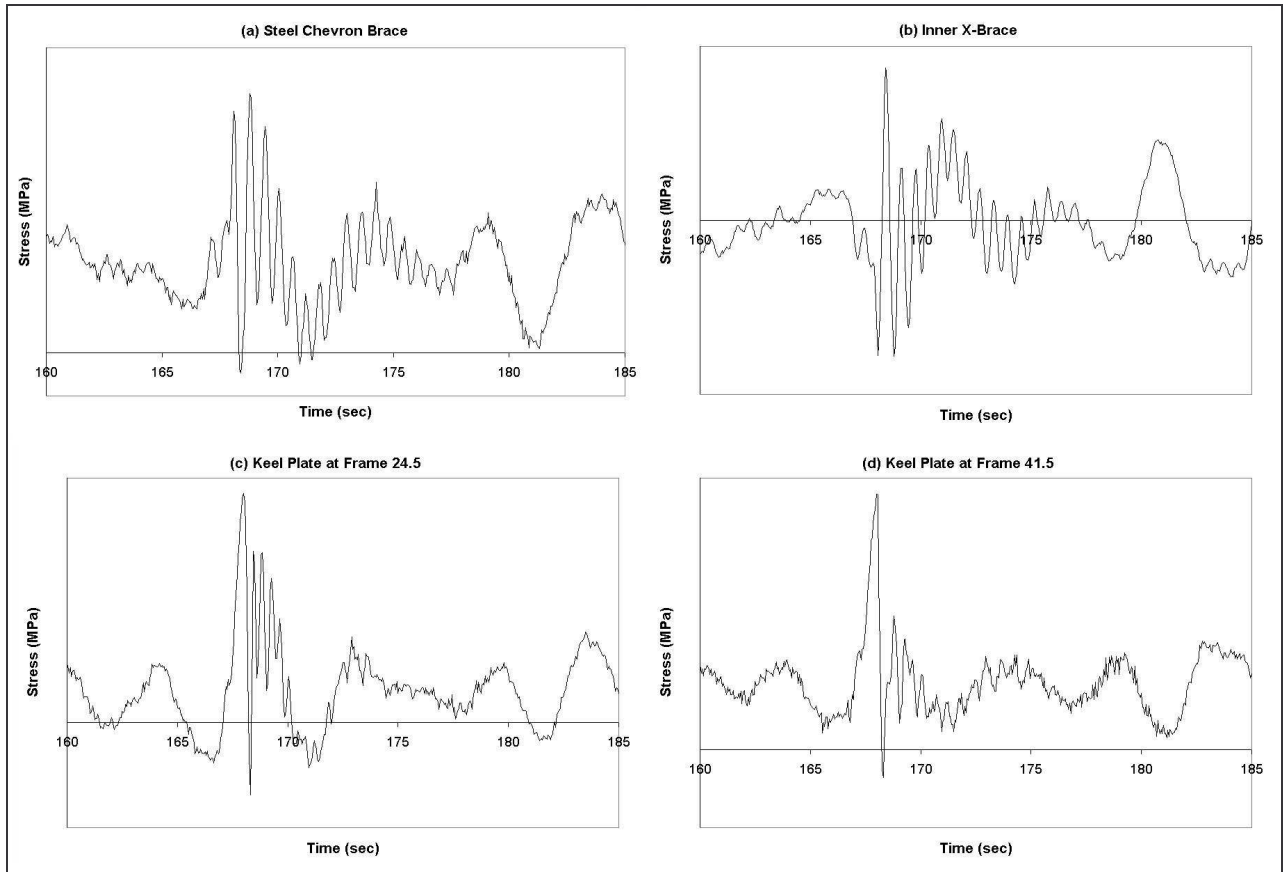


Fig. 5: Slam Event – Hull 042 Raw Strain Gauge Data Traces

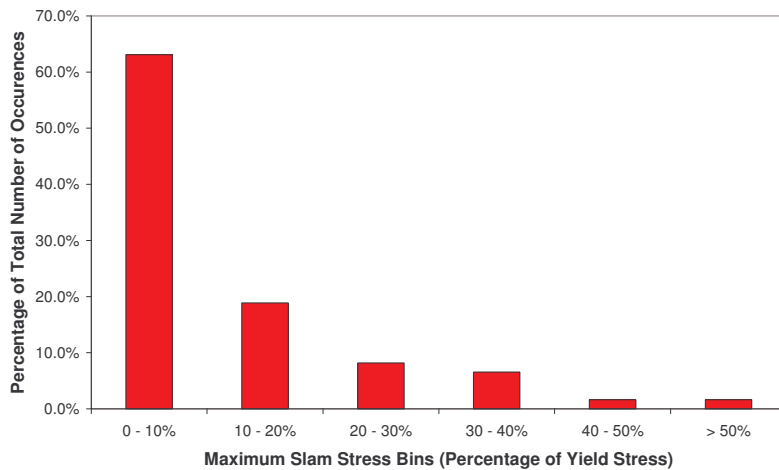


Fig. 6: Distribution of Slam Peak Stress for Slam Events for Hull 050

The average decay coefficients for Hull 042 are shown in Fig. 9 for the signals from four strain gauges: inner cross brace at frame 14 (lateral torsion mode), transverse girder at frame 35 (first longitudinal mode) and frames 24.5 and 41.5 at the keel (first longitudinal mode), where the average values from a number of slam events are shown with range bars. The decay of the signal for the inner cross brace strain gauge at frame 14 appears to be fairly constant across the number of detectable cycles at approximately 0.1. This gauge only exhibited the lower frequency and therefore it appears that this frequency has lower damping levels than the higher frequency mode. The decay coefficient for the transverse girder strain gauge at frame 35 tends to start at a higher level of approximately 0.25,

and then this slowly decreases until the 7th cycle, when the coefficient turns negative before growing rapidly to diminish the whipping response. The gauge at frame 24.5 at the keel appears to have three distinct parts: the large decay coefficient (between 0.3 and 0.4) for the 1st cycle, a negative coefficient for the 2nd cycle and then a relatively steady lower coefficient (between 0.05 and 0.2) for the subsequent cycles until the signal becomes indistinct. It should be noted that a negative decay coefficient simply means that the signal amplitude of the subsequent cycle of the point of measurement increases. The decay at the gauge at the keel at frame 41.5 is similar to that at the keel at frame 24.5 although the value at the 2nd cycle does not appear to be so low.

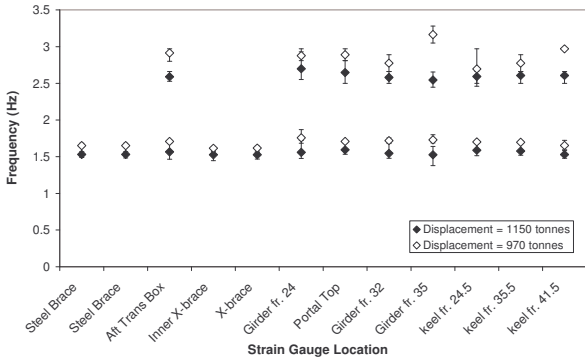


Fig. 7: Hull 042 whipping frequencies

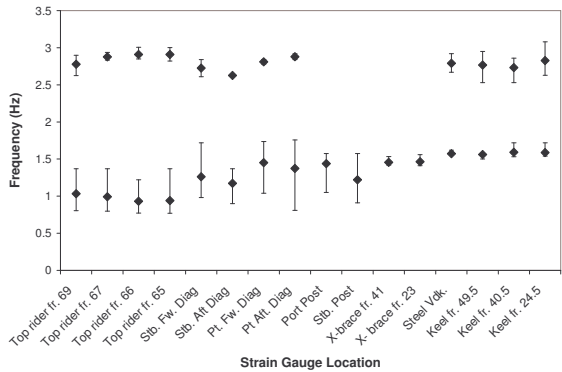


Fig. 8: Hull 050 whipping frequencies

The average decay coefficients are shown in Fig. 10 for the signals from four strain gauges for the first longitudinal mode of Hull 050: frame 67 in the centre bow, frame 41 at the keel, frame 25 at the keel (all first longitudinal mode) and frame 23 on the starboard portal crossbrace (lateral torsion mode). The decay of the signal at frame 67 has two parts: the large decay coefficient (between 0.3 and 0.4) for the first 2 cycles and then the steady lower coefficient (less than 0.15) for the subsequent cycles until the signal becomes indistinct. Since this strain gauge was situated in the centre bow, and was very close to the slam impact region on the hull, the initial large decay value was most likely to be due to transient energy transfer in the beam-like structure towards the aft of the vessel in order to set up the modal vibration. This effect is borne out further in the strain gauge results from further aft in the vessel where the initial decay factor is negative (see the second cycles in Figs. 10(c) and (d)), meaning an increase in oscillation strength, as the energy is transferred aft. After this initial effect the decay coefficient for the gauges at frames 23, 25 and 41 are consistently low at less than 0.15.

3. Exciter Tests

Vibration exciter tests were conducted on the two vessels to determine the frequency, damping and modal shape of the primary longitudinal mode. Unfortunately Hull 042 was not available for testing and hence Hull 045, an identical sister ship, was utilised instead. These tests were carried out in controlled conditions with the vessels being stationary in calm water. The vessels' anchors (050 mass = 1.8 tonnes, 045 mass = 1.4 tonnes) were used to excite the longitudinal mode of vibration by dropping the anchor and then instantaneously restraining it with the electric winch. Four accelerometers, distributed along the length of the vessel on the centreline, measured the structural response. Unfortunately, due to practical constraints, it was not possible to conduct exciter tests for the torsional modes.

Hull 045 was in the lightship condition (see Table III) whilst the displacement of Hull 050 was close to that recorded from the full-scale trials.

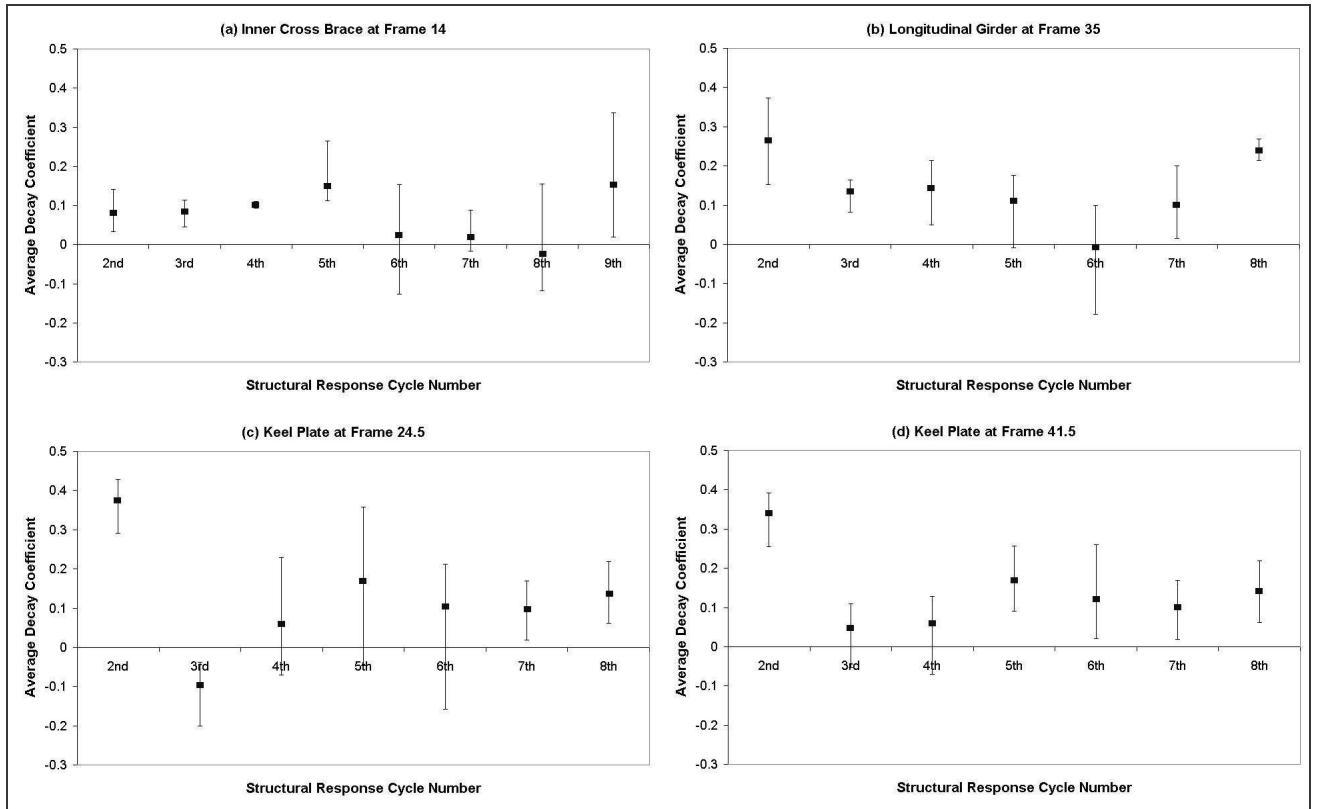


Fig. 9: 042 full-scale slam decay coefficients

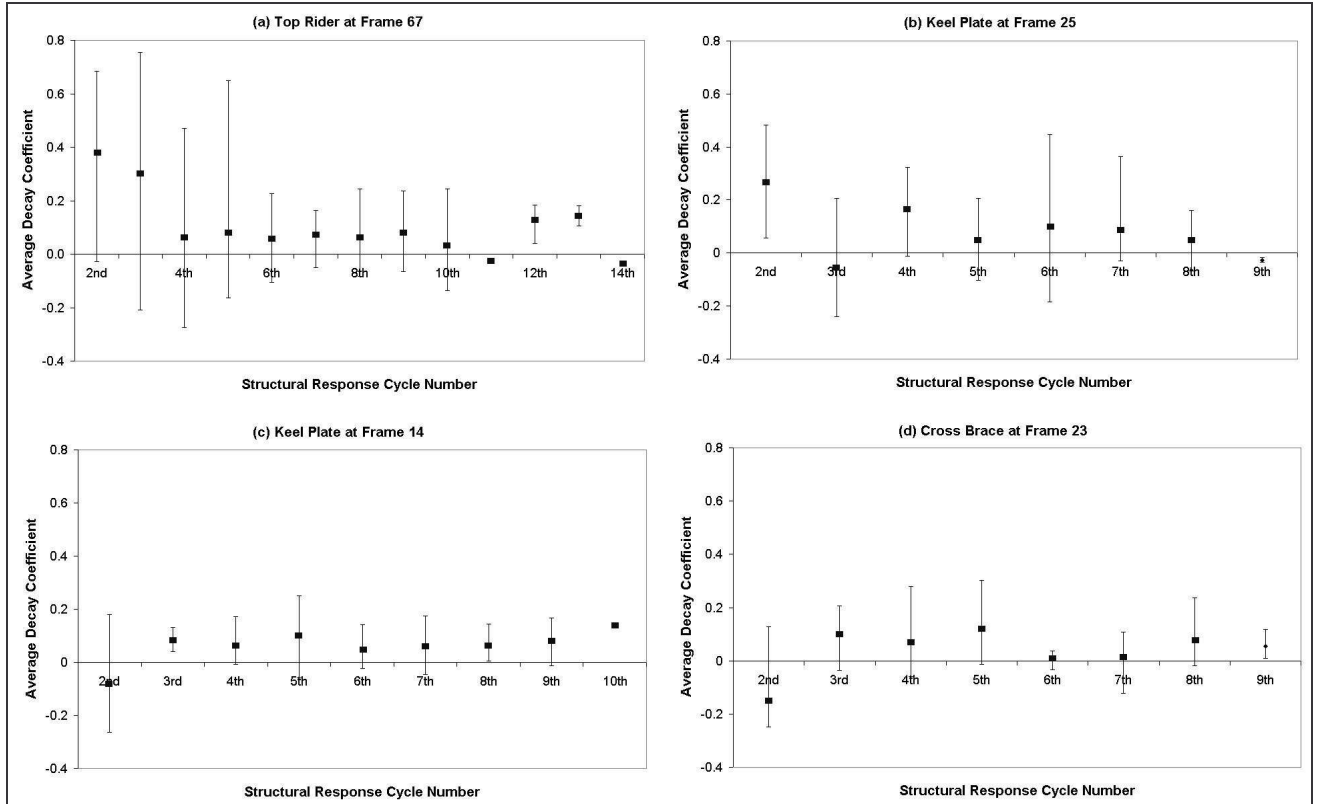


Fig. 10: 050 full-scale slam decay coefficients

3.1. Data Analysis

The 100 Hz raw data was highpass filtered at 0.6 Hz to remove low frequency drift. The power spectra for the accelerometer records were then determined and used to identify the modal response of the vessel. The decay coefficients were estimated from the decaying oscillation by determining the amplitude reduction between successive peaks. The modal shape of the dominant structural response was found by comparing the response at the four accelerometers distributed along the centreline with regard to magnitude and phase.

3.2. Results

The average first longitudinal natural frequencies from the tests were 3.01Hz for Hull 045 and 2.89Hz for Hull 050. For Hull 045 the decay coefficient ranged between 0.007 and 0.14, as shown in Fig. 11, with an average value of 0.069. The Hull 050 results shown in Fig. 12 indicate that the decay factor was generally in the range of 0.01 to 0.06 with an average decay coefficient for all cycles of 0.035. These values of decay coefficient fall within the range determined through the analysis of the full-scale slam events.

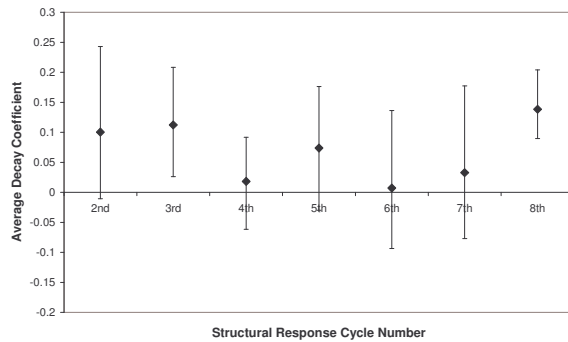


Fig. 11: 045 exciter test decay coefficients

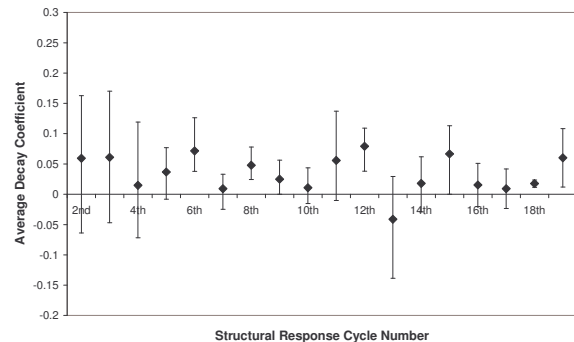


Fig. 12: 050 exciter test decay coefficients

The range of results appear to be smaller for Hull 050 than for Hull 045 which may be due to the heavier anchor used for the excitation producing a larger and clearer structural response. This is also borne out by the number of cycles that the data was able to be analysed for: 19 cycles for Hull 050 and 8 cycles for Hull 045.

The damping level recorded for Hull 050 is significantly smaller than that measured for Hull 045, although it falls within the measured damping range of Hull 045. The measured mode was identified as the first longitudinal mode of vibration. Results for the exciter test mode shape are shown in Section 5 where the exciter test and full-scale results are compared with those obtained from normal mode analysis.

4. Normal Mode Analysis

Normal mode analysis was conducted to determine the primary low frequency dry and wet modes of the two vessels, with the hydrodynamic added mass of the surrounding fluid being calculated by a two dimensional panel method coupled with a strip theory.

The solution of the equation of motion for natural frequencies and normal modes requires a special reduced form of the equation of motion (MSC Software 2001). If there is no damping and no applied loading, the equation of motion in matrix form reduces to

$$[M]\{\ddot{u}\} + [K]\{u\} = 0 \quad [1]$$

where $[M]$ is the mass matrix and $[K]$ is the stiffness matrix. Equation 1 may be solved using a finite element approach to obtain the dry natural frequencies, ω_i (where $i = 1, 2, 3, \dots$), and principal mode shapes. For the wet modes, where the fluid-structure interaction is included, Equation 1 becomes

$$([M_s] + [M_A])\{\ddot{u}\} + [K]\{u\} = 0. \quad [2]$$

Where M_s represents the ship displacement and M_A is the ship added mass, representing the inertia properties of the surrounding water. The normal mode analysis was carried out using the Lanczos method within the PATRAN/NASTRAN finite element package.

In order to determine the wet modes of Hulls 042 and 050, the added mass of the surrounding fluid needed to be included in the normal mode analysis. The added mass represents the effective inertia of the water surrounding the oscillating hull, and may be defined as the component of force in phase with the body's acceleration exerted by the hull on the water for a unit amplitude acceleration of the hull. It was calculated utilising a steady periodic Green function panel method (Holloway et al. 2003). A summary of the various vessel loading conditions and total added masses may be found in Table III. This shows that the added mass of each vessel configuration was found to be close to the corresponding displacement of the vessel.

Table III: Displacements & Added Masses of Hulls 042 & 050

	Displacement (t)	Total vessel added mass (t), 1st longitudinal mode
Hull 042, Trials 1	1150	978
Hull 042, Trials 2	970	910
Hull 045, Exciter Test	880	875
Hull 050, Trials/Exciter Test	1100	1085

4.1. Normal Mode Analysis Results

The first two global modes found were the lateral torsion mode and the first longitudinal mode, see Figs. 13 and 14. The dry and wet modal frequencies for these modes are shown in Table IV. As expected the natural frequencies reduced significantly due to the effect of the added mass.

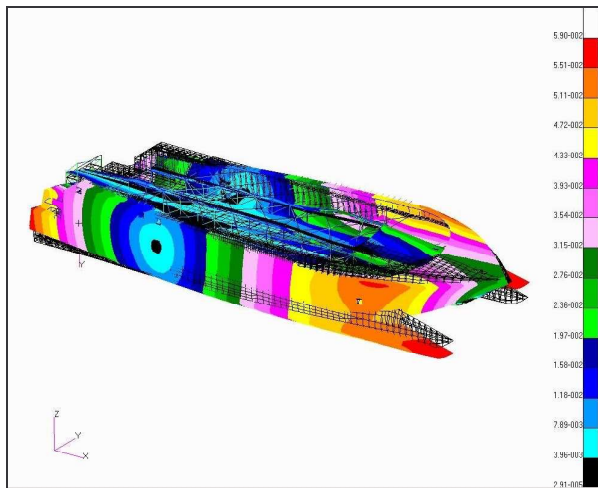


Figure 13: Hull 050 lateral torsion mode
total relative deflection amplitude

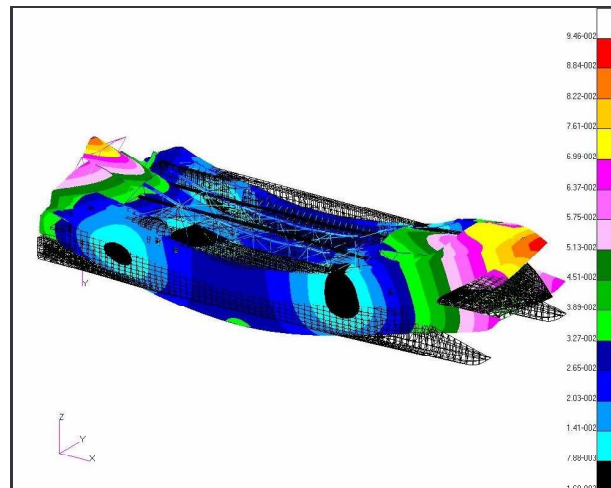


Figure 14: Hull 050 1st longitudinal mode
total relative deflection amplitude

5. Comparison of Full-Scale, Exciter Test and Normal Mode Analysis Results

The results from the full-scale trials measurements and exciter tests were compared with the output from the normal mode analysis incorporating the fluid structure interaction.

The comparison for Hull 042 in the trials condition 1, see Fig. 15(a), shows that the predicted natural frequencies correlate closely with the two main frequencies measured during the full-scale trials. The

exciter test and full-scale results are average values for a number of readings, with bars showing the range of results. The mode measured at approximately 2.6 Hz correlates with the first longitudinal mode as predicted by the finite element analysis, whilst the mode at approximately 1.5 Hz matches with the calculated lateral torsion natural frequency. Similar correlation may be found in Fig. 15(b) for Hull 042 in trials condition 2, with the first longitudinal mode at approximately 2.9 Hz and the lateral torsion mode at approximately 1.7 Hz, both matching with the finite element results. These results clearly highlight that different vessel loading conditions result in changes in natural frequency, with the frequencies generally increasing as the vessel displacement decreases. The influence of the distribution of the mass changes is also significant. The long distance fuel tanks were located close to modal nodes for both the identified modes and a change in displacement due to loading/unloading of long range fuel would not be as significant as a change in mass at a modal anti-node. For example, if the difference in fuel mass between trials condition 2 and trials condition 1 were loaded evenly at the bow and stern of the vessel, as opposed to the centrally located long range fuel tanks, the finite element modal analysis estimated the lateral torsion and first longitudinal modes as 1.39 Hz and 2.27 Hz respectively. These values are significantly different from those measured and calculated for delivery condition 1 where the fuel is loaded close to amidships.

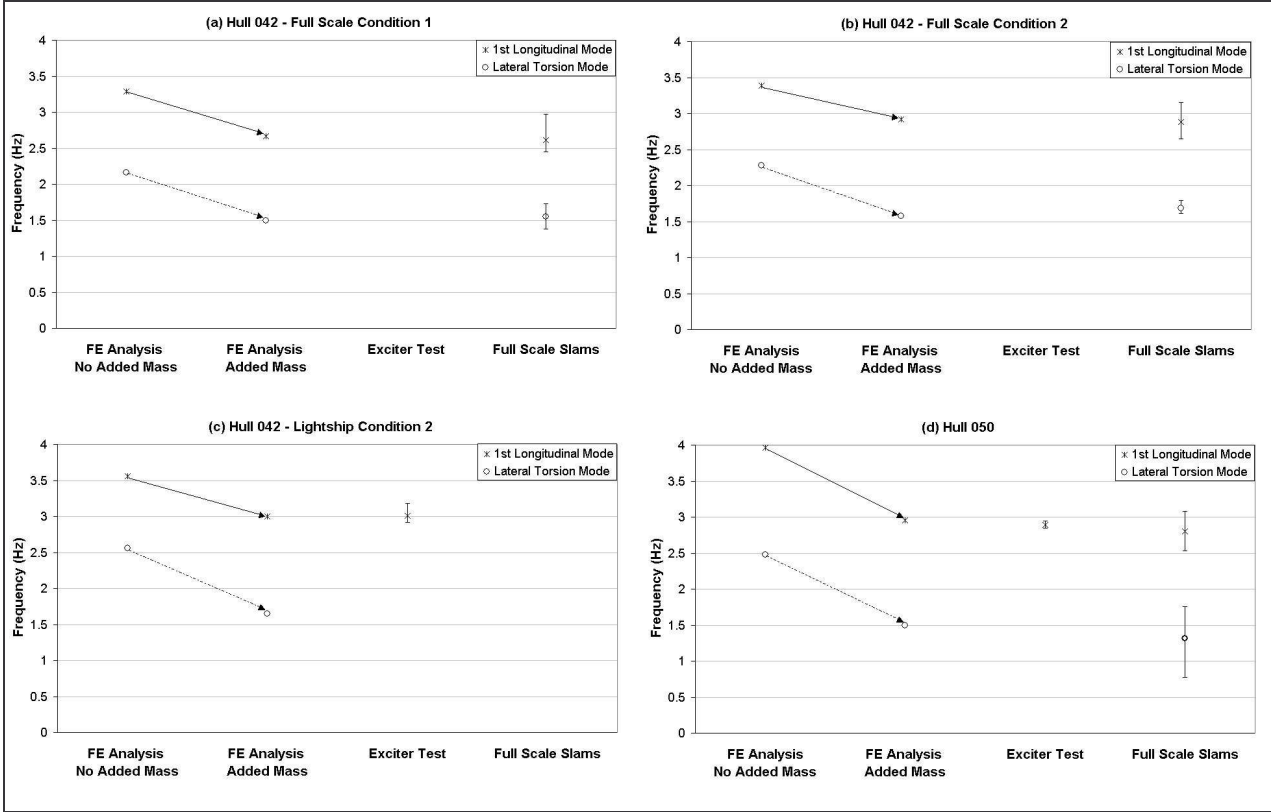


Fig. 15: Hulls 042 & 050 natural frequency comparisons.

Table IV: Predicted natural frequencies

Hull Condition	Dry Modes		Wet Modes	
	Lateral Torsion	First Long.	Lateral Torsion	First Long.
Hull 042, Trials 1	2.16 Hz	3.29 Hz	1.50 Hz	2.56 Hz
Hull 042, Trials 2	2.28 Hz	3.39 Hz	1.58 Hz	2.92 Hz
Hull 045, Exciter Test	2.56 Hz	3.56 Hz	1.65 Hz	3.00 Hz
Hull 050, Trials/Exciter Test	2.48 Hz	3.97 Hz	1.50 Hz	2.96 Hz

From the exciter tests on Hull 045 the first longitudinal mode for this type of vessel was identified at

approximately 3 Hz. This frequency matches closely with that found by the finite element analysis for Hull 042 in the lightship configuration, as seen in Fig. 15(c). This confirms that the mode at approximately 2.6 Hz in the trials results is the first longitudinal mode, and the difference in frequency between the trials measurements and the exciter test is again due to the vessel loading variation.

It should be noted that the added mass formulation is conducted for the vessel's calm waterline. This assumption was applicable for the exciter test measurements where the waterline variation was minimal. However the waterline would have varied significantly when the vessel was operating in waves, particularly in waves large enough to cause slamming. A change in local draft affects the vessel's total added mass value and this factor may have contributed to the spread in the measured natural frequencies for the full-scale trials.

Fig. 15(d) shows that the first longitudinal mode found from the normal mode analysis of Hull 050, with the added mass incorporated, matches up well with the frequency determined from the exciter test. This confirms that the mode identified from the trials measurements at approximately 2.8 Hz is the first longitudinal mode. It is also evident that the mode at approximately 1.4 Hz in the trials results is the lateral torsion mode since it compares well with the frequency identified by the finite element analysis.

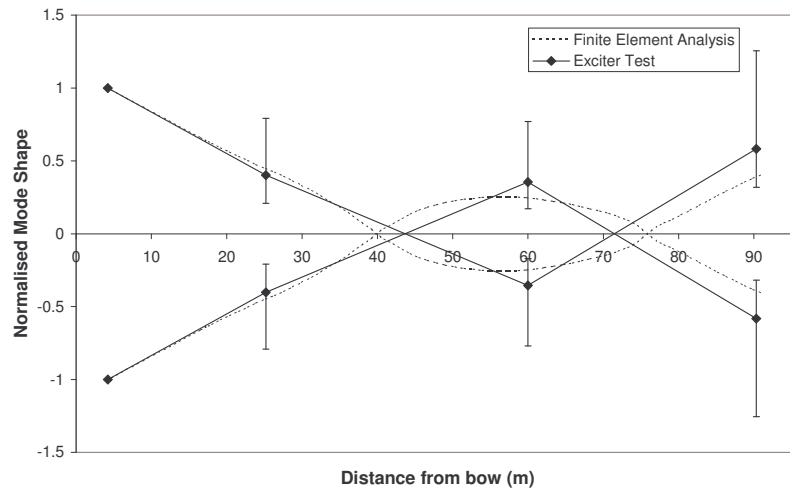


Fig. 16: Hull 050 mode shape comparison

The mode shapes for the first longitudinal mode, as measured on Hulls 045 and 050 through the exciter tests, were compared with the mode shapes as predicted through the finite element normal mode analysis including the added mass. An example for Hull 050 is shown in Fig. 16. The magnitudes of the mode was normalised about the response level at the forward accelerometer location from the exciter test. The correlation appears to be satisfactory with the theoretical predictions lying within the range of the measured results along the length of the vessel.

The comparisons of the trials measurements and exciter tests with the theoretical predictions indicate that the method utilised in this study for determining the natural frequencies of large catamarans including added mass provides satisfactory results.

6. Fatigue Implications of Whipping

The influence of whipping behaviour on the expected fatigue life of part of a large high-speed aluminium catamaran has also been investigated. Whilst knowledge in the design process of the fatigue strength of large aluminium vessels is crucial (Tongue 1998), there are several reasons why prediction of a vessel's fatigue life span is difficult. The main difficulties are estimating the lifetime sea spectrum and load regime that the vessel will be exposed to. These difficulties are avoided in this study by concentrating on the differences in estimated fatigue life for different whipping behaviour, rather than attempting to estimate the absolute fatigue life.

A series of realistic simulated stress traces resulting from slam events, for a strain gauge on the keel

plate, were developed for differing decay coefficients and slam peak stresses (Fig. 17). Slam peak stress and slam frequency of occurrence data gained from the sea trials was utilised (Thomas et al. 2001, 2003) to build up realistic slam scenarios. It should be noted that the stress records took no account of the underlying wave induced global loads, and only the slams and subsequent whipping were included.

The Rainflow method (Sharp et al. 1996) was utilised to determine the number of stress cycles for specific stress ranges. The fatigue life was then estimated using the British Standard BS8118 (British Standards 1992), which is based on Miner’s Law, which states that failure will occur when

$$\sum \frac{n_i}{N_i} = 1. \tag{3}$$

where n_i is the number of cycles in the i th stress range and N_i is the number of cycles to failure at the i th stress range. The Miner’s Law technique is predominantly used by Classification Societies to estimate fatigue life because it is a simple concept. However since the correct assessment of the amount of damage incurred by given stress levels and cycles is not straightforward there is difficulty utilising it in practice. For example experimental values for Miner’s sum at the time of failure often range from approximately 0.6 to 1.6 for quasi-random cyclic stress amplitudes (Collins 1993). Nonetheless it is suitable for use in this study in order to give comparative values of fatigue life for differing stress cycle regimes. A number 24 weld detail, which corresponds to a typical end fillet weld that might experience the simulated stresses, was utilised for the fatigue predictions. It was assumed that the vessel would operate for 5000 hours per year of life which corresponds to approximately 15 hours of service per day for 48 weeks of service per year.

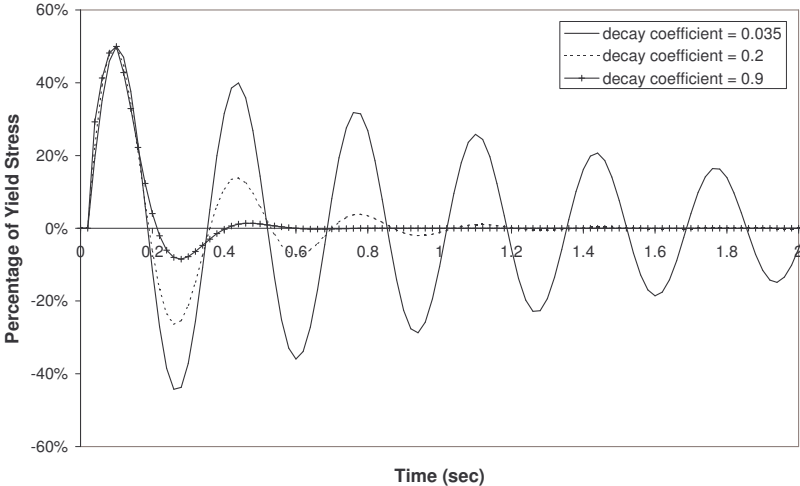


Fig. 17: Example simulated slam events

For a slam peak stress of 25% of the yield stress the fatigue life was determined for a varying number of slams per hour throughout the vessel’s life for a range of decay coefficients. The results, as shown in Fig. 18, clearly indicate that as the decay coefficient increases the fatigue life increases. For a slam rate of 7.5 per hour (for the whole operational life of the vessel), a change in decay coefficient from 0.035 to 0.025 brings about a reduction in fatigue life of approximately 25%. As expected the fatigue life also reduces as the number of slams per hour increases.

For a decay coefficient of 0.035 (which was the value determined for Hull 050 through the exciter test), the fatigue life for varying slam peak stress was found for a range of slam occurrence rates (Fig. 19). This plot shows that the fatigue life reduces rapidly as the slam peak stress is increased. For example, at a slam rate of 7.5 per hour, the fatigue life reduces from 56 years to 0.72 years as the slam peak stress is increased from 12.5% to 50% of the yield stress. It is clear that slam events with large peak stress have a significantly greater influence on fatigue life than smaller slam events. It should be remembered though that the Hull 050 trials data showed that the majority of slam events resulted in

low maximum stress levels (Fig. 6). Again an increase in slam occurrence rate is shown to cause a reduction in fatigue life.

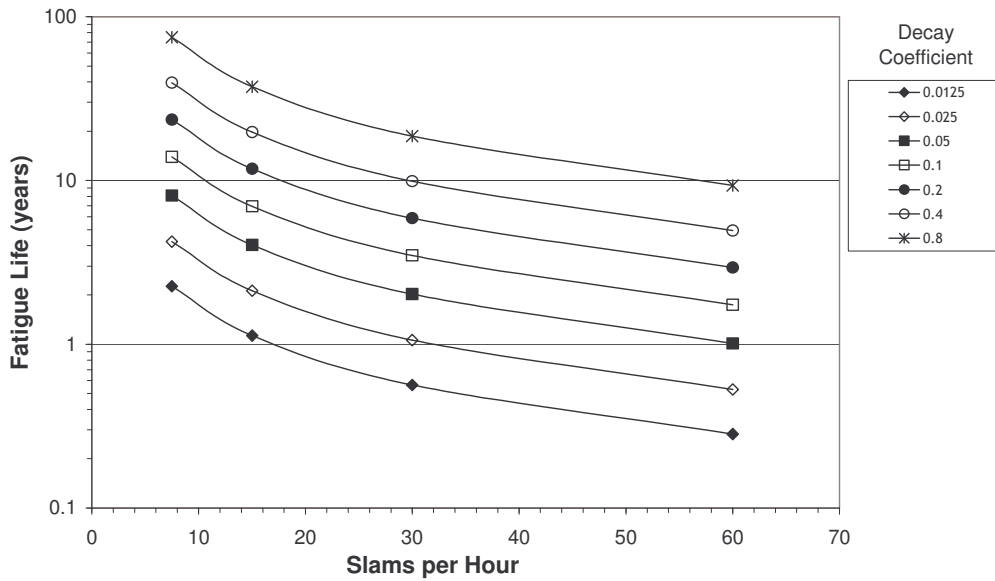


Fig. 18: Fatigue life for varying slams per hour rate and decay coefficient

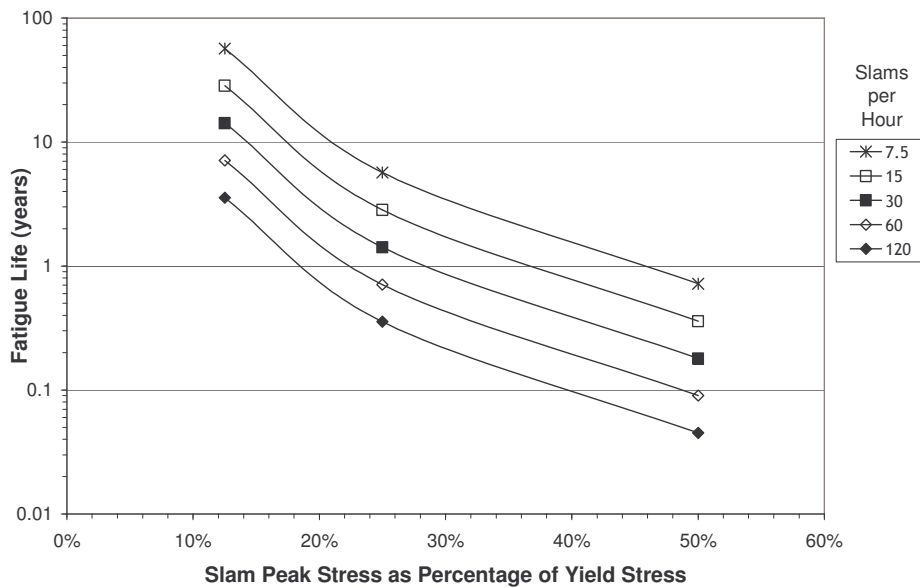


Fig. 19: Fatigue Life for varying slams per hour rate and slam peak stress

The fatigue life values calculated in this study appear to be realistic. Operational experience for this type of vessel has demonstrated a wide range of fatigue life. Depending on the structural detail and loading regime fatigue lives as low as two years have been observed. This study highlights the strong influence of whipping on fatigue life. The methods and results shown give guidance to designers when estimating the fatigue life of large high-speed catamarans for a given operating scenario.

7. Conclusions

The whipping behaviour of large high-speed aluminium catamarans has been investigated through trials measurements of slam events, exciter tests conducted in calm water and finite element modal analysis. A fatigue study was also conducted to estimate the effect of whipping on a large high-speed vessel's fatigue life.

The good correlation between the finite element analysis results for the wet modes and the full-scale and exciter test results indicates that the method utilised for deriving the flexible global modes is suitable for this style of vessel. It can be concluded that, for the two major frequencies identified in the vibratory whipping through the trials measurements of slam impacts, the lower frequency (approx. 1.5 Hz) corresponds to the lateral torsion mode whilst the higher frequency (approx. 2.5 - 3 Hz) is the first longitudinal mode. This finding was supported by the good match between the finite element results and the exciter test results for Hulls 042/045 and 050 when changes in loading condition were taken into account. Significant changes in natural frequency were apparent due to changes in vessel mass loading.

The whipping decay coefficients for Hulls 042/45 and 050 were found through full-scale slam measurements and exciter tests. From the exciter measurements, for Hull 045 the average decay coefficient was 0.069, whilst for Hull 050 it was 0.035. It is recommended that further work be conducted on the modal damping with regard to identifying the contribution of various sources of damping (e.g. structural damping, hydrodynamic damping, viscous damping and radiated pressure wave damping).

It was found that whipping behaviour has a strong influence on the theoretical fatigue life of such vessels, with the fatigue life increasing as the decay coefficient increases, and the fatigue life reduces as the number of slams per hour increases.

Acknowledgements

This work has been partly supported by an Australian Research Council SPIRT grant. The authors would like to acknowledge the help of their colleagues at the University of Tasmania, Incat Tasmania and Revolution Design Pty Ltd.

References

- AERTSSEN, G. (1979), *An Estimate of Whipping Vibration Stress based on Slamming Data of Four Ships*, International Shipbuilding Progress, Vol. 26, No. 294.
- BETTS, C.V., BISHOP, R.E.D., PRICE, W.G. (1977), *A Survey of Internal Damping*, Transactions RINA, Vol.119.
- BRITISH STANDARDS (1992), *Structural Use of Aluminium, BS 8118, Part1, Code of Practice for Design, 1992: Part 2, Specification for Materials, Workmanship and Protection*.
- CLARKE, J.D. (1982), *Measurements of Hull Stresses in Two Frigates during a Severe Weather Trial*, Transactions RINA, Vol. 124.
- CLARKE, J.D. (1987), *Prediction of Fatigue Cracking in Warship Hulls*, Third International Symposium on Practical Design of Ships and Mobile Units.
- COLLINS, J.A. (1993), *Failure of Materials in Mechanical Design*, John Wiley & Sons.
- EVANS, J.H. (1982), *Preliminary Design Estimation of Hull Girder Response to Slamming*, Transactions SNAME, Vol. 90.
- FRIIS-HANSEN, P., JENSEN, J.J., PEDERSEN P.T. (1995), *Long Term Springing and Whipping Stresses in High Speed Vessels*, FAST '95.

FUKASAWA, T., YAMAMOTO, Y., FUJINO, M., MOTORA, S. (1981), *Motion and Longitudinal Strength of a Ship in Head Sea and the Effects of Non-Linearities*, Transactions Society of Naval Architects Japan, No. 150.

HOLLOWAY, D.S., THOMAS, G., DAVIS, M.R. (2003), *Added Mass of Whipping Modes for Ships at High Froude Number by a Free Surface Boundary Element Method Coupled with Strip Theory*, International Congress on Industrial and Applied Mathematics.

HUMPHREY, R., NYBØ, T. (2002), *Det Norske Veritas - Direct Calculation Methods for High Speed, Light Craft and Naval Surface Craft*, Pacific 2002.

KANNARI, P., KLINGE, P., RINTALA, S., KARPPINEN, T., MIKKOLA, T.P.J., RANTANEN, A. (1998), *Comparison of Simulated Global Stresses with Full-Scale Measurements on an Aluminium Fast Patrol Vessel*, Hydroelasticity in Marine Technology.

KAWAKAMI, M., MICHIMOTO, J., KOBAYASHI, K. (1977), *Prediction of Long-Term Whipping Vibration Stress due to Slamming of Large Full Ship in Rough Seas*, International Shipbuilding Progress, Vol. 24, No. 272.

LOUARN, F., TEMAREL, P. (1999), *An Investigation of the Structural Dynamics of a Racing Yacht*, 14th Chesapeake Sailing Yacht Symposium.

McTAGGART, K., DATTA, I., STIRLING, A., GIBSON, S., GLEN, I. (1997), *Motions and Loads of a Hydroelastic Frigate Model in Severe Seas*, Transactions SNAME, Vol. 105.

MORRIS, J.A. (1991), *A Three Dimensional Structural Analysis of a Large Wave Piercing Catamaran Design*, IMAS 91 High Speed Marine Transportation.

MSC SOFTWARE (2001), *NASTRAN Basic Dynamic Analysis*, Los Angeles, USA.

OCHI, M.K., MOTTER, L.E. (1973), *Prediction of Slamming Characteristics and Hull Responses for Ship Design*, Transactions SNAME.

OEI, T.H. (1976), *Finite Element Ship Hull Vibration Analysis Compared with Full Scale Measurements*, Netherlands Maritime Institute Report.

PRICE, W.G., TEMAREL, P. (1994), *Hydroelastic Analysis of a SWATH in Waves*, Hydroelasticity in Marine Technology.

SHARP, M.L., NORDMARK, G.E., MENZEMER, C.C. (1996), *Fatigue Design of Aluminium Components and Structures*, McGraw-Hill.

THOMAS, G., DAVIS, M.R., WHELAN, J., ROBERTS, T.J. (2001), *Dynamic Response of Large High Speed Catamarans*, FAST '01.

THOMAS, G., DAVIS, M.R., HOLLOWAY, D. S., WATSON, N.L., ROBERTS, T.J. (2003), *The Slamming Response of a Large High Speed Wave-Piercer Catamaran*, SNAME Marine Technology Journal, Vol. 40, No. 2.

TONGUE, E. (1998), *Fatigue Assessment of Aluminium Fast Craft*, Third Forum on Aluminium Ships, Norway.

Damage Stability as a Safety Criterion for Optimisation Tools

Deniz Saydan, University of Southampton, Southampton/UK, deniz@soton.ac.uk
Grant E. Hearn, University of Southampton, Southampton/UK, grant@ship.soton.ac.uk

Abstract

This paper is primarily concerned with the fact that seakeeping and resistance based optimisation of hull forms, at the conceptual stage, do not appear to highlight any other behavioural disadvantages. Whilst some aspects of intact stability are included within the optimisation process, damage stability is not considered. The situation of a damaged optimised hull form being less safe than a damaged non-optimised hull form would seem perverse and so this paper presents a methodology to investigate this situation. The methodology is applicable to any ship type.

1. Introduction

A ship is designed to transport a certain amount of cargo between specified ports on a chosen route. An important step in the earlier stages of design is the selection of the ship sizing parameters. At this stage of design few naval architectural tools can be applied. Traditionally, these initial challenges are overcome by applying various empirical formulae to assign the initial sizing of parameters. Thereafter, the design is developed iteratively. However, any approach based on empiricism and experience restricts the ability of the designer to be innovative. Fundamental changes in key hull form parameters may not be evident until detailed analyses are undertaken far down the design path. Consequently, changes may not be made due to the level of commitment to the design and the perceived costs in design re-development. The failure to reflect the results of the more accurate analysis in the design process limits the usefulness of empiricism and experience based methods. An alternative approach is to apply computer-based search or optimisation tools in the earlier stages of the design to improve seakeeping and resistance qualities.

The earlier background information presented in the next section will indicate that whereas the search and optimisation methods address seakeeping, various aspects of resistance, in some cases manoeuvring with due regard for intact stability requirements, no consideration is given to damage stability. This paper presents an initial investigation of the changes in damage stability characteristics as a design progresses from its initial selected hull form to the optimised hull form. The motivation for the research is the concern that the optimisation methods appear to improve seakeeping, resistance and intact stability qualities without, so far, having identified any seriously undesirable behavioural characteristics. It would be extremely perverse if one were to find that the damaged optimised hull form was less survivable than the damaged conceptual form. This concern is the prime motivator for the reported research.

2. Research Background

In the late 1980s, *Hearn et al (1988)* developed a strip theory based seakeeping analysis for use by British Shipbuilders design offices. Since there was little familiarity with boundary element based solutions of Fredholm integral equation within these design offices, the computer system developed '*Lynette Suite (Hearn and Colton 1990)*' required automatic spline fitting through arbitrary defined waterplanes and transverse sections to generate required data at regular stations consistent with needs of strip theory. This in turn also required automatic discretisation of the stations to allow the necessary hydrodynamic analysis. Availability of robust friendly software with error detection and recovery was thought to be a necessary tool to allow improved initial designs within British Shipbuilders. It was soon evident that undertaken seakeeping analysis with ease was insufficient. There appeared to be an inability to readily identify what hull form parameter changes were required to remove unfavourable seakeeping characteristics. Whilst public literature contained considerable anecdotal advice, the immediate need of the design team was to identify specific solutions to their particular problems. This

academic industrial interaction was the catalyst to a fruitful research programme concerning new developments in the application of analysis tools for initial/conceptual design.

In particular, a design chart based search methodology was developed by *Hearn et al (1990, 1991)* for monohulls and by *Hearn et al (1994)* for catamarans to analyse the desired engineering responses for the ‘designer permitted’ variations of the selected hull form parameters. The design charts provide a graphical representation of the ‘cause and effect’ relationship for different engineering responses as a function of different pairs of hull parameters. The design charts were either concerned with the ‘secondary variables’ of LCB, C_{WP} , LCF and C_p or the ‘primary parameters’ of L and B/T. The selection of these parameters is based on reading some forty years worth of different experimental investigations and noting the perceived dependence of different hull form performance indicators with various hull form parameters. The disadvantage of this approach is that equal amounts of effort may be spent studying both non-beneficial and beneficial portions of the searched parameter spaces. Also whilst interaction between the pairs of selected hull form parameters could be readily appreciated, understanding of interactions between different pairs of parameters was not produced by this approach. Optimisation methods allow one to seek out beneficial parameter changes and to concentrate effort in such regions whilst simultaneously changing in turn all of the hull form parameters. Hence any unappreciated interactions are automatically eliminated by the Optimisation Software. Having perceived which changes are beneficial for the vessel designed, the continuous iteration of the selected parameters was undertaken by using an automated algorithm to produce a new hull form (see *Hearn et al (1995)*).

The mono-hull Hooke and Jeeves (see *Cooper and Steinberg (1970)*) based optimisation analyses performed by *Hearn et al (1990, 1991 and 1992)* and *Sarioz et al (1992)* were deliberately restricted to vertical plane motions in head seas. In these studies, strip theory based seakeeping analysis facilitated using a database of pre-calculated hydrodynamic coefficients with automatic generation of alternative hull forms consistent with parameter changes requested by the optimisation method. Michell’s thin-ship theory provided estimates of wave-making resistance and the International Towing Tank Conference (ITTC) 1957 correlation curve was used for the frictional resistance calculations. Intact stability checks were based on the International Maritime Organisation’s criteria namely, IMO A-287.

Outside of the above cited University of Newcastle based research, one finds other examples of analysis being used in the context of optimisation. Space unfortunately does not permit a complete review of the current literature. *Mandel and Leopold (1966)* undertook optimised economic analysis of ships. *Liu et al (1981)* provides an early example of optimised ship hull structural strength using the finite element method. The wave resistance computations are incorporated into the earlier stages of the design cycle by *Keane et al (1991)* and *Doctors and Day (1995)*.

The role of safety within the design spiral is highlighted by *Cramer and Tellkamp (2002, 2003)*. In traditional design, safety is partially addressed through the requirements of the intact stability and the regulations addressing damage stability. When there is sufficient statistics concerning a particular ship type, a probabilistic approach to damage stability may also be undertaken. In the context of the optimised design for seakeeping and resistance, it is assumed that the ship being investigated is novel and hence the probabilistic method to damage stability cannot be meaningfully included within the optimisation process.

To help the decision concerning what damage must be applied and where requires some appreciation of ship damage statistics per se. Analysis of currently available damage statistics is considered next.

3. Damage Statistics

Two different sources of damage statistics are investigated to gain a general appreciation of accidents leading to capsize or total loss of the ship. The first source is the UK Marine Accident Investigation Branch (*MAIB (2000, 2001)*) and the second database is that due to *Lutzen (2002)*. The databases are

analysed to provide insight concerning vulnerability to damage, as a function of ship type, and the extent and location of damage.

The pie-charts presented in Figures 1 & 2 and Figures 3 & 4 are based on merchant vessel and fishing boat damage statistics provided by MAIB for different time periods.

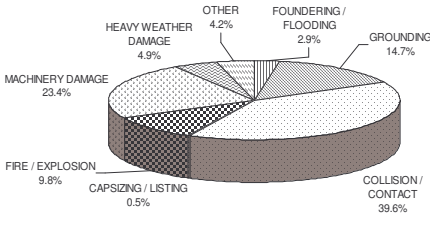


Fig.1: Merchant Ship Statistics 1992-2000.

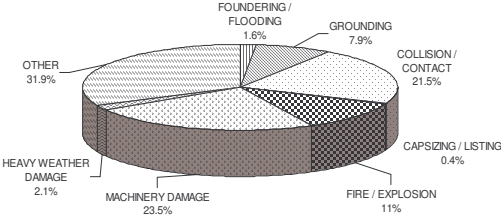


Fig.2: Merchant Ship Statistics 1994-2001.

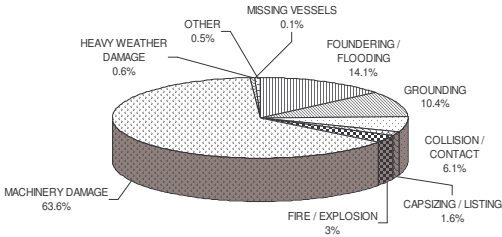


Fig.3: Fishing Boats Statistics 1995-2000.

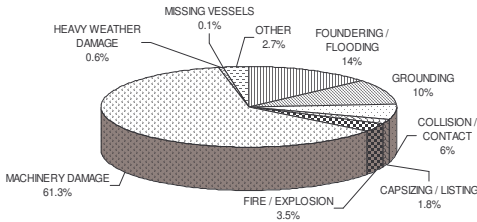


Fig.4: Fishing Boats Statistics 1994-2001.

The significance of machinery damage versus collision/contact changes from Figure 1 to Figure 2 but it is relatively constant in Figures 3 & 4. For fishing boats machinery damage is particularly significant compared with all other causes. For merchant ships collision/contact appears to have reduced due to the increase use of the classification ‘other’.

Within these statistics, ‘damage’ means the damage to the hull structure. Consideration of damage stability appears much more important for merchant vessels than fishing boats.

Since the MAIB statistics do not provide guidance on location and extent of damage, the *Lutzen (2002)* damage database was analysed. Analysis undertaken at Southampton University suggests that general cargo ships, tankers, containerships and bulk carriers account for approximately 85.5 % of all accidents reported and these merchant vessels suffer mostly from collision and grounding. Furthermore general cargo ships, tankers and containerships experience more collisions than other ship types; whereas general cargo ships, tankers and bulk carriers suffer more grounding problems. Statistics concerning the location, extent, height, penetration and vertical position of the damage were determined from the statistics of *Lutzen (2002)* and currently exist as an internal report *Saydan (2003)*. This information is used to create a damaged parent hull and optimised hull in the remaining sections of this paper.

4. The Choice of the Candidate Design

Considerable technical detail is required to model the dynamic motions of a damaged ship since the loss of geometric symmetry necessitates inclusion of cross products of inertia (generally neglected in most intact motion analyses). Such calculations require knowledge of mass distribution. For the fluid-structure interaction, the full 3-D hydrodynamic analysis *Matthew Diffraction Suite* (Hearn 1978) will be applied since trim and heel angle changes and (in later papers) the holed hull due to applied damage are less readily dealt with using strip theory. The *Lutzen 2002* damage statistics imply that bulk carriers have the third highest recorded number of damage incidents. The Derbyshire (for other reasons) has been investigated in some depth and therefore it is readily possible to access the technical details required to undertake a realistic intact and damage analysis.

5. Optimisation Process

Prior to initiating the optimisation procedure, preliminary studies are undertaken to estimate the maximum practical alterations permissible in the primary parameters. The changes that led to impractical transverse sections were identified. Hence the upper and lower bounds on the changes in L and B/T were $\pm 10\%$.

An optimised form of the Derbyshire was generated using the *Optistanbul Suite* (Sarioz 1993). This software represents an extension of the method originally developed at the University of Newcastle upon Tyne. Having provided an initial description of the hull form, only the primary parameters were modified since L and B/T significantly affect the stability characteristics. Generation of alternative hulls in this case is undertaken using linear distortion methods (see Hearn *et al* (1991)). Had secondary parameters been altered, the Lackenby transformation method *Lackenby* (1950) would have been applied.

The objective function selected is the peak relative bow motion (RBM) in head seas subject to the constraint that calm water resistance is not increased. Other constraints imposed were fixed C_B , fixed displacement and fixed depth. As the Hooke and Jeeves algorithm proceeds, the hull form is modified and the resulting hydrostatic properties, resistance (wave and frictional) and RBM values are determined. In this case the process converged after 52 iterations. After the termination of the optimisation process, a family of the candidate designs is created. For the current study, a sub-optimum hull form was selected on the basis that its object function value was midway between that of the parent hull and of the optimal hull. The body form for the parent hull, sub-optimised hull and full optimised hull are presented in Figure 5. Clearly, as the ship is optimised the section curves expand.

The hull form parameters for the parent hull, for the selected sub-optimum design and for the optimum design are presented in Table I. Comparisons of the RBM for these hulls are provided in Figure 6. These motion responses are based upon 3-D hydrodynamic data generated using the *Matthew Diffraction Suite* (Hearn 1978). The quality of the discretisation process is deemed acceptable when the hydrodynamic reactive cross terms, the hydrostatic restoration cross terms and the wave excitation forces and moments determined directly and by means of the Haskind relationship agree to within 1%. The resulting minor differences are removed by averaging the cross terms and the independent measurements of excitation loads. This ensures that no asymmetry is introduced into the equations of motion through the assignment of hydrostatic and hydrodynamic quantities.

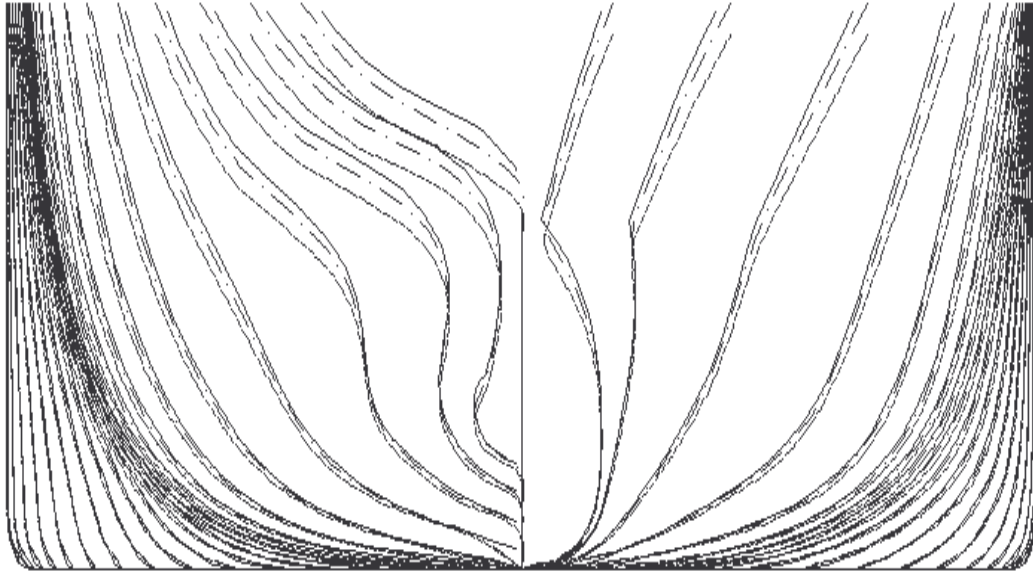


Fig.5: The Parent (continuous), the Sub-optimised (dashed dot) and Optimised (dashed) Hull Forms.

Table I: Parameters for the Parent, Sub-optimum and Optimum Hull Forms.

Geometric Parameters	Parent Form	Sub-optimised Form	Optimised Form
Length Between Perpendiculars (m)	281.94	292.51	310.13
Beam (m)	44.20	44.00	43.99
Draught (m)	17.97	17.32	16.34
Depth (m)	24.99	24.99	24.99
Block Coefficient	0.84	0.84	0.84
Displacement (tonnes)	199480.20	199480.20	199480.20
Resistance (KN)	14617.33	11196.28	14579.87

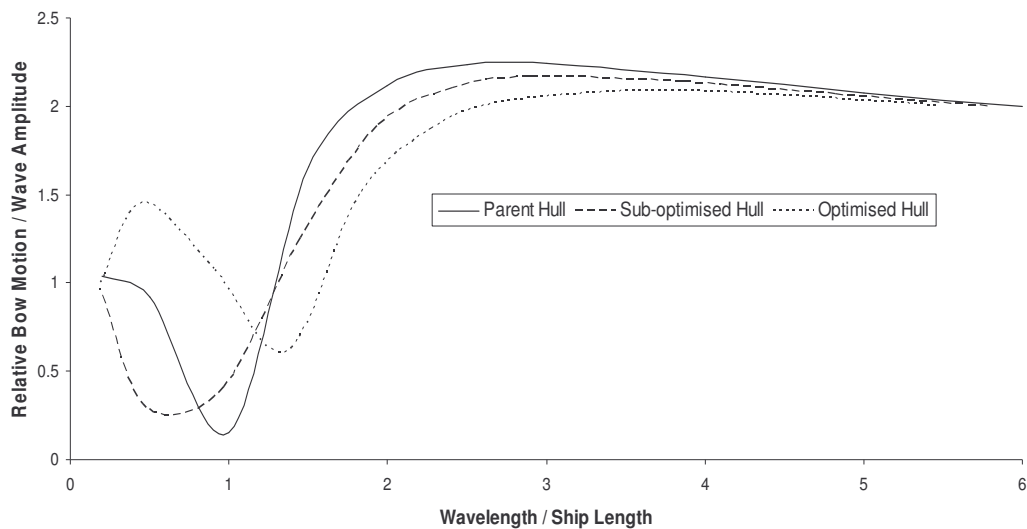


Fig.6: RBM Motion for the Parent, Sub-optimised and Optimised Hull Forms.

6. IMO Intact Stability Requirements and Related Analysis

The IMO intact stability requirements (A-287 criteria) are as follows,

- The area under the GZ curve up to 30 degrees should be equal to/or greater than 0.055 m.rad.
- The area under the GZ curve between 30 and 40 degrees should be equal to/or greater than 0.030 m.rad.
- The area under the GZ curve up to 40 degrees should be equal to/or greater than 0.090 m.rad.
- Initial GM should be equal to/or greater than 0.15m.
- Maximum GZ should be at an angle equal to/or greater than 30° .
- Maximum GZ should be equal to/or greater than 0.2m.

The last three A-287 criteria are not included in the optimisation process, but will be checked in the analysis presented.

The intact stability curves for the parent hull form, sub-optimum and optimum configurations are illustrated in Figure 7. Details related to areas under the intact stability (GZ) curve for these three hulls are presented in Table II.

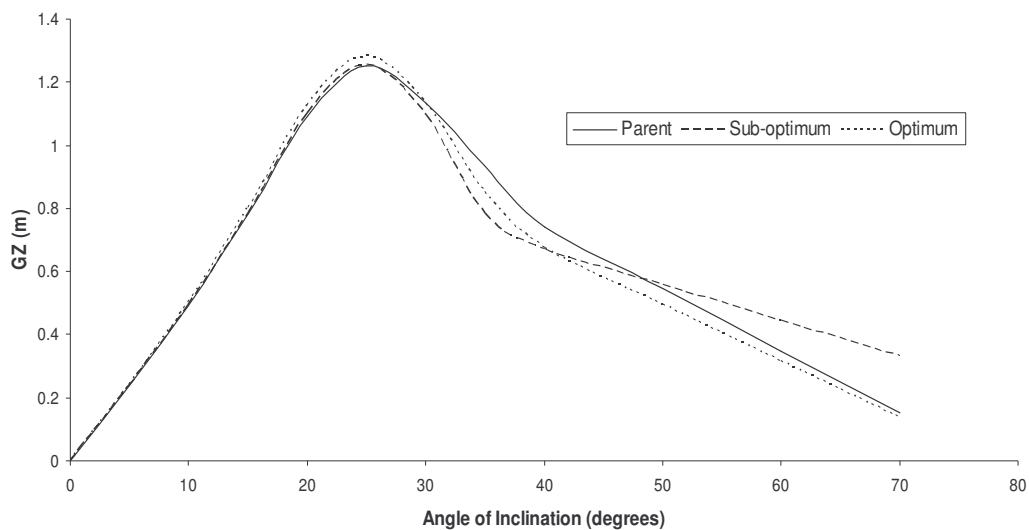


Fig.7: The Intact Stability Curves for the Parent, for its Sub-optimum and Optimum Configurations.

Table II: Calculated IMO Intact Stability Curve Areas.

Area under GZ Curve (m.rad)	Parent Form	Sub-optimised Form	Optimised Form
Up to 30 Degrees	0.379	0.379	0.388
Up to 40 Degrees	0.554	0.532	0.548
Between 30 and 40 Degrees	0.175	0.153	0.160

All three hull forms satisfy the first three cited IMO intact stability area requirements.

The calculated values of the initial GM and the location and value of the maximum GZ are provided in Table III.

Table III: Calculated IMO Intact Stability Curve Properties.

Hull Forms	Initial GM (m)	Angle of the Maximum GZ (degrees)	Maximum GZ (m)
Parent Hull Form	0.471	25	1.250
RBM Sub-optimised Hull Form	0.494	25	1.255
RBM Optimised Hull Form	0.400	25	1.284

According to the cited IMO criteria, all three hull forms significantly exceed the minimum limits for initial GM and for the maximum value of GZ. However, none of the hulls fulfils the angle requirement for location of maximum GZ. Whilst this situation cannot be explained, the use of public domain (rather than actual) hull form geometry allows all but one of IMO conditions to be satisfied. To date the papers accessed on the stability of the Derbyshire do not discuss maximum GZ location properties.

7. Mass Distribution Characteristics of Derbyshire

The longitudinal mass distribution given in *Bishop et al (1990)* leads to a longitudinal centre of gravity (LCG) of 147.6 metres from the aft perpendicular. This does not coincide with the longitudinal centre of buoyancy (LCB). The difference implies a bow down trim. To create a level trim ballast water is added to the wing tanks in holds 9, 8, 7, 6 and in the after peak tank. The resulting longitudinal distribution of mass for the Derbyshire is given in Figure 8.

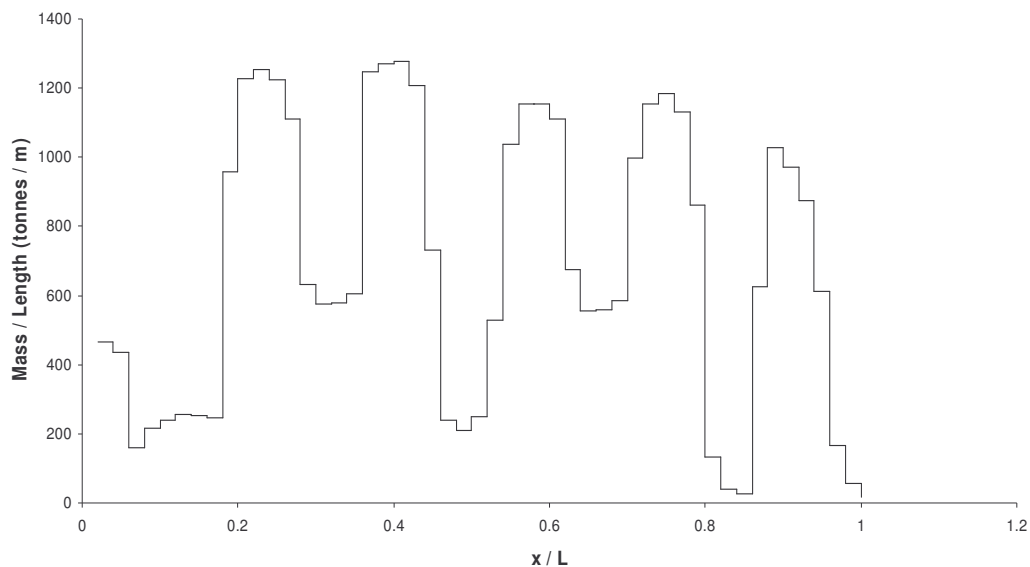


Fig.8: The Longitudinal Mass Distribution of the Derbyshire.

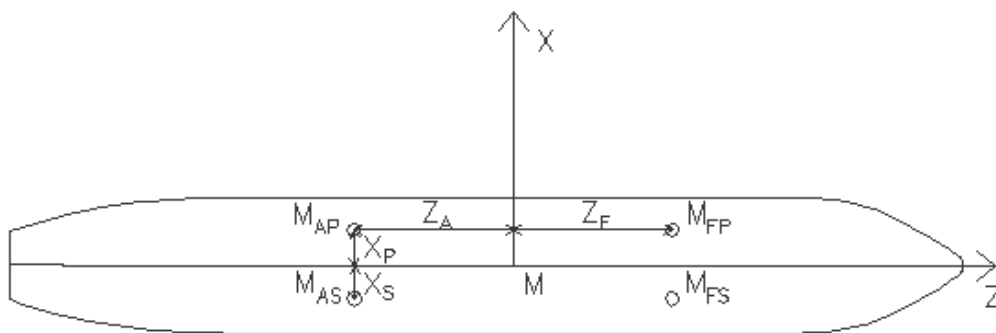
The mass distribution is very peaky and quite unlike the often assumed coffin diagrams. For accurate calculation of the products of inertia, corresponding sectional distributions are required at a representative number of stations. To allow comparison of motion responses for different loading conditions, the equations of motion are usually determined at a reference point other than the centre of gravity. This means that the translational and rotational degrees of freedom are coupled as a consequence of the moments generated by the inertial forces acting through the centre of gravity. On the other hand, the products of inertia are responsible for the coupling of the rotational degrees of freedom. Hence, if one is to compare the motions of a hull in its intact condition with the motion responses of the damaged hull, it will be necessary to determine the products of inertia for at least the damaged ship even if the cross products of inertia are assumed zero for the intact case. Since the

authors were unable to locate any published procedures to complete this task a new proposed method of calculation is suggested.

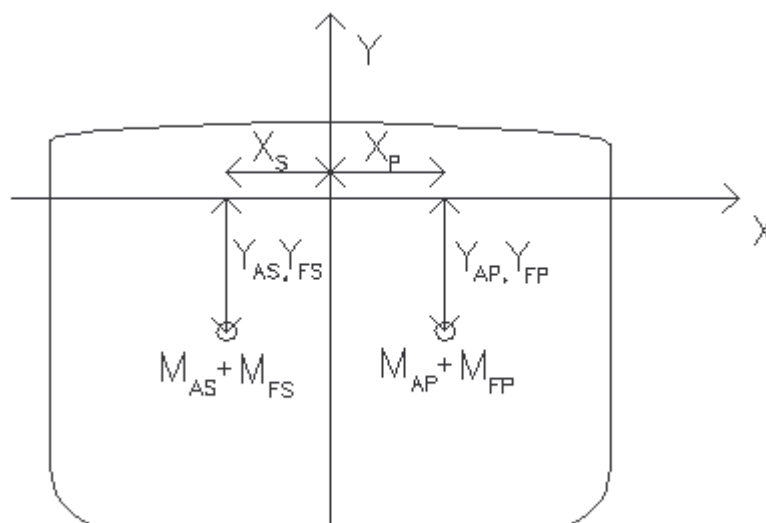
8. Novel Method of Determining the Products of Inertia of a Damaged Ship

The mass moment of inertia calculations are usually undertaken subject to the ‘implicit’ assumption of port-starboard and/or fore-aft symmetry of the ship mass. This results in zero valued products of inertia of the ship. However, this is not the case for the damaged hull form, even if the ship in its intact form displayed such mass symmetry. The water flooding into the damaged compartment(s), the structural loss occurred in the damaged part of the ship and the change of the distances of the unit masses forming the actual mass of the ship will change as a consequence of the resulting trimming and heeling moments. Consequently, the assumed symmetry of the mass with respect to the MZ and MX axes defined in Figure 9 will no longer exist.

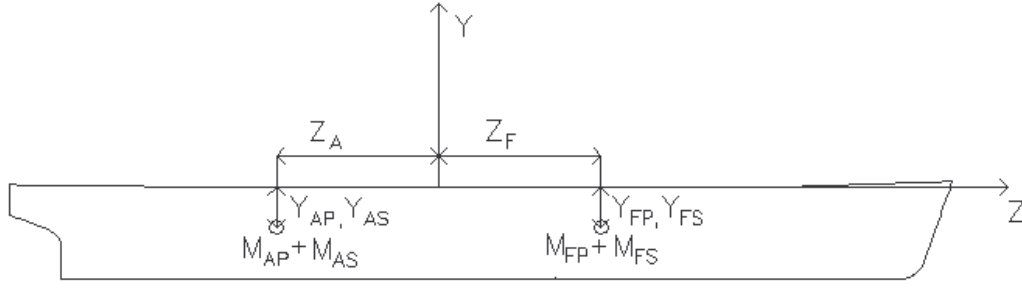
To assist with the task of determining how the products of inertia have changed from their zero intact ship values to their non-zero damaged ship values, the actual total mass of the ship is regarded as being composed of the four representative point masses M_{AP} , M_{FP} , M_{AS} and M_{FS} defined in Figure 9 with respect to the earth-fixed right-handed coordinate system MXYZ. The origin of the mass reference system (M) is located in the still water plane on the longitudinal axis of the intact ship vertically above the centre of gravity.



(a) Plan View



(b) Transverse View



(c) Side View

Fig.9: Total Intact Mass of the Ship Presented as Four Equivalent Point Masses.

Irrespective of the geometry and thus the condition of the ship (intact or damaged), the product of inertias are symmetric; that is, $I_{XZ} = I_{ZX}$, $I_{XY} = I_{YX}$ and $I_{ZY} = I_{YZ}$ (see, for example, *Housner and Hudson (1966)*). Using the point mass equivalence illustrated in Figure 9(a) it follows that:

$$I_{XZ} = M_{AP} Z_A X_P + M_{FP} Z_F X_P + M_{AS} Z_A X_S + M_{FS} Z_F X_S. \quad (1)$$

The right side of the Equation (1) can be equal to zero only if:

$$M_{FP} = M_{FS}$$

and (2)

$$M_{AP} = M_{AS}$$

subject to $X_S = -X_P$.

That is, irrespective of the relationship between Z_A and Z_F , port-starboard symmetry of mass forward and aft of the mid-ship section implies that $I_{XZ} = I_{ZX} = 0$.

Similarly, on appealing to Figure 9(b), it may be argued that:

$$I_{XY} = M_{AS} Y_{AS} X_S + M_{FS} Y_{FS} X_S + M_{AP} Y_{AP} X_P + M_{FP} Y_{FP} X_P. \quad (3)$$

The port-starboard symmetry assumptions of Equation (2) for the intact ship mass distribution implies that

$$I_{XY} = M_{AS} \times X_S \times (Y_{AS} - Y_{AP}) + M_{FS} \times X_S \times (Y_{FS} - Y_{FP}). \quad (4)$$

Clearly, M_{AS} and M_{FS} are positive quantities, X_S is non zero and port-starboard symmetry of the mass also means that $Y_{AS} = Y_{AP}$ and $Y_{FS} = Y_{FP}$. That is, port-starboard symmetry of the mass implies that $I_{XZ} = I_{ZX} = 0$ and $I_{XY} = I_{YX} = 0$.

Thus assuming that port-starboard geometric symmetry implies port-starboard mass symmetry, one can readily appreciate that four of the cross products are zero valued. This is a common assumption when solving the equations of motion of an intact floating structure.

Next, the implications of assuming $I_{YZ} = I_{ZY} = 0$ are considered with the aid of Figure 9(c). The products of inertia I_{YZ} may be written in the form:

$$I_{YZ} = M_{AP} Z_A Y_{AP} + M_{AS} Z_A Y_{AS} + M_{FP} Z_F Y_{FP} + M_{FS} Z_F Y_{FS}. \quad (5)$$

By writing M_A for $(M_{AP} + M_{AS})$ and M_F for $(M_{FP} + M_{FS})$ it follows that:

$$I_{YZ} = M_A Z_A Y_{AS} + M_F Z_F Y_{FS}. \quad (6)$$

If I_{YZ} is to be assumed zero for the intact case, Equation (6) suggests two possibilities. Either the ship may have a fore-aft mass symmetry, which is not the case for most of the ships, or there should be a relationship between Y_{AS} and Y_{FS} to make the equation equal to zero. This point will be discussed again, once equivalent expressions have been generated for the pure moments of inertia.

With M equal to the total mass and k_Y denoting radius of gyration, I_{YY} is usually expressed as:

$$I_{YY} = M k_Y^2 \text{ subject to } k_Y \approx 0.225 \times L, \quad (7,8)$$

where L is the waterline length of the ship (see *Lloyd (1998)*).

I_{YY} may also be written, upon appealing to Figure 9(b), in the form:

$$I_{YY} = M_{AP} (Z_A^2 + X_P^2) + M_{FP} (Z_F^2 + X_P^2) + M_{AS} (X_S^2 + Z_A^2) + M_{FS} (Z_F^2 + X_S^2). \quad (9)$$

Equation (2) implies that:

$$I_{YY} = M_A (Z_A^2 + X_P^2) + M_F (Z_F^2 + X_P^2). \quad (10)$$

Equating Equations (7) and (10) and assuming the veracity of Equation (8) implies that:

$$M_A (Z_A^2 + X_P^2) + M_F (Z_F^2 + X_P^2) = (M_A + M_F) (0.225 \times L)^2. \quad (11)$$

Since the details of the longitudinal mass distribution is usually more readily available than the transverse distribution of the mass, it is reasonable to assume that Z_A , Z_F , M_A and M_F are known. Hence, Equation (11) can be used to determine X_P .

Similarly, I_{ZZ} can be approximated by the formula:

$$I_{ZZ} = M k_Z^2 \text{ with } k_Z \approx 0.4 \times B, \quad (12,13)$$

where B is the maximum waterline beam.

I_{ZZ} can also be written, upon appealing to Figure 9(b), as:

$$I_{ZZ} = M_{AS} (X_S^2 + Y_{AS}^2) + M_{FS} (X_S^2 + Y_{FS}^2) + M_{AP} (X_P^2 + Y_{AP}^2) + M_{FP} (X_P^2 + Y_{FP}^2). \quad (14)$$

Again using Equation (2) with $Y_{AS} = Y_{AP}$ and $Y_{FS} = Y_{FP}$ and equating Equations (12) and (14) results in;

$$M_A \times (X_S^2 + Y_{AS}^2) + M_F \times (X_S^2 + Y_{FS}^2) = M \times (0.4 \times B)^2. \quad (15)$$

Thus both equations (6) and (15) provide a relationship between Y_{AS} and Y_{FS} .

I_{XX} can also be approximated by the formula:

$$I_{XX} = M k_X^2 \text{ with } k_X \approx 0.225 \times L. \quad (16,17)$$

Finally, I_{XX} can also be written in the form:

$$I_{XX} = M_{AP} (Z_A^2 + Y_{AP}^2) + M_{AS} (Z_A^2 + Y_{AS}^2) + M_{FP} (Z_F^2 + Y_{FP}^2) + M_{FS} (Z_F^2 + Y_{FS}^2). \quad (18)$$

Again using Equation (2) with the equivalence of Equations (16) and (18) yields the expression:

$$M_A (Z_A^2 + Y_{AS}^2) + M_F (Z_F^2 + Y_{FS}^2) = M \times (0.225 \times L)^2. \quad (19)$$

Since Z_A , Z_F , M_A and M_F are known from a knowledge of the longitudinal mass distribution (whether it be from actual data or an assumed Coffin diagram), Equation (19) provides a third relationship between Y_{AS} and Y_{FS} . Hence, from Equations (6) and (15) or (19), Y_{AS} and Y_{FS} can be evaluated as there are two unknowns and three independent equations.

The above equations and assumption can be used to determine the equivalent four point masses and related geometric coordinates using the mass distribution of Section 7. The calculations are extremely sensitive to the fineness of the graticule superimposed upon the mass distribution to determine forward and aft total masses and related moments. Once the damage condition has been selected and its impact upon ship attitude determined, the new positions of the point masses and structural changes can be used to determine the cross products of inertia and the new moments of inertia.

9. Damage Stability Analysis

The assignment of damage longitudinally, vertically and horizontally specific to Derbyshire is based on the analysed damage statistics. The damage is relatively minor and will therefore be modelled as a change in mass distribution in the damaged region. Other more complex damage scenarios can be undertaken but it is not necessary to demonstrate the approach adopted and has the advantage of not having to analyse fluid flows within the structure as well as external to the damaged ship. For the sample calculations presented, the damage is assumed to occur on the starboard side of the bow.

With the position and extent of the damage known it is possible to decide where to place the additional weight, which is a combination of the mass of water flooding into the damage compartment(s) and/or the structural loss due to the hull damage. The influence of the additional starboard weight is simply expressed as:

$$M'_{FS} = M_{FS} + w_{add} \cdot \quad (20)$$

The other three distinct point masses remained the same and hence $M'_{AP} = M_{AP}$, $M'_{FP} = M_{FP}$ and $M'_{AS} = M_{AS}$.

The distances of the four distinct masses with respect to the reference origin designated point M change as the ship experiences parallel sinkage, trim and heel. The new positions of the four distinct masses were found by applying an appropriate set of Euler angles.

In order to compare the motion responses of the optimised and non-optimised hulls in the damaged condition, the equilibrium angles have to be iterated correctly. For this reason, the equilibrium angles are determined by combining the lost buoyancy and added weight methods (see, *Saydan (2003)*). The damage properties and the associated angles of heel, trim and parallel sinkage are given in Tables IV and V.

Table IV: The Damage Properties for the Derbyshire and for its Optimum Hull Form.

Damage Properties	Parent Form	Optimised Form
Length of Damage (m)	5.639	6.203
Height of Damage (m)	4.999	4.546
Penetration of Damage (m)	8.800	8.797

Table V: Attitude of the Damaged Derbyshire and its Damaged Optimised Hull Form.

Attitude of the Damaged Structure	Parent Form	Optimised Form
Parallel Sinkage (m)	1.037	0.939
Trim Angle (degrees)	0.964	0.796
Heel Angle (degrees)	1.224	1.273

10. Influence of Damage upon Motion Characteristics

The motion characteristics for the parent and optimised forms of the Derbyshire are obtained using the *Motion Suite (Saydan 2003)*. The hydrodynamics coefficients, hydrostatic restoring coefficients, wave excitation forces and the moments for the equations of motions are evaluated using the *Matthew Diffraction Suite (Hearn 1978)*.

The relative bow motion is non-dimensionalised with respect to the wave amplitude. The relative bow motion characteristics are plotted in Figure 10 for the damaged parent and optimised forms of the Derbyshire.

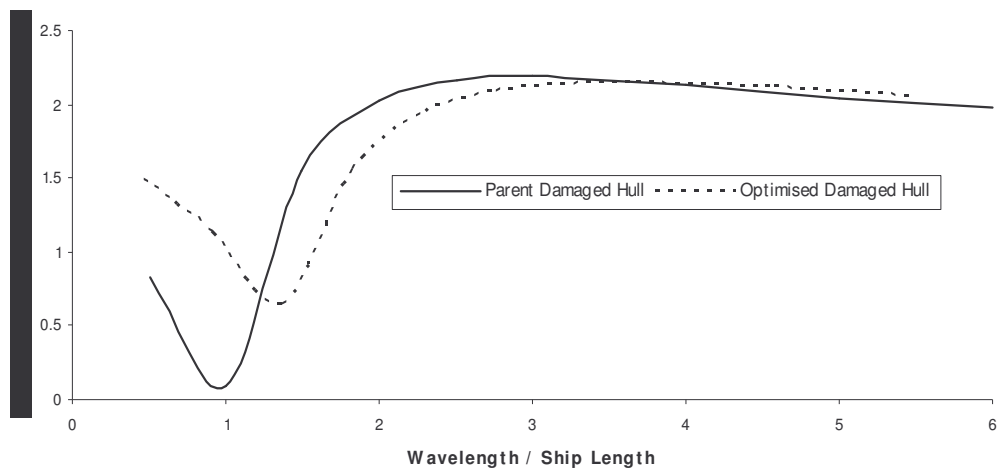


Fig.10: Relative Bow Motion Responses for the Damaged Hull Forms.

Comparison of Figures 6 and 10 indicate that the differences between the intact and damaged hull relative bow motion in head seas for parent and optimised hull forms are very minor. However; whereas the RBM motions of the parent hull form decrease when the structure is damaged, the RBM increases for the damaged optimised hull form relative to the parent optimised hull form. The magnitudes of the changes are small but this is to be expected, since the damage inflicted was itself quite minor and modelled as an addition of a single weight at the starboard bow. For more complex scenarios involving the modelling of the impact of the internal structure on the hydrodynamic reactive and excitation loads would lead to a greater number of terms in the equations of motion being influenced by the existence of damage.

11. Conclusions and Final Comments

The methodology presented includes a novel way of estimating the cross products of inertia of a damaged ship assuming that such terms are neglected in the intact response motion analysis. Simple checks to ensure that practical optimised hull forms are generated have been highlighted. The simple worked example included shows that for a very simple damage scenario, the RBM of the damaged optimised hull form increases whereas RBM of the damaged parent hull is reduced. More complex scenarios modelling the internal structure of the ship within the hydrodynamic analysis due to hull penetration are likely to show more significant changes and perhaps exacerbate the different behaviours of damaged parent and damaged optimised hull forms.

References

- BISHOP, R.E.D.; PRICE, W.G.; TEMAREL, P. (1991), *A theory on the loss of the mv Derbyshire*, Trans. of RINA, Vol 127, pp 389-453
- COOPER, L.; STEINBERG, D. (1970), *Introduction to methods of optimisation*, W.B. Saunders, London, UK
- CRAMER, H.; TELLKAMP, J. (2002), *Towards the direct assessment of a ship's intact stability*, Proc. of 6th International Ship Stability Workshop, Glen Cove, New York, USA
- CRAMER, H.; TELLKAMP, J. (2003), *Towards safety as performance criteria in ship design*, Passenger Ship Safety, pp 17-25, London, UK

DOCTORS, L.J.; DAY, A.H. (1995), *Hydrodynamically optimal hull forms for river ferries*, RINA, Proc. of International Symposium on High Speed Vessels for Transport and Defence, pp 20, London, UK

HEARN, G.E. (1978-onwards), *Matthew Diffraction Suite*, The University of Newcastle upon Tyne, UK

HEARN, G.E.; COLTON, P. (1990-onwards), *Lynette Suite*, The University of Newcastle upon Tyne, UK

HEARN, G.E.; HILLS, W.; COLTON, P. (1988), *Incorporating a seakeeping capability in a computer aided preliminary design system*, Soc. Naval Arch. Mar. Eng STAR Symposium, pp 179-194, Pittsburgh, USA

HEARN, G.E.; HILLS, W.; SARIOZ, K. (1990), *Making seakeeping analysis work for the designer: a new practical approach*, Proc. of SSMH 90, Vol 2, pp.69, pp (69-1)-(69-8), Varna, Bulgaria

HEARN, G.E.; HILLS, W.; SARIOZ, K. (1991), *A hydrodynamic design methodology for conceptual ship design*, Proc. of ICCAS 91, pp. 113-129, Rio de Janeiro, Brazil

HEARN, G.E.; HILLS, W.; SARIOZ, K. (1992), *Practical seakeeping for design: a ship shape approach*, Trans. of RINA Spring Meetings, Vol 134, pp 225-244

HEARN, G.E.; WRIGHT, P.N.H.; HILLS, W. (1994), *Seakeeping for design: the demands of multi hulls in comparison to mono hulls*, Proc. of ICCAS 94, Vol 2, pp 11.125-11.144, Bremen, Germany

HEARN, G.E.; WRIGHT, P.N.H.; HILLS, W. (1995), *Seakeeping for design: development and application of an inverse analysis design methodology to multi hull forms*, RINA International Conference on Seakeeping and Weather, 23 pp, London, UK

HOUSNER, G.W.; HUDSON, D.E. (1966), *Applied mechanics dynamics*, D. Van Nostrand Company, New York,

KEANE, A.J.; PRICE, W.G.; SCHACHTER, R.D. (1991), *Optimisation techniques in ship concept design*, Trans. of RINA, Vol 133, pp 123-139

LACKENBY, H. (1950), *On the systematic geometric variation of ship forms*, Trans. of INA, Vol 92, pp 289-316

LIU, D.; HUGHES, O.; MAHOWALD, J. (1981), *Applications of a computer-aided, optimal preliminary ship structural design method*, Trans. Soc. Naval Arch. Mar. Eng., Vol 89, pp 275-294, USA

LLOYD, A.R.J.M. (1998), *Seakeeping: ship behaviour in rough weather*, Ellis Horwood Limited, London, UK

LUTZEN, M. (2002), *Discussions on damage statistics*, Private Communication

MAIB (2000), *Marine accident investigation branch*, Annual Report, UK

MAIB (2001), *Marine accident investigation branch*, Annual Report, UK

MANDEL, P.; LEOPOLD, R. (1966), *Optimisation methods applied to ship design*, Trans. Soc. Naval Arch. Mar. Eng. , Vol 74, pp 477-521

SARIOZ, K. (1993), *Optistanbul Suite*, The University of Newcastle upon Tyne, UK

SARIOZ, K.; HEARN, G.E.; HILLS, W. (1992), *Practical seakeeping for design: an optimised approach*, Proc. of PRADS 92, Vol 1, pp 1.233-1.246, Newcastle, UK

SAYDAN, D. (2003), *Motion Suite* , The University of Southampton, UK

SAYDAN, D. (2003), *MPhil to PhD Transfer Report*, The University of Southampton, UK

Floodable Length Curves based on Probability of Survival

Maciej Pawłowski, School of Ocean Eng. & Ship Technology, TU Gdansk, mpawlow@pg.gda.pl

Dracos Vassalos, SSRC, Universities of Glasgow & Strathclyde, d.vassalos@na-me.ac.uk

Daria Cabaj, SSRC, Universities of Glasgow & Strathclyde, daria.cabaj@na-me.ac.uk

Cantekin Tuzcu, Universities of Glasgow & Strathclyde, cantekin.tuzcu@na-me.ac.uk

Dimitris Konovessis, Universities of Glasgow & Strathclyde, d.konovessis@na-me.ac.uk

Abstract

The paper reports on calculating floodable lengths understood as lengths of compartments after flooding of which the ship has given value of the factor s , treated as parameter. The factor s represents the conditional probability of a ship surviving flooding the compartment under consideration. At the moment, the floodable lengths are calculated for transverse compartments only. These new types of floodable length curves, accounting for damage stability, have been obtained using NAPA macros, specially developed for the purpose. It is expected that the use of this new curves of floodable lengths will significantly ease the optimisation of ship subdivision in the light of the probabilistic concept, in a similar manner as it was done in the case of the classical curve of floodable lengths, applied widely within the factorial system of subdivision.

1. Introduction

Historically, the classical floodable length curves, accounting only for the damage freeboard defined by the so-called *margin line*, were widely applied in the preliminary design stage for identifying the allowable length of the compartment that protected the ship against excessive sinking beyond the margin line in case of collision damage. However, as the classical floodable length curve does not account for stability of the ship in the damaged condition, it became obsolete with the advent of the probabilistic concept of ship subdivision. Nowadays, it is no longer used.

The paper proposes a new approach for effective ship subdivision at the early stages of design, based on floodable lengths of new type, calculated for a constant value of the survivability factor s , which is treated as parameter in this respect. The floodable length can be basically calculated for a wing compartment with given height, resulting from a fixed horizontal subdivision, for various locations along the ship's length and breadth. At the moment, however, the floodable lengths are calculated for transverse compartments only.

The availability of advanced computational and numerical tools in optimization of the ship has resulted in significant changes in the traditional ship design. The new trends resort to integrated optimization procedures for maximizing ship survivability in the damaged condition. This is basically achieved by designing hundreds or even thousands of alternative ship designs with various layouts but with the same design constraints, and selecting afterwards the best design in terms of profitability and safety. However, to fully consider the performance-based multiple criteria approach to design without excessive calculating times, development of a more direct method is crucial for optimisation of the watertight subdivision. It is expected that floodable lengths can be useful for that purpose, as they remain unchanged for given ship size and form.

2. Probabilistic concept of ship subdivision

One of the principal assumptions of the current probabilistic subdivision regulations is that two different ships achieving the same attained (global) indices of subdivision are equally safe. The global index represents the mean probability of survival for all feasible cases of flooding, comprising single compartments and groups of adjacent compartments. The philosophy behind the probabilistic concept is that two different ships with the same index of subdivision have equal *overall* safety with respect to

flooding, although these ships may have quite different actual capabilities for withstanding damage in some parts of their length. Different capabilities along the length occur, particularly in cases with relatively low values of *A*-indices. To prevent such a situation, the basic requirement regarding the level of the attained *global* index of subdivision should be supplemented by a requirement regarding the distribution of local indices along the ship's length, so that no part of the ship is left with unacceptable vulnerability to flooding.

Protection against local vulnerability is equally as important as overall safety – for passenger ships in particular. Ideally, the ability of any part of the ship to survive damage measured in the form of a *partial* or *local* subdivision index, defined later, should be the same throughout the ship length, but this is rather difficult to achieve. As in the case of the overall index, the rules should set a minimum standard for the value of the local index, best as a fraction of the required value of the global index. On the other hand, insofar as practicable, the regulations, *IMO (1971)*, should not impose unnecessary design restrictions, therefore in the case of cargo ships this requirement might be largely relaxed.

One of the fundamental statements of the probabilistic concept of subdivision of ships is the assumption that the ship is damaged. This is a very important assumption worth emphasizing; it means that the interest is not on the absolute damage safety of the ship or *total* ship safety but on the *conditional* safety. In other words, beyond the interest of knowing how big the risk of collision is that results in flooding or hull breaching, emphasis is placed on the overall safety of the ship in the case of an accidental collision. For this reason, the regulations require the same level of safety irrespective of the area of operation that can be of varying density of shipping (congestion of traffic), and thus of various levels of collision risk. However, some other aspects of shipping (e.g. environmental hazard due to harmful cargo, size of the ship, number of persons on board the ship) can be accounted for in the expression for required level of subdivision, albeit in an approximate manner.

Under such circumstances the probability of a ship surviving a collision is given by the equation for the entire probability:

$$A = \sum_{i \in I} p_i s_i, \quad (1)$$

in which the sum is taken for all cases of flooding in which one, two, three or more adjacent compartments are involved, where *i* is an index representing each compartment or group of compartments under consideration, *I* is the set of all feasible cases of flooding, comprising single compartments and groups of adjacent compartments, *p_i* is the probability that only the compartment(s) under consideration are flooded; and *s_i* is the (conditional) probability of surviving the flooding of compartment(s) under consideration.

It is clear that the summation in equation (1) may cover only those cases of flooding for which both *p_i* and *s_i* are positive (i.e., which contribute to the summation). The *p_i* factor has thus the meaning of the maximum possible contribution of a given compartment group to index *A*. Because the attained subdivision index *A* is the entire probability, therefore

$$\sum p_i = 1,$$

that is, the sum of probabilities of all cases of flooding equals 1. This reflects the fact that the ship is damaged, that is to say, the probability of some damage is certain. The index *A* is therefore the average probability of survival, given that some damage takes place. In other words, the probability of survival, as given by equation (1), is nothing else than the *mean* probability of surviving (the mean *s* factor). Hence, equation (1) can be succinctly written as $A = E(s)$, where *E* stands for the averaging operator. The factors *p_i* in equation (1) are therefore nothing else than weighting factors.

For describing the effectiveness of local subdivision *local* indices of subdivision of two kinds (not in use in the regulations yet), reflecting the degree of subdivision for individual parts of the ship, can be

used. They denote mean probabilities of survival either for the cases of flooding in which a given (wing, if any) compartment is flooded, or in which a given transverse bulkhead is involved. For this reason we talk about *one-compartment indices* of subdivision and *minor damage indices*. The formers express the so-called one-compartment standard on the ground of the probabilistic concept, while the latter, the two-compartment standard, so regarded by the practitioners.

The local (partial) indices of the two kinds are defined by the equations

$$A_j = \frac{\sum p_i s_i}{\sum p_i}, \quad \text{for } j = 1, 2, \dots, n \quad (2)$$

$$B_j \equiv A_{j,j+1} = \frac{\sum p_i s_i}{\sum p_i}, \quad \text{for } j = 1, 2, \dots, n-1 \quad (3)$$

In equation (2) the summations are limited to the cases of flooding in which the given j -th (wing, if any) *compartment* (damage zone) is involved and n is the number of damage zones along the ship length. In equation (3) the summations are limited to the cases of flooding in which the given j -th *bulkhead* is damaged. Hence, like the overall subdivision index, the two kinds of local indices are also the average values of the s -factor corresponding to individual *subsets* of damage scenarios associated with a given compartment or a given bulkhead. Hence, the three expressions for indices of subdivision can be summarized neatly, as follows:

$$\begin{aligned} A &= E(s) \text{ on } I, \\ A_j &= E(s) \text{ on } I_j, \\ B_j &= E(s) \text{ on } I_{j,j+1}, \end{aligned} \quad (4)$$

where E is the averaging operator for the s -factor, whereas I_j and $I_{j,j+1}$ are subsets of the set I that are connected, made up of the cases of flooding in which a given j -th compartment (pair of compartments) is involved alone or with any combination of adjacent compartments. The idea of local indices is simple in practical application as it makes use of previously calculated values of p_i and s_i needed for determination of the overall subdivision index A , Pawlowski (1997), Karaszewski and Pawlowski (2003).

3. New floodable length curves

The most difficult part of the probabilistic regulations is the calculation of the stability related factor s . For a typical ship, even with not a particularly complicated subdivision, there are normally hundreds of cases of flooding, for which it is necessary to calculate each time the stability of the ship with a flooded compartment or group of compartments that is obviously tedious and time consuming. Here arises then a question whether these calculations could be significantly reduced.

It seems that there is such a possibility if we resort to the idea of a floodable length for the compartment, well established in the old factorial system. The traditional *floodable length curve* indicates a maximum length of the compartment under consideration that can be symmetrically flooded at given location along the ship length without immersing the margin line, Lewis (1988). As the traditional curve does not account for damage stability, it is useless for designing subdivision of the ship, based on the probabilistic concept and is, therefore, no longer used. Following the same idea, it is possible now to define a floodable length understood differently as a maximum length of the compartment under consideration at given location along the ship length after flooding of which the ship assumes given values of the factor s , say $s = 0, 0.5$, and 1 . Hence, instead of the distinct old curve of floodable length, we obtain now a fuzzy curve, with a lower band defined by $s = 1$, and an upper band, defined by $s = 0$, as it is shown in Fig.1. The factor s can be SEM- or GZ-based, according to the newly proposed harmonised regulations for damage stability calculations (SLF 47).

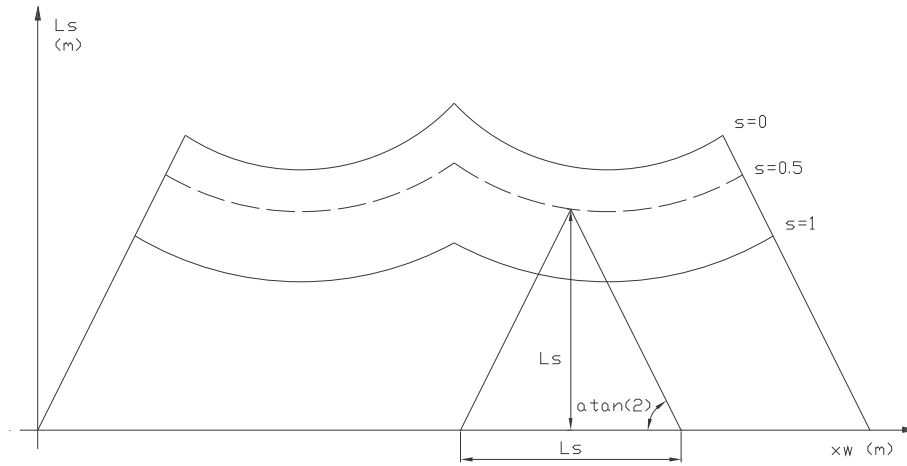


Fig.1: Floodable lengths accounting for damage survivability via factor s

4. Calculation of the s factor in NAPA

According to the SEM, the factor s is a function of the water head h on the vehicle deck, understood as the elevation of water on deck above the sea level at the critical heel of equilibrium, as shown in Fig.2. The critical heel is such at which the heeling moment exerted by water on deck reaches maximum. The said elevation has been calculated with the help of NAPA, where space on the vehicle deck is treated like an undamaged tank, containing some amount of liquid cargo. The heeling moment is created by weight of the total amount water on deck p_3 (blue and yellow colours in Fig.2), passing through its centre of gravity C_3 .

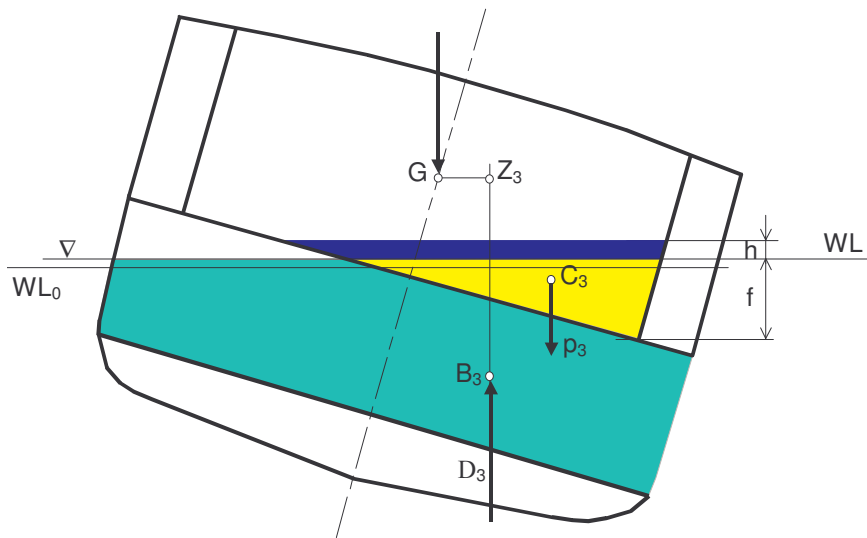


Fig.2: Calculation of heeling moment by NAPA

The entire weight of the ship, including weight of water on deck, is balanced by the entire buoyancy force $D_3 = D + p_3$ below the actual waterplane, including buoyancy given by the undamaged vehicle deck (yellow colour in Fig.2). The entire buoyancy force passes through the centre of buoyancy B_3 for the ship damaged only below the vehicle deck. Hence, the resulting moment (restoring) is given by:

$$M = D_3 GZ_3 - p_3 l_3, \quad (5)$$

where GZ_3 is the righting arm for a freely floating ship, with the undamaged vehicle deck, p_3 is weight of total water on deck, and l_3 heeling lever due to water on deck, equal to the horizontal dis-

tance between centre of gravity of the intact ship G and centre of gravity of water on deck C_3 , measured perpendicularly to the axis of rotation. For the ship at equilibrium, the above equation yields

For the ship at equilibrium, the above equation yields

$$v_3 l_3 = V_3 GZ_3, \tag{6}$$

where v_3 is total volume of water on deck, and V_3 is volume displacement of the ship with the undamaged vehicle deck.

The outcome of the calculations for given amount of water on deck is the angle of loll ϕ , trim, water head h , freeboard f at the opening at the heel angle (depth of the deck edge), volume of the elevated water v_{el} , etc. Knowing volume of the elevated water the sinkage of the ship δT can be found from equation $\Delta T = v_{el}/A_{WLd}$, where A_{WLd} is the (mean) waterplane area, excluding the part occupied by the water. Next, running software again, the traditional righting lever GZ can be found, corresponding to the damaged waterplane WL_0 (before parallel sinkage), shown in Fig.2, with free flooded water on the vehicle deck up to WL_0 , *Pawlowski and Tuzcu (2004)*.

A macro called “list .critwod_CT_ACV8”, calculating the factor s based on the elevation of water on deck, as described in the foregoing, was used as a subroutine in a floodable lengths macro.

5. A sample ship

For fast calculations of the floodable lengths a computer program is needed, iterating length of the compartment under consideration so as to get an assumed value of the factor s . Rather than developing a special program it was decided to write an automatic macro (*NAPA Basic*). The methodology was tested using a sample ship (PRR1), taken from the ROROPROB project, *Lefebvre and Dauce (2004)*. All calculations were performed with the assistance of NAPA – naval architects software.

Table I: Main particulars of the sample ship

Overall length	194.30 m
Length between pp	170.00 m
Breadth	27.80 m
Design draught	6.23 m
Car deck high	8.80 m
Displacement to summer draught	16949.50 t
KG	12.892 m
GM intact	2.91 m
Permeability of cargo spaces	0.90

For testing the methodology for calculating the floodable lengths a general arrangement for the ship investigated `FLS_ARR` was generated that is shown in Fig.3. Once the general arrangement is defined (without internal transverse compartments), a set of calculation is performed, varying length of the compartment under consideration: `comptest_fl` so as to attain the length of the compartment resulting in given value of the factor s for the loading condition given in Table I. To obtain the results along the whole ship’s length, longitudinal position of the compartment was varied. The permeability for all the compartments was assumed to be 90%.

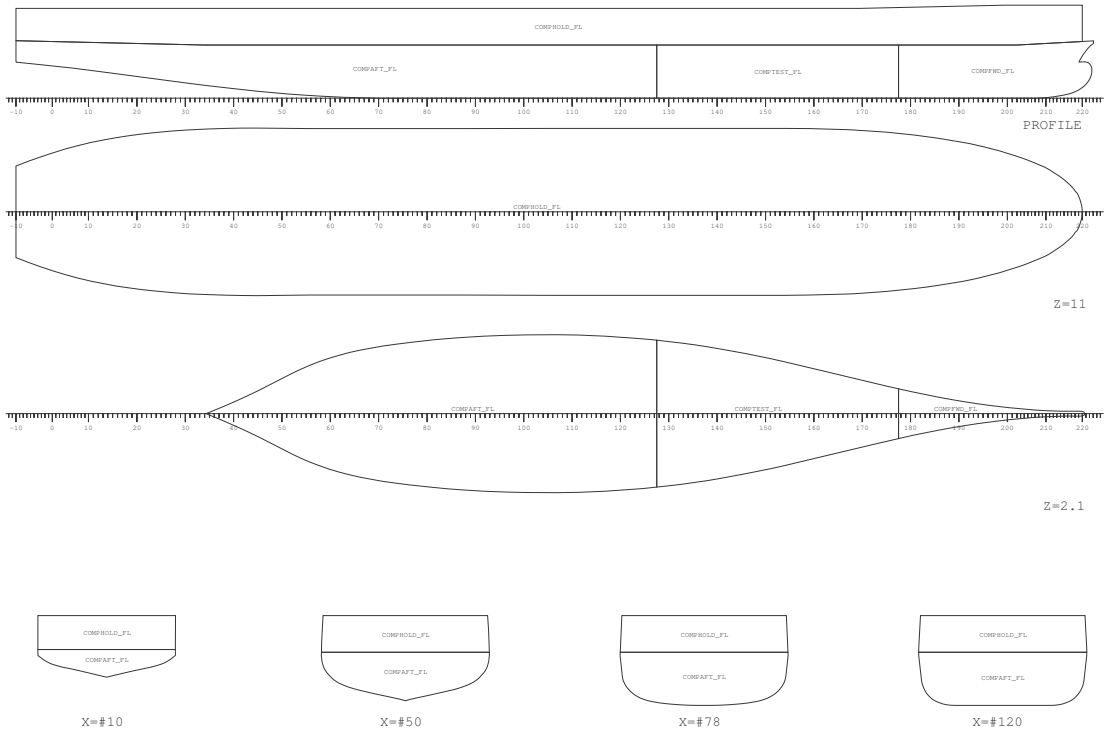


Fig.3: FLS_ARR arrangement for the sample ship

6. Results and discussion

Fig.4 to 6 present the output of the FLS macro for one loading condition, corresponding to the summer draught and $KG = 12.892$ m. In addition to floodable lengths for a range of the s_i values, defined by the SEM and draft SOLAS regulation II-1/7-2, *SLF-ISCG (2004)*, for comparison purposes curves corresponding to $GZ_{max} = 0$ and $GZ_{max} = 0.12$ m are also shown. For reference, the traditional floodable lengths are presented as well. Longitudinal location of the compartment was varied by 5 to 10 m.

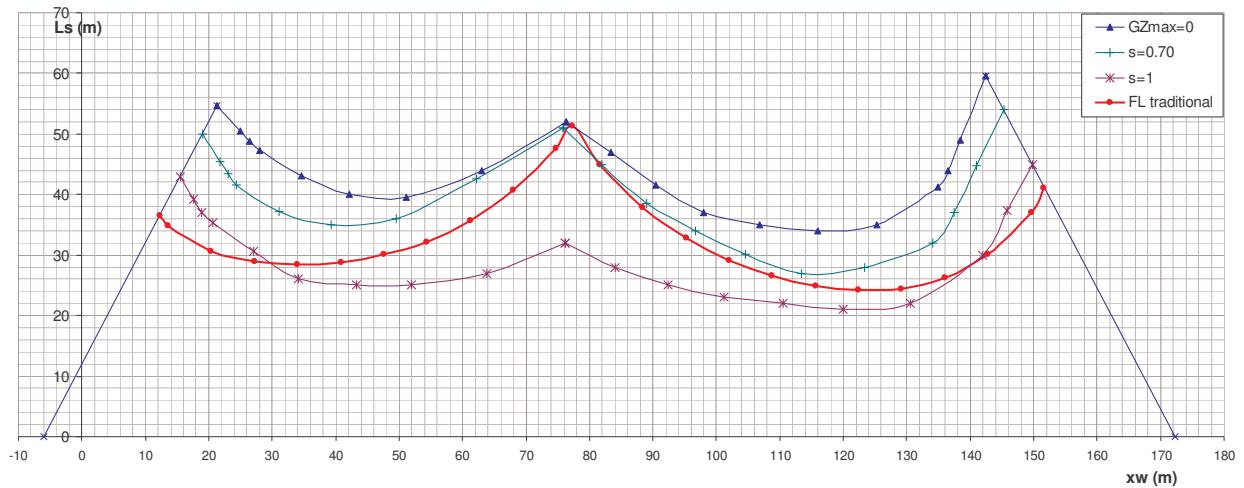


Fig.4: Floodable lengths according to 'SEM macro'

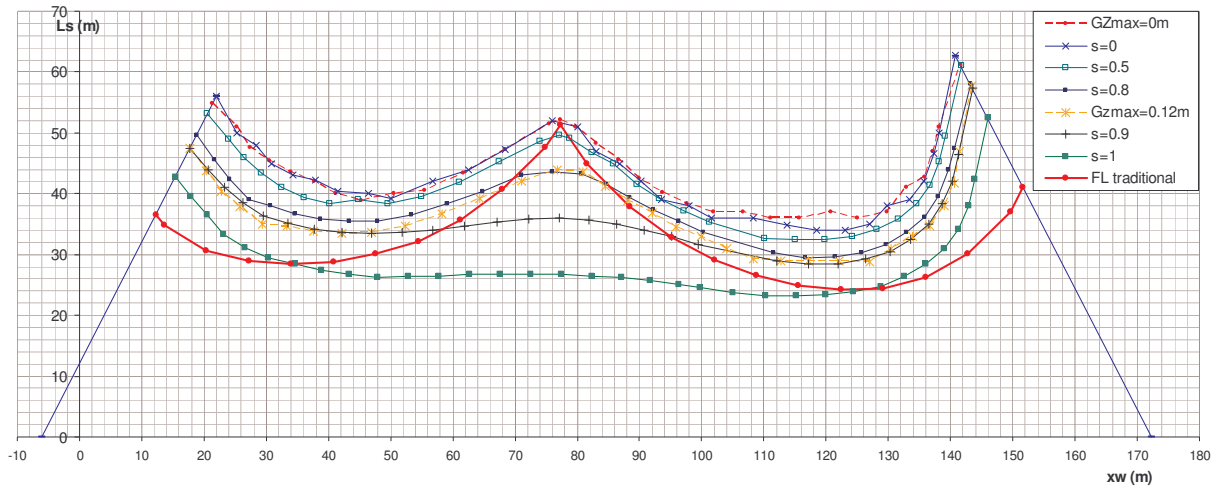


Fig.5: Floodable lengths according to draft SOLAS regulation II-1/7-2

It is amazing that the traditional floodable length curve yields the upper band values ($s = 0$) for a midships compartment, when the ship is at a level keel after flooding, whereas for compartments away the midships the values shift towards the lower band ($s = 1$) or even less for end compartments. This is a result of the increase of residual stability for a trimmed ship.

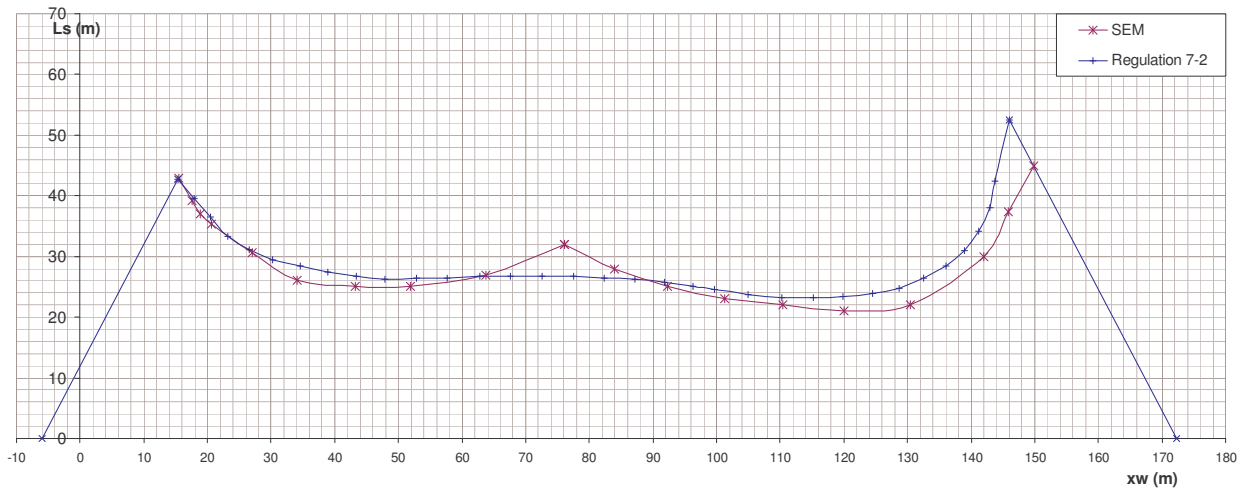


Fig.6: Floodable lengths for $s = 1$ according to 'SEM macro' and draft SOLAS regulation II-1/7-2

The NAPA environment appears to be not stable. Also a bug in the compiler was found, probably in line numbering sequence. The instability of calculations increases particularly for a small tolerance of the results. As a consequence of this instability, for the same case and the same initial condition results might vary quite significantly. The same instability is obviously exhibited by the macro used for calculating floodable lengths. The reason for the said instability can be attributed chiefly to the indirect method used for calculating the heeling moment due to water on deck, described briefly in section 0. To make the calculation procedure fast and accurate, this procedure should be based on a direct method of calculating the heeling moment, resorting to the mechanism of the heeling moment due to water on deck, as discussed in *Pawlowski and Tuzcu (2004)*.

Values of floodable length for $s = 1$ according to 'SEM macro', shown in Fig.4, are approximate. Due to the time-consuming process, a rough tolerance had to be applied. The same applies as well to a curve for $s = 0$, based on $GZ_{max} = 0$. For other s values there was no problem with convergence.

Maximum values of the floodable lengths, irrespective of the condition used, occur for the same longitudinal location of the compartment, around a midships, after flooding of which the ship floats at a level keel.

7. Conclusions

New curves of floodable lengths based on the factor s open up a new way of addressing efficiency of subdivision. Floodable lengths are inherent characteristic of the ship and can be calculated in advance before optimising the watertight subdivision of the ship. While calculating the indices of subdivision, the required values of the factor s can be obtained by interpolation. The current macros developed for calculating these curves have to be reviewed to account for better performance.

Curves of floodable lengths allow for easy illustration of the various effects, such as the effect of intact freeboard, a change of intact stability (variation of the KG value), the effect of deck sheer, and so on, which were not illustrated here. The current research was focused on exploring the problem.

The floodable lengths are calculated at the moment for transverse compartments but can be calculated also for wing compartments of given breadth and location along the ship's length. As the compartment in such a case is described by two independent variables: the longitudinal location and breadth, the floodable length is also a function of these two variables. A graph of such a function represents a surface in a two-dimensional domain, which by analogy to the previous curve can be called as "the surface of floodable lengths". It is expected that the use of such concepts will ease significantly the optimisation of ship subdivision

Acknowledgements

The first author stayed over a period of three months from July to September 2004 as academic visitor at the SSRC. The Overseas Research Student Award and the University of Glasgow is acknowledged for the financial support throughout the duration of studies of Miss Daria Cabaj.

References

- GRAHAM, A.; TUZCU, C. (2003): *The use of probabilistically based regulations in determining the level of subdivision and damage stability*, Total ship safety course, Ship Stability Research Centre/Safety at Sea Ltd
- IMO (1971), Resolution A.265 (VIII): *Regulation on subdivision and stability of passenger ships*
- KARASZEWSKI, Z.; PAWŁOWSKI, M. (2003): *A general framework of new subdivision regulations*, 8th Int. Marine Design Conf. IMDC 2003, , Athens, Vol. I, pp. 254-265
- LEFEBVRE, Y.M.; DAUCE, F. (2002): *Probabilistic Rules-Based Optimal Design of Ro-Ro Passenger Ships*, ROROPROB project, Optimisation tool – user guide WP3
- LEVIS E.V. (1988): *Principles of Naval Architecture, Vol. I Stability and Strength.*, SNAME, pp. 149-158
- SLF–ISCG (2004): *Calculation of the factor s_i* , Draft SOLAS regulation II-1/7-2
- PAWŁOWSKI, M. (1997): *Outline of probabilistic concept of Ship Subdivision*, Department of Naval Architecture & Offshore Engineering, Technical University of Denmark
- PAWŁOWSKI, M.; TUZCU, C. (2004), *Stability of the ship with water on deck*, to be published in Marine Technology

Numerical Models of Water Impact

Hajime Kihara, National Defense Academy, Japan, hkihara@nda.ac.jp

Abstract

This paper presents a numerical method for studying water impact of a two-dimensional body of arbitrary cross-section. The global simulation procedure based on the boundary element method is constructed. The attention is focused on the computational description of the jet flow in the framework of a potential flow assumption. The proposed computational model makes the numerical analysis more stable, in addition, enables the simulation of the flow deformation due to the gravity effect. Water impact problems due to the vertical impulsive motion of an initially floating body are considered. The prediction of hydrodynamic pressure is found to be in good agreement with similarity solutions for wedges with different dead-rise angle.

1 Introduction

Water impact is one of the critical phenomena from a viewpoint of the structural design of ships or offshore structures. Since the further development of von Karman's theory was made by Wagner (1932), considerable attention has been turned to broad studies on the water impact problems. The similarity solutions for a two-dimensional wedge were first obtained by Dobrovolskaya (1969), which were the complete ones based on the nonlinear theory. The jet flow is generated due to the impulsive motion of a floating body or the water entry of a body. It is one of characteristic features in water impact phenomena. The theoretical approach using asymptotic expansions can recover the effect of the jet flow, which was made by, for example, Armond and Cointe (1987), Howison et al. (1991), Chapman et al. (1997), Faltinsen (2002), and Iafrati and Korobkin (2002). As related works, the compressibility of the fluid in a moment of impact was discussed by Korobkin (1996)(2004). On the other hand, the numerical approach by the boundary element method (BEM) is also one of practical procedures in which the jet region can be taken into account. However, it is well-known that the velocity is singular at an intersection between the body and the free surface. The ordinary computation often gives rise to some problems on the accuracy or the stability of solutions. Accordingly, it is one of challenging issues how the jet flow is dealt with in computation.

Zhao & Faltinsen (1993) proposed the so-called "cut-off" model, in which a new computational segment is introduced at the jet root position and the upper part of the jet region is removed from the computation. This model provides so good prediction of the hydrodynamic pressure on wedges with various deadrise angles that it is adopted in the studies by Lu et al. (2000) and Battistin and Iafrati (2003). This operation is very practical from an engineering viewpoint, because the hydrodynamic pressure on the body in the jet region is almost equal to atmospheric one. As studies with the similar concept where the jet flow was ignored, the practical method based on the generalized Wagner theory was presented by Zhao & Faltinsen (1996) and Mei et al. (1999). However, as the jet flow is cut off at the spray root, we cannot obtain the information, for instance, the evolution of the jet flow and the separation from the body surface. Recently the interesting method that can make up with the drawback of the model was presented by Battistin and Iafrati (2004). The jet region is divided into several small panels and the velocity potential on each panel is computed by using local Taylor expansions and matching with the other domain.

The present study is intended to develop the numerical procedures by the BEM, by which we can describe the evolution of the jet flow in the water impact as well as the prediction of the hydrodynamic pressure. For this purpose, we introduce a computational model about the jet flow. It is regarded as a kind of cut-off models, but the cut-off operation is restricted only to

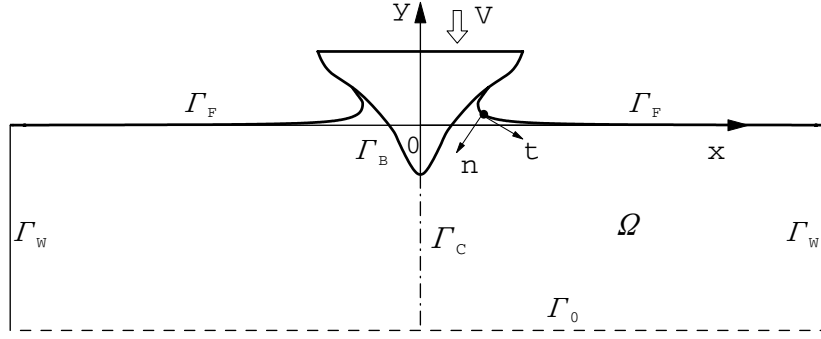


Fig. 1: Definition of coordinate system.

the jet tip in order to keep the computed information. Our idea may be conceptually similar to the model by Fontaine & Cointe (1997), although their computational results near jet tips are different from ours judging from their published results. As we describe this computational model of the jet flow in section 2.3.2, we'd like to emphasize that such a manner is arbitrary to some extent. It suggests that the exact description of the flow is not always necessary within the jet region.

2 Numerical simulation for water impact

2.1 Formulations of problems

We consider the water entry problem of a two-dimensional symmetrical body, in which the initially floating body on the free surface moves down with impulsive vertical motion, that is, abruptly starting motion. The x and y axes are taken along the undisturbed free surface and along the body centerline pointing upward, respectively, as is shown in Fig.1. The water entry velocity $\mathbf{v}_B = -V\mathbf{e}_y$ is assumed to be constant during the impact, the \mathbf{e}_y being the unit vector along the y -axis. The fluid domain Ω is surrounded by boundaries consisting of the free surface Γ_F , the body surface Γ_B , side walls Γ_W , and the bottom Γ_0 . Assuming the fluid is incompressible and the flow is irrotational, the fluid motion is specified by the velocity potential ϕ . The problem of the velocity field is governed by the following equations:

$$\nabla^2\phi = 0 \quad \text{in } \Omega \quad (1)$$

$$\frac{\partial\phi}{\partial n} = \mathbf{v}_B \cdot \mathbf{n} = -Vn_y \quad \text{on } \Gamma_B \quad (2)$$

$$\frac{D\phi}{Dt} = \frac{1}{2}|\nabla\phi|^2 - gy \quad \text{on } \Gamma_F \quad (3)$$

$$\frac{D\mathbf{x}}{Dt} = \nabla\phi \quad \text{on } \Gamma_F \quad (4)$$

$$\frac{\partial\phi}{\partial n} = 0 \quad \text{on } \Gamma_W, \Gamma_0, (\Gamma_C) \quad (5)$$

where g is the acceleration of gravity and the position vector of arbitrary point in the domain is expressed by $\mathbf{x} = (x, y)$. The gravity term in equation (3) is retained for the realistic description of the problem, while it is neglected in ordinary analysis on the water impact because the gravity effect is considered small during the impact.

The hydrodynamic pressure can be computed by using the Bernoulli equation. On that occasion, the time derivative of the velocity potential is necessary. Although it can be obtained by using

the finite difference method to the velocity potential, the computational accuracy of the pressure is generally said to be not good. For more accurate prediction, the boundary value problem as for $\partial\phi/\partial t = \phi_t$ is also considered in the present study. The validity of such an approach is demonstrated widely, for example, in results of the ISOPE benchmark test (1999). Such a boundary problem related with the acceleration field can be described as follows:

$$\nabla^2 \phi_t = 0 \quad \text{in } \Omega \quad (6)$$

$$\frac{\partial \phi_t}{\partial n} = \kappa |\nabla \phi|^2 + \frac{\partial \phi}{\partial n} \frac{\partial^2 \phi}{\partial s^2} - \frac{\partial \phi}{\partial s} \frac{\partial}{\partial s} \frac{\partial \phi}{\partial n} \quad \text{on } \Gamma_B \quad (7)$$

$$\phi_t = -\frac{1}{2} |\nabla \phi|^2 - gy \quad \text{on } \Gamma_F \quad (8)$$

$$\frac{\partial \phi_t}{\partial n} = 0 \quad \text{on } \Gamma_W, \Gamma_0, (\Gamma_C) \quad (9)$$

where $\partial/\partial s$ is the tangential derivative along the boundary, and κ denotes the local curvature of the body contour. The general form about the normal derivative of ϕ_t on the body in motion was shown by Tanizawa (1995). The condition is simplified to equation (7) for the translational motion with constant velocity. Although the similar conditions are shown by by Cointe et al. (1990), van Daalen (1993) and Wu and Eatock Taylor (1996), these lead to the same condition for a body shape without curvature like a wedge.

The initial conditions of the free surface are necessary to complete the problems. Although the small portion of the body is already submerged into water, there is no initial disturbance on the free surface. Such conditions are given by:

$$\phi = \phi_t = \eta = 0 \quad \text{on } \Gamma_F \quad \text{at } t = 0 \quad (10)$$

where η denotes the free surface elevation. The treatment of the initial condition is important to discuss the nonlinear wave-body interaction due to the impulsive motion, because the prediction of the hydrodynamic pressure on a body is affected at the early stage of the impact. This point is discussed more in section 2.3.1, and the practical approach to complement such influence is presented in section 4.

Thus the water entry problems of a body are formulated as the initial value - boundary value problems. Considering the symmetrical property of the problem, we can reduce the fluid domain to analyze to half, that is, the fluid domain in $x \geq 0$, where the boundary Γ_C on the y -axis is newly complemented.

2.2 Numerical procedures

2.2.1 Solution procedure of integral equation

Two sets of boundary value problems in equations (1)-(5), (6)-(9) can be solved using the BEM. Applying Green's theorem to the boundary value problems, the integral equations with the same form are derived as follows:

$$C(\boldsymbol{\xi}) \begin{Bmatrix} \phi(\boldsymbol{\xi}) \\ \phi_t(\boldsymbol{\xi}) \end{Bmatrix} + \int_{\Gamma} \begin{Bmatrix} \phi(\boldsymbol{x}) \\ \phi_t(\boldsymbol{x}) \end{Bmatrix} \frac{\partial G(\boldsymbol{\xi}, \boldsymbol{x})}{\partial n(\boldsymbol{x})} d\Gamma(\boldsymbol{x}) = \int_{\Gamma} \begin{Bmatrix} \phi(\boldsymbol{x}) \\ \phi_t(\boldsymbol{x}) \end{Bmatrix} d\Gamma(\boldsymbol{x}) \quad (11)$$

where $\boldsymbol{\xi}$ and \boldsymbol{x} are an observation point and an integral point, respectively. The free term $C(\boldsymbol{\xi})$ is given by:

$$C(\boldsymbol{\xi}) = - \int_{\Gamma} \frac{\partial G(\boldsymbol{\xi}, \boldsymbol{x})}{\partial n(\boldsymbol{x})} d\Gamma(\boldsymbol{x}) \quad (12)$$

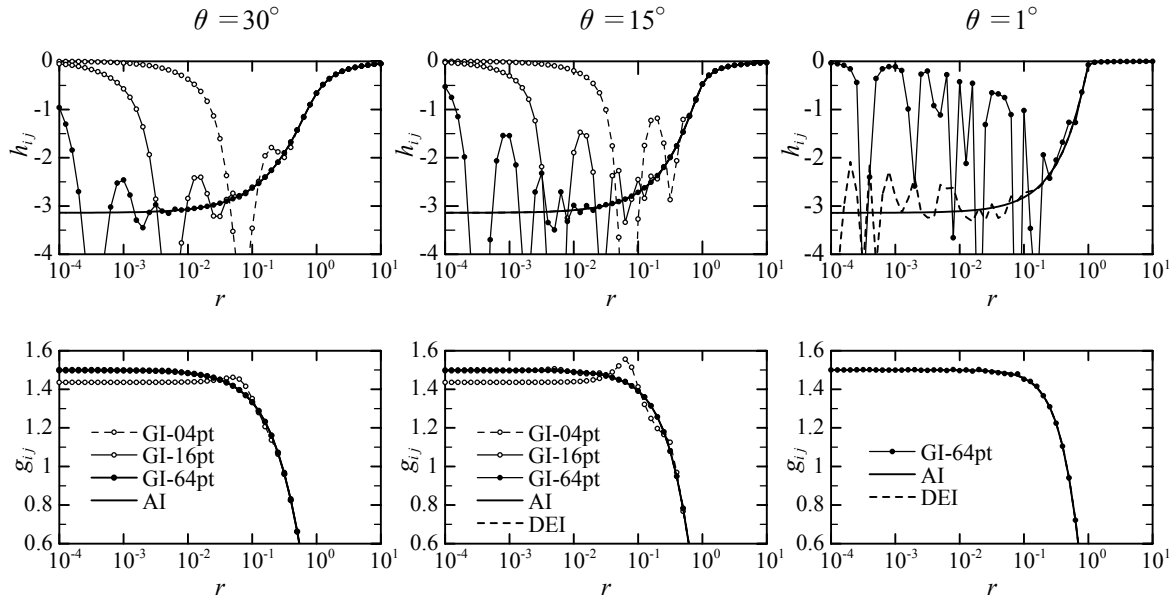


Fig. 2: Evaluation of influence coefficients for the distance r and the angle θ between $(\mathbf{x} - \boldsymbol{\xi}_i)$ and $(\mathbf{x}_{j+1} - \mathbf{x}_{j-1})$, where the internal angle between Γ_j and Γ_{j+1} is π and the length of each element is unity. GI:Gaussian integration, AI:Analytical integration, DEI:Double exponential integration.

The integral contour Γ means the boundary surrounding the fluid domain, that is, $\Gamma = \Gamma_B \cup \Gamma_F \cup \Gamma_W \cup \Gamma_C$. It is noted that the bottom boundary Γ_0 is excluded from computation here. Then the Green function $G(\boldsymbol{\xi}, \mathbf{x})$ is expressed by using the source as follows:

$$G(\boldsymbol{\xi}, \mathbf{x}) = \frac{1}{2\pi} \ln \frac{1}{|\mathbf{x} - \boldsymbol{\xi}|} + \frac{1}{2\pi} \ln \frac{1}{|\mathbf{x} - \boldsymbol{\xi}^*|} \quad (13)$$

where $\boldsymbol{\xi}^*$ denotes the image point of $\boldsymbol{\xi}$ about the bottom Γ_0 . Additionally, the boundary Γ_C can be excluded from the computation by introducing other source images. However, it doesn't result in the effective reduction of computational time in using the free surface boundary with a long distance.

The linear isoparametric elements are used for the discretization of the boundary Γ in the present study. Adjacent nodes \mathbf{x}_j and \mathbf{x}_{j+1} connect an element Γ_j , on which the variations of both the geometric shape and the physical quantity, such as the velocity potential, are assumed linear. The influence coefficients can be evaluated by the following equations:

$$h_{ij} = \int_{\Gamma_j} f^{(2)}(l) \frac{-1}{r(l)} \frac{\partial r(l)}{\partial n} d\Gamma(l) + \int_{\Gamma_{j+1}} f^{(1)}(l) \frac{-1}{r(l)} \frac{\partial r(l)}{\partial n} d\Gamma(l) \quad (14)$$

$$g_{ij} = \int_{\Gamma_j} f^{(2)}(l) \ln \frac{1}{r(l)} d\Gamma(l) + \int_{\Gamma_{j+1}} f^{(1)}(l) \ln \frac{1}{r(l)} d\Gamma(l) \quad (15)$$

where $r = |\mathbf{x} - \boldsymbol{\xi}_i|$, the variable l is the local coordinate along each element, and $f^{(1)}(l)$ and $f^{(2)}(l)$ are interpolation functions which are given by:

$$f^{(1)}(l) = \frac{1}{2}(1 - l), \quad f^{(2)}(l) = \frac{1}{2}(1 + l), \quad -1 \leq l \leq 1 \quad (16)$$

The computational accuracy of these integrals is extremely important in the BEM analysis. Some results of the evaluation for equations (14) and (15) are shown in Fig.2. Since we have to deal with the special geometric shape of the jet region in water impact problem, it is guessed that the numerical integration leads to the instability easily. Therefore the analytical integration

is adopted in the present study. When the integrals in equations (11) and (12) are performed on each element, the following matrix equations concerning the velocity potential and its flux can be derived:

$$[H_{ij}] \{\phi_j\} = [G_{ij}] \{\phi_{nj}\} \quad (i, j = 1, 2, \dots, N) \quad (17)$$

where ϕ_n denotes the normal derivative of the velocity potential and H_{ij} and G_{ij} are the influence coefficients in using equation (13). On the free surface Γ_F , the velocity potential is known and its flux is unknown. On the other hand, the velocity potential is unknown and its flux is known on the other boundaries. Transforming equation (17) to the simultaneous equations concerning unknowns, we can solve these numerically by using an ordinary scheme for the linear system, such as the Gaussian elimination method. As for ϕ_t and its flux ϕ_{tn} , we can solve in the same manner as the problem for the velocity field. Since the influence coefficients in equation (17) are available in common, it does not lead to increase of large computational loads.

Once the boundary value problem of velocity field is solved at a certain time step, the boundary conditions of the boundary value problem for ϕ_t can be set. Solving two kinds of boundary value problems, we can compute the pressure on a body by:

$$\frac{p}{\rho} = -\frac{\partial\phi}{\partial t} - \frac{1}{2} |\nabla\phi|^2 - gy \quad (18)$$

where ρ is the fluid density. The hydrodynamic loads can be obtained by integrating the pressure over the instantaneous wetted surface of a body.

2.2.2 Time integration procedure

The boundary conditions have to be updated for the computation at next time step. This is achieved by the integration of equations (3) and (4). By using values at the former time step, the position \mathbf{x}_j and its velocity potential ϕ_j at the next time step, can be written as:

$$\mathbf{x}_j(t + \Delta t) = \mathbf{x}_j(t) + \int_t^{t+\Delta t} \left\{ \mathbf{t} \frac{\partial\phi(\tau)}{\partial s} + \mathbf{n} \frac{\partial\phi(\tau)}{\partial n} \right\} d\tau \quad (19)$$

$$\phi_j(t + \Delta t) = \phi_j(t) + \int_t^{t+\Delta t} \left\{ \frac{1}{2} |\nabla\phi(\tau)|^2 + gy(\tau) \right\} d\tau \quad (20)$$

where \mathbf{t} and \mathbf{n} denote a tangential and a normal vector on the free surface, respectively. The tangential derivative of the velocity potential can be computed by using the numerical differentiation:

$$\left. \begin{aligned} \left(\frac{\partial\phi}{\partial s} \right)_j &= \left(\frac{\partial\phi}{\partial j} \right)_j / \left(\frac{\partial s}{\partial j} \right)_j \\ \left(\frac{\partial x}{\partial s} \right)_j &= \left(\frac{\partial x}{\partial j} \right)_j / \left(\frac{\partial s}{\partial j} \right)_j \\ \left(\frac{\partial y}{\partial s} \right)_j &= \left(\frac{\partial y}{\partial j} \right)_j / \left(\frac{\partial s}{\partial j} \right)_j \end{aligned} \right\} \quad (21)$$

where the index j corresponds to the node number of \mathbf{x}_j , and each term is evaluated using the Lagrange five point interpolation formula. As a time-marching scheme, the fourth-order Runge-Kutta method is employed in the present study. Then the time step size Δt is chosen in consideration of the following condition:

$$\max\{ |\nabla\phi_1|, |\nabla\phi_2|, \dots, |\nabla\phi_{N_F}| \} \times \Delta t \leq c_s \times \min\{ \Delta s_1, \Delta s_2, \dots, \Delta s_{N_F-1} \} \quad (22)$$

where $\nabla\phi_j$ and Δs_j are the velocity of a node \mathbf{x}_j and the length of an element Γ_j , respectively, and N_F is node numbers of a moving boundary Γ_F . The coefficient c_s is set to 1/3. Since we

encounter the occasion that a time step size is not adequately small, the computational scheme that the time step is automatically divided to smaller one is adopted.

Finally, the control of the spatial discretization during computation is indispensable in following fluid particles in a Lagrangian manner. A high density of nodes is needed to describe a small-scale feature with high curvature. However, it is not preferable that a node density is too high or too low at the part of the moving boundary, because the drop of computational accuracy may lead to the instability, specially in the region where the velocity gradient is so high. The quasi-uniformity condition for the node distribution is significantly effective, and this can be formulated as:

$$\frac{\Delta s_{j-1}}{c_u} \leq \Delta s_j \leq c_u \Delta s_{j-1} \quad (23)$$

where c_u is a constant sufficiently large than 1 and always set to 3 in the present study.

2.3 Computational model of jet flow

2.3.1 Treatment of the intersection

In the studies of nonlinear wave-body interactions, specially considering the fluid behavior due to abruptly starting motion, the treatment of a wave-body surface intersection has been discussed by Lin et al. (1984), Yim (1985), Greenhow (1987) and Takagi et al. (1989). Summarizing those, the problems are collected to the following two points: (i) Computational accuracy, (ii) Stability of computation. That is, when computational points are increased near the intersection, computational results get closer to the analytical solutions, but the solutions are easy to become unstable. On the other hand, when computational points are decreased near the intersection, a computational scheme becomes hard to be broken down, but the mass or the energy are hard to be conserved. Generally, It is explained that these problems result from the presence of singularities at the intersection.

The first point becomes important at the early stage of water impact. It means that a very high resolution is needed in the computation near the intersection, because the free surface part with high curvature due to the jet is formed within a small time scale. The asymptotic behavior of the fluid at $t \rightarrow 0^+$ is studied by Roberts (1987) for the horizontal impulsive motion of a vertical plate, and by Iafrati and Korobkin (2000) for the vertical impulsive motion of a wedge. Korobkin (2004) concludes that the compressibility of the fluid should be taken into account at the early stage of the water impact. It suggests that the initial disturbance should be taken into account in the water impact analysis of the incompressible fluid. In the water impact analysis of a wedge, it is well-known that self-similarity solutions can be obtained in considering the problem in the dimensionless plane, which is called the similarity plane in the present work for simplicity. Especially, we can avoid the above-mentioned resolution problem in this approach, because there is no scale of disturbance changed by time, in principle. Self-similarity solutions for the wedge impact can be obtained using the iterative numerical method by Tanizawa (1985), Ohtsubo and Fukumura (1987), Wu et al.(2004) and Battistin and Iafrati (2004). The similar approach is also studied in the present study, and it is discussed in section 4. The computational scheme is designed for nodes to be arranged intensively near the boundary with high curvature in the present simulation method on the physical plane. Nevertheless we can expect the better results in using the similarity solutions as the initial condition.

The second point in the water impact problem is considered to have close relation to the contact angle which is made between the body and the free surface. The introduction of analytical integration for the influence coefficients ensure stable computation as shown in section 2. Actually even though the contact angle becomes less than 1° , the computation does not break down unless both boundaries touch each other. Therefore, although the substantial cause cannot be

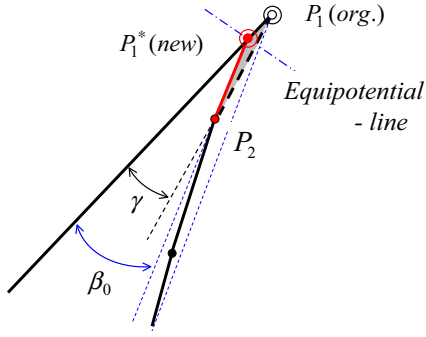


Fig. 3: Cut-off operation of a jet tip.

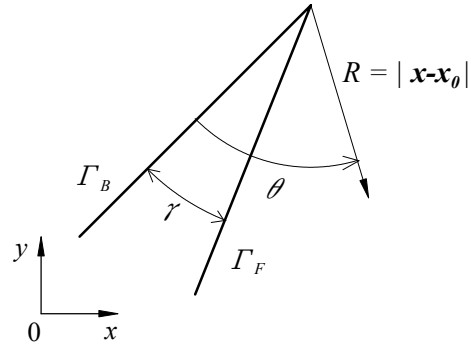


Fig. 4: Local coordinate system,

specified here, we can conclude that the four numerical factors should be evaluated for success computation, which consists of the numerical description of the geometric shape of the moving boundary, the setting of time step size, the control of nodal arrangement and the integration of boundary elements.

2.3.2 Modified cut-off model

The impulsive motion of a body induces very large acceleration near the intersection and then the fluid runs up along the body surface quickly. Theoretically the velocity is singular at the intersection in a moment of the water impact. It means that the velocity is infinite there. However, the computed velocity values based the nonlinear theory are finite, and numerical errors are inherent in the computation of the intersection for the short duration after the water impact. It implies that there is the arbitrariness to a certain extent. Considering actual fluid phenomena on the jet, the fluid is disintegrated into clouds of droplets, which is no longer the continuous fluid domain. We can trace the motion of a jet tip to some extent, but computational efforts will be added more and more because of an increase in a computational domain. At last, such a situation leads to the numerical instabilities bringing the small negative pressure and the contact of boundaries causing the computational break . From the above-mentioned considerations, we introduce the cut-off model to describe the jet flow practically. We assume that the body surface is approximately straight near the intersection. The cut-off operation in a thin triangle layer with an apex at the intersection is illustrated in Fig.3. Since the velocity potential comes to have almost symmetry values on both boundaries, the flow can be considered one-dimensional toward the intersection. The tip shape of the jet region is controlled only by the contact angle γ . The execution of the cut-off operation is judged by the condition:

$$\gamma \leq \beta_0 \quad \text{at} \quad P_2 \quad (24)$$

The shadow area in Fig.3 is removed when the above condition is violated. So the contact angle γ is always monitored during computations. The results by Dobrovol'skaya (1969) are adopted as the threshold angle β_0 in the present work. We expand the velocity potential ϕ in Taylor series around the intersection \mathbf{x}_0 as follows:

$$\phi(\mathbf{x}) = \phi(\mathbf{x}_0) + (\mathbf{x} - \mathbf{x}_0) \cdot \nabla \phi(\mathbf{x}_0) + \frac{1}{2!} \{(\mathbf{x} - \mathbf{x}_0) \cdot \nabla\}^2 \phi(\mathbf{x}_0) + \dots \quad (25)$$

Two terms in the above equation are considered sufficient to describe the jet flow near the intersection. By the local coordinate system in Fig.4, if the following conditions:

$$\left. \begin{aligned} \phi(R, 0) &= \phi(R, \gamma) \\ \frac{\partial \phi(R, 0)}{\partial R} &= \frac{\partial \phi(R, \gamma)}{\partial R}, \quad \frac{\partial \phi(R, 0)}{R \partial \theta} = \frac{\partial \phi(R, \gamma)}{R \partial \theta} \end{aligned} \right\} \quad (26)$$

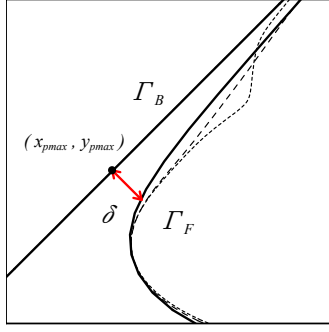


Fig. 5: Sketch near a jet root.

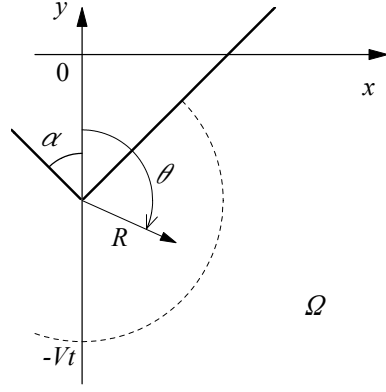


Fig. 6: Sketch around a bottom apex.

are approximately satisfied closely near the intersection, the mass and energy conservation are within the acceptable range even in cutting off the jet tip.

2.4 Matching of analytical solutions for a bottom singularity

In the water impact of a body with a sharp apex at the bottom, such as a wedge, we need to pay attention to the presence of a singularity at the apex, as pointed out by Yim (1987). It turned out that the prediction of the local hydrodynamic pressure around the apex was subject to be affected by computational errors. It is more remarkable as the apex angle becomes small. In the numerical approach, the shift of a source point inside from the apex brings some improvements, for example, by using a constant element or a non-conformity element as the element adjacent to the apex. However, it still remain the influence of the numerical differentiation, the type of its scheme and the choice of nodal intervals. Therefore, to reduce such disadvantage, the analytical expression of velocity potential is adopted in the local domain around the apex, as shown in Fig.6. Such analytical solutions are expressed as:

$$\phi = V \sum_{m=1}^M a_m R^{\frac{(m-1)\pi}{\pi-\alpha}} \cos \left\{ \frac{(m-1)(\theta-\alpha)\pi}{\pi-\alpha} \right\} - VR \cos \theta \quad (27)$$

where a_m is a coefficient to be determined by matching with the solutions in the other domain. Equation (27) satisfies both the Laplace equation and the body boundary condition. The discretized form can be written as:

$$\{\phi_k\} = [F_{km}] \{a_m\} + \{b_k\} \quad (k, m = 1, 2, \dots, M < N) \quad (28)$$

The matrix and vector of right-hand side are given by

$$\begin{cases} F_{km} = VR_k^{\sigma_m} \cos \{ \sigma_m(\theta - \alpha) \}, & \sigma_m = \frac{(m-1)\pi}{\pi - \alpha} \\ b_k = VR_k \cos \theta \end{cases} \quad (29)$$

Let the local boundary (M nodes) locate in the first half of the total boundary (N nodes). Substituting equation (29) to the left-hand side of (17), the matrix form is

$$\left[\begin{array}{c|c} H_{ik} & H_{il} \end{array} \right] \left\{ \begin{array}{c} \phi_k \\ \phi_l \end{array} \right\} = \left[\begin{array}{c|c} H_{im}^* & H_{il} \end{array} \right] \left\{ \begin{array}{c} a_m \\ \phi_l \end{array} \right\} + \left\{ b_i^* \right\} \quad (30)$$

The new matrix and vector with the symbol* can be computed by

$$[H_{im}^*] = [H_{ik}] [F_{km}] \quad (31)$$

$$\{b_i^*\} = [H_{ik}] \{b_k\} \quad (32)$$

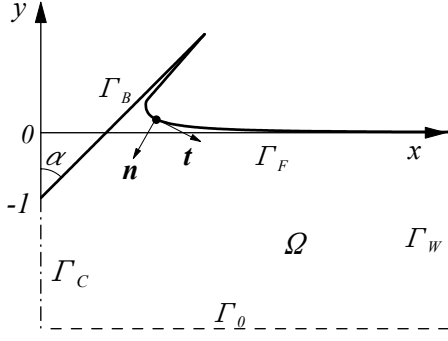


Fig. 7: Definition of coordinate system.

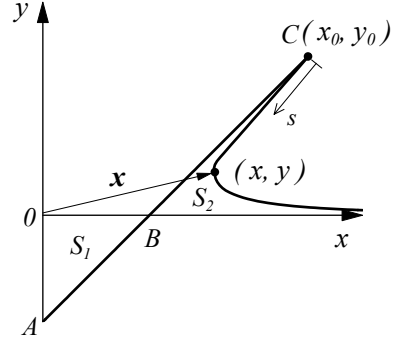


Fig. 8: Sketch of self-similarity flow.

The total number of unknowns is the same as that before introducing equation (27). Therefore, using equation (30), we can solve the simultaneous equations with unknown coefficients a_m matched with the velocity potential ϕ_l in the remaining domain. In the present work, the radius distance of the local domain is set to $Vt/2$.

3 Similarity solutions of wedge impact problem

3.1 Formulation of the problem

We studies the wedge impact problem here by following two reasons. One is for purposes of comparison with the computational results by the nonlinear simulation method, and the other is for the use of similarity solutions as initial conditions in the nonlinear simulation method. This concept is based on the assumption that these similarity solutions are applicable as initial conditions in spite of the arbitrary-shaped body.

We consider the water impact problem for a symmetrical wedge with half apex angle α . When the velocity V is constant and the gravity is neglected, the solution is self-similar and the independent variables \bar{x} and t are reduced to a dimensionless variable \mathbf{x} defined by:

$$\mathbf{x} = \frac{\bar{\mathbf{x}}}{Vt} \quad (33)$$

The velocity potential $\bar{\phi}$ in the physical plane is related to the dimensionless one ϕ defined by:

$$\phi = \frac{\bar{\phi}}{V^2 t} \quad (34)$$

By using these variables, the boundary value problem (1)-(5) can be rewritten as follows:

$$\nabla^2 \phi = 0 \quad \text{in } \Omega \quad (35)$$

$$\frac{\partial \phi}{\partial n} = \mathbf{v}_B \cdot \mathbf{n} = -n_y = \sin \alpha \quad \text{on } \Gamma_B \quad (36)$$

$$\phi - \mathbf{x} \cdot \nabla \phi + \frac{1}{2} |\nabla \phi|^2 = 0 \quad \text{on } \Gamma_F \quad (37)$$

$$\frac{\partial \phi}{\partial n} = \mathbf{n} \cdot \mathbf{x} \quad \text{on } \Gamma_F \quad (38)$$

$$\frac{\partial \phi}{\partial n} = 0 \quad \text{on } \Gamma_W, \Gamma_0, (\Gamma_C) \quad (39)$$

where \mathbf{v}_B is dimensionless velocity of a wedge and equal to $-\mathbf{e}_y$ in the present case. The problem is illustrated in Fig.7. The kinematic free surface condition (38) provides

$$\nabla \phi = \mathbf{x} - s\mathbf{t} \quad (s \geq 0) \quad \text{on } \Gamma_F \quad (40)$$

where s is the parameter along the free surface as shown in Fig.8. The gradient of the dynamic free surface condition (37) gives $-(\mathbf{x} \cdot \nabla)\phi + (\nabla\phi \cdot \nabla)\nabla\phi = 0$, in addition, by the substitute of equation (40) and the consideration that the gradient of s means the tangential vector, the sign of the second term in equation (40) can be decided as the negative. When $s = 0$, it corresponds to the intersection \mathbf{x}_0 . Taking the scalar product of equation (40) with \mathbf{t} , the tangential velocity on the free surface is given by:

$$\frac{\partial\phi}{\partial s} = \mathbf{t} \cdot \mathbf{x} - s \quad \text{on } \Gamma_F \quad (41)$$

Substituting equation (40) to the dynamic condition (37), the velocity potential can be written by:

$$\phi = \frac{1}{2}(|\mathbf{x}|^2 - s^2) = \frac{1}{2}(r^2 - s^2) \quad \text{on } \Gamma_F \quad (42)$$

where $r = |\mathbf{x}| = \sqrt{x^2 + y^2}$. The above equation can be also derived from integrating equation (41) in s . It should be noted that equations (40), (41) and (42) are respectively derived from the combination of both free surface conditions (37) and (38).

From the above-mentioned consideration, the problem can be formulated as the Neumann boundary value problem: (35), (36), (38) and (39), or the mixed boundary value problem: (35), (36), (39) and (42), alternatively. More careful treatment is necessary in the Neumann problem as referred to in the next section.

3.2 Numerical procedures by iterative computations

For the mixed boundary problem, the solution procedure by the boundary integral equation is available, which is already presented in section 2.2.1. Initially the free surface shape being given, the similarity solutions are computed by the iterative procedures until the solutions converge. On the other hand, for the Neumann problem, an additional condition is indispensable for the uniqueness of solutions, which is complemented by giving the ϕ on a point on the boundary. For example, we can do so by using equation (42) to the intersection. However, the position of the intersection sensitively affect the velocity potential ϕ on the body surface, and more careful treatment is necessary in judging the convergence of computations. Therefore, we recommend dealing with the mixed problem.

It should be noted that there are no physical meanings in the computation on the similarity plane under iterative process. We employ the Wagner's solutions as the initial free surface shape.

$$y = \frac{x}{c} \sin^{-1} \left(\frac{c}{x} \right) - 1, \quad x \geq c \quad (43)$$

where $c = (\pi/2) \tan \alpha$. The modification of the free surface shape is performed in the similar manner to the time-stepping scheme as follows:

$$\mathbf{x}_j(t + \Delta t) = \mathbf{x}_j(t) + \int_t^{t+\Delta t} \mathbf{t} \frac{\partial\phi(\tau)}{\partial s} d\tau \quad (44)$$

where Δt is a quasi-time step size and not sensitive to the computation. The integrand can be computed using equation (41). In these steps, with the nodes shifted, the shape is modified in order to satisfy the free surface condition. The slip condition is imposed on the intersection along the body surface. When the convergence is achieved to some extent, the following equation

$$\mathbf{x}_j(t + \Delta t) = \mathbf{x}_j(t) + \int_t^{t+\Delta t} \left(\frac{\partial\phi(\tau)}{\partial n} - \mathbf{n} \cdot \mathbf{x} \right) d\tau \quad (45)$$

is employed in order to satisfy the kinematic condition much more. Every time the free surface is updated, the velocity potential on it can be computed from equation (42).

As for the treatment of the jet flow, the cut-off method in section 2.3.2 can be applied. However, we are not interested in the free surface deformation due to the gravity effect here, and cut off it at the jet root position \mathbf{x} on the free surface. Substituting $\nabla\phi(\mathbf{x}_0) = \mathbf{x}_0$ to the two term expansions in (25), we obtain

$$\begin{aligned}\phi(\mathbf{x}) &= \phi(\mathbf{x}_0) + (\mathbf{x} - \mathbf{x}_0) \cdot \mathbf{x}_0 \\ &= \frac{1}{2} \left\{ |\mathbf{x}|^2 - |\mathbf{x} - \mathbf{x}_0|^2 \right\}.\end{aligned}\quad (46)$$

This relation satisfies the free surface condition (42) under the assumption of two term expansions. In addition, substituting equation (42) to the kinematic condition equation (38), we obtain the following form:

$$\mathbf{n} \cdot \nabla \left\{ \frac{1}{2} |\mathbf{x}|^2 - \frac{1}{2} |\mathbf{x} - \mathbf{x}_0|^2 \right\} - \mathbf{n} \cdot \mathbf{x} = \mathbf{0} \quad \Leftrightarrow \quad \mathbf{n} \cdot (\mathbf{x} - \mathbf{x}_0) = \mathbf{0} \quad (47)$$

where \mathbf{n} is the normal vector at \mathbf{x} . This means the free surface shape in the jet region, which is the straight line connecting \mathbf{x}_0 and \mathbf{x} .

The convergence of solutions are judged from the mass conservation rule. For similarity solutions, this can be expressed by the simple condition that two area S_1 and S_2 are equal, that is, $S_1 = S_2$. Finally, the hydrodynamic pressure can be computed by using:

$$\frac{p}{\rho V^2} = -\phi + \mathbf{x} \cdot \nabla\phi - \frac{1}{2} |\nabla\phi|^2 \quad (48)$$

4 Numerical results

In advance, we mention to the computational size dealt with the present numerical study. As the radiation condition is not imposed, the side wall Γ_w are needed to be far away from the body to avoid the influence of the reflection from the boundary Γ_w . Only setting it to $x = 10.0m$ in Fig.1 and $x = 10.0$ in Fig.7, we can do the computation within a practical range. The water depth is set to be $y = 2.0m$ and $y = 3.0$, respectively. In the numerical simulation, the computation is started initially submerged into water slightly, then the bottom is located at $y = -0.01m$. The total number of nodes is about 360 points, particularly, 20, 60 (initially 40), 260 and 20 are shared on Γ_c , Γ_B , Γ_F and Γ_W , respectively. On the free surface, the element size gradually becomes coarse as far from the body.

Considering the water impact of a wedge, the problem is solved by the nonlinear simulation method in the time domain and the iterative method for similarity solutions. We compared both results of the pressure distribution on the wedge with different deadrise angle α . These results are shown in Fig.9. We can recognize good agreement and specially the prediction in the jet region is acceptably stable. Corresponding results of the free surface profiles by the numerical simulation method are shown in Fig.10. Since we make the cut-off operation to the jet tip, the too much jet ejection is not observed, but the total length of the free surface is reduced to a certain extent.

Next we investigate the influence of the initial condition to the computation. It is demonstrated in Fig.11. Results of the left hand of the figure were obtained by using the initial condition (10). We can observe the formation of the convex on the free surface under the jet root just after the moment of water impact. Although the convexity of the free surface on the impact of a wedge was discussed by Mackie (1962), this is partly because the resolution of the computation near the intersection is insufficient. Another reason is probably the lack of the consideration on the

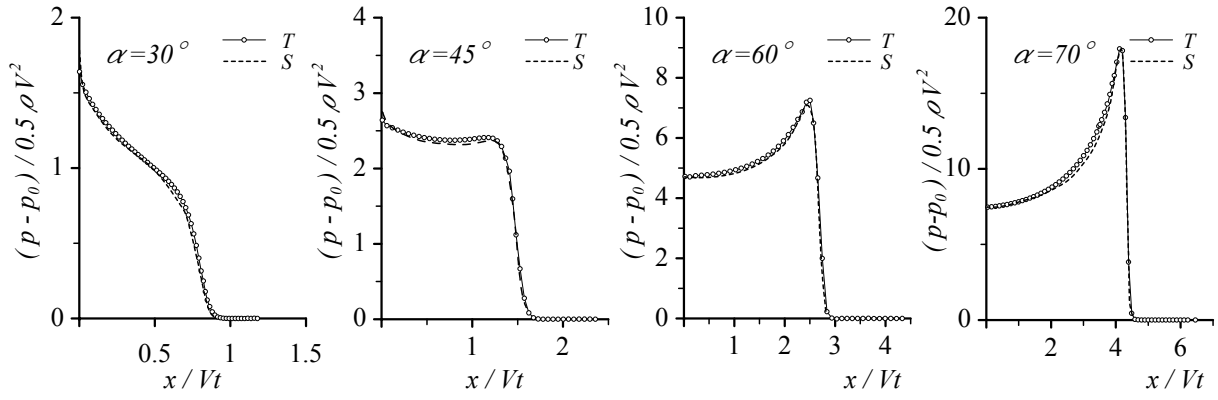


Fig. 9: The pressure distributions on the wedge in disregarding the gravity effect. (T: time domain solution, S: similarity solution)

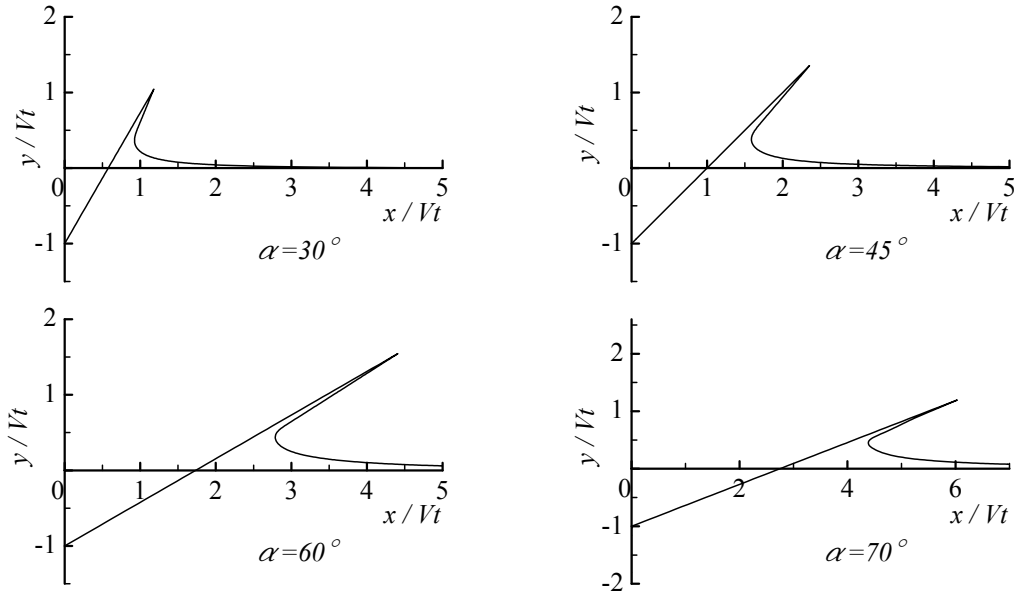


Fig. 10: The free surface profiles in disregarding the gravity effect.

compressibility of the fluid as discussed by Korobkin (2004). The computed pressure indicates the small negative value and the high peaked value in the transient process to the steady value. On the other hand, the results of the right hand were obtained by taking account of the initial disturbance, particularly which was computed by the iterative computation in section . In these cases, such a convex are not observed and the peak value is also smaller. The influence of the initial condition should be taken into account in predicting the maximum pressure

Retaining the gravity term in the problem, we can simulate the evolution of the free surface from the jet formation up to the re-entry against the underlying free surface. Such computational results are shown in Fig.12 and Fig.13. So far the gravity effect has been always neglected in the water impact analysis based on the potential theory for the rational reason. The present numerical procedures hopefully enable the global simulation combining the hydrodynamic analysis with the free surface flow analysis. The adopted cut-off model doesn't disturb the evolution of the free surface as shown in Fig.5.

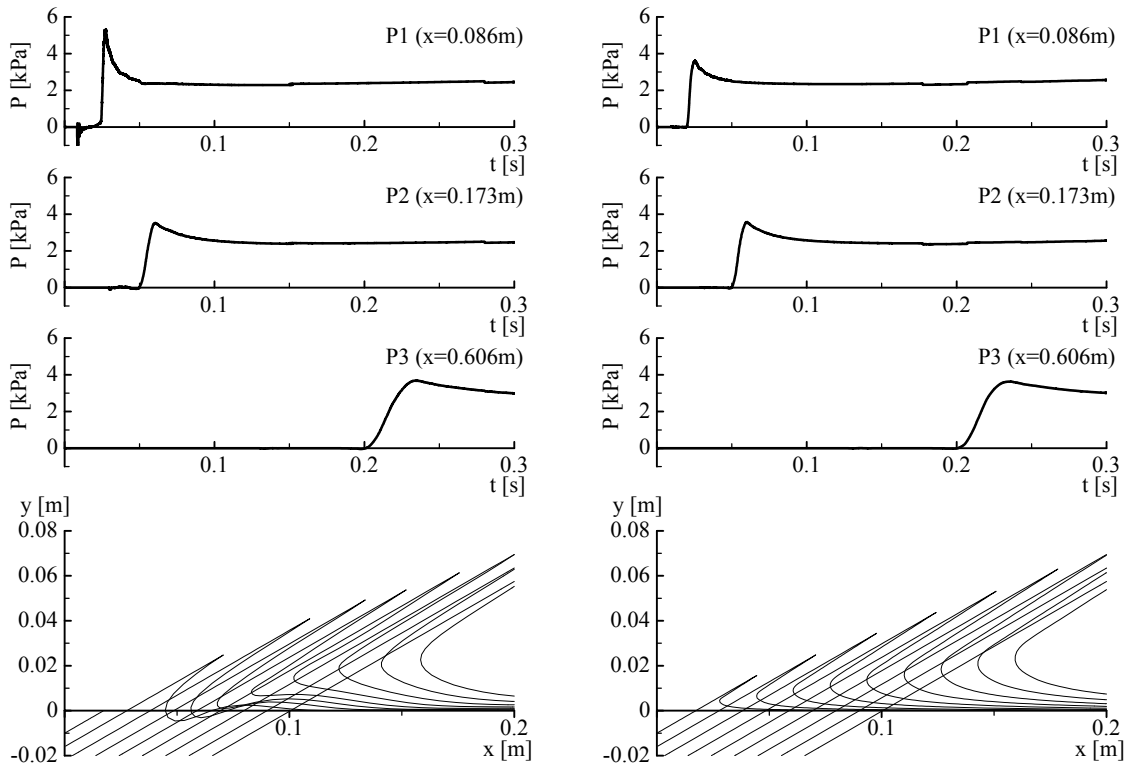


Fig. 11: Time histories of the pressure at fixed points on the wedge with $\alpha = 60^\circ$ and $V = 1m/s$, and free surface profiles at an early stage of the impact, from 0.0s to 0.048s every 0.006s, are shown. Left figures are the computations without initial disturbance, and right ones are the computations with initial disturbance.

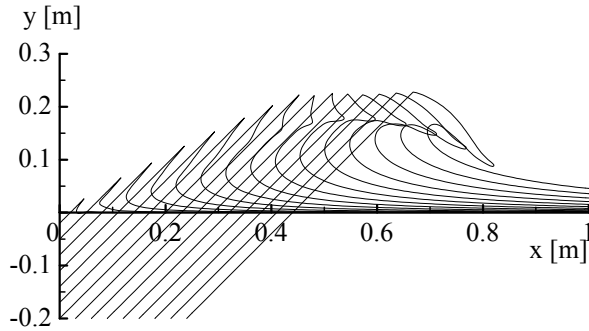


Fig. 12: Free surface evolution ($\alpha = 45^\circ$).

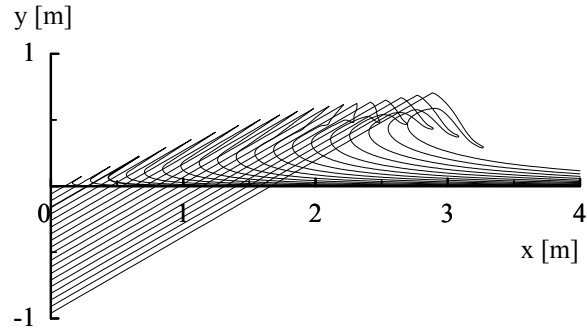


Fig. 13: Free surface evolution ($\alpha = 60^\circ$).

5 Conclusions

Water impact problems for the wedge at the constant speed have been analyzed numerically in the frame of the potential flow assumption. The construction of numerical procedures in the time domain were intended to enable the global simulation combining the hydrodynamic analysis with the free surface flow analysis. For purposes of it, the computational model of the jet flow has been proposed and its availability was demonstrated for the wedge impact case. The iterative numerical procedure for similarity solutions was also studied to obtain the initial condition for the numerical procedure in the time domain. Both numerical methods can provide good agreement for similarity solutions. Related to the initial condition, its treatment is significant particularly in predicting the hydrodynamic pressure.

6 References

- ARMOND, J.-L.; COINTE, R. (1987), *Hydrodynamic impact analysis of a cylinder*, Journal of Offshore and Mechanics and Arctic Engineering, ASME, Vol.9, pp.237-243.
- BATTISTIN, D.; IAFRATI, A. (2003), *Hydrodynamic loads during water entry of two-dimensional and axisymmetric bodies*. Journal of Fluid and Structures, Vol.17, pp.643-664.
- BATTISTIN, D.; IAFRATI, A. (2004), *A numerical model for the jet generation by water impact*, Journal of Engineering Mathematics, Vol.48, pp.353-374.
- CHAPMAN, S .J.; GILLOW, K. A.; HOWISON, S. D.; OCKENDON, J. R (1997), *Asymptotics of violent surface motion*, Philosophical Trans. of the Royal Soc. , Series A, Vol.355, pp.679-685.
- COINTE, R.; GERYER, P.; KING, B.; MOLIN, B.; TRAMONI, M. (1990), *A nonlinear and linear motions of a rectangular barge in a perfect fluid*, Proceedings of 18th Symp. on Naval Hydrodynamics, Ann Arbor, pp.85-99.
- DOBROVOL'SKAYA, Z. N. (1969), *On some problems of similarity flow of flow with a free surface*, Journal of Fluid Mechanics, Vol.36, pp.805-829.
- FALTINSEN, O. M. (2002), *Water entry of a wedge with finite deadrise angle*, Journal of Ship Research, Vol.46, No.1, March, pp.39-51.
- FONTAINE, A.; COINTE, R. (1997), *A slender approach to nonlinear bow waves*, Philosophical Trans. of the Royal Soc. , Series A, Vol.335, pp.565-574.
- GREENHOW, M. (1987), *Wedge entry into initial calm water*, Applied Ocean Research, Vol.9, No.4, pp.214-223.
- HOWISON, S. D.; OCKENDON, J. R.; WILSON, S. K. (1991), *Incompressible water-entry problems at small deadrise angles*, Journal of Fluid Mechanics, Vol.56, pp.173-192.
- IAFRATI, A.; KOROBKIN, A. (2000), *Liquid flow close to intersection point*, Proceedings of 15th Intl. Workshop Water Waves and Floating Bodies.
- IAFRATI, A.; KOROBKIN, A. A. (2002), *Hydrodynamic loads at the early stage of a floating wedge impact*, Proceedings of 17th Intl. Workshop Water Waves and Floating Bodies.
- ISOPE NUMERICAL WAVE TANK GROUP (1999), *Report of the workshop of ISOPE Numerical Wave Tank Group*, <http://www.isope.org/conferences/conferences.htm>
- KOROBKIN, A. A. (1996), *Water impact problem in ship hydrodynamics*, Ch.7 in Advance in Marine Hydrodynamics, M. Ohkusu, Ed., Computational Mechanics Publishing, Southampton, Boston.
- KOROBKIN, A. A. (2004), *Jetting by floating wedge impact*, Proceedings of 19th Intl. Workshop Water Waves and Floating Bodies.
- LIN, W. M.; NEWMAN, J. N.; Yue, D. K. (1984), *Nonlinear Forced Motions of Floating Bodies*, Proceedings of 15th Symposium on Naval Hydrodynamics, pp.33-49.
- LU, C. H.; HE, Y. .S.; WU,G. X. (2000), *Coupled analysis of nonlinear interaction between fluid and structure during impact*. Journal of Fluid and Structures, Vol.14, pp.127-146.
- MACKIE, A. G. (1969), *The water entry problem*, Qurut. Journ.Mech. and Applied Math., Vol.22, pp.1-17.
- MEI, X.; LIU, Y; YUE, D. K. P. (1999), *On the water impact of general two-dimensional sections*, Applied Ocean Research, Vol.21, pp.1-15.
- OHTSUBO, H.; FUKUMURA, M. (1987), *Simplified analysis of impact pressure taking account*

- of splash.*(in Japanese), Journal of the Society of Naval Architects of Japan, Vol.162, pp.374-380.
- ROBERTS, A. J. (1987), *Transient Free-Surface Flows Generated by a Moving Vertical Plate*, Q. J. Mech. Appl. Math., Vol.40 pp.129-158.
- TAKAGI, K.; NAITO, S. (1989), *An Application of Boundary Element Method to the Fluid-Body Interaction Problem*, Proceedings of 18th International conference on Offshore Mechanics and Arctic Engineering, pp.504-516.
- TANIZAWA, K. (1985), *Self-similar solution of wedge entry problem by BEM* (in Japanese), Journal of the Kansai Society of Naval Architects, Japan, Vol.196, pp.147-154.
- TANIZAWA, K. (1995), *A nonlinear simulation method of 3-D body motion in waves -1st report-*, Journal of the Society of Naval Architects of Japan, Vol.178, pp.179-191.
- WAGNER, H. (1932), *Über Stoß- und Gleitvorgänge an der Oberfläche von Flüssigkeiten*, Zeitschr. für Angew. Math. und Mech., Vol.12, 4, pp.193-235.
- WU, G. X.; EATOCK TAYLOR, R. (1990), *Transient motion of a floating body in steep water waves*, Proceedings of 11th Intl. Workshop Water Waves and Floating Bodies.
- WU, G. X.; SUN, H.; HE, Y. S. (2004), *Numerical simulation and experimental study of water entry of a wedge in free fall motion*, Journal of Fluid and Structures, Vol.19, pp.277-289.
- YIM, B. (1985), *Numerical solution for two-dimensional wedge slamming with a nonlinear free-surface condition*, Proceedings of 4th International Conference on Numerical Ship Hydrodynamics, pp.107-116.
- ZHAO, R.; FALTINSEN, O. (1993), *Water entry of two-dimensional bodies*. Journal of Fluid Mechanics, Vol.246, pp.593-612.
- ZHAO, R.; FALTINSEN, O.; AARSNES, J (1996), *Water entry of arbitrary two-dimensional sections with and without flow separation*. Proceedings of 21th Symp. on Naval Hydrodynamics, pp.408-423.

Multi-Attribute Decision Techniques in Ship Design

Marcello Barone, mabarone@unina.it

Carlo Bertorello, bertorel@unina.it

Mario Stella, mastella@unina.it

Department of Naval Architecture, University of Naples "Federico II"

Abstract

In this paper a review of the most commonly adopted Multi Attribute Decision Making (MADM) procedures is presented. Some comments are given on the main aspects of their implementation, that are the criteria for the choice of the attributes to be considered, the different techniques for attribute normalization, and the choice of the decision rule to be applied for ranking the design alternatives. Different methods for designer preference communication are also described. Special attention is given to the Ma-Fan-Huang method which allows the designer to assign preferences in terms of a combination of subjective and objective weights to be given to the different attributes. The application of a MADM procedure to a trimaran fast ferry already performed in previous works is analysed, pointing out the influence of the above mentioned aspects on the final result.

1. Introduction

The design of a new ship is a complex process in which the designer, from given information and available resources, deals with the problem of generating feasible designs, i.e. proposals able to meet specified functional requirements. The final design is generally achieved through a process of repeated generation and evaluation of different alternatives with the aim to select that one which best fits designer expectations. The usual way of facing this problem has been, so far, to use a sequential and iterative approach in which the different design aspects as, e.g., powering, strength, stability and seakeeping are considered in sequence. While quite intuitive and rather effective in most of cases, this approach holds the main disadvantage of requiring too much guess work to the designer when looking for the best compromise; the limits of this method are particularly evident when different design features influence ship performances in counteracting ways. In such cases a much more effective approach would require a procedure able to simultaneously handle several design criteria. Furthermore the designer should be allowed to get to the best result considering both objective criteria as well as his experience and personal intuition.

Over the last thirty years a large number of design procedures with such features have been developed and applied in several fields. Most of them have been thought to deal with a single criterion or measure of merit; the marine field needs optimisation schemes allowing the simultaneous consideration of the largest possible number of the design effectiveness relevant measures

Multicriteria decision making (MCDM) procedures seem therefore particularly suitable to be applied in this field. Among them, particular attention has been recently paid, at the Department of Naval Architecture and Marine Engineering of Naples, towards multiattribute design procedures (MADM). They have been shown to be useful tools to compare existing or proposed design alternatives, especially in the case of complicated hullforms considered at the stage of the design of new HSC proposals.

The ship concept intrinsically implies the definition of general specifications and technical features relative to a mission profile. The ship design can approach this final target through different ways and different values of the meaningful design parameters.

Within this frame ship design can be seen as a multidisciplinary action implying different aspects sometimes reciprocally counteracting; available data and resources are used to generate alternatives that must be feasible and acceptable.

Design optimisation is the development and the evaluation of design alternatives. In this case “evaluation” means a cognitive activity, performed in intentional way, apt to give a judgement about a the design itself and aimed at rationalizing a decisional process.

Usually, in the marine field, design alternatives have been developed and evaluated through sequential procedures based primarily on designer experience and preferences and able to consider available data.

Recently, the strong competition due to a dynamic market and the availability of new design methodologies developed in different technical fields have lead to new design techniques able to consider simultaneously several design features and on this basis to identify an optimal result. Furthermore designer preferences can be inserted or not into such design procedures and the relative weights finely tuned.

This approach has been already used in technical and social fields and these techniques are generally defined as multicriterial. The Multiple Criteria Decision Making (MCDM) can be defined as the choice of an acceptable design option performed on the basis of two or more criteria. The criterion is an indication to evaluate the option performance. MCDM aim is to identify the best compromise solution on the basis of any design option or to rank existing designs. MCDM approach can be divided into Multiattribute (Multi Attribute Decision Making, MADM) and Multiobjective (Multi Objective Decision Making, MODM). While MADM implies the selection among a number of options, MODM performs the design of the best option among any possible option which is not necessarily explicitly known. MADM and MODM methods have a basic common structure as shown in Fig.1.

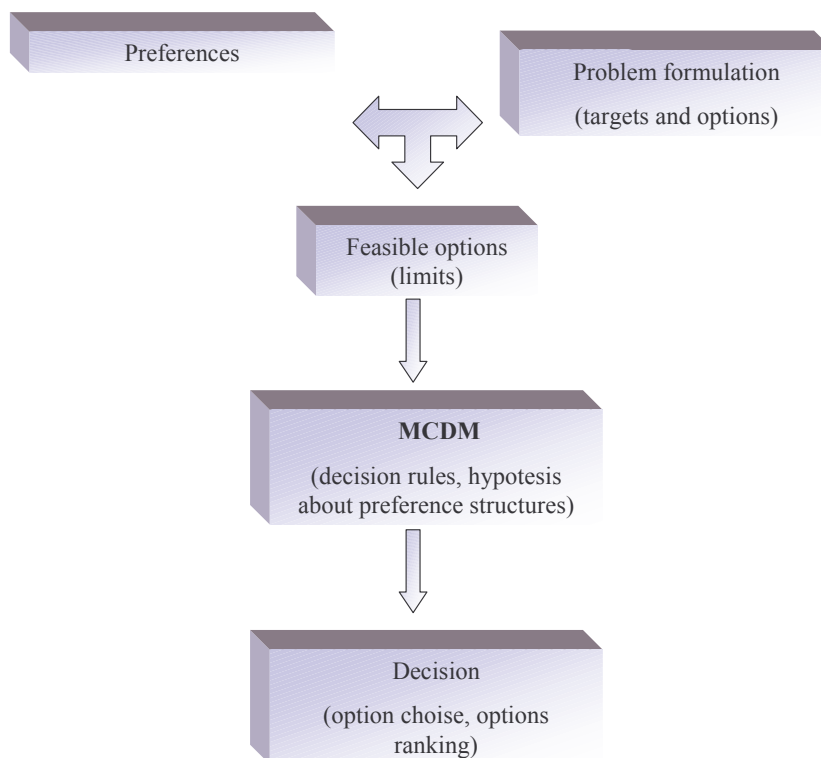


Fig 1: MCDM general structure

Recently the use of both techniques has been proposed in the marine field also. In this paper MADM is considered. MADM technique seems suitable to basic and general ship design as well as to rank existing ships or designs. It needs the definition of a design model constituted by several design moduli that allow to evaluate the performances of the design itself. MADM technique is based on the following elements:

- Variables: input data for the design model, that are modified one by one;
- Parameters: input data similar to the variables, but not subjected to any modification;
- Attributes: output data used to rank the obtained result;
- Limits: Similar to attributes or attribute values used to limit the results to the feasible ones.

A large number of feasible designs is developed through a corresponding number of elaborations of the design model each with different variable values inside the defined limits. Among the obtained feasible designs only the so called dominant are retained. The dominance concept is fundamental within MADM. A design option is considered dominant in respect to an other when an improvement of any attribute can be obtained only with a detriment of at least one of the remaining attributes. The surface union of the dominant options in a K dimensional space, where K is the number of the adopted decisional criteria, is called Pareto frontier. The Pareto frontier will divide the space into two regions of feasible and unfeasible designs respectively. In the region of unfeasible designs a point will represent the design with each attribute at the best possible value. This design, or this point, is generally called “utopia”. The best design option will be the nearest to utopia, belonging to Pareto frontier. These concepts are summarised in Fig. 2 for the case of three attributes. B, C, A are the points representative of the design options obtained optimising only one of the three attributes, CBA is the Pareto frontier and P could be representative of the nearest point to utopia, that is the best feasible design option. The Pareto frontier can be influenced by some elements that, consequently, affect the procedure final result:

- attribute selection and choice depending on available database and/or design model;
- attribute normalization formula, which is evidently necessary to commensurate different attributes;
- different relative weights assigned to each attribute; they can be representative of designer subjective preferences, consider objective attribute hierarchy, or combine both criteria.

Finally the used technique for the evaluation of the distance from utopia can influence the final options ranking. Each of these elements will be considered in the following and its influence evaluated in the frame of a case study.

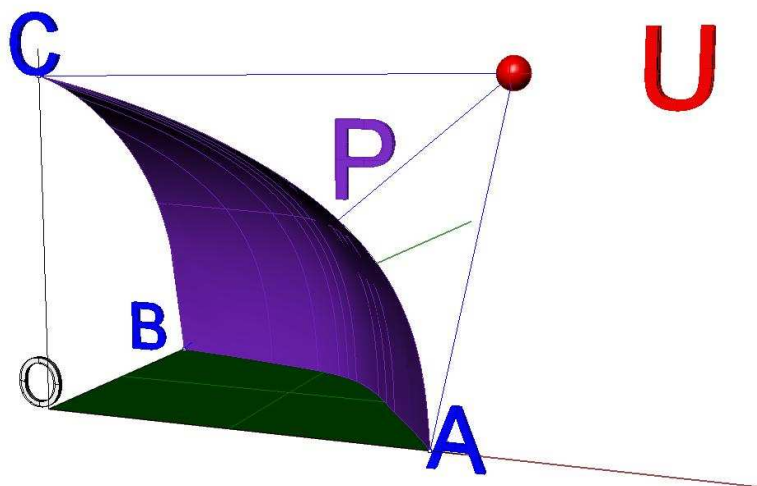


Fig. 2: Pareto frontier in the case of three attributes

2. Peculiarities in MADM applications and their influence on the results

2.1 Parameters and attributes selection

The ability of the MADM technique to consider simultaneously several design options based on conflicting criteria, make it an effective design methodology and a useful tool to compare existing designs. To such extent, it is important to emphasize that, MADM techniques allow to select the best option taking into account the main characterizing elements of the design. When dealing with the optimisation of a new design, the worthiness of the found solution is also subordinated to other factors as the proper formulation of the procedure and representative design modules according to the selected criteria. Each design module, whose scope is to supply a functional link between parameters and attributes, is the first step towards the resolution of a MADM problem; it has to provide a mathematical description of a physical phenomena related to the ship. The choice of the parameters characterizing the models is affected by the designer cultural background and by the availability of data from previous experiences. The appropriate selection of meaningful parameters, guarantees the effectiveness of the module and of the criteria used to solve problem. The link between the goal and the alternatives allows the choice of the parameters on the basis of similar ships, and for similar mission profiles.

2.2 Attributes relative weights

To keep into account the importance of each attribute in the selection of the best solution, some MADM techniques use preference structures through assigned attribute weights. When the method does not consider the attribute relative weights explicitly, the preferences of the designer can be equally expressed implicitly within MADM methodology. The preference structures can keep into account the taste, the experience and the designer intuition but the objective importance of each attribute must be also considered. In the case objective approach the weights are obtained through a mathematical model which is detailed in *Fan (1988)*. The result will be different if the adopted technique takes into account for each attribute the designer preferences exclusively (subjective approach), the objective importance (objective approach) rather than both, as in the integrated approach proposed by Ma Fan Huang method *Fan (1988)*. In this case attribute weights are obtained through a mathematical procedure that considers subjective and objective approaches through two coefficients α and β . The final result will be strongly influenced by the relative importance given to the two approaches.

2.3 Attribute normalization

The most widely formulas adopted are:

$$p_{ij} = \frac{x_{ij}}{x_j^{\max}} \quad (2.0) \quad p_{ij} = 1 - \frac{x_{ij}}{x_j^{\max}} \quad (2.1) \quad p_{ij} = \frac{x_j^{\max} - x_{ij}}{x_j^{\max} - x_j^{\min}} \quad (2.2)$$

Where

p_{ij} = i_{th} attribute normalized value relative to j_{th} option

x_{ij} = i_{th} attribute value relative to j_{th} option

x_j^{\max} = i_{th} attribute maximum value relative to j_{th} option

In (2.0) and in (2.1) the normalization is made considering one extreme of the range of attributes, in (2.2) the full range. At this step of the procedure attributes have to be separated into two classes. The first is composed by attributes that are better when maximized, the second by attributes that are better when minimized. Usually the attributes are identified and treated as “benefits” and “costs”. As an example (2.2) became for “benefits”

$$p_{ij} = \frac{x_{ij} - x_j^{\min}}{x_j^{\max} - x_j^{\min}} \quad (2.3)$$

and “for costs”

$$P_{ij} = \frac{x_j^{\max} - x_{ij}}{x_j^{\max} - x_j^{\min}} \quad (2.4)$$

2.3 Option ranking

The selection of the best solution is based on distance between considered and ideal design; basically, it can be performed through three methodologies Weighed Sum, Euclidean Distance from the Utopia Design, Chebychev’s distance. Each method supplies a final ranking of options that considers all attributes and weights, and leads to choose the best option basing on all elements simultaneously. In the Weighted Sum method the designer assigns a weight w_j to each attribute, according to his own preferences. The weight vector must be such that:

$$\sum_{j=1}^n w_j = 1 \quad (2.5)$$

the rank of i_{th} option is given by

$$R_i = \sum_{j=1}^n w_j p_{ij} \quad (2.6)$$

R = ranking

i = option index

w = attribute weight

p = attribute normalized value

Evidently the best option is that with the highest R value. This method needs attribute normalization

The Euclid Distance from Utopia method considers the quantity:

$$R_i = \sqrt{\sum_{j=1}^n (w_j p_{ij})^2} \quad (2.7)$$

In this case R is the Euclid Distance from Utopia design. The meaning of the other symbols is the same as in (2.6). The best option is that with the lowest R value. This method also needs attribute normalization.

Chebychev’s method is based on the difference between coordinates; each alternative is represented only through the maximum difference between its attribute value and the corresponding attribute of the ideal design. The Chebychev method leads to a final ranking based on one attribute and so it do not considers the whole information supplied from the attributes value. The attribute selected as representative can be chosen because maximize a benefit but also because minimize a cost.

In this paper Chebychev’s method have been applied in a different way for costs and benefits, in particular, the distance from ideal design characterized from zero value for each attribute is valued through:

$$L_{\infty}^* = \min_j \left\{ \max_i \left[\frac{p_i}{1 + K(w_{\max} - w_i)} \right]_{i=1,K} \right\}_{j=1,N} \quad \text{for costs} \quad (2.8)$$

$$L_{\infty}^* = \min_j \left\{ \max_i \left[\frac{p_i}{1 + K(w_i - w_{\min})} \right]_{i=1, K} \right\}_{j=1, N} \quad \text{for benefits} \quad (2.9)$$

Where:

L_{∞} = Chebychev distance

I = attribute index

J = option index

w_i = is the subjective weight assigned to the normalized attribute

K = number of the attributes .

The analyzed methodologies are in general different and lead to the similar results only if, for the considered option, one weighted attribute is much heavier than the others.

3 Some examples of MADM application of for ship basic design or for ranking existing ships.

In the marine field MCDM is still at the first steps. Some examples of MODM applications aimed at specific architectural or structural problems optimisation are reported in literature. MADM seems much more suitable to basic or preliminary design and the most known papers, mostly focused on Small Craft are synthetically reviewed in the following. In “Multi Attribute Concept Design Model of the Adriatic Type of Fishing Vessel” *Grubisic (2001)*, the application of MADM to Adriatic sea fishing vessels with length ranging from 10 to 30 m. is performed. Design options are represented by input parameters (Lwl, Bx, Cp, etc.) and by output attributes. Design model is controlled through seven variables representative of hull principal dimensions, random generated with upper and lower limits by the formula:

$$v = \text{ran}_j v_{\min} + (1 - \text{ran}_j) v_{\max}$$

where ran_j is the j th random consecutive number in the range (0,...,1).

Attributes have been chosen among those characteristics able to define ship intrinsic utility as cruising speed, payload etc. Design feasibility has been evaluated considering a minimum allowed payload. The final design has been selected according to the attribute values among non dominated options. The importance of each attribute in respect to the others has been determined on the basis of their relative comparison.

In “Multi Attribute Concept Design Model of Search and Rescue Vessel” *Grubisic (2002)* 230 Search and Rescue Vessels (SAR), are ranked on the basis of formula (2.7). Attribute normalization has been performed according to (2.0) and (2.1). Design model takes into account brake horsepower, seakeeping, structural weight and cost.

In “Multi Attribute Concept Design Model of Search, Rescue and Antiterrorist Craft” *Grubisic (2003)* use Monte Carlo Method for random generation of parameters as L_p , B_{px} , β_x , within given limits. So that restrained attribute values allowing for design feasibility are generated. Feasible designs are then selected according to Pareto frontier logic. In this case final ranking has been obtained by the Chebyshev formula and attribute weights have been assigned according to their relative importance.

MADM approach has been used in “Feasibility Study on a Hight Speed Catamaran: Comparison with Aquatsrada” (*Trincas 1995*), to investigate new design configurations for high speed car/passenger mediterranean transportation. Considered attributes are cruising speed, payload, service quality and easy ship loading/unloading. Final result consists in high speed catamaran with jet propulsion and load capability of 300 passengers and 300 cars. The flow chart used to get this results is typical MADM as reported in Fig. 1 using Monte Carlo Method for random generation of parameters, within given limits. Attribute values are normalized and non dominated options are selected. Saaty method for preference

matrix is applied. Finally a comparison with Aquastrada construction, management and maintenance costs is performed.

An application of AHP (Analytic Hierarchy Process) can be found in “Marine Design: The Multiple Criteria Approach” *Sen (1991)*. The paper is focused on the best choice for a ship to be used for coastal transportation in developing countries. The first hierarchy level is the choice itself, followed by the three subjects acting the choice that are ship manager, ship owner and Classification Society. Then the hierarchy goes on considering attributes as service quality, comfort parameters, cost parameters, physical aspects and external factors. Each attribute is reconsidered at lower level by some other more detailed attributes as shown in Fig. 3, the last level is composed by the types of ships to be chosen. Applying AHP the authors perform a ranking list of different options.

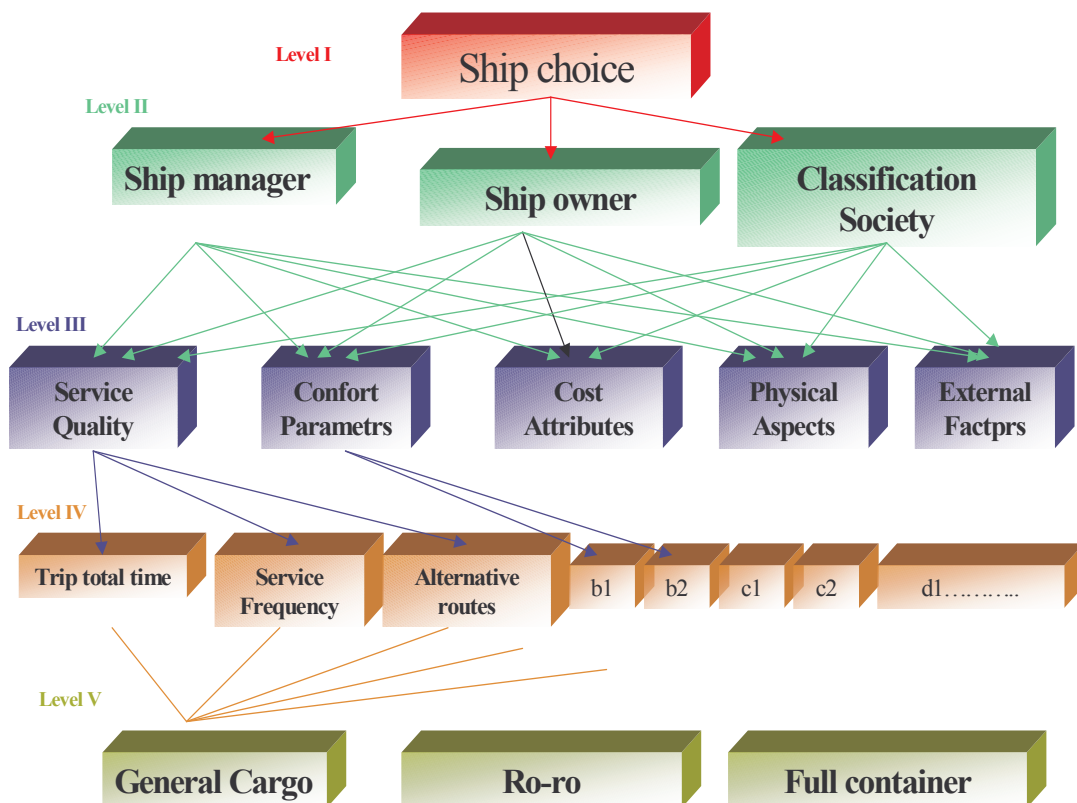


Fig. 3: AHP applied to ship for coastal transportation

A meaningful example of MADM application is reported in “Multiattribute Concept Design Model of a Trimaran Hull Form” *Barone (2003)*, in which the stagger optimisation for a trimaran fast ferry is performed. The design model contains resistance, seakeeping global/local loads and stability modules. Attribute weights are assigned through Ma-Fann-Huang Integrated methods where the final weight vector is obtained combining a subjective factors taking into account the designer preferences and objective factors considering the quantitative information given by the decision matrix relative to the design optimisation. For the attributes normalization an equally distributed formulation on the whole interval $x_j^{\max} - x_j^{\min}$ was used both for “costs” and “benefits”. The final ranking list of design options has been evaluated according to Euclid distance through the formula (2.7)

A Concept Exploration Model is a mathematical scheme able to model the design procedure and to evaluate a large number of options within a given dimensional range. Finally C.E.M. will identify the best fitting option according to adopted criteria. In “A Concept Exploration Model For Sailing Yacht” (*Van*

Oossanen 2003) a C.E.M. is used to investigate the dimensional range for a sailing yacht. The result evaluation is based on a decisional matrix able to consider adopted criteria and the attributes relative to a single criteria. The obtained matrix is normalized by (2.3) and (2.4).

4. MADM Application to a trimaran fast ferry

During the last years research in the marine field has been increasingly focused on new concept vessels able to guarantee a further improvement of the hydrodynamic performances of HSC. Particularly a noticeable attention has been paid toward the trimaran hull because of its large deck area, easy machinery arrangement and promising power performances. Its complex hull geometry needs, at the early design stage, the assessment of several key parameters. Particularly the definition of the optimal outrigger longitudinal position (stagger) has been clearly proven to be one of the most important aspects to be investigated in the vessel performance optimisation: early results of the research showed that stagger is able to affect not only hydrodynamic resistance but also intact and damage stability characteristics, global and local loads and seakeeping performances, and this often happens to be in counteracting ways. In this section, the results of the application of a multi-attribute procedure aimed at performing such optimisation for a small trimaran passenger ferry are reported. In the following, the ship main characteristics are briefly described. The main steps of the applied MADM procedure as well as the results of its application are also reported paying particular attention to the influence of the main aspects of the procedure on the final results.

4.1 Ship Main Characteristics and Hull Form

Main hull and outrigger geometrical features have been determined taking into account the ship service characteristics. Round bilge hull form with transom stern have been found to be suitable for both main hull and outriggers. Different L/B ratios have been chosen, anyway, according to their different Froude number: main hull has been selected from Series 64 while outriggers have been chosen from Series 64 and stretched by geometrical affinity so as to increase the L/B ratio. Outriggers immersed volume is 6.5% of the trimaran hull volume. Table I details the principal main hull and outrigger characteristics; the trimaran hull body plan is represented in Figure 4.

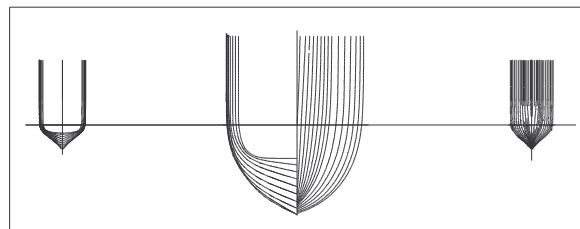


Fig. 4: Main hull and outriggers body plan

Table I: Principal characteristics of the trimaran ship

	MAIN HULL	SIDE HULL	TRIMARAN
L _{OA} (m)	47.700	23.850	47.700
L _{WL} (m)	46.940	23.470	46.940
B _{WL} (m)	3.336	1.092	11.700
T (m)	1.670	0.460	1.670
WS (m ²)	194.8	25.2	245.2
Displ. (t)	120.489	4.259	129.007
C _B	0.45	0.35	
L/B	14.070	21.500	
B/T	2.000	2.356	
Fn	0.839	1.187	

Stagger has been defined according to the following formula:

$$\text{Stagger} = 20 y / L_{WL} \quad (4.1)$$

being y the longitudinal distance between main hull and outrigger transoms as shown in Fig 5. The examined range of stagger values is [0; 10].

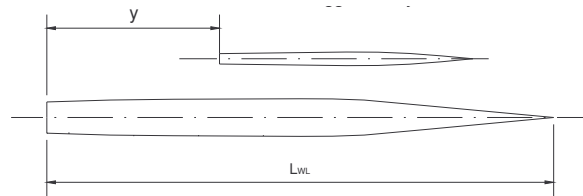


Fig. 5: Stagger evaluation scheme

4.2 MADM Procedure for stagger optimisation

The principled scheme of the applied MADM procedure is represented in Fig. 6. At the stage of the problem definition, the stagger value has been set as the design variable to be optimised. An accurate selection of the attributes representing the design evaluation criteria has been performed as well being this choice generally capable of noticeably affect the final result. In this case eight different attributes have been chosen, which are thought to fairly account for all the relevant aspects of the design directly influenced by stagger. They are:

1. Hydrodynamic resistance (kN)
2. Area A_1 under the righting arm curve (m rad)
3. Operability @ centre of passenger accomm. area (%)
4. Maximum longitudinal shear (kN)
5. Maximum longitudinal bending moment (kN m)
6. Transversal torque moment (kN m)
7. Bottom impact pressure @ 0.75 L_{wl} from after perpendicular (kN/m²)
8. Impact pressure on cross-deck @ 0.75 L_{wl} after perpendicular (kN/m²)

Four different design modules concerning Hydrodynamic Resistance, Seakeeping, Global and Local Loads, Ship Intact Stability have been therefore developed. The aim was to provide those tools necessary to calculate the value of any attribute with respect to any design alternative obtained by changing the outrigger longitudinal position. The application of these modules to a given number of proposed designs allows therefore to evaluate the decision matrix of the optimisation problem. Normalisation of attributes values has been always performed, unless otherwise stated in the following, using the (2.3), (2.4) formulas. Designer's preferences have been elicited in terms of fixed weights to be assigned to the considered attributes. Particularly the choice has been made of assigning weights through the Ma-Fan-Huang method *Fan (1988)*.

Following the structure given to the four design modules the optimisation procedure has been applied referring to different ship speeds, trip durations, and sea conditions, with the aim to evaluate the influence of these factors on both the final classification of alternatives and the best design proposal. This choice allowed to get a measure of the sensitivity of the whole procedure to the ship operational conditions. In the following, being the main purpose of this paper to investigate the influence of the main aspects of the multi-attribute procedure rather than extensively report the results of the trimaran stagger optimisation, only the results relative to the case of 29 knots of cruising speed and 30 minutes trip in Western Mediterranean in summer conditions are reported. For such case, some comments about the influence on the final results of the applied normalization formulas, the selected decision rule and the assigned weights are given.

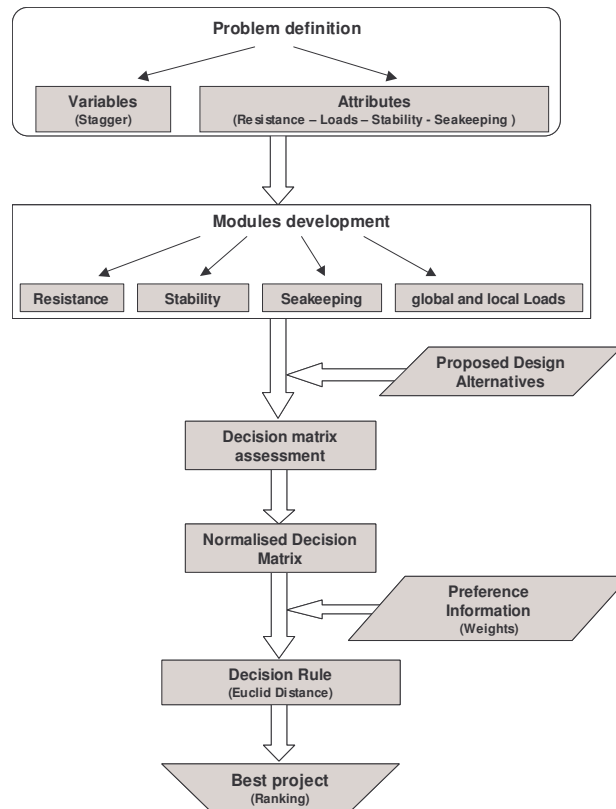


Fig. 6: Multi-attribute procedure principled scheme

Diagrams reported in Figs 7-9 show respectively the influence of normalization formulas, attribute weights and decision rule on the final ranking of the 21 design alternatives generated by changing the outrigger longitudinal position between the extreme values 0 and 10 with a 0.5 step. Fig. 7 shows how the change of the applied normalization formulas seems to be actually capable of noticeably affect the final result at least in terms of the best design alternative if not in terms of the final classification of the competing designs: by using the (2.0) or (2.1) formulas the best stagger is pointed out as stagger 0, while making use of the (2.2) formula the best alternative comes out to be stagger 1; nevertheless the general trend of the curves seems to be rather similar always pointing out forward staggers as the worst alternatives. Particularly, if exception is made for staggers falling within the $0 \div 2$ range, in both cases results show that the greater is the stagger, the greater is the distance from the ideal design, i.e. the less performing the design solutions are.

The diagrams in Fig. 7 allow to enhance the influence of the assigned weights on the final classification of the proposed alternatives. The four different curves represent the final Euclid distance from ideal design (d_i) in case that no weights are provided or weights are assigned through the Ma-Fan-Huang method (three curves accounting for the subjective, objective or integrated approach respectively). The trend of the curves clearly shows the importance of designer preference communication: starting from the no weights case, the final classification of alternatives significantly changes as whatever set of weights (from subjective, objective or integrated approaches) is generated through the Ma-Fan-Huang procedure. Anyway the best compromise solution still has to be sought within a very narrow range of after staggers, being it represented by stagger 0, 0.5 or 1 depending on the considered curve. Subjective and integrated approaches lead to very similar results while a completely different trend is obtained when assigning weights on the basis of the objective approach.

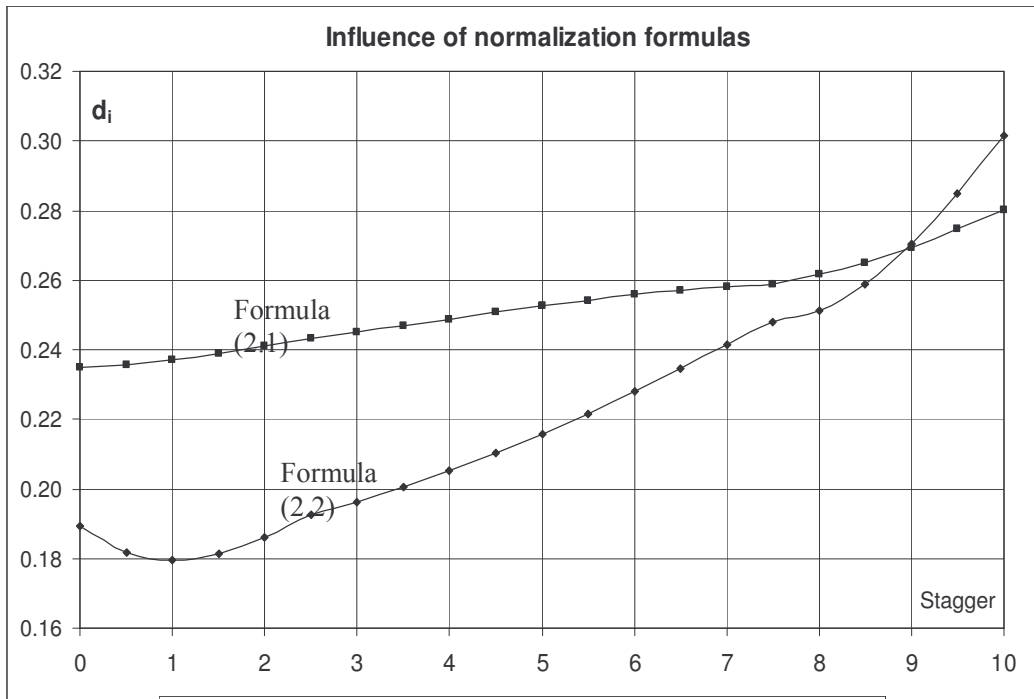


Fig. 7: Euclid distance versus stagger, the effect of different normalization formulas (weights given by Ma-Fan-Huang integrated approach)

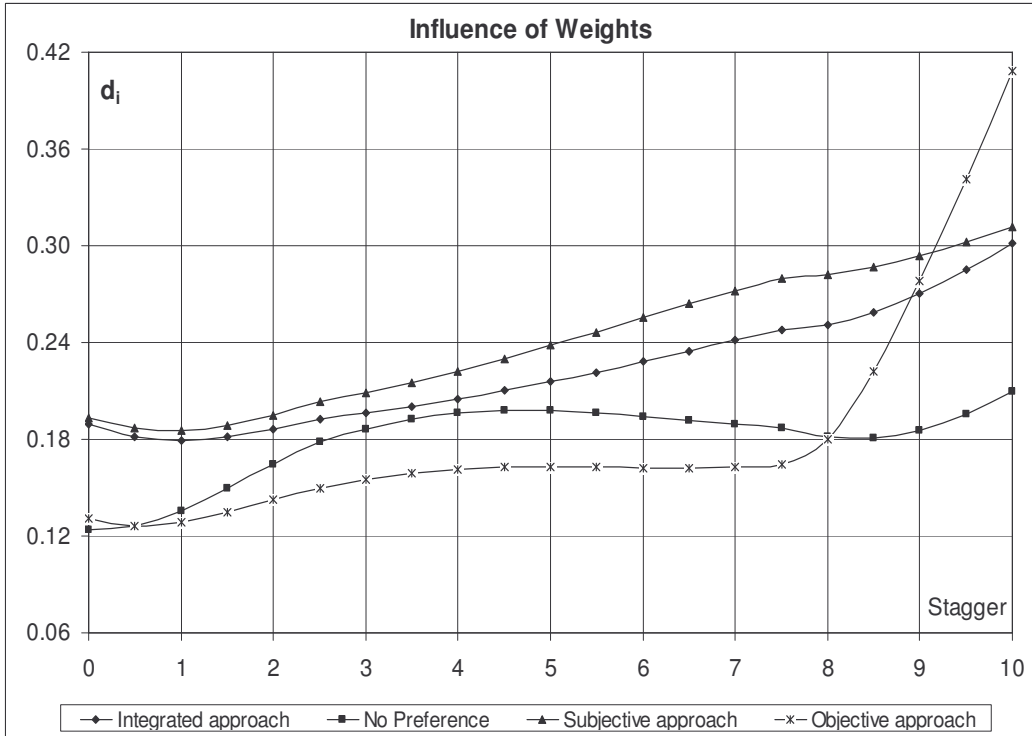


Fig. 8: Euclid distance versus stagger – different methods for weight assignment

Finally diagrams in Fig. 9 allow to evaluate the influence of the applied decision rule on the final result. In any of the considered cases, weights are assigned through the Ma-Fan-Huang integrated approach. The curves are obtained by ranking the proposed design alternatives through the Euclid distance from ideal design (formula 2.7), the weighted sum (formula 2.6) and the Chebychev's distance, here implemented following the (2.8),(2.9) formulas.

Again Euclid distance and weighted sum lead to similar results when ranking the proposed design alternatives, pointing out stagger 1 (respectively stagger 0) as the best alternative and forward staggers as really unworthy solutions. Completely different results are obtained, on the other hand, when the Chebychev distance is considered. In this last case the best stagger is actually pointed out as stagger 7, while after staggers come out to be heavily penalized. This last result can be easily justified considering that, unless the weighted sum and the Euclid distance, the Chebychev's distance doesn't make use of the entire quantitative information provided by the decision matrix of the problem, identifying each alternative just through one of the considered attributes. While useful in some particular cases, i.e. when the distance between each alternative from the ideal point in the k -dimensional space of the k considered attributes is significantly represented by the maximum distance between the relative mono-dimensional coordinates, in this application it doesn't appear to be an effective tool, leading to neglect an amount of quantitative information which eventually bears misleading results. As such, it should be considered, within this context, just as an attempt to propose a more complete review of the available technique for a MADM procedures implementation.

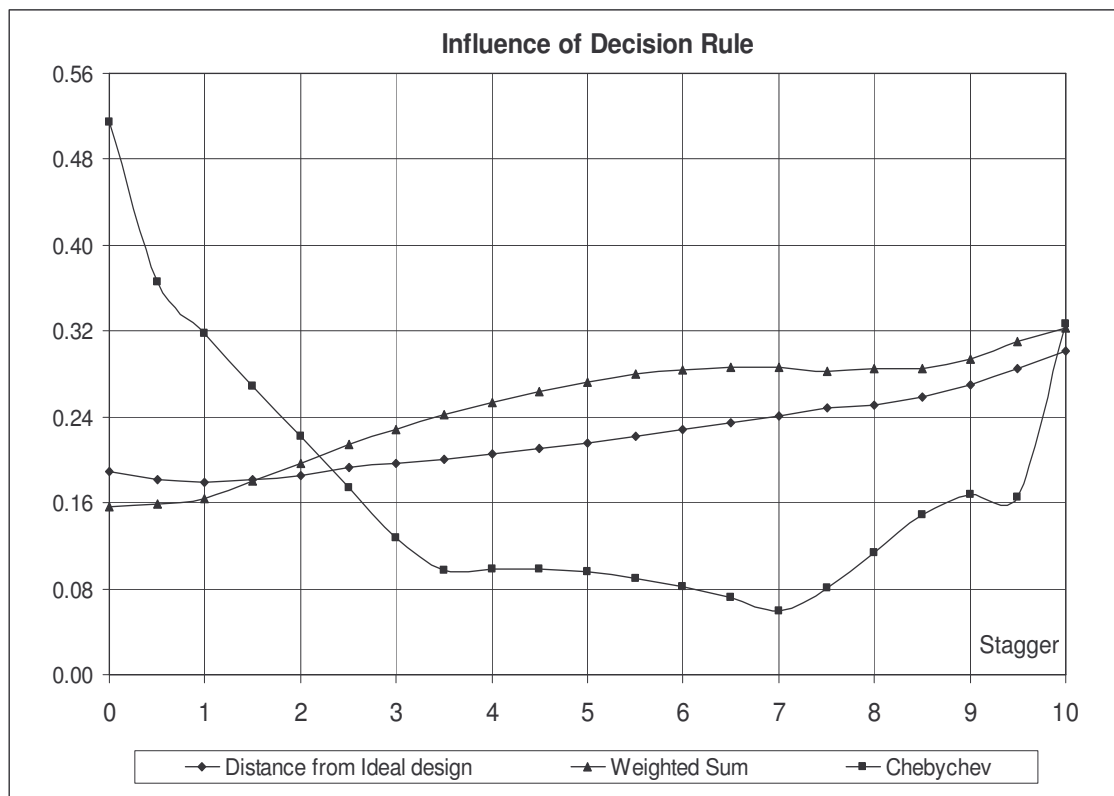


Fig. 9: Weighted Euclid distance, weighted sum and Chebychev distance versus stagger

5. Conclusions

Within MCDM available procedures, MADM seems useful and effective in the marine field. Meaningful rankings of existing ships as well as optimised basic design proposals can be easily performed by this technique. No limit is given in the parameter choices apart the availability of a dedicated design modulus. This calls for further investigations on the technical economical design aspects, at the moment poorly considered with such tools. Presently, different choices are possible for almost any step of the procedure. Their influence on the final results, must be carefully taken into account. These factors have to be trimmed according to ship design specific aspects through the comparison with well known reliable results. A wider interest on the matter is witnessed by the number of recent paper and let us hope for a quick implementation of this technique in the usual professional practice.

Acknowledgments

This work has been financially supported by University of Naples "Federico II" within the frame of 2003-2004 research program.

References

- BARONE, M.; BEGOVIC, E.; BERTORELLO, C. (2003), *Multiattribute Procedure for Basic Design of Trimaran Fast Ferries*, NAV, Palermo, Vol 2
- BARONE, M.; BERTORELLO, C. (2004), *Design Optimisation of Trimaran Hull by Multiattribute Concept*, PRADS 2004, Lübeck Travemünde, Germany
- BARONE, M. (2003), *Multiattribute Concept Design Model of a Trimaran Hull Form*, P.h.d. thesis, Department of Naval Architecture and Marine Engineering, University of Naples "Federico II", Italy
- BEGOVIC, E.; BERTORELLO, C.; BRUZZONE, D.; CASSELLA, P.; AND ZOTTI, I. (2001), *High Speed Trimarans Validation of Numerical Results by Geosim Tests*, Proc FAST, Southampton, Vol 2, pp 285-294
- BERTORELLO, C.; BRUZZONE, D.; CASSELLA, P.; AND ZOTTI, I. (2001), *Experimental Performance Investigation on Different High Speed Crafts: Monohull Catamaran and Trimaran*, HIPER, Hamburg, pp 107-114
- CALLAGHAN, A.R.; LEWIS, K.E. (2000), *A Phase Aspiration Level and Utility Theory Approach to Large Scale Design*, DETEC2000/DTM-14569
- FAN, Z.P.; MA, J.; HUANG, L.H. (1998), *A subjective and objective integrated approach to determine attribute weights*, ([http://www.is.cityu.edu.hk/Research/ Working Papers /working_paper98.htm](http://www.is.cityu.edu.hk/Research/Working_Papers/working_paper98.htm))
- GRUBISIC, I. (1995), *Multi criteria concept design model of fast catamaran*, IMAM, Dubrovnik, Croatia
- GRUBISIC, I.; BEGOVIC, E.; KRILIC, T. (2002), *Multi-attribute concept design model of search and rescue vessels*, HSMV, Napoli, Italy
- GRUBISIC, I.; BEGOVIC E.; ZANIC, V. (1997), *Concept design model of an outrigger trimaran ferry*, IMAM, Istanbul, Turkey

- GRUBISIC, I.; BEGOVIC, E. (2001), Multi-attribute concept design model of the Adriatic type of fishing vessel, *Brodogradnja*, Vol. 49, No. 1, pp. 39-54
- GRUBISIC, I.; BEGOVIC, E.; KRILIC, T. (2000), Multi-criteria ship selection procedure, *International Design Conference*, Dubrovnik
- GRUBISIC, I.; BEGOVIC, E. (2003), *Multi-attribute concept design model of patrol, rescue and antiterrorist craft*, FAST 2003, Ischia, Napoli, Italy
- KORHONEN, P. (1998), *Multiple Objective Programming Support*, Interim Report, IR-98-010/March
- PAOLUCCI, M. (2000), *Metodi Decisionali Multi Criterio*, DIST, Università di Genova
- SEN, P.; YANG, J.B. *Engineering design and Multiple Criteria Decision Making*, (<http://www.sciencedirect.com>)
- SEN, P. (1992), *Marine Design: The Multiple Criteria Approach*, Transactions of RINA, Vol. 134 pt. B, pp. 261-276
- SEN, P.; YANG, J.B. (1998), *Multiple Criteria Decision Support in Engineering Design*, Springer-Verlag
- TRINCAS, G.; BIRIACO, A.; GRUBISIC, I.; PONOMAREV, A. (1995), *Feasibility Study on a Hight Speed Catamaran: Comparison with Aquastrada*, FAST 95, Lübeck – Travemünde, Germany
- VAN OOSSANEN, P. (2003), *A Concept Exploration Model for Sailing Yacht*, Transactions of RINA, pp.17-28
- WHITCOMB, C.A. (1998), *Naval Ship Design Philosophy Implementation*, Naval Engineers Journal

Experimental and CFD Resistance Calculation of a Small Fast Catamaran

Marcos Salas¹; Richard Luco¹; Prasanta K Sahoo²; Nicholas Browne²; M. López³

¹ University Austral of Chile. msalas@uach.cl

² Australian Maritime College. P.Sahoo@mte.amc.edu.au

³ Nautatec, Spain. nautatec@nautatec.com

Abstract

Catamarans continue to increase in size and application, with proposals circulating within the ship-building industry for bigger and better designs than the present generation of catamarans. The present paper attempts to show a comparison of resistance calculation of a small fast catamaran carried out by experimental and CFD techniques. Experimental tests were carried out with a scaled model at the Towing Tank facilities at University Austral of Chile. CFD simulation using the RANSE code TDYN and Potential Flow code SHIPFLOW was used to calculate the resistance of a prototype catamaran for high-speed operation. The code includes automatic modification of the free surface and therefore dynamic trim and sinkage changes are considered in the solution. Several published articles in well-known journals have detailed various procedures to estimate the resistance characteristics of catamarans. Since few published articles are in existence regarding experimental data on catamarans, it is the aim of this research to undertake a CFD analysis to predict the wave resistance and ultimately the total resistance. Experimental investigation appears to provide very good agreement as has been observed in the resistance curves showing that CFD methods may adequately deal with the problem of wave interference produced by both demihulls. A further conclusion by the authors is that panel density on free surface needs to be defined adequately to capture the waves in the transom at higher Froude numbers.

1. Introduction

This paper compares between CFD and experimental methods in the prediction of calm water resistance of a small fast catamaran. The comparison is restricted to an existing hull form with fixed demihull separation; therefore the results presented here are not intended to be representative of an optimization approach. Moreover the discussion should be viewed simply as a validation test on the reliability of CFD methods for this particular catamaran. Although it is possible to carry out a hydrodynamic optimization using purely numerical methods (López et al. 2000; Kim et al. 2000), is it considered much safer to compare CFD results against experimental data (Stern et al. 1998). A multidisciplinary approach including CFD is thought to be the way forward in hydrodynamics optimization (Peri 2003, Maisonneuve et al. 2003), however the accuracy of CFD methods is still not completely reliable and current research is being devoted to validate CFD techniques (Mehta 1998, Coleman and Stern 1998). It is then necessary to be cautious when performance predictions are involved, although the necessary validation procedures are being developed (Stern et al. 1999; Larsson et al. 2003). In order to evaluate and confront both experimental and theoretical results, two different CFD codes are used to calculate calm water resistance for a small fast catamaran. Both sets of numerical results are then compared to experimental results obtained for scaled model at the towing tank at University Austral of Chile.

2. Catamaran main characteristics

The tested vessel corresponds to a small fast catamaran built by Alwoplast in Chile. The hull, decks and bulkheads are sandwich panels made of composite materials with foam core. The structural configuration of this craft has been illustrated by Ojeda et al. (2004).

Main particulars of the vessel are given in Table 1 below while Figures 1 and 2 depict the built vessel and the hull geometry respectively:

Table 1: Geometrical Parameters of full scale vessel

Parameters	Dimensions
Length over all	16.76 m
Beam maximum	6.00 m
Depth	2.40 m
Draught	0.80 m
Displacement	19 tonnes
Service Speed	22 knots



Figure 1: The tested catamaran

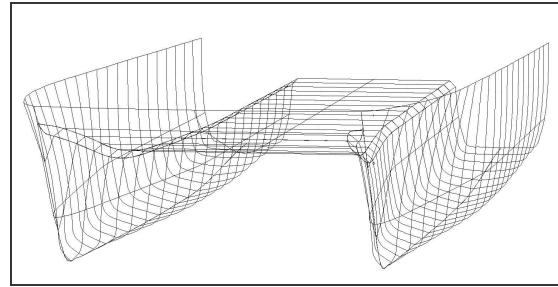


Figure 2: Hull geometry

3. CFD Method

From the mathematical point of view, the equations governing the fluid motion around a vessel are known since the 19th century. Although the equations have practical applications they cannot be solved analytically. In recent times Navier-Stokes equations have been solved using numerical algorithms. Nowadays contour elements or singularity methods are the base of most numerical algorithms used in the prediction of calm water resistance of ships.

3.1 RANSE code Tdyn

Primarily the CFD investigation was carried out using Tdyn (2004) CFD code. It is beyond the scope of this paper to show the mathematical details of the code. López et al. (2000) and García et al. (2002) have provided an extensive discussion on this aspect. However some general description of the solver algorithm may be of interest. The CFD code is based on the FEM and may use almost any type of element, but it is optimized for using linear tetrahedra. An unstructured grid is used to enhance geometry flexibility and to speed up the initial modeling time.

3.1.1 Free surface discretization

The discretization of a general three-dimensional computational domain into an unstructured assembly of tetrahedra is accomplished by means of an advancing front grid generation procedure. This procedure requires the geometry of the computational domain to be defined in terms of an assembly of surface patches. In this case the surface definition of a complete computational domain, consisting of hull and appendages surfaces, free surface, inflow plane, exit plane, and bottom and lateral surfaces is based on NURBS patches (Kim and Shin 2003).

3.1.2 Boundary conditions

Boundary conditions are allowed to be assigned directly on the geometrical entities and automatically transferred to the grid. This utility permits not to re-assign boundary conditions every time a new grid is generated. Furthermore, boundary conditions may be defined by analytic functions. This fact allows performing different drift angle analyses using the same grid, by changing the inflow condition. Other kind of phenomena like non-uniform flows may also be simulated in a similar way.

3.1.3 Control Volume

Finite element solution of a fixed control volume is in most cases accurate enough for design purposes. However, a great quantitative performance of results may be obtained in some cases by updating the domain, taking into account free surface deformations and a dynamic sinkage and trim of the boat. The procedure used to update the domain is now summarized.

- 1) The hull model is first considered in an estimated steady state position. A planar or quasi-planar surface is used as reference for free surface calculations. An automatic unstructured grid generator based on the advancing front technique is used to generate a surface mesh and a volume mesh. A steady state simulation is performed with the hull in this initial position.
- 2) The net heave force and trim moment acting on the hull are calculated from the previous converged solution. The sinkage and trim corrections required by the equilibrium of this force and moment are evaluated. Free surface is updated accordingly to previous results. This is made at CAD level, generating a new NURBS surface based on the previous triangulation of the free surface. A new domain is then created within the preprocessor, repositioning the hull and using the new free surface. This process is automatic, but if necessary may be controlled by the user by means of a *wizard*-type tool. Finally, a new mesh is automatically generated.
- 3) A steady state simulation is performed again in the new domain. A converged free surface is obtained for this given hull position at the end of the present step. This process should be repeated until a convergence of the results. Experience shows that one iteration is enough in most of the cases to obtain forces results within the uncertainty band.

The sinkage and trim corrections are expressed in terms of the net heave force and trim moment using the following relations:

$$\Delta z = \frac{F_z}{\rho g A_{wp}}$$
$$\Delta \alpha = \frac{M_y}{\rho g I_y}$$

Δz is a correction of the sinkage at a center of gravity, $\Delta \alpha$ is a trim angle correction, F_z and M_y are a net heave force and a trim moment. A_{wp} is the water plane area, and I_y is the corresponding moment of inertia about the transverse y-axis. The heave force and the trim moment are defined in terms of the pressure p and the viscous stress tensor components τ_{ij} , which can be obtained directly from the flow solver.

New free surface NURBS definition, taking the resulting deformation into account, is generated in three steps:

1. NURBS Cartesian support grid of $M \times N$ points is created. M and N are calculated in terms of the number of local maximum in the X and Y axis directions.
2. Z coordinate of the points, representing the wave elevation, is interpolated into the grid. This interpolation is based on a weighted function of the nearest points. The nearest points are easily located by using a quad-tree structure.
3. Finally, the NURBS surface based on the support grid is generated. Boundaries of the NURBS are defined by projecting the original ones in the Z direction.

3.2 Potencial Flow code SHIPFLOW

Shipflow uses panel methods to calculate the co-efficient of wave resistance, and therefore it is necessary to define the grid of panels that will be used for the analysis. The module X_MESH is used to define the groups/surfaces that are to be considered. To define the grid of panels representing the body, the number of stations to be used along the length of the hull and the number of points across each station must be specified.

Results of CFD simulations were then confronted with experimental measurements of hull resistance in order to validate the numerical predictions.

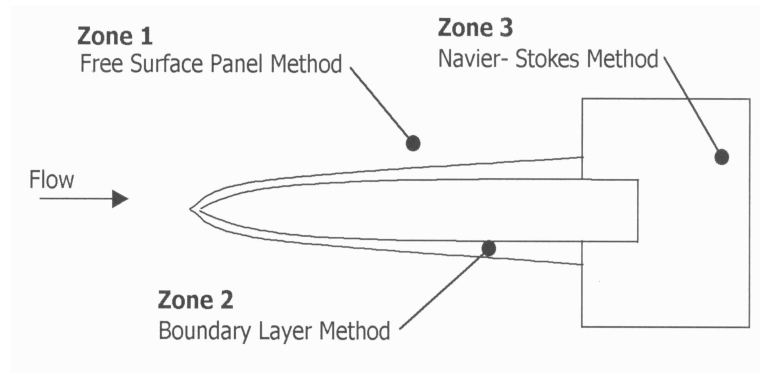


Figure 3: Zonal Approach in SHIPFLOW Solver

The theoretical wave resistance coefficient, C_w , is calculated by splitting the flow into three regions where an efficient approximation of the flow equations may be made and a complete flow calculation may be accomplished in a few hours using the potential flow, as described by Larsson (1993). Figure 3 represents the zonal approach or regions used by SHIPFLOW to maximise computational efficiency.

- Flow in Zone 1 is calculated using a higher order panel method with linear or non-linear free surface boundary conditions.
- Flow in Zone 2 is calculated using momentum integral methods for laminar and turbulent boundary layers.
- Flow in zone 3 is calculated using the Reynolds-Average Navier-Stokes method with a k-epsilon turbulence model and a numerically generated body fitted coordinate system.

4. Model and Experimental Procedure

A FRP model, of scale factor $\lambda = 17$, was built to carry out the towing tank tests. No appendages were installed on the model, and all the experiments were done to the full load displacement, of 19 tons. Experiments were conducted for the range speed of 8 to 28 Knots, corresponding to F_N of 0.35 to 1.2. Tests were carried out in the towing tank of the Institute of Naval and Maritime Sciences at the University Austral of Chile. Tank dimensions are 45 m in length, 3 m width and 2 m water depth. Model was towed at the required speed (same full-scale F_n) by a cable connected to a dynamometer where drag is measured and directly recorded into a computer. Models are free to trim and trim angles may be measured if required. Results from model experiments were extrapolated to the full-scale craft using the ITTC extrapolation procedure and ITTC ship model correlation line, correlation allowance of ATTC of 0.0004 over the friction coefficient of the prototype and zero over the friction coefficient of the model. All data presented in this investigation corresponds to the full-scale craft, floating in smooth, deep salt-water conditions, with a uniform standard temperature of 15° C. To induce turbulent flow along the length of the model hull, 16 turbulence stimulator studs were placed at both demihull bows, as can be seen in Figure 4. No particular turbulence transition location was aimed with this stud configuration. Figure 5 shows the scaled model undergoing towing tank tests.

5. Results

Figures 6 and 7 depict the results of wave height and free surface obtained under different simulated speeds of Tdyn CFD. Finally resistance predictions from experimental tests and both CFD codes are presented in Figure 8. In Shipflow results wave resistance of the model has been calculated based on the regression equation developed by Sahoo et al. (2004).



Figure 4: The model fitted with studs



Figure 5: Towing tank test

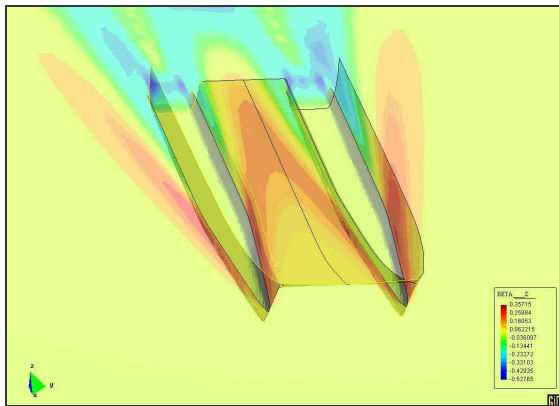


Figure 6: CFD wave height at 28 knots

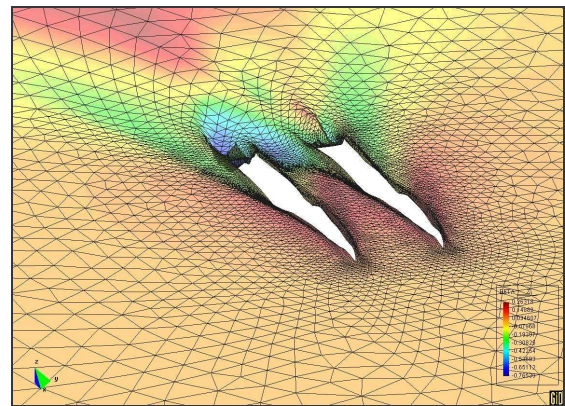


Figure 7: Free surface at 16 knots

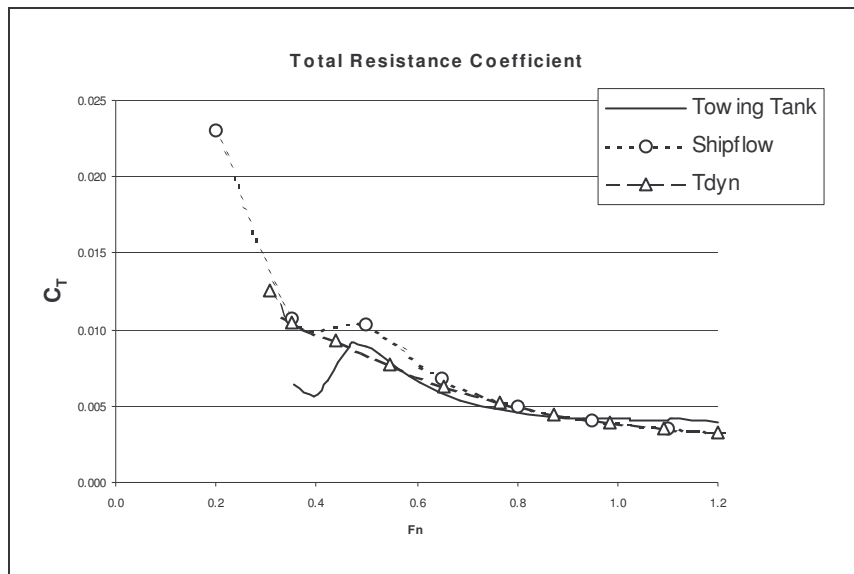


Figure 8: CFD and Towing Tank resistance predictions

6. Conclusions

In the low speed range both CFD codes predict higher C_T than the towing tank. The disagreement may be due to trim angle being affected by pulling cable in the experimental tests. Between Fn 0.5 and Fn 0.9 Tdyn agrees closely with experimental results as both total resistance curves are almost identical. Shipflow resistance estimates are slightly higher than CFD Tdyn and Towing Tank resistance results in this speed range. Both CFD codes, i.e. Tdyn and Shipflow, produce very close total resistance coefficients all over the speed range. CFD codes and experimental results are in remarkable good agree-

ment above F_n 0.5 and up to F_n 1.0, for higher speeds numerical results predict lower resistance than the towing tank. The difference is about 20% for F_n 1.2

Acknowledgements

We express our sincere gratitude to The University Austral of Chile and The Australian Maritime College, Australia for their support, encouragement and financial help throughout the course of this research work.

References

- Coleman, H.W.; Stern, F. (1998). "Uncertainties in CFD Code Validation". *ASME J. Fluids Eng.*, Vol. 120, pp. 635-636.
- García, J.; Luco, R.; Salas, M.; López, M.; Oñate, E. (2002) "An Advanced finite element method for fluid-dynamic analysis of America's Cup boat", *High Perf. Yacht Design Conf.*, pp.21-29. Auckland
- Kim, B.; Shin Y. (2003). "A NURBS Panel Method for Three-Dimensional Radiation and Diffraction Problems". *J. Ship Research*, Vol. 47. N°2. pp.177-186.
- Kim, W.; Kim, D.; Van, S. (2000). "Development of wave and viscous flow analysis system for computational evaluation of hull forms" *Ship and Ocean Technology*, Sept. 2000, Vol. 4, N° 3, pp. 33-45.
- Larsson, L.; Stern, F.; Bertram, V. (2003) "Benchmarking of Computational Fluid Dynamics for Ship Flows: The Gothenburg 2000 Workshop". *J. Ship Research*, Vol. 47, N°1, pp. 63-81.
- Larsson, L. (1993), "Resistance and Flow Predictions Using SHIPFLOW Code". 19th WEGEMT School, Nantes
- López, M.; García, J.; Oñate, E. (2000) "Recreational craft optimization using a CFD code" (In Spanish) Barcelona, Spain. Technical workshop on sport craft.
- Maisonneuve, J. ; Dauce, F. ; Alessandrini, B. (2003). "Towards Ship Optimal Design Involving CFD". *CFD 2003: Comp. Fluid Dynamics Technology in Ship Hydrodynamics*, London, pp. 31-41.
- Mehta, U.B. (1998). "Credible Computational Fluids Dynamics Simulations". *AIAA J.*, Vol.36, pp.665-667.
- Ojeda, R.; Prusty, B. G.; Salas M.. (2004) "Finite Element Investigation on the Static Response of a Composite Catamaran under Slamming Loads". *Ocean Engineering*, Vol. 31. pp. 901-929
- Peri, D.; Campana, E. (2003). "Multidisciplinary Design Optimization of a Naval Surface Combatant". *J. Ship Research*, Vol 47. N°1. pp. 1-12.
- Sahoo, P.K.; Browne, N.A.; Salas, M. (2004). " Experimental and CFD Study of Wave Resistance of High-Speed Round Bilge Catamaran Hull Forms". *4th Int. Conf. High Perf. Marine Vehicles*, Rome
- Stern, F.; Longo, J.; Abdel-Maksoud, M.; Suzuki, T. (1998). "Evaluation of Surface-Ship Resistance and Propulsion Model-Scale Database for CFD Validation". *1st Symp. Marine Application of CFD*, McLean
- Stern, F., Wilson, R.V., Coleman, H. and Paterson, E. (1999). "Verification and Validation of CFD Simulations". *3rd ASME/JSME Joint Fluids Eng. Conf.*, San Francisco
- Tdyn-Compass, (2004) ref. URL www.compassys.com

The Applicability of Advanced Ship Types in the Dutch SAR Operations

Koos Frouws, Delft University of Technology, Delft/The Netherlands, J.W.Frouws@wbmt.tudelft.nl

Fons Huijs, Delft University of Technology, Delft/The Netherlands, F.A.Huijs@student.tudelft.nl

Abstract

Recent research investigated which advanced ship types could improve the performance of the Dutch search-and-rescue (SAR) fleet. For each ship type the advantages and disadvantages regarding the whole scope of aspects including speed, range, endurance, sea keeping, draft, space for victims and operational aspects in waves and during rescue operations were evaluated. Ship types considered included monohulls, catamarans, trimarans, SWATH's, Stolkraft, hydrofoils, air cushioned vehicles and surface effect ships. Unexpected advanced ship types turned out to be well applicable in certain areas, adding substantial speed and as such decreasing the reaction time of the rescue organisation, and decreasing the required time from volunteers. The paper presents the findings in terms of criteria matched against possible alternatives for the current RIB's and/or possible improvements of monohulls in SAR service.

1. Introduction

The “Royal Netherlands Sea Rescue Organization” KNRM (Koninklijke Nederlandse Reddings Maatschappij) is a private institution that is responsible for the rescue boats in the Dutch Search-and-Rescue (SAR) fleet. The development of shipping, ship types, politics and the public opinion asks for a reconsideration of the service and equipment needed in the future.

Delft University of Technology performed a research project for the KNRM. The aim of the research was to investigate the possibilities to improve the SAR fleet. First an analysis of the performed SAR operations was made, using detailed statistical data of twelve years of SAR actions. Based on shipping statistics, harbour information, economical predictions and political plans, a prediction of the intensity of shipping, recreation and fishery in 2010 was made. In the second part of the research the functional requirements of the ships and equipment were established. Those are based on operational aspects, harbour facilities, draft restrictions, and sea states and weather conditions the rescue craft will face during operation. The final part of the research was focussed on the fields where improvements can be made or developments can be implemented. Possibilities to improve the fleet, vessels and equipment were investigated. This led to recommendations and a plan for further technical research.

This paper focuses on the applicability of advanced ship types in the Dutch SAR fleet, mainly investigated in the final part of the research.

2. The Dutch SAR Fleet

The Netherlands Coast Guard is responsible for the search and rescue of crew and passengers of vessels, offshore plants and aeroplanes in problems in the Dutch waters. According to an agreement between the Netherlands Coast Guard and the KNRM, the latter provides the lifeboats for SAR-operations, *NCG (1999)*. The vessels are owned by the KNRM and operated by their crew, mainly consisting of volunteers. The Royal Dutch Navy provides aeroplanes (Lockheed Orion) and helicopters (Lynx) for SAR operations when necessary. Furthermore there are a lot of so-called 'non-declared units', being ships from governmental organisations like customs, police, navy and coast guard or smaller private rescue organisations. The availability of those units depends on their other activities and is not always guaranteed. Fig.1 shows that KNRM vessels are involved in 80% of all SAR operations, *Frouws (2004b)*. In 18% of the operations, the KNRM is co-operating with other parties, mainly commercial or recreational vessels that are in the vicinity of the accident.

The coast guard operates a Rescue Control Centre at IJmuiden for the operational co-ordination of SAR activities. During most SAR operations, one of the rescue units is assigned as On Scene Co-ordinator and has the command over the other units involved.

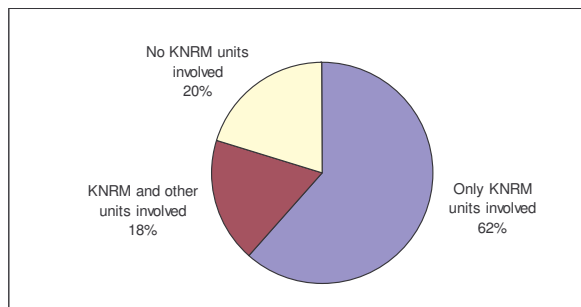


Fig.1: Involvement of the KNRM in the Dutch SAR operations



Fig.2: Largest vessels of the KNRM in line: Valentijn class, Johannes Frederik class and Arie Visser class

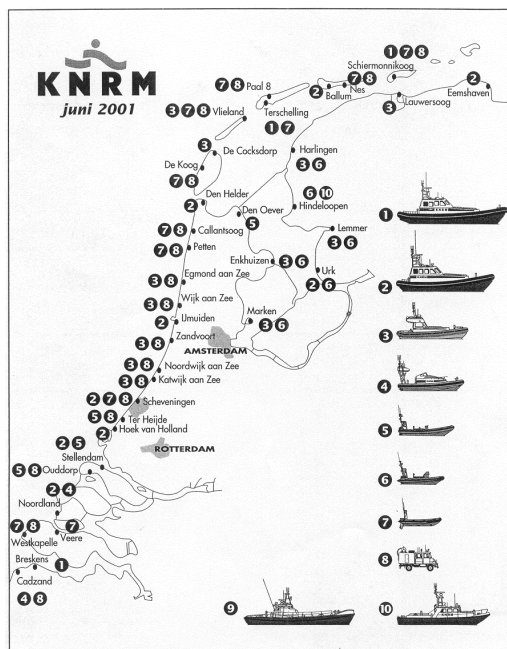


Fig.3: The SAR fleet of the KNRM (2001)

The fleet of the KNRM consists of planing monohull Rigid Inflatable Boats (RIB's) along the coastline of the Netherlands. Fig.2 shows the largest types of those vessels. These are the so-called "all-weather ships", operational at any weather or sea condition. Fig.3 shows the locations of the rescue stations and the vessels in service. Table I gives some technical information of the ships. The numbers of the classes correspond to the numbers on the map. Most of these vessels have top speeds around 35 knots. Relevant for this article are the first three vessel types. In seaway however this speed is often not reached, because the severe ship motions force the crew to slow down.

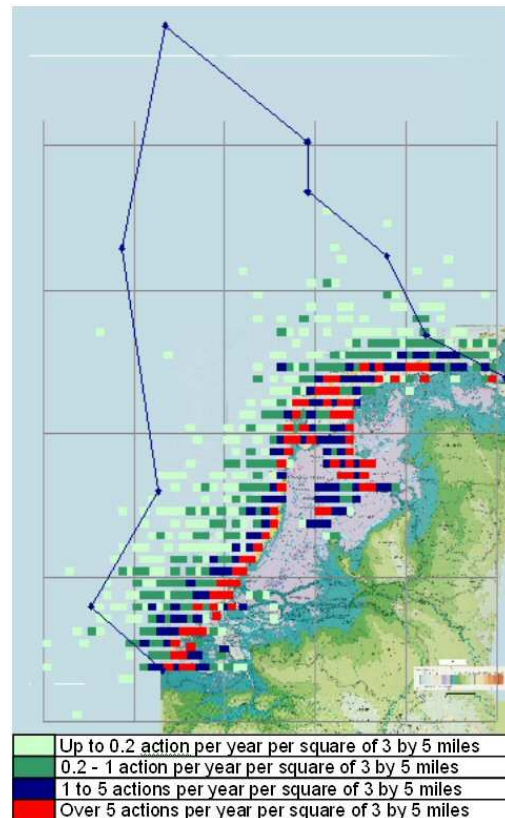
3. Analysis of Performed SAR Operations

The operations of the Dutch SAR fleet were analysed using the statistical data of twelve years search-and-rescue actions. This data included for example the location, duration and cause of over 14.000 actions. Fig.4 shows the geographical location of the SAR operations, *Frouws (2004a)*.

Table I: The SAR vessels of the KNRM, www.knrm.nl.

Class	1. Arie Visser	2. Johannes Frederik	3. Valentijn	4. Harder	5. Atlantic	6. Avon	7. Floot 500	8. Wippertruck	9. Koningin Juliana	10. Jansje Bart
Length [m]	18.8	14.4	10.6	9.1	6.5	5.4	5.1	-	21.1	14.9
Beam [m]	6.1	5.4	4.1	3.3	2.3	2.1	2.0	-	4.6	4.2
Draft [m]	1.0	0.8	0.8	0.5	0.7	0.4	0.3	-	1.5	1.1
Displacement [ton]	28.0	15.0	7.6	3.5	1.5	1.0	0.5	-	54.5	23.0
No. of engines	2	2	2	2	2	1	1	-	2	1
Power installed [kW]	735	507	321	172	52	67	37	-	127	189
Maximum speed [kn]	35.0	34.0	34.0	36.0	30.0	40.0	25.0	-	10.7	9.0
Waterjets	yes	yes	yes	no	no	no	no	-	no	no
Material	Alu	Alu	Alu	Rub	Rub	Rub	Rub	-	Steel	Steel
Crew	6	4	4	3	3	2	3	-	5	4
Space for victims	120	90	50	20	12	8	5	-	120	50
Vessels in service	5	8	15	1	6	6	10	-	17	0
Back-up vessels	0	1	0	1	2	2	5	-	0	2
Total no. of vessels	5	9	15	2	8	8	15	-	17	2

Fig.4: Average number of SAR actions per year



90% of all accidents take place within 10 miles out of the coast of the North Sea or on the protected waters of the Waddenzee, IJsselmeer and Zeeuwse stromen. In 98% of the operations of the KNRM, the number of rescued persons is under ten. Over 60% of those accidents take place with recreational vessels. Larger accidents are very rare. The highest number of rescued persons between 1990 and 2001 was 118 in case of an accident with a passenger ship. The chance of a large incident is small; the impact can however be enormous. In summertime every day 47 ferries with 312 up to 1750 passengers travel between the mainland and the Wadden islands. Yearly 3800 ferries sail between the Netherlands and England with numbers of passengers varying from 150 to 1500 passengers and 100 cruise ships cross the Dutch waters. Daily some 450 aeroplanes heading for or leaving Schiphol Airport fly over the Dutch waters. The possibility of an accident with up to 4000 victims cannot be neglected. The routes of the large passenger vessels and aeroplanes are shown in Fig.5. This gives an indication of the possible locations of large accidents.

The SAR operations database of the KNRM was coupled on a wind measurement database of the Royal Netherlands Meteorological Institute, www.knmi.nl/samenw/hydra/. The real time wind data during operations were analysed, leading to the results presented in Fig.6. It shows that most operations take place under medium wind forces, but the ratio operational time versus wind occurrence time grows substantially with increasing wind forces. 94% of the operational time is spent at wind forces under 7 Beaufort. (Mainly assisting recreational vessels)

The same operation is carried out for the wave climate. The database of the KNRM is coupled with wave measurements of the National Institute for Coastal and Marine Management (RIKZ), www.golfklimaat.nl, leading to very detailed information about the waves the SAR vessels will be operating in. Table II: shows the resulting wave scatter diagram during SAR operations on the North Sea. This is not just an ordinary wave scatter diagram of the North Sea; it is the wave scatter diagram during operational time.

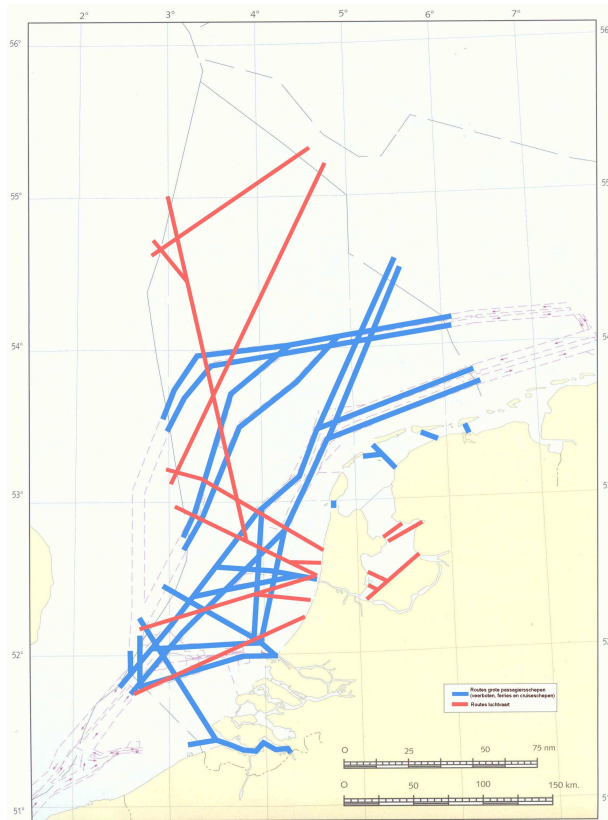


Fig.5: Routes of large passenger vessels (blue) and aeroplanes (red)

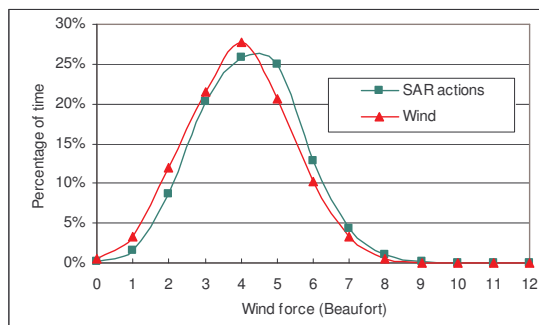


Fig.6: Distribution of wind occurrence whole year round and wind occurrence during actions.

Table II: Wave scatter diagram during SAR operations on the North Sea

$h \ 1/3 \ (m)$	T (s)	3	4	5	6	7	8	9	10	11	12	total
0.25		0.36	4.53	4.52	1.14	0.28	0.23	0.06				11.10
0.5		1.16	7.09	6.00	3.30	0.93	0.54	0.08	0.03			19.14
0.75		0.10	5.47	5.26	3.44	1.69	0.43	0.11	0.03			16.54
1			2.41	5.81	2.96	1.14	0.29	0.02	0.01			12.63
1.25			0.47	4.67	2.46	1.23	0.18					9.00
1.5			0.02	3.05	3.91	1.00	0.15	0.01				8.14
1.75				0.73	3.89	1.14	0.19	0.01				5.95
2					0.07	3.27	1.04	0.06	0.01	0.02		4.47
2.25						2.09	0.79	0.10		0.01		2.98
2.5						0.81	0.84	0.06	0.03			1.73
2.75						0.17	1.31	0.29	0.06			1.82
3						0.01	0.67	0.39	0.03			1.09
3.25							0.80	0.67	0.18			1.65
3.5							0.20	0.31	0.16			0.67
3.75							0.04	0.41	0.31	0.10		0.86
4								0.33	0.18			0.51
4.25								0.16	0.10	0.12	0.03	0.41
4.5								0.09	0.22	0.10	0.03	0.43
4.75								0.01	0.22	0.07		0.30
5									0.05	0.04	0.01	0.10
5.25									0.18	0.01	0.19	0.38
5.75										0.05		0.05
6.5											0.01	0.01
6.75											0.03	0.03
total		1.62	19.99	30.10	27.43	13.08	4.89	1.94	0.62	0.32	0.01	100

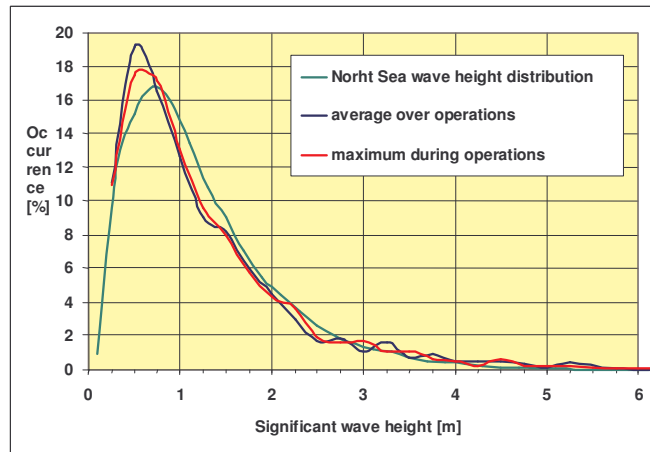


Fig.7: Average and maximum significant wave heights during SAR operations on the North Sea

Fig.7 shows that the distribution of wave heights over the operational time of the SAR vessels on the North Sea differs little from the ordinary North Sea distribution of wave heights. The majority of the incidents take place at medium wave heights. The SAR vessels spend 86% of their time offshore at significant wave heights up to 2.0 m. The scatter diagram of the SAR vessels shows a higher occurrence of wave heights exceeding 3.0 m, which indicates that those wave heights lead to an increased number of accidents.

4. Functional Requirements

The analysis of the performed SAR actions shows that the KNRM faces different accidents, asking for different rescue vessels.

Most incidents appear close to the coast and involve only a small number of victims. For those accidents and for search operations, the KNRM needs small vessels distributed along the coastline. Operations further offshore and accidents with large numbers of victims ask for large and very fast ships. The reaction time is important and the ship motions should be smooth in order to maintain a speed over 30 knots in seaway. Those ships should have an endurance of at least 6 hours at full speed.

Table III: functional requirements of large rescue vessels

length	< 20 m
draft	< 1.0 m
speed in waves	> 30 kn
endurance (full speed)	> 6 hrs
stability	self-righting
vertical accelerations	< 0.2 g
manoeuvrability	good
maximum wind force (hourly average)	10 bft
wind force < 7 bft	94 % of time
maximum significant wave height	6.75 m
significant wave height < 2.0 m	86 % of time
communication equipment	advanced
space for victims	> 100persons

All rescue vessels should be self-righting to ensure the safety of the crew and passengers. The seaworthiness and manoeuvrability should be good. Vertical accelerations over 0.2g are to be avoided for the crew to do their job. There should be enough redundancy installed in the propulsion system. The towing capacity is important as well, because small damaged or grounded vessels need to be towed back to harbour. Because of the shallow coastal waters, the draft of all KNRM vessels is limited by 1.0 m. Depending on the location, the length of the vessel might be limited by the boathouse or the harbour. The KNRM and its coxswains prefer a maximum overall length of 20 m, based on their experience with handling vessels in the coastal waters, *Velde et al. (1999)*. A stable platform and advanced means of communication are needed for the larger vessels, so that they will be able to perform the task of On-Scene-Coordinator. All free space should be available to take as many victims aboard as possible.

The functional requirements for the large “all-weather vessels” the ship types 1 and 2 (Arie Visser and Johannes Frederik) are collected in Table III. Those large vessels operate further offshore than the small vessels, so speed is extremely important.

5. The Applicability of Certain Ship Types

Monohulls

The KNRM currently operates fully planing Rigid Inflatable Lifeboats. They have a low resistance when planing and can reach speeds of about 35 knots, but the vertical accelerations in seaway are too heavy and force the crew to slow down. According a master the speed has to be reduced to 15/18 knots in case of front waves of 3 meter. These ship types have a very good over all performance, but should be improved on the field of vertical accelerations.

This might be established by increasing the deadrise from 25° to 30°. The penalty on ship resistance caused by this change of design is calculated using the prediction methods of Mercier-Savitsky (semi-planing speed range) and Savitsky (fully-planing speed range). Calculations have shown that the resistance increases between 10% and 15%, but the decrease of vertical accelerations might be worth taking this penalty. For these calculations the displacement and the length were kept constant, so the draft increased and the breadth decreased with increasing deadrise. The increase of draft is about 11%, which might cause problems because of the draft restrictions on the shallow coastal waters. The breadth decreased with 10%, which might cause stability problems. Both aspects should be looked after in following technical research. A way to compensate for the loss of lift could be a transversely trepped hull, a prototype of this approach is sailing in Germany.

Another possibility to decrease the vertical accelerations is to apply the Enlarged Ship Concept. The vessel is enlarged, but the extra space should not be utilised, in that case the displacement stays almost the same. In 1999 Delft University of Technology performed a design study on a RIB according to this concept, *Velde et al. (1999)*. A RIB of the 'Johannes Frederick' class of 14.40 meters was compared with two enlarged versions of 16.80 and 19.20 meters. The enlarged vessels would have a lower resistance caused by the higher Froude number, lower vertical accelerations at the bridge, less draft and extra space for saved victims. The difference between those enlarged vessels and the already existing 18.80 meter RIB's of the 'Arie Visser' class is that the latter are heavier and have a larger breadth, undoing the positive effects of the enlargement.

The motions of fast monohulls can be improved even further by giving the bow the shape of an axe, *Keuning and Pinkster (2002)*. This so-called Axebow concept is not applied on vessels yet, but the test results are promising. This development was mainly done for frigates. The change of shape would however increase the draft at the bow and the directional stability, which makes this ship type vulnerable in shallow water, less manoeuvrable, and as such less suitable for the KNRM.

Concluding one might say that the monohull RIBs of the KNRM have proven to be very successful, but should be improved on the field of motions in seaway. Further technical research for the application of the Enlarged Ship Concept or an increase of the dead-rise, possibly in combination with a transversely trepped hull is recommended.

Catamarans

The catamaran consists of two slender hulls and on top of the hulls a beamy deck. This offers a large stable platform area and a lot of space for victims. The wave making resistance is smaller than for a monohull, because of the slender hulls, but the wetted surface is larger, leading to a larger frictional resistance, relevant at low speeds. In order to lower the wave making resistance the distance between the hulls should increase which is not compatible with self-righting properties. The accelerations in waves and the consequent speed reduction are larger than for monohulls, *Nigel (1990)*, this makes further research for the applicability of this ship type in severe seaway obsolete, because these motions and speed reductions are actually the main items to improve of the current ships.

Trimarans

The trimaran is a ship type with a centre hull and two outriggers, recently proposed for frigates, *Andrews and Zang (1995)*. The centre hull takes the largest part of the displacement and is shaped according the thin hull ideas in order to reduce the wave resistance, the outriggers take care of the required stability. The draft of such a hull will be larger than for a comparable monohull. Manoeuvres close too vessels, to rescue people, will be limited due to the vulnerable outriggers. These aspects make this hull form less suitable for SAR actions in the shallow Dutch waters.

SWATH

The Small Waterplane Area Twin Hull (SWATH) is designed to minimise the motions in seaway. The submarine shaped structures deep under water delivers most of the buoyancy. The waterplane area is very small, leading to minimal influence of waves on the vertical accelerations. This concept is applied successfully on patrol ships, hydrographical research vessels, ferries and recently pilot tenders. Although there are publications that recommend this ship type for SAR service, there has not one been built one vessel yet, *Hussey and Inan-Ul Majid en Wight (1990)*. The big disadvantage for use in the Dutch coastal waters is the necessity to increase the draft in order to place the buoyancy sufficiently far enough under water. Furthermore SWATHs are not as fast as planing monohulls or catamarans, because of the large wetted area. On the other hand the sustained speed in seaway is excellent, with head waves of 3 meter they can sustain the same speed as the existing monohulls (around 15 to 18 knots). Further on using the gained experience with the pilot tenders *Döse* and *Duhnen* build by *Abeking and Rasmussen* they are very stable, have extremely low acceleration levels and a surprising ability to take over or deliver people to seagoing vessels up to beaufort 8 as proven in the Elbe area. On one hand due to its ability to raise, lower or heel the vessel by its ballast system, on the other hand because the motions are limited and in its magnitude comparable with the motions of the bigger ship. The tenders operating in the Elbe area are equipped with a lift in order to rescue people from the water. This stable and large platform is an advantage when performing the role of On-Scene-Coordinator or when a lot of victims have to be taken on board. When a lot of people are taken on board, the draft may however increase too much, because of the small waterplane area. When the deck comes to close to the waterplane, the motions will increase.

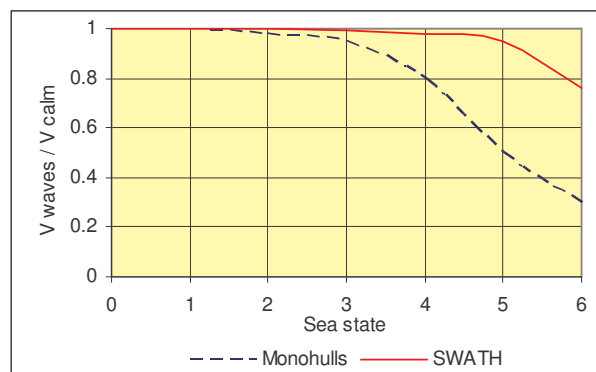


Fig.8: Speed loss in head waves

The natural frequency for heave of a SWATH is about half that of a monohull or catamaran of the same displacement. Since the maximum vertical accelerations are a function of the square of this frequency, the accelerations will be about four times smaller. Furthermore are low frequency waves not so much present in the wave spectrum and is excitation at the natural frequency unlikely to occur. Fig.8 shows that the speed loss of SWATHs in head waves is much smaller than the speed loss of monohulls, *Hawkins and Sarchin*. The calculation is made for vessels from 4000 to 8000 tons, but the general picture is valid for all sizes of vessels.

SWATHs have a very good manoeuvring capacity at low speeds, because of the large distance between the two propellers. At higher speeds however, manoeuvring is difficult because of the extreme straight-line stability of the SWATH. Self-righting abilities, not yet investigated in detail by me, are still considered as possible.

To conclude, SWATH's are an improvement in SAR operations if the sustained speed in head waves is of primary importance and a draft of 2 till 2.5 m is acceptable. For example the vessel *Döse* has a design draft of 2.7 m., actually variable due to the ballasting system. The top speed can be improved because of a lower equipment level in SAR service than in pilot tender service.

Stolkraft

The hybrid ship type Stolkraft is a merging of the fore body of a trimaran with the aft body of a catamaran, Fig.9, and moves very efficiently at high speeds. The airflow, generated by forward motion of the vessel, is ducted through two symmetrical scoops formed by the tri-hulled fore body. A vacuum caused by an amidships step combined with flow phenomena behind the three hulls, creates a fusion of air in the aft body recess between the two outer hulls, significantly reducing frictional resistance and subduing hull generated wake and wash,

<http://www.artanderson.com/Stolkraft%20Technical%20Paper.pdf>.

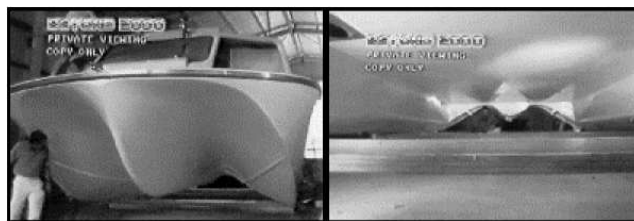


Fig.9: Stolkraft hull

This hull type offers minimal wake and wash, good speed – power characteristics, high maximum speeds, good manoeuvrability, shallow draft, normal sea keeping performance, a large deck area for victims and good stability at all speeds.

The draft at zero speed is smaller than conventional catamarans and deep-vee monohulls and this draft is further reduced by about 67% when the vessel is at speed. Motions and accelerations in high seas are comparable to those of planing monohulls or slightly better due to the cushioning airflow between the hulls. The vessel does hardly take green water over the bow. Creating a self-righting ability without jeopardizing the design could be a challenge.

The shallow draft and economic fuel consumption makes this ship type possibly good applicable for the Dutch SAR fleet and worth further research. Special attention should be paid on the motions in seaway.

Hydrofoils

Hydrofoils are vessels that are lifted out of the water by their foil, decreasing the resistance and thus enabling very high speeds. They consume a lot of fuel, but are economic at speeds between 30 and 50 knots. There are two kinds of hydrofoils: with a surface piercing foil and with a submerged foil.

Surface piercing hydrofoils have the advantage that the foil stabilises the vessel and no active stabilisation for heave, pitch and roll motions is needed. Ships with surface piercing foils can however only operate on calm water and are thus useless as lifeboat, *Johnston (1985)*.

Because the submerged foil is placed deeper under the water surface, it suffers less from waves and submerged hydrofoils can be operated up to sea state 6. An active stabilisation system is however needed for this kind of hydrofoil.

Hydrofoils are designed to survive severe weather conditions as a displacement ship. In this case the speed advantage of the hydrofoil is lost. The manoeuvring properties of hydrofoils are even better than for monohulls. Sharp curves are felt as a little increase of the gravity, without any lateral force.

When a hydrofoil is sailing slower than half its design speed, it is not lifted out of the water. In this case the draft is very large, because the foil should be placed far under the deck of the ship in order to operate in waves. This large draft and the vulnerability of the foils in low depth conditions make the hydrofoil not suitable as lifeboat on the Dutch shallow coastal waters.

Hovercraft

The amphibious properties of hovercrafts may offer great advantages in the Dutch coastal waters. The craft can be launched from the beach without a truck; it can cross banks and sand plates and operate on partly frozen waters. A hovercraft has a large deck area, as an effect of the large beam. The beam of a hovercraft is in general about half its length. Air propellers, able to rotate around their vertical axis to manoeuvre, usually deliver the propulsion. Especially hovercrafts with four propellers have good manoeuvring properties and can move sideward, *Lavis (1985)*. Maintaining the pressure under the cushion does however cost a lot of energy, which makes the propulsion efficiency significantly lower than the current planing monohulls. But speeds up to 50 knots can be reached, enabling short reaction times and effective search operations.



Fig.10: SAR hovercraft CCG SIPU-MUIN

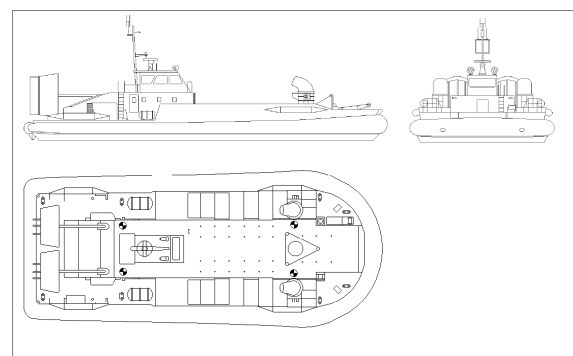


Fig.11: General plan of CCG SIPU-MUIN

The Canadian Coast Guard operates hovercrafts for SAR aims since 1969, *Wade (1989)*. Among the activities are search actions, towing of damaged vessels and taking wounded persons on board. Nowadays the Canadian Coast Guard operates four hovercrafts, www.ccg-gcc.gc.ca, that are used for SAR activities as well as for hydrographical research, transport of inspectors and buoy maintenance. Technical details are given in Table IV: *T* The hovercrafts are still operational at wind speeds of 40 knots (Beaufort 8) and significant wave heights of 1.5 m (Sea state 4), *Grady (2004)*. Hovercrafts are not limited to protected waters, but operate over the whole area of the Canadian Coast guard, up to 200 miles out of the coast. Heavy motions, forcing the crew to reduce thrust, mainly cause speed reductions in seaway. Experience shows that in those cases, higher speeds can be made on shallow water.

Table IV: Technical details of the Canadian SAR hovercrafts

Vessel	Length [m]	Beam [m]	Range [nm]	Endurance [h]	Cruising speed [kn]	Maximum speed [kn]	Bollard pull [t]
CCG WABAN-AKI	24.5	12	600	24	35	50	5
CCG SIPU-MUIN & CCG SIYAY	28.5	12	-	24	45	48	n.a.
CCG CG-045	14.8	7	300	8	50	50	n.a.

The use of hovercrafts seems especially suitable for the Waddenzee. This sea is full of banks and many of them get above water at low tide. A hovercraft would not need to follow the tidal channels and can reach yachts that are grounded on very shallow water or people who are walking the banks and get surprised by the tide. When Beaufort 8 is taken as the limit for operation of the hovercraft, 2168 of the 2292 actions of the period 1997 – 2001 could have been carried out by hovercrafts. In 645 cases the hovercraft would have had great advantages over the current vessels. Those are the operations for surfers, canoes, bank walkers, swimmers, aircrafts, medical transport and search operations. The very high seasonal load on the volunteers in summertime, especially in august in this area, could be lightened by the application of one or two hovercrafts. However, at this moment the use of hovercrafts in this area is forbidden for environmental reasons by law.

Hovercrafts can use their full thrust as bollard pull, but will not be able to reach high speeds when towing, because they can not pass the humps in the resistance characteristics, *Yun and Bliault (2000)*.

Further technical research for a SAR hovercraft at the Waddenzee is recommended. The potential number of operations where hovercrafts can help is substantial and can decrease the required time from the current volunteers.

Surface Effect Ships

Like hovercrafts, Surface Effect Ships (SES) rides the sea on an air cushion. The difference is that the longitudinal sides of the cushion are solid floaters for the SES. It is actually a hybrid hull type, a combination between the catamaran and the hovercraft. As an effect, the SES is not amphibious, but less air pressure is lost, the longitudinal stability is larger and underwater propulsion systems can be used. Speeds up to 91.9 knots have been reached with SES, but for most ships the maximum speed is about 40 knots. The speed loss in waves is substantial due to slamming. The SES with the record speed of 91.9 knots had to slow down to 35 knots in waves between 1.8 and 2.4 m, *Butler (1985)*.

The draft of the hull of the SES is small when on-cushion, but this advantage is diminished by the rudders that need a larger draft to achieve enough manoeuvrability. When the rudders are large enough, the SES has good manoeuvring properties, even at low speeds.

SES vessels have more freeboard than conventional monohulls, so there is little green water on deck. Furthermore the ships are stable and have reasonable motions in seaway, because most waves pass through under the cushion. When a wave passes the pressure over the whole bottom changes, causing just heave motions, no roll or pitch motions.

Although this craft is not amphibious, it still has many of the advantages the hovercraft has. When the draft of the rudders could be minimized, use of a SES on the Waddenzee might be possible. However besides their speed they do not offer advantages above the current existing monohulls, a speed paid by means of complexity and money.

Wing in Ground

Wing in Ground planes would have to be relative big in order to fly high enough above the waves to be useful for SAR operations, *NN (1985)*. The only application in SAR service I can think of is as a platform for sensors (for finding people) which has to be situated just above the water for reasons of sensitivity.

Submarines

The British Royal Navy operates a submarine to rescue people from sunken submarines, Figs.12 and 13, www.royal-navy.mod.uk/static/pages/1252.html. There is no need for more than one of those vessels in the North Sea.



Fig.12: Royal Navy LR5 Rescue Submarine

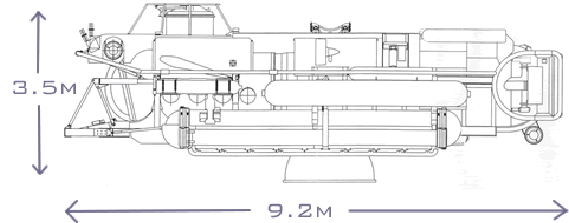


Fig.13: LR5 Rescue Submarine side view

Remotely Operated Vehicles

The Canadian company International Submarine Engineering Ltd has built a prototype of a ROV rescue vessel. The vessel is dropped into the water by an aircraft, inflates itself and starts the engines. The vessel is remotely operated from a helicopter and directed to the victim. The victim has to board the vessel by his own power. Then the vessel sails to a safe place where the helicopter can take the victim on board. The vessel returns to harbour.

The vessel offers space for five or six persons and the endurance is 24 hours with a cruising speed of 5 knots, <http://www.ise.bc.ca/SearchNRescue.html#sarpalvideo>. Disadvantages of the system are that the victim cannot be unconscious, planes and a helicopter are needed and the system is technically complex. The advantage of this ship type is that it can be used when the weather is too heavy to take victims on board of the helicopter and when no lifeboats can be present in time. This is an uncommon situation in the Netherlands. However, if considered it could be considered in cooperation with foreign states in order to be able to cope with extreme situations.

6. Conclusions

Table V compares the performance of the different ship types on the various functional requirements. Also an indication of the building and maintenance cost is given, based on the paper on Stolcraft, <http://www.artanderson.com/Stolcraft%20Technical%20Paper.pdf>.

Increasing the deadrise or applying the Enlarged Ship Concept can possibly improve the monohulls currently used. The Axebow concept is not very suitable because of the large draft.

Catamarans have worse motions and larger speed reductions in waves, which make them less useful. Trimarans are not applicable either, because of the large draft.

A SWATH could be applied and does offer advantages on top of the existing monohull but not in all conditions.

The new concept of Stolcraft might offer good opportunities for the smaller vessels of the KNRM. The shallow draft and economic fuel consumption makes them attractable. Motions in waves and dif-

difficulties in reaching the self-righting ability makes this ship type however less useful as “all-weather” rescue craft.

Hydrofoils are not applicable for the Dutch SAR fleet, because their draft at rest makes them useless for the majority of actions, performed on shallow water.

Hovercrafts offer great opportunities because of their minimized draft and very high speeds. They are not applicable as “all-weather” vessel, but might be very useful on the protected shallow Waddenzee. Surface Effect ships have the disadvantage of a larger draft, caused by the rudders, but if this is minimized, they might as well be applicable on the Waddenzee.

Table V: Comparison of different ship types

Functional requirement		Current monohull	Monohull with increased deadrise	Enlarged ship concept	Axebow	Catamaran	Trimaran	SWATH	Stolkraft	Fully submerged hydrofoil	Hovercraft	Surface Effect Ship
length	< 20 m	+	+	+/-	+/-	++	+/-	+	+	+	++	++
draft	< 1.0 m	+	+/-	+	-	+/-	-	--	+	--	++	+/-
speed in waves	> 30 kn	-	+	++	++	-	+/-	++	+/-	+/-	-	-
endurance (full speed)	> 6 hrs	+	+	++	++	+	+	++	+	+	+/-	+
stability	self-righting	++	++	++	++	-	-	+/-	+/-	+	--	--
vertical accelerations	< 0.2 g	-	+/-	+	++	-	+/-	++	+/-	+	-	-
manoeuvrability	good	++	++	+/-	+/-	+	+	+/-	+	++	++	+
Ability to withstand max. wind force	10 bft	++	++	++	++	-	+/-	++	+/-	-	--	--
maximum significant wave height	6.75 m	+	++	++	++	--	-	++	+	-	-	-
significant wave height < 2.0 m	86 % of time	+	++	++	++	+	+	++	+	-	+	+
space for victims	> 100 persons	+	+	++	++	++	++	++	++	+	+	+
building cost	-	++	++	++	+	+	-	-	+	--	--	--
maintenance cost	-	++	++	++	++	+	+	++	++	-	--	--

7. Recommendations

Following from the conclusions, detailed technical research for the application of increased deadrise, the Enlarged Ship Concept, hovercrafts, SWATH’s and may be Stolkraft is recommended.

The KNRM might improve their service by building two Enlarged Ship Concept vessels and stationing them at the ports of Hoek van Holland and Den Helder. Those “all-weather” vessels would be able to maintain a very high speed in waves and decrease the reaction time for accidents further offshore on the North Sea. The large number of victims that can be taken on board of those vessels is very useful in case of a large accident with a lot of victims.

Furthermore, a hovercraft can be very useful on the Waddenzee. This unit can be operational up to Beaufort 8 on the more protected waters. The very high speed and the ability to cross shallow water and sand banks decrease the reaction time. It is worth considering using a paid crew on this vessel. This would mean that the hovercraft is full time operational during summertime, which would relieve the work pressure for the volunteers.

Most of the existing ships can be maintained because they perform quite well. When vessels are getting old and need replacement, applying an increased deadrise or transversely stepped hulls could be considered.

A SWATH could be considered as a very useful and flexible platform in open sea during emergency operations as a coordination centre in case of major accidents, its function should be combined with other services for example supplying people to windmill parks or pilot tendering in order to get the economics right.

An overview of this possible future SAR fleet of the KNRM is given in Fig.14. ‘A’ indicates the Enlarged Ship Concept vessel; ‘B’ indicates the hovercraft.

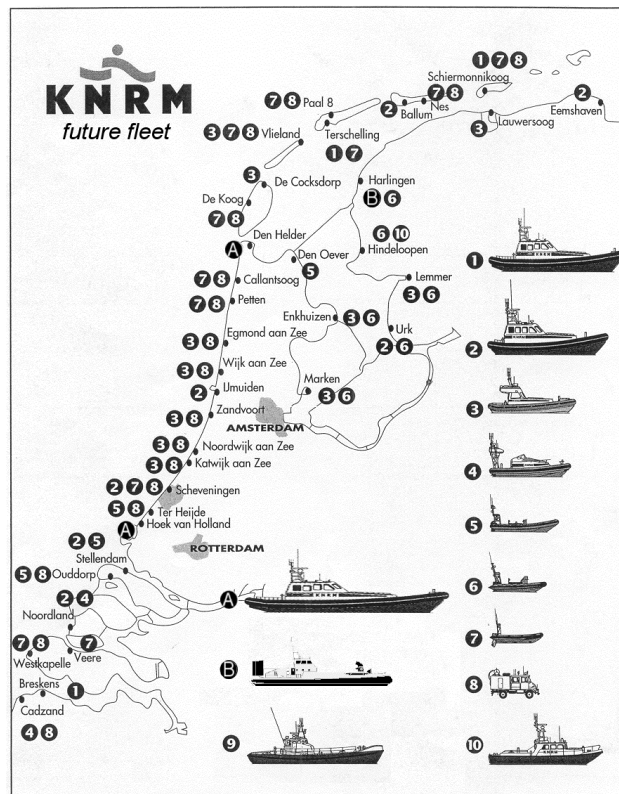


Fig.14: Possible new fleet configuration for the KNRM

Acknowledgement

The authors would like to thank the Koninklijke Nederlandse Reddingsmaatschappij (KNRM) and the Netherlands Coast Guard for their cooperation in this research project.

References

- ANDREWS, D.J.; ZANG, J.W. (1995), *Trimaran ships - The configuration of the frigate for the future*, Naval Engineers J., May, pp.77-93.
- BUTLER, E.A.(1985), *The surface effect ship*, Naval Engineers J., Feb.
- FROUWS, J.W. (2004a), *KNRM Reddingsboot 2010, rapport fase 1*, Delft University of Technology.
- FROUWS, J.W. (2004b), *KNRM Schepen en de Vloot, rapport fase 3*, Delft University of Technology report
- GRADY, R.(2004), *Canadian Coast Guard*.
- HAWKINS, S.; SARCHIN, T., *The small waterplane area twin hull (SWATH) program - A status report'*.
- HUSSEY, D.J.; INAN-UL MAJID en WIGHT, D.C. (1990), *An evaluation of the swath vessel Frederick G. Creed to the missions of the department of fisheries and oceans off the Canadian East Coast*, Mari-Tech Conf., Victoria, Paper no. 6.
- JOHNSTON, R.J. (1985), *'Hydrofoils'*, Naval Engineers J., Feb., pp.143-199.
- KEUNING, J.A.; PINKSTER, J. (2002), *The Axebow, a further improvement on the seakeeping performance of a fast monohull*, Schip en Werf de Zee 1, pp.31-36.
- LAVIS, D. (1985), *Air cushion craft*, Naval Engineers J., Feb.
- NCG (1999), *Operationeel Plan Search-And-Rescue (OPPLAN-SAR)*, operationans plan Netherlands Coastguard.
- NIGEL, G. (1990), *Design for speed, economy and comfort - The role of the independent designer in the design of high speed surface craft*, 7th Int. High Speed Surface Craft Conf., London
- N.N. (1985) *Wing-in-ground vehicles introduction*, Naval Engineers J., Feb.
- VELDE, J. van der; PINKSTER, J.; KEUNING, J.A. (1999), *Enlarged Ship Concept applied to a fully planing SAR Rigid Inflatable Lifeboat*, Fast Sea Transportation Conf., pp.495-509.
- WADE, R.G. (1989), *Operational experience of hovercraft in the Canadian Coast Guard*, Seminar on Hovercraft to the Rescue, London, Paper no. 1.
- YUN, L.; BLIAULT, A. (2000), *Theory and design of Air Cushion Craft*, London: Arnold.

Design development and model testing of new patented Air Supported Vessel (ASV) designs – leading to the construction of a 24 m ASV full-scale demonstrator

Ulf Stephen Tudem, SES Europe AS, Sandefjord, Norway, ulf.tudem@brygga.no
Hans Liljenberg, SSPA Sweden AS, Gothenburg, Sweden, hans.liljenberg@sspa.se

Abstract

For more than 6 years SES Europe AS has conducted various R&D on air assisted vessel solutions. Two years ago the Air Supported Vessels (ASV) concepts were patented “world-wide”. The partly EU funded innovation process (EU project EFFISES) has demonstrated highly encouraging ASV performance and results, particularly in the high-speed ranges. Several tank-testing models have been developed, instrumented and thoroughly tested in the towing tank of SSPA Sweden AB in Gothenburg. The results from the model tests have been used to optimise and refine the ASV detail solutions. A leading design goal has been to create simple, yet robust solutions offering improved capabilities over current State of the Art conventional fast crafts. The end users requirements have been given high priority. As an example most of the ASV’s have been designed for water jet propulsion. In addition the designs have been optimised for improved sea keeping and reduction in onboard motions. (Improved comfort.)

The model testing covers fast ASV solutions from smaller fast boats to larger (125 m +) express cargo ship designs. The ASV’s may be built in both monohull- and multihull configurations.

A scaled manned model – 9 m in length – of a 40 m and 70 knots fast ASV catamaran – is built and tested at the Technical University of Athens. (NTUA). Another similar size model of a 125 x 45 m ASV ROPAX is under construction, and will undergo similar testing.

To illustrate the span of applications, a fast Landing Craft (LC) design has also been developed on request from a European navy. Denoted ASV MonoCat, this design is also configured for water jet propulsion, and represents a large step up in performance from the conventional medium lift LC’s. Loaded speed is 40 knots, ballast speed almost 50 knots. The ASV landing craft delivers performance comparable with the much more vulnerable hovercraft LC – without the disadvantages of rubber skirts and bags.

To demonstrate the ASV concept in full scale, a 24,0 x 7,4 m aluminium catamaran demonstrator is under construction at Swede Ship – Djupviks Varv in Sweden. This vessel will be thoroughly tested. The development- and construction cost are financed by Effect Ships International AS (the patent holding company) with support from the Norwegian Research Council. The boat will be ready for the water early 2005.

The demonstrator will be used to exhibit and document the ASV concept advantages and features, and an international market introduction of the technology – including establishment of licensing agreements with leading HSC yards – will then follow.

1. Introduction

In 2002, Effect Ships International AS (ESI) patented the ASV concept in more than 50 countries worldwide. ESI and SES Europe AS (SE) have performed considerable R&D on the technology, supported by EU (5th Framework R&D program EFFISES) and Norwegian Research Council. In the EFFISES project ASV catamarans have been investigated.

In the EFFISES project, two quite different groups of ASV designs have been investigated. One is aiming at very high speed vessels – exemplified and scaled to represent 40 m LOA passenger ferries with a design speed of 70 knots (tested to 80 knots), while the other main group of ASV ships are 125 x 45 m large ROPAX / express cargo catamarans, designed to operate at 50 + knots. In this paper focus will be given to the small and medium size ASV catamarans, operating at $F_n = 1,0$ to $2,0$ +.

The ASV conceptual features may also be used on various ASV monohull and combination designs – all covered by the ESI IPR and patents.

Several renown collaborating partners have contributed with valid input as they foresee commercial potential in applying the ASV technology to various fast vessel applications– both commercial/civil and naval.

The ASV catamarans have - according to the general preference of the market - been configured for Water Jet propulsion, but also other propulsion systems may be used. Several of these designs have been thoroughly tank-tested at SSPA Sweden during the last years, and the ASV hullforms are exhibiting very competitive data on resistance, motions and general vessel behavior. These properties and features have captured the interest of quite a few potential end users, including several of the world leading navies.

Although high quality unbiased tank testing results and other type of documentation are important, the market would like more tangible hardware, tested under real life conditions. With a 24 m ASV demonstrator vessel, now commissioned by the aluminum shipyard - Swede Ship, ESI / SE will start the international marketing of the technology. Potential commercial as well as naval yards and end users will be invited for test runs, and the vessel will also be subject to very comprehensive test- and documentation programs.

2. Model testing of ASV designs suitable for fast small to medium size vessels at SSPA

2.1. Background

In line with other types of Air Assisted Vessels (AAV), the ASV uses air lift to reduce resistance /increase speed / improve efficiency. The stationary running condition in calm waters is easier to monitor than the dynamic behavior in a seaway. The calm water, stationary hull resistance can be substantially reduced by reduction of wetted surface by means of air cushion support (lifting otherwise wetted portions of the hull out of the water) and “air lubrication” of the remaining semiwetted surfaces. The reduction of the displacing solid hull portion also reduces the residual resistance but the air cushion itself has a displacement resistance.

In a seaway the AAV concepts work up to a point where the cushion ventilation deteriorates the characteristics to, or below, those of conventional high-speed craft.

The ASV does not have any flexible skirts, so the ASV will not suffer skirt wear / replacements and high maintenance cost as seen on other AAV's .

The ASV concept tries to trade off some of the god resistance performance for better seakeeping and reliable propulsion. Model tests to date have shown very good high-speed resistance data for hull shapes intended for surface piercing propeller propulsion. But for the time being the required propulsion power is still above what is commercially available for a 40 m vessel. The market asks for WJ-propulsion, well proven for high speeds and available in a range from small units to very high power.

2.2. Concept ideas

Three ASV tank testing models – representing 40 m LOA and 70 knots fast ferry hull forms - have been developed by ESI/SE and later tested in the SSPA towing tank in Gothenburg.

Several ideas listed below are shared for the 3 above-mentioned ASV hull concepts. In addition there are also considerable and markedly differences between the designs.

- All designs are high-speed solutions – suited for F_n above 1,0, and preferably between F_n 1,5 and 2,0.
- The operational displacement and payload should be at least of the same level as comparable conventional catamarans.

- A significant part of the displacement – some 70 – 90 % - should be supported by pressurised air in air cushions arranged as integrated parts of the hull . No troublesome flexible skirts, bags or the like should be used.
- The design should not rely on dynamic lift (in the forward part of the hull) as a main source of support.
- Designed to avoid high levels of bow pitching, i.e. as a result of large dynamic areas forward as frequently seen on planing and semiplaning vessels.
- The running trim to be close to neutral.
- The air cushion support to be “balanced “ i.e. with more support in the aft end to accommodate the heavier machinery / propulsion.
- The step and the surface in front of the step should together create the forward sealing of the air cushion chamber.
- The step should be located in a plane that is close to horizontal (no part of the step is to ventilate before the other)
- The bow section to be slender in order to reduce displacement forces in a seaway.
- The bow to incorporate a voluminous part above a built-in chine/spray rail, producing water deflection and reserve buoyancy in a pitch diving motion.
- Side keels of varying height, extending from just ahead of the step to the transom stern, the height of the keels to be adjusted to the observed/expected shape of the air cushion. The main purpose of the side keels is to fence in the air cushion, but they will also have a course stabilizing effect.
- The whole air cushion periphery to be arranged close to the same vertical position to avoid ventilation and reduce fan power requirement.
- Spray rails on the outside of the side keels, at a height partly to deflect the water without wetting the rails on the upper sides (finding best balance between wetted surface).
- A cushion ceiling at a height to minimize the frequency of the sea hitting the ceiling when the vessel moves in a seaway. Simple shape for cost efficient production.
- A slope of the ceiling aft end in order to deflect passing waves in a seaway and an adjustable flap in line with the sloped portion of the ceiling to fence in the rear part of the air cushion chamber/create dynamic lift and motion damping.
- Designed to allow various propulsion systems – also WJ.

The hull geometries of the models are quite diverse and the performance and behaviour of the models also diverge. However, without a clear definition of the vessel / end user / operational requirements one cannot rank one model relative to the other. They have their individual pros and cons.

2.3. Model investigations

The procedure for performing a test runs involved decisions and selection of several variables prior to each test run, including displacement, LCG / change of ballast weight, flap angle, fan rate of revs, speed to be investigated based on previous results etc.

New zero readings were taken if displacement and/or LCG had been changed or something in the measurement equipment had been adjusted.

The fan reference pressure taps and connecting were inspected prior to each run, including blowing all pressure taps and connecting air tubes (to cushion as well as fans) free of possible water by applying pressurised air (any amount of water left would distort the measurement).

The fans were run up to close to the decided rate of revs prior to starting the run, then fine tuned to the determined level during the acceleration phase.

Zero speed were always measured prior to the start up of the run with model on cushion.

Then the model was run up to speed and all measurements, including video, still pictures (above and below water) and wave recording where completed.

The results were checked – measurements, wave cut, under water photo, video etc – after each run, and in case of problems repeated.

Preliminary evaluation of measurements, predict full scale power components where then done after

each run in order to progress to next run and carry out decisions on changes to the parameters etc.

2.4. General comments

The tank testing models representing ASV 40m vessels were all 2.5 m long, thus carried out in a scale of 1:16. These models were all built from carbon fiber reinforced resin and painted. The actual model speed in the 270 m long towing tank at top speed was close to 10 m/s. Both calm water tests and testing in head seas were carried out.

The testing is complicated in that a number of parameters have to be investigated for each speed. So has the LCG position an influence in that the ventilation of the air cushion is affected and thus the airflow and fan power.

The fan power, in terms of rate of revs, was varied. Using a high airflow rate will reduce the resistance, at least up to a point, but increases the cushion fan power to an unrealistic extent. The ESI patented features have addressed this general problem in order to reduce the ventilation and fan power requirement. A general observation was that a higher flow rate appears to be beneficial for high speeds in calm water. In full-scale vessels it is recommended to install fan systems with more power than demonstrated to be the optimum in calm water because the air leakage in a seaway will be larger.

Another parameter is the rear sealing flap angle. Apart from sealing off the cushion chamber there is a lift by some water being deflected, causing a bow trim. This is sought for in conditions where the bow step is on the verge to ventilate. A combination of LCG, flap angle selection and the best air flow rate will be determined to give the optimum running condition – for each speed and displacement – will be required. It is obvious that the test program then becomes very large and expensive. Luckily, one eventually gets a feeling for how to make short-cuts to the best combinations in the towing tank environment, and the same is expected to be the case in practical full scale operation of an ASV – particularly on how to combine and operate the flaps and fans.

The 3019 design, demonstrated exceptional calm water high speed efficiency, but were not as good as the models 3036 and 3052 with regards to onboard motions and seakeeping at high speed. The 3019 design would have been a highly capable candidate for high speed operation with small vessels operating in protected waters, where efficiency has higher priority than seastate capability.

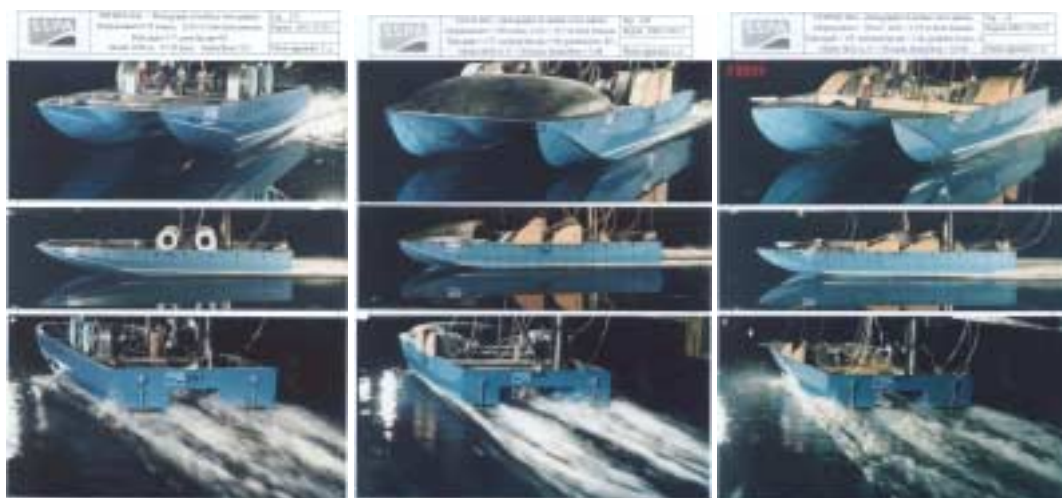


Fig.1: Left: Model 3019 – ASV suited for SPP during SSPA tank testing at 70 knots..

Fig.2: Middle: Model 3036 – during SSPA tank testing at 70 knots.

Fig.3: Right: Model 3052.

The 3036 design was the first ASV configured for WJ propulsion. The tested model must not be regarded as final design, rather a testing tool for initial investigations into WJ gondola shape and location in order to develop commercial designs as outlined in the ESI ASV patents. The main challenge will be to establish the best balance between resistance, motions and shielding of the WJ intakes from air ingestions. It is clear that the more loaded the vessel is the less critical this balance becomes. This hull form had low increase in hull resistance when operated in a sea state.

The 3052 was the second ASV designed to incorporate WJ, and the first with a separate WJ gondola located inside the air cushion chambers. Also this design should be regarded a test design, where i.e. the shape of the WJ gondola and the shielding of the WJ intake in now way is fully optimised. From a construction and WJ intake optimisation point of view this design is relatively easy to modify and optimise as WJ and engines are located along the centre line of each demihulls,. The WJ will be an integrated part of the WJ gondola where the vertical immersion of the gondola and WJ intake could be adjusted without too large modification to the global construction and lay-out.

The goal for the model testing was to conclude on the feasibility of the patented solutions.

3. Main results and conclusions – 40 m ASV model tests

3.1. Speed vs. power – propulsive power and lift fan power

The most striking results for the ASV's are of course the reduction in resistance and consequently reduction in propulsion power. Below are summaries in tables and diagrams of all predictions for a 40 m vessel. It should be noted that some versions are also tested with at load conditions differing from the set standard of 170m³. Of significant interest to the commercial HSC users where payload capability is one of the main success criteria will be the testing of the ASV's with heavy load, and the results obtained.

Test were done with 50 m3 extra load – in commercial terms equivalent to the weight of some 30 – 40 passenger cars ! – this on a modest size 40 m vessel.- normally only capable of carrying passengers.

Each result for a specific speed and loading condition is the best one found in optimizing the combination of LCG/fan rate of revs/flap angle.

The diagrams also contains predictions for one semi-displacement catamaran and one planing catamaran of the following dimensions:

Cat type	LWL(m)	BWL _{dh} (m)	B _{CL-CL} (m)	T (m)	∇ (m ³)	Speed range (knot)
Semi – dipl.	39,5	3,6	7,6	1,4	170	20 - 45
Planing	35,5	3,5	7,5	1,3	170	35 - 55

The predictions are based on the statistically best results from model tests achieved for similar catamaran vessels. The propulsion system is anticipated to be water jet.

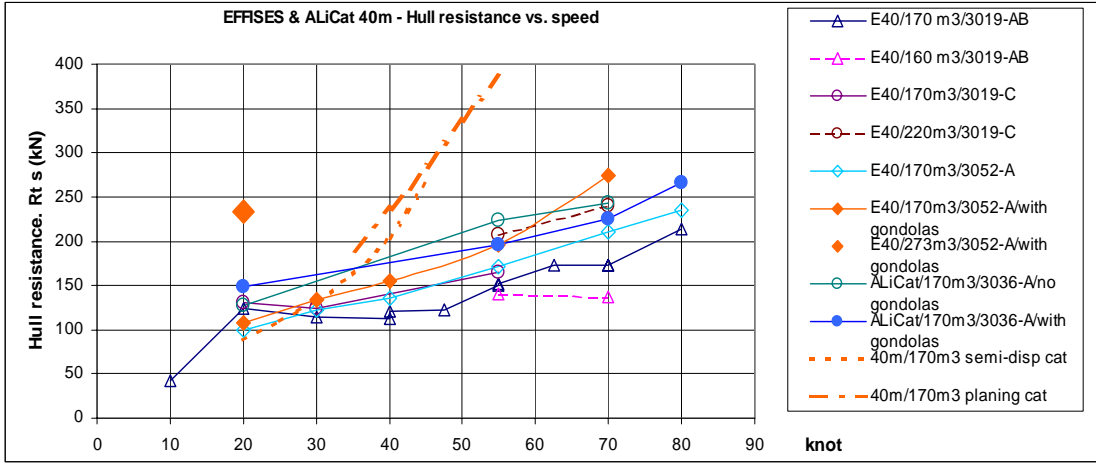


Fig.4: Hull resistance vs. speed for three ASV hulls with various displacements compared with SOA conventional catamarans.

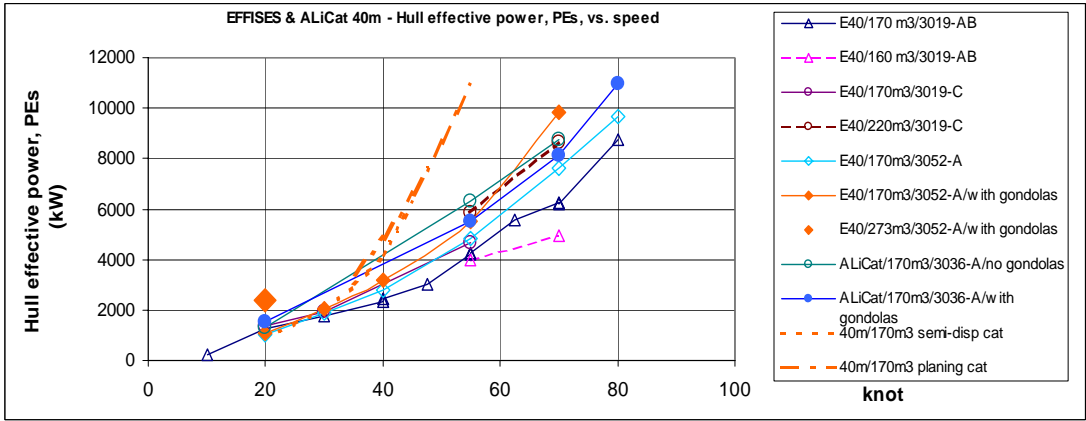


Fig.5: Hull effective power vs. speed for three ASV hulls with various displacements compared with SOA conventional catamarans.

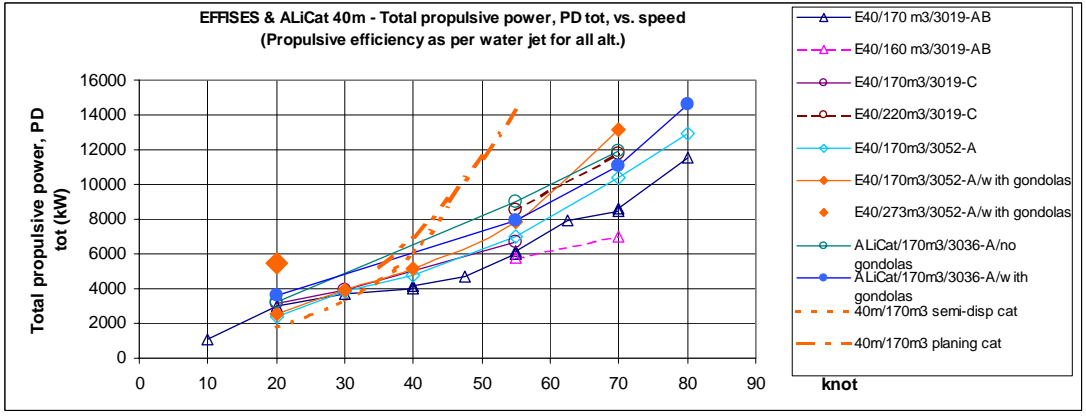


Fig.6: Total power vs. speed for three ASV hulls with various displacements compared with SOA conventional catamarans.

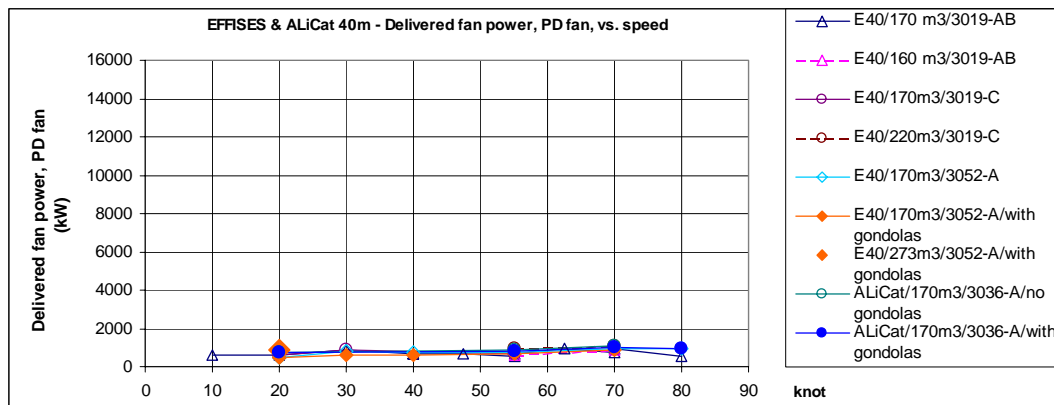


Fig.7: Fan power vs. speed for three ASV hulls with various displacements.

The three tested ASV's were designed for speeds corresponding to 70 knots in a 40 m scale. From the tabulations it is clear that these ASV's are competitive first above 35 -40 knot. At speeds from 50-55 knot up to 70-75 knot, their performance is quite outstanding compared with conventional catamarans.

In all predictions above of propulsion power efficiencies as per water jet is presupposed. This is of course not correct for the 3019-A to -C and the 3052-A hulls without gondolas as they are intended for surface piercing propeller drive. However, the 3036-A and 3052-A with the motor gondolas on are representative for a water jet propulsion. Tests with/without gondolas indicate that the gondolas demand some 15% added resistance/increase of power as an average, but that percentage varies with speed. For low speeds the motor gondolas stands for only a few % resistance increase while at the tested top speeds e.g. the gondolas of model 3052 stands for as much as 30% increase.

The gondola shape and position are expected to have considerable potential for optimization in order to reduce the added resistance of these hull parts. The optimum gondola position and trim angle can be expected to depend on speed (in the model tests it was the same through the speed range) and should be optimized for the design speed of each very application.

For the 3019 and 3052 models, at high speeds, the residual drag ought to be a small portion of the total, and so it mostly is. It is mainly about 10-30 knots where it is of greater magnitude. At higher speeds the residual resistance many times becomes negative when the friction, cushion wave and wind resistance is deducted from the total measured resistance. The reason may be

- an over-estimate of the wetted surface leading to too small total drag coefficient
- the anticipated model friction coefficients are too high, which means deducting too much friction drag from the total
- the calculated air cushion wave drag is too high
- the drag due to wind is over-estimated (N.B. that $C_{D\text{ air}}$ was based on wind tunnel measurement on a similar configuration; wind speed measurements under the towing carriage had been performed with a similar set-up)

When testing the 3036 model without gondolas a comparatively high calm water resistance was measured, which may not be quite representative. When this model was tested without any of the gondola configurations mounted there were no spray rails mounted on the inner sides of the side hulls. At the tests the water therefore climbed and wetted the demi-hull inner sides, apparently as high as the wet deck. It is not astonishing that the advantage of a ship concept based on reduction of wetted surface suffers from the above-described situation. One should notice that with the gondolas mounted the resistance is actually lower than without gondolas! The gondolas work as creators of dynamic lift as well as spray deflectors, though none of the gondolas had spray rails along the chines. In commercial ASV design using the 3036 type of designs the gondolas will be designed as streamlined

integrated parts of the inner side hulls, intended to allow a smooth flow of water through the tunnel.

The propulsion power, PD , is the power needed by the propulsor to overcome the resistance when air borne, using the efficiency of the intended propulsion system (here WJ all the time). To obtain the total propulsion power, PD_{tot} , one always has to add the fan power, PD_{fan} , not only the net power but with a fan efficiency and a transmission efficiency, thus a “braked” fan power. This is a price one has to pay for a reduced resistance, which unloads the propulsor and is partly regained as an increased efficiency.

In the best operational speed range the braked power of the fan motor is typically around 10 % of the total propulsion power, PD_{tot} .

3.2. ASV concept behaviour during tank testing

In line with the patents claims of the ASV concepts, the air cushion(s) seems to work well both in calm water and in a seaway. A video camera was located in the fore end of the cushion chamber, looking aft towards the rear flap. The observations were:

- The bottom of the air cushion looks fairly flat when running in calm water
- There is some wave making originating from the side keels
- The oblique angle of the keels in relation to the direction of travel, when not too steep, does not appear to create any excessive cross flow over the keels
- The air flow from the fan shafts cause some depression of the water just below the shafts. The depression is not very large in spite of no attempt being made to deflect the air horizontally.
- For most cases the rear flap is partly in contact with the water and partly leaves a gap for exit of air
- For a majority of running attitudes there is a tendency towards air escaping below the rear part of the side keels (that is a reason for making the side keels a little deeper in the aft end)
- In a seaway the cushion water surface moves vertically as the seas pass by, but the height of the cushion chamber appears to be sufficient for avoiding the water hitting the ceiling. Thus an air pressure is always at hand over most of the cushion chamber projected area.

Another video camera was located in the center body between the side hulls, looking aft for observing how the waves from the side hulls interfered. The waves behaved very much as for other twin hulls: bow waves interfering, forming a substantial crest at low speeds that moves aft and flattens out with increased speed. It is located well aft of the transom at and above design speed. There were no waves hitting the wet deck. The waves between hulls were in general low in spite of the hull distance being fairly small - unless when passing “hump speed”.

One gets the impression that the surface wave generation of this ASV is lower than for a traditional twin hull vessel in the high-speed range but there are not many measurements to compare with. About hump speeds the picture may be the opposite, indicating a fairly large resistance. The latter must be paid attention to, not to create a situation where the vessel gets stuck on the hump due to limited propulsor thrust. Using the surplus of installed fan air power (needed in rough sea) when accelerating may help overcome this problem.

Under water still pictures were taken continuously at a fixed position in the tank, in calm water as well as in a seaway. The under water photography is necessary for evaluating the wetted surface and extrapolation to full scale of the hull resistance. The pictures give a clear view of what is happening momentarily but is well completed by the video cameras in the cushion and between the hulls. Attempts to use an under water video camera was not very successful, the resolution of the picture was insufficient for detailed observations. The introduction of a digital under water camera gave immediate information about a test run that could be used for deciding about the next test configuration.

Measurements of the cushion pressure along the length of the hull was also made. An example (model 3019) is shown. On this model the pressure varies slightly with position in the cushion, on other models the pressure is quite uniformly distributed along the length of the air cushion. The cushion chamber section area increasing rearwards, reducing the static pressure in a potential flow mainly being directed aft.

The direct fan outlet flow into the cushion may disturb a smooth variation.

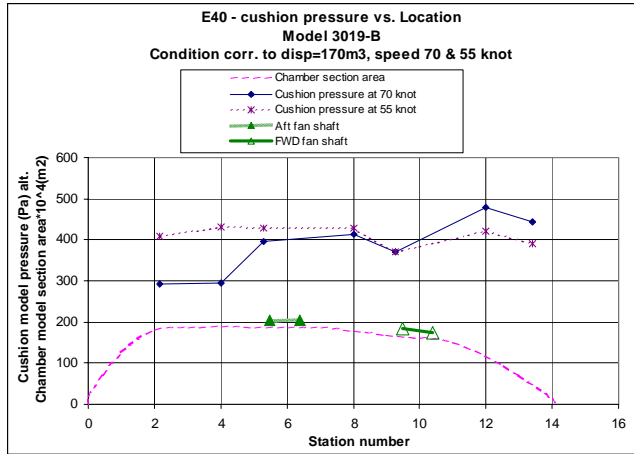


Fig.8: Pressure distribution and air cushion area distribution for the ASV model 3019.

The below tabulation to illustrate the average cushion pressure in relation to total propulsive power. In addition one will find the cushion pressure to be nearly proportional to the boat weight for the speeds where comparisons can be made.

Model 3019	Mean cushion pressure (kPa) at speed (knot):					Total propulsive power (MW) at speed (knot):				
	20	30	40	55	70	20	30	40	55	70
Displ (m³)										
160	-	-	-	6.2	5.3	-	-	-	5.74	7.02
170	6.9	7.1	6.7	6.6	5.7	3.02	3.66	3.98	6.18	8.64
220	-	-	-	8.6	7.5	-	-	-	8.52	11.79
	Total air volume flow (m³/s) at speed (knot):									
	20	30	40	55	70					
Displ (m³)										
160	-	-	-	78	128					
170	68	92	75	75	121					
220	-	-	-	85	111					

Fig 9: Model 3019 cushion pressure, total propulsive power and total air volume flow.

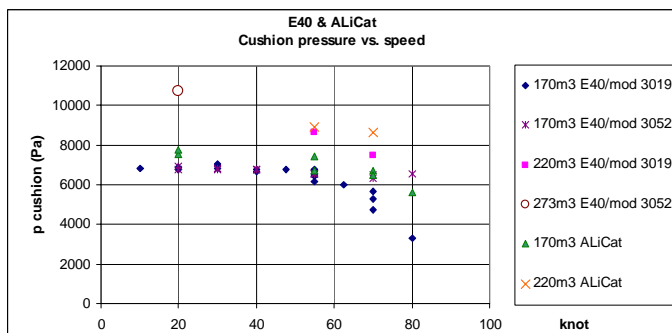


Fig.10: Cushion pressure vs speed for ASV 40 m models with different displacements.

The 20 knot case corresponds to “hump” speed for the 40 m ASV which may explain the relatively

high figure there. It has generally been observed that a relatively larger flow rate is beneficial at the highest tested speeds. At the same time the cushion pressure falls off a little.

3.3. Running behaviour

The running behavior of the ASV 40 m versions shows some consistency regarding trim and sinkage. All versions rises out of water increasingly much with increasing speed. The rise of CG increases almost linearly with speed. The trim angles vary somewhat more between versions but mostly the trim angle is between 0.5 and 1°. Above hump speed the trim angle for each version is nearly constant. The 3052 model runs flatter (smaller trim) and raises more out of the water. The latter may partly depend on less buoyancy in the fore body for a given draught when off cushion (as all sinkage figures are related to the off-cushion condition).

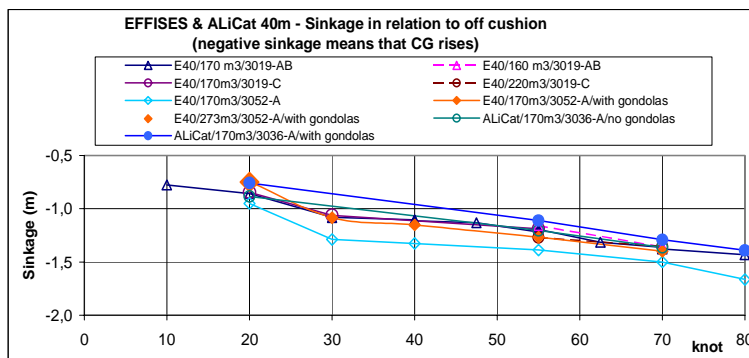


Fig.11: Sinkage in relation to off cushion for the ASV 40 m designs.

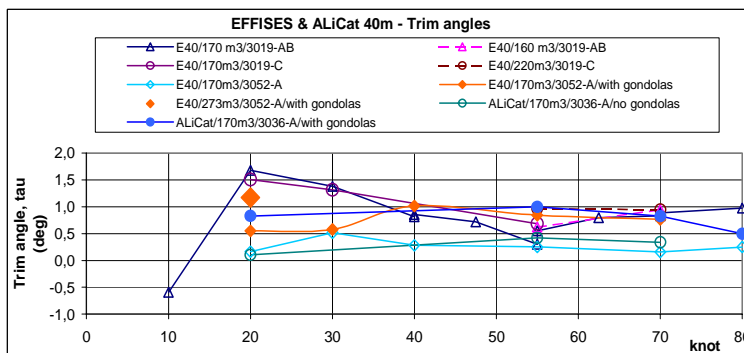


Fig.12: Trim angles for the ASV 40 m designs relative to vessel speed.

3.4. Sea keeping

The seakeeping investigations have so far been limited to model tests in head seas in a towing tank, with the models towed in long elastic strings to allow for a certain amount of surge movement. The models were by a mechanical arrangement kept on a straight course, but allowing for roll, pitch and heave while sway and yaw were restricted.

Two vertical accelerations, two vertical motions and the towing force were measured. The same air pressures as measured during the calm water test (cushion and fan flow reference) were recorded. A wave recorder, the same as used for the wash wave registration, measured the generated waves in the far end of the test track, not to disturb the measurements by wash waves. The measurement was stopped when the model passed the recorder. By this connection between waves and model position, the part of the wave spectrum that the model has passed through during the measurement sequence can be determined.

From measurements of response amplitude and phase angle in two locations fore and aft on the model

it is possible to determine the variation of the response along the length of the model.

In addition calm water resistance reference runs with the seakeeping test set-up were made for determining wave added resistance. The resistance was generally very close to the corresponding measurement with the calm water test set-up.

The generated waves were calibrated in the empty tank, in order to adjust the wave energy spectrum to the theoretical one. Wave spectra of Pierson-Moscowitz (equal to ITTC/ISSC and Bretschneider) type were used.

The 40 m models were tested in sea state 3 corresponding to $H_{1/3}=0.88\text{m}$ and $T_z=4.0\text{s}$. A variation of T_z was made comprising tests in 4.8 and 6 s.

All seakeeping tests were carried out for a boat weight corresponding to 180 m^3 displacement. The LCG position was the one found as optimum for the design speed, 55 knot. The flow rate was increased in relation to that in calm water corresponding to about 10 rps of the model fans. In retrospect several within the team behind the ASV concept development is of the opinion that it might have been beneficial to have carried out the tests with higher air flow, partly to ensure the boat riding higher in the water and partly to improve the motion damping effect of the air cushions. Tests to verify if this theory is correct will be carried out with the 9 m operational model currently undergoing tests at NTUA.

The results below are generally given as significant 1/3 response (single amplitude) per meter significant 1/3 wave height (double amplitude).

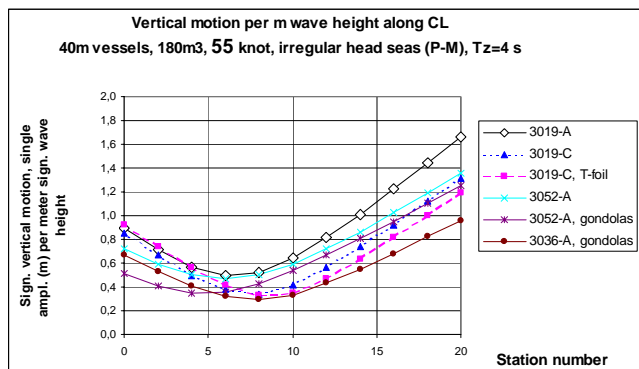


Fig. 13: Vertical motion pr m wave height along CL of the various ASV 40 m design at 55 knots in irregular head seas with $T_z = 4\text{ s}$.

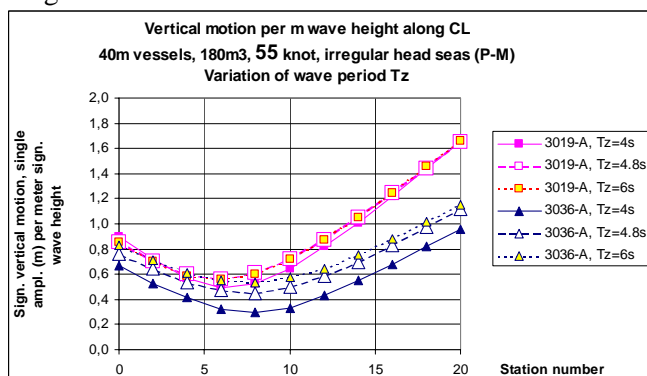


Fig.14: Vertical motion pr m wave height at 55 knots.

The above are only examples of some of the work carried out at SSPA on sea keeping performance for the 40 m ASV models.

Given the selected air flow (that might not have been the optimum to obtain best possible results), one can generally conclude that the first tested ASV 40 m model (3019-) had CG accelerations in SS 3 allowing only half an hour duration of a journey in relation to the ISO limit lines. The model 3036 and model 3052 had a finer bow entrance, shows clearly a reduction of accelerations.

The use of small motion damping T-foils (passive) on the 3019 model had very little effect. The foil angle of attack was set at -1 , 0 and $+1^\circ$ respectively in relation to the BL plane. 0° appeared to be the best but on the whole the foils had very little influence on the vertical accelerations.

The model 3019 performance could probably be acceptable in 55 knots during $\frac{1}{2}$ + hour due to the high response frequency. The model 3036 may be acceptable for a 2 hours journey. The model 3052 could be acceptable for $1\frac{1}{2}$ hour. The presence of propulsion gondolas might add some damping effect at high speed (cf. model 3052 and remembering that model 3036 also had gondolas). In waves of higher period than 4 s the tolerance of motion sickness is less.

Below is the ratio between resistance in waves and resistance in calm water presented for both EFFISES concepts; first the E40 version:

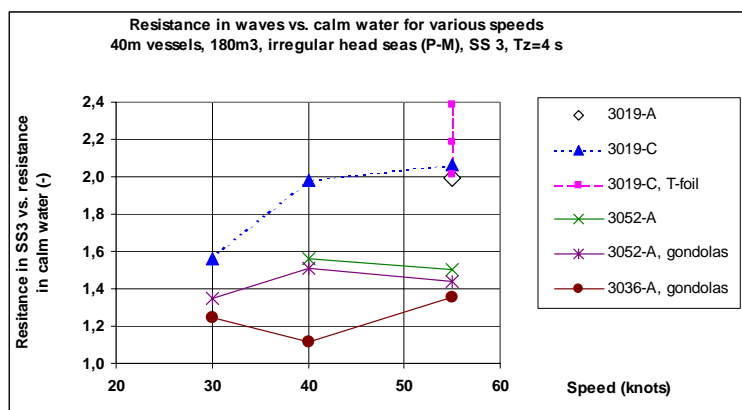


Fig.15: Added resistance in waves vs. in calm water for the ASV 40 m designs.

The 40m versions with sharp bows show less resistance due to less motion in a seaway. Especially the 3036 model appears to be very good in this respect.

4. Design development first full scale ASV demonstrator

The ASV demonstrator will be closely based upon the model 3052 hull configuration. Although the 3036 may be a long term stronger ASV candidate, the 3052 hull form is easier to optimize and refine without carrying out too large changes to arrangement and structures.

In the initial design phase, the demonstrator had a size of 15 m x 5.5 m. Both composite materials and aluminium were discussed as suitable building materials. As the Demonstrator is the first ever full-scale ASV with water jet propulsion to be built, some adjustments, modifications and optimisations when the vessel is in the water is expected. In favour of the composite alternative were somewhat lower hull weight and a potential very high level of exterior finish.

On the other hand as the main target with the demonstrator was to demonstrate the scaling capability from the smaller tank testing models to full scale vessels, the aluminium solution was selected, as no production of a male plug and female mould tools was required prior to actually building the vessel. The aluminium choice also enables quite easy modifications of e.g. water deflection lists, water jet intake and shielding. The cost aspects are also in favour of the aluminium solution. Aluminium is a popular choice among the owners/operators of smaller fast vessels. The efficient construction principles available when using the Hydro Marine Aluminium extruded profiles also helps cut

building cost and time. As it has been frequently used before in similar size of vessels, the classification approval process is also expected to be somewhat easier with aluminium than with composite materials.

As the ASV to a large extent utilise air cushion lift in supporting the hull weight, a careful balance between air cushion area, cushion pressure distribution, cushion pressure, hull weight and weight distribution is required.

The accuracy of the weight calculations one will first see when the boat is completed. In our case we have had quite a few rounds of weight estimates, along with changes in specifications, class requirements etc. Unfortunately the weights almost always go up. The cushion area of a 24 m hull length vessel is more than twice that of the 15 m vessel, while many of the onboard systems remain almost the same. After a careful evaluation of the design parameters, it was concluded that the 24 m vessel size, built in aluminium was a good and capable size, with acceptable building cost compared with the expected performance of the test vessel and very suitable for several commercial and military fast vessel applications.

A similar evaluation of the size of main engines, lift fan powering, fan size/capacities and water jet size was made.

5. 24 m ASV demonstrator main particulars and general arrangement

The ASV prototype / demonstrator will be presented as a candidate design for fast passenger transport, workboats of different kinds, patrol boat duties and naturally due to the very high-speed capability – as a fast combat boat. The low draft, air-lift capabilities and WJ propulsion may even enable the vessel to be beached. The design will be closely compared with current market leading monohull designs, and the higher efficiency, larger platform and low draft are expected to be appreciated by several end users. The vessel is under construction at Swede Ship in Sweden.

The vessel will have the following main specifications:

Building material - hull and superstructure: Hydro Marine Aluminium – extruded aluminium profiles.

Length of hull: 24.0 m. (exclusive Water jets.).

Beam of hull: 7.3 m

Expected lightweight displacement (as a demonstrator vessel): 41 tons.

Estimated operational displacement: 50 - 53 tons (subject to final specification / no of passengers.)

Main propulsion engines: 4 x Volvo Penta D 12-715. 4 x 520kW at 2.300 RPM

Propulsion: 2 x Rolls-Royce Kamewa A 45 waterjets.

Transmission between engines and WJ: Gates Polychains.

Lift fan engine: 1 x Volvo Penta TAMD 63 – 230 kW at 2800RPM

Lift fans: 2 x Flekt Woods. Type: Backward curved Centrifugal fans, in tandem configuration.

Transmission between engine and fans: Gates Polychains.



Fig 16: Demonstrator vessel – artist impression.

Expected vessel performance and capabilities:

Estimated full speed (at 41 tons): 48 knots at 100% MRC.

Operational speed (at 53 tons): 40 + knots at 90% MCR

The D 24 is expected to be a very important milestone in the documentation and demonstration of the new ASV catamaran with WJ's. The vessel will following the first in-house tests and trials complete a comprehensive scientific test program, according to suggestions and recommendations from SSPA, where a long list of aspects including air cushion ventilation aspects, details in the air cushion chamber design, fan requirements under different conditions and operations, WJ location / air ingestions, trim and air cushion flap arrangement, sensitivity to load and to changes in LCG /TCG etc will be investigated. In addition motions / accelerations, maneuvering capabilities etc will be carefully monitored and documented. The project is supported by Norwegian Research Council.

The project partners will assist in optimizing the different subsystems and overall vessel performance following the first tests.

When the D 24 has completed the documentation trials, the vessel will be used to promote the new concept internationally, at conferences, trade shows/exhibitions and also as part of active approach towards potential end users as well as construction yards.

The data and operational experience from the D24 will be utilized in the further R&D to improve the technology in general and towards targeted vessel types and applications.

It is the opinion of the authors that the best and most convincing way to convince the sceptic is to actually take them for a ride in a variety of operational conditions.

6. Alternative hull form to fast ASV vessels

To illustrate how a complete ASV design of the model 3036 may look like, on request from navy interests a 24 m ASV troop transport vessel has been developed. As will be seen from the illustration, the WJ gondolas are here integrated into the inner side keels, located towards the vessel main centre line.



Fig.17: 24 m ASV troop transport vessel – hull form.

To illustrate another ASV hull form covered by the ESI ASV patents, the below illustration of the ASV landing craft, in a “monoCat” configuration, should demonstrate one of the ways the concept could be used.

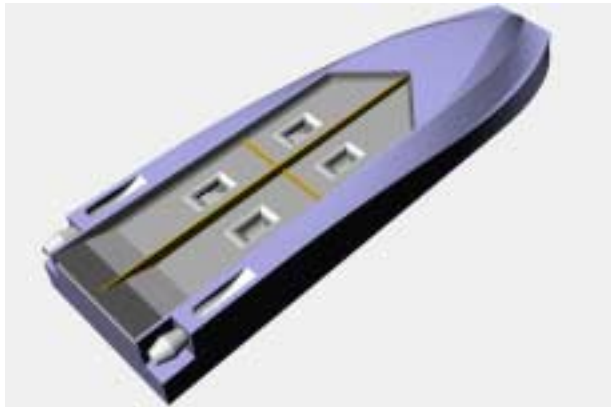


Fig.18: 27 m 40 + knots fast ASV Landing Craft.

7. Conclusions

Several innovative ASV designs have been developed and thoroughly model tested at SSPA during the last years. Tank testing results and other conclusions on main concept features are very conclusive and positive. The ASV's represent a shift in fast vessel technology, not only for the efficiency but as importantly for the overall robust performance without too high complexity, maintenance and introduction of new concepts and/or systems.

Propulsion systems in line with the markets preference – Water Jets – is another key factor in the new ASV designs. Proper sea keeping capabilities has been yet another feature targeted in the concept development.

The construction of the D 24 is expected to bring the ASV technology to the next development phase. It is the intention, following design optimization and documentation of the performance of the D 24, to develop a wide range of ASV's to suit various types of end user requirements and missions, and allow leading yards to produce the ASV designs in accordance with licencing agreements with ESI / SE.

8. References

ALLENSTROEM, B, LILJENBERG, H, TUDEM U. 'An AirLifted Catamaran'. FAST '01, Southampton. Sept 2001

ALLENSTROEM, B, LILJENBERG, H, TUDEM U. "Concept development and model testing - new generation Air Assisted Vessels (AAV) with Water Jet propulsion", FAST 03, Ischia, Oct 2003

EILERTSEN. A, MOE, OM, TUDEM, U. "Medium Lift landing Craft ", proposal Qinetiq / UK MOD, Dec 2003.

EILERTSEN, A, TUDEM U. "Design development – 23 m Air Supported Vessel (ASV) with WJ", Int Air Cushion Technology and Exhibition, Southampton Oct 2003

EILERTSEN, A, GRIEG EIDE, J, TUDEM, U. "Design development of advanced air supported Vessel (ASV) designs. " RINA WARSHIP, June 2004.

Multi-Objective Hull Form Optimization of High-Speed Vessels

Gregory Grigoropoulos, Dimitris Chalkias, Christos Tikkos, NTUA, gregory@central.ntua.gr

Abstract

Modern techniques for parametric hull form modelling of high-speed vessels, for assessing their hydrodynamic performance in calm water and in waves have been combined with two alternative optimization software systems implementing genetic algorithms, neural networks and evolutionary strategies to develop an automated procedure for the hull form optimization using multi-objective criteria. Using a modern high-speed naval vessel and a double chine planing hull as test cases, various optimization strategies have been applied and the effect of various parameters involved, on the efficiency of the optimization scheme to derive the hull forms with optimum performance after investigating the characteristics of a reasonable number of intermediate variants.

1. Introduction

The efficiency of the hull form both in calm and rough water is a major concern for the naval architect. The seakeeping performance of the vessel depends primarily on global hull form parameters and, thus, it should be taken into consideration during the preliminary design stage. The resistance and propulsion characteristics, on the other hand, are influenced both by the global and the local form parameters of the vessel. The incorporation of both local and global hull form parameters in an automated optimization process can only be accomplished if a powerful tool for the parametric modelling of the hull is available.

Grigoropoulos (2004) reviewed past attempts for hull form optimization, especially for seakeeping and evaluated a semi-automatic methodology developed during his PhD Thesis (1989) for optimizing of hull forms with respect to their hydrodynamic performance in calm and rough water. The method is based on an initial optimization of a parent hull form for seakeeping and the improvement of the resulting optimum hull form for calm water resistance. In the first part of the method, variant hull forms differing from a parent in the main dimensions and/or in one or more hull form parameters such as C_{WP} , LCF, C_B , LCB, KB, C_p are automatically generated by modifying the respective curves (sectional area, waterline, profile and longitudinal distribution of KB) by an extension of Lackenby method (1950) and their seakeeping qualities evaluated. When appropriate ranges for the principal characteristics and parameters of the hull form under investigation are prescribed, a formal optimization procedure is used to obtain the variant with the best seakeeping behaviour. The weighted sum of the resonant values of the Response Amplitude Operators (RAOs) for selected ship responses, at a grid of ship speeds and headings in regular waves forms the objective function. Hooke and Jeeves algorithm (1961) in conjunction with external penalty method accomplish the optimization. The procedure results in a set of optimum values of the selected hull form parameters, within the specified constraints, which are approached by suitable modification of the lines of the parent hull form. This hull form can be further modified locally to improve its calm water resistance or, as it should be done, its propulsion characteristics. The method has been implemented in two cases: a conventional reefer ship and a naval destroyer. Scaled models of the parent and the optimized hull forms have been tested for calm water resistance and seakeeping with satisfactory results.

Although the method is quite efficient in deriving hull forms with superior seakeeping qualities after the direct evaluation of the seakeeping responses of less than 100 variants, it has two major shortcomings:

- 1 The necessity to design an optimized hull form on the basis of the optimum set of parameters derived. This task can be accomplished either manually or using a CAD software.
- 2 The difficulty to handle multi-objective optimization. Especially, the set of parameters used are not sufficient to evaluate the calm water resistance of the variants.

In order to overcome both of these shortcomings, FRIENDSHIP Modeller has been used in this paper, in conjunction with multi-objective optimization strategies. FRIENDSHIP Modeller incorporates a modelling technique based on a parametric curve generation approach developed by Harries and Abt (1997) and capable of modelling the hull form in sufficient detail. In addition, the software allows for the generation of variant hull forms with some of the form parameters modified and the rest of them kept constant. If the magnitude of the modifications is reasonable, the variants represent realistic hull forms. Two different tools implementing evolutionary strategies, modeFRONTIER (2002), a well-known software and EASY (Giannakoglou, 2002) are used for the optimization of the hull form. In both cases Genetic Algorithms form the basis of the optimization. The hydrodynamic evaluation of the hull forms was carried out by the Rankine source panel code SWAN (Sclavounos, 1996) and the NTUA standard seakeeping code (SPP-86, 1994) implementing the classical strip theory method (Salvesen et al, 1970).

In this work, the above methodology is implemented in the hull form design of two fast vessels, the parent hull form of NTUA series of double-chine high-speed vessels and a naval combatant. In both cases, a sensitivity analysis is carried out regarding the parameters that should be modified. The results are presented in graphical format and are discussed.

Recently, Abt et al. (2003) presented an application of hull form optimization, where FRIENDSHIP Modeller was used in conjunction with SHIPFLOW (1999) for CFD calculations and modeFRONTIER as the optimization tool. However, their application was restricted in the optimization of a fast ferry hull form with respect to its calm water resistance only.

2. Hull form representation

As it is described in the previous section, a major concern of the optimization procedure was to replace the set of the hull form parameters used to identify the variants and the final outcome of the methodology by faired hull forms. This could only be accomplished by replacing them by their parametric model. This model ensures that at each stage of the optimization a feasible model is produced. Then, state-of-the art algorithms can evaluate its hydrodynamic performance both in calm and rough water.

FRIENDSHIP Modeller software has been selected for the parametric representation in this paper. Harries (1998) presented the prototype of this Modeller, which is the outcome of long-lasting investigations at the Technical University of Berlin, initiated about 15 years ago, to develop new techniques of parametric hull design. In order to properly handle the design parameters of the double chine hull form used as test case in this work, the inventors of the software have carried out additional work.

The system follows the naval architect's classic technique of describing the hull through longitudinal curves, the so-called *basic curves*, from which all the design sections are produced. These basic curves include topological, differential and integral information. The design waterline, the centreplane curve and the deck curve are clear examples of topological basic curves. A differential basic curve is that of the distribution of the sections' inclination angles at the waterline level, while the most characteristic integral curve is that of the section area. These basic curves are enough to describe correctly different hull topologies.

The shape of the desired hull is determined exclusively by form parameters from which the basic curves are created. These curves constitute all the necessary information needed for the creation of the design sections.

FRIENDSHIP Modeller is fully based on B-spline curves and surfaces. Every B-spline is determined by the form parameters and through an optimization procedure of suitable fairness criteria. The control

points of the curves are treated as free variables and the form parameters as equality constraints. Since fairness is a characteristic incorporated in the whole procedure, all surfaces are smooth and have exceptional quality. There is no need for manual handling of any control point.

The advantage of the above approach compared to the traditional modelling methods is that the hulls are created and modified on a high level, which means that the alteration of selected form parameters is enough to cause either local or global modifications. Of course, some global parameters of the hull form, which are not directly involved in the modelling, should be evaluated by the optimization scheme, in order to satisfy the associated imposed constraints of the optimization.

3. Hydrodynamic tools

The seakeeping qualities of the variant hull forms are assessed using two-dimensional (2-D) strip theory and three-dimensional (3-D) panel methods. The SPP-86 code (1994), the standard software of the Laboratory for Ship and Marine Hydrodynamics of the National Technical University of Athens (NTUA) has been used for the strip theory calculations. It uses the modified strip theory of Salvesen, Tuck and Faltinsen, S-T-F (1970), disregarding the transom stern terms, coupled with the close-fit hull form representation proposed by Frank (1967). As is well known, strip theory remains a solid basis for seakeeping calculations and competes successfully with newer and more rigorous methods (Bailey et al, 2000, Grigoropoulos et al., 2000), even at high speeds, when compared with experimental (Blok and Beukelman, 1984) and full-scale results (Grossi and Dogliani, 2000). The usefulness of strip theory is more pronounced in the prediction of the shape of the RAO curve in the vicinity of the resonance for the vertical ship responses (Bruzzzone et al, 2000), which is essential for the proposed optimization procedure.

In addition, the 3-D panel code SWAN1 (1999) described in detail by Sclavounos (1996) is used to assess the calm and rough water performance of a hull form. A suitable interface to automatically prepare the detailed description of the hull form fed to that code has been devised. However, this code is quite time-consuming when used for seakeeping calculations. Furthermore, for some of the variants of the modern high-speed hull forms used as test cases, with wide and shallow transom, the code failed to provide the dynamic responses, thus, creating problems to the optimization software. Following this criticism, which is directly related to the detailed input necessary for the panel method and by no means depreciates the value of the code compared to the robust and reliable strip theory code, the latter has been used in most of the sensitivity seakeeping runs, while the former is used for the estimation of calm water resistance of the variants and for the a posteriori evaluation of the seakeeping characteristics of the parent and the optimum hull forms. The incorporation of SWAN was facilitated by automating the iterative procedure it uses converging to the actual dynamic draft and trim of the vessel at each speed.

Finally, the analytical assessment of the hydrodynamic performance of a candidate design in calm water and in waves should be accompanied by careful experimental verification before proceeding to the final design of the hull form.

4. Optimization strategies

Classic optimization methods are based on the approach of keeping the best solution found so far and attempting to improve it further, using deterministic or stochastic rules. By introducing probabilistic processes in some of the traditional algorithms or by inventing brand new algorithms, methods for solving complex optimization problems over multi-modal solution landscapes are now fully operational.

Instead of processing and improving only a single solution at a time, evolutionary algorithms maintain a population of several candidate solutions simultaneously. Separate analysis tools are used to determine the relative merit of each population member. Populations evolve according to the principles of natural

selection and the survival of the fittest concept; through encoded natural processes, while fittest individuals increase their presence in successive generations. So, the most promising parts of the search space are explored by exploiting knowledge gained during previous explorations and the optimal solution is finally located.

The theory of evolution and the survival of the fittest concept gave rise to the so-called Evolutionary Algorithms (EA). Genetic Algorithms (GA) and Evolution Strategies (ES) are the two most widely used EA. EA work with populations of individuals, which evolve according to the principles of natural selection and the probabilistic processes which are implicit to them. Nowadays, evolutionary algorithms (EA) are used in solving a wide range of complex problems in engineering, manufacturing, computer sciences, logistics, business, etc. Their readily understood methodology along with the fact that they may handle difficult problems, among them multi-objective and multi-disciplinary ones, not susceptible to solution by traditional methods, drags in new users from a variety of scientific fields. New comers to the field of EA may profit of their indisputable advantages, such as:

- their robustness,
- their ability to escape from local optima and to locate the global optimal solution,
- their ability to easily accommodate any analysis software which scientists are accustomed to use, just acting as the driving mechanism towards the sought for optimal solution,
- their ability to locate feasible optimal solutions, in optimization problems with constraints, and
- their ability to handle optimization problems with more than one contradictory objectives or problems related to more than one disciplines, provided that the user supplies analysis tools for each one of the involved disciplines.

Multi-objective optimization is a major feature of modern optimization systems to cope with problems involving several non-commensurable or/and competing objectives that should be optimized simultaneously. An optimal performance according to one objective often implies unacceptably low performance in one or more of the other objectives, calling for a compromise between them. A family of non-inferior, alternative solutions, known as the Pareto optimal front, characterizes multi-objective problems. Optimization software may handle an unlimited number of objectives, providing a multi-dimensional Pareto front of optimal solutions as well as post-processing tools for getting answers and making critical decisions. Furthermore, they may handle any kind and number of constraints by penalizing unfeasible solutions that emerge during the evolution process by reducing their fitness value in proportion to the degree of constraint violation. Thus, infeasible solutions are gradually eliminated and optimal solutions or a front of optimal feasible solutions are provided.

In an EA, the individuals forming the current population compete and the most successful among them will have a relatively larger number of offspring in the next generation. Through encoded natural processes, fittest individuals increase their presence in the forthcoming generation, while unfit ones are likely to die out. The next generation is formed by breeding them together using operators borrowed from natural genetics. This process leads to the evolution of populations of individuals that are better suited to their environment than the individuals that they were created from, just as in natural adaptation. Thus, EA models natural processes, such as selection, recombination and mutation. By doing so, the most promising parts of the search space are explored by exploiting knowledge gained during previous explorations.

Basic EA phases are the formation of the initial starting population, generated through sampling randomly from the search space, the objective function that is used to judge the quality of the population members as well as the process for creating offspring.

An EA-based computation starts by randomly generating a number of individuals (the starting

population). Through calls to the evaluation software each one of the starting individuals is associated with its own cost value. If the optimization criteria are not met the creation of a new generation starts. Individuals are selected according to their fitness for the production of offspring, through recombination. In the GA the whole parent population is replaced by their offspring and their cost value is then computed. In ES selected only members of the parent population are replaced by offspring, while others last for more than one generations, with the possibility to have even life span. In both cases, this cycle is performed until the optimization criteria are met.

From the above discussion, it can be seen that EA differ substantially from the traditional search and optimization methods. The major differences are listed below:

- 1 EA handle population of individuals, instead of a single individual, at a time.
- 2 EA do not ask for cost function derivatives' evaluations.
- 3 Since EA employ probabilistic transition rules, local optimal solutions can be skipped.
- 4 EA (and, in particular, the EASY software) can be employed with negligible preparation cost whenever the evaluation tool is available.
- 5 In multi-objective optimization problems, the EA can provide a number of potential solutions to a given problem. The final choice is left to the user.

In this work, two alternative optimization software systems, based on the aforementioned methodologies are employed to seek for the optimum hull form: the modeFRONTIER package (2002) and the Evolutionary Algorithms System (EASY) developed and brought to market from a research group in NTUA (Giannakoglou, 2002).

modeFRONTIER is commercial, general-purpose software for the search of optimal solutions in single- or multi-objective problems. modeFRONTIER provides a wide range of optimisation technologies and strategies, in one of the following four categories:

- 1 Techniques for preliminary exploration of the range of possible design configurations, including algorithms derived from the theory used to design experiments, such as surrogate models (response surfaces).
- 2 Techniques for multi-objective optimisation; these are based on evolutionary algorithms known as genetic algorithms (GA), or evolutionary strategies, standard and modified.
- 3 Techniques for local refinement i.e. single-objective methods, which search for local maxima or minima, employing the so-called hill-climbing algorithms (sequential quadratic programming, quasi-Newton, conjugate gradient, and direct search methods).
- 4 Plugged in, special-purpose methods, encompassing a wide range of externally provided optimisation algorithms, which can be introduced, if appropriate for particular problems (in this case all the normal functions of modeFRONTIER are still available).

EASY software, although it not so widespread as modeFRONTIER, it has also been extensively used in engineering applications. It provides to the advanced user the capability to specify every aspect of the evolution while it guides the beginner by offering preset values. It supports single and multiple objectives, function approximation through Artificial Neural Networks (ANN) for time consuming problems and a rich set of options that may define algorithms such as Genetic Algorithms or Evolutionary Strategies. The user is assumed to be reasonably acquainted with Evolutionary Algorithms and programming. EASY user interface is built on the Java™ platform while the core evolutionary system is programmed in C++ for maximum performance. Its documentation includes modules for maintenance (defect corrections and new revisions), training and consultation on its usage.

In general, CFD analysis tools used in ship hydrodynamics are quite time consuming. Thus, the reduction

of the number of evaluations during the optimization process is essential for its completion within reasonable time. The strategy implemented in EASY seems to be very efficient in this respect. Contrary to modeFRONTIER, where ANN are trained at the beginning of the optimization process using a great amount of evaluations (about 200), EASY invokes the use of dynamically trained, built in, simple ANN. ANN permit the reduction of the number of calls to the evaluation tool by substituting them with Inexact Pre-Evaluations (IPE). The most promising IPEs are then re-evaluated using the exact CFD tool and they are inserted in the database used to train the ANN. Finally, extra user-defined or automatically computed coefficients, denoted as importance factors, can be incorporated in the network to account for the importance of some of the design parameters over the rest of them.

5. Test cases

5.1. Naval Corvette

The first test case is the hull form of a naval corvette with a service speed corresponding to Froude number = 0.50. On the basis of an existing parent hull form optimization has been carried out using the method described in the introduction (Grigoropoulos, 1989). The procedure resulted in a hull form for which the average of the RAO peak values of the vertical acceleration and the relative motion at the forward perpendicular (FP) in head waves was 9% better than that of the parent one. The body plans of the parent and the optimized hull form are shown in Fig.1.

The same parent hull has been used as the starting point for the evaluation of the proposed methodology. Considering a single objective optimization focusing on the same seakeeping responses as above, successive runs of modeFRONTIER and EASY codes were executed with various sets of options. The design hull form parameters investigated and their respective range of variation is given in Table I. The main particulars of the hull were kept constant in all runs, while the divergence of the displacement from its initial value was penalized properly. Strip theory was used to evaluate the seakeeping responses in all cases.

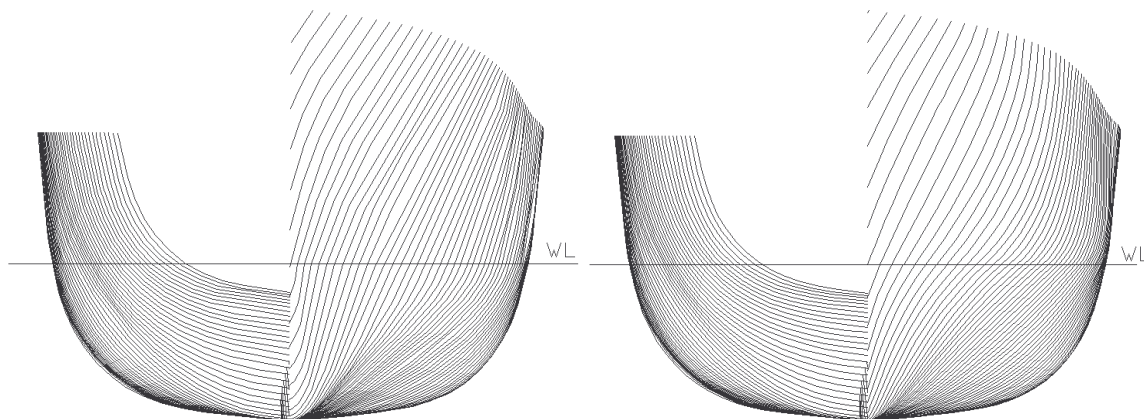


Fig.1: Body plan of the parent and the optimized hull form using the semi-automatic method proposed by Grigoropoulos (1989)

Table I: Design variables of the naval corvette investigated and their range of variation

Design Variable	Initial Value	Units	Lower Limit	Upper Limit	Variation Range	
Centroid shift of sectional area curve (SAC)	0	[%]	-1	1	-	-
Forebody prismatic coefficient	0.57	[-]	0.56	0.58	-1.75%	1.75%
Sectional area coefficient of a reference frame in the bow region	0.38	[-]	0.36	0.5	-5.26%	31.58%
Tangent of SAC at FP	0	[deg]	0	30	-	-
Transom section coefficient up to deck	0.54	[-]	0.5	0.6	-7.41%	11.11%
Longitudinal centre of gravity of aftbody SAC up to deck	28.25	[m]	28	28.6	-0.88%	1.24%
Transom draft	0.8	[m]	-0.3	1.3	-137.50%	62.50%
Transom beam at deck	9.9	[m]	9	11.5	-9.09%	16.16%
Flare at deck of the reference frame in the bow region	60	[deg]	30	90	-50.00%	50.00%
Tangent at bow of the design waterline	10	[deg]	8	25	-20.00%	150.00%
Area coefficient of the forebody design waterline	0.67	[-]	0.66	0.75	-1.49%	11.94%
Gradient of the distribution curve of the flare at waterline, at the for end of parallel body	25	[deg]	10	50	-60.00%	100.00%
Flare at waterline at the reference frame in the bow region	70	[deg]	35	75	-50.00%	7.14%

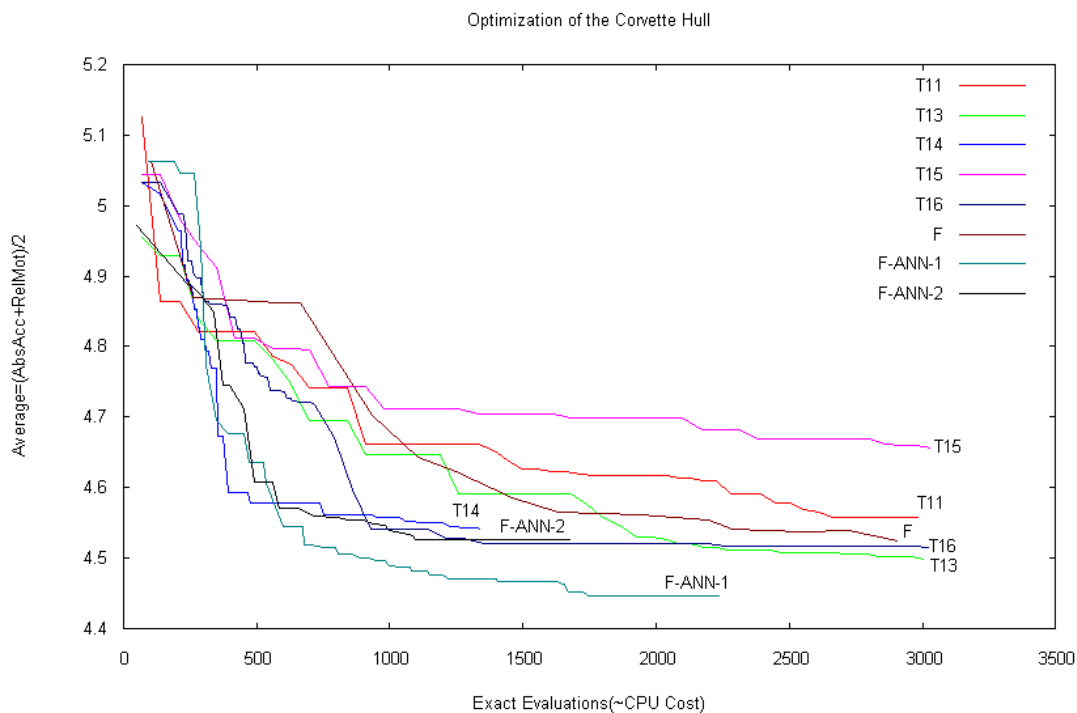


Fig.2: Optimization progress using modeFRONTIER and EASY software with various options.

The progress of the optimization process via the achieved reduction of the objective function (OF) value versus the evaluated variants is demonstrated in Fig.2. According to this figure, the GA implemented in modeFRONTIER (F) with ANN (F-ANN-1) support achieves the largest part of the reduction of the OF after about 500 evaluations, while it needs more than 2000 evaluations to reach its minimum. In the absence of the ANN the method is not very efficient, since the convergence to the optimum is more

smooth, while the final result after about 3000 evaluations is comparable with the one reached after 500 in the case where ANN are used. However, a repetition of the method resulted in slightly inferior results. On the other hand, the GA applied in EASY code is quite efficient in cases T14 and T16 where the GA is associated with IPEs of the OF and automatically generated importance factors (IF). If the same GA without the IPE and IF is executed (T11, T13, T15) the results are inferior. In general significant differences between successive optimization runs with the same parameters are apparent both in the first part of the process where the major reduction of the OF happens as well as to the final outcome. In Fig.3 the body plans of the optimum hull forms derived by modeFRONTIER (F-ANN-1) and EASY (T16-IPE-IF) are depicted. It seems that both of them are quite similar with the one derived by EASY being slightly smoother.

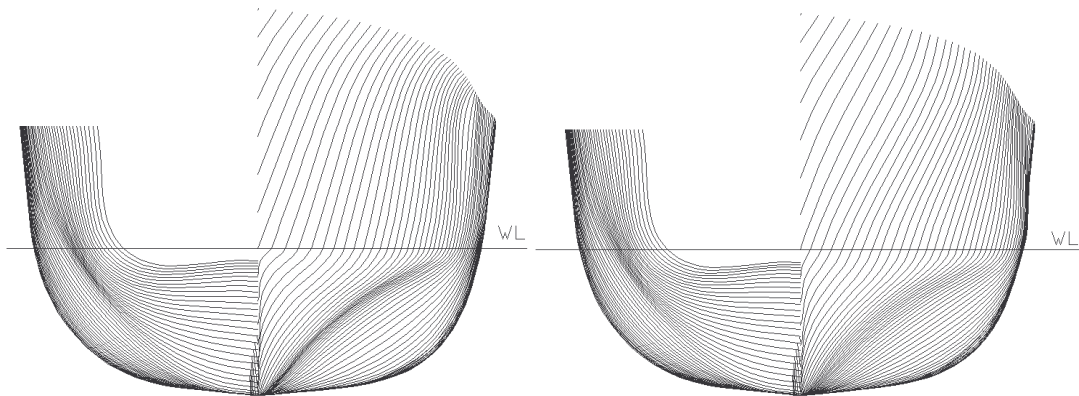


Fig.3: Body plan of F-ANN-1 and T16-IPE-IF optimum hull forms.

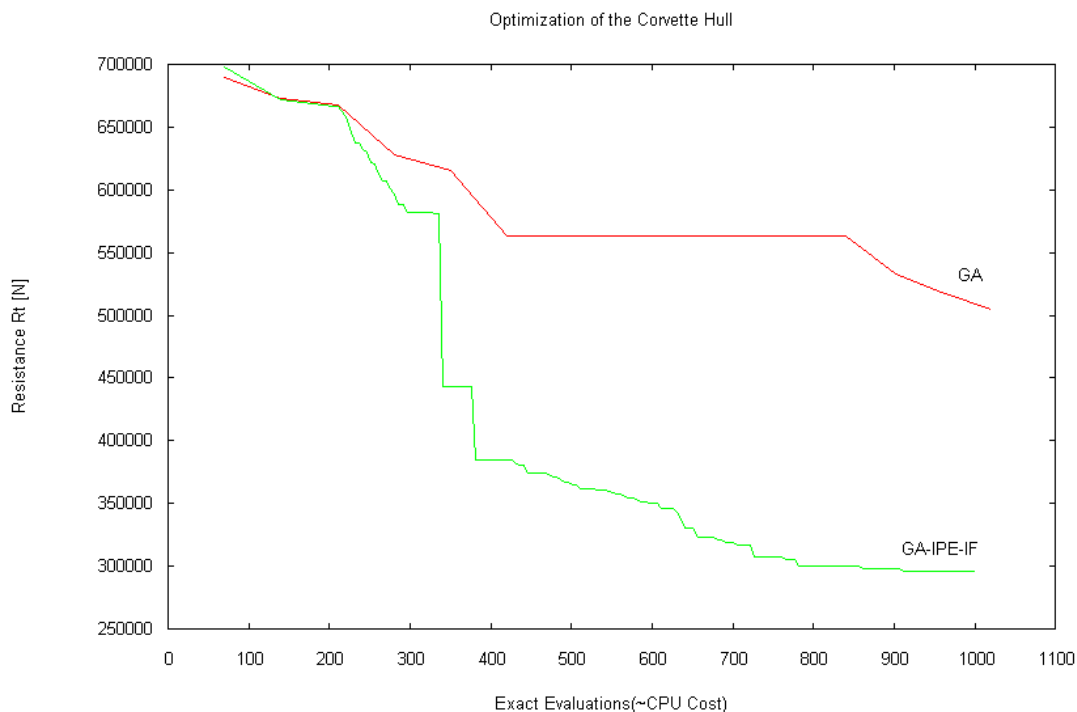


Fig.4: Progress of the optimization procedure for resistance at Froude number = 0.50, using EASY software with and without IPE and IF options.

As a next step to the demonstration of the capabilities of the proposed method, the calm water resistance calculated using SWAN code has been used as the OF. The calm water resistance is assumed to be the sum of the calculated wave resistance and the frictional resistance, both based on the calculated wetted surface. The course of the optimization procedure in successive runs of EASY code, with and without IPE and IF, is shown in Fig.4. It is clear that IPE and IF options enhance drastically the efficiency of the method. The resulting optimum hull form, using IPE and IF, is shown in Fig.5a. This hull form is quite different both from the parent one and the one optimized for seakeeping. The formation of a bow bulb is apparent in the fore body of this hull form. However, the estimated reduction in resistance is quite unrealistic to be accepted without verification by model tests.

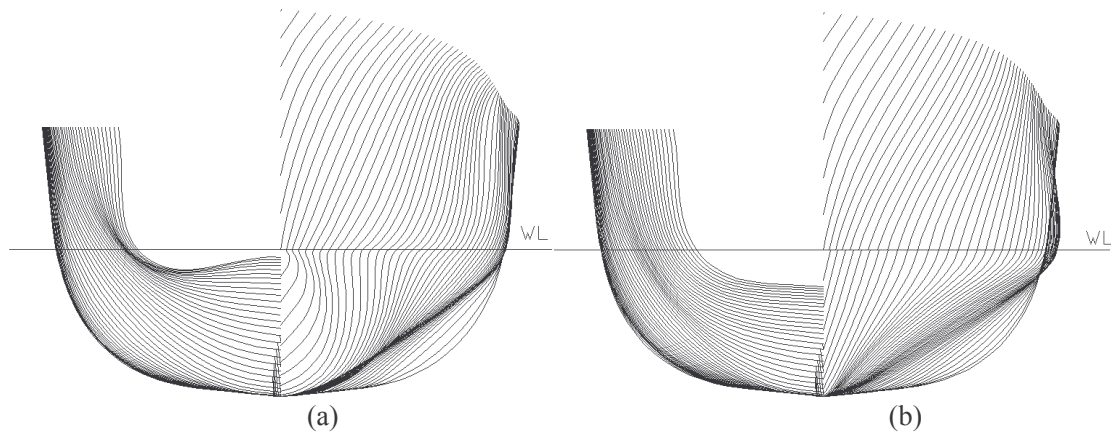


Fig.5: Body plan of the optimum corvette hull forms on the basis of calm water resistance (a) and the one derived multi-objective (seakeeping and resistance) optimization (b).

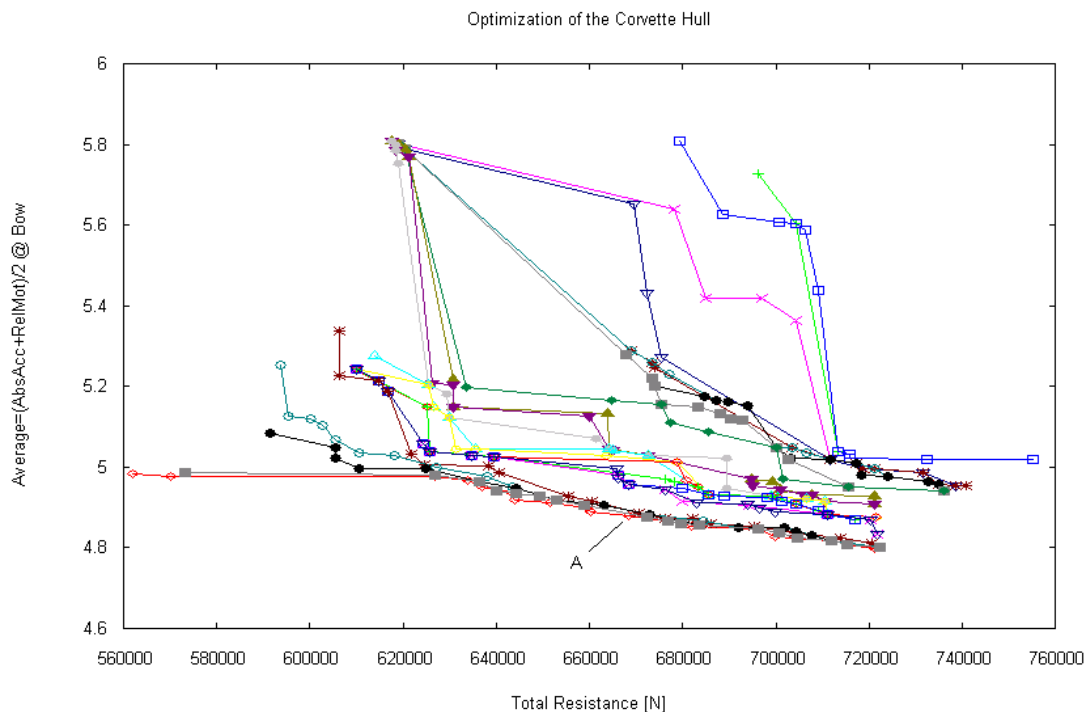


Fig.6: Pareto front for the multi-objective optimization procedure for resistance and seakeeping using EASY software with IPE and IF options.

Finally, in order to demonstrate the full capabilities of the developed procedure, multi-objective optimization for both resistance and seakeeping has been carried out. The successive Pareto fronts are presented in Fig.6. As it is obvious from this figure, the final Pareto front is slightly only inclined with respect to the horizontal line. Keeping in mind the comment about the reliability of the analytical resistance estimation, the shape of the final Pareto front leads to the conclusion that, the significant improvement of the resistance can be achieved at a very low seakeeping performance expense. Thus, a hull form with significantly improved resistance and seakeeping performance can be designed. The derived optimum hull form denoted as A in the figure, which is located at an intermediate point of the final Pareto front is shown in Fig.5b. As it was expected the hull forms that correspond to the two ends of the front, with minimum resistance and dynamic responses are similar with the respective hull forms optimized for resistance and seakeeping, only.

5.2. High-speed double chine planing hull form

As a second test case the parent hull form of double chine, planing NTUA series has been selected. Although this hull form has constantly increasing warp in the stern to bow direction, it is composed of relatively simple lines and curves (Fig.7). Furthermore, the immersion of the upper and lower chine is critical for the hydrodynamic performance of the hull form at high speeds. Thus, in this case the margins of the varied parameters are limited.

Grigoropoulos and Loukakis (2002) demonstrated that the available analytical tools for the prediction of calm water resistance, at the high speeds and the light displacements at which these hull forms operate, are not quite reliable. Thus, it was decided to carry out the optimization of the hull form only for seakeeping at a speed corresponding to Froude number = 0.68. The same figure of merit for the seakeeping performance assessment has been used as in the case of the naval corvette.

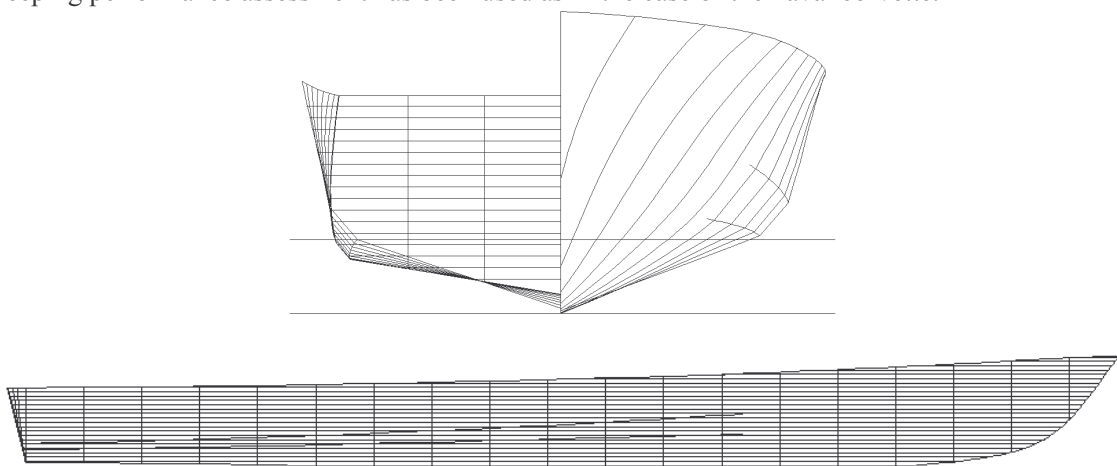


Fig.7: Body plan and profile (in different scale) of the parent hull form of the NTUA systematic series.

The design parameters varied during the optimization, along with the range of their variation are listed on Table II. In this case, where the hull lines are quite simple, the draft should be modified for each variant in order to keep the displacement constant. Both available optimization software packages modeFRONTIER and EASY have been used, the former without and the latter with active the enhancing options IPE and IF. These options seem to make the difference in the optimization course and the final outcome, as it is shown in Fig. 8.

Table II: Design variables of the double chine hull form investigated and their range of variation

Design Variable	Initial Value	Units	Lower Limit	Upper Limit	Variation Range	
Longitudinal Position of FP	34.95	[m]	34.95	37	0.00%	5.87%
BEVEL.depth at transom (distance of chines-connecting line from the hypothetical intersection of bottom and side)	0.14	[m]	0.1	0.4	-28.57%	185.71%
Area coefficient of forebody deadrise angle distribution curve	0.8	[-]	0.8	1	0.00%	25.00%
Area coefficient of the forebody distribution curve of the flare at deck angle	0.75	[-]	0.55	1	-26.67%	33.33%
Angle of entrance of design waterline	10	[deg]	0	20	-100.00%	100.00%
Inclination of the transom wrt the vertical in the profile view	14	[deg]	5	25	-64.29%	78.57%

The resulting body plan, profile and a perspective view of the optimum hull form derived using EASY code are given in Fig. 9. By comparing Figs. 7 and 9, it can be concluded that the optimized for seakeeping hull form has slightly higher deadrise angle at the transom, modified stem profile and increased distance between the chines, while the lower chine has been lowered even more. The associated reduction in the seakeeping figure of merit is about 30%.

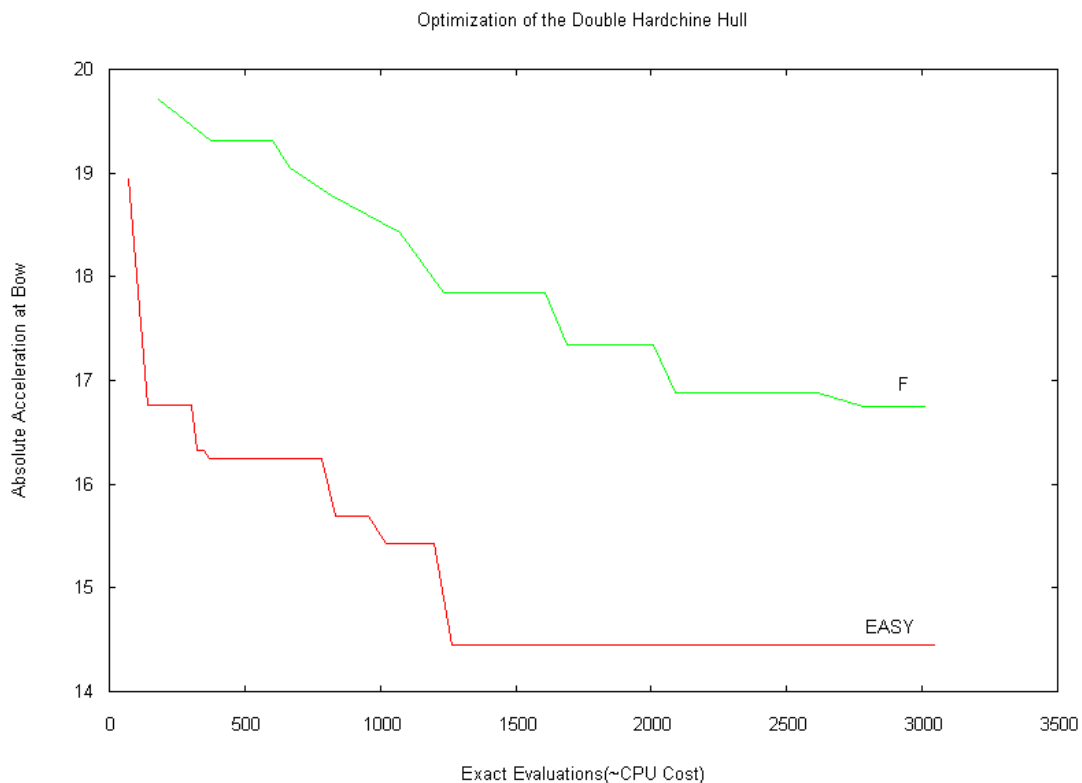


Fig.8: Progress of the optimization procedure for seakeeping using EASY software and modeFRONTIER.

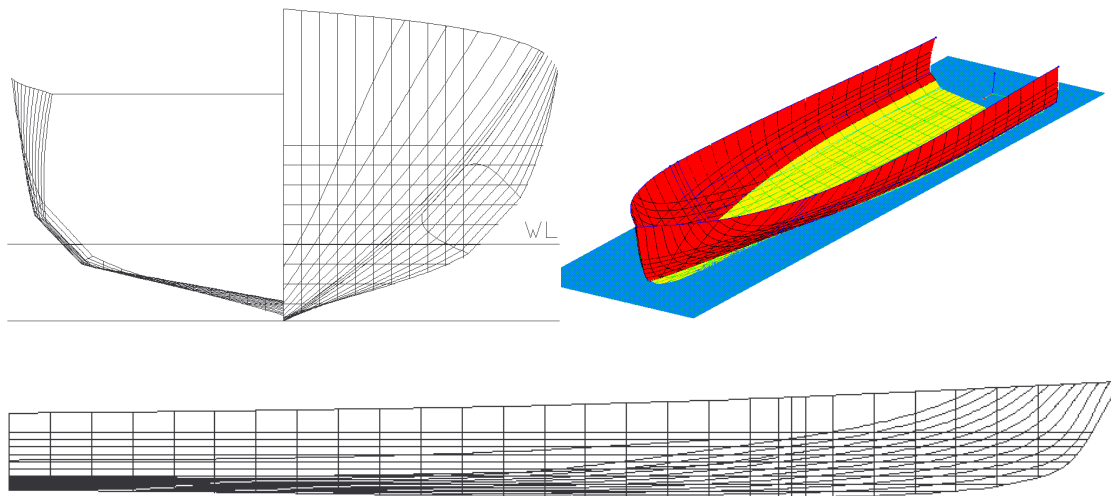


Fig.9: Lines plan, profile and perspective view of the optimized hull form of the NTUA series using EASY optimization package.

Conclusions

A series of numerical tests have been carried out to investigate the effectiveness of the combination of software for the parametric representation of a hull form, the hydrodynamic evaluation in calm water and in waves and the single and multi-objective non-linear optimization.

In order to demonstrate the power of the optimization methods, the principal hull form characteristics (main dimensions, displacement) were kept constant.

On the basis of the results presented in the previous section, the following conclusions are drawn:

- The parametric representation of the hull form enables the automatic generation of variants, which represent fair hull forms and feasible designs.
- Modern stochastic multi-objective optimization system permit the derivation of optimum hull form after a large number of evaluations, although successive runs are necessary to confirm the process ends with a global and not a local optimum.
- The hull form optimization for seakeeping can be associated with reduction of the calm water resistance at the same time.
- The use of ANN and IPE are essential tools for speeding up the process, since CFD codes are still quite time-consuming.
- Special treatment is necessary to accomplish the automatic modification of hard chine semi-planing and planing hull forms.

The authors believe that the proposed methodology will form the way ahead in the hydrodynamic ship design.

References

ABT, C.; HARRIES, S.; HEIMANN, J.; WINTER, H. (2003), *From Redesign to Optimal Hull Lines by means of Parametric Modelling*, 2nd Int. Conf. Computer Applications and Information Technology in the Maritime Industries, COMPIT2003, Hamburg

- BAILEY, P.A.; HUDSON, D.A.; PRICE, W.G.; TEMAREL, P. (2000), *Comparisons between Theory and Experiment in a Seakeeping Validation Study*, Trans. RINA, Vol. 142, pp. 44-77.
- BLOK, J.J.; BEUKELMAN, W. (1984), *The High-Speed Displacement Ship Systematic Series Hull Forms – Seakeeping Characteristics*, Trans. SNAME, Vol. 92, pp. 125-150.
- BRUZZONE, D.; GUALENI, P.; SEBASTIANI, L. (2000), *Application of Green's Function Methods to the Seakeeping Computations for High-Speed Vehicles*, Intl. Conf. Ship and Shipping Research NAV 2000, Paper 9.1, Venice, September 19-22.
- FRANK, W. (1967), *Oscillation of Cylinders in or Below the Free Surface of Deep Fluids*, NSRDC, Rep. No. 2375, Washington, D.C.
- modeFRONTIER (2002), *Mode modeFRONTIER Multi-Objective Design Environment. User Manual*, ES.TE.CO s.r.l.
- GIANNAKOGLU, K.C. (2002), *Design of optimal aerodynamic shapes using stochastic optimization methods and computational intelligence*, Progress in Aerospace Sciences, Vol. 38, pp. 43-76.
- GRIGOROPOULOS, G.J. (2004), *Hull form optimization for hydrodynamic performance*, Marine Technology, Vol. 41, No. 4, October.
- GRIGOROPOULOS, G.J. (1989), *Hull form optimization with respect to seakeeping*, PhD Thesis, NTUA
- GRIGOROPOULOS, G.J.; LOUKAKIS, T.A. (2002), *Resistance and Seakeeping characteristics of a Systematic Series in the Pre-planing Condition (Part I)*, Trans. SNAME, Vol. 110, Sept.
- GROSSI, L.; DOGLIANI, M. (2000), *Load and Seakeeping Assessment of HSC Based on Full-Scale Monitoring*, Intl. Conf. On Ship and Shipping Research NAV 2000, Paper 2.8, Venice, Sept. 19-22.
- HARRIES, S.; ABT, C. (1998), *Parametric Curve Design applying fairness criteria*, Intl. Workshop on Creating Fair and Shape-preserving Curves and Surfaces, Network Fairshape, Berlin/Potsdam; Teubner
- HOOKE, R.; JEEVES, T.A. (1961), *Direct search solution of numerical and statistical problems*, Journal of Assoc. for Computing Machinery, Vol.8, No.4, p. 212.
- LACKENBY, H. (1950), *On the systematic geometrical variation of ship forms*, Trans. INA, Vol. 92
- SALVESEN, N.; TUCK, E.O.; FALTINSEN, O. (1970), *Ship Motions and Sea Loads*, Trans. SNAME, Vol. 78, pp. 250-287.
- SCLAVOUNOS, P.D. (1996), *Computation of Wave Ship Interactions*, *Advances in Marine Hydrodynamics*, edited by M. Qhkus, Computational Mechanics Publ.
- SHIPFLOW (1999), *Users Manual, Rev. 2.4*, 1999 FLOWTECH, Gothenburg, Sweden, June.
- SWAN1 (1999), *User Manual Vs.3.1. Ship Flow Simulation in Calm Water and in Waves*, Boston Marine Consulting Inc., Boston MA 02116, USA.
- SPP-86 (1994), *User's Manual*, Report No: NAL-114-F-94. Lab. Ships and Marine Hydrodyn., NTUA

Field and Laboratory Investigation of High-Speed Ferry Wake Impacts in New York Harbor

Michael S. Bruno, Brian J. Fullerton, Raju Datla, Peter A. Rogowski

Center for Maritime Systems, Davidson Lab., Stevens Inst. of Technology, Hoboken, N.J. 07030
mbruno@stevens.edu

1. Introduction

The last 10 years have witnessed a tremendous growth in passenger ferry service in the New York metropolitan region, a growth that is mirrored in many other areas of the world as more and more urban shorelines experience revitalization – some would say a transformation. This revitalization has in a very real sense been brought about by success in restoring our urban waterways. Estuaries like the Hudson-Raritan Estuary are once again vital and vibrant habitat, and offer recreational and commercial opportunities to thousands of residents and visitors. Urban waterways also serve as hosts to the US Marine Transportation System (MTS), a system that is responsible not only for passenger ferry transportation, but also for more than 95% of U.S. international trade. The Port of New York and New Jersey, among the largest in the nation, is a critical component of the national and global MTS.



Fig.1: Ferry route map for NY Waterways

The mixed use of the urban estuary – including marine transportation, commercial and recreational fishing, and pleasure boating, among others - creates complex user needs and, unfortunately, conflicts. The recent rapid growth in high-speed ferry service in the Hudson River (see Fig.1 for a route map of the primary ferry service) has created the potential for one such conflict – the need to provide reliable waterborne passenger transportation while at the same time ensuring that wave-sensitive shoreline facilities and activities are not adversely impacted. Of particular concern are:

- Impact to vessels in exposed and partially-protected dock areas and marinas
- Damage to bulkheads and other shoreline structures
- Erosion of natural shorelines and wetlands
- Impacts to sea grass and shellfish beds
- Safety of passing vessels, particularly small craft

In response to this issue, the State of New Jersey requested that Stevens Institute of Technology conduct a comprehensive study of the New York Harbor wake problem with a view toward developing recommendations to enable efficient passenger ferry service while also minimizing any identified adverse impacts associated with ferry wakes. The Stevens study is now complete and has been approved by the Harbor Operations Committee of New York – New Jersey Harbor. We here summarize our findings and recommendations, and also provide the preliminary findings from more recent field measurements in the Harbor.

2. Study description and results

The study of ferry-generated wakes in New York Harbor involves the consideration of various factors: complicated bathymetry, ambient wave field, various types of vessels, their speed, acceleration and course changes. With this in mind, it was decided to study the problem by a combination of qualitative and quantitative field measurements, and laboratory measurements of wake wash from small-scale models.

The study contained several elements, including:

- field observations of wave characteristics in the Hudson River over a multi-week period;
- visual observations of ferry wake generation, ferry routing, docking and departing procedures, etc.;
- scale model studies of ferry wake generation using the Stevens high-speed towing tank and scale models representing a variety of ferry hull forms, including monohulls and catamarans, operating over a wide range of speeds;
- meetings with the full range of stakeholders, including ferry captains, marina owners and operators, commercial vessel captains, the New York Harbor Operations Committee, and Federal, State and local government officials.

2.1. Field Observations, July, 2002

A field study was undertaken in July, 2002. High-resolution pressure gauges were deployed for slightly over eight days beginning the afternoon of July 10th. Two gauges were situated so as to obtain time series pressure records that would provide a description of the wave heights and wave periods found in the Harbor. The Harbor bathymetry is characterized by a deep (~20 m) channel flanked in most areas by a narrow, flat, and shallow (~3 m) shelf. One gauge was placed at a depth of 11 m in the channel, approximately 100 m seaward of the pier head line. The second gauge was placed at a depth of 4 m, inshore of the pier head line. The two gauges were located near the NY Waterways Lincoln Harbor ferry terminal (see Fig.1) and as such near an active fast ferry route.

The 8-day surface elevation time series for the offshore gauge is given in Fig.2. The time series indicates a strong diurnal pattern of relatively calm overnight periods followed by very energetic periods. The highest waves in the day occur during two peak periods. The first peak period of each day begins as a gradual increase starting at approximately 0530 EDT and peaking at approximately 0915 EDT,

which corresponds to the morning rush hour. Wave heights then gradually diminish, but only to levels well above the typical overnight values, until approximately 1245 EDT when they again begin to increase as the evening rush hour is approached. After the second and typically highest peak of the day at approximately 1745 EDT, the wave heights gradually diminish until they reach the typical overnight values some time shortly after 2330 EDT. Overnight maximum wave heights range from 4 inches to 6 inches (10 to 15 cm). The morning peak heights are typically between 12 inches and 16 inches (30 to 40 cm). Similar behavior was observed by the inshore gauge, although the inshore gauge typically recorded wave heights between 5% and 10% higher than the offshore gauge, likely because of the effect of shoaling and/or wave reflections from the shoreline.

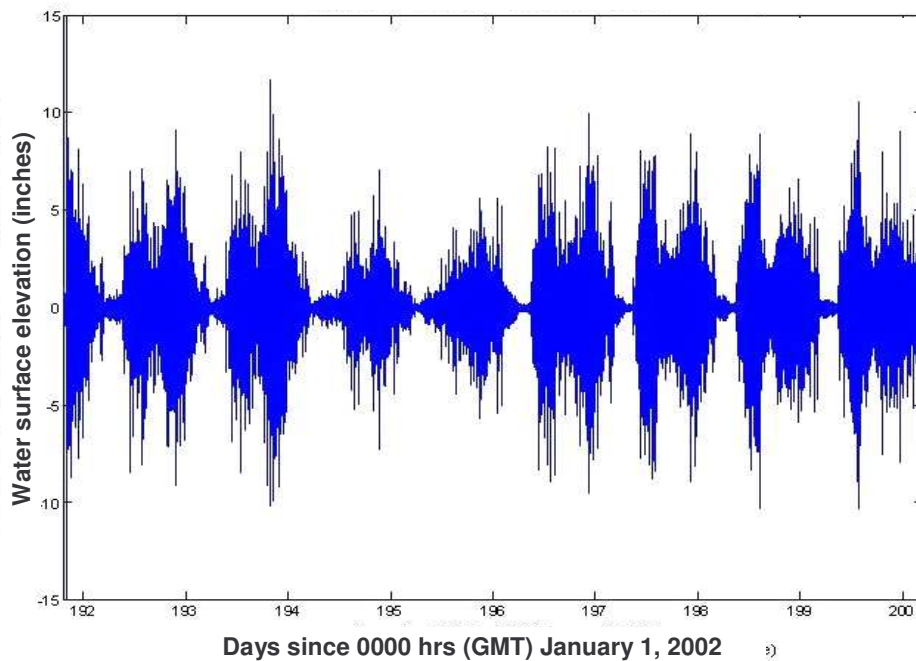


Fig.2: Time history of water surface elevation for 8-day period

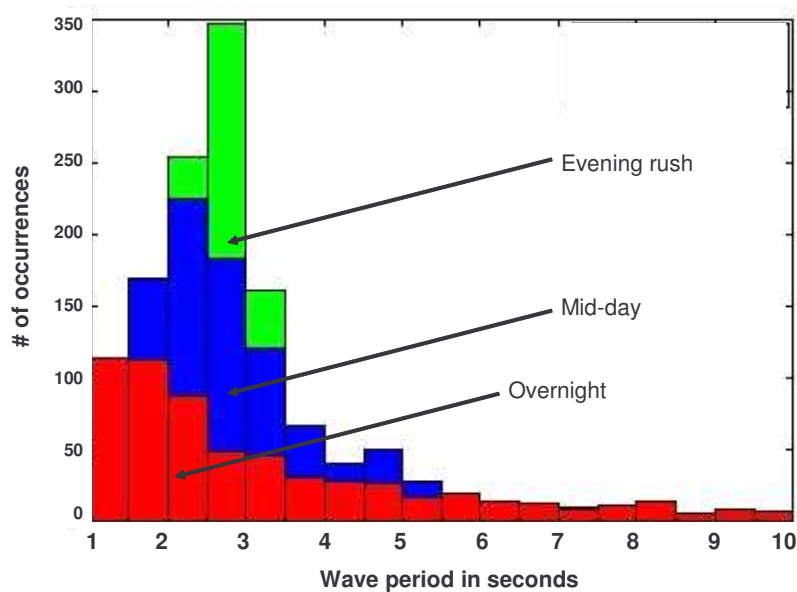


Fig.3: Histogram of wave period

Until this point in the report, discussion of the observed waves has been limited to describing wave height. However, wave period is a critical measure not only of the energy contained in the wake field, but also of the potential influence of the wakes on vessels and shoreline infrastructure. In addition, the performance of partial wave barriers, such as floating breakwaters, is strongly affected by wave period. Observed wave periods ranged from 1 to 10 seconds. Histograms of wave period for different time periods are presented in Fig.3. The peak of the histogram falls in the 1 to 2 second range during a typical overnight hour. During the typical midday hour, the peak moves to the 1.5 to 3.0 second range and the number of occurrences in the 3 to 5 second range increases by nearly 50%. During a typical hour in the evening rush, the peak period again moves up, now to the 2.5 to 3.0 second range. During the evening rush, the number of occurrences of periods greater than 3.0 seconds is very similar to that which was observed during the midday, which is significantly greater than is observed in the calm overnight hours.

2.2. Field Observations, July, 2004

A follow-up field study was conducted in July, 2004 in order to obtain a higher-resolution dataset regarding wake characteristics, and the relationship between time of ferry vessel passage and associated wave characteristics. In order to accomplish this task, an ultrasonic acoustic water level gauge operating at a frequency of 10 Hz was used to measure wave activity in New York Harbor. The gauge was located at the western Hudson River Shoreline just south of the Hoboken North ferry terminal, Fig.1. Wave data was logged on July 20th starting at 5:20 am before any boat activity in the harbor. Times of ferry vessel passage were noted, and measurements were taken throughout the day until 7 pm.

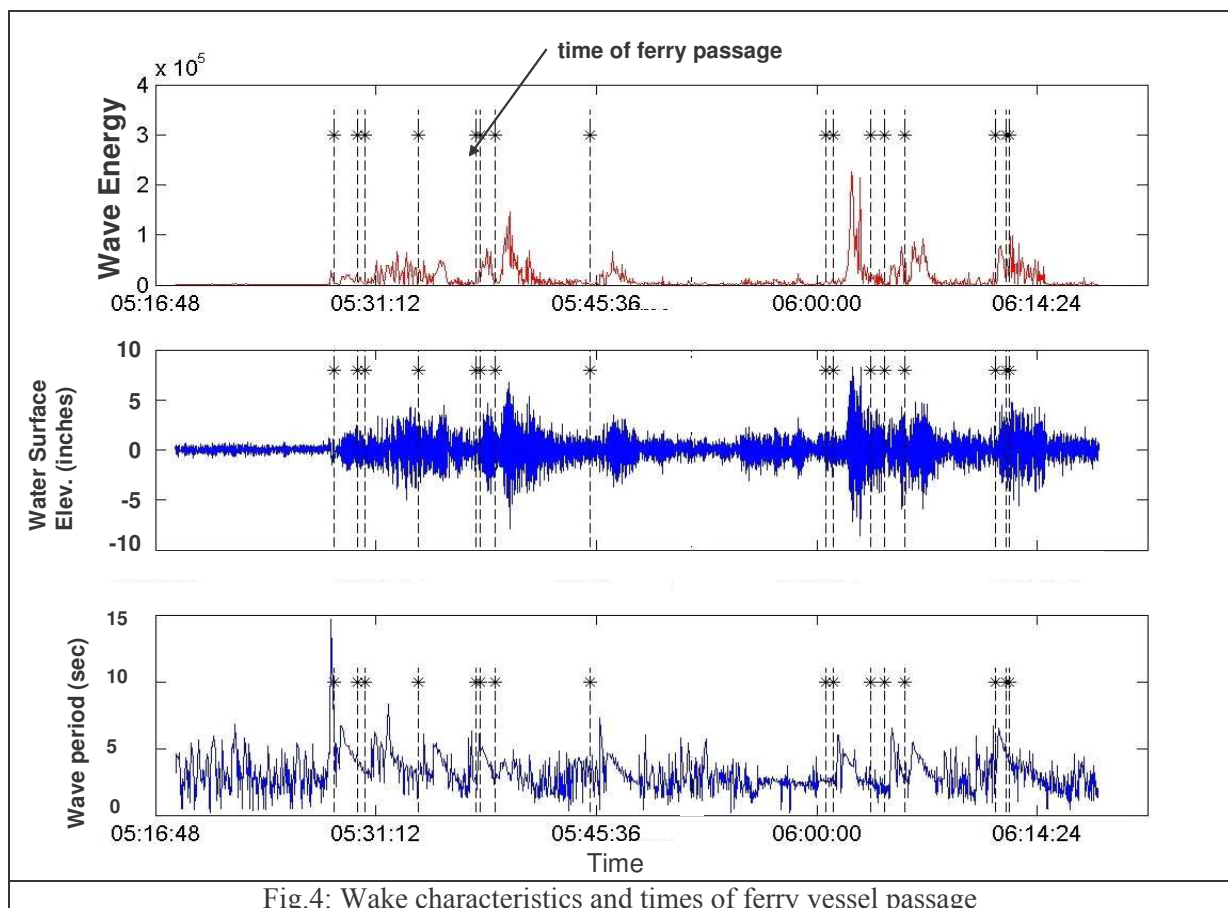


Fig.4 illustrates the wave energy, water surface elevation (with tide removed) and wave period for the first hour of measurements, at the start of the morning rush hour. Clearly, the times of vessel passage are associated with sudden increases in the measured wave energy, with maximum wave energy levels experienced during time periods when several vessels passed in close proximity to one another. This

finding is likely at least in part attributable to the wave summation associated with reflections from the shoreline. The figure does not indicate the type and speed of the ferry in each instance, although these records do exist. A computer modeling effort is underway to examine the wake generation characteristics of each vessel type under the observed speed and water depth conditions. This analysis will help explain the variability in wave height and period observed here.

2.3. Laboratory studies

Tests were conducted in the Davidson Laboratory High-Speed Towing Tank, which is 313 ft (95.5 m) long, 12 ft (3.7 m) wide and 6 ft (1.8 m) deep, and has a top speed of 100 ft/s (30.5 m/s). Four different vessels, whose characteristics are given in Table I, were tested to study their wake characteristics in addition to the standard resistance and seakeeping performance characteristics.

Table I: Model characteristics

Hull	Catamaran	Monohull	Catamaran	Catamaran
Length	71.2 ft (21.7 m)	65 ft (19.8 m)	105 ft (32 m)	90 ft (27.4 m)
Beam	27.5 ft (8.4 m)	14 ft (4.3 m)	28.4 ft (8.7 m)	34 ft (10.4 m)
Draft	3.4 ft (1 m)	3 ft (0.9 m)	3.45 ft (1.1 m)	5 ft (1.5 m)
Model scale	1/12	1/12	1/20	1/16

The first model, that of the 71 ft Catamaran, was tested in October 2000 but NY Waterway decided not to consider it for their fleet. The 65 ft Monohull, “The Sea Otter”, was tested in April 2001 and NY Waterway currently operates 3 of these vessels. The 105 ft catamaran design was tested in July 2001 and NY Waterway is in the process of commissioning a few of these vessels. Finally, the 90 ft Catamaran that was tested in September 2002 will be part of the future NY Waterway fleet.

Each model was free to trim and heave, but fixed in yaw, roll, surge and sway. The vertical motion of the tow-point was measured using a motion transducer attached to the free-to-heave apparatus. Trim of the model keel relative to the horizon was measured using an inclinometer mounted on the connecting platform. Resistance was measured using a drag balance located directly above the pivot box. Two accelerometers were mounted near the bow and CG to record vertical acceleration in wave tests. Wake height measurements were made in calm water tests using two resistance-type wave probes at fixed locations in the tank. The two probes were located in that section of the tank where the model runs at constant speed and at transverse distances of 3 ft and 5 ft (model scale) from the ship centerline. The time history of the wake was recorded as the model passed by. A video camera was located on the carriage and video recordings were made of each run. Still photographs using a camera mounted on the carriage were also taken for most of the runs. Data were acquired at 250 Hz in a 100 ft “data trap”.

The full-scale wake heights measured from each of the model test are presented in Tables II to V. Some of the typical trends that can be observed are: the wake heights increase with the displacement, the newer designs tend to have lesser wake heights, the wake heights are higher at the transition (hump condition) speeds and decrease at higher speeds, wake heights depend on the location of the center of gravity and the running trim. To emphasize the wake height variation with speed, the data from the 71 ft Monohull “Sea Otter” is presented in Fig.5.

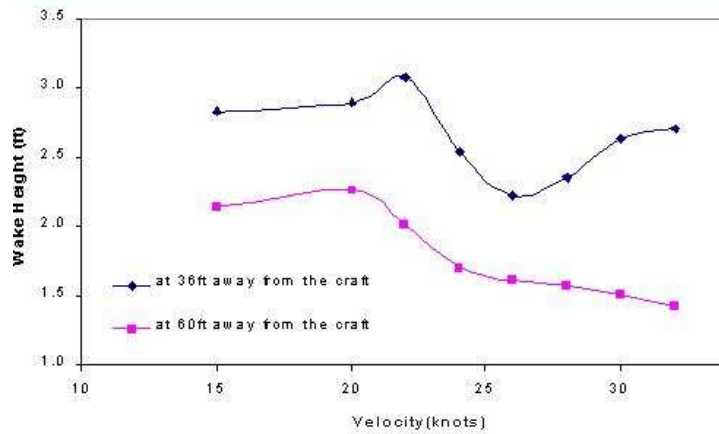


Fig.5: Wake characteristics for the 71 ft. monohull ferry: wake height vs. speed

Table II: Wave heights for 71 ft catamaran (different displacements and LCGs)

Run #	Speed (knots)	Wake Heights (ft)		Run #	Speed (knots)	Wake Heights (ft)	
		Measured at 36 ft	at 60 ft			Measured at 36 ft	at 60 ft
55 LT - 3 ft				65 LT - 3 ft			
27	15	2.9	2.9	64	15	2.8	2.6
28	20	3	2.8	66	20	3.6	3.2
29	22	2.8	2.8	67	22	2.8	2.8
30	24	2.2	2	68	24	2.6	2.6
31	26	2.2	1.8	69	26	2.2	2.2
55 LT - 5 ft				65 LT - 5 ft			
33	20	3.2	2.8	71	15	2.8	2.8
34	22	2.8	2.4	72	20	3.6	3.2
35	24	2.4	2.2	73	22	3	2.8
36	26	2	1.8	74	24	2.6	2.6
37	28	1.8	1.7	75	26	2.2	2.2
38	30	1.6	1.5				
60 LT - 3 ft				65 LT - 7 ft			
41	15	2.5	2.4	77	20	2.7	2.7
42	20	3	3	78	22	3.4	2.9
43	22	3.2	3	79	24	2.8	2.6
44	24	2.8	2.7	80	26	2.5	2.5
45	26	1.9	1.9				
46	28	1.8	1.7	55 LT - 3 ft			
47	30	1.4	1.3	82	20	3	2.8
60 LT - 5 ft				83	22	2.8	2.5
49	15	2.5	2.5	84	24	2.4	2.1
50	20	2.9	2.9	85	26	2	1.9
51	22	3.2	2.8				
52	24	2.8	2.8	50 LT - 5 ft			
53	26	2.4	2.3	88	15	3.2	2.9
54	28	2	2	89	20	2.8	2.6
55	30	1.8	1.7	90	22	2.5	2.3
60 LT - 7 ft				91	24	2	1.7
59	20	2.7	2.7	92	26	1.9	1.6
60	22	3.2	2.8	93	28	1.5	1.3
61	24	2.8	2.6	94	30	1.4	1.2
62	26	2.4	2.2				

Table III: Wave heights for 65 ft monohull (different displacements and LCGs)

Run # No.	Velocity (kn)	Wake Height(ft)		Run # No.	Velocity (kn)	Wake Height(ft)	
		at 36ft	at 60ft			at 36 ft	at 60 ft
73,990lb. - 39.8 ft				62,500 lb. - 39.8 ft			
4	15	2.8	2.1	49	20	2.5	2.0
5	20	2.9	2.3	50	22	2.4	1.6
6	22	3.1	2.0	52	24	2.2	1.3
7	24	2.5	1.7	53	26	2.2	1.2
8	26	2.2	1.6	54	30	2.3	1.2
9	28	2.4	1.6	55	32	2.2	1.1
10	30	2.6	1.5	<u>40.8 ft</u>			
11	32	2.7	1.4	63	30	2.4	1.2
<u>repeat check</u>				Tests using 2.75" interrupters at 62,500 lb.			
13	24	2.7	1.6	<u>1/16" projection - 39.8 ft LCG</u>			
Tests with LCG variation at 73,990 lb.				57	15	1.9	0.8
<u>37.8 ft</u>				59	26	1.7	1.3
15	26	2.4	1.6	<u>1/16" projection - 40.8 ft LCG</u>			
<u>38.8 ft</u>				61	26	1.9	1.3
17	26	2.3	1.6	62	30	1.9	1.1
<u>41.8 ft</u>				<u>1/32" projection - 40.8 ft LCG</u>			
21	26	2.7	1.8	67	30	1.8	0.9
<u>40.8 ft</u>				Tests using interrupters at 73,990 lb.			
19	26	2.7	1.6	<u>2.75" long - 1/32" projection - 39.8 ft LCG</u>			
23	28	2.7	1.5	70	26	1.2	1.8
24	30	2.7	1.5	<u>1.4" long - 1/32" projection - 39.8 ft LCG</u>			
25	32	2.7	1.5	72	26	2.3	1.6
49,640 lb. - 39.9 ft				73	30	2.3	1.4
27	10	0.7	0.2	<u>1.4" long - 1/32" projection - 40.8 ft LCG</u>			
28	15	1.5	0.7	75	30	2.3	1.3
29	20	2.0	1.6	76	26	2.5	1.6
30	22	1.9	1.3	Tests using Trim Wedges at 73,990 lb. And 39.8 ft			
31	24	1.7	1.1	<u>3.5"X1" - 5 deg. Wedges</u>			
32	26	1.5	1.2	79	26	2.0	1.5
33	28	1.8	1.0	<u>3.5"X1" - 3 deg. Wedges</u>			
34	30	1.8	1.0	82	30	2.4	1.4
35	32	1.8	0.8				
<u>repeat check</u>							
36	24	1.8	1.2				
49,640 lb. - 40.9 ft							
40	26	1.8	1.0				
41	28	2.0	1.0				
42	30	1.9	0.9				
43	32	1.8	0.9				
44	40	1.6	0.7				
45	42	1.5	0.8				

3. Results and discussion

The wake heights and periods found in the field measurements agree qualitatively with what was observed during the physical model tests. For this reason, it would be expected that modification of operational parameters such as speed and trim to be more in line with the optimum values predicted by the physical model tests would lessen wakes created by a particular vessel. For vessels currently operating in their most inefficient regimes, the potential reduction in wake energy can be substantial.

Table IV: Wave heights for 105 ft catamaran (different displacements and LCGs)

Run # No.	Vs (kn)	Wake Heights (ft)		Run # No.	Vs (kn)	Wake Height (ft)	
		at 60ft	at 100 ft			at 60ft	at 100 ft
195,610 lb - 59.5 ft				195,610 lb - 59.5 ft			
9	10	0.6	0.5	49	20	4.0	3.2
10	15	1.5	0.9	50	24	2.5	2.0
11	20	2.2	1.0	51	27	2.2	1.9
12	22	2.6	1.5	52	30	1.9	1.6
13	24	2.6	2.5	55	34	1.6	1.1
15	26	2.5	1.9	150,850 lb. - 61.25 ft			
14	28	2.2	1.8	57	19	3.1	1.3
16	30	1.8	1.6	58	20	2.3	1.7
195,610 lb - 62.5 ft				59	24	2.0	1.5
19	20	2.9	2.2	60	28	1.7	1.4
21	24	2.7	2.4	61	30	1.5	1.2
22	26	2.4	2.1	62	32	1.4	1.1
23	28	2.0	1.8	64	36	1.2	0.9
24	30	2.0	1.5	66	40	1.1	0.8
25	32	2.0	1.4	150,850 lb. - 63.25 ft			
26	34	1.8	1.4	68	20	2.2	1.7
27	36	1.6	1.1	69	24	2.1	1.5
28	38	1.7	1.1	70	24	2.1	1.5
29	40	1.6	1.0	71	28	1.8	1.3
30	41	1.6	1.0	72	30	1.6	1.2
* Chines Widened near the Bow				73	32	1.5	1.1
195,610 lb - 62.5 ft				75	41	1.3	0.8
32	20	1.6	1.2	225,000 lb. - 62.5 ft			
33	24	2.5	1.9	77	20	2.3	1.1
34	28	1.9	1.8	78	24	2.9	2.2
35	30	1.8	1.6	79	28	1.7	2.0
37	32	1.7	1.4	80	30	2.4	1.7
38	34	1.7	1.2	81	32	1.9	1.4
195,610 lb - 59.5 ft				82	34	1.8	1.4
40	20	2.2	2.1	225,000 lb. - 64 ft			
41	24	2.6	1.9	84	24	2.9	2.2
44	26	2.0	1.8	85	28	2.3	2.1
45	30	1.9	1.6	86	32	2.0	1.4
46	32	1.8	1.3				

The largest amount of wake energy created per unit time occurs during the transition from displacement to planing mode. This was observed in the physical model tests and suggested in the qualitative field study. In many cases (especially the newer hulls), higher speeds result in lower wave energy. Again, with the guidance provided by physical model tests of hulls, these optimum speeds must be known and adhered to by vessel operators whenever possible to minimize wake. As little time as possible should be spent in the transition zone. Again, for vessels that are currently being operated for long periods of time at the very high end of displacement (very low end of planing) substantial decreases in wake energy will be possible by this optimization.

Table V: Different loads and trims

Run #	Vel (fps)	Wake Height (ft) (at 80 ft)	Run #	Vel (fps)	Wake Height (ft) (at 80 ft)
100 LT - Level Trim			110 LT - Level Trim		
1	0.00	0.0	19	0.00	0.0
2	4.02	--	20	8.37	3.2
3	6.23	2.8	21	10.52	--
4	8.37	3.1	22	11.38	--
5	10.52	--	23	12.69	1.1
6	11.36	2.1	24	13.54	1.2
7	12.68	1.3	25	14.82	1.2
8	13.51	1.2	26	15.69	1.2
9	14.82	1.1	27	16.99	0.9
10	15.67	1.1	90 LT - Level Trim		
11	17.00	0.9	28	0.00	0.0
12	12.67	1.2	29	8.38	2.9
100 LT - 2 deg Trim			30	10.54	2.5
14	0.00	0.0	31	11.39	--
15	8.37	3.5	32	12.70	1.2
16	10.52	--	37	13.55	1.2
17	12.67	1.1	34	14.86	1.2
18	14.84	0.8	35	15.71	1.1
			36	17.01	0.9

The qualitative field study also strongly suggested that sharp turns in the transition phase could result in the focusing of wave energy, especially to the inside of turns. The qualitative evidence is strong enough on its own in this specific area to warrant the minimization of any sharp turns during the transition phase if any wake-sensitive areas are located on the inside of the turn.

Wave shoaling is taking place during at least some stages of the tide in the shallowest areas of the shorelines, some of which contain marinas. Deepening (dredging) these specific areas has the potential to reduce wave heights by 30% in some of the shallowest regions. Deepening by itself will not completely mitigate any wake problem in this harbor, but should be considered part of the total approach.

In places where reflective shorelines (vertical or near vertical walls) border water deeper than 2 feet MLLW, most of the incoming wave energy is simply reflected back into the Harbor. Efforts should be taken wherever possible to limit reflective shorelines. Again, simply replacing reflective shorelines with dissipative shorelines will not completely mitigate the wake problem, but will prevent exacerbating the situation and is an important part of any total approach.

Our study indicated that ferry wakes are responsible for a good portion of the wave energy in the ferry operating region, with maximum contribution during the weekday rush hours. Our analysis indicates that the wakes produced by high-speed ferry vessels differ in many important respects from wakes produced by more slowly moving vessels. The most damaging wakes, in terms of height, occur at low speeds, particularly during the transition from low-speed displacement mode to planing mode, and during certain turning maneuvers. The length of the ferry wakes is in general significantly longer than the length of wakes associated with even larger, slow-moving (displacement-mode) vessels operating in the Harbor. It is this large wavelength that allows wake energy to pass through the various wave protection devices in use at marinas along the Hudson River shoreline, including floating barriers and partial-depth wave screens.

Wake characteristics vary not only as a function of the vessel's speed, trim, and direction of travel, but also as a function of hull characteristics. Hull designs that more easily achieve high-speed planing are far more energy efficient and generate far lower wake energy than less efficient hull designs. Clearly, hull designs that minimize wake production are desirable from both an adverse impacts standpoint and an operational standpoint.

These findings have led to the following recommendations:

- 1) Ferry Operators
 - Assign the most efficient hulls to the most wake-sensitive areas.
 - Determine the most efficient operating range (speed and trim) for each vessel class and operate each vessel within this range as much as is practicable, with as little time as possible spent in the transition phase between the displacement and planing modes.
 - Ferry routing should be carefully evaluated, and modified to ensure minimal time spent in the transition phase while adjacent to or pointing toward wake-sensitive shoreline areas, and to avoid turning with a wake-sensitive area inside the turn. In general, a ferry should proceed from the dock to the center of the navigation channel at a speed well below transition (that is, well within displacement mode), then make its turn to proceed in an along-channel direction, rapidly accelerate to high-speed planing mode until adjacent to the next stop, decelerate to a speed well within displacement mode, then turn toward the dock.
 - We recommend against blanket speed restrictions, as such restrictions will very likely have the unintended effect of increasing the height of wakes produced by ferry vessels that are designed for efficient operation at high speeds.
- 2) Marina Operators
 - Should be permitted to construct wave protection systems that can protect the dock areas from waves exceeding 20 inches in height and 4.25 seconds in period. An example of such a system is a full-depth timber wave screen.
 - Avoid reflective side banks to the degree possible.
 - Optimize entrance channel design to avoid direct exposure to wakes produced by passing vessels.
- 3) Regulatory Authorities
 - Examine permitting requirements that prohibit the installation of effective wave protection systems along marina and other wake-sensitive shoreline areas.
- 4) General Public
 - As the revitalization of waterways and shorelines continues, and as more people take to the water in vessels of all sizes and types, there will be an increasing need to educate the boating public about the rules of the road when operating a vessel in a commercial harbor. The production and widespread dissemination of Harbor maps that clearly delineate active navigation channels, loading and unloading areas, and ferry routes, would be an important first step in this regard, as would public outreach activities that would include the participation of commercial vessel operators in the Harbor.

A Boundary Element Method (BEM) for the Wave Making Resistance of Displacement Catamaran

Sayyad-Hamid Sadathosseini, Mohammad S. Seif

Sharif University of Technology, Mech. Eng. Dept., Tehran, Iran 11365-9567, seif@sharif.edu

Abstract

A boundary element method based on the Green function method approach is presented for the steady, free-surface flow simulations around catamarans. Results for a Wigley hull agree well with published data. The simulation code is used for parameter studies investigating the influence of speed on wave patterns. The code is suitable for hull form optimizations with respect to wave making resistance.

1. Introduction

Waves created by ships cause an important drag component, namely the wave resistance. Several methods are used to compute wave resistance. Due to the complicated hull forms and intricate boundary conditions, analytical methods are not applicable. As wave resistance can be influenced often by moderate design modifications, we like to investigate it already early in design before more expensive and time-consuming model tests are performed.

Modern computer technology enables simulations of free surface flows around a realistic ship hull and greatly improves the accuracy of the predictions of linear ship motions. With the schemes of finite difference, finite element, and boundary element as the choice for the numerical algorithm, the boundary element method has been established as a popular approach for free surface wave computations due to its efficiency, accuracy and flexibility. Potential flow based panel method are based on Green's theorem which relates properties of flows within a domain to the domain boundary conditions. *Hess and Smith (1962)* pioneered panel methods for the numerical simulation of potential flows for bodies of general shapes. There are two main approaches towards the numerical solution of free surface flows:

1. Linearized free-surface wave Green Function as elements are distributed on the submerged hull surface, being superposed to a uniform base flow. The approach is particularly popular for time-harmonic (quasi-steady) simulation in seakeeping, e.g. *Liapis (1986)*, *King (1987)*, *Beck and Magee (1990)*, *Korsmeyer (1988)*, *Bingham (1994)*. While the Green function method (GFM) is elegant in enforcing free-surface conditions and radiation conditions (the linearized free-surface conditions are satisfied automatically and there is no need to discretize the free-surface domain), it is difficult to extend the scheme to nonlinear solutions, *Sclavounos (1988)*.
2. The Rankine Panel Method (RPM) approach for free-surface flows was first introduced by *Gadd (1976)* and *Dawson (1977)*, who employed the double body flow as the basis for linearization, chosen primarily through physical intuition. The free surface is discretized into (typically quadrilateral) panels and covered by the Rankine sources and dipoles. The RPM provides much flexibility for different kinds of free-surface formulations and numerical algorithms, and models both steady and unsteady wave flows, e.g. *Jensen et al. (1988)*, *King et al. (1988)*, *Nakos (1990)*, *Raven (1992)*. This approach is usually preferred for steady wave resistance computations in practice, *Bertram (2000)*.

Here we describe a GFM for the steady, free-surface potential-flow problem to calculate wave resistance and wave pattern of ships.

2. Governing equations

We can develop the boundary element method for the solution of Laplace's Equation ($\nabla^2\phi = 0$) in a three-dimensional domain Ω . We form an integral equation from the Laplace's Equation by using a weighted integral equation and then use the Green-Gauss theorem:

$$0 = \int_{\Omega} \nabla^2 \phi \cdot w d\Omega = \int_{\partial\Omega} \frac{\partial \phi}{\partial n} w d\Gamma - \int_{\Omega} \nabla \phi \cdot \nabla w d\Omega \quad (1)$$

ϕ is the velocity potential, w the weight function, Ω the boundary of the domain, n the normal direction on the boundary. To derive the starting equation for the boundary element method we use the Green-Gauss theorem again on the second integral. This gives:

$$\begin{aligned} 0 &= \int_{\partial\Omega} \frac{\partial \phi}{\partial n} w d\Gamma - \int_{\Omega} \nabla \phi \cdot \nabla w d\Omega \\ &= \int_{\partial\Omega} \frac{\partial \phi}{\partial n} w d\Gamma - \int_{\partial\Omega} \phi \frac{\partial w}{\partial n} d\Gamma + \int_{\Omega} \phi \nabla^2 w d\Omega \end{aligned} \quad (2)$$

For the boundary element method we choose w to be the fundamental solution of Laplace's Equation. The fundamental solution for Laplace's Equation is a solution of:

$$\nabla^2 w + \delta(\xi - x, \eta - y, \zeta - z) = 0 \quad (3)$$

(ξ, η, ζ) are the coordinates of a singularity point, (x, y, z) the coordinates of a field point, δ is the Dirac-Delta function.

We solve the above equation without reference to the original domain, the Green function G , or the original boundary conditions. In other words, the method is to try and find solution to $\nabla^2 w = 0$ in 3-d which contains a singularity at the point (ξ, η, ζ) . If w satisfies the linearized free surface conditions there is no need to discretize the free-surface domain. *Wehausen and Laitone (1962)* obtained the solution for linear free surface around ships. They introduced w as:

$$\begin{aligned} w &= \frac{1}{2\pi} G \\ G(x, y, z, \xi, \eta, \zeta) &= \frac{1}{r} - \frac{1}{r_1} \\ &- \frac{4}{\pi} K \int_0^{\pi/2} d\theta \sec^2 \theta \int_0^{\infty} dk \frac{\exp k(y+\eta)}{k - K \sec^2 \theta} \cos[k(x-\xi)\cos\theta] \cos[k(y-\eta)\sin\theta] \\ &- 4K \int_0^{\pi/2} d\theta \sec^2 \theta \exp[K(z+\zeta)\sec^2 \theta] \sin[K(x-\xi)\sec\theta] \cos[K(y-\eta)\sin\theta \sec^2 \theta] \end{aligned} \quad (4)$$

$$r = [(x-\xi)^2 + (y-\eta)^2 + (z+\zeta)^2]^{1/2}$$

$$r_1 = [(x-\xi)^2 + (y-\eta)^2 + (z-\zeta)^2]^{1/2}$$

K is the wave number, θ a direction on the free surface. Thus we get the boundary integral equation:

$$c(p)\phi(p) + \int_{\Gamma} \phi \frac{\partial w}{\partial n} d\Gamma = \int_{\Gamma} \frac{\partial \phi}{\partial n} w d\Gamma \quad (5)$$

$$c(p) = \begin{cases} 1 & p \in \Omega \\ \frac{1}{2} & p \in \Gamma \\ \frac{\alpha}{4\pi} & p \in \Gamma \end{cases} \quad (6)$$

If the point p happens to lie at a corner, the coefficient $c(p)$ is replaced by $\alpha/4p$ where α is the internal angle at point p .

Eq.(6) involves only the surface distributions of Φ and $\partial\Phi/\partial n$ and the value of Φ at a point p . Once the surface distributions of Φ and $\partial\Phi/\partial n$ are known, the value of Φ at any point p inside Ω can be found since all surface integrals in Eq.(6) are then known. The procedure is thus to use Eq.(6) to find the surface distributions of Φ and $\partial\Phi/\partial n$ and then (if required) use Eq.(6) to find the solution at any point $p \in \Omega$. Thus we solve for the boundary data first, and find the volume data as a separate step.

Since Eq.(6) only involves surface integrals, as opposed to volume integrals in a finite element formulation, the overall size of the problem has been reduced by one dimension (from volumes to surfaces). This can result in huge savings for problems with large volume to surface ratios (i.e., problems with large domains). Also the effort required to produce a volume mesh of a complex three-dimensional object is far greater than that required to produce a mesh of the surface.

3. Geometry and Grid

The ship model employed in this study is the Wigley hull form. The Wigley parabolic hull is characterized by sharp edges at the bow, stern and keel. Its form is defined by:

$$\begin{aligned}
 |y| &= \frac{B}{2} \left(1 - \frac{4x^2}{L^2}\right) \left(1 - \frac{z^2}{T^2}\right) \\
 -\frac{L}{2} &< x < \frac{L}{2} \\
 -T &< z < 0 \\
 0 &< y < \frac{B}{2}
 \end{aligned}
 \tag{7}$$

In the (x,y,z) coordinates system with increasing values of x in the direction opposite to the ship's forward motion, z vertically upward, and the origin at the undisturbed level of the free surface. Here L is the length of the model, B is the beam at midship and T is the draft. For the selected form, the parametric values are $L/B = 10$ and $B/T=1.6$, Fig. 1.

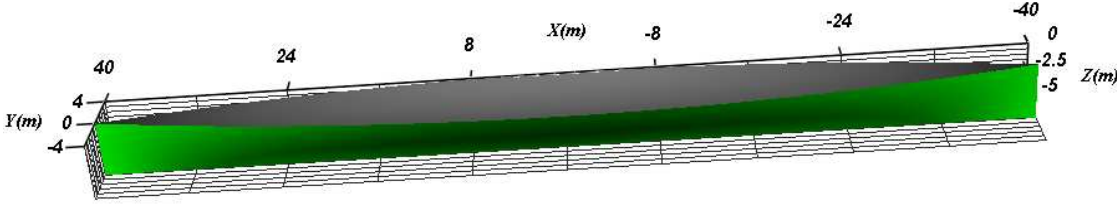


Fig.1: Wigley hull form

The numerical solutions use discretized geometry employing triangular elements in our method, Fig.2. Due to symmetric condition of hull form, only half body is modeled.

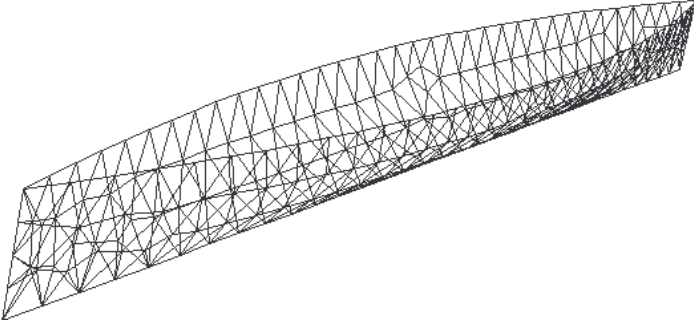


Fig.2: Triangular elements on hull form

4. Results

The solution algorithm outlined in the preceding sections has been applied to the prediction of wave making resistance coefficient at a short range of Froude numbers Fr . The wave drag was computed by integrating the pressure over the wetted surface. The results are obtained due to Froude numbers $0.2 \leq Fr \leq 0.4$. As in any numerical method, the first step for getting correct data is checking grid independency. Fig.3 shows the wave resistance coefficient due to element number on half body. Beyond 200 elements, results for wave resistance became grid independent.

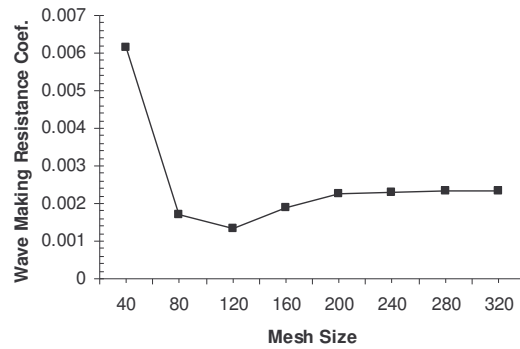


Fig.3: Grid Independency

Four Froude numbers are considered for modeling. Fig.4 compares computed wave profile for Wigley hull form with experimental data at $Fr=0.25$. The wave length of computed and experimental wave profiles agree fairly well, but the linearized free-surface condition causes a considerable error near the bow. The Kelvin wave angle coincides well with the theoretically expected value, Fig.5.

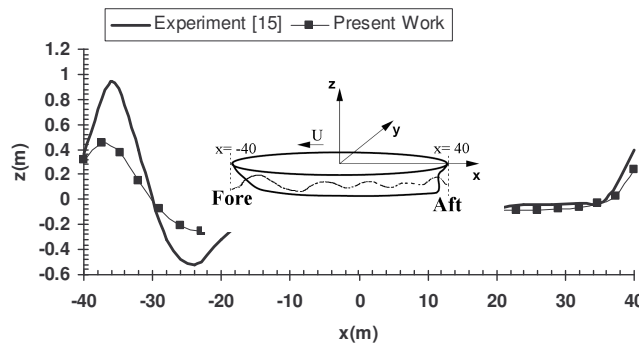


Fig.4: Computed and experimental wave profile at $Fr=0.25$

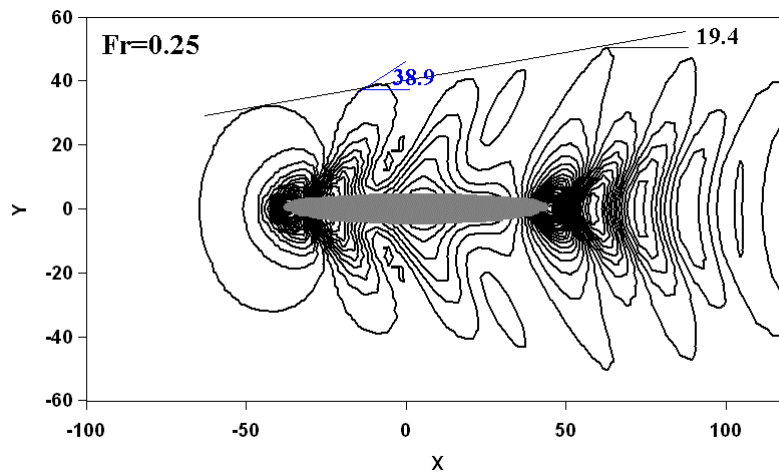


Fig.5: Wave pattern at $Fr=0.25$

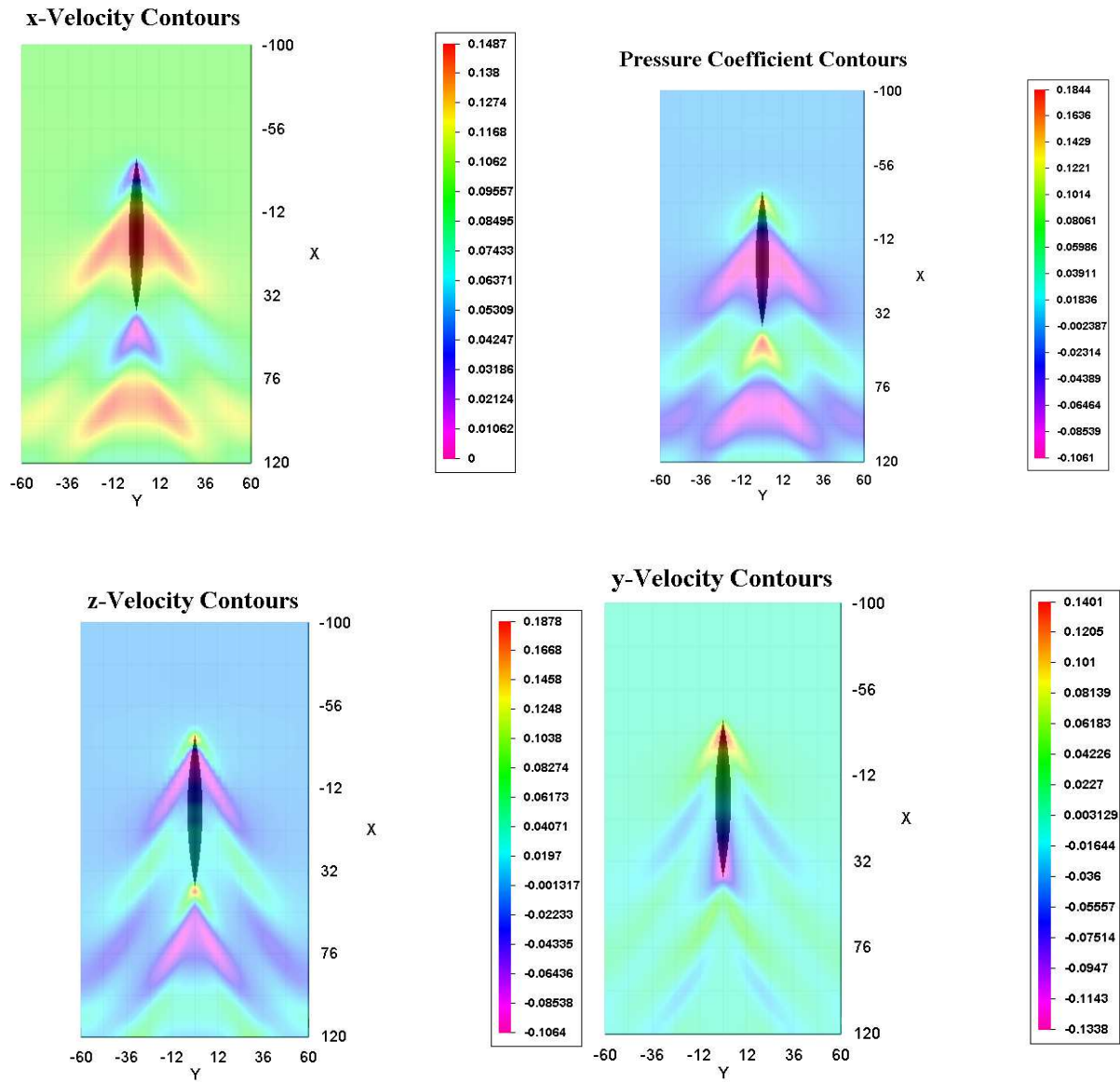


Fig.6: Contours of pressure coefficient and component of velocity

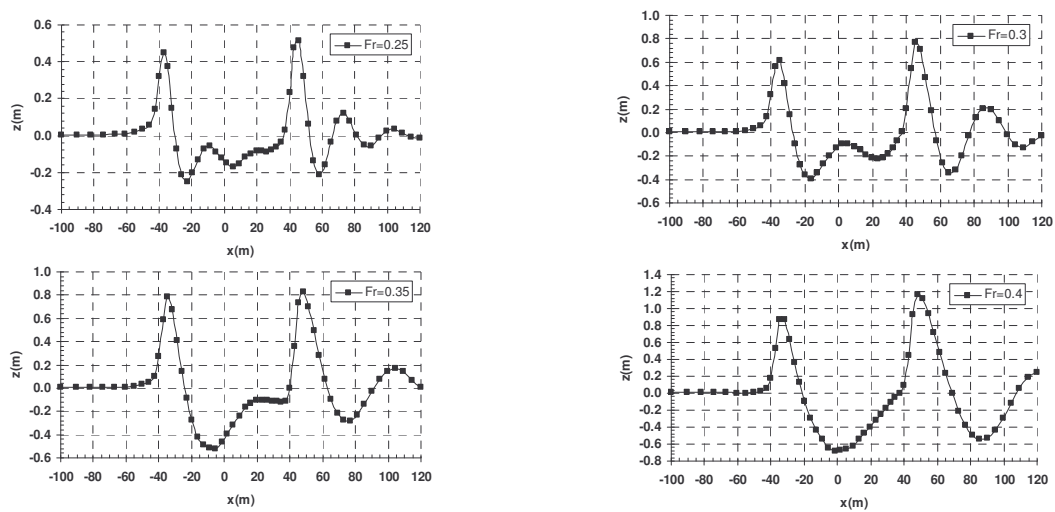


Fig.7: Wave profile on centerline

Fig.6 shows contours of pressure coefficient and components of velocity on the free surface at $Fr=0.4$. Fig.7 shows the calculated free surface elevations along the centerline of the domain, showing the effect of a variation in Froude number. The bow (or front) of the hull is located at $x=-40$ and the stern (or rear) is located at $x=40$. As shown, the Froude number has a strong effect on the wave profile. Fig.8 compares computed and measured wave drag coefficients which agree fairly well.

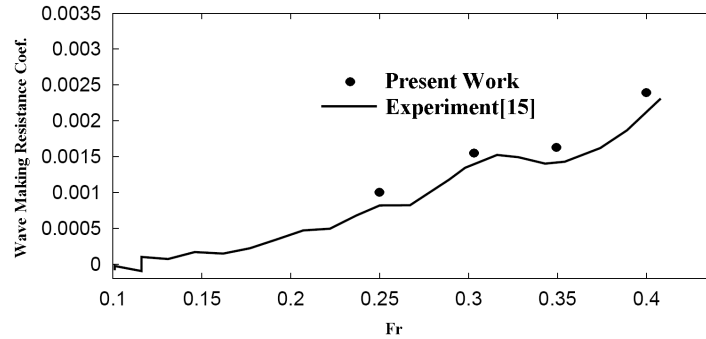


Fig.8: Wave making resistance coefficient

Fig.9 shows the grid for the catamaran hull form, in which $s=0.35L$ is the distance between the centerlines of the demihulls. Again, only one demihull is modeled in the computations exploiting symmetry. Fig.10 shows contours of pressure coefficient and free surface elevation at $Fr=0.25$ for catamaran hull form. Fig.11 shows a comparison between computed wave profile on the body of monohull and catamaran at $Fr=0.25$. The great difference in wave profiles suggests a strong interaction between the hulls of the catamaran.

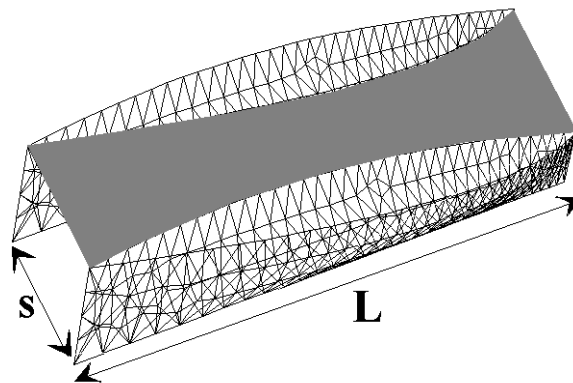


Fig.9: Catamaran Hull Form

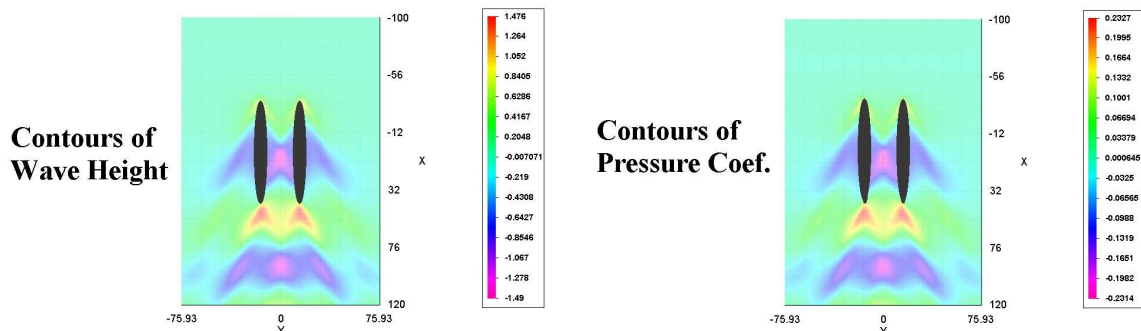


Fig.10: Contours of pressure coefficient and free surface elevation

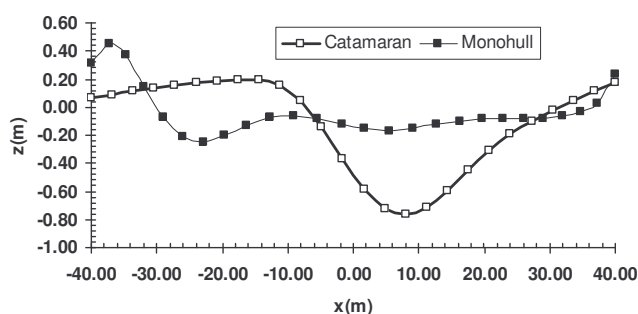


Fig.11: Wave profiles of monohull and catamaran

5. Conclusion

A Green Function Method for wave resistance computations has been applied to a Wigley monohull and a Wigley catamaran. The wave profiles and wave drag computed using this approach agree well with model test measurements for a range of low to medium Froude numbers. The wave angles are as those predicted by Kelvin's ship wave theory. The computer code is efficient and can be used to optimize wave resistance of catamaran or monohull hull forms.

References

- BECK, R.F.; MAGEE, A.R. (1990), *Time domain analysis for predicting ship motions*, IUTAM Symp. Dynamics of Marine Vehicles and Structures in Waves, London
- BINGHAM, H.B. (1994), *Simulating ship motions in the time domain*, Ph.D. thesis, MIT
- DAWSON, C.W. (1977), *A practical computer method for solving ship-wave problems*, 2nd Int. Conf. Numerical Ship Hydrodynamics, Berkeley
- GADD, G.E. (1976), *A method of computing the flow and surface wave pattern around full forms*, Trans. RINA
- HESS, J.L.; SMITH, A.M.O. (1962), *Calculation of non-lifting potential flow about arbitrary three-dimensional bodies*, Technical Report No. E.S. 40622, Douglas Aircraft Co., Inc., Long Beach, CA
- JENSEN, G.; BERTRAM, V.; SÖDING, H. (1988), *Ship wave resistance computations*, 5th Int. Conf. Numerical Ship Hydrodynamics, Hiroshima
- KING, B.W., (1987), *Time domain analysis of wave exciting forces on ships and bodies*, Technical Report 306, Dept. NAME, University of Michigan.
- KING, B.W.; BECK, R.F.; MAGEE, A.R. (1988), *Seakeeping calculations with forward speed using time domain analysis*, 17th Symp. Naval Hydrodynamics, The Hague
- KORSMEYER, F.T. (1988), *The first and second-order transient free surface wave radiation problems*, Ph.D. thesis, MIT
- LIAPIS, S.J. (1986), *Time domain analysis of ship motions*, Technical Report 302, Dept. NAME, University of Michigan
- NAKOS, D. E., (1990), *Ship wave patterns and motions by a three dimensional Rankine Panel Method*, Ph.D. thesis, MIT

RAVEN, H.C. (1992), *A practical nonlinear method for calculating ship wave making and wave resistance*, 19th Symp. Naval Hydrodynamics, Seoul

SCLAVOUNOS, P.D. (1988), *Radiation and diffraction of second-order surface waves by floating bodies*, J. Fluid Mech., Vol. 196, pp. 65-91.

WEHAUSEN, J.H.; LAITONE, E.H. (1962), *Surface Waves*, Handbuch der Physik 9, Springer

YANG, C.; LÖHNER, R.; NOBLESSE, F.; HUANG, T. (2000), *Calculation of Ship Sinkage and Trim Using Unstructured Grids*, European Congr. Comp. Methods in Applied Sciences and Eng., Barcelona

Corrosion and Damages on High Speed Craft

Karsten Fach, Germanischer Lloyd AG, Hamburg/ Germany, fa@gl-group.com

Abstract

Lightweight construction has always been of great significance in shipbuilding. The introduction of car carrying high speed craft in the early nineties lead to a worldwide revolution in short sea passenger transport and consequently an increased need for lightweight design . Although steel is employed in some types and sizes of HSC, aluminum has become the material of choice for most designs. The corrosion protection strategy applied to conventional ships does not apply to HSC for numerous reasons. Therefore special attention for both lightweight steel and aluminum structures are required to insure a long service life. The paper shall mark the often conflicting requirements involved in corrosion protection of HSC craft and offers solutions. Structural damages related to lightweight design will be described .

1. Introduction

One of the factors influencing the service life and reliability of marine structures exposed to seawater and sea atmosphere is corrosion. High corrosion rates of uncoated or improperly coated steel surfaces may significantly reduce the scantlings of structural elements, so that within a relatively short period the required minimum wall thickness is no longer present. Other materials such as stainless steels, aluminum alloys and copper or nickel alloys may also be attacked by marine corrosion under particular conditions. Extensive knowledge about the corrosion characteristics of the materials and service conditions of the structures is required to avoid deterioration.

Reducing the weight of ship structures increases the risk of under dimensioning with respect to possible failure modes. Classification Societies work together with designers and shipyards to realize the demand for lightweight structures in shipbuilding, especially for high speed craft. However, in any case sufficient strength has to be proven to withstand static and dynamic loads.

Lightweight construction has always been of great importance in shipbuilding. For high speed craft weight saving is absolutely essential. Reducing the weight of ship structures requires increased effort in the selection and application of sophisticated materials and manufacturing processes. For ship operation and survey activities it must be remembered that reducing the weight increases the risk of under dimensioning with respect to possible failure modes such as fatigue, buckling and corrosion. For high tensile steels or aluminum alloys applied for lightweight construction, it is important to realize that traditional strategies for design and survey should be adapted to the characteristics of the material in question.

Conventional ships like container ships and oil tankers are normally designed for a lifetime of about 30 years. Safe ship operation with regard to classification societies requirements can be achieved through out the life of the ship by applying a complex set of measures. These measures are based on the material properties, careful engineering and fabrication technology. Additionally, such measures must be combined with periodic surveys which take into consideration ship type, age, structural condition etc. In this context the corrosion allowance presents a significant gain in the safety margin of the structural design.

High speed craft typically operate in considerably different conditions compared to conventional vessels. Hull, machinery and equipment are highly loaded and tight operating schedules give limited opportunity for maintenance. The planned operating life of high speed craft (HSC) is usually much shorter than for conventional ships. In addition, the operating profile is more often changed to meet changing market conditions. This may result in more intense operation and a shorter operational

lifetime. Additionally HSC are build to special classification rules (Germanischer Lloyd) which take into account the needs and demands for reliable construction and safe ship operation.

As defined in the SOLAS regulations a High Speed Craft (HSC) is a craft capable of a speed equal to or exceeding $3.7 V^{0.1667}$ (m/s). As an example Fig. 1 shows the typical construction of an HSC with a cruising speed in excess of 40 knots. Reduction in light-ship weight can be achieved by optimization of the scantlings, by innovative design and by the use of higher strength to weight ratio structural steels, aluminum alloys or composite materials (fiber-reinforced plastics, FRP). In the endeavor to obtain structures of increasingly lighter weights adequate strength must, of course, be ensured with respect to possible failure modes. Optimized scantlings are obtained using highly sophisticated design and analysis tools. The corrosion allowances normally applied to conventional ships are not used for HSC due to weight constraints. Therefore the margin of structural safety at delivery is considerably less than that for conventional vessels (Engel/Holland, Fach/Rothe).



Fig. 1: Light Weight Structure

2. Metallic Materials

Ordinary and higher-tensile steels (HTS), materials traditionally employed in shipbuilding, are also frequently used in present-day lightweight structures. For seagoing ships of approx. 150 m in length and over, higher-tensile hull structural steels with minimum yield strength of up to 390 N/mm^2 are employed. This permits the amount of required material to be considerably reduced and also avoids forming and welding problems associated with excessive plate thickness. HTS is generally applied only in larger high speed craft where the minimum thickness criteria for steel is at least 4mm.

Aluminium alloys are currently the most commonly employed materials for high speed craft. All aluminium vessels of over 100 meters in length with cruising speeds of over 40 knots are becoming common. In shipbuilding, aluminium alloys of the 5000 series (AlMg alloys) and the 6000 series (AlMgSi alloys) are employed both for ships' hulls and superstructures. These aluminium alloys are characterized by good weld ability and corrosion resistance. For superstructures such as the wet decks of catamarans coatings and/or cathodic protection are not necessarily required. However if aluminium alloys are in direct contact or immersed in seawater for a prolonged period, corrosion protection measures are absolutely necessary to avoid critical corrosion attack. The so-called fully seawater resistant aluminium alloys which are often mentioned have yet to be developed

When employing higher-tensile steel and aluminum alloys in lightweight ship construction, special attention must be paid to the particular characteristics of these materials regarding fatigue strength, buckling and corrosion behavior(Engel/ Holland, Fach/Rothe).

3. Corrosion behaviour

3.1 High Tensile Steel

Unprotected carbon steels such as high tensile steels in direct contact with seawater are normally attacked by uniform corrosion. No significant difference in corrosion rates can be observed between mild and high tensile steels. Under the worst conditions corrosion rates of 1.5 to 2 mm/year may be assumed. Since such corrosion can ultimately result in a reduction of the structural strength or induce leakage in watertight boundaries, organizations like IMO and classification societies have introduced measures to deal with this problem. Regulations and rules have been adopted providing suitable corrosion control systems such as protective coatings and/or cathodic protection. In addition surveys have been adjusted to account for structural deterioration due to corrosion. Fig.2 shows the relatively uniform corrosion of an uncoated steel ballast tank.

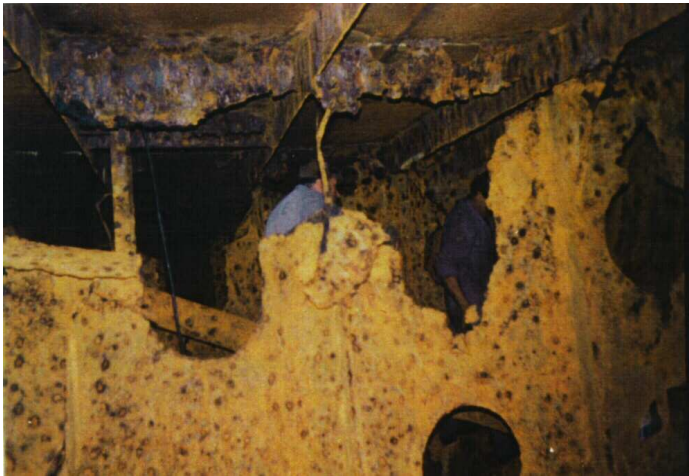


Fig. 2: Uniform Corrosion in a Ballast Tank

In the design phase structural scantlings are calculated under consideration of classification requirements. A corrosion allowance is required when following Germanischer Lloyd's Rules for Classification and Construction of Seagoing Ships. Plate thicknesses up to 10 mm require a corrosion allowance of $t_k=1.5$ mm. For plate thickness above 10 mm, the corrosion allowance is determined by $t_k = 0.1 \times t' / k^2 + 0.5$ or a maximum of 3 mm. The t' is the thickness required to provide adequate strength. Introducing a corrosion allowance is equivalent to increasing the time frame available for safe ship operation.

Coated carbon steels behave much like passive materials such as stainless steels and aluminium alloys. The coating system or rather the passive layer is normally able to protect the material from uniform corrosion. When the passive layer is damaged and not recoated, localized corrosion will attack the base metal. Such attacks are characterized by being extremely localized and the penetration is deep in relation to the area attacked. Corrosion rates in such situations will depend on factors such as the size of the breakdown and the availability of oxygen. It can generally be assumed that significantly increased corrosion rates compared to uniform corrosion will result.

In such cases a corrosion allowance will not enhance longevity. Because it is impractical to apply a perfect coating without some defects and given the harsh environmental conditions and service which ships operate in, it is unlikely that local corrosion attack can be totally prevented. Therefore coated carbon steels submerged in seawater need additional measures to protect the material from localized corrosion. A cathodic protection system is able to provide suitable protection against pitting corrosion in cases where the coating has broken down. Briefly one method of cathodic protection is the use of

sacrificial anodes made of Zinc or aluminium alloys. Another method of protection is through an active impressed current system (Engel/ Holland).

3.2 Aluminum alloys

Aluminum is a reactive metal with a high affinity for oxygen. The corrosion of aluminum is dependent on the pH value of the immersing electrolyte. Since the pH value of seawater is close to neutral, the natural oxide film which forms on unprotected aluminum is normally stable. The exact chemical composition of the aluminum alloy and the related presence and absence of other elements which are used to produce the alloy also determines the way in which aluminum will suffer corrosion. The very limited copper content combined with magnesium of the 5000 and 6000 series alloys provides the good corrosion resistance in the marine environment. However, where no corrosion measures are taken aluminum alloys may be attacked by pitting corrosion when permanently immersed in seawater. The susceptibility to corrosion is mainly related to the time of exposure, the alloy's chemical composition and its grain structure.

According to the galvanic series in seawater zinc and aluminum are the least noble materials. This means aluminum alloys combined and in contact with other more noble materials such as carbon steel or stainless steels will suffer bimetallic corrosion. The corrosion which can be observed can be described usually as enhanced pitting or swallow pitting corrosion. This phenomenon is most visible in areas where stainless steels or copper alloys are present. Fig.3 shows the bimetallic corrosion of a waterjet flange welded to the transom of a HSC. The waterjet has a high percentage of stainless steel components.



Fig. 3 Bimetallic Corrosion of Aluminum

If aluminium alloys are utilized in a marine environment, special corrosion protection measures must be applied. Coatings applied to aluminium ships are frequently used for corrosion protection as well as for decorative purposes. Products such as epoxy polymer and epoxy glass flake coatings can be used to reduce the risk of pitting corrosion. These coatings can also be used to provide an electrically non-conductive surface. The application of coatings can also be used to achieve an electrical isolation between aluminum and, for example, stainless steels in order to avoid bimetallic corrosion. Of course the specified coating procedure must be closely observed. Usually surfaces on which epoxy coatings are applied must be blasted and the coating should be applied in two or possibly three coats to achieve a long-standing protection against bimetallic and pitting corrosion. If coatings are applied on aluminum it is important to realize that any coating failure will concentrate the corrosion on the exposed corrosion cell, leading to deeper and faster penetration of the pit. Therefore during

construction and maintenance considerable attention must be paid to the coating application. It is also essential that any mechanical damage to the coating during construction be repaired before launching.

Aluminum protected by coatings and immersed in seawater should always be combined with cathodic protection to avoid pitting corrosion where the coating has broken down. Cathodic protection by means of sacrificial anodes made from aluminum or zinc can be used. Additionally, bimetallic corrosion can be avoided with anodes. The protective potential applicable for AlMg and AlMgSi alloys has to be limited to $U_H = -0.55$ V versus the standard hydrogen electrode. Any shift in the protective potential may result in an altered pH- value leading to accelerated corrosion rates. If anodes are used to protect aluminum against bimetallic corrosion, for example in the presence of large stainless steel components, the design of cathodic protection must be thoroughly investigated.

Impressed current systems (ICS) have so far not been used for the corrosion protection of aluminium ship's hulls. As mentioned above the electrochemical potential necessary for the corrosion protection of aluminium has to be precisely adjusted. Traditionally designed impressed current systems with one or maximum two impressed anodes will not be able to achieve or adjust to an acceptable current distribution. Thus, unacceptable potentials may result in corrosion being accelerated by the ICS (Engel/Holland).

4. Corrosion protection strategies

4.1 Protection of Steel

All surfaces of high speed craft built of carbon steel should be protected against uniform corrosion. This includes high tensile steels and is applicable for all surfaces in direct contact to seawater and to sea atmosphere. The protective coatings employed are traditionally epoxy and polyurethane based. Surfaces immersed in seawater such as ballast tanks and the underwater hull are to be protected by coatings with a dry film thickness of at least 300 μm before antifouling. For these areas cathodic protection is additionally required to avoid corrosion in case of a coating break down. If coatings are combined with cathodic protection their compatibility must be checked. For ballast tanks sacrificial anodes (zinc or aluminum) can be used. Impressed current systems are not permitted in confined spaces such as ballast tanks due to the possible development of hydrogen gas. As with ballast tanks, the underwater hull should be protected by cathodic protection. Sacrificial anodes (zinc or aluminum) or an impressed current system may be utilized.

Insulated interior areas exposed to dry heat such as passenger spaces normally receive only shop primer. Areas susceptible to sweating should receive a protective coating in addition to the shop primer.

For newbuildings the corrosion protection specification has to be submitted to class for approval. The specification must contain information about the intended surface preparation before coating application, coating types (name and manufacturer), number of layers, film thickness, etc. Coatings used for immersed areas are to be type approved. The design and layout of cathodic protection measures must be specified to obtain approval. The specification of the cathodic protection system should follow the requirements given in GL's rules for classification. For surfaces immersed in seawater the application of the corrosion protection system has to be documented. Surface preparation as well as activities connected to coating application must be fixed in a protocol. If applicable, a functional test of the impressed current system has to be undertaken during sea trials (Engel/Holland).

4.2 Protection of Aluminum

4.2.1 Surfaces Exposed to the Atmosphere

Surfaces which are exposed to sea and interior atmospheres do not necessarily need corrosion protection by means of coating systems. The corrosion behavior of aluminum alloy employed on

HSC's has demonstrated no uniform corrosion. In some cases, local corrosion attack may be observed as an uneven appearance of the surface. However, the depth of the corrosion penetration is rather limited and the corrosion rates are slowed through the formation of an oxide layer. Current practice is to coat all visible surfaces above the waterline on HSC to improve the visual appearance for passengers. The coatings are usually well maintained thus avoiding local corrosion. Suitable coatings are generally epoxy or polyurethane based. A phosphate wash primer with a polyurethane top coat or similar makes a durable and very lightweight coating system for such areas.

If aluminum is used in combination with other materials in a sea atmosphere it is recommended that stainless steels such as 316 grades be used. Carbon steel should not be combined with aluminum (Engel/Holland).

4.2.2 Surfaces Immersed in Seawater

For the corrosion protection of aluminum surfaces immersed in seawater suitable coating systems combined with cathodic protection is required. The corrosion protection of ballast tanks on HSC's is not as critical as for conventional ships as these craft rarely use water ballast. Therefore the corrosion protection strategies should be focused on the protection of the underwater hull to avoid local and bimetallic corrosion.

The requirements applicable for HSC's using aluminum are basically similar to those for using steel. For coating systems on underwater surfaces of aluminum the dry film thickness required is 300 μm without antifouling. The coatings are to be type approved. As the coatings are required to be combined with cathodic protection, the coating must be compatible for the chosen cathodic protection system. Vinyl epoxies or similar are generally suitable for this type of service.

The corrosion protection specification must be submitted for approval to class for each newbuilding project. Information about the intended surface preparation, coating types (name and manufacturer), number of layers, film thickness, etc. must be provided. The application of the coating system has to be documented. The protocol must include the surface preparation, environmental conditions as well as complete activities connected with the coating application.

The cathodic protection of aluminum can be assured by using zinc or aluminum sacrificial anodes. Due to the risk of overprotection magnesium anodes should not be used. The anodes are generally flush mounted to the surface to avoid increased resistance. In the presence of stainless steel components such as waterjets a calculation of anode mass is required to avoid bimetallic corrosion. The calculation has to consider the exposed area of the stainless steel as well as water velocities, alloy characteristics, coating system, etc. The distribution and size of the anodes should be laid out for a protective potential of $U_H = -0.55 \text{ V}$. For the approval of cathodic protection measures the design and layout of the system has to be specified and approved.

The use of sacrificial anodes for waterjet propulsion systems is rather limited due to the very high water velocities and limited space for attaching anodes. Recently, impressed current protection systems have been used to protect aluminum against bimetallic corrosion for such systems. These areas are highly susceptible to bimetallic corrosion as the propulsion systems are normally manufactured from stainless steel. Such impressed current systems use a stable anode manufactured from an inert material coated with an active layer of platinum or metal oxide. The surfaces which are to be protected are connected to the negative supply while the positive supply is connected to the anode, thus forming an electrolytic cell. Potentially harmful corrosion is prevented by introducing a negative charge onto the aluminum surface thus returning the potential to nearly the passive potential.

The potential and current flow has to be adjusted by a control system using reference electrodes cells. This control system is similar to those for impressed current systems used to protect steel structures. It is absolutely essential that the correct potential be maintained to obtain sufficient protection on the one hand and avoid overprotection on the other hand. Any shift in the potential generated on the aluminum

surface may introduce areas of over- or under protection resulting in rapid corrosion attack. The protective potentials which have to be achieved to avoid bimetallic as well as pitting corrosion in the presence of highly divergent velocities were recently investigated. The final conclusions of this study are still outstanding. However, recent experience has improved our understanding of the mechanics involved and the future application of impressed current systems for propulsion units looks promising (Engel/Holland).

5. Structural damages

Due to the fact that lightweight structures, no matter whether of steel or aluminium are often dimensioned close to the yield strength and on the basis of exactly defined load cases, unforeseen events may cause local damages of partial hull structures.

A problem in connection with aluminium structures in shipbuilding that could become critical is the failure under dynamic loads like pressure fluctuations in the waterjet inlet ducts. Beside The 1st harmonic cavitation will excite especially 2nd but also 3rd and 4th harmonics of the blade frequency which can lead to resonance responses in the hull structure. Such resonance can cause fatigue problems (Fach, Spiliotis, Ulken). Therefore the design of the waterjet area is more a stiffness than a strength problem.

Not only sea loads have to be considered but also loads due to vehicles acting on the deck structures and ramps may cause problems. In view of the high rates of utilization of present-day lightweight structures special regard has to be paid to fatigue strength in areas exposed to high dynamic loads. Fig.4 shows a stern ramp which fails due to overload.



Fig. 4 Stern Ramp Damage



Fig. 5 Optimized Construction Detail

Smooth transitions of transverse joints, soft brackets, single-bevel and/or double-bevel welds with full root penetration and well rounded free edges all improve the fatigue strength properties of highly stressed structures. For special structures analysis of structural details on the basis of finite element models is required to ensure adequate fatigue strength. Fig.5 shows the fatigue optimized connection of a stanchion supporting an extruded aluminum deck.

The design of intersecting structural members employing fillet welds and the welded connections of highly stressed transverse and longitudinal members must be considered with respect to fatigue.

Following the problems on buckling mentioned for lightweight steel structures, aluminium structures have carefully to be checked as well in the design and structural plan approval phase. Buckling of highly loaded longitudinal and transverse structures located at the fore end of high speed craft has been surveyed several times, especially on vessels sailing frequently in rough sea condition. Fig.6 shows buckling of a longitudinal bulkhead due to slamming events on the wet deck structure of a high speed catamaran operating at the Baltic Sea.



Fig. 6 Bulkhead Buckling

Many time collision of the vessel with harbour facilities happen. Due to the lightweight construction extensive repair work is required to restore the original shape. Traditionally built structures may have less damage on the other hand the higher weight of the conventional ship will result in a higher impact force. Fig.7 shows the damaged aft structure of an aluminium catamaran



Fig. 7 Damaged Hull of HSC Catamaran

Special consideration must also be given during the design phase to the vibration behaviour of lightweight structures. Because of the possibility of reduced scantlings with unchanged unsupported length achieved by use of increased strength materials for transverse and longitudinal girders or alternatively an increased girder length with unchanged scantlings, the natural frequency of these large "weak" structures can lie within the resonance range of low-frequency exciters, such as propellers. Vibration analyses of critical structures during the design phase are nowadays more or less a matter of routine and are increasingly performed, using the finite element method.

In this connection the noise behaviour of light-weight structures has also to be mentioned. The reduction of weight and stiffness often lead to uncomfortable noise levels which is well known on HSC. Additional stiffeners and material at the main engine foundation can reduce the noise level considerable. The additional weight for this matter is often less than the weight for insulation necessary for comparable noise reduction. A noise prediction performed by a competent partner can optimise the noise behaviour of light-weight structures.

More and more windows on HSC and passenger ships were glued to the superstructure to reduce the weight of the construction. Up to now the experience with this procedure is positive. It is important to use trained staff for this work, failures in the working procedure cause significant loss of the strength of the connection. It has to be noted that glued windows are only allowed in areas which are not affected by International Load Line (Fach/Rothe).

6. Damage Statistics

GL's statistic about structural damages on HSC since 1996 of ships operating in the Skagerak, Baltic Sea, North Sea, Irish Sea, Mediterranean Sea, Red Sea, Indonesia, North and South America, Polynesia etc. shows about 40% of the reported damages are caused by collision(70%) or grounding (30%). Most of these accidents happen during harbour manoeuvring (collision with harbour facilities). About 20% of the damages are caused by unexpected loads during operation. About 15% are reported as overload, operating above the design limits. Another 15% are caused by bad workmanship or material failures. At the end there are about 10% which are reported as unknown reason. All of these damages were local and most of the repairs were done without longer interruption of operation.

8. Conclusion

In order to reduce weight and improve performance their structures often are dimensioned solely on the basis of strength regardless of the corrosion resistance of the material employed. A corrosion allowance is not usually considered. This imposes the demanding requirement for a highly reliable corrosion protection system as well as thorough inspection and supervision of the vessel and its protection system. Additionally, it is important for the owner and operator to realize that the increased safety margins due to a corrosion allowance are not present. Where local corrosion is discovered, immediate action to repair the damage and mediate the cause of the corrosion is imperative.

Lightweight structures are often dimensioned close to the yield strength and on the basis of exactly defined load cases. It is GL's experience that these damages were local and most of the repairs were done without longer interruption of operation.

Acknowledgement

Thanks to Daniel Engel (GL), John Holland (GL) and Falk Rothe (GL) who mainly supported the content of this paper.

References

FACH, K.; ROTHE, F. (2000), *High Speed Craft- Applications and Damages*, High-Speed Vessels 2000 & Beyond, Victoria

ENGEL, D.; HOLLAND (2001), *Corrosion Protection Strategies for High Speed Craft*, SNAME

FACH, K.; SPILLOTIS, G.; ULKEN (1999), *Fast Ship Construction – Special Challenge for Class Surveyors*, HIPER 1999, Zevenwacht

Seakeeping Analysis of a Trimaran Fast Ferry

Dario Boote, Tommaso Colaianni, University of Genova/Italy, boote@dinav.unige.it
Enrico Pino, CETENA, The Italian Ship Research Centre, Genova, Italy

Abstract

In the context of a concept design of a trimaran fast ferry developed together by the University of Ancona, Genova, Naples and Trieste, a procedure for the determination of global design loads by a seakeeping long term analysis has been studied. In this paper seakeeping calculations, carried out by a 3D panel method, have been performed on two hull geometries of two different loading conditions corresponding to the maximum hogging and sagging bending moments.

1. Introduction

The market of passenger fast ships for Mediterranean Sea can be classified in two main fields: the longer routes, for which the new large passenger vessels and ferries are commonly utilized, and the short and/or medium range lines for which medium and small size fast ferries are most suitable, carrying up to about 800 passenger and 250 cars, displacement in the range of 800 - 2000 tons, length between 70 and 120 m, service speed of 35-55 knots. A great interest exists on medium range lines where the tourist traffic is increasing every year. For this kind of activity classic monohulls, hydrofoils, catamarans and SWATH have been studied and compared each other. Recently a new typology, the trimaran, gained a certain interest among owners and designers. Recent studies and comparisons, Ackers et al; (1997); Benvenuto et al. (2001); Porta (2003) demonstrate that the trimaran could offer some advantages if compared to existing deep-V monohulls and catamarans of the same size, such as better seakeeping performances in short seas, lower specific resistance and larger initial transverse stability especially with respect to monohull fast ferries.

A concept design of a trimaran fast ferry, Table I, was developed by DINAV within a joint research project together with the Italian Universities of Ancona, Napoli and Trieste. Further details relevant to the concept design solutions adopted can be found in Boote and Colaianni (2002). In the first phase of the project, attention has been particularly devoted to the definition of the main hull and outrigger geometry. The most recent developments on this matter can be found in Cardo (2003).

As far as structural aspects are concerned, much information are available from Dubrovsky and Lyakhovitsky (2001), Brizzolara and Rizzuto (2001), Coppola et al. (2002), Kohlmoos et al. (2003). The structural design, almost in the preliminary phase, has been faced making reference to the High Speed Craft Codes (HSC), together with additional prescriptions of Classification Societies. Nevertheless, as trimaran ships are not explicitly considered in the rules, in a second phase, a verification of the obtained structure geometry has been performed by using a finite element model of the ship loaded by a parametric quasi-static sinusoidal wave. Once the most important parameters of the hull geometry and strength have been defined, a more refined load investigation has been carried out by a three-dimensional seakeeping analysis based on panel methods. In this paper attention has been focused on the values of hogging and sagging long term vertical bending moment obtained from two different calculation procedures.

2. Preliminary Structural Design

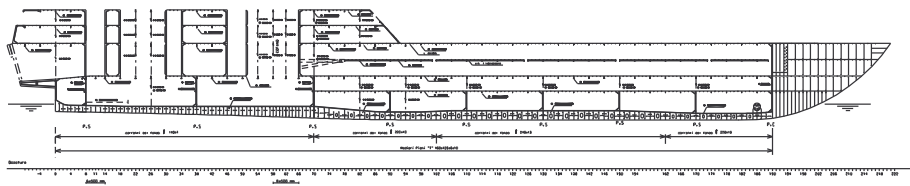
The structure of the trimaran, Fig.1, consists of a mixed longitudinal and transversal stiffening with 2400 mm spacing between reinforced frames and 600 mm spacing between ordinary ones. Starting from this geometry a complete numerical model of the vessel has been created by using the Maestro FEM code (Hughes, 1995) in order to better evaluate the behavior of the whole structure accounting simultaneously for hull girders and local stresses on structural elements, Fig.2. A series of calculation have been performed loading the model with a quasi static parametric wave ranged as follows:

- Wave length: 50%, 100% and 150% of ship length;
- Wave height: 2%, 3%, 4% and 5% of wave length;
- Headings: 0° to 180° step 15°.

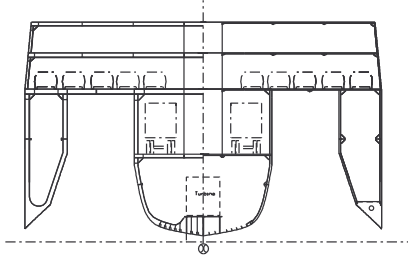
Table I: Trimaran fast ferry main design characteristics

					
Length bet. Perpendiculars	L_{pp}	120.0 m	Service speed	V	40 knots
Maximum total breadth	B	28.0 m	Side hulls displacement		abt 5%
Depth to main deck	D	12.0 m	Main hull geometry		L/B>10
Full load draft	T	3.0 m	Payload: 800 passengers and 240 cars		
Full load displacement	Δ_{PC}	2250 t	Propulsion: TAG 1 x 25 MW + Diesel 2 x 5.5 MW		

LONGITUDINAL SECTION

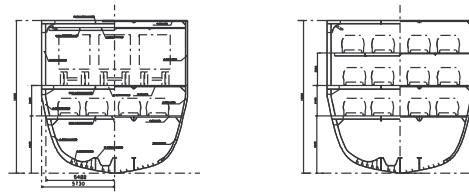


RE INFORCED FRAME ORDINARY FRAME



HOISTED CAR DECK

HOISTABLE CAR DECK LOWERED



UPPER GARAGE DECK

PASSENGER DECK

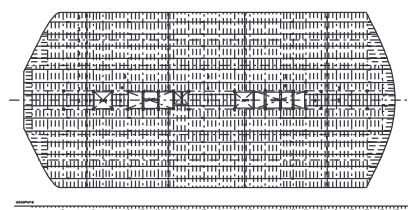
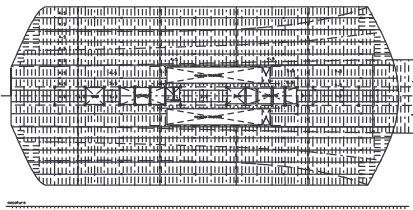


Fig.1: Longitudinal section, main section and cross decks structures

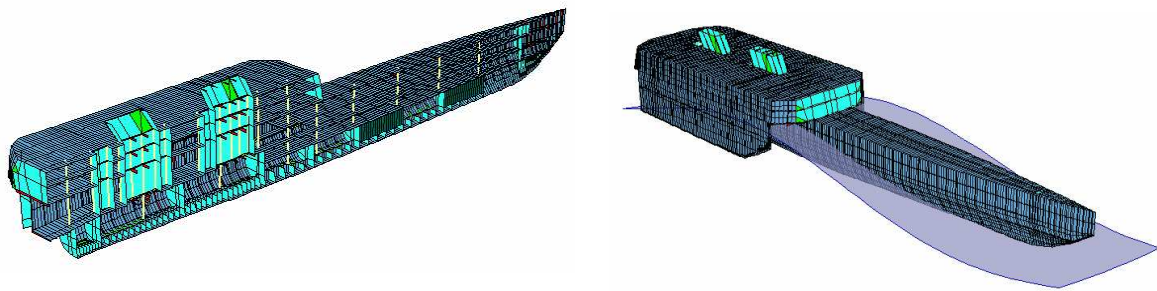


Fig. 2: Half ship numerical model made by Maestro FEM code and complete model on wave crest

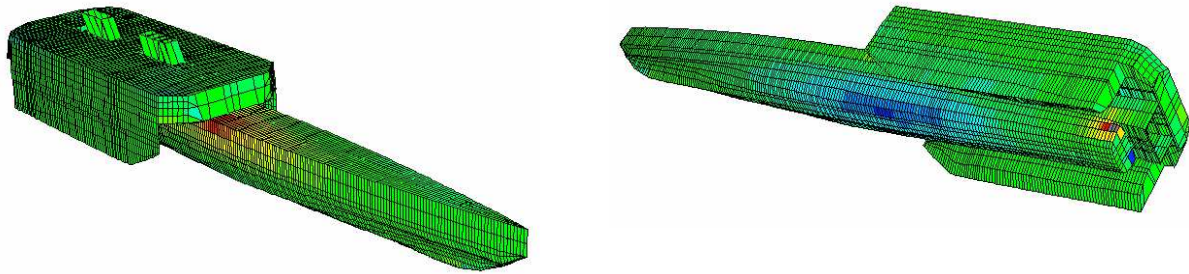


Fig. 3: Longitudinal stresses on the main hull

The performed investigation, Boote (2003a,b), showed the most critical aspect for trimaran structure is the longitudinal strength, particularly stressed by the high slenderness of the central hull, Fig.3. For this reason a more refined investigation on the longitudinal bending moment became necessary in order to establish the proper degree of safety for hull structures and, consequently, the minimum hull weight. With this objective in mind a long term analysis of wave loads has been planned.

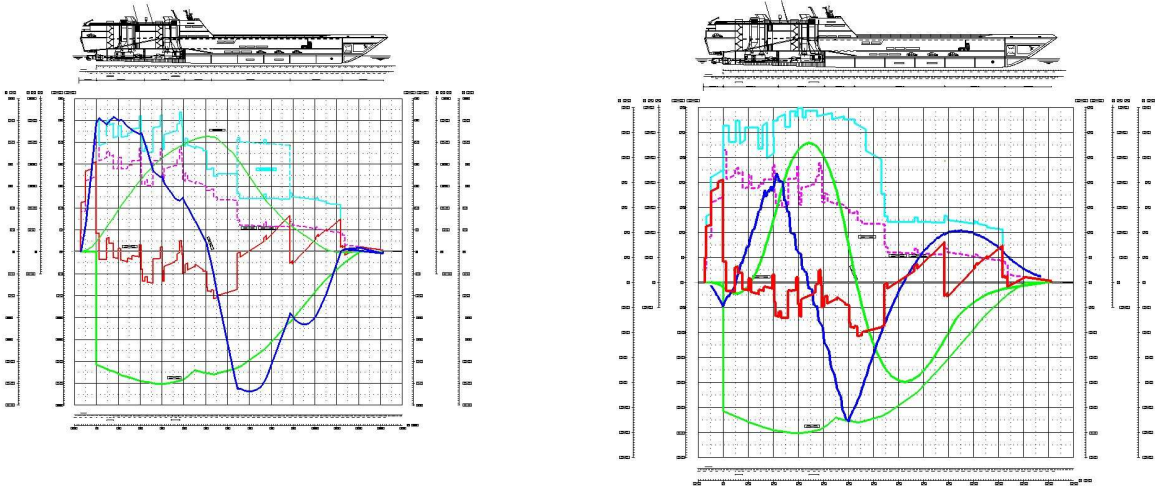
3. Seakeeping Calculations

A complete seakeeping analysis of the vessel was performed with particular attention to the vertical bending moment. Both short term and long term values were calculated; all the different sea states the ship is expected to encounter in its operative life were considered. In the context of a continuous scientific collaboration between the Department of Naval Architecture of the University of Genova and CETENA, the Fincantieri research center, it was decided to perform the seakeeping investigation utilizing the software available at CETENA hydrodynamic department. The ship response was determined with the 3-d seakeeping code PRECAL, Van't Veer (2003), developed within the international consortium CRS (Co-operative Research Ships) which CETENA is an active member of. PRECAL can deal with several typologies of displacement ships: conventional mono-hull, SWATH, catamaran, multi-hulls (trimaran/ pentamaran). For multi-hulls, it can provide the linear transfer functions of the longitudinal loads at transverse cuts (longitudinal force, vertical shear force, vertical bending moment, torsion moment) and of the transverse loads at longitudinal cuts (horizontal shear force, horizontal 'yaw splitting' bending moment, transverse torsion 'pitch connecting' moment, transverse 'prying' bending moment). The PRECAL results were post-processed using the Seakeeping Operability Analysis Program package (SOAP) developed by CETENA as a general statistical post-processor of linear frequency-domain seakeeping codes, Sebastiani and Caprino (1998).

3.1 Hull Geometry and Loading Condition

The wetted hull geometry can be described by a proper numerical mesh made of quadrilateral flat panels. Starting from the offset of the submerged body plan, a dedicated routine included in the software generates the mesh automatically. Boote et al. (2004) performed seakeeping calculations on the wetted body plan derived from the full load condition. In this case the ship experiences the highest hogging bending moment. Both short term and long term results were obtained from a unique hull

geometry. As a consequence the total long term values of hogging and sagging VBM are derived from the combination of still water hogging and sagging bending moments with a unique value of long term wave VBM relative to the hogging hull geometry. The aim of this work was to calculate the long term values of VBM considering two different hull geometries corresponding to the loading conditions producing the highest hogging and sagging VBM in still water. Besides the long term values of VBM it was considered interesting to investigate also on the differences between other typical seakeeping characteristics such as ship motion response amplitude operators and accelerations. The most severe hogging and sagging conditions in still water have been individuated with an iterative procedure by using the Maestro software. In fig.4 the main parameters of the two cases, named “a” (hogging) and “b” (sagging) conditions, are resumed.



	(a) hogging		(b) sagging
Displacement	2240 t	Displacement	2240 t
Fore draft	3.12 m	Fore draft	4.40 m
Aft draft	2.77 m	Aft draft	1.50 m
CoG from aft Pp	49.20 m	CoG from aft Pp	38.25 m

Fig.4: Still water longitudinal strength:

The resulting hydrodynamic meshes are shown in Figs.5 and 6. For the “a” condition the mesh consists of 400 panels for the central hull and 81 panels for the outrigger, with a total of 562 panels for the entire vessel. For the “b” condition the mesh consists of 650 panels for the central hull and 110 panels for the outrigger, with a total of 870 panels for the entire vessel.

3.2 Transfer Functions of Motions and Loads

Seakeeping calculations have been carried out for a wide range of speeds and heading angles:

- Speeds: 0, 5, 10, 15, 20 and 30 kn;
- Headings: 0° to 180° step 15°.

The response amplitude operators of vertical motions were plotted in order to evaluate their shape and to individuate the most severe headings. For heave response, as expected, the most severe values occur for 90° heading at low speeds. Fig.7 shows e.g. the heave RAOs at 20 knots speed over frequency and heading. At this speed, critical values appear at 120° heading. Fig.8 shows the heave RAOs for this condition for three speed values, 0, 10 and 20 knots. The trends are very similar for “a” and “b” conditions. There are the same peaks for the same frequencies; in general the “sagging” values seem to be lower the “hogging” values.

Figs.9 and 10 provide the same information for pitch. In this case the most severe heading corresponds to 150°. The differences between “a” and “b” conditions are not significant; there is the same trend in the two conditions and the numerical values are very similar as well.

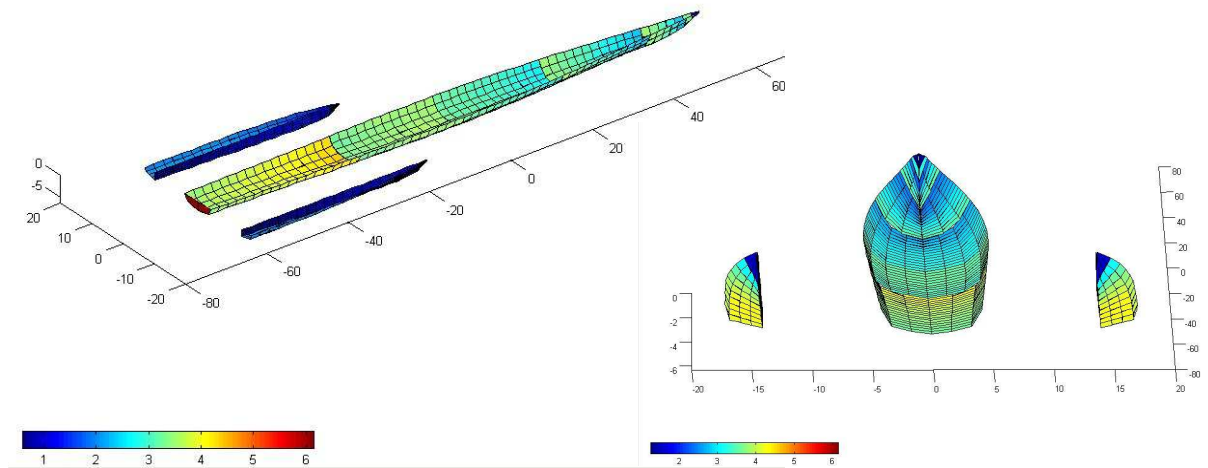


Fig. 5: Trimaran hydrodynamic mesh in hogging condition

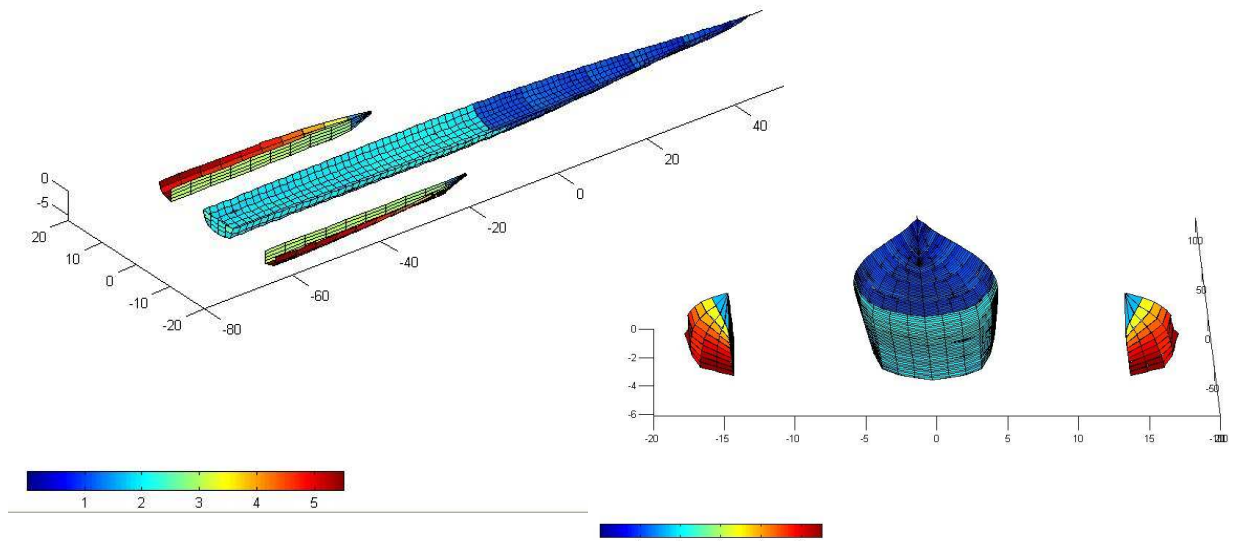
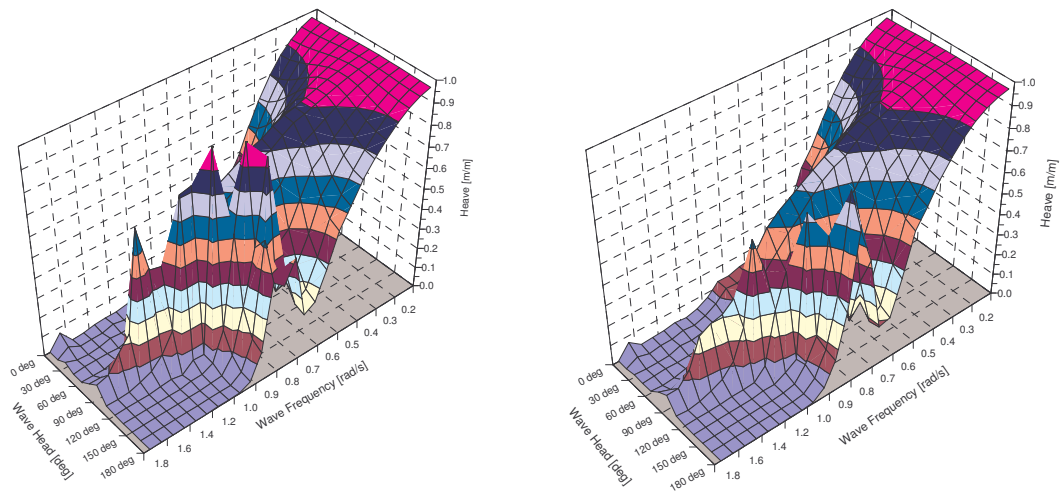


Fig. 6: Trimaran hydrodynamic mesh in sagging condition



(a) hogging

(b) sagging

Fig.7: 3D plot of heave RAO at 20 kn speed

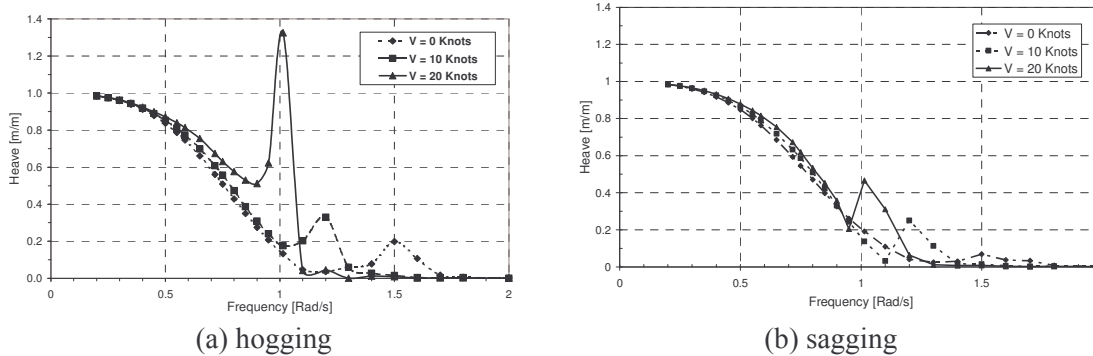


Fig.8: Heave RAO for 120° heading

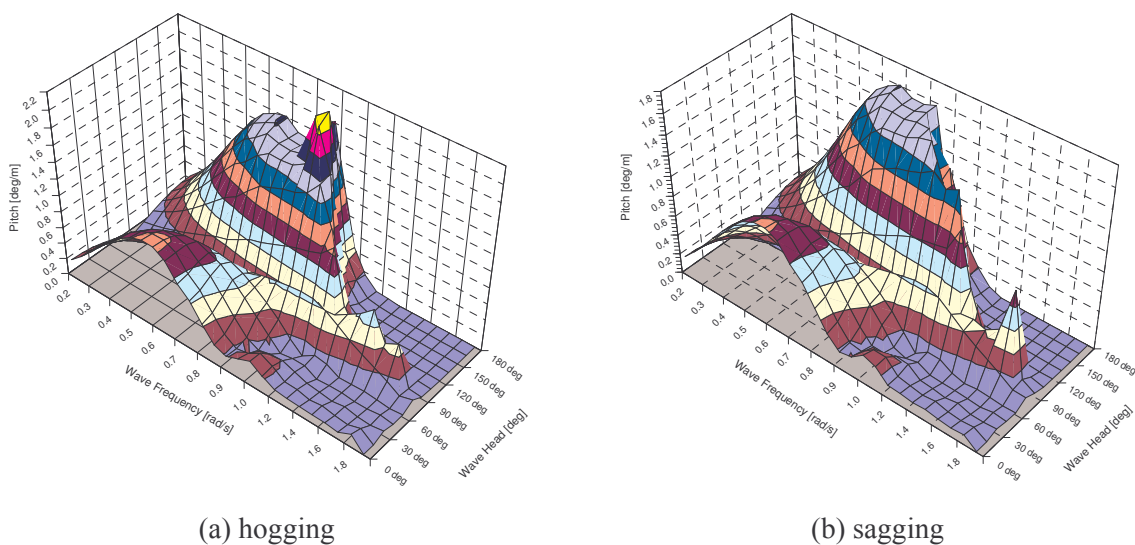


Fig. 9: 3-d plot of pitch RAO at 20 kn speed

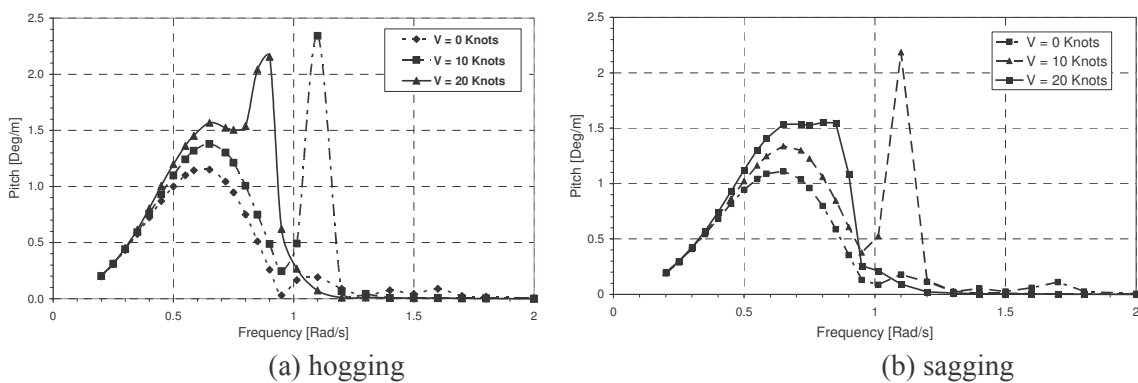
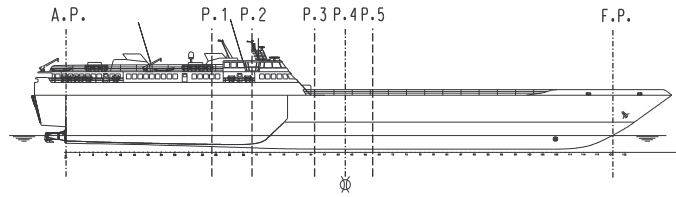


Fig. 10: Pitch RAO for 150° heading

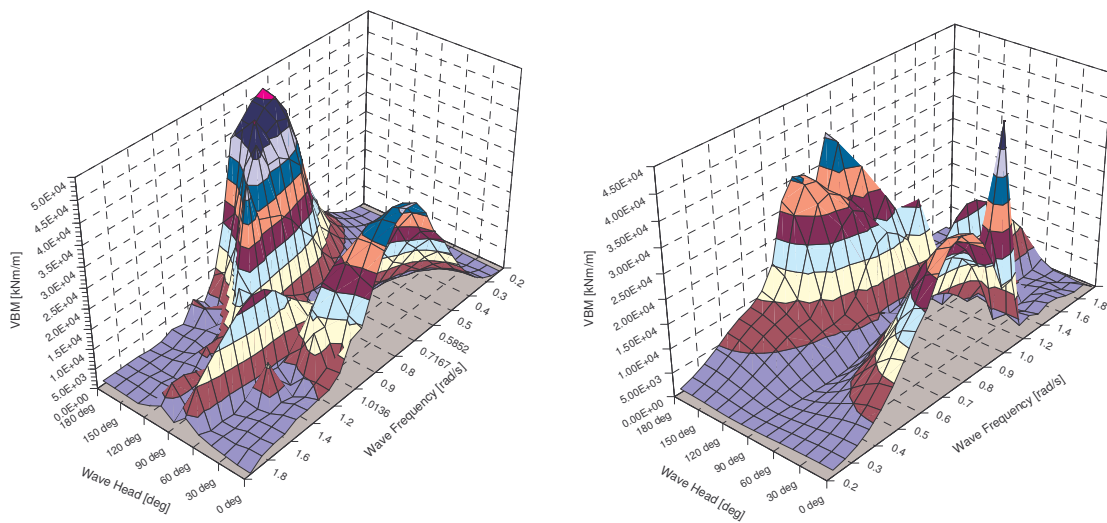
The wave vertical bending moment has been computed in five different stations close to the midship section in order to individuate maximum values. Fig.11 shows the calculation sections. Section 3 corresponds to the location where the maximum longitudinal bending moment has been individuated in the previous FEM analyses.

Also for wave VBM 3-d plots of RAOs were produced to better evaluate the trend as a function of speed and heading. In Fig.12 the 3-d RAO diagram of VBM at 0.445 L section and at 20 kn speed is shown as an example. As it is possible to see maximum values take place at 180° heading. In fig. 13 the vertical bending moment RAO for 180° heading is reported for 0, 10 and 20 kn speed. In this case the differences between “a” and “b” condition is quite significant and, in the case of 180° heading, it corresponds to about 30%.



VBM Calculation Stations		
STATION	Distance from Aft Perpendicular [m]	Percentage from Aft Perpendicular
1	32.10	0.261L
2	40.96	0.333L
3	54.74	0.445L
4	61.50	0.500L
5	67.53	0.549L

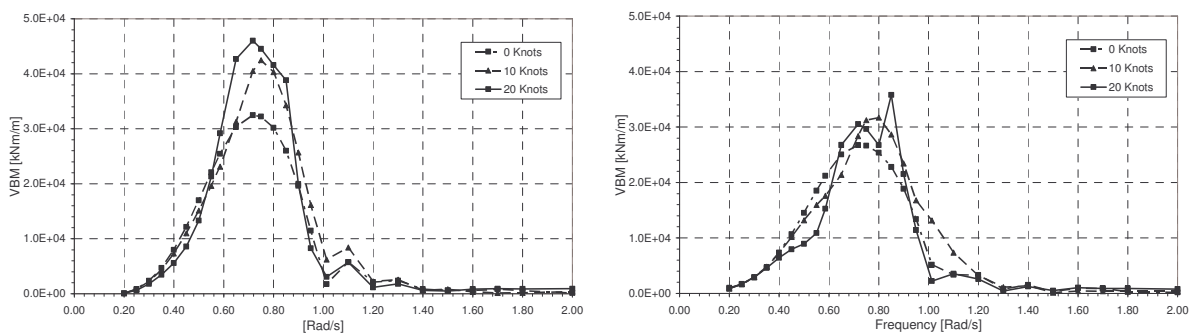
Fig.11: Calculation sections of vertical bending moment



(a) hogging

(b) sagging

Fig.12: 3-d plot of VBM RAO at 0.445 L at 20 kn



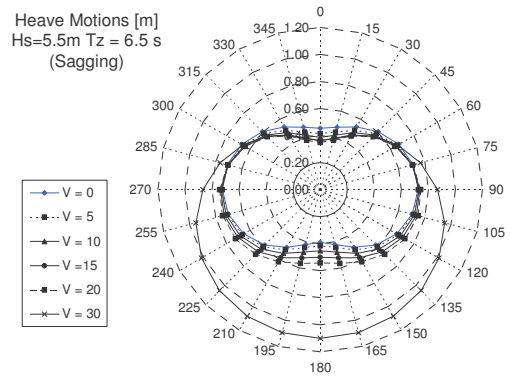
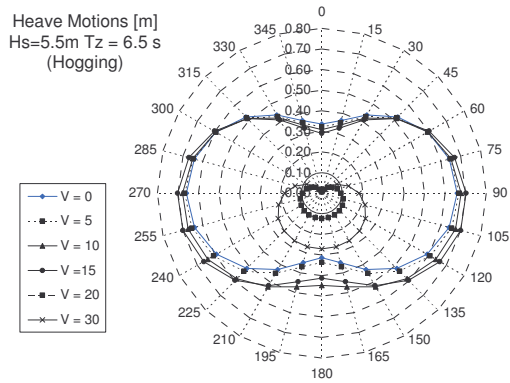
(a) hogging

(b) sagging

Fig.13: VBM RAO for head sea at 0.445 L

3.3 Short Term Statistics

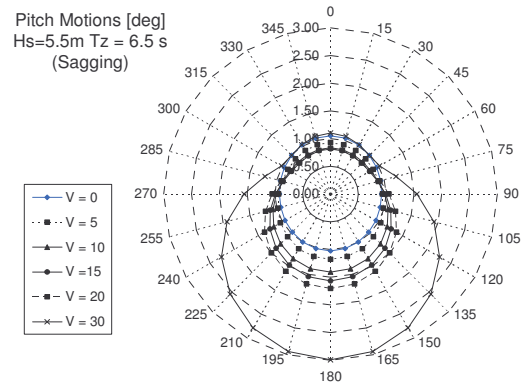
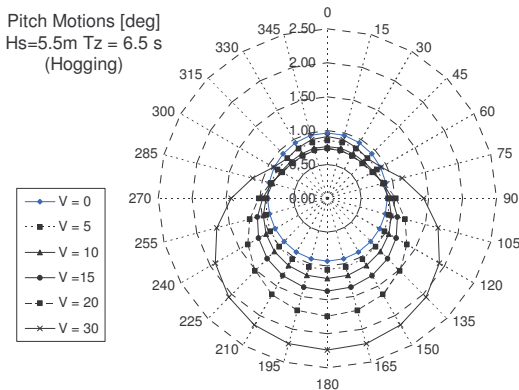
The short-term statistics refer to an interval of time spanning the typical duration of one sea state. It is customary to display the results of the short-term statistics in terms of polar diagrams representing the standard deviation of the relevant quantities versus relative wave heading at several speeds for each sea state. This allows the designer to have an overall assessment of the ship response and quickly identify the critical operational conditions in terms of unfavorable headings and combinations of ship speed and wave period.



(a) hogging

(b) sagging

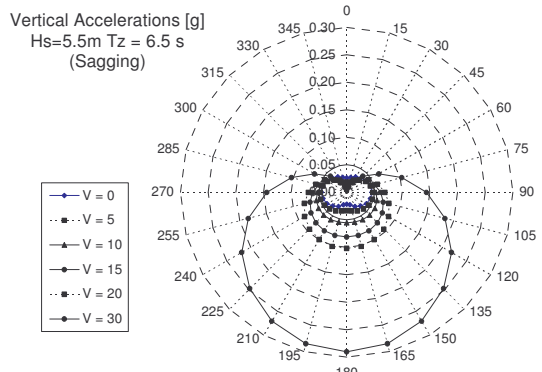
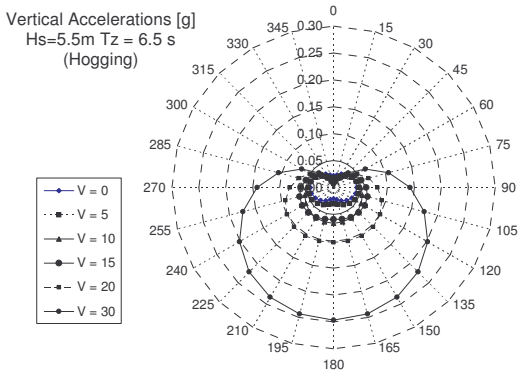
Fig.14: Polar diagrams of heave motions at CoG



(a) hogging

(b) sagging

Fig.15: Polar diagrams of pitch motions at CoG

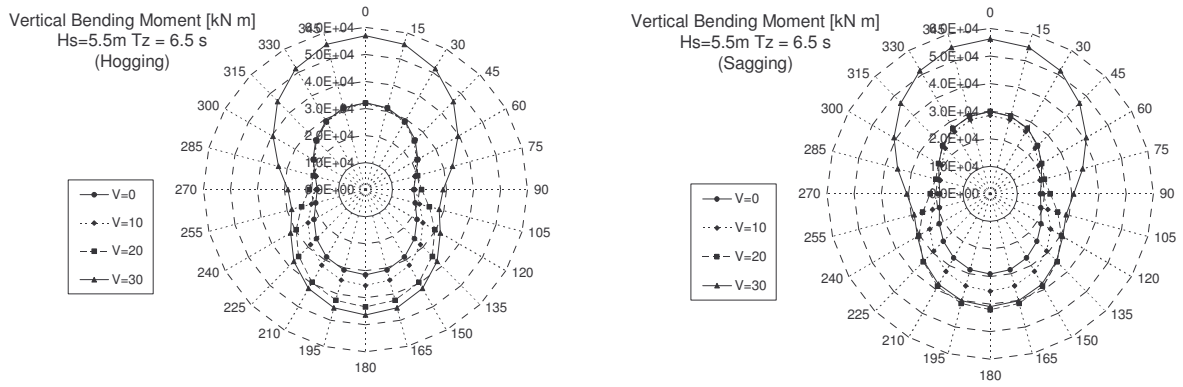


(a) hogging

(b) sagging

Fig.16: Polar diagrams of vertical acceleration at CoG

As an example, Figs.14-17 shows the polar plots of the standard deviations of heave and pitch motions, vertical acceleration and vertical bending moment for a representative sea state of $H_s = 5.5\text{m}$ and $T_z = 6.5\text{s}$. The spread of the wave direction by the cosine-squared function determines the shape of the curves in the polar diagrams; this is particularly evident for VBM values at 90° heading. Some differences exist between “a” and “b” conditions; for almost all ship responses, for 30 knots speed and head sea, the values of sagging condition are higher than those of hogging condition.



(a) hogging (b) sagging
Fig.17: Polar diagrams of vertical bending moment

3.4 Long Term Analysis

While short-term statistics refer to a specific sea state, long-term statistics must consider several sea states. The necessary information for distribution of sea states and regions is found in a wave atlas. Long-term calculations of the vertical bending moment were carried out for the following conditions:

- reference operative geographic area 26 GWS of Western Mediterranean Sea , Fig.18;
- no limitation on significant wave height: the full wave scatter diagram was considered;
- three-parameters JONSWAP spectrum;
- short-crested sea with a cosine-squared spreading function.
- speeds of 20 and 25 knots corresponding to 1/2 and 2/3 of the maximum value.

The analysis was carried out for a probability level of 10^{-8} , corresponding to 20 years of service.

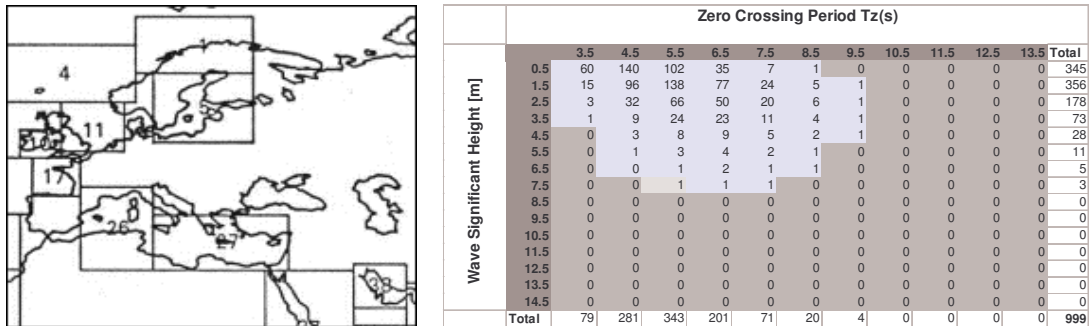
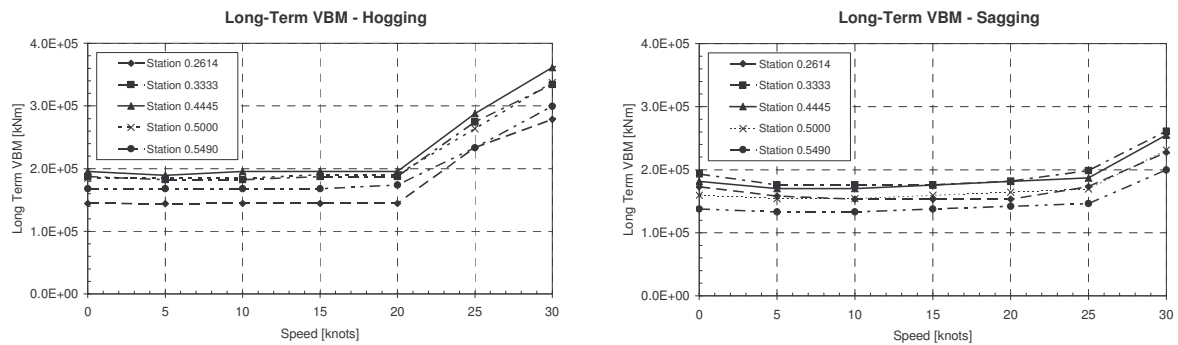


Fig. 18: Statistics of Mediterranean area n° 26 (BMT,1986)



(a) hogging (b) sagging
Fig. 19: Long-term wave VBM

The long-term wave VBM was calculated for all the considered sections, Fig.19. As expected, for “a” case, the highest value occurs in section n°3 (0.445 L from aft perpendicular) at the end of cross deck, in the same place where the maximum longitudinal stresses were detected in the FEM analysis. In “b” case the maximum values occur in section n°2 (0.333 L). The differences are significant especially for higher speeds. Making reference to section n°3, for 20 kn speed, the difference is 7% while, for 25 kn speed, the difference is 54%.

The final results are resumed in Table II. The first column of the table contains the hogging VBM values, the second column contains the sagging VBM calculated by using a unique hull geometry; in this case the total VBM is the sum of the wave long term VBM plus the still water sagging VBM. The third column reports the sagging VBM results obtained by two hull geometries; in this case the total sagging long term VBM is the sum of the long term sagging VBM plus the still water sagging VBM. The first rows of the table show the highest hogging and sagging VBM in still water together with the total bending moment determined by DNV and RINA HSC rules on the basis of the still water VBM. These last values are not to be considered as a reference because neither DNV nor RINA HSC codes make specifically reference to trimaran type configuration. The last row shows the hogging and sagging ultimate bending moment in correspondence of section at 0.445L, Boote (2003b).

Table II – Total bending moments in hogging and sagging conditions

	VBM Hogging [kN m]	VBM Sagging “a” (One hull geometry) [kN m]	VBM Sagging “b” (Two hull geometries) [kN m]
SWBM	0.427 E+5	0.305 E+5	
DNV	3.315 E+5	4.973 E+5	
RINA	2.021 E+5	2.150 E+5	
Long term wave VBM at 20 knots speed	1.9542 E+05		1.8133 E+05
Tot long term VBM at 20 knots speed	2.386 E+5	2.259 E+5	2.118 E+5
Long term wave VBM at 25 knots speed	2.880 E+05		1.870 E+05
Tot long term VBM at 25 knots speed	3.307 E+5	3.185 E+5	2.175 E+5
Ultimate bending moment at 0.444 L	3.73 E+5	2.36 E+5	

Table II shows significant differences between the total long-term sagging VBM computed using one or two hull geometries: 6% for 20 knots speed and 46% for 25 knots speed. For the “a” condition, the ultimate hull strength satisfies both hogging and sagging total long term VBM for 20 knots speed; for 25 knots speed the ultimate strength is 75% of the total sagging VBM. For the “b” condition is concerned the ultimate bending moment is higher than the total long term VBM both for 20 and 25 knots speed.

Even if neither DNV nor RINA HSC code make specifically reference to trimaran configurations, some considerations can be made on the comparison between the values provided by the two HSC codes and the long term VBM derived from direct calculations. In the case of 20 knots speed, the maximum bending moment provided by RINA is very close to the long-term values, both in hogging and sagging conditions. DNV values are higher by 38% in hogging and by 200% in sagging.

For 25 knots RINA code values are lower by 60% for hogging condition; in sagging, RINA is lower by 67% in “a” case, while it matches very well the “b” case. DNV matches the hogging condition and overestimates in sagging by 56% in “a” case and by 220% in “b” condition. In any case, the speed assumed in a long term analysis is very important: 20 or 25 knots, i.e. 1/2 or 2/3 of the operational speed. Having considered the full scatter diagram of area 26, a 20 knots speed seems to be more adequate for a vessel with such a mission profile.

3.5 Vertical Accelerations

The first scantling of trimaran structures was based on the rules of DNV HSC code, Boote (2003b). Keeping in mind that trimaran typology is quite outside the HSC standard, it should be said that the obtained results were not so far from an acceptable scantling, as highlighted by FEM structural analysis. In this respect some considerations can be very interesting regarding the value of the vertical accelerations suggested by the HSC rules and the value coming from seakeeping analysis. The leading criteria for load and force calculation in the DNV HSC Code (2003) is based on the vertical acceleration provided by the following relationship:

$$a_{cg} = \frac{V}{\sqrt{L}} \frac{3.2}{L^{0.76}} f_g g_0$$

where:

- f_g = acceleration factor (1 for car ferry unrestricted notation);
- g_0 = standard acceleration of gravity;

As in the case of the trimaran the value provided by the previous relationship with maximum speed (40 kn) is 0.318g, the assumed design value should be not less than 1.0 g, as stated by DNV rules.

The design acceleration a_v at different positions along the craft's length is provided by the following:

$$a_v = k_v a_{cg}$$

where k_v is given by the diagram in Fig.24.

To achieve a complete range of values, vertical accelerations have been calculated for a set of points distributed along the main hull and on the outriggers. The positions where vertical acceleration has been evaluated is schematically indicated in Fig.20.

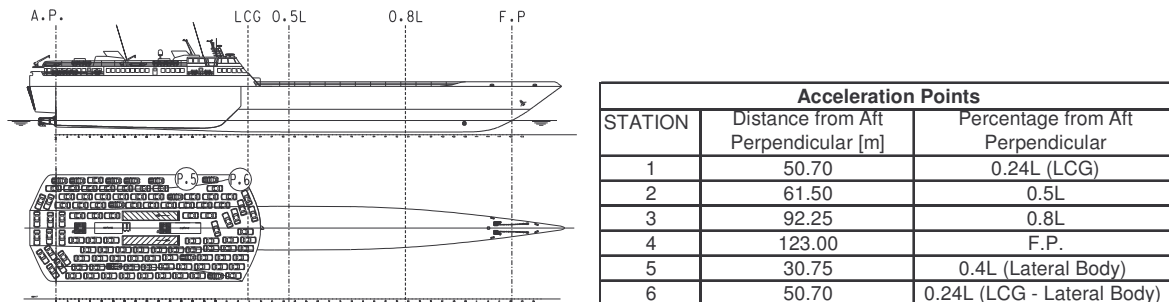


Fig. 20: Vertical acceleration calculation points

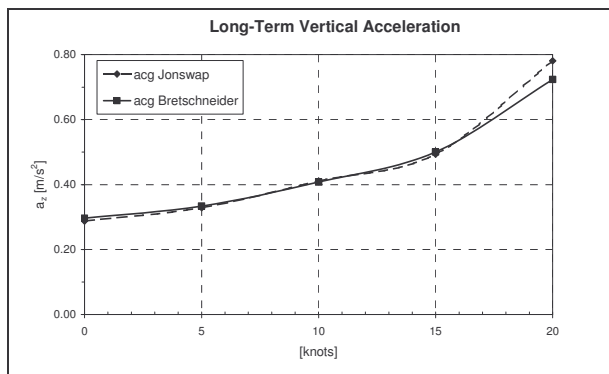


Fig. 21: Long term values of accelerations calculated with Jonswap and Bretschneider spectra

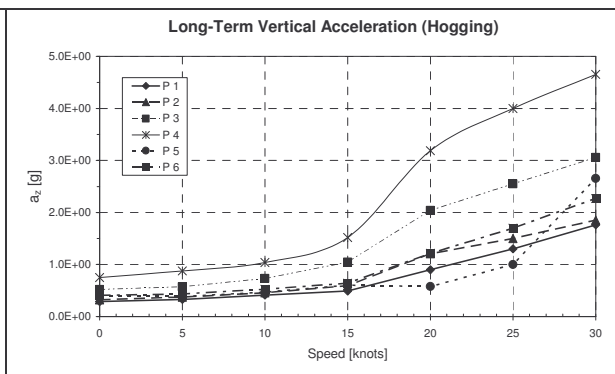


Fig. 22: Long term accelerations in all calculation points (case "a" hogging).

Long term calculations of vertical acceleration have been carried out by utilising both JONSWAP and Breitschneider sea spectra. An operative life of 20 years of the ship was assumed. The results, reported in diagram of Fig.21, show that JONSWAP spectrum gives a slightly higher value of design acceleration. In any case, it is quite close to 1 g which is the reference design value suggested by all

HSC codes. The long term vertical accelerations in the 6 points are reported in the diagram of fig. 22 for “a” condition. Besides the very high values in points n°3 and 4, the long-term acceleration values in correspondence of the centre of gravity; in the diagram of Fig. 23 the values for “a” and “b” conditions have been plotted together. Sagging values are slightly higher for 20 knots speed and quite similar for lower and higher speeds.

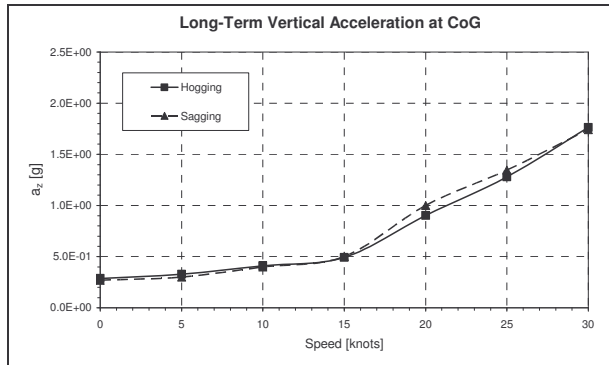


Fig.23: Long-term vertical accelerations at CoG for hogging and sagging conditions

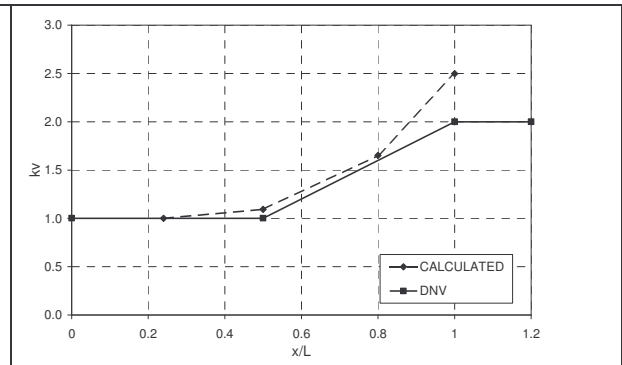


Fig.24: Longitudinal distribution factor for vertical design acceleration, DNV (2003)

From the acceleration values calculated in the points other than the centre of gravity, a “calculated” distribution factor “ k_v ”, relative to JONSWAP spectrum, was derived as shown in Fig.24 together with the DNV “ k_v ” factor.

4. Conclusions

In this paper the seakeeping calculations for the evaluation of all the most significant ship responses of a trimaran-type fast ferry has been presented. In particular, as HSC codes do not make reference specifically to trimaran-type vessels, a direct calculation of vertical bending moment load has been performed by a long term analysis based on a seakeeping panel code, in cooperation with CETENA. The long term bending moments in hogging and sagging conditions have been determined making reference to a unique wetted hull geometry and to two different wetted hull geometries. A wide range of seakeeping parameters have been considered: for what the speed value is concerned, attention has been focused on 20 and 25 knots, respectively equal to 1/2 or 2/3 of the operational speed. The results have been compared each other and with the total maximum vertical bending moments provided by RINA and DNV HSC codes.

The results show that a significant difference exists between the total long term sagging VBM computed using one or two hull geometries: 6% for 20 knots speed and 46% for 25 knots speed. Comparing these results with ultimate bending moment values it appears that:

- considering the “a” condition, the ultimate hull strength satisfies both hogging and sagging total VBM in the case of 20 knots speed; for 25 knots speed the ultimate strength is 75% of the total sagging VBM;
- for what the “b” condition is concerned the ultimate bending moment is higher than the total long term VBM both for 20 and 25 knots speed.

Despite a certain difference between HSC and seakeeping values of VBM, the scantling of the trimaran structures seems to be adequate and, as a consequence, the light weight requirements of this kind of unit partially satisfied. A further strengthening of deck longitudinal structures, however, is advisable and under course in the new version of the trimaran hull and cross deck structure.

Acknowledgements

The research work reported in this paper was partly carried out with the financial support provided by the Italian Ministry of Education, University and Scientific and Technological Research in a joint research project together with the University of Ancona, Napoli and Trieste.

References

- ACKERS, B.B.; MICHAEL, T.J.; TREDENNICK, O.W.; LANDEN, H.C.; MILLER, E.R.; SODOWSKY, J.P.; HADLER, J.B. (1997), *An investigation of the resistance characteristics of powered trimaran side-hull configuration*, SNAME Trans., Vol. 105, pp.349-373
- BENVENUTO, G.; BRIZZOLARA, S.; FIGARI, M.; PODENZANA, C. (2001), *Fast trimaran ships: some example of applications for commercial vessels*, 2nd HIPER Conf., Hamburg, pp.64-78
- BMT (1986), *Global Wave Statistics Atlas*, British Maritime Technology, Feltham, GB.
- BOOTE, D.; COLAIANNI, T. (2002), *Structural analysis of a trimaran fast ferry*, DINAV Report, Genova.
- BOOTE, D.; COLAIANNI, T.; RIZZO, C. (2003a), *Strength assessment of trimaran fast ferries*, NAV 2003 Conf., Palermo
- BOOTE, D.; COLAIANNI, T.; RIZZO, C. (2003b), *Structural analysis of a trimaran fast ferry*, FAST 2003, Naples
- BOOTE, D.; COLAIANNI, T.; PINO, E.; RIZZO, C. (2004), *A procedure for wave load assessment of fast trimaran ships*, PRADS 2004, Travemunde.
- BRIZZOLARA, S.; RIZZUTO, E. (2001), *Global loads for a trimaran ship*, FAST 2001
- CARDO, A.; FERRANDO, M.; PODENZANA-BONVINO, C. (2003), *Influence of hull shape on the resistance of a fast trimaran vessel*, FAST 2003, Naples
- COPPOLA, T.; MANDARINO, M.; SIMEONE, F. (2002), *A preliminary study for trimaran ship structural design*, 6th Symp. High Speed Marine Vehicle, Naples
- DNV (2003), *Rules for Classification of High Speed, Light Craft and Naval Surface Craft*, Hovik, Norway.
- DUBROVSKY, V.; LYAKHOVITSKY, A., (2001), *Multihull ships*, Backbone Publ., ISBN 0-9644311-2-2
- HUGHES, O. (1995), *Maestro User and Application Manuals*, Maryland USA.
- KOHLMOOS, A.; VIEJO, F.; PEREZ, A. (2003), *Prediction of global wave induced loads for structural analysis of IZAR high-speed pentamaran*, FAST 2003, Naples
- PORTA, F. (2003), *Il trasporto passeggeri con navi veloci: il caso di un mezzo innovativo*, Graduation Thesis, Univ. Genova
- RINA, (2002), *Rules for the classification of High Speed Craft*, Genova.
- SEBASTIANI, L.; CAPRINO, G. (1998), *Seakeeping Operability Analysis Program (SOAP)*, Report CETENA, Genova
- VAN'T VEER, R. (2003), *A new ship type for PRECAL V6.0: trimaran*, MARIN, Report No. 17926-4-CPS.

Classification Aspects of HSC Multihulls

Karsten Fach, Germanischer Lloyd AG, Hamburg/ Germany, fa@gl-group.com

Abstract

End of September, the biggest Trimaran ever build, the Fred Olsen line Trimaran (Fig. 1) is envisaged to be launched in Australia. Germanischer Lloyd (GL) is entrusted to classify this vessel. GL did hydrodynamic investigations for the Nigel Gee ADX Pentamaran and had the chance to compare these results with towing tank measurement. Also for the IZAR Pentamaran a hydrodynamic analysis was performed. From many points of view HSC Trimaran and Pentamaran are similar to monohulls and/or catamarans. This paper will give some ideas of the specialities of Pentamaran and Trimaran from classification point of view and will also inform about multihull navy activities .



Fig. 1: Fred Olsen Line Trimaran

1. Introduction

The introduction of car carrying high speed craft in the early nineties lead to a worldwide revolution in short sea passenger transport Nowadays these HSC are also used for military purpose. Some years ago Nigel Gee introduced the Pentamaran design and small Trimarans were built for passenger transport. The biggest HSC Trimaran is presently under construction at Austal Ships in Australia.

2 Pentamaran

Some years ago GL participated in an extensive investigation of the innovative Nigel Gee Pentamaran design and performed a prediction of global wave induced response for the ADX Express high-speed Pentamaran. The results where presented in. In 2003 GL started the prediction of the global wave induced loads for the Analysis of IZAR high-speed Pentamaran. Figures 2 and 3 show animations of the Pentamarans. As the ASX is designed for container transport the full breadth of the ship is not used. in contrast the IZAR Pentamaran uses the full breadth of the vessel for car and passenger decks. For the ASX wet deck slamming is negligible, for the IZAR Pentamaran minor. General advantages of the Pentamaran concept are: Drag is minimised, improving the speed-power curve. Speed may be achieved at a relatively low cost and comfort is assured since it behaves like a very slender monohull. Equating this advantage in different terms, steel may again be on the picture for a still attractive speed, increasing the overall reliability of the platform.



Fig. 2: Nigel Gee ADX Express

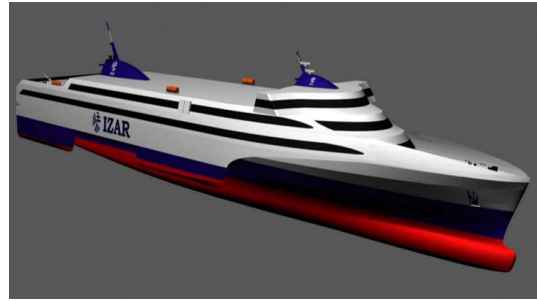


Figure 3: IZAR Pentamaran

The concept has an inherent depth. The vehicle deck is naturally placed high enough to permit the use of medium speed diesels without interrupting vehicle traffic. And these diesel engines, burning HFO instead of MDO, provide what operators are really expecting: a low operating fuel bill and a competitive increase in ship reliability.

A Pentamaran structure shares some of the peculiarities of slender monohull and multihull ships: large vertical bending moments, torsional and transverse loads in oblique/beam seas, wet-deck arrangement, etc. Prediction of global design loads for NG's and IZAR's high-speed Pentamaran at an early stage of the project was of paramount importance not only for strength and fatigue reasons, but also to determine the steel mass of the vessel and its structural configuration. The standard long-term statistical method was applied to calculate these design loads. So-called nonlinear pseudo transfer functions and the wave climate of the Western Mediterranean Sea served as input for the statistical analysis together with a significant wave height restriction of 4 metres. Figure 4 shows a cross section of the IZAR Pentamaran.

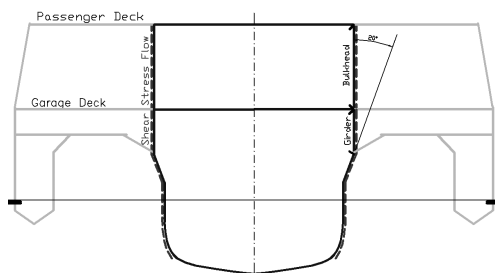


Fig. 4: Cross section of IZAR Pentamaran

The great flexibility of the Pentamaran concept allows for different designs with length up to 250m and deadweight up to 7000 t. Navy applications, as well as container and cruise designs, are also envisaged.

Prior to developing an exhaustive analysis of the Pentamaran structure, some conceptual aspects were studied to make initial decisions in the design. Most important of these aspects consists in the way in which buoyancy loads raise from the bottom of a narrow central hull to a significantly wider upper deck. The efficiency presented by this upper deck depends on the structural solution implemented between upper and garage decks.

Another effect associated to the non-standard hull configuration was detected. While the fore body is nearly a monohull, the aft body is more like a Trimaran. This means that, during a complete hogging-sagging cycle, the loads flow in the structure in a quite different manner, depending on the number of sponsons submerged at each time step, leading to peculiar shear lag effects.

3 Trimaran

For the investigation of hydrodynamic loads the vessel is similar to the Pentamaran designs. Comparing the forward main deck of the Pentamarans (figs 2 and 3) and the Trimaran (fig 5) it is obvious that for this Trimaran wetdeck slamming was an issue to be investigated. The occurrence of wetdeck slamming couldn't be neglected and an additional longitudinal wave bending moment had to be considered. In this respect modifications of the shape of the forward car deck were investigated and a slight design change resulted in a significant reduction of the additional bending moment.

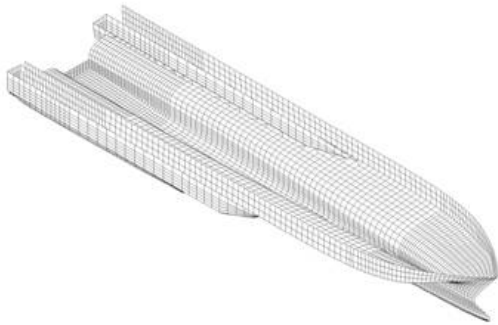


Fig 5: Hydrodynamic Model of Trimaran

In Tasmania a 55 meter Trimaran (Fig. 6) was built by North West Bay Ships which carry 420 people at a cruising speed of 40 knots between South Korea and Japan.

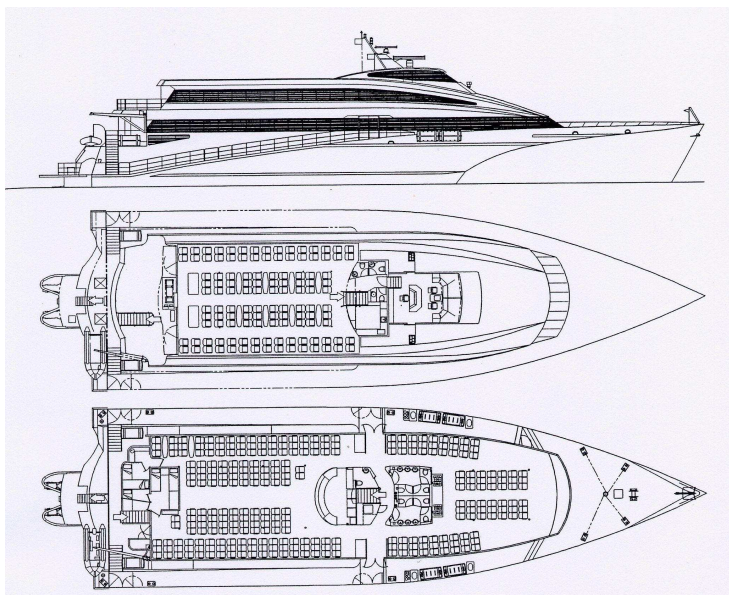


Fig. 6: Arrangement of NWBS 55m Trimaran (Tulk and Quigley)

Tulk and Quigley state that possibly the biggest disadvantage of the Trimaran platform are constraints placed on the machinery installation. The centre hull, whilst slightly wider than a comparable catamaran demi-hull, has to accommodate an additional of 50% propulsive power. In addition, as a category B craft, the vessel must maintain two independent sources of propulsion, thus providing a get-home function should get one engine room become unserviceable (Fig. 7)

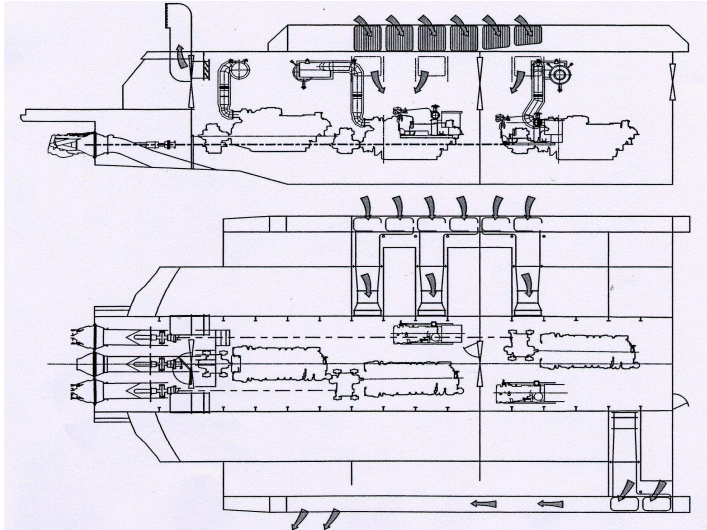


Fig 7: Machinery Arrangement of MWBS 55m (Tulk and Quigley)

The other disadvantage (Tulk and Quigley) of main machinery located in the centre hull is the difficulty in meeting ventilation requirements. Whilst it would be possible to simply vent vertically, this imposes a large structure in the centre of an otherwise spacious passenger cabin. This is unacceptable from both an aesthetic and noise transmission viewpoint.

4. Navy Ships

Several navies are looking for HSC like Westpac Express, Jervis Bay or others. They are used as Theatre Support Vessel (TSV), which will deliver a much broader package of dominant manoeuvre. They will allow the transportation of combat units as a complete package, and the ability to insert them without the need for a large combat service support soldier package to assist on the shore executing reception, staging, onward movement and sustainment.

The Littoral Combat Ship (LCS) is a fast, manoeuvrable, surface combatant geared to supporting mine detection/ elimination, anti-submarine warfare and surface warfare. Some of the key characteristics of the LCS include the following:

- Modular payload with rapid changeover capability to switch from one focused mission to another
- Up to 50-knot sprint speed and max ranges exceeding 5000 nautical miles
- Very low core manning (15 to 50) for all ship navigation, engineering and self-defence functions
- Very shallow draft to allow operations in littoral regions

A design team of General Dynamics, Austal, BAE Systems, CAE and MAPC was established in 2002. Austal are the platform designer and builder. The platform that has been submitted to Navy is a Trimaran similar in concept and overall size to the 126 m commercial Trimaran (Armstrong), see also fig.8.



Fig. 8: Artist impression of Austal's LCS Trimaran design

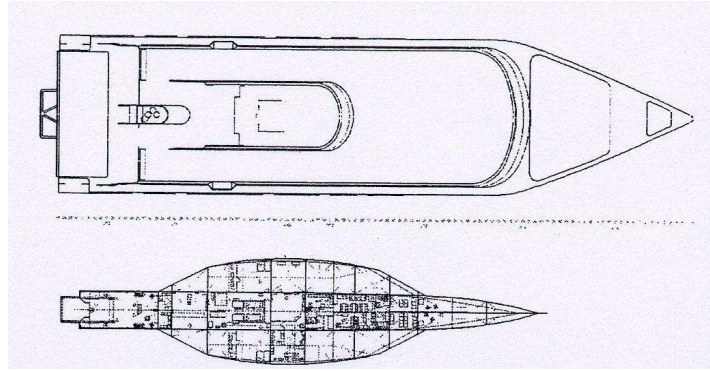


Fig. 9: Comparison of the relative sizes of the 126m Trimaran and RV Triton

In Europe(UK) the advantages and disadvantages of the Trimarans for future surface combat ships were assessed by several research projects, e.g. RV Triton. Fig. 9 shows the comparison of Austal's Trimaran and Triton (Armstrong).

5. Fred Olsen Line Trimaran

The biggest Trimaran at the moment is presently under construction for Spanish ferry operator Fred. Olsen, SA, at Austal Ships in Australia (see figure 1). Launching is expected end September 2004 and delivery in November 2004. It will be operated in the area of the Canary Islands where the effect of the islands on the wind and wave environment can produce rough conditions

GL is entrusted with the classification of this vessel with a length of 126.7 m, which will be larger than any existing diesel-powered fast ferry – catamaran or monohull. It is also believed to be the world's largest all-aluminium ship.

Providing capacity for 1,350 passengers, over 340 cars and more than 400 freight lane-metres, the aluminium ferry will feature a quadruple diesel engine main machinery package coupled to a trio of waterjets. This will enable it achieve in excess of 40 knots loaded when it is delivered to the Canary Islands in the second half of 2004. MTU Friedrichshafen will supply four 20V 8000 diesels, each rated to 8,200kW but with the agreement to increase their output to 9,100kW during the first quarter of 2006.

After weight estimates Austal decided for an aluminium structure with a steel strong back. Also for the structural design GL and Austal are in close collaboration. Several visits from GL Head Office plan approval engineers to the shipyard and the excellence co-operation in previous projects resulted in a fruitful progress of the project.

Some specific issues are welding of 40 mm aluminium plates, the integration of the steel strong back (cross bracings), the cut-outs for the bow thruster and local loads. Pictures of the construction of the will be shown in the presentation.

The vessel will be classed as an HSC category B craft. For catamaran with engine rooms in each hull it is no problem to separate the engine rooms. A Trimaran has to be considered as a monohull. The slender centre hull has to carry all systems with regard to the HSC code which is a challenge for the designer, see also figure 10. Contrary to Tulk and Quigley Austal stated that this was not one of the major problems for the Fred Olsen Trimaran.

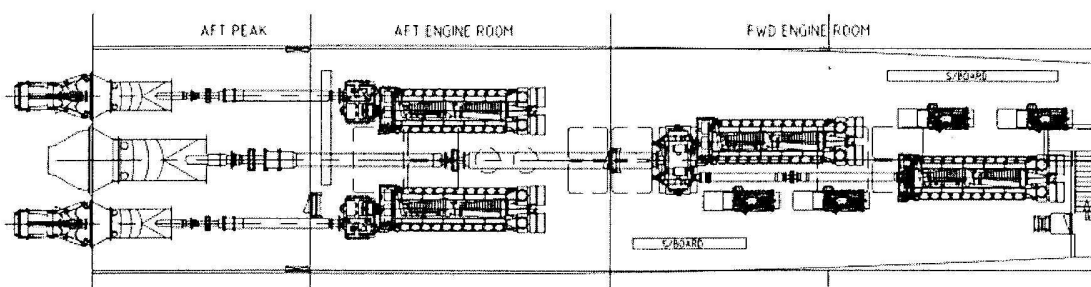


Fig. 10: Trimaran engine room layout

Several other issues beside the normal classification process were discussed or are under discussion. Some of them are evacuation, the lashing of the vehicles on the car deck, manoeuvrability investigations and the open car deck configuration.

Armstrong reported about some difficulties with the interpretation of the safety regulations, which have not been written with any thought towards a vessel having three hulls. It was clarified with IMO that the 126m Trimaran is considered as a monohull for purpose of stability, despite being a craft with multiple hulls. The stability characteristics are more similar to those of a monohull. Another challenge according to Armstrong has been the passenger evacuation. Lifeboats or life rafts must not be allowed to come too close to the amahs when the vessel is rolling during evacuation.

Together with Seastate, the Australian Maritime College Tasmania and with Marintek in Norway Austal performed comprehensive investigations about seakeeping, intact and damage stability. A manned model (10.7 m) was built to get more knowledge about the design.

6. Conclusion

After numerous fast monohulls and catamarans were built over the past years fast slender hull Trimaran and Pentamaran designs are developed for passenger/ RoRo transport and for military purpose. Some Trimaran were already built and the biggest HSC Trimaran is presently under construction at Austal Ships in Australia. From machinery and safety point of view these vessels are more comparable with monohulls than with catamarans. Several technical and safety issues makes the design and construction of Pentamaran and Trimaran a real challenge for shipyards, class societies and flag authorities. From hydrodynamic and load generation point of view sophisticated tools are necessary to cover influence of these specific ship types.

Acknowledgement

The reader of this paper will understand that GL can not give detailed information about the classification of the Fred Olsen Trimaran.

References

- TULK, R.J.; QUIGLEY, S.g. (2004), *Development of the North West Bay Ships Trimaran*, Design & Operation of Trimaran Ships, RINA London April 2004.
- ARMSTRONG, T (2004), *Coming soon to a Port near You – The 126 Metre Austal Trimaran*, Design & Operation of Trimaran Ships, RINA London April 2004.
- FACH, K. (2004), *Classification of HSC Multihull Vessels*, Design & Operation of Trimaran Ships, RINA London April 2004.

Numerical and Experimental Investigations on Semi-displacement Mono- and Multi-hulls.

C. Lugni¹, A. Colagrossi¹, G. Colicchio¹, O.M. Faltinsen²

¹INSEAN, *The Italian Ship Model Basin*, Roma - Italy, c.lugni@insean.it

²Centre for Ships and Ocean Structures, NTNU, Trondheim - Norway)

ABSTRACT

Present work aims to analyze the behavior of semi-displacement mono- and multi-hulls (catamarans and trimarans) in calm water. The mono-hull geometry is used to investigate the interaction both between the demi-hulls of the catamaran, and among the inner hull and the two smaller lateral ones in the trimaran arrangement. To do this, the mono-hull, the catamaran demi-hulls and the trimaran inner-hull were shaped identically. Experimental studies of the mono-hull steady wave pattern have been carried out for several Froude numbers, $F_n = 0.3 - 0.8$ with step $\Delta F_n = 0.1$. A smaller number of speeds, corresponding to $F_n = 0.3, 0.4, 0.5, 0.6$, has been considered for the catamaran.

The model test results were compared with nonlinear 2D+t and linear 3D Rankine Panel Method computations where trim, sinkage and dry transom conditions are taken into account. The combined use of experimental and numerical tools allowed to investigate the relevance of the demi-hull interaction and of nonlinear effects on the vessels generated waves. Numerically the study has been extended to the trimaran geometry.

1 INTRODUCTION

Aiming to increase the cruise speed of the ships, designers have created a wide variety of arrangements where the weight of the vessel can be supported by submerged hulls, hydrofoils, air cushion effects, or combinations of them.

Mono-hulls and catamarans are geometries commonly adopted. These two designs present advantages and drawbacks. High-speed mono-hulls are characterized by rather large beam-to-draught ratios (B/D), *i.e.* from around 5 to values greater than 7. This implies more limited accelerations in heave and pitch motions, (FALTINSEN, 1990). However the roll motions of mono-hulls can be critical and need special attention.

Among the catamarans we can list: the wave-piercing, the semi SWATH (Small Water-plane Area Twin Hull) style hulls and the Surface Effect Ships (SES). A SWATH vessel has higher heave and pitch natural periods and generally lower vertical excitation loads than a comparable catamaran. On the other hand, if control surfaces are not introduced, a threshold Froude number exists beyond which the SWATH is dynamically unstable in the vertical plane. In head-sea conditions, this vessel behaves better than a corresponding catamaran. But its seakeeping properties are not generally more advanced. When the combination of sea state, speed and heading, leads to resonant vertical motions, the SWATH may actually not have a good seakeeping behaviour. Surface Effect Ships (SES) use an air cushion mechanism to obtain the desired cruise velocity and performances. The excess pressure in the air cushion between the two SES hulls lifts the vessel and carries about 80% of its weight. On the other hand, it reduces the metacentric height and causes wave generation and additional wave resistance. However the latter is sufficiently limited so that a SES experiences a total calm water resistance smaller than a catamaran with similar dimensions. As a drawback, SES can have more pronounced speed loss in waves than for instance catamarans, and suffer easily damages of the bow skirts.

More recently, trimarans and pentamarans with a large center hull combined with smaller outrigger

hulls start to be considered as promising innovative concepts. Trimarans, consisting in a slender central hull and two lateral smaller hulls, can have length-to-displacement ratios (L/∇^3) rather high. Even for L/∇^3 larger than 9 such vessels do not experience any stability problem. This partially explains why the interest on trimarans is getting massive and makes them a widespread concept, although the first prototype models were designed just 15 years ago. Their features motivated pioneer enterprises and allowed a new record for under-powered circumnavigation. Moreover their handling characteristics opened them to the business of fast passenger ferry transportation, for example between Korea and Japan, and to military applications, within the RV Triton project.

The choice among different designs is the result of comparing ship performances in several contexts, like powering, seakeeping ability, stability, survivability, maneuverability, space, cost. As new ship concepts are introduced, numerical and experimental investigations are needed to quantify and characterize the related properties.

In the case of mono-hulls and catamarans, comprehensive experimental studies have been performed by MOLLAND *et al.*, 1995, DOCTORS, 2003, KEUNING, 1988 and OHKUSU and FALTINSEN, 1991. The first paper refers to calm-water conditions and discusses the effect of a forward speed on trim and sinkage when ship-length Froude numbers are around 0.35. This is relevant for the vessel performances since trim and sinkage are directly connected with the resistance and matter also for the wetdeck slamming on multi-hull vehicles. DOCTORS, 2003 conducted calm water-tests on five different transom-stern mono-hull models to investigate the transition from wet to dry transom. The author identified the transom-draft Froude number as the parameter governing such transition. A dry transom is generally beneficial and affects the trim and rise, as well as the damping of vertical ship motions. KEUNING, 1988 performed high-speed mono-hull experiments in calm water and head sea waves and analyzed the wave elevation near the vessel and the distribution of the hydrodynamic coefficients along the ship hull. Forced heave and pitch model tests on a high-speed catamaran were presented in OHKUSU and FALTINSEN, 1991. A weak interaction between the demi-hulls was suggested by the fairly good agreement of the measured hydrodynamic forces with numerical $2D+t$ results based on the assumption of hydrodynamically independent demi-hulls.

Limited amount of experimental data is available for trimarans, essentially due to the work by MIGALI *et al.*, 2001. Several other model-test activities have been done, but most of them are covered by military secrecy. MIGALI *et al.*, 2001 analyzed the forces acting on a commercial ship arranged as a trimaran configuration. The interference effects for different transverse and longitudinal positions of the side hulls have also been investigated and discussed in terms of an interference factor.

In the numerical context, most of the studies of wave resistance and wave induced ship motions on mono-hulls and catamarans are based on the assumptions of incompressible fluid in irrotational motion. In fact, the solution of the more general unsteady Navier-Stokes Equations still presents problems linked with the CPU time required for the computations, the large amount of grid points necessary for the discretization of the fluid domain, and the modelling of the turbulence. Linear wave resistance analysis based on the Michell's thin-ship theory (MICHELL, 1898) and accounting for the transom effect have been presented by different researchers (*i.e.* MOLLAND *et al.*, 1994, and DOCTORS and DAY 1997). The developed methods have been applied to high-speed mono- and multi-hull vessels. In the latter case, the diffraction of the waves generated by one demi-hull due to the presence of the other demi-hull is not accounted for, *i.e.* the waves generated by the separated hulls are simply superimposed. This type of analysis is very efficient and important at a pre-design stage. However, the role played by the nonlinearities increases with the Froude number. The same is true for the interaction between steady and unsteady flows when the seakeeping is of concern. In principle three-dimensional effects should be accounted for. Several numerical codes exist handling them properly for the linear seakeeping case. However, the solution of the fully nonlinear three-dimensional problem is still challenging due to numerical and CPU time requirements. In terms of nonlinear effects, simplifications are often made, for instance, by including nonlinearities associated with hydrostatic and Froude-Kriloff loads. In terms of three-dimensional effects, quite accurate approximate solutions may be achieved by following physical considerations. For instance the wave

pattern around a semi-displacement vessel in deep water is dominated by divergent waves. The main 3D effects can therefore be adequately captured by using a $2D+t$ (also referred to as 2.5D) theory. In this case the longitudinal flow variations are assumed smaller than the transverse ones, leading to a sequence of 2D problems in the ship cross-planes. The 3D information travels from the bow to the stern only, that is the solution in each cross-plane is influenced just by the flow upstream. (FALTINSEN, 2001) pointed out the relevance of 3D flow effects in the close vicinity of both the bow and the transom stern. These aspects represent a limitation for the $2D+t$ theory since it assumes that both velocity potential and free-surface elevation are zero at the bow and is not aware of what happens downstream. The latter implies a predicted pressure at the transom stern different from the atmospheric value. These considerations are also relevant in unsteady flow conditions. FONTAINE *et al* (2000,) accounted for the bow wave elevation by combining a 3D bow model with the 2.5D theory. A domain decomposition method (see *i.e.* GRECO *et al*, 2002) can be introduced to couple a global $2D+t$ modeling with a local 3D analysis for the description of the transom-stern flow. The same strategy can also be applied to handle other phenomena characterized by three-dimensional flow features, *i.e.* the water on deck and the wetdeck slamming. If the water-hull interaction is not characterized by particularly small angles between the impacting free surface and the hull, slamming loads can be modeled as an integrated part of the analysis. Otherwise local hydroelasticity will matter. In this case, the rather small time scales involved allow to investigate the slamming separately from the global analysis. On the other hand, such phenomenon can induce global elastic effects that must be included in the global analysis for a proper estimate of the whipping occurrence. Springing, *i.e.* steady-state wave induced global resonant hydroelastic vibrations, may be a relevant fatigue issue for larger high-speed vessels. Since the natural frequencies are high, head sea are of major concern in this context. Springing may be excited by linear and nonlinear wave effects. The linear wave excitation corresponds to small incident wave lengths relative to the ship length. The spatial oscillations of head-sea waves cause strong variations of the flow in the longitudinal ship direction. As a result, in this case a $2D+t$ theory is not suitable.

Our research activity is aimed to contribute on characterizing and comparing the performances of different high-speed vessels, and it is based on the combined use of numerical and experimental tools. In (LUGNI *et al*, 2004) the steady and unsteady wave patterns around a mono-hull and a catamaran have been analyzed and compared through dedicated model tests. The mono-hull geometry was chosen identical to a catamaran demi-hull to analyze the interaction effects in the catamaran arrangement. This implies a beam-to-draught ratio much smaller than the one normally used for mono-hull high speed vessels. Several Froude numbers, wave amplitudes and wave frequencies have been selected. Detailed measurements of the steady and unsteady wave-field features have been made both along the hull and downstream the transom stern. Also the flow area between the two demi-hulls of the catamaran was studied. The information from the experiments have been checked, interpreted and integrated by means of two numerical tools: (i) a nonlinear $2D+t$ solver and (ii) a linear 3D Rankine Panel Method. In the numerics trim and sinkage were not accounted for. The comparison allowed also the validation of the used codes and of the models behind them. The results confirmed the relevance of a nonlinear flow description and the validity of a parabolized approach in case of sufficiently large Froude numbers. The interaction between catamaran demi-hulls appeared substantial. The same is true for the interaction between steady and unsteady flows. For the considered speeds and within the heave and pitch resonance ranges, the experiments showed that the mean trim and sinkage of the catamaran are mainly governed by the steady flow. This is relevant for instance for the wetdeck slamming.

Presently we are at the second stage of the investigation. This concerns the seakeeping properties of fast ships, with emphasis on the occurrence and effects of impact phenomena. The latter include both ship-deck and bottom slamming. For the purpose, experimentally a catamaran model will be equipped with different measuring devices on the deck and tested both with and without head-sea waves. In this framework, occurrence of hydroelastic phenomena will be also analyzed. In the present paper, the steady model tests for the mono-hull and the catamaran cases are further investigated and new numerical analyses are carried on due to the further development of our solvers. The latter represents the numerical part of this second-stage activity. It is a logical continuation of the work reported in LUGNI *et al* (2004,)

and concerns: (a) the improvement of the linear 3D simulations of mono-hull and catamaran by including the trim and sinkage from the experiments, (b) and by modelling the dry transom condition for Fn higher than 0.4 with a *false body* shaped as the hull hollow obtained by the 2D+t results; (c) the extension of the 2D+t algorithm to handle multi-hull (more than two) arrangements and its specialization for the trimaran case. Through the former the relevance of trim and sinkage has been further analyzed. The latter allowed to investigate numerically the interference effects for trimaran designs. As a next step, also the 3D linear code will be generalized to treat trimaran systems. Then, trimaran model tests will be performed and the related information will be combined and compared with the numerical results.

2 2D+t THEORY

The 2D+t theory leads to a sequence of 2D problems to be solved in the transverse cross-sectional planes of the vessel. The 3D effects are partially accounted for since the generic cross-section is influenced by the flow in the upstream cross-sections of the hull. The nonlinearities of the problem are retained. For vertical ship motions and steady symmetric flows (straight coarse), this approach is suitable at sufficiently large Froude numbers, let us say larger than 0.4, so that the ship transverse wave system is not dominating. For horizontal wave induced motions and steady antisymmetric flows (maneuvering), the transverse waves are less important also at small Froude numbers, *i.e.* the 2D+t theory can be used for Froude number smaller than 0.4. FALTINSEN and ZHAO, 1991 used the 2.5D method to study the ship motions of high speed mono-hulls. Nonlinear steady and linear unsteady analysis were considered and the interaction between steady and unsteady flows was accounted for. MARUO and SONG, 1994 retained also the nonlinearities in the unsteady problem but assumed linear incident waves. In our case, the 2D+t theory is applied to investigate the steady flow patterns for mono-hulls and catamarans. In the latter case the interaction between the demi-hulls is accounted for. No correction of the local flows at the bow and at the transom stern is introduced. Damping foils, trim tab and interceptors are not modeled. In the following the solution method is briefly outlined under the assumptions of inviscid steady flow induced by a ship with constant forward speed and fixed trim and sinkage.

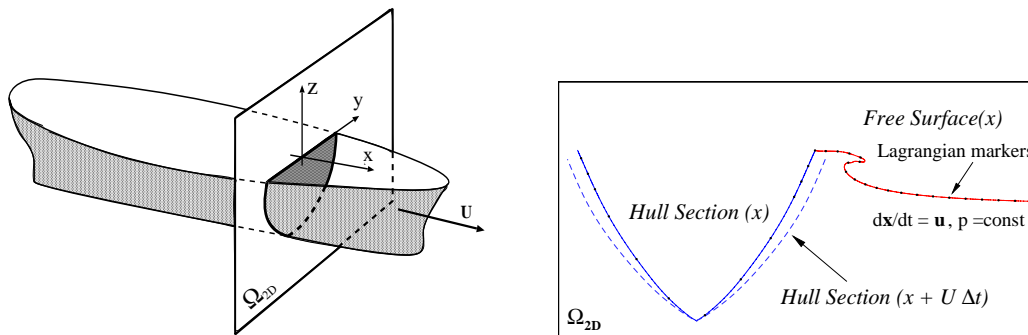


Figure 1: Qualitative sketch of the 2D+t approximation for the steady three-dimensional flow around a ship with constant forward speed \vec{U} . Left: 3D ship problem. Right: equivalent unsteady 2D problem (2D+t).

Let us consider a ship moving with constant velocity \vec{U} (see left sketch in Figure 1). We assume a beam-to-draft ratio $B/D \sim \mathcal{O}(1)$ and both B and D individually much smaller than the ship length L , say $\varepsilon = B/L, D/L \ll 1$. We also assume the Froude number $Fr = U/\sqrt{gL} = \mathcal{O}(1)$. In a ship-fixed frame of reference, the hull geometry is given implicitly as $\mathcal{H}(x, y, z) = 0$ and the *a priori* unknown free surface can be represented as $\mathcal{W}(x, y, z) = z - \zeta(x, y) = 0$. Assuming that the fluid is in irrotational motion, the flow field is described by the Laplace equation combined with the kinematic hull (\mathcal{H}) boundary condition

$$\nabla \Phi \cdot \nabla \mathcal{H} = 0 \quad (1)$$

and the kinematic and dynamic free surface (\mathcal{W}) boundary conditions

$$\nabla\Phi \cdot \nabla\mathcal{W} = 0 \quad \text{and} \quad p = 0 \quad (2)$$

respectively. The statement of the problem is completed by the upstream radiation condition

$$\Phi \rightarrow -Ux \quad \text{as } x \rightarrow \infty . \quad (3)$$

It is convenient to formulate the problem in terms of the perturbation potential φ , linked to Φ by $\Phi = -Ux + \varphi$. The longitudinal gradient $\partial/\partial x$ can be neglected with respect to those in the transverse plane. Therefore, the problem for φ reduces to a sequence of two-dimensional problems in the ship cross planes. The related boundary conditions imply the generic cross plane Ω_{2D} is influenced by the upstream solution and unaware of the following cross sections. The problem sequence can be solved once given the conditions at the bow and the far-field behavior of the solution at each hull cross section. In a fixed frame of reference with respect to the unperturbed fluid the problem can be re-written as a two-dimensional time-dependent problem. This is fully equivalent to the unsteady problem of the free-surface flow generated by a body deforming in time (see right sketch in Figure 1). Consistently, the resulting approximation is called here $2D+t$. The 2D unsteady problem is solved through the Mixed Eulerian Lagrangian method (LONGUETT-HIGGINS and COKELET 1976, FALTINSEN 1977, and originally suggested by OGILVIE 1967), that is the problem is split in a kinetic and a time evolution step. The kinetic problem for φ is solved by means of the Green's second identity used as integral representation of the velocity potential. Applying the latter at the domain boundary leads to an integral equation for the unknown boundary data $\partial\varphi/\partial n$ and φ , on the free surface and body boundary, respectively. The continuity of the velocity potential is enforced at the intersection points between the body and the free surface. A Boundary Element Method (BEM) with linear shape functions for the geometry and boundary data is then introduced. The relevant integrals are computed analytically, and after some manipulations the discretized integral equations lead to a system of linear algebraic equations for the unknowns at the collocation points. The system influence matrices are only dependent on the geometry of the problem. In the time evolution step, the free-surface boundary conditions, expressed in a Lagrangian form, and the body velocity are integrated in time to provide the new boundary configuration and related data for the next time instant. The time stepping is performed by a fourth-order Runge-Kutta method. The discretization of the free surface is controlled through numerical regridding and the grid refinement is adapted to the evolution of the solution. If the angle between the body and the free surface becomes too small, the jet-like flow created is partially cut to avoid numerical errors (*cf.* ZHAO and FALTINSEN 1993). Unphysical reflection of the outgoing waves is prevented by using a damping layer technique (for short waves) and a panel stretching (for longer wave components) toward the edges of the computational domain. Invariance of the solution under mesh refinement and size changes of the computational domain has been widely checked. Since a BEM is used, bow wave post-breaking phenomena cannot be studied. The breaking is limited by cutting off the jet flow in the plunging bow waves. This is not believed to be an important error source.

3 LINEAR 3D METHOD

In our analysis of the steady and unsteady mono-hull and catamaran flows, we used a linear 3D method as additional numerical instrument. In the following its features are briefly outlined, for more details see *i.e.* NAKOS, 1990.

We consider the free-surface flow generated by a ship advancing at constant forward speed U in regular incoming waves. The problem is solved by using the potential flow theory and neglecting the nonlinearities connected with the wave-body interactions. In case of vessels with transom stern, the latter is modeled as shown in the following. Two different base flows can be considered: the Double-Model (DM) and the Neuman-Kelvin (NK) linearization (see *i.e.* NAKOS, 1990). These are, respectively, a low-speed and a slender-body approximation. In this way, the free-surface boundary conditions can be transferred

on the undisturbed free surface and the steady problem may be solved. Once this is accomplished, the pressure can be evaluated from the Bernoulli's equation. Finally, the wave pattern is calculated from the related kinematic free-surface conditions. Because the high Fr considered, in the following NK linearization will be adopted.

The potential is represented in terms of source distributions on the body \mathcal{H} and the free surface \mathcal{W} . The problem is then solved numerically by using a lower order Rankine Panel Method (*RPM*, HESS and SMITH, 1996). This leads to a system of algebraic equations for the unknown source strengths at the collocation points. The collocation points on \mathcal{H} are placed at the centers of the corresponding panels. The same is made for those along the free surface but additionally they are rigidly shifted one panel downstream in order to enforce numerically the radiation condition (see *i.e.* BERTRAM, 1990).

When a transom stern is present, special care is used for its modelling. In the case it is dry (as seen by experimental observations, or, when not available, from Doctors's formula (DOCTORS, 2003)), a false body is introduced. Practically the trim and sinkage of the hulls are set as from the experimental observation, while the length of the hull hollow calculated at the centerline of the hull L_{hh} and obtained by the 2D+t calculations is used to smoothly prolong the hull of the same length. Figure 2 shows how the hull is prolonged for different Froude numbers. A new part of hull is added to the original hull form.

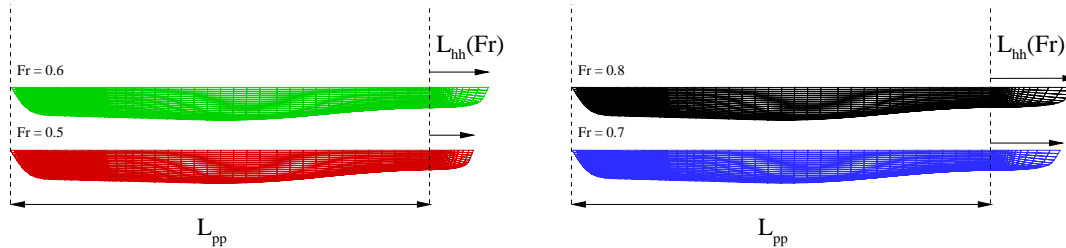


Figure 2: Sketch of the *false body* added at the transom stern of the monohull for several Froude numbers.

The latter has been modeled by using the shape of the hull hollow obtained through the 2D+t theory. Of course this part of the hull is not taken into account when integrating the pressure for calculation of the forces on the body.

4 EXPERIMENTAL SET-UP

A dedicated and comprehensive experimental investigation has been performed to analyze the behaviour of semi-displacement mono-hulls and catamarans. A catamaran model was built consistently with the geometric ratios normally used for semi-displacement catamarans. The main characteristics are reported in table 1. The same parameters have been considered for the mono-hull geometry coinciding therefore with a catamaran demi-hull. This leads to a shape finer than those of the existing semi-displacement mono-hulls. The experimental activity has been carried out at the INSEAN basin No. 2: 220 m long, 9 m large and 3.6 m deep. During the tests, each model was towed by the carriage through a constant force mechanism. Trim and sinkage were free while the center of rotation was fixed to the center of gravity of the vessel. The model tests analyzed the forward motion in calm water and investigated Froude numbers $Fr = U/\sqrt{gL} = 0.3 - 0.8$ with a step $\Delta Fr = 0.1$, for the mono hull, $Fr = 0.3, 0.4, 0.5, 0.6$, for the catamaran. A capacitance wave probe system fixed to the carriage was used to measure the wave field near the hull, composed by an array of 40 transducers located transversally to the basin and with a uniform distance of 4 cm between the probes. More refined reconstruction of the wave pattern has been achieved by shifting the sensor array of 2 cm transversally to the vessel axis and repeating the same run. With this set-up, the wave field was recorded within a lateral distance of $0.5L$ from the model hull, including the area between the two demi-hulls in the catamaran case. Figure 3 gives a sketch of the wave probe arrangement along the vessel central axis and along the external profile of a catamaran demi-hull, at a distance of 3 cm.

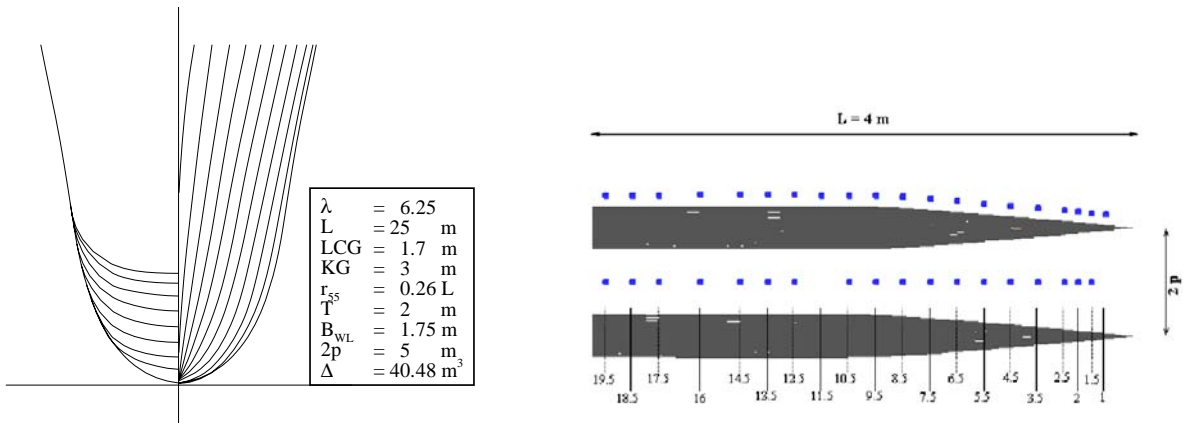


Figure 3: Left: Body plan of the demi-hull and hydrostatic properties. $2p$ indicates the distance between the centrelines of the catamaran demi-hulls. Right: Top view of the wave probes (indicated by the dots) used along the external profile of a catamaran demi-hull and along the vessel central axis.

Each test condition was repeated between 5 and 10 times to ensure repeatability and a precision error analysis has been performed.

5 DISCUSSION

This study is aimed to a better understanding of the steady wave pattern features and to verify the validity and limits of the numerical methods presented in sections 2 and 3. The NK linearization is used for the linear 3D (*3D RPM*) results, that is the basis steady flow is assumed given just by the uniform flow due to the ship speed. The results of the repeatability analysis for the model tests are reported by presenting the experiments as mean measured values and error bars. The latter are given as $\pm\sigma$, with σ the standard deviation. The wave profiles along the mono-hull for $Fr = 0.5$ and $Fr = 0.7$ are given in figure 4.

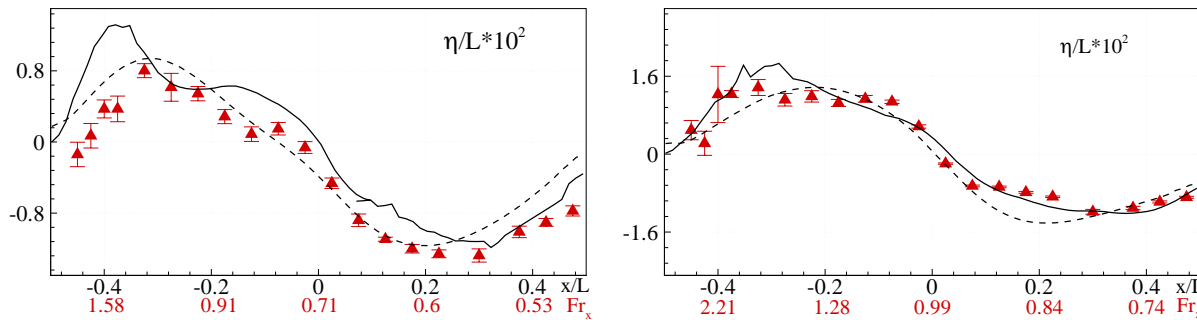


Figure 4: Wave profile along the mono-hull for $Fr = 0.5$ (left) and $Fr = 0.7$ (right). Experiments (symbols: mean value and error bar) and numerical results obtained by the *3D RPM* (dashed line) and *2D+t* (solid line) methods. $Fr_x = U/\sqrt{gx}$, with x the longitudinal distance from the bow.

Numerically the wave elevation was calculated at a distance of 3 cm from the ship profile, consistently with the measurements. Globally the agreement between the experiments and the numerical results is satisfactory. Locally large discrepancies are detected in the bow area between the model tests and the *2D+t* theory at $Fr = 0.5$. The former predict a negative wave elevation, the latter gives a quite large free-surface rise along the hull. This disagreement can be partially explained by ventilation of the sensors in the bow area, indirectly confirmed by a larger experimental error bar near the bow. Ventilation leads to more dry conditions for the probes and so to an underestimate of the wave elevation. The two results fit quite well at $Fr = 0.7$, when the *2D+t* model is able to capture the bow splash phenomenon. Similarly as for $Fr = 0.5$, also in this case the experiments are less repeatable near the bow. The stern wave

disturbance is predicted correctly by the nonlinear method for both the speeds. The *3D RPM* results agree better with the experiments at the smaller speed, when the nonlinearities are less important and the three-dimensional effects are stronger. At the larger Fr the agreement is still satisfactory but a smoother bow rise-up and a deeper trough near the stern are predicted as a consequence of the linear formulation.

In (LUGNI *et al*, 2004) the stern and downstream flows were not properly described when the transom was dry while it was assumed wet. As explained before, here the real transom flow condition has been properly reproduced using the *false body* technique. In figure 5 the results of this technique are compared with those obtained using a wet transom. By the comparison of the two data sets with the experimental results, right plot of figure 5, the importance of the proper trim, sinkage and wetness conditions is highlighted. The role of these parameters had already been estimated with the $2D+t$ theory.

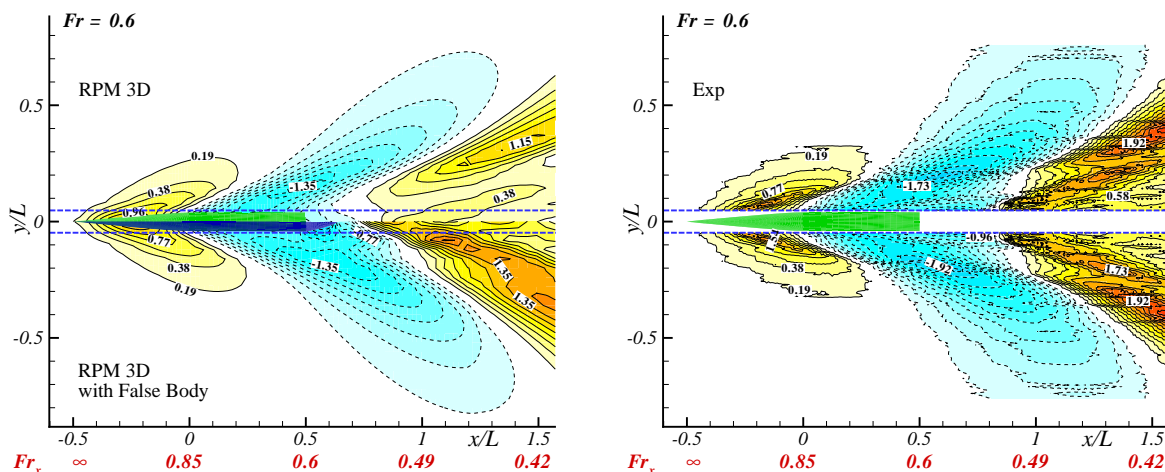


Figure 5: Left: Comparison between 3D RPM results without (top) and with *false body* (bottom). Right: Experimental results.

The steady wave patterns at $Fr = 0.5, 0.6, 0.7$ and 0.8 are reported in figures 6 and 7 where the experiments are compared with the $2D+t$ and $3D RPM$ results, respectively. For the smallest ship-length Froude number shown, the linear 3D computations capture correctly the phasing of the wave pattern and give reliable quantitative information in the bow area and along the ship hull. The $2D+t$ results agree fairly well with the experiments along the hull in terms of the phasing of the wave system generated. The predicted amplitudes are close to the measurements near the bow but underestimate them going downstream. A global extension of the lobes (contour lines with constant elevation) is observed, not shown by the measurements. The comparison slightly improves behind the stern, suggesting the relevance of nonlinearities in the wake and the need of handling the dry stern condition. In this context, the $2D+t$ theory assumes that the flow leaves tangentially the transom stern in the downstream direction. This approximation appears suitable to capture the transom flow behavior. OHKUSU and FALTINSEN, 1990 showed that theoretically the $2D+t$ theory should not be applied for ship-length Froude smaller than 0.4 since the method neglects the transverse wave system generated by the ship. The latter is important at such speeds while becomes less important than the divergent system at higher speeds. FALTINSEN, 2000 defined a local Froude number $Fr_x = U/\sqrt{gx}$, with x the longitudinal distance from the ship bow, and used it to estimate the goodness of the $2D+t$ theory for the ship bow waves prediction. A similar local Froude number should be introduced for the transom waves, with x defined as longitudinal distance from the stern. For a given Fr , the $2D+t$ results can be considered suitable within the region where Fr_x is sufficiently large, say greater than 0.4. Obviously such region enlarges as the ship speed increases. The local bow Froude number is reported in the figures. According to our results, the $2D+t$ model gives reliable results for Fr at least larger than 0.5 and they are globally better than the ones from the $3D RPM$ code. This is due to two factors: the transverse waves become progressively less relevant and the importance of nonlinearities increases. The linear results underestimate the peaks and troughs along the

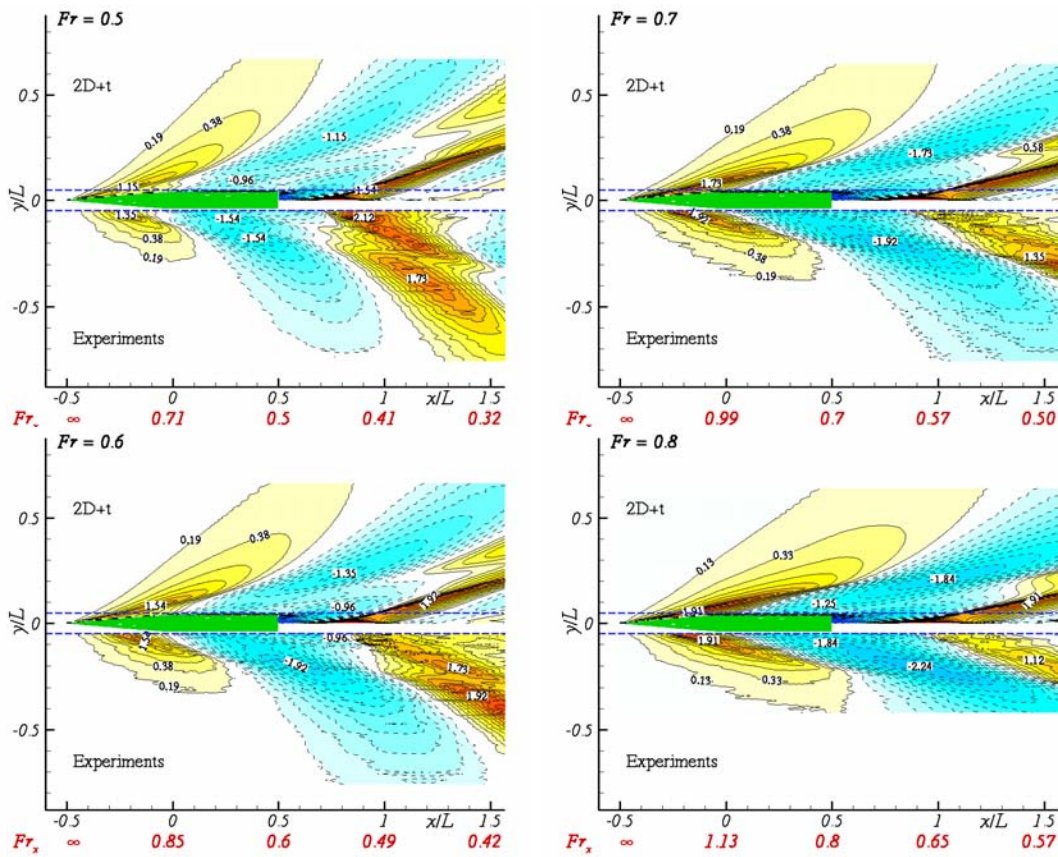


Figure 6: Contour lines of the mono-hull steady wave pattern. From top to bottom and from left to right: $Fr = 0.5, 0.6, 0.7$ and 0.8 . In each plot the experiments (bottom) are compared with the $2D+t$ results (top). $Fr_x = U/\sqrt{gx}$, with x the longitudinal distance from the bow.

hull and in the wake. However the dimension of the lobes of the global wave system is reproduced quite nicely while the $2D+t$ results show a wider extension of the lobes even at the largest speed.

The steady wave patterns for $Fr = 0.5$ and 0.6 are reported in figures 8 and 9 where the experiments are compared, respectively, with the $2D+t$ and $3D$ RPM predictions. The linear $3D$ code is more able to capture the global picture of the wave field along the vessel, showing that the transverse waves play still a role. However, for both the speeds, it does not quantify correctly the free-surface disturbance due to the ship forward motion. This implies that nonlinear effects matter. The $2D+t$ theory shows a wide extension of the lobes near the bow, similarly to the mono-hull case, and it has a relevant phase difference with respect to the experiments at the lower Froude. Despite this, even at $Fr = 0.5$ the peaks and troughs are closer to the measured values than the results obtained with a linear method. Top picture of figure 10 shows the experimental wave field behind the transom for the mono-hull at $Fr = 0.5$. The dry transom causes the formation of a hollow just behind the vessel. The water reaches a minimum value and then rises to form a rooster tail developing into a divergent breaking wave system. The mono-hull transom flow features have been thoroughly investigated by LANDRINI *et al*, 2001 due to the practical relevance of the resulting breaking phenomena. These lead to vortical structures responsible of the visible signature left downstream by the ship. In their study, the authors used the $2D+t$ theory. The transom was enforced to be dry. A nonlinear BEM solver, as used in the present study, was adopted to simulate the flow evolution until the incipient wave breaking and a Smoothed Particle Hydrodynamics (SPH) method was initialized by the BEM to handle the post-breaking evolution of the wave system. In the bottom of the figure 10, the results obtained by using just the BEM $2D+t$ method for $Fr = 0.5$ are given. As we can see, the $2D+t$ formulation is able to reproduce the flow scenario behind the transom: hull hollow, rooster tail and incipient breaking divergent wave system. Nevertheless, since the plunging jet is cut to

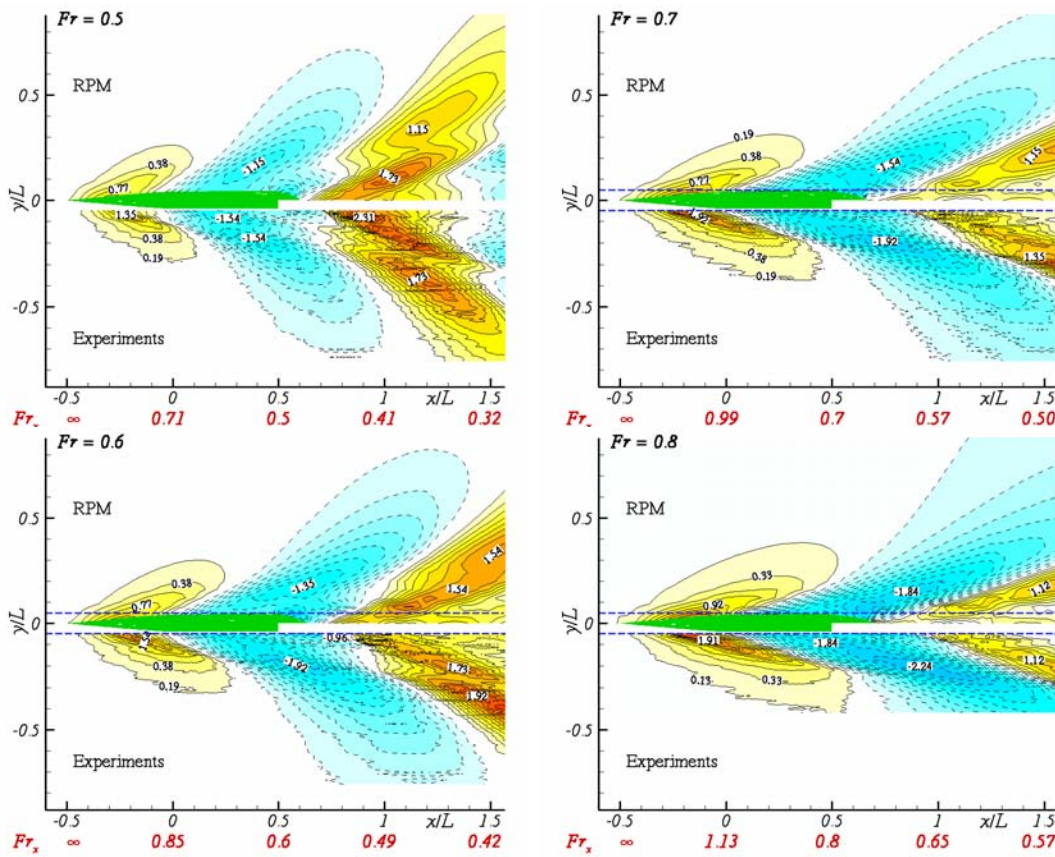


Figure 7: Contour lines of the mono-hull steady wave pattern. From to bottom and from left to right: $Fr = 0.5, 0.6, 0.7$ and 0.8 . In each plot the experiments (bottom) are compared with the $3D$ RPM results (top). $Fr_x = U/\sqrt{gx}$, with x the longitudinal distance from the bow.

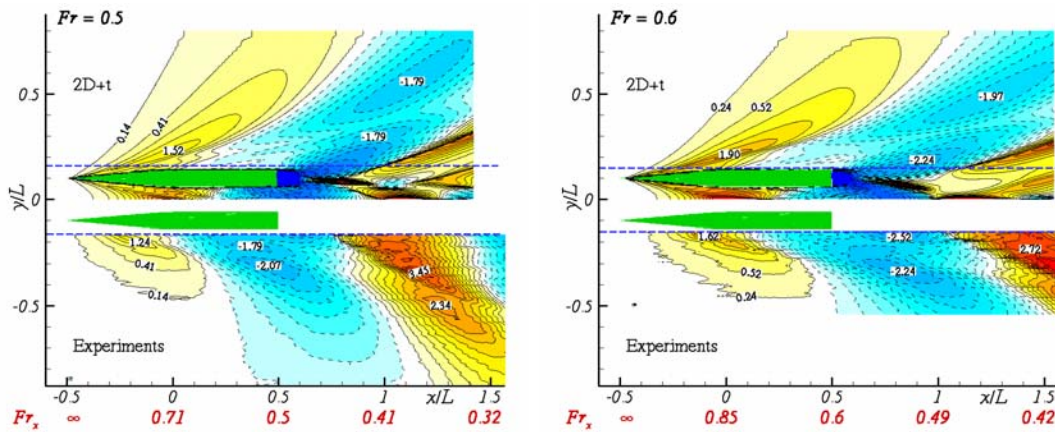


Figure 8: Contour lines of the catamaran steady wave pattern. Left: $Fr = 0.5$. Right: $Fr = 0.6$. In each plot the experiments (bottom) are compared with the $2D+t$ results (top). $Fr_x = U/\sqrt{gx}$, with x the longitudinal distance from the bow.

avoid the occurrence of impact on the underlying water, the energy of the wave system is focused close to the crest of the divergent wave. Differently, in the physical phenomenon the breaking causes a spatial spread of the wave energy.

The previous discussion has shown as the $2D+t$ theory gives useful information for the wave pattern around both the mono-hull and the catamaran. The results are reliable especially behind the stern, while in the aft part of the vessels they give a qualitative indication of the flow features. This suggested the

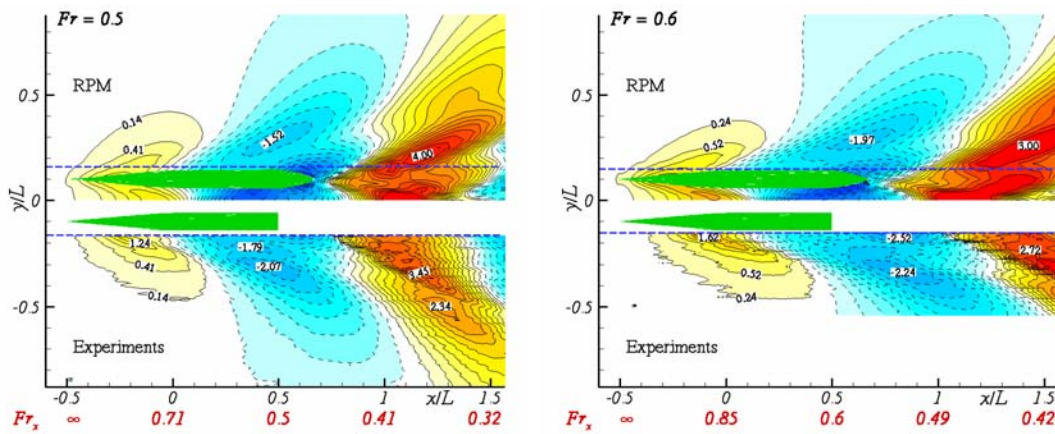


Figure 9: Contour lines of the catamaran steady wave pattern. Left: $Fr = 0.5$. Right: $Fr = 0.6$. In each plot the experiments (bottom) are compared with the 3D RPM results (top). $Fr_x = U/\sqrt{gx}$, with x the longitudinal distance from the bow.

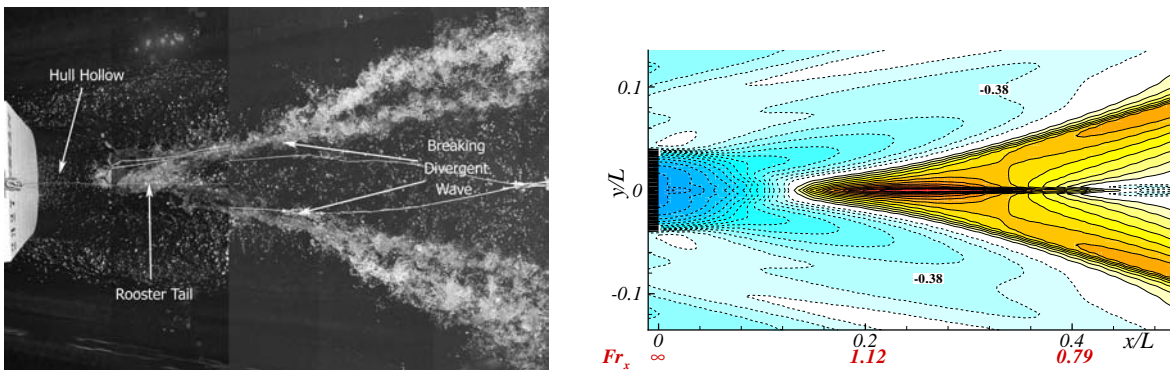


Figure 10: Mono-hull: transom stern wave field at $Fr = 0.5$. Experimental picture (left) and contour lines of the steady wave pattern predicted by 2D+t theory (right). $Fr_x = U/\sqrt{gx}$, with x the longitudinal distance from the transom.

possibility of using the 2D+t model for investigating numerically the flow pattern around a trimaran.

The ship arrangement considered is shown in figure 11 together with the relevant geometrical parameters for the main hull and the outrigger.

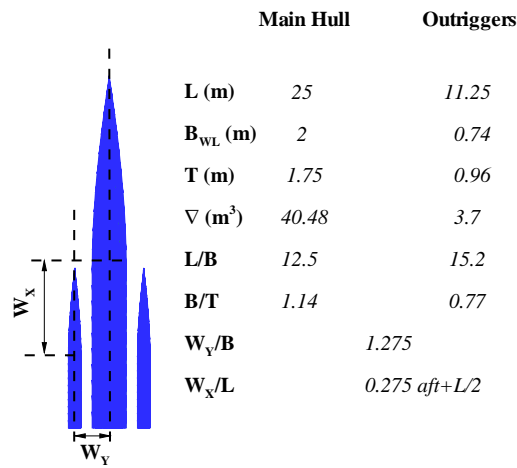


Figure 11: Main geometrical features of the analyzed trimaran.

The latter have been identified through a study of the stability properties of the vessel.

In the following, we discuss the preliminary results obtained for the calm water tests at $Fr=0.5$ and 0.6.

The influence of the outriggers on the ship wave field at $Fr = 0.5$ is analyzed in figure 12 through the comparison of the steady wave pattern generated by the trimaran with the wave system due the main hull

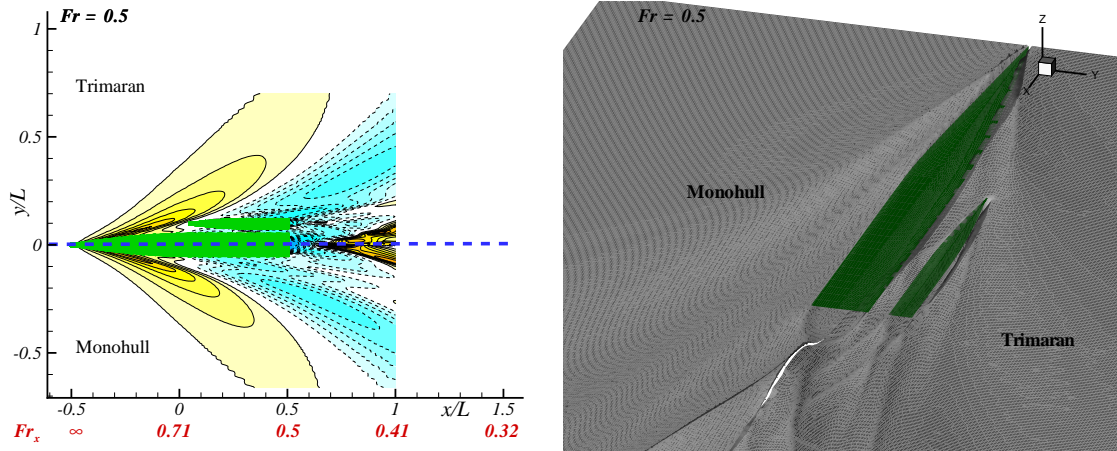


Figure 12: Steady wave pattern of a monohull and of a trimaran at Froude number 0.5. Left: contour plots of the wave height. Right: three-dimensional view.

only. At this Froude number the main effects are concentrated near the ship, in particular in the regions between the center-hull and the outriggers and at transom. For $y/L > 0.2$ the two wave patterns are instead quite similar. In the inner areas between the main and the side hulls, there is a complex interaction between the outrigger bow wave and the shoulder wave coming from the main hull. In the downstream region the flow differences with respect to the mono-hull case become even more significant. Here, the wake developing at each side hull interacts with the one shed from the main hull and this leads to: (a) a lower height of the rooster tail (see right figure 13) similar as for the catamaran, (b) a second rooster tail behind the side-hull, and (c) kind of local islands formed where main-hull diverging transom wave is reached by the ones caused by the outriggers. These flow areas are characterized locally by high steepness, with the occurrence of breaking phenomena.

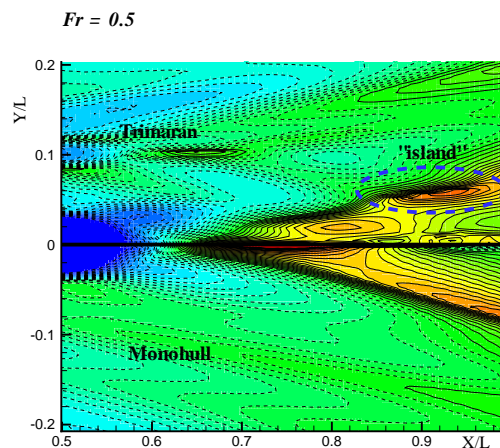


Figure 13: Contour plots of the wave height behind the transom at $Fr = 0.5$.

Similar results are obtained for the $Fr = 0.6$, as shown in figures 14 and 15. The former figure gives both three-dimensional views and contour plots of the wave patterns generated by the mono-hull and

trimaran.

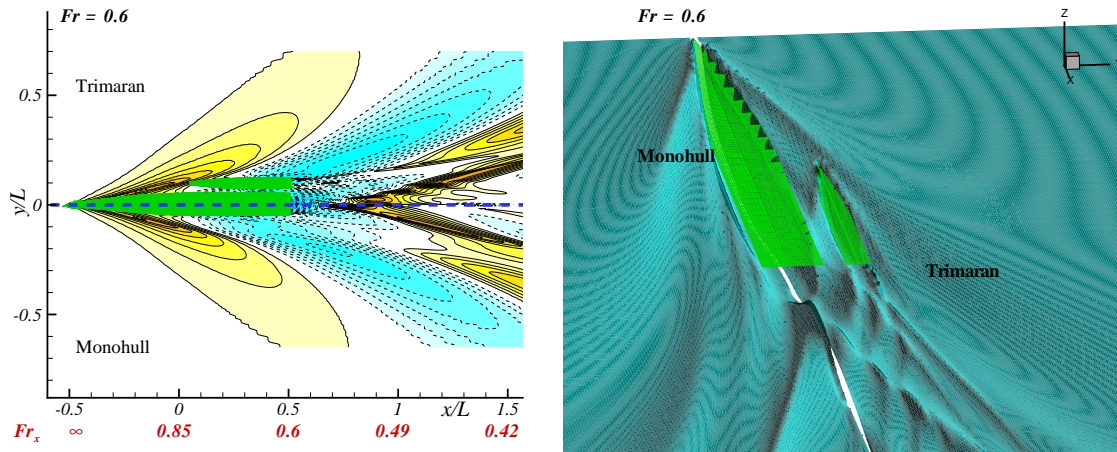


Figure 14: Steady wave pattern of a monohull and of a trimaran at Froude number 0.6. Left: contour plots of the wave height. Right: three-dimensional view.

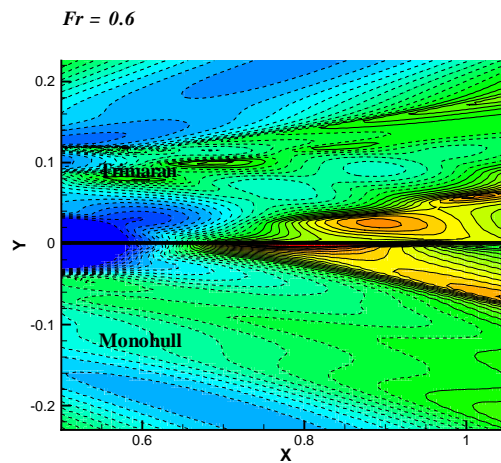


Figure 15: Contour plots of the wave height behind the transom at $Fr = 0.6$.

In this case, beyond $y/L=0.26$ the wave pattern is almost unaffected by the presence of the outriggers. The highest interactions interest the wakes released by the different hulls in the trimaran arrangement. The height of the rooster tail is further reduced with respect to the $Fr = 0.5$ case. So its flow region is not characterized by any breaking phenomenon. The side-hull transom waves develop in a spilling breaker just behind the stern.

Further investigation of the interaction phenomena connected with the trimaran arrangement is presently under development and will be discussed at the conference.

A more detailed analysis of the flow scenario behind the transom stern for several hulls arrangement is given in figure 16. There the longitudinal wave cut obtained through the $2D+t$ theory along the centre-line of the different configuration are shown. The left picture (relatively to the mono-hull) shows that the rooster tail height is not affected by the Froude number while both its horizontal width and the extension of the hollow increase with the speed. The hollow extension can be measured as the longitudinal distance between the transom position and the location where the free surface becomes zero. The wave elevation downstream a catamaran demi-hull transom (see central part of figure 16) shows a quite different behaviour. Except for the smaller speeds, showing an increase of the hollow extension

with the Froude number, the hollow width is not particularly affected by the speed. The rooster tail height is lower than the corresponding value for the mono-hull. It shows a non monotonic but rather limited variation with the Froude number. This demi-hull wave behaviour behind the transom is due to the presence of the other demi-hull. The arrangement of the two demi-hulls causes three rooster tails downstream the catamaran, respectively, in correspondence of the demi-hull transom sterns and of the catamaran centre-line (cf. $2D+t$ contour plots in figures 8). Finally, in the trimaran configuration the hull

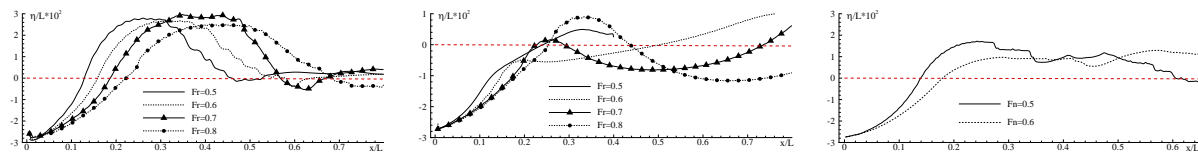


Figure 16: Cut of the steady wave pattern along the centre-line of the demi-hull transom stern. x is the longitudinal distance from the transom. Left: mono-hull, center: catamaran, right: trimaran.

hollow of the main hull resembles the one obtained for the mono-hull. The height of the rooster tail is influenced by the interaction with the side hull. The higher is the Froude number, the lower is the height of the rooster tail. The interaction continues downstream with a wavy profile.

It is important to understand if the main responsible mechanisms are connected with the hydrodynamic interaction between the demi-hulls or if they are related to the demi-hulls interference only. The latter means the diffraction caused by one demi-hull on the waves generated by the other demi-hull is negligible and the catamaran wave pattern is just given by the sum of the wave fields produced by each demi-hull as if the other was not there. In LUGNI *et al*, 2004 it has been evidenced that the interference is not the governing mechanism. The interaction between the two demi-hulls plays a fundamental role. This interaction is mainly nonlinear as evidenced both by difficulties of the linear solution in capturing the first peak and by the phase shifting existing between the linear and nonlinear results accounting for the demi-hull interaction.

As previously discussed, the $2D+t$ model enforces a dry transom stern condition independently from the forward speed. In reality the flow at the transom stern can be quite complicated at sufficiently small Froude numbers, involving partial or full ventilation phenomena. A detailed discussion of this phenomena can be found in LUGNI *et al*, 2004.

CONCLUSIONS

The steady wave pattern around semi-displacement mono-hulls, catamarans and trimarans has been investigated numerically by using a nonlinear $2D+t$ method. In particular the cases relatively to the mono-hull and catamaran have been studied also through a linear $3D$ RPM code. For these ones, a dedicated experimental activity has been performed and the measurements have been compared with the numerical results. The mono-hull model has been shaped identically to a catamaran demi-hull to investigate the interaction between the demi-hulls of the catamaran and the related influence on the rooster tail developing from the transom stern. The physical investigation was focused on the wave-field features at the bow, along the hull, in the area between the two catamaran demi-hull, and downstream the transom stern. The influence of the Froude number has been analyzed in a wide range. For the mono-hull and the catamaran, the $3D$ RPM simulations are able to capture the wave pattern along the hull to handle the stern and wake flows by adopting a *false body* in case the transom is dry. At $Fr \geq 0.6$ the nonlinearities become relevant and the linear method can fail in modeling some details of the flow. The opposite trend is shown by the $2D+t$ results. These are not satisfactory at the smaller Froude due to the relevance of the transverse wave pattern. For Fr greater than 0.6 they fit well with the experiments. The stern and wake flows are properly described since a dry transom condition is enforced. For the catamaran, the same trend is observed but the $2D+t$ theory gives globally the best agreement at smaller speeds than for the mono-hull. For both

geometries this model predicts a wide extension of the lobes near the bow region. This is not observed in the measurements. The $2D+t$ model has been used to investigate the physical mechanisms causing the flow features downstream the transom, and to quantify the related influence of the interaction between the catamaran demi-hulls.

The comparison between the numerical and experimental data has shown the reliability of the $2D+t$ results and suggested the use of such model also for the trimaran configuration. In this case the main-hull has been assumed identical to the mono-hull tested in the experiments and the effect of the outriggers on the evolution of the stern waves has been investigated.

Future work will be focused on the experimental study of the trimaran configuration. The experimental data will be used for a better understanding of the physical phenomena. The trim and sinkage measured in the physical model will be used for the numerical simulations, as already done for the catamaran. It is likely that the introduction of this parameters will deeply influence the evolution of the waves interactions between the hulls and behind the stern. Seakeeping tests will be performed to evaluate the influence of the incident wave on the mean trim and sinkage.

As done for the catamaran, the trimaran configuration will be studied also through a linear three-dimensional Rankine Panel Method. A dedicated error analysis of the tests has been performed confirming a general reliability of the measurements.

ACKNOWLEDGEMENTS

Present research activity is partially supported by the Centre for Ships and Ocean Structures, NTNU, Trondheim, within the *Green Water Events and Related Structural Loads project*, and partially done within the framework of the *Programma di Ricerca sulla Sicurezza* funded by *Ministero Infrastrutture e Trasporti*.

References

- BERTRAM, V. (1990). *Fulfilling Open-Boundary and Radiation Condition in Free-Surface Problems Using Rankine Sources*. Ship Technology Research 37(2).
- DOCTORS, L. J. (2003). *Hydrodynamics of the flow behind a transom stern*. In Hydrodynamics of the flow behind a transom stern, Haifa, Israel, pp. 1–11.
- DOCTORS, L. J. AND A. H. DAY (1997). *Resistance prediction for transom-stern vessels*. In Resistance prediction for transom-stern vessels, Volume 2, Sydney, Australia, pp. 743–750.
- FALTINSEN, O. M. (1977). *Numerical solutions of transient nonlinear free-surface motion outside or inside moving bodies*. In Numerical solutions of transient nonlinear free-surface motion outside or inside moving bodies.
- FALTINSEN, O. M. (1990). *Sea loads on ships and offshore structures*. Cambridge, England: Cambridge University Press.
- FALTINSEN, O. M. (2000). *Sea loads on High Speed Marine Vehicles*. Trondheim, Norway: NTNU.
- FALTINSEN, O. M. (2001). *Steady and vertical dynamic behaviour of prismatic planing hulls*. In Steady and vertical dynamic behaviour of prismatic planing hulls, Varna, Bulgaria.
- FALTINSEN, O. M. AND R. ZHAO (1991). *Numerical predictions of ship motions at high forward speed*. Phil. Trans. R. Soc. Lond. A Vol. 334, pp. 241–252.
- FONTAINE, E., O. M. FALTINSEN, AND R. COINTE (2000). *New insight into the generation of ship bow waves*. J. Fluid Mech. Vol. 421, pp. 15–38.

- GRECO, M., O. M. FALTINSEN, AND M. LANDRINI (2002). *Water Shipping on a Vessel in Head Waves*. In *Water shipping on a vessel in head waves*, Fukuoka, Japan, pp. 1–14.
- HESS, J. L. AND A. M. O. SMITH (1996). *Calculation of non-lifting potential flow about arbitrary bodies*. *Prog. Aero. Sci. Vol. 8*, pp. 1–138.
- KEUNING, J. A. (1988). *Distribution of added mass and damping along the length of a ship model at high forward speed*. Technical report, Report No. 817-P, Delft University of Technology: Ship Hydrodynamics Laboratory.
- LANDRINI, M., A. COLAGROSSI, AND M. P. TULIN (2001). *Breaking bow and transom waves: numerical simulations*. In *Breaking bow and transom waves: numerical simulations*, Hiroshima, Japan.
- LONGUETT-HIGGINS, M. S. AND E. D. COKELET (1976). *The deformation of steep surface waves on water. I A numerical method of computation*. In *The deformation of steep surface waves on water. i a numerical method of computation*, Volume 350, pp. 1–26.
- LUGNI, C., A. COLAGROSSI, M. LANDRINI, AND O. M. FALTINSEN (2004). *Experimental and numerical study of semi-displacement mono-hull and catamaran in calm water and incident waves*. In *Experimental and numerical study of semi-displacement mono-hull and catamaran in calm water and incident waves*, St. John's, Canada, pp. 104–119.
- MARUO, H. AND W. SONG (1994). *Nonlinear analysis of bow wave breaking and deck wetness of a high speed ship by the parabolic approximation*. In *Nonlinear analysis of bow wave breaking and deck wetness of a high speed ship by the parabolic approximation*. National Academy Press.
- MICHELL, J. H. (1898). *The wave resistance of a ship*. *Philosophical Magazine Vol. 45*, pp. 106–123.
- MIGALI, A., S. MIRANDA, AND C. PENSA (2001). *Experimetal study on the efficiency of trimaran configuration for high speed very large ships*. In *Experimetal study on the efficiency of trimaran configuration for high speed very large ships*, Southampton, UK.
- MOLLAND, A. F., J. F. WELLCOME, AND P. R. COUSER (1994, September). *Theoretical prediction of the wave resistance of slender hull forms in catamaran configurations*. Technical report, Report No. 72, Southampton University: Ship Science.
- MOLLAND, A. F., J. F. WELLCOME, AND P. R. COUSER (1995). *Resistance experiments on a systematic sense of high speed displcement hull forms: Variation of length-displacement ratio and breadth-draught ratio*. The Royal Institution of Naval Architects.
- NAKOS, D. E. (1990). *Ship Wave Patterns and Motions by a Three Dimensional Rankine Panel Method*. Ph. D. thesis, MIT, Cambridge.
- OGILVIE, T. F. (1967). *Nonlinear high-Froude-number free surface problems*. *J. of Engineering Mathematics 1(3)*, pp. 215–235.
- OHKUSU, M. AND O. M. FALTINSEN (1990). *Prediction of radiation forces on a catamaran at high froude number*. In *Prediction of radiation forces on a catamaran at high froude number*, Washington D.C., USA, pp. 5–20. National Academy Press.
- OHKUSU, M. AND O. M. FALTINSEN (1991). *Prediction of radiation forces on a catamaran at high froude number*. In *Prediction of radiation forces on a catamaran at high froude number*, Washington D.C., USA, pp. 5–20. National Academy Press.
- ZHAO, R. AND O. M. FALTINSEN (1993). *Water entry of two-dimensional bodies*. *J. Fluid Mech. Vol. 243*, pp. 593–612.



**5th INTERNATIONAL CONFERENCE
ON HIGH-PERFORMANCE MARINE VEHICLES**

Launceston, Tasmania, Australia 8 -10 November 2006
www.amc.edu.au/hiper06

The 5th International Conference HIPER'06 presents an unique opportunity to present and discuss developments in design, construction and operation of high-performance marine vehicles in the island state of Tasmania, which is also home to the first ever high-speed wave-piercing catamaran built in Australia.

As in previous years this forum provides a prestigious platform to present and discuss research findings in several areas of interest to academics, scholars, practicing naval architects, high-speed craft builders as well as transporters.

This is the first announcement being made for submission of abstracts on all aspects of the development, design, construction and operation of high-performance marine vehicles.

The HIPER'06 will be the first to be organised in the Asia-Pacific region of the world and will attract the full spectrum of academic, professional and commercial interests of the maritime sector.

Suggested Symposium Topics

- 1. Transport & Economics of Fast Sea Transport*
- 2. Design and Production Technologies*
- 3. Hydrodynamics (Resistance, Seakeeping and Manoeuvring)*
- 4. Safety (Regulations, Comfort)*
- 5. Structures (loads, strength, materials, composites)*
- 6. Propulsion (engine, propellers, water-jets, noise and vibration)*
- 7. Automation and Control Systems*
- 8. Ecological and Environmental Aspects*

An international scientific committee will review the abstracts and papers prior to publication in the bound proceedings. Further details about HIPER'06 will be available on the web in early 2005. In the meantime address all your queries to the convenor of HIPER'06.

Convenor: Dr. Prasanta K Sahoo
Phone +61-(0)3-6335 4822
Fax +61-(0)3-6335 4720
Email P.Sahoo@mte.amc.edu.au

Index by authors

Barone	215	Stella	215
Begovic	68	Tanaka	103
Bertorello	215	Thomas	162
Bertram	5,18,28,83	Tikkos	264
Boccadamo	68	Toderan	129
Boote	304	Tudem	249
Brizzolara	119	Tuzcu	192
Browne	55,229	Vassalos	192
Bruno	277	Viviani	140
Bruzzo	119	Yoshida	44, 103
Cabaj	192		
Chalkias	264		
Colagrossi	323		
Colaiani	304		
Colicchio	323		
Constantinescu	83		
Datla	277		
Davis	162		
El Moctar	5		
Fach	295, 317		
Faltinsen	323		
Figari	140		
Frouws	235		
Fullerton	277		
Grigoropoulos	264		
Hearn	177		
Holloway	162		
Huijs	235		
Jensen	95		
Junalik	5		
Kihara	200		
Klemt	95		
Konovessis	192		
Liljenberg	249		
Lindenau	95, 152		
Lopez	229		
Luca	229		
Lugni	323		
Mesbahi	18		
Neme	83		
Nusser	5		
Paik	129		
Pawlowski	192		
Pino	304		
Richir	129		
Rigo	129		
Roberts	162		
Rogowski	277		
Sadathosseini	287		
Sahoo	55,229		
Salas	55,229		
Saydan	177		
Seif	28, 287		